Process Mapping and Optimal Process Window Identification for Laser Powder Bed Fusion of Invar36

by

Thanh Ma

A thesis
presented to the University of Waterloo
in fulfillment of the
thesis requirement for the degree of
Masters of Applied Science
in
Mechanical and Mechatronics Engineering

Waterloo, Ontario, Canada, 2018

AUTHOR'S DECLARATION

I hereby declare that I am the sole author of this thesis. This is a true copy of the thesis, including any required final revisions, as accepted by my examiners.

I understand that my thesis may be made electronically available to the public.

Abstract

The development of Additive Manufacturing (AM) has reached a point where it is positioned to be disruptive for the manufacturing sector, with a majority of manufacturers having leveraged the use of AM in their operations. Laser powder bed fusion (LPBF) is one subclass of AM in particular that has seen tremendous growth and adoption in the past decade. This is due to the increased needs for customized metallic parts and the demand for light-weighting and performance optimization. However, the adoption of LPBF (and in extension, AM) is challenging because of numerous issues that affect the quality of LPBF-built parts, where the complex interactions between parameters make it difficult to predict part quality behaviour. To ensure low risk of deployment of this technology, progress still needs to be made in the design of strategies for process window identification of new materials, of process predictive tools, and of process control strategies to ensure process stability and traceability.

Within this work, the optimization of LPBF-built parts is performed for a novel material for LPBF, such that it may be possible to garner new insights into process development for future material adoption in the AM space. The material in question is Invar36, which is an iron-nickel alloy that is known for its low thermal expansion behaviour, and it is used in applications that require such dimensional stability over a temperature range. Its applications include metrology, cryogenic storage, and precision mounting applications. However, the material is known to have challenges with manufacturability. The material has a tendency to crack during solidification and reheating, and its high nickel content results in unfavorable work hardening characteristics that increase machining costs. Through the use of LPBF and its unique capabilities, it may be possible to sidestep the manufacturing difficulties of the material, and potentially further improve on the material's uses by reducing costs through optimized design strategies.

The work performed within uses a gas-atomized blend of Invar36 powder. After characterization, the powder was found to conform to the particle size distribution, as specified by the manufacturer and defined by ASTM standards. It is also found that the powder size distribution adhered to a bimodal distribution with centers about 27 μm and 40 μm. The rheology of the powder was also examined, with overall observations suggesting that the material displays good flowability behaviour.

The experimentation work was split into two separate experiments. The first experiment was structured to develop a process map and then identify an optimal process window for the LPBF of

Invar36 that could characterize the performance of the material on the following process outcomes: density, and thermal expansion. The parameters of focus within this experiment were chosen such that they directly affect the energy input within the material. These parameters are laser power, point and hatch distance, and laser exposure time. Techniques used for this experiment included detailed pore space analysis through computed tomography (CT) and thermal expansion measurements through thermomechanical analysis (TMA). The experiments were created using factorial design metholodology and were analyzed using statistical techniques.

From the results, it was found that the material tended towards optimal solid fraction at lower power levels (250 W), larger point and hatch distances (80 μm), and lesser exposure times (60 μs), with the best performing parts reaching ≈99.92% solid fraction. However, upon observation it was found that a large number of pores within the samples were biased towards the border region of samples, and appeared to be affected by parameters that were uncontrolled in the first experiment. Re-analysis of the results without these uncontrolled areas showed that, within the core regions, optimal samples had solid fractions of 99.99% once a minimal power threshold was met (>250 W). In terms of thermal expansion, the material was found to have ideally low thermal expansion at lower energy density ranges, and as a whole, all parts performed better than conventional Invar36.

The second experiment focused on eliminating the pores created at the border regions. From observations, it was found that parameters such as power, border power, fill contour offset, and hatch compensation are significant parameters in the aforementioned regions. CT analysis was once again employed in this experiment, and parts were fabricated adhering to a factorial design.

As a result, it was found that the general trend for low porosity parts had low power (275 W), low border power (250 W), low fill contour offsets (50%), and low hatch compensations (25%). The improvement on the solid fraction in the overall part increased to 99.99%. When considering only the border regions, the majority of pores were eliminated, with the border solid fraction increasing to up to 99.94%. However, one difficulty during analysis is that the errors were not normally distributed; and thus, the results presented for this chapter may not have been entirely representative of the complexity of the process and process parameter interactions at the border of the parts.

As a final study, a numerical modelling approach that was taken to investigate the possibility of using simulations to predict part quality behaviour (through melt pool analysis) of Invar36 parts. The results show that the model under-predicts the melt depth, and is most likely due to the approximations made within the model.

Acknowledgements

I would first like to express my sincerest gratitude to my supervisor, Dr. Mihaela Vlasea, for her enthusiasm and guidance along the way. Even through her busy schedule, she has always found time to assist her students however she can. Without her continued support, I could not have developed my abilities to the point they are at today.

I would like to thank the backing and expertise by Dr. Adeola D. Olubamiji and Burloak Technologies for their extensive support of our team and their technical mentorship throughout the course of this work.

I am very grateful to Dr. Hamed Asgari Moslehabadi and Dr. Ehsan Marzbanrad for their help and commitment with the chemical composition analyses and all microscopy work within this thesis, especially knowing that an arduous amount of time was required to prepare and analyze the samples.

I would like to extend my appreciation to Mike George and Dr. Mehrnaz Salarian for their tutelage with computed tomography. I have learned a great deal from them and I greatly appreciate the time they made for me from their busy schedules.

I would also like to acknowledge Dr. Geoffrey Rivers from the University of Waterloo Advanced Composites and Adhesives Thermal Analysis Laboratory for the training, the provided system time, and his guidance during the thermomechanical analysis of my many samples. Without his assistance, I could not have prepared my data in time.

As well, I would like to thank Kelly Huang for her help with gathering all of the powder size distribution and rheology results.

I would particularly like to thank Dr. Allan Rogalsky and Evan Wheat for all of their words of advice throughout the course of my thesis. Within all stages of this work and whenever I was caught in the unknown, their expertise has helped guide me and my work to completion.

I wish to thank all of my friends and family for their unrelenting support and encouragement throughout my degree. I would not have been able to make it out the door without you all by my side.

Lastly, this work could not have been performed without sponsorship and funding from the Federal Economic Development Agency for Southern Ontario, in partnership with Burloak Technologies, and I am grateful for the opportunity that this has given me.

Table of Contents

List of Figures

xiii

xvi

List of Tables

List of Abbreviations

AM	Additive Manufacturing
ANOVA	Analysis of Variance
BCC	Body-Centered Cubic
BFE	Basic Flowability Energy
BPP	Beam Parameter Product
CAD	Computer-Aided Design
CBD	Conditioned Bulk Density
CT	Computed Tomography
CTE	Coefficient of Thermal Expansion
DMLS	Direct Metal Laser Sintering
DOE	Design of Experiments
EBM	Electron Beam Melting
FCC	Face-Centered Cubic
FRI	Flow Rate Index
GE	General Electric
ICP-AES	Inductively Coupled Plasma Atomic Emission Spectroscopy
LPBF	Laser Powder Bed Fusion
ODE	Ordinary Differential Equation
PBF	Powder Bed Fusion
PREP	Plasma Rotating Electrode Process
SE	Specific Energy
SEM	Scanning Electron Microscopy
SLM	Selective Laser Melting
SLS	Selective Laser Sintering
TD	Tap Density
TMA	Thermomechanical Analysis
WATLab	Waterloo Advanced Materials Laboratory

Chapter 1 Introduction

Additive Manufacturing (AM) is a technology that has seen tremendous growth since its inception, and it is poised towards disruption in the manufacturing sector. Based on the AM corporate annual industry growth in 2016, the AM industry grew by 17.4% to $6.063 billion, with reports indicating that more than 70% of manufacturers have adopted or leveraged AM processes in their operations [1]. The underpinning cause of this paradigm shift can be understood by the core operating principle behind all AM processes, which is the "process of joining materials to make parts from [three-dimensional] model data, usually layer upon layer, as opposed to subtractive manufacturing and formative manufacturing methodologies" [2]. From this definition, it is clear to see why the technology is so alluring. Within today's competitive economy, a product's success can be dictated by even the minutest of details. For example, the launching of a product before a competitor or the improvement of a product's efficiency can position a company to secure valuable market share. AM can cater to this environment by reducing the steps required in the design-to-manufacturing cycle. During the prototyping stage, AM offers the ability to quickly shift from design to fabrication, possibly within a single step. The resulting prototypes give engineers important visual and tactile indicators to more effectively improve on the design iterations of their products. Moreover, the AM process and its layer-by-layer approach can also offer significant savings associated with material usage, since unused material during the process can be re-used for future builds. Arguably, the most important and unique advantage of AM is that it is conceivable to fabricate complex geometries unachievable by more conventional methods—such as casting, forming, or machining. This allows engineers to design more efficient geometries or system configurations. Companies like General Electric (GE) are already leveraging the advantages of AM in their designs. For example, before utilizing AM, GE was manufacturing jet engine fuel nozzles that had extraordinarily complex interiors, which required over 20 distinct parts that had to be welded and brazed together [3]. After optimization for AM, GE was able to print a fuel nozzle that limited the assembly into a single component, with a weight reduction of 25% and a fivefold durability increase [3]. Moreover, the company continued its endeavors with AM and was able to consolidate the components in its advanced turboprop engine from 855 to a dozen parts, reduce the engines weight, increase fuel efficiency by 25%, and give the engine 10% more power [4]. The mentioned parts by GE were created using a rapidly growing subcategory of AM known as powder bed fusion.

Powder bed fusion (PBF) is an AM technology that involves the solidification of powder laid upon a substrate into solid material. When the solidification is performed using a laser through thermal interaction, the technology is known as laser powder bed fusion (LPBF). LPBF was first developed at

the University of Texas in the 1980s, and at the time it was referred to as selective laser sintering (SLS) [5]. Since then, many similar technologies have arisen, such as selective laser melting (SLM), which uses more powerful lasers than SLS, and electron beam melting (EBM), which uses an electron beam instead of a laser as the heat source. However, all PBF systems function using the same fundamental principles; layers of powder are spread across a build bed and are then fused together, typically with a focused beam of electromagnetic radiation. As well, a method of controlling the location of melting regions is employed based on a raster pattern generated from input three-dimensional (3D) computer-aided design (CAD) models. Although polymer based AM technologies have been dominating the market, metal AM technologies such as LPBF have seen tremendous growth within the past decade. In 2017 alone, the metal AM sector grew by 79.8% with the sales of over 1768 systems compared to 983 in 2016 [6]. A key driver for the growth in the metal AM space is with the aerospace and automotive industry. With the increased need of customized metallic parts, as well as the demand for light-weighting and performance optimization, metal AM provides the necessary tools to fill the gap in the industry. Even with the positive sentiment towards LPBF (and AM, in general) there is still a lot of progress to be made before the technology can be widely accepted in the industry.

Even with the unique advantages that AM provides, there are many challenges with finding optimal process parameters and with designing for AM. Although AM can theoretically offer increased design complexity and flexibility, there are currently many factors that must be taken into account when designing complex shapes and optimizing the process parameters for AM to ensure manufacturability. For LPBF processes in particular, the part orientation and layout play an important role in overall part quality and material properties. As well, overhanging features often need sacrificial support structures to prevent failure during fabrication. This is because the absorption and dissipation of energy varies between powder and solid substrate. Interior channels and chambers within parts must also consider the method for removal of unprocessed material and internal support structures from the final solidified part. For LPBF processes, there may be hundreds of other material and process considerations that play a role in the final part quality [7]. Because of this, significant time and financial investment may be required before a feasible design, coupled with a set of ideal process parameters, can be considered production-ready. In general, LPBF-built part quality is often inhibited by failures to meet dimensional tolerances, high surface roughness, internal defects, and anisotropy in compositional and mechanical properties [8], [9]. Presently, there are many research and industrial efforts to enhance the understanding behind the complex laser-material interaction of LPBF processes

2

in order to quickly iterate and identify process windows and designs that can leverage the benefits of AM while maximizing part performance. Without significant headway in the understanding of the LPBF process, adoption in the industry may be hindered. For example, when considering the case of AM technology adoption for GE, it required over a decade of engineering before a suitable product was achieved [3]. Part of the difficulty with producing components for LPBF is with the different scales of phenomena that occur during processing. Parts designs are manufactured over time frames that span hours/days, in a layer-by-layer fashion, with materials experiencing cyclic thermal loading with each manufactured layer. On the other hand, the laser interaction time, the melt pool formation, and the laser speed occur in orders of magnitude between $10\ \mu s - 100\ \mu s$, $10\ \mu m - 100\ \mu m$, and ≈ 1 m/s ranges, respectively [7]. Depending on the material used and the design employed, the multi-physics phenomena, combined with the disparity in scale, make it difficult to accurately predict part quality behavior [7]. Due to this, there have been challenges with the identification of process windows and the development of robust design-specific process window optimization strategies, ultimately resulting in a limited portfolio of established materials for LPBF AM [10].

1.1 Problem Statement

Laser powder bed fusion is a technology that will be a major disruptor in the industry, however adoption of this technology has been challenging due to the numerous issues that affect part quality. This is because of the large number of parameters that may affect the final outcome of the process. As well, the complex interactions between these parameters make it difficult to predict part behaviour. As a result, the manufacturing design cycle and optimized process parameter development requires iterative empirical manufacturing runs. For this technology to be more successful, significant progress must be made in the development of strategies for process window identification for new materials, process predictive tools, and process control strategies to ensure process stability and traceability.

1.2 Motivation and Objective

The motivation for this thesis is to lower the barrier for adoption of LPBF, by applying a strategy for process mapping and process window identification based on part quality characteristics. This strategy is deployed for a novel LPBF material. In this context, the material of interest is an iron-nickel alloy, Invar36. This material is known for having a low coefficient of thermal expansion, with a direct application in aerospace industries. Since this material has challenges in terms of machinability, the selection of this material for LPBF makes it possible to highlight the capabilities of

LPBF, and garner new insights into process development for future material adoption in the AM space. In terms of the objective, this work aims to look at optimizing AM-built parts in process regions that obtain part quality that are near to conventionally-built parts. Through the use of comprehensive microcomputed tomography, thermomechanical analysis (TMA), and statistical design techniques, the goal is to reveal details of the process at a more refined level.

1.3 Thesis Outline

The scope of work discussed in this thesis highlights several different areas of the research.

Chapter 2 discusses relevant background on the pertinent aspects of the LPBF process, relevant material characteristics, and theory required to understand the research material. Topics within this chapter include a thorough review of the LPBF process, Invar36, previous work of AM on Invar36, and of the application of statistical design of experiments for AM. Chapter 3 describes work investigating the characterization of Invar36 powder, with analysis into chemical composition using inductively coupled plasma atomic emission spectroscopy (ICP-AES), particle size analysis through optical imaging, particle morphology observations through scanning electron microscopy (SEM), and powder rheology characteristics. Chapter 4 describes the manufacturing plan, design of experiments (DOE), and analysis of part characteristics, with a focus on developing a process map and optimal process window for process parameters that maximize the performance of manufactured artefacts. Within this chapter, the effects of input process parameter variation on density and thermal expansion were established using statistical analysis techniques, and the overall part performance was found using a weighted decision-making model. In Chapter 5, an appropriate process window is identified from the process map developed in Chapter 4, with a shifted focus on process parameters for features nearby and at the border region of samples. In this chapter, the parameter of focus is only on the part density. To investigate the potential for process validation and part quality prediction purposes, a finite element modelling approach was developed and discussed in Chapter 6. The model is intended to reduce the number of empirical tests to construct a process map and narrow-down a process window of interest. 0 provides concluding remarks and recommendations for future work.

Chapter 2

Background

Within this chapter, an overview of the laser powder bed fusion process will be discussed, including critical design considerations concerning the system, the material, the build setup, and the process parameters. Background information discussing the history, the material properties, and the potential applications of Invar36 (the material of focus) for LPBF is also presented. This chapter continues with the demonstration of the analysis techniques used within this work, and through the introduction of these concepts, the goal of this chapter is to provide a comprehensive summary to supplement understanding of this work. To conclude, this chapter introduces relevant terminology and definitions for LPBF process optimization that will be useful in describing the experimental methods and results within this work. These terms have been defined previously by Evan Wheat (Research Associate, Multi-Scale Additive Manufacturing Lab) as standard nomenclature to be used for the group.

2.1 Laser Powder Bed Fusion

The origins of laser powder bed fusion (LPBF) began in the 1980s at the University of Texas in Austin, USA, where the first system was developed and named as selective laser sintering (SLS) for its ability to induce sintering of powders through laser-material interaction [5]. Since then, many LPBF technologies have been developed, such as selective laser melting (SLM), laser cusing, and direct metal laser sintering (DMLS) [5]. Although each of these technologies has its own variation on the LPBF process, they function using the same core methodology, as described in Figure 1.
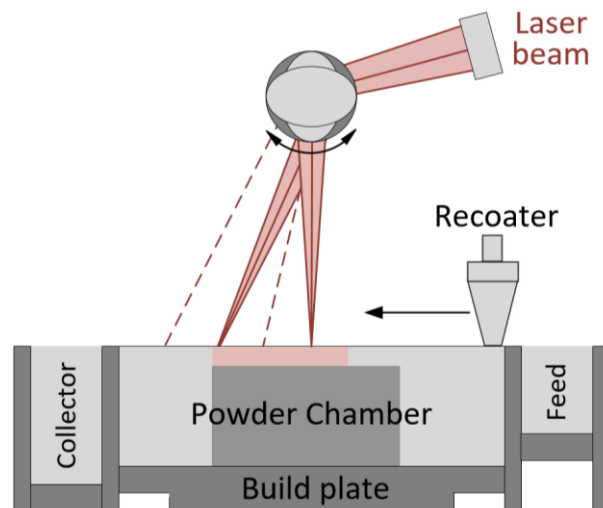
Figure 1. Generic layout for describing core functionalities of LPBF systems.

As with all AM processes, the first step involves the translation of 3D CAD data to a file format that can be understood by the AM machine. The models are first oriented in a space that parallels their ensuing physical location within the build volume of the machine. Depending on the location and orientation, support features may be required to provide structural integrity and serve as heat dissipaters for overhanging features or free-floating parts. Afterwards, a build file is created that describes the laser scan path characteristics, layer thickness, and other manufacturing details based on the selected machine capabilities and design features of the part. To facilitate the layer-by-layer manufacturing approach, the build file is discretized along the part height in increments equal to the thickness of each printed layer. The data is then exported and transferred to the AM machine, where a build file interpreter and execution engine are deployed using industrial controllers. Before executing a build, powder material needs to be supplied to the build volume using a powder feed system. Figure 1 shows a piston-based feed system that raises to provide material; however, additional technologies such as gravity-fed hopper systems exist as well. Currently, the market is split 64% for piston-based systems (EOS, Concept Laser, 3D Systems), 34% for hopper based systems (Arcam, Renishaw, Realizer), and the remaining 2% for other system types [11]. The supplied powder is carried from the feed bed to the build bed powder chamber using a recoater system. The recoater often takes the form of a blade or roller. Excess material from the build bed powder chamber is carried off to a collection system for material recycling. Resting at the bottom of the build bed powder chamber is a build plate, which serves as the structural foundation for the build as well as a heat sink during thermal processing. To provide height clearance for additional powder layers, the build plate is able to translate in the vertical direction. The material is melted at select locations by a laser beam that is directed by a system of optical lenses. The process of layer spreading and selective laser melting is repeated until the entire build is completed. Although the principles described here appear simple, the process parameter selection and design considerations for LPBF are complex and multifaceted.

2.1.1 Manufacturing and Design Considerations for LPBF

Process parameter selection and optimal design for LPBF is challenging due to the many machine and process specific factors that must be taken into account. These factors include, but are not limited to, the physical differences between LPBF technologies, the size distribution, morphology, and rheology of powder feedstock, the multitude of processing parameters, the geometry of parts and their spatial orientation in a build, and lastly, the post-processing considerations.

2.1.1.1 System considerations

Several of the most important system considerations, as relevant to this thesis, are described below. In this work, a commercial LPBF system from Renishaw is used, and all of its relevant specifications pertaining to this section can be found in section 2.1.2.

Recoater: The choice of material and method for the recoater has been shown to be noteworthy. If there are layer fabrication defects resulting in raised features in the build bed, a recoater blade may impact those features, resulting in powder re-coating damage, part quality issues, or the dislodging of the underlying part. These defects can potentially propagate through subsequent layers. On the contrary, a roller-based recoater, may roll over raised features without damaging them [12]. Additionally, a roller based recoater has the advantage of providing powder compaction, with the disadvantage of being more complex than blade systems due to the number of moving parts. A soft polymeric recoater blade is often deployed in machines, as it is less sensitive to underlying surface irregularities and may prevent recoater or part damage when striking raised edges, but may not spread powder layers as consistently [13].

Feed system: There are differing types of feed systems for LPBF, such as with raised platform systems or gravity-fed hopper systems [11]. Compared to the former, hopper systems provide the advantage of being able to hold large volumes of material, to quickly supply the material, and to isolate materials in a controlled gas atmosphere. In some systems, the hopper is connected with a powder re-circulation circuit, capable of recovering powders from the build zone. However, with hopper systems the rheological characteristics of the feedstock powder are of critical importance, since the powder is gravity-driven and resistances in flow will interrupt ideal hopper behaviour. In particular, effects such as internal vibrations in the equipment, hopper temperature, humidity, electrostatic charge buildup, particle aeration, and container surface effects have been shown to influence the consistency of powder flow through hopper systems [14]. Thus, careful consideration must be given to powder characteristics to ensure a uniform and continuous hopper flow regime.

Build Plate: When selecting a build plate, the material and its thickness must be taken into account. Using separate materials for the build plate and specimen has benefits for post-processing. For example, when using a Stainless Steel 304 build plate for Ti-6Al-4V parts, the brittle interface created between the part and substrate facilitates the ease of part removal [15]. However, the use of different materials also means that there is a difference in coefficients of thermal expansion, which causes interfacial stress from unequal shrinkage rates [16]. Ultimately this may cause warping or

7

delamination due to thermal residual stress development during solidification [16], [17]. To counter-act warping of the build plate, increasing the thickness can offer further structural integrity. Other considerations within literature include the use of rougher build plate surfaces to increase first layer densification and adhesion, vibrating build plates to increase powder compaction, and heated build beds to reduce thermal shock [14].

Powder Collection and Re-circulation: Many commercial machines employ the usage of recirculation systems to capture unused powder for future prints. Although reusing material can potentially reduce costs, there are several factors that must be taken into account with their repeated material use. Upon layer spreading, for example, particles that are larger than the layer thickness or powders that are agglomerated do not get distributed within the build area and are pushed away for re-use. Because of this, it has been found that over repeated builds, the distribution of particle size becomes more shifted towards larger particle sizes [18]. Also, re-used powders become less spherical with increased usage cycles, possibly due to the compounding presence of partially melted powder or powder satellites from processing [19]. Lastly, some materials suffer surface chemical composition changes with re-use. For example, with titanium, the powder may encounters embrittlement issues due to increases in oxygen absorbed in the material during processing [19].

Laser: The use of lasers is ubiquitous in powder bed fusion processes, due to the ability of lasers to deliver energy in a focused area with precision and high intensity. This ability is derived from the spatial coherence of laser radiation, which allows lasers to be focused into high resolution beams that can be propagated over long distances. Specifications such as the laser wavelength, intensity, efficiency, the operating mode, and the beam shape, quality, and focused spot size are all important parameters for the LPBF process, however many of these are machine dependent and cannot be controlled for a process. For reference, a full review of these parameters and their effects can be found in [20], while in this work, only several critical aspects will be discussed.

One of the most important factors to consider for a laser for LPBF is the operating wavelength. The reason for this is because materials interact differently to varying laser wavelengths. As a comparison, Figure 2 shows the absorptivity of various materials as a function of wavelength. For efficiency, higher absorptivity is desired for LPBF, since less input energy would be required to melt the material. Within AM, there are different types lasers used for LPBF, with the most notable being CO_2 gas lasers, neodymium-doped yttrium aluminum garnet (Nd:YAG) lasers, and ytterbium-doped (Yb-doped) fiber lasers [20]. Table 1 shows the lasers used for LPBF and their representative specifi-

cations. CO_2 lasers can potentially achieve high output powers, but have issues maintaining stable power output, and this is because pumping energy into a large volume of CO_2 gas results in turbulence that causes volume fluctuations in the laser system [21]–[23]. As well, their higher operational wavelengths are not well absorbed by some materials (Figure 2). Nd:YAG lasers operate at a much lower wavelength than CO_2 lasers, and can thus be used for a wider range of materials because of higher laser absorption. Additionally, the lower wavelength operation allows Nd:YAG lasers the ability to be delivered through optical fibers, and this makes it possible to have more compact and efficient systems than CO_2 lasers [23]. However, when pumping Nd:YAG lasers using xenon lamps, they are known to have low power efficiency due to thermal losses, and the resulting thermal effects negatively influence beam quality [24]. The usage of diode-pumped lasers has since been used to mitigate these disadvantages [25], [26]. Recently, Yb-fiber lasers have been replacing Nd:YAG lasers in additive manufacturing due to their high efficiency and compactness [20].
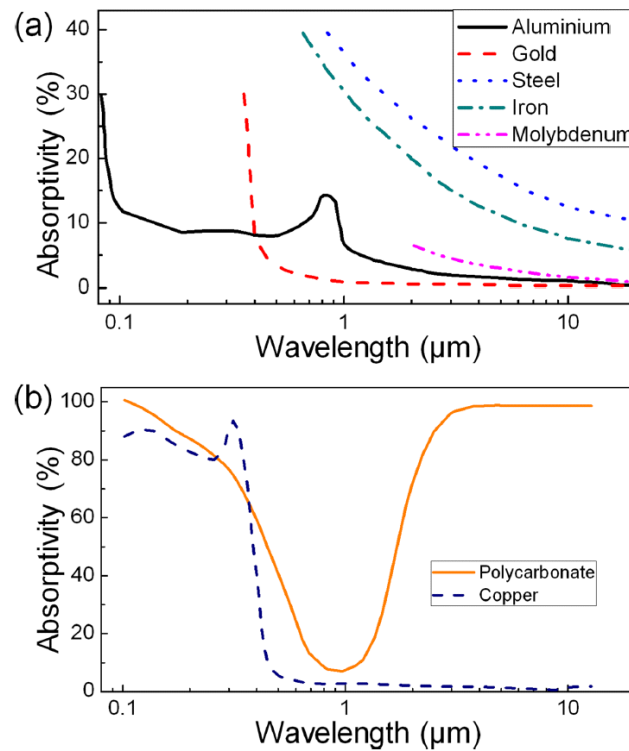
Figure 2. Wavelength dependency of absorptivity for (a) various metal and (b) polycarbonate and copper [20], [27], [28].

The amount of power is also another critical factor to consider for lasers, as it quantifies the energy output delivered by the laser. All materials must be excited to a certain energy threshold before they

can be melted and fused, and higher laser powers allow this threshold to be met quicker. However, it should be noted that with higher energy inputs, obtaining high feature resolution becomes an issue. This is because the input energy may penetrate deeper and melt more material than expected. The role of laser power as a processing parameter is further discussed in section 2.1.1.3.

Table 1. Representative specifications of laser types in laser powder bed fusion [20].

Laser Type	CO_2	Nd:YAG	Yb-fiber
Operation wavelength	9.4 & 10.6 μm	1.06 μm	1.07 μm
Efficiency	5 – 20%	Lamp pump: 1– 3% Diode pump: 10 – 20%	10 – 30%
Output power (continuous-wave mode)	≤20 kW	≤15 kW	≤10 kW
Pump source	Electric discharge	Flashlamp or laser diode	Laser diode
Operation mode	Continuous-wave or pulsed		
Pulse duration (order of magnitude)	100 ns – 10 μs	10 ns – 10 ms	10 ns – 10 ms
Beam quality factor (mm· rad)	3 – 5	0.4 – 20	0.3 – 4
Fiber delivery	Not possible	Possible	
Maintenance periods	2, 000 hrs	200 hrs (lamp life) 10, 000 hrs (diode life)	25, 000 hrs

Aside from the power output, a laser's operational mode affects the method of energy delivery and the mode can be classified into two different types: continuous-wave and pulsed emission. Continuous-wave lasers emit their radiation at a constant rate, independent of time, while pulsed emission lasers send discrete packets in repeating intervals. Compared to continuous-wave lasers, pulsed emission lasers offer the benefit of increased process control with the ability to exactly specify the location and amount of heat input for any particular location within a build [29]. However, due to its intermittent nature, pulsed lasers are prone to generating melt pool instabilities [30]. Depending on the laser technology, the mode of pulsed lasers can also vary [20]. However with current fiber laser technology, pulsed emission is generated through direct power modulation of the laser by controlling the electrical current sent to the pumping diodes [29].

Lastly, the beam quality is an important factor to consider when trying to achieve optimal part precision. The Beam Parameter Product (BPP) is commonly used to measure beam quality and it is

defined as, "the product of beam radius (measured at the beam waist) and the half angle of beam divergence (measured in the far field) with the units of mm·mrad" [20]. Generally, the lowest possible BPP is desired. Another indicator of beam quality is the M^2 factor (beam quality factor), which is the BPP divided by $\frac{\lambda}{\pi}$, where λ represents the wavelength and π is Archimedes' constant. The output of this calculation gives the comparison of the laser beam to a perfect Gaussian beam, where a value of one is generally desired. Depending on the application, smaller spot diameters may be preferred due to the ability to create finer geometric features. Unfortunately, obtaining high quality laser beams is difficult due to disparaging influences in-situ, such as optical surface deformations and gradients in refractive index [20].

Build Chamber Atmospheric Conditions: The use of controlled build atmospheres are vital to the success of the LPBF process, especially because many materials are prone to accelerated oxidizing conditions under high temperatures. To control the atmosphere, inert gas environments are typically used. With many LPBF systems, inert environments consist of either argon or nitrogen, with the gas flowing through the process chamber to reduce oxygen content to a set threshold. As well, the gas is directed to flow immediately above the build surface to ensure melt pool stability by further inhibiting oxidation, by dispersing fumes and ejected particles, and by reducing the size of plasma [15]. The use of a vacuum environment has also been used in other PBF processes, such as Electron Beam Melting, where a vacuum environment is required to maintain electron beam quality [15]. Similarly to inert gas environments, vacuum environments for LPBF reduce the oxygen content and inhibits oxidation, and it also presents the benefit of improving reducing scatter of the laser beam from refractive index transitions [15]. However, vacuum environments also present several difficulties. The use of vacuum environments increase the heat input within the system, and also removes the method of heat removal to the ambient environment. Due to this, melt pool depths and widths are much larger in vacuum environments, which may decrease feature resolution [31]. The amplified heat input also results in increased melt vaporization, which may condensate and damage the optics system [31].

2.1.1.2 Material Considerations

The outcome of a LPBF process is also dependent on the characteristics of the feedstock material. Due to challenges in process window identification, and in development of robust design-specific process window optimization strategies, there is a limited portfolio of established materials for LPBF AM [10]. For reference, Table 2 shows a catalogue of materials available from four different

commercial LPBF system providers; Concept Laser, EOS, Renishaw, and Trumpf. It should be noted that the exact blend and chemical composition of powders vary between suppliers, and that not all suppliers provide the full range of alloys described in Table 2. The reason behind the limited portfolio is because the chemical composition and morphological characteristics of the input powder affect the thermophysical properties, which in turn influences melt pool behaviour and solidification processes [7], [32]. In addition, the blend, morphology, size, and rheological characteristics of the feedstock powder are key influencers as well.

Table 2. List of available powders from several representative LPBF suppliers [33]–[36].

Type of Material
Variety of CrCo alloys
Variety of Stainless Steel alloys
Maraging Steel
AlSi12
AlSi10Mg
Pure Titanium
TiAl6V4
Inconel 625
Inconel 718
Hastelloy X
Bronze
Gold
Platinum
Silver

Note: List of materials available as of July 2018 from online catalogue of Concept Laser, EOS, Renishaw, and Trumpf [33]–[36].

Within the context of this work, a gas atomized Invar36 powder is used in the development of a process map and in the process window identification for various product quality metrics. The additional specifications for this powder can be referenced in Chapter 3.

Powder Production Method: Various methods are used to produce powders which include, but are not limited to, gas atomisation, water atomisation, plasma atomisation, and plasma rotating electrode process (PREP). Images gathered from [37] and [38] are shown in Figure 3 and Figure 4, and highlight the differences between water atomized, gas atomized, plasma atomized, and PREP powders, respectively.
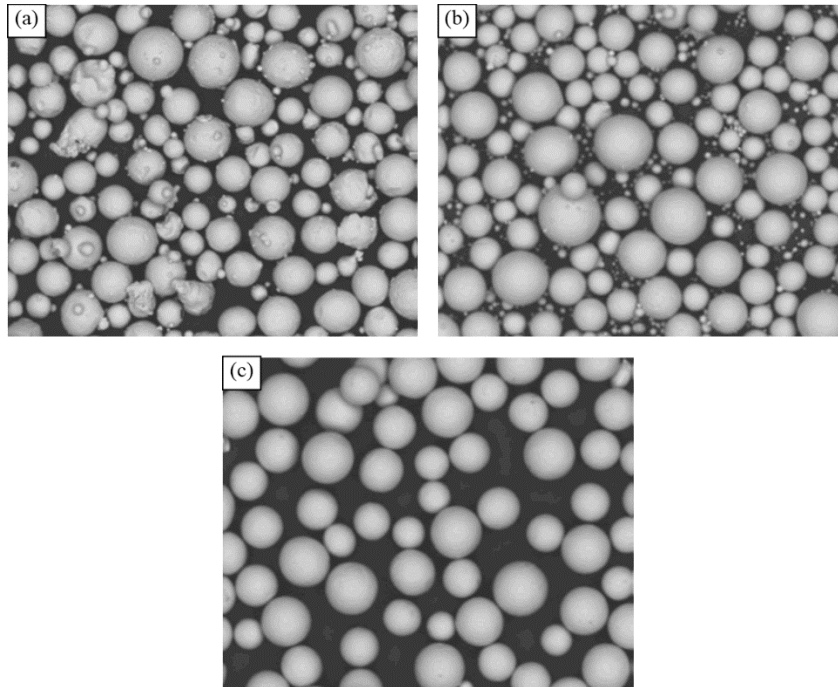
Figure 3. Example SEM images of powders obtained from (a) gas atomization, (b) plasma atomization, and (c) plasma rotating electrode process [37]. Not to scale, for visualization of powder morphologies only.
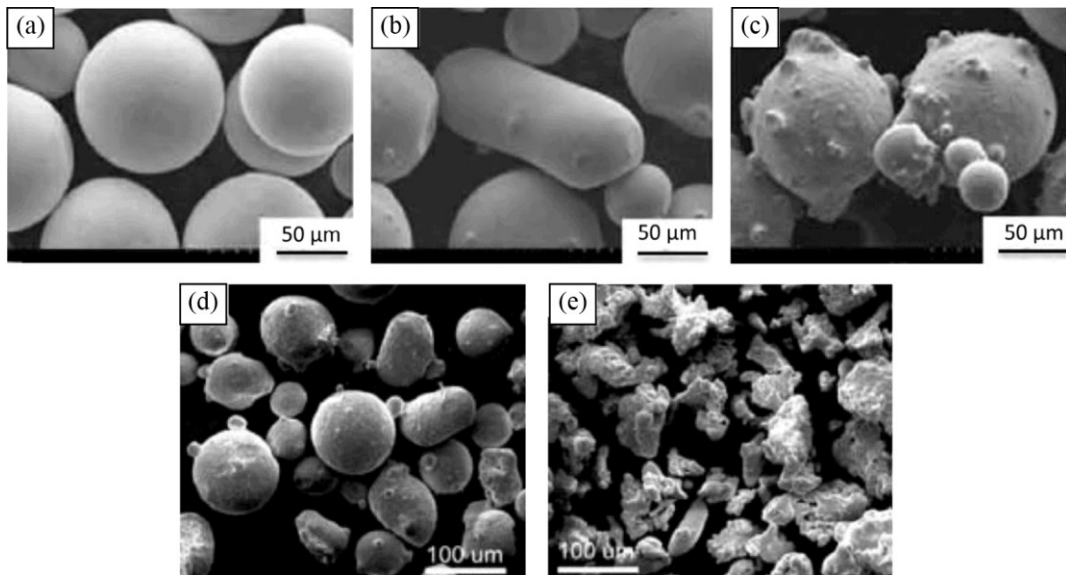
Figure 4. Example SEM images of powders obtained from (a) plasma rotating electrode process, (b) rotary atomization, and (c) gas atomization, and a comparison between (d) gas atomization and (e) water atomization [38].

Gas atomisation is the commonly used method of atomisation for LPBF because of the high particle sphericity obtained [39]. However, gas atomized powders are also prone to the occurrence of satellites, as well as internal pores due to entrapped inert gasses [15], [38], [40]. Water atomisation is another technique that is commonly used due to its ease and low cost [39]. However, because of the rapid cooling and high impact energies associated with using water, powders generated using this technique can be irregularly shaped [39]. PREP is known to create highly spherical particles, but with increased costs. In addition to the size considerations presented here, many other considerations must be taken into account with the production method, including the cost, productivity, acquired particle distribution range, and compatibility with specific chemical compositions. Typical particle sizes of powders created using different atomization techniques are described in Table 3.

Table 3. Typical particle size ranges for a variety of powder atomization techniques [37].

Manufacturing Process	Particle Size Range [μm]
Water atomization	0 – 500
Gas atomization	0 – 500
Plasma atomization	0 – 200
Plasma rotating electrode process	0 – 100

Powder Material Type: The use of pre-alloyed powders are generally used for LPBF processes because of their homogeneous composition, but blended powders can be used as well. Blended powders create a specific composition by mixing different powder materials (e.g. a blended Invar36 powder would contain 36-wt. % of nickel powder, and 64-wt. % iron powder). Since it is costly to obtain custom compositions of pre-alloyed powders for material development, the use of blended powders is sometimes used for material development [41]. The idea of in-situ alloy blending has also been investigated as an option to print functionally graded materials [41]. A common concern with blended powders is in obtaining homogeneous compositions. Even before processing, if a blended powder is poorly mixed or becomes segregated, it is possible to obtain inhomogeneity upon LPBF processing. Furthermore, the mixing of blended powders occurs on a meso-scale, and thus enough energy and time must be supplied during processing to ensure that the material fully homogenizes upon melting and solidification. Lastly, since blended powders exist as separate powder materials, the interaction of the powder with the environment may be different than if the powder was pre-alloyed. For example, some materials are prone to oxidation, but become corrosion resistant when alloyed.

Size Distribution and Morphology: In addition to the previously mentioned factors, the size distribution and morphology play a critical role in LPBF. When considering the morphology of

powders, spheres can achieve the greatest packing density, and thus any irregularities will serve to decrease powder bed compaction [42], [43]. The flowability of particles are also affected by their morphology, with deviations from perfect spheres negatively influencing particulate flow [43]–[45]. In terms of particle size, larger particles require more energy input to melt, due to the lower surface-to-volume ratio and the higher reflectivity [46]–[48]. Additionally, because of their larger volumes they also fill spaces less efficiently than smaller particles when spread onto a substrate. In the context of powder spreading, larger particles tend to flow better than smaller particles, because small particles are known to have issues with agglomerations and are more influenced by electrostatic charge [14], [49]. Although finer particles are more proficient at absorbing energy than larger particles, they also present a risk to vaporize upon laser interaction [14]. Other than with quality concerns, the fineness of powders also presents as a safety hazard, where powders may combust during processing. Also, finer powders can potentially diffuse through and damage machine components, and cause biological harm if inhaled [14]. The distribution of particles also has a role as well. Particularly, wider distributions of particles have been shown to have improved packing density, since smaller particles can fill the voids created by larger particles [50]. Bimodal distributions also increase packing density in a similar fashion. Thus, an optimal powder distribution has to be identified for the material system at hand with flowability, powder packing, absorptivity, and safety considerations in mind.

2.1.1.3 Build Setup and Process Parameter Considerations

There are a multitude of distinctions that need to be made when considering the process parameters and build setup. While this section covers several of these influencing factors, it does not serve as a comprehensive summary. More complete lists can be referenced in literature, such as in [51] or [52].

Build File Setup: Depending on the spatial orientation and geometry of parts within the build volume, the quality of the final part may be affected. For example, material anisotropy is a well-known issue, with tensile properties significantly affected by the build direction of components or by the scanning strategy [53]–[56]. To account for anisotropy related to the scanning direction, a parameter known as 'hatch angle' is used (Figure 5), which offsets the scanning direction of the laser in any individual layer by an angle, θ. To minimize the chance that any particular layer has the same orientation as a previous layer, an angle such as 67° can be used, where a layer orientation is repeated only every 360 layers [55]. Anisotropy due to build direction may be unavoidable and thus must be carefully considered before manufacturing. Figure 6 illustrates a possible range of build orientations.
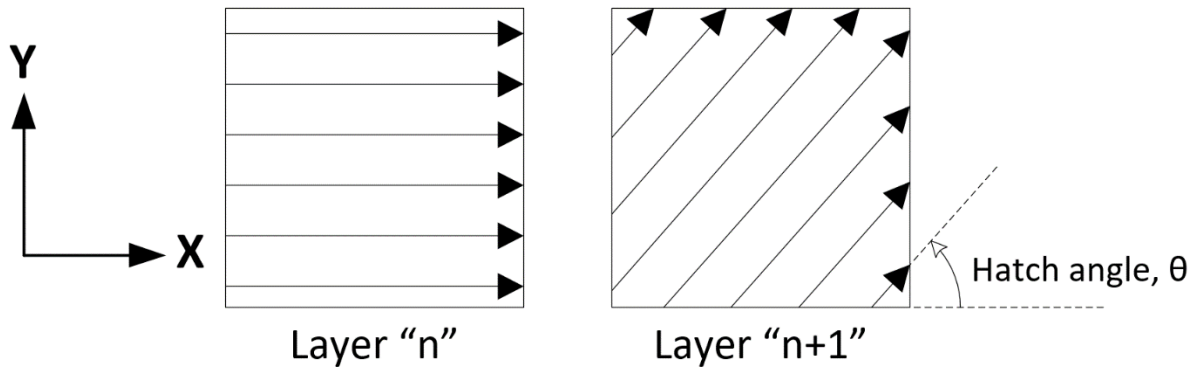
Figure 5. Schematic demonstrating the effect of hatch angle on consecutive layers.
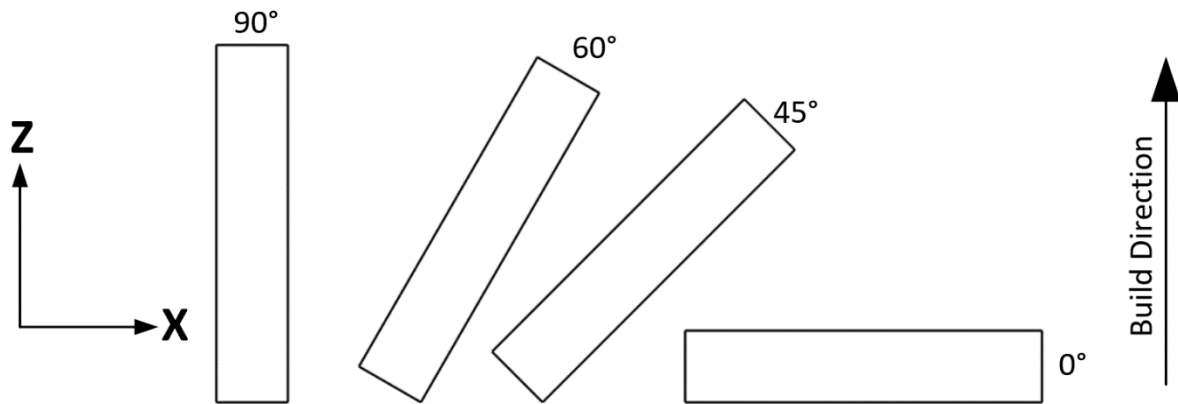
Figure 6. Schematic demonstrating build orientation.

Depending on the local orientation of the part, additional support structures may be required as well, and the purpose of support structures is twofold. Similar to the build plate, they provide structural integrity and serve as heat sinks to conduct heat away from the melting region [51]. They can also facilitate part removal by creating scaffolds that can be easily removed from the part upon solidification. Since support structures cannot conduct heat away as effectively as a solid part, and since they present as an additional post-processing step, it is still ideal to prevent the need for support structures when possible through design considerations and part orientation in the build layout [51].

The orientation of the part within the build layout is important as well. Upon solidification, the edges of parts may become more raised than the core regions of parts, and it may be possible for the recoater blade to strike these edges upon layer deposition [57]. In particular, to minimize the part contact with the recoater, multiple part edges or long singular edges that are parallel to the recoater blade can be rotated by several degrees (Figure 7). Similarly, it may be possible for the recoater to

16

propagate defects as it spreads new layers, and thus it may be beneficial to avoid aligning parts directly behind another.
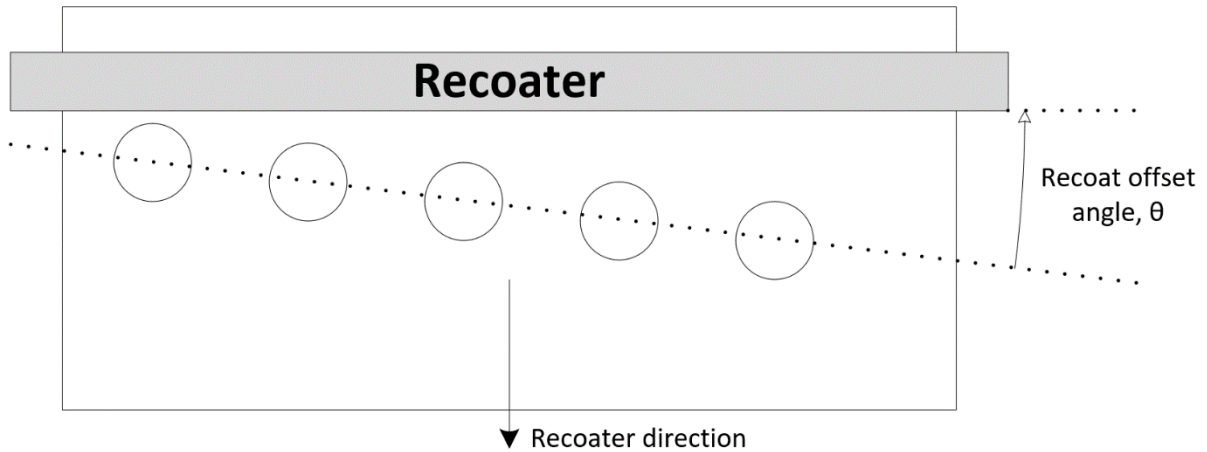
Figure 7. Schematic demonstrating recoater offset angle.

When considering the geometry of parts, it is highly dependent on the situation. For instance, it was mentioned previously that overhanging or angled features may require support structures. Support structure removal depends on the geometry of the part, and parts should be designed such that support structures can be easily accessed. In addition, thin walls solidify quickly and are more prone to issues related to residual stress. Thin walls are also limited by the resolution of the laser beam spot diameter. Height resolution is also limited by the layer thickness on deposition. Depending on if there are hollow chambers within a part, features must be designed to allow de-powdering or to allow internal support material removal, where gaps that are too small may result in material being trapped within the part.

To reiterate, described above are only several factors that must be taken into account, and more complete lists can be found in literature, such as with [51] or [52].

Process Parameters: The choice of process parameters during printing is essential, with over one hundred parameters that have an influence on LPBF part quality outcomes [14]. Studies have shown, however, the most important factors have been limited to the oxygen level, laser beam quality, dynamic viscosity of molten metal, surface tension of molten metal, melt enthalpy of the material, thermal diffusivity of the material, powder bed density, laser power, spot size, scan spacing, scan velocity, and layer thickness [58]. Out of these parameters, only a handful are controllable as a parameter setting before the process, or are continuously controlled during the process. Within

literature, energy density is a common variable that describes the effect of controllable input parameters, and shown below is the relevant relationship [59]–[61]:

$$E_D \left[\frac{J}{mm^3} \right] = \frac{P}{v \times d_h \times T_l}$$

E_d, above, describes the volumetric energy density in terms of, P, input power $[W]$, v, scanning velocity $[\frac{mm}{s}]$, d_h, hatching distance $[mm]$, and T_l, layer thickness $[mm]$. Depending on the phenomenon being observed, layer thickness and hatch distance may be neglected to quantify two-dimensional and one-dimensional equivalents of energy density, respectively. The term itself is used to describe the amount of input energy that is given to the system per unit volume (volumetric energy density), per area (surface energy density), or length (linear energy density).

Energy density is widely used in literature, with the advantage of being a relatively simple and reliable indicator of part quality [62]–[65]. However, the scientific rigor of the term is questionable because of inconsistencies found in literature. For example, in experiments with printing Al-12Si samples with constant values of energy density but varying laser power and velocity settings, discrepancies between results were reported [66]. This issue becomes apparent when one considers the temporal dependence of energy input, as well as the fact that the energy density does not capture the melt pool dynamics. Depending on the length scale of the part, for example, adjacent hatch lines may be delayed or expedited by several milliseconds. Additionally, with slower scan velocities, the energy is given time to penetrate in the material, affecting the thermal distribution within the part and changing the dynamics within the melt pool. Although it has its drawbacks, energy density has been used to successfully optimize parameters for AM-built parts [59]–[61], [67].

Within the context of this work, the effect of part design on process window is not explored, however the best practices with respect to hatch orientation and recoater offset angle have been taken into account. Also, since build orientation has not been investigated within this thesis, a singular orientation has been selected for all parts and the layout within the build space has been randomized in order to ensure robust comparisons between parts. This work mainly explores the usage of the energy density equation to explore the effects of energy input and part quality outcomes, and more on this topic can be referenced in section 4.1.

2.1.2 LPBF System of focus

For all experiments performed within this work, a Renishaw AM 400 SLM system was used, and all details within this section have been gathered from [35]. A diagram showing its external layout is shown in Figure 8.

Figure 8. External machine layout for the Renishaw AM 400 [35].

The system has a build volume of 250 mm × 250 mm × 250 mm with a controlled inert gas atmosphere. Prior to part fabrication, the system creates a vacuum of -968 mbar gauge pressure, and then backfills the chamber with argon gas. The powder delivery is performed via a gravity fed hopper system, and the powder is spread via a replaceable silicone recoater blade. To make clearance for additional layers, the build plate can be actuated in height increments of as low as 20 μm, and the build plate can be preheated to 170 °C to mitigate thermal stresses. All powder handling within the system is performed under argon atmosphere and through metallic flasks to maintain safety and avoid entrapped contaminant gasses. The system has isolation valves in place to allow the ability to remove and reintroduce new material during the process. Lastly, the laser system is powered by a 400 W Ytterbium fiber laser that has a wavelength of 1070 nm and a spot size of 70 μm. A full list of specifications can be referenced in Table 4.

Table 4. System specifications for the Renishaw AM 400 [35].

List item	Specification
Build volume (X × Y × Z)	250 mm × 250 mm × 300 mm
Maximum build size	248 mm × 248 mm × 285 mm
Build rate*	Up to 20 cm³/hr
Powder layer thickness	Between 20 μm and 100 μm
Laser type, wavelength	Ytterbium fiber, 1070 nm
Laser class	Type 1
Laser power	400 W
Laser spot size diameter	70 μm
Scan speed	Up to 2 m/s
Speed positioning	7 m/s
External dimensions without accessories	853 mm × 1700 mm × 2115 mm
Weight (gross / net)	1225 kg / 1100 kg
Argon consumption (after fill)	< 30 L/hr
Argon consumption (on fill/purge)	600 L
Power Supply	220 V to 240 V, 16 A, 45 Hz to 60 Hz single phase
Compressed Air	6 bar, regulated to 1.6 – 2.4 bar, 10 L/min
Available commercial materials	AlSi10Mg, CoCr, In625, In718, Stainless Steel 316, Ti6Al4V

* Build rate dependent on geometry and material

The Renishaw system has approximately 140 system parameters that can be modified to fabricate components. The list of parameters can be referenced in Appendix A. One interesting factor to note is that the Renishaw AM 400 system uses a pulsed emission mode for the laser output. Because of this ability, the scanning speed variable for Renishaw systems is split up into two variables: point distance and exposure time. This pulsed mode gives users an additional degree of control within the process, among other benefits previously discussed in section 2.1.1.1. For further clarification, Figure 9 and Figure 10 describe the operating methodology of laser scans in the Renishaw AM 400, where P describes the laser power [W], t_e describes the amount of time that the laser is exposed to the material [μs], t_d describes the latent time where the laser is off and repositioning to the next exposure point (known as drill delay) [μs], d_p describes the distance between adjacent exposure points [μm], and d_h describes the distance between adjacent hatch lines [μm]. Also, due to the differences in operational mode, the energy density equation for Renishaw's pulsed laser is slightly different than originally proposed in section 2.1.1.3. Essentially, the velocity term is just replaced to obtain the following:

$$E_D \left[\frac{J}{mm^3}\right] = \frac{P}{\left(\dfrac{d_p}{t_e}\right) \times d_h \times T_l}$$
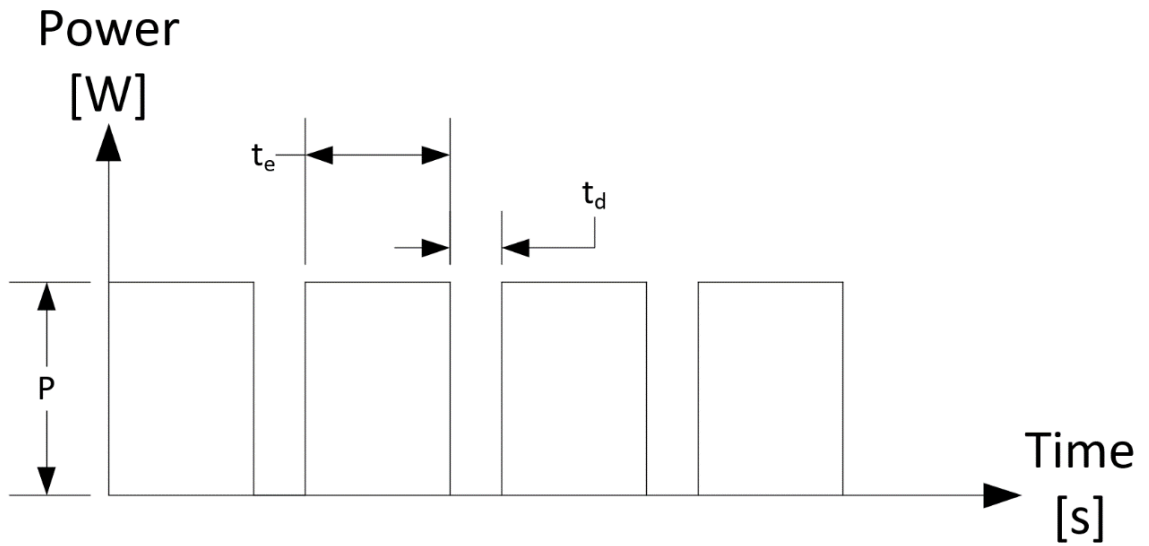
Figure 9. Schematic representing the time dependence of laser pulses for the Renishaw AM 400.
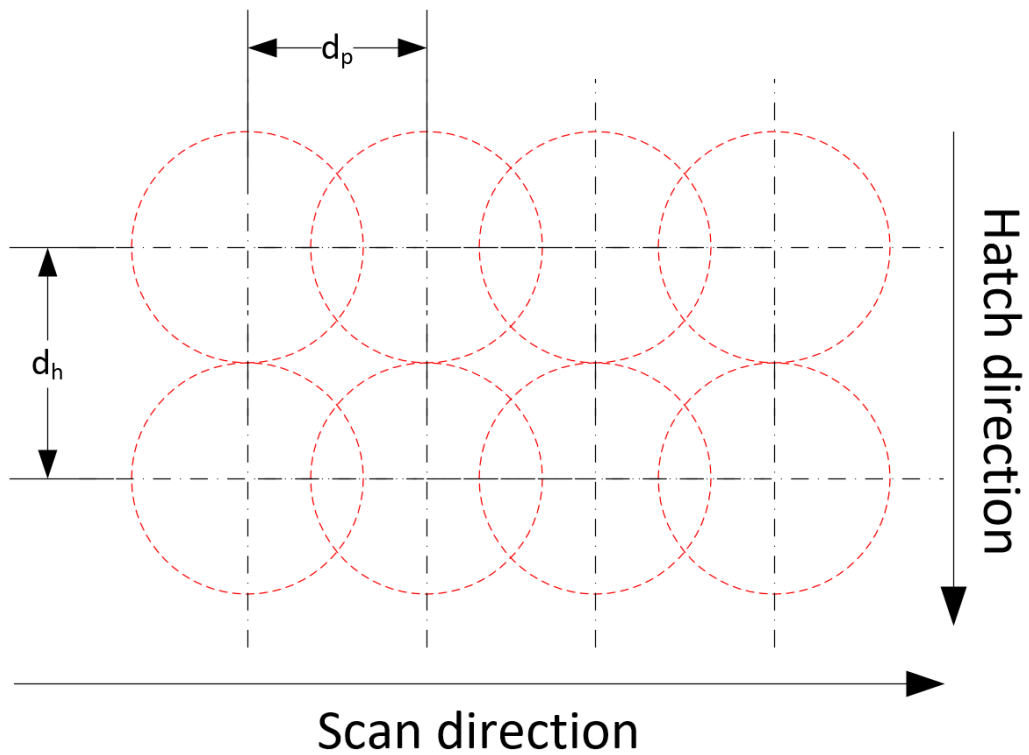
Figure 10. Schematic representing the spatial distribution of laser pulses for the Renishaw AM 400.

It should be noted that the t_d term (drill delay) is accounted for within the modified energy density equation, but does not appear within the equation because the effective power knockdown from the drill delay and the effective velocity decrease from the drill delay cancel each other out.

As shown in Table 4, the Renishaw system is capable of processing a variety of materials. Within this work, however, a novel material that may benefit from the LPBF process will be investigated. The material of focus is called Invar36 and section 2.2 will detail the background on the material, and how it may benefit from the LPBF process.

2.1.3 Relevant Terminology for LPBF Process Optimization

Described below are various terms used within this work. Some may have been previously defined in earlier sections but are catalogued below to serve as a point of reference.

Build variable: These are the variables that affect the LPBF process in some capacity. For the purpose of this research, the variables are specifically defined for the Renishaw AM 400 SLM system. Because of the complexity of the process, not all possible variables will be defined within this work. For the experiments performed in this work, the build variables include, but are not limited to: laser power, exposure time, point distance, hatch distance, and scanning strategy.

Process map: The process map is a representation (either quantitatively or qualitatively) of the results of the LPBF process with respect to the variation of build variables. The build variables will be represented over a range of values, and the results can be shown as either binary "pass/fail" conditions or of a range of values indicative of quality. The process map, while it may be indicative of certain build variable combinations that produce desirable outcomes, is simply meant to document observations. The process map serves as a representation of the whole process, and is not an optimized range.

Process window: The process window is a narrow range of combinations of build variables that can be tailored to achieve specific process outcomes from the LPBF process. The process window is narrowed based on specific desired outcomes, and is not representative of the process as a whole, or any other result. The process window may be made smaller or larger depending on the type of performance desired, or the accuracy and precision required.

Recipe: For the purposes of this research, a recipe is a combination of selected values for build variables that are used with the Renishaw AM 400 system to produce a specific desired process

outcome from the LPBF process. In the context of the statistical design of experiments, it may be referred to as a "treatment".

Process outcome: A process outcome is some result that is obtained from the LPBF process, which describes a specific part quality that can be measured quantitatively (such as porosity, dimensional accuracy, linear CTE), or qualitatively (number of successful parts per build, etc). Within this work, the process outcomes include porosity and coefficient of thermal expansion, and the goal is to minimize them.

Standardized artefacts: Standardized artefacts are specific part geometries that are designed to compare the effect of different build variables. For example, a standardized artefact for testing the elastic properties of a material would be a tensile coupon.

Manufacturing plan: The manufacturing plan is the full process of producing a LPBF part, including but not limited to: the selection of powder, system setup, build variable selection, quantity and layout of parts along the build plate, removal of parts and support structure from the build plate, and any post-processing steps.

2.2 Invar Alloys

Invar alloys are iron-nickel alloys that take their name by their invariance of certain properties with temperature. The properties of Invar were first discovered near the end of the 19th century, where several groups observed that iron-nickel alloys displayed anomalous thermal expansion characteristics [68]. Noting these discoveries, a physicist named Charles Édouard Guillaume began to investigate the possibility of creating an alloy that could rival the dimensional stability of an existing alloy, Pt–10 wt.% Ir, but at a much lower cost [69]. From Guillaume's work, it was determined that an Fe-Ni alloy with nickel composition of $\approx$35.6 wt. % was found to have superior thermal expansion characteristics [69]. To illustrate Guillaume's findings, Figure 11, as found by Chevenard, shows the thermal expansion behaviour of an Fe-Ni binary system [70]. The alloy composition displaying the minimal thermal expansion is known as Invar36. To compare, the platinum alloy used at the time has a coefficient of thermal expansion (CTE) of $\approx 8.84 \times 10^{-6} \left[\frac{\mu m}{m\,^\circ C} \right]$ between 0-1000 °C, while Invar36 displays a CTE of $\approx 1.19 \times 10^{-6} \left[\frac{\mu m}{m\,^\circ C} \right]$ and remains minimal for temperatures up to 200 °C [69]. The origins of this effect remained unknown for many years, but originally Guillaume postulated that the Invar phenomenon arose from a $\gamma \rightleftharpoons \alpha$ transformation between γ-phase face-centered cubic (FCC)

23

and α-phase body-centered cubic (BCC) iron, where the increasing nickel would delay and diminish the effects of the $\alpha \rightarrow \gamma$ contraction over a large range of temperature [68]. More recent insights have placed the Invar phenomenon as a property that exists purely in the γ-phase region, and that the mechanism behind its properties rely on magnetic phenomenon [69], [71].

According to Rancourt, this is because of interactions between high magnetic moment and low magnetic moment γ-Fe [71]. For reference, Figure 12 shows the phase diagram for an Fe-Ni binary system. At the Invar composition and upon solidification, the alloy forms γ-Fe and nickel, and remains metastable due to high cooling rates. From calculations by Rancourt, it can be shown that the
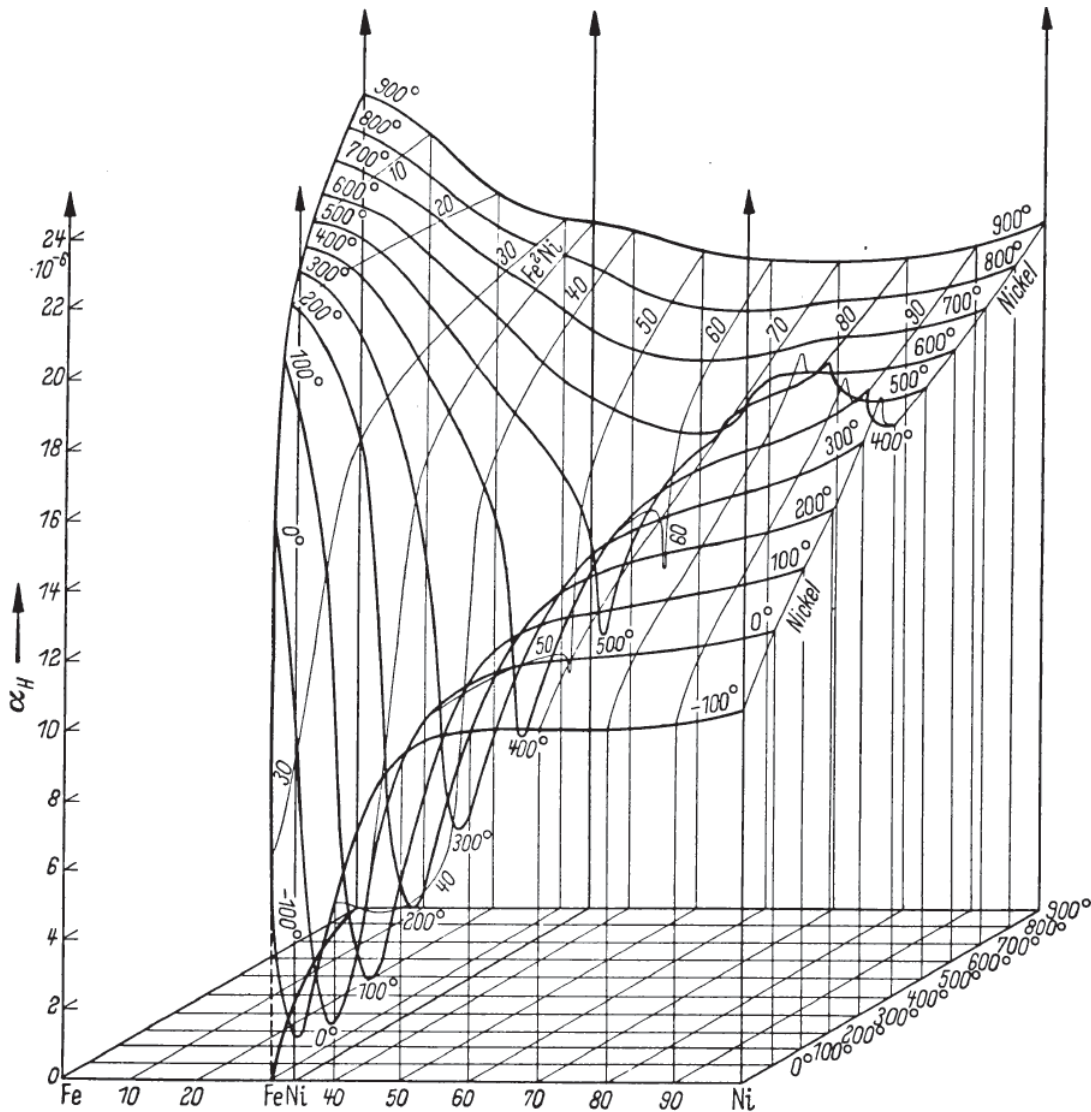
Figure 11. Thermal expansion behaviour of an iron-nickel binary system with varying temperature [70].

24

fraction of Fe-Fe nearest-neighbour magnetic exchange bonds that are energetically unsatisfied at the Invar composition is high (≈80%) [71].

Resulting from this, Rancourt conjectured that it is due to the resulting large degree of frustration between Fe-Fe bonds expresses a magnetovolume force that opposes the thermal expansion of the alloy [71]. For Invar, this effect is strong below the material's Curie temperature, with the change in CTE being minimal and linear, and understandably, normal expansion behavior dominates once the material is heated above the Curie temperature [69], [70], [72].
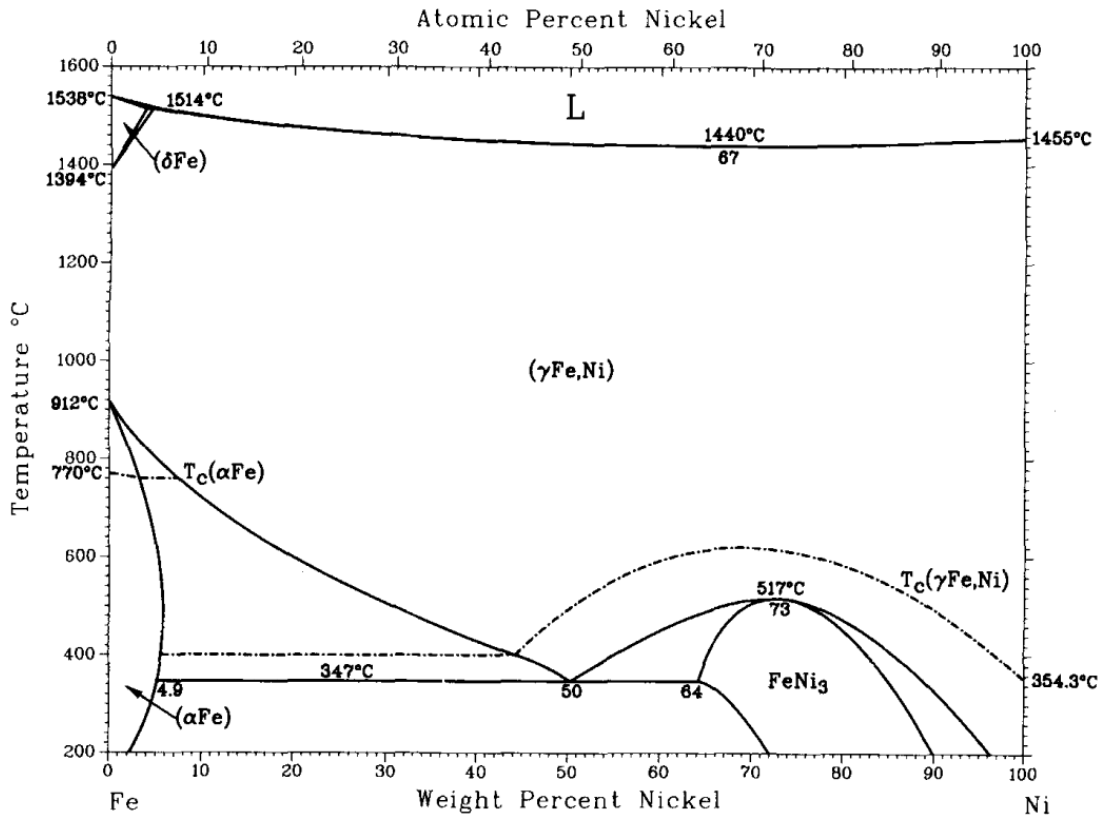
Figure 12. Phase diagram of a binary Fe–Ni system at temperatures of 200–1600 °C [73].

It should be noted that the low thermal expansion behaviour of Invar is strongly affected by its composition. As seen in Figure 11, a slight change from the optimal composition of nickel shifts the CTE dramatically. The presence of impurities affects the composition as well. For example, the inclusion of chromium to increase corrosion resistance has the drawback of increasing the CTE [74]. In general, any added trace elements negatively affect the CTE, but there is one exception. In 1927, Masumoto found that the CTE of Invar could be further decreased with the addition of cobalt to create a mixture of Fe-32 wt. % Ni-5 wt. % Co that resulted in an alloy with even lower CTE than

25

standard Invar36 at temperatures between -65 °C and 100 °C [69]. This mixture is now known as "Super Invar". Shown below in Table 5 is the standard composition of Invar, according to ASTM Standard F1684-06, "Standard Specification for Iron-Nickel and Iron-Nickel-Cobalt Alloys for Low Thermal Expansion Applications" [75]. Additional elements are added in trace amounts to the composition to improve on the mechanical and metallurgical properties of the alloy [69], [76].

Table 5. Chemical composition requirements for conventional Invar36 (UNS No. K93603), as per ASTM Standard F1684-06 [75].

Element	Composition, wt. %
Iron, nominal	Remainder
Nickel, nominal	36
Cobalt, maximum	0.50
Manganese, maximum	0.60
Silicon, maximum	0.40
Carbon, maximum	0.05
Aluminum, maximum	0.10[A]
Magnesium, maximum	0.10[A]
Zirconium, maximum	0.10[A]
Titanium, maximum	0.10[A]
Chromium, maximum	0.25
Phosphorus, maximum	0.015[B]
Sulfur, maximum	0.015[B]

[A] The total sum of aluminum, magnesium, titanium, and zirconium shall not exceed 0.20%
[B] The total sum of phosphorus and sulfur shall not exceed 0.025%

2.2.1 Mechanical and Thermodynamic Properties

The mechanical and thermodynamic properties for Invar36 are listed in Table 6. In comparison to the mechanical properties of a material such as 304 Stainless Steel, Invar36 has lower specific stiffness and ultimate tensile strength, but with a linear thermal coefficient of expansion that is of an order of magnitude lower [77], [78]. As such, it is clear that the material is not as suitable for load-bearing applications, and is more appropriate for applications requiring high dimensional stability over a range of temperatures. When considering the manufacturability of Invar36, there are several challenges. It has a tendency to crack during solidification and reheating, and due to its high nickel content, the material also displays unfavorable work hardening characteristics [72], [79]–[81]. When machining Invar36, the resultant tool wear issues that arise due to work hardening is further exacerbated by the presence of highly ductile invar chips created during processing that may build up on the cutting face [82].

In this work, Invar36's properties are used in order to determine appropriate ranges for the experimental setups. Particularly, the Curie temperature serves as a maximum bound for thermal expansion testing, and the coefficient of thermal expansion values are useful as a baseline to compare to LPBF-built parts. The thermal properties are useful input parameters in the modelling chapter to determine the behaviour of the material under laser interaction. Although, it should be mentioned that the material properties have been specified for bulk annealed material, and that the material may behave differently when processed under LPBF. Although the mechanical properties are not directly used within this work, they are presented for possible future reference in the event that additional testing is performed on the LPBF-built parts.

Table 6. Mechanical and thermal properties for Invar36 under annealed condition, unless specified otherwise [78].

Property	Unit	Value
Density	$[\frac{kg}{m^3}]$	8.05
Thermal conductivity	$[\frac{W}{m \cdot K}]$	10.5
Curie Temperature	$[°C]$	280
Melting temperature	$[°C]$	1425
Specific Heat	$[\frac{kg}{kJ \cdot K}]$	0.515
Thermal Expansion Coefficient (30 – 100 °C)	$[\frac{\mu m}{m°C}]$	1.18
Ultimate Tensile Strength	$[MPa]$	450
Yield Strength	$[MPa]$	280
Elongation	[2 inch, %]	35
Hardness	[Rockwell]	B-70
Elastic Modulus	$[GPa]$	141
Specific Stiffness	[-]	17.5
Poisson's Ratio	[-]	0.290

2.2.2 Applications

Invar alloys are typically deployed in applications where high dimensional stability over a temperature range is a requirement. One of Invar's earliest uses was for precision measurement in geodesy, due to the variance of environmental conditions on a day-to-day basis [69]. By creating levelling staves out of Invar, measurements were able to be reliably taken and compared against other measurements in any weather condition [69]. Another notable use of Invar was to replace platinum in the manufacturing of glass sealing wires with an Invar alloy with Fe- 45wt. % Ni composition [69]. At the time, this simple material replacement was a cost-saving initiative that resulted in millions of pounds of savings by the 1920s, and today Invar is still used in glass-to-metal hermetic seals [69].

More recently, Invar has seen usage in cryogenic storage by including Invar in the inner lining of liquid nitrogen storage tanks to mitigate the effects of periodic heating and cooling during loading/unloading [83]. Within the space industry, Invar has found uses with optics, where the alignment of lenses and other critical components are required to be stable and precise over a large range of temperatures [79]. This is especially true with optics systems within satellites, where the system is subjected to periodic heating and cooling cycles from the sun as the satellite orbits the earth. On a similar note, waveguides used in satellites suffer from similar heating cycles, and the use of Invar can help maintain the dimension stability of parts from temperature drift.

As mentioned previously, Invar's poor mechanical properties have limited its use to very specialized applications. Particularly, because of the material's poor machinability and high density, the machining and launch-costs may be prohibitive. It is with these challenges in mind that motivates this work to optimize the additive manufacturing process for Invar36, because it may be possible to sidestep difficulties with machining and also reduce mass costs through optimized design strategies. As a tool for this optimization process, a statistical design of experiments approach will be used and introduced in the following section.

2.3 Statistical Design of Experiments

The process optimization for additive manufacturing is difficult due to the sheer number of factors (as discussed in section 2.1.1) that influence part qualities. With increasing number of variables, experiments focused on single factor effects quickly become inefficient and experiments must start to consider the effects of parameter interactions. One method to resolve situations involving multiple factors is to use a design of experiments (DOE) approach, which quantifies the effects of each factor and all interactions simultaneously using statistical analysis. Designed experiments have been successfully used in many diversified fields, including optimization for thermal energy storage applications [84], for optimal metrological measurement and uncertainty analysis [85], for optimal material grinding processes [86], and for manufacturing of medicinal compounds [87]. The DOE approach has also been used extensively for AM as well, for example, to optimize for properties such as fatigue life or tensile strength [88], for maximizing density [67], [89], [90], for minimizing surface roughness [91], and for other part qualities [60], [92]–[94]. To develop experiments, an effective design method that can be used is the factorial design. Factorial designs are experiments set up so that responses are measured for every possible combination of parameter levels. As an example, consider an experiment that observes the sweetness of a beverage based on sugar levels (factor A)

28

between 5%/10%/15%, and on salt levels (factor B) of 1%/2%/3%. A factorial experiment designed with these two factors at the three respective levels would result in a 3^2 factorial experiment with the following setup and nine unique samples (Table 7).

Table 7. Example 3^2-factorial design table.

Sample ID	Factor A	Factor B
1	5%	1%
2	5%	2%
3	5%	3%
4	10%	1%
5	10%	2%
6	10%	3%
7	15%	1%
8	15%	2%
9	15%	3%

The benefit of factorial designs is that they make efficient use of experimental data, since each sample permutation within an experiment provides unique information about the effect of parameters. Also, due to the way they are constructed, the data can be easily interpreted through statistical analysis with analysis of variance (ANOVA). However, when constructing factorial designs (and DOEs), the effectiveness of the experiments are limited by informed decisions about the response variable, the number of factors and their levels, the presence of uncontrollable nuisance factors, the model for statistical analysis, and the interpretation of results [95]. Unfortunately, factorial designs get increasingly unwieldly as the number of factors increase. For instance, a factorial experiment with four factors at two levels results in $2^4 = 16$ samples, but at five factors the number of samples exponentially increases to $2^5 = 32$ samples. To mitigate the number of samples, designs known as fractional factorial experiments can be constructed, where only a subset of a full factorial is measured, with the caveat that some main effects and interaction effects become confounded. However, the retrieval of these main and interaction effects can be performed simply by measuring the response variable for the missing subset of parameter levels.

As mentioned previously, the results of a factorial design experiment can be interpreted through ANOVA. The structure of a factorial design makes it possible to isolate individual effects of interest from the response variable using a technique known as sum of squares decomposition [95]. This is proven and discussed in detail in [95], however a small excerpt will be included here as reference. The analysis for a factorial experiment is generally conducted by the process shown below in section 2.3.1 [95].

2.3.1 Analysis of Factorial Experiments

Assume an experiment that is set up with controlled factors A, B, and C, and a response variable y. Factor A has $i = 1, 2, \ldots, a$ levels, factor B has $j = 1, 2, \ldots, b$ levels, and factor C has $k = 1, 2, \ldots, c$ levels. With the experiment repeated (or replicated) a total number of $l = 1, 2, \ldots, n$ times, the resulting total number of observations for this experiment will be $N = a \times b \times c \times n$. The statistical model for the analysis can be written in many ways, but the traditional model that is used is the 'effects model', as shown below:

$$y_{ijkl} = \mu + \alpha_i + \beta_j + \delta_k + (\alpha\beta)_{ij} + (\alpha\delta)_{ik} + (\beta\delta)_{jk} + (\alpha\beta\delta)_{ijk} + \epsilon_{ijkl}$$

Where y_{ijkl} is the response at factors A, B, and C at levels i, j, and k, respectively, and at the lth replicate. Continuing, μ describes the overall mean, while α_i, β_j, and δ_k denote the effects of factors A, B, and C at their respective levels, and $(\alpha\beta)_{ij}, (\alpha\delta)_{ij}, (\beta\delta)_{jk}, (\alpha\beta\delta)_{ijk}$ the interaction effects between the factors, respectively. Lastly the ϵ_{ijkl} is the error term. Under the assumption that the purpose of the experimental design is to determine the significance of the parameter effects and their interactions, the following null hypothesis is then defined:

$$H_0: \alpha_i = 0 \; for \; all \; i \; ; H_0: \beta_j = 0 \; for \; all \; j \; ; H_0: \delta_k = 0 \; for \; all \; k$$
$$H_0: (\alpha\beta)_{ij} = 0 \; for \; all \; i, j \; ; H_0: (\alpha\delta) = 0 \; for \; all \; i, k \; ; H_0: (\beta\delta) = 0 \; for \; all \; j, k$$
$$H_0: (\alpha\beta\delta)_{ijk} = 0 \; for \; all \; i, j, k$$

Which states that all the effects (main and interaction) are equal to zero. Before continuing, let $y_{i\ldots}$ be the sum of all observations at treatment i, let $y_{.j\ldots}$ be the sum of all observations at treatment j, let $y_{ij\ldots}$ be the sum of all observations at treatments i and j, and etc. for all possible combinations of letters and dots ($\cdot$). Similarly, $\bar{y}_{i\ldots}$ is the grand average of the observations at treatment i such that $\bar{y}_{i\ldots} = \frac{y_{i\ldots}}{bcn}$ and likewise for all possible combinations of letters and dots. Therefore, the total corrected sum of squares of the response variable can be expressed as follows:

$$SS_T = \sum_{i=1}^{a} \sum_{j=1}^{b} \sum_{k=1}^{c} \sum_{l=1}^{n} \left(y_{ijkl} - \bar{y}_{\ldots} \right)^2$$

It is proven in [95] that through sum of squares decomposition, SS_T can also be written as

$$SS_T = SS_A + SS_B + SS_C + SS_{AB} + SS_{AC} + SS_{BC} + SS_{ABC} + SS_E$$

Moving forward, the mean squares for the effects can then be found as

$$MS_A = \frac{SSA}{a-1}; MS_B = \frac{SSB}{b-1}; MS_C = \frac{SSC}{c-1}$$

$$MS_{AB} = \frac{SSAB}{(a-1)(b-1)}; MS_{AC} = \frac{SSAC}{(a-1)(c-1)}; MS_{BC} = \frac{SSBC}{(b-1)(c-1)}$$

$$MS_{ABC} = \frac{SS_{ABC}}{(a-1)(b-1)(c-1)}; MSE = \frac{SS_E}{abc(n-1)}; MS_T = \frac{SS_T}{abc(n-1)}$$

Lastly, with the decomposed sum of squares and their respective mean square values, the following test statistic can be used to determine the significance of any particular effect:

$$F_0 = \frac{MS_{effect}}{MS_E}$$

This test statistic is distributed as $F_{a-1,(a-1)(b-1)}$ if the null hypothesis is true. Therefore the critical test statistic F_{crit} would be distributed as $F_{\alpha,a-1,(a-1)(b-1)}$, and a comparison showing that $F_0 > F_{crit}$ means that the null hypothesis can be rejected, implying the significance of the effect. For the above formulation to apply, however, the error within the model must conform to the normality assumption, where the distribution must be normally and independently distributed such that $\epsilon \sim NID(0, \sigma^2)$. To ensure this outcome, randomizations are added in as many aspects of experiments as possible, such as with fabrication or measurement order, to mitigate any bias due to operators, or uncontrollable factors.

Within this work, a factorial design will be used to investigate the effects of various parameters on the thermal expansion coefficient and density of Invar36 parts built through LPBF, and will be further discussed in section 4.1.5.

Chapter 3

Powder Analysis

In this chapter, an analysis of the chemical composition, particle size morphology, and rheology for the Invar36 powder is performed. As discussed in section 2.1.1.2, it is critical to distinguish the characteristics of the feedstock material because it may affect the behaviour in-situ. The techniques used within this chapter are inductively coupled plasma atomic emission spectroscopy (ICP-AES) for the chemical composition, scanning electron microscopy (SEM) for particle morphology, optical imaging techniques with a Camsizer X2 for particle size analysis, and dynamic flow testing with an FT4 rheometer for the particle rheology. The data gathered for all SEM and ICP-AES results presented in this work has been performed by Dr. Hamed Asgari Moslehabadi (Post Doctorial Fellow, Multi-Scale Additive Manufacturing Lab).

3.1 Experimental Methods

For all work performed for this research, the material used was a gas-atomized Invar36 powder. According to the supplier specifications, the powder size conformed to US Standard Mesh No. 325 (approximately equal to sieve mesh size of 44 μm). For all stages of this research, the powder was used in its as-received state without any preprocessing in advance of analysis or fabrication. The as-received powder was reported to contain the following chemical composition:

Table 8. Chemical composition of the Invar36 powder, according to supplier specifications.

Element	Composition, wt. %
Iron	Remainder
Nickel	36.12
Cobalt	0.01
Manganese	0.44
Silicon	<0.01
Carbon	0.010
Aluminum	<0.01
Magnesium	<0.01
Zirconium	<0.01
Titanium	<0.01
Chromium	0.12
Phosphorus	0.02
Sulfur	0.003
Copper	<0.01
Molybdenum	0.05
Selenium	<0.003

3.1.1 Chemical Composition Analysis

The verification of the chemical composition was directed an external analytical laboratory for ICP-AES analysis. The chemical analysis was performed according to ASTM E1019-11, ASTM E1097-12, and ASTM E1479-16 standards. The resulting compositional information was compared against the ASTM Standards for conventional Invar36. For reference, according to the ASTM Standard F1684-06, "Standard Specification for Iron-Nickel and Iron-Nickel-Cobalt Alloys for Low Thermal Expansion Applications", the received powder conforms well to the standard composition for Invar36 (UNS No. K93603) [75]. The outlined requirements are shown previously in Table 5, but are also repeated below in Table 9. It should be noted that the received powder deviates from the standards with the inclusion of the following three elements not reported by the standards: selenium, molybdenum, and copper. It should be noted that although copper and selenium were measured, they were under reportable limits.

Table 9. Chemical composition requirements for conventional Invar36 (UNS No. K93603), as per ASTM Standard F1684-06 [75].

Element	Composition, wt. %
Iron, nominal	Remainder
Nickel, nominal	36
Cobalt, maximum	0.50
Manganese, maximum	0.60
Silicon, maximum	0.40
Carbon, maximum	0.05
Aluminum, maximum	0.10[A]
Magnesium, maximum	0.10[A]
Zirconium, maximum	0.10[A]
Titanium, maximum	0.10[A]
Chromium, maximum	0.25
Phosphorus, maximum	0.015[B]
Sulfur, maximum	0.015[B]

[A] The total sum of aluminum, magnesium, titanium, and zirconium shall not exceed 0.20%
[B] The total sum of phosphorus and sulfur shall not exceed 0.025%

3.1.2 Particle Size

The particle size distribution of the powder was found using a Retsch Camsizer X2 Optical Particle Size Analyzer with the X-Jet dispersion module [96]. The Camsizer is capable of reporting multiple different measures of particle size, but since the supplier specified the particle size in terms of US

Standard mesh sizing, the selected particle size indicator was based on chord size measurements. To clarify, for any given direction in a particle, the maximum possible chord length was found as x_c. Out of the entire set of x_c measurements, the minimum value was selected as $x_{c,min}$. A representation of this measurement process is shown in Figure 13. This measure of particle size was chosen because it is the minimum possible diameter of a hole that the particle is able to pass through. Thus, this measure of particle size can be compared against particle size measurements attained through sieving.
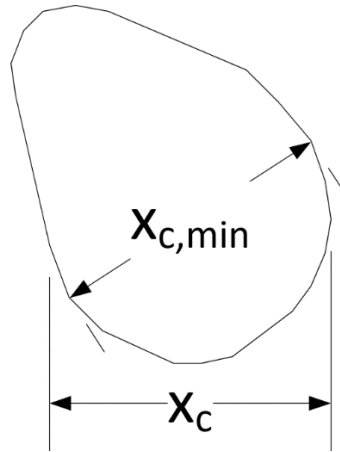
Figure 13. Reference illustration for maximum chord, x_c, and minimum measurement of maximum chord, $x_{c,min}$.

Before taking a sample of powder for analysis, the container was agitated for 10 minutes using a tumbler system to promote the homogenization of the particle distribution. Afterwards, approximately 2000 mg of sample was measured and poured through a funnel and onto the Camsizer's vibrational feed ramp. The equipment was then allowed to automatically perform its run, and the experiment was terminated after at least 500 consecutive empty measurements were captured by the system. To obtain a statistical relevant representation of the distribution, this process was repeated for a total of three runs.

3.1.3 Particle Morphology

The morphology of the powder was observed through micrographs taken by scanning electron microscopy (SEM). The micrographs were taken at the University of Waterloo Advanced Technology Laboratory (WATLab), using a LEO FESEM 1530. To obtain the most visual clarity, the equipment was set to secondary electron mode at an operating voltage of 15 kV and working distance of 8.5 mm. After agitating the powder in the same fashion as in section 3.1.2, a small amount of powder was sampled and adhered to a carbon substrate. Micrographs were then taken at randomized locations to

eliminate selection bias from the operator. Depending on the observed feature, magnification in the orders of 100× to 1000× was used.

3.1.4 Powder Rheology

The rheological properties of the powder were characterized with a FT4 powder rheometer by Freeman Technology [97]. The FT4 functions using "a patented blade principle [with] a twisted blade displacing powder as it moves along a helical path through the sample", and during the movement of the blade, force measurements along the axial and rotational directions are used to assess the flow characteristics of powders [98]. Within industry, the FT4 has successfully been used to assess and compare flow characteristics of powders inside and outside of additive manufacturing [98]–[101]. Within this work, several methods are performed to evaluate the flowability of the powder; stability and variable flow rate testing, aeration testing, compressibility testing, permeation testing, and shear cell testing. To explain their significance, insights from [98]–[101] have been taken and summarized below.

In the stability and variable flow rate test, two separate tests are run in series. The stability test is run so the powder can reach a steady flow state upon testing. The default testing sequence involves an initial conditioning sequence, a splitting sequence to remove excess powder, and then seven alternating sequences of conditioning and testing to determine the steady state flow energy of the powder. To explain, a figure is described below:
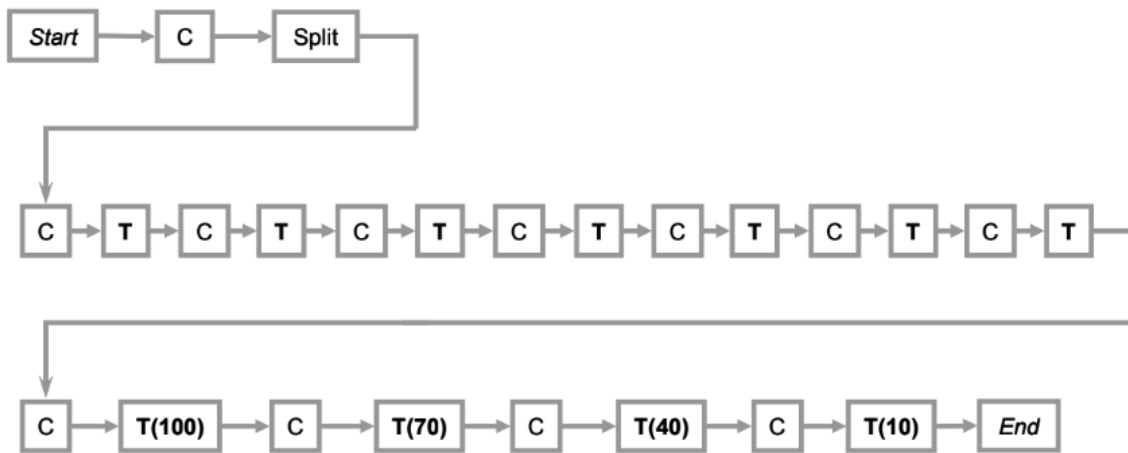
Figure 14. Schematic describing the stability and variable flow rate testing sequence.

In the above figure, the term 'C' describes a conditioning cycle, 'T' describes a testing cycle, 'Split' denotes the removal of excess powder to attain a precise measurement volume, and the numbers within the brackets describe the blade speed used for testing, in millimeters per second. Unless otherwise specified by the brackets, the blade speed for all cycles are at 100 mm/s. During the variable flow rate testing, the blade is run at steadily decreasing speeds, and based on the energy recorded, additional information about the powder flow state is gained. Simply put, lower energies are associated with less cohesive powders, and thus better flow. The aeration test measures the energy required for the blade to travel through the powder, with the powders subjected to injected air during testing. With the added aeration, less energy should be required to move the testing blades through the powder. Non-cohesive powders should easily allow aeration to occur, indicated by a large subsequent reduction in measured energy during testing. The compressibility testing measures the amount of volume change that is possible in the powder samples when subjected to a compressive force. As such, it functions as a measure of packing efficiency of the powder and an indirect measure of flowability; powders that have high compressibility are indicative of more cohesive powders as they have additional degrees of freedom to realign before flowing. Permeability is used to measure how easily a fluid can be transmitted through the powder bulk, with lower permeability associated with powders that are more cohesive. Lastly, the shear testing is used to determine the amount of shear stress required to induce flow in a powder. This is an important measure since the primary mode of powder flow is in shear. Thus higher values during shear testing are associated with particles more resistant to flow. In order to determine these values, the following procedure was taken:

Before taking a sample of powder for analysis, the container was agitated for 10 minutes using a tumbler system to promote the homogenization of the particle distribution. Afterwards, depending on the test, a suitable vessel was then selected (based on the manufacturer guidelines), and then the appropriate standardized test was initialized within the FT4 software package. From there, the rotary blade was inserted into the machine, and then the vessel was filled with powder, attached to the machine, and then the test was run. For each test, a total of three runs were performed to obtain a statistically significant set of measurements.

3.1.5 Tap Density

In addition to the tests performed by the FT4 rheometer, the tap density (packed density) of the powder was found using a tap density apparatus, constructed according to ASTM B527-15, "Standard Test Method for Tap Density of Metal Powders and Compounds" [102]. Figure 15 shows the required

specifications. To perform the testing, the powder container was agitated for 10 minutes with a tumbler system, and then a sample mass ($m_{initial}$) of 100 g was weighed and then added to a graduated cylinder. Afterwards, a periodic tapping at a frequency of 200 taps per minute at a stroke height of 3.0 ± 0.2 mm was applied until there was no observable change in powder volume (V_{final}), in millilitres, for over 5 minutes. The tap density was then calculated as follows:

$$\rho_{tap} \left[\frac{g}{cm^3} \right] = \frac{m_{initial}}{V_{final}}$$
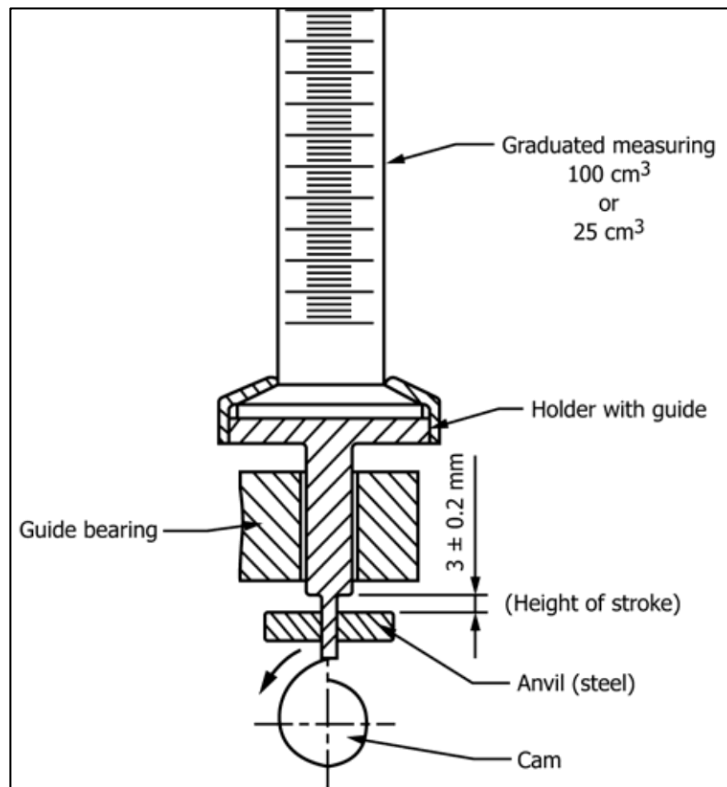
Figure 15. Tap density apparatus standard specifications, as per ASTM B527-15 standards [102].

The results of the tap density measurements were used to compare against the conditioned bulk density measurements from the FT4 testing. Based on the increase of density from conditioned to tap density, an idea of the packing state of powders upon layer deposition was obtained.

3.2 Results and Discussion

3.2.1 Chemical Composition Analysis

The tested chemical composition of the powder with comparisons to the reported and ASTM chemical composition are shown below in Table 10.

Table 10. Chemical composition of the powder as measured, and compared against supplier and ASTM specifications.

Element	Tested Composition, wt. %	Supplier Composition, wt. %	ASTM Specifications, wt. %
Iron	63.3	Remainder	Remainder
Nickel	35.6	36	36 nominal
Cobalt	< 0.01	0.01	0.50 max
Manganese	0.35	0.44	0.60 max
Silicon	0.17	<0.01	0.40 max
Carbon	Not measured	0.010	0.05 max
Aluminum	< 0.01	<0.01	0.10[A] max
Magnesium	Not measured	<0.01	0.10[A] max
Zirconium	Not measured	<0.01	0.10[A] max
Titanium	< 0.01	<0.01	0.10[A] max
Chromium	< 0.01	0.12	0.25 max
Phosphorus	0.010	0.02	0.015[B] max
Sulfur	< 0.005	0.003	0.015[B] max
Copper	< 0.01	<0.01	Not in standard
Molybdenum	< 0.01	0.05	Not in standard
Selenium	Not measured	<0.003	Not in standard

[A] The total sum of aluminum, magnesium, titanium, and zirconium shall not exceed 0.20%

[B] The total sum of phosphorus and sulfur shall not exceed 0.025%

Unfortunately, the techniques at the external lab did not have the capabilities to measure several of the elements such as carbon, magnesium, zirconium, and selenium. However, in terms of the primary elements, the overall composition remains largely unchanged, with a deviation from the nominal nickel content of 0.4 wt. %. Based on Figure 11 (section 2.2) this would result in a negligible increase of the thermal expansion coefficient. Although the measured trace elements deviate from the composition listed by the supplier, their specifications are still within the allowed maximum and should not influence the thermal expansion behaviour of the material to a large degree. In fact, the lower amount of the majority of the listed trace elements is expected to lower the thermal expansion

of the material even further. However, since these trace elements are normally used to enhance the mechanical properties, there may be a decrease in those properties, if measured in the future.

3.2.2 Particle Size

The particle size distribution for the powder is shown in Figure 16. The error bars for the distribution represent one standard deviation from the mean, as calculated from the three repeated runs through the Camsizer X2. The dotted red line (Mean Q3) describes the cumulative percentage of all measured particles below a specific particle size. The other curves on the plot describe the volume fraction of particles of a specific size and is plotted on the secondary y-axis scale on the right hand side. There were also fitted curves generated (marked by ──▲── and ──✕──, respectively) that extract the distribution of powder size. The sum of the fitted curves is shown by a dotted curve ⋯✳⋯, which appears to fit well to the underlying data.
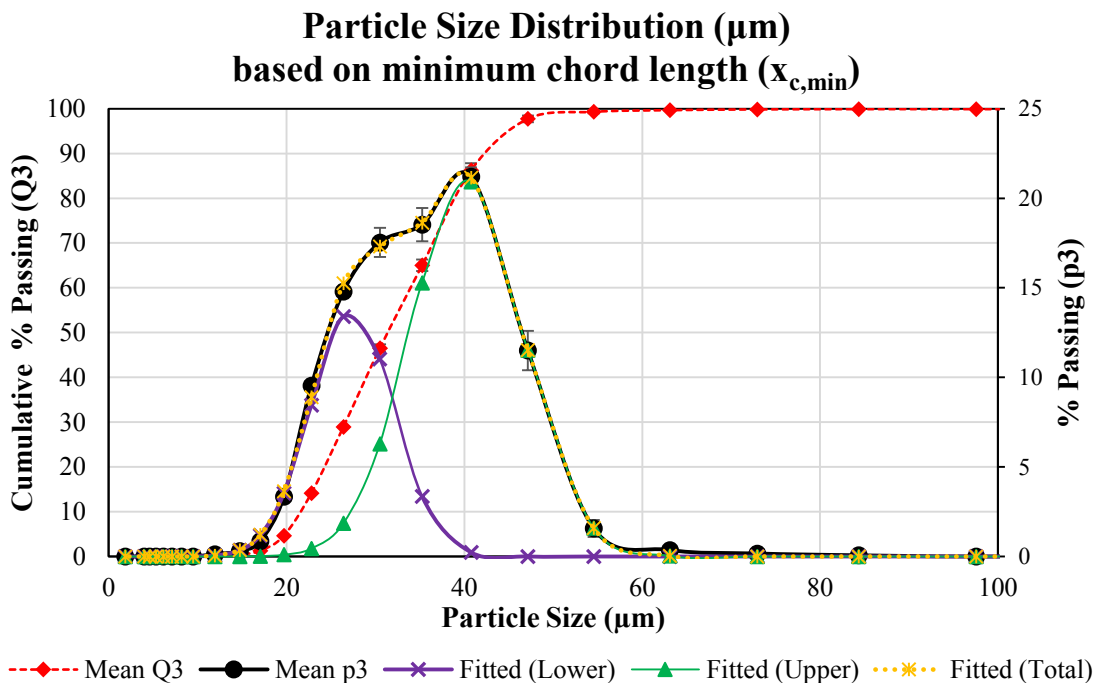
Figure 16. Measured particle size distribution of the Invar36 powder, with a mixed Gaussian model fitted to the data to demonstrate the bimodal distribution of the powder.

It is immediately clear that, based on the D_{10} (10% cumulative passing) and the D_{90} (90% of cumulative passing) of the powder, the powder size spans a range between 21–40 μm. Overall, the size distribution conforms well to the supplier specifications, stating a maximum size of 45 μm, and a

well-centered D_{50} of 30 μm. However, there are a few causes of concern. Particularly, the remaining 10% cumulative passage of particles above the D_{90} displayed larger sizes than the reported values. The reasoning for this may be because of powder agglomeration that may have occurred since initial acquisition of the powder. As mentioned in section 2.1.1.2, this is a phenomenon that is known to happen in LPBF, especially for finer powders. When considering the impact this may have on the experiments, larger layer thicknesses will have to be selected to account. Another cause of concern is that upon fitting a mixed Gaussian model to the data, it can be seen that the powder appears to follow a bimodal distribution, centered about 27 μm and 40 μm. It has been discussed previously that bimodal distributions have better compaction and absorption than single mode distributions of the same size range, and as such, well-performing recipes generated with single mode powders may become over melted with bimodal powders.

3.2.3 Powder Morphology

The SEM micrograph in Figure 17 illustrates one representative image taken for the powder morphology. A detailed set of images is presented in Appendix B. Upon initial observation, it appears that the particles are mostly uniform and spheroidal in nature. There is also a noticeable presence of particles with satellite features, oblong particles, agglomerated particles, and non-uniformity in general. Furthermore, some particles are clearly shown to be porous, with hollow voids extending from their internal to external areas. These morphologies are shown in detail in Figure 18. The presence of pores in the particles is most likely due to the gas atomization technique used to create the powder, as discussed in section 2.1.1.2, and may be a concern if the porosity gets translated to final bulk parts. In terms of the non-uniformity, the larger surface-to-volume ratio of the non-spherical particles will result in greater laser absorption, and may result in excess heat input during processing. Additionally, there may be concerns with the rheological properties of the powder due to the abnormal particle shapes.
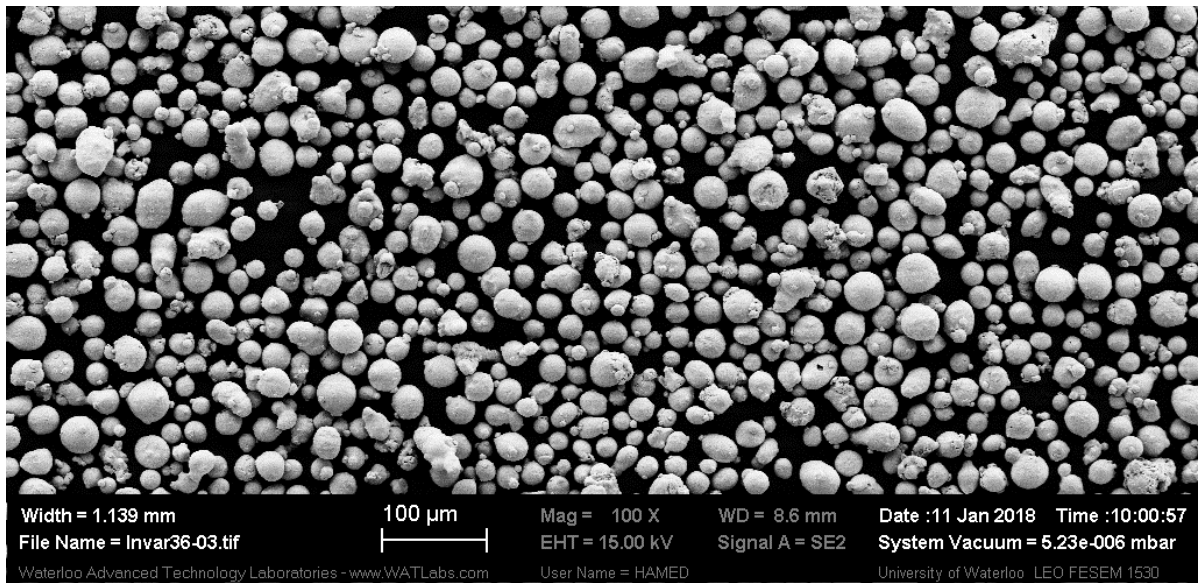
Figure 17. SEM micrograph taken of the Invar36 powder distribution.
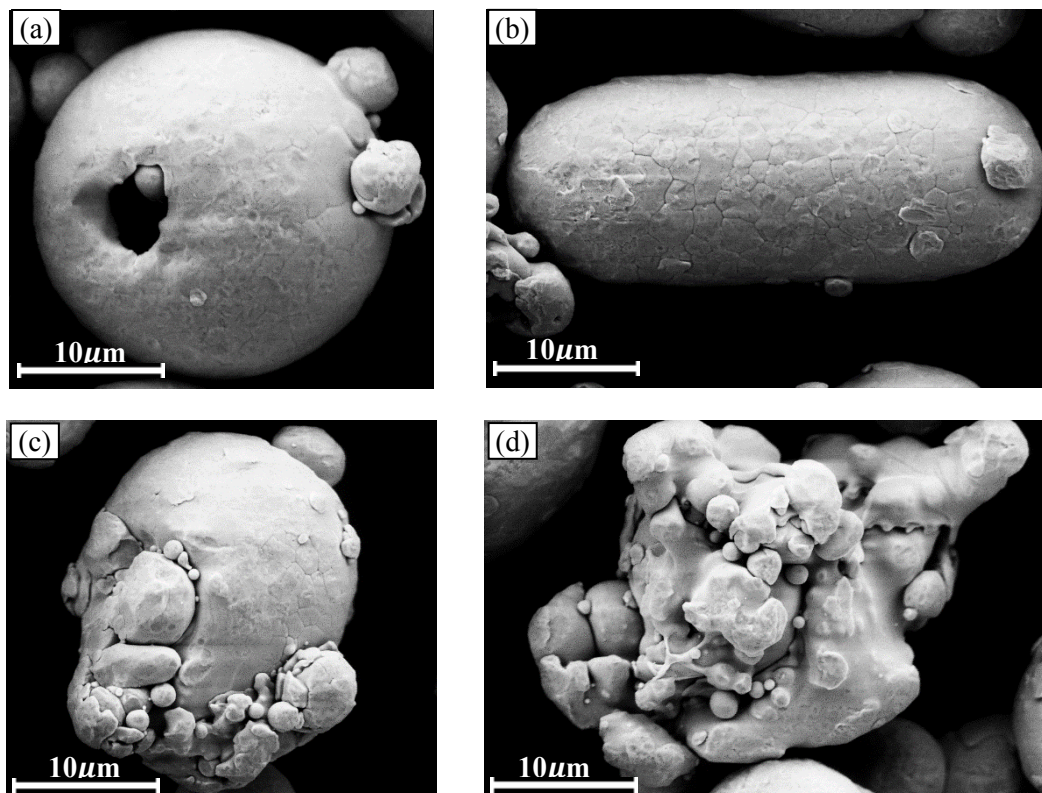
Figure 18. Representative particles showing various morphologies including (a) pores and satellites, (b) oblongated, (c) agglomerated, and (d) general non-uniformity.

3.2.4 Powder Rheology

Shown below in Table 11 are the general properties of the powders used as comparison in this section. As well, presented below in Table 12 is a table summarizing the various indicators calculated from the stability and variable flow rate tests, and Figure 19 shows the measurements taken for it. Figure 20 to Figure 23 plot the measurements taken for the various experiments. For the measured statistics in the table, a 95% confidence interval was calculated based on a three sample t-distribution. Also, data from literature is also provided as comparison, when available.

Table 11. General powder properties of literature material, as referenced from [98].

Material Description	D_{50} [μm]	Shape
GL glass beads	174	Spherical
GS glass beads	68	Spherical
Aluminum powder	134	Irregular
Tungsten powder	4	Angular

When observing the results in Table 12, it can be seen that Invar36 has a similar basic flowability energy (BFE) and specific energy (SE) to the glass samples from literature, within the bounds of error. These two values are derived from the stability and variable flow rate testing, and are indications of the shear forces preventing the material from flowing in low stress flow conditions [98]. Its low value indicates that the powder behaves non-cohesively, especially when compared to the cohesive tungsten powder. The flow rate index quantifies the difference in flow energy required between the fastest blade speed test and the slowest blade speed test. Higher flow rate indices show a powder's sensitivity to flow stress, and is indicative of increase cohesion within the powder. For the Invar36 powder, it performs in a similar regime to the GL and GS glass material in literature, which were examples of non-cohesive powders. Lastly, the conditioned bulk density (CBD) and the tap density (TD) give an idea of the powder density in an unpacked and packed state. CBD values near TD values indicate a powder that is efficiently packed. For the values of Invar36, it has the worst values of all the other listed materials. This may be due to the non-uniformities present within the powder, as discussed previously.

Upon observation of the aeration tests in Figure 20, the Invar36 powder performs very similarly to the GS Glass sample, and the quick tendency for both of the powders to reach zero energy state indicate their non-cohesivity. In contrast, the tungsten powder is shown to have much higher energies, and does not reach a zero energy state. This is because the material may be forming air-channels and rat-holes instead of becoming fluidized; this behaviour is indicative of cohesive powders [98].

42

Table 12. Powder flow properties for the Invar36 powder, supplemented literature values [98].

Indicator	Unit	Invar36 (measured)	GL Glass (literature)	GS Glass (literature)	Aluminum (literature)	Tungsten (literature)
Basic Flowability Energy (BFE)	$[mJ]$	726.25±202.02	1431	899	3300	5964
Specific Energy (SE)	$\left[\frac{mJ}{g}\right]$	3.03±1.014	3.36	2.36	4.40	6.70
Flow rate index (FRI)	$[-]$	1.18±0.096	1.04	1.02	1.48	1.40
Conditioned Bulk Density (CBD)	$\left[\frac{g}{mL}\right]$	4.17±0.148	1.44	1.46	1.24	4.17
Tap Density (TD)	$\left[\frac{g}{mL}\right]$	5.07±0.154	1.50[A]	1.49[A]	1.34[A]	4.97[A]

[A] Consolidated with 20 taps

The compressibility plot gives an idea of how much the powder can compress with increasing normal loads applied to it. Larger compressibility values are associated with materials that are less efficiently packed, more cohesive, or both. The values for Invar36 appear to be relatively similar to the aluminum powder, but are much lower than the cohesive tungsten powder. Since the value is much lower than with tungsten, it appears as if the powder is much less cohesive than the tungsten, but is still not as efficiently packed as it can be, compared to the glass materials.

The measurement tests for permeability is used as an indicator of how easy it is to transmit a fluid through the powder, and it is affected by many different factors. Generally, finer powders are known to decrease permeability, because of the absence of large voids characteristic of larger particle sizes. Irregular shaped powders are also more permeable for the opposite reason, with the larger amount of void structures within them. Cohesive powders are also known to increase permeability as the entrapment of air within the powder bed is increased. For the Invar36 powder, it appears to lie within a median zone between the most permeable powders (GL glass and aluminum) and the least (tungsten). This is most likely due to its relatively small particle size (D_{50} of 30 μm) in comparison with the other materials, and not the general cohesiveness of the powder. However, even with its smaller particle size, it performs similarly to the GS glass, which has a D_{50} of 68 μm. Thus, it may indicate that the Invar36 powder performs well for a material in its particle size regime.

Lastly, the shear testing results measure the amount of shear stress to induce flow in the powder at any given applied normal stress. Since shear is the primary method of flow for powders, higher values of shear stress indicate powders with less propensity to flow. In Figure 23, the Invar36 powder

appears to be following a similar trend to the aluminum samples, but it is difficult to distinguish because the literature materials were measured at lower applied normal stresses. However, the higher values for the material may be a concern when initiating powder flow during processing. This is especially important as the amount of powder in the hopper becomes low and gravity becomes less effectual for inducing powder flow.

To conclude, the results found within this chapter indicate that the Invar36 powder is generally non-cohesive, which is beneficial for power flow. However, the larger compressibility, the larger differential between tap and conditioned bulk density, and the larger permeability values indicate that the powder is not as efficiently packed as it can be. It has been hypothesized that this is due to the non-uniformities present in the powder samples, as discussed previously. The higher values obtained in shear testing results also indicates that the powder may behave non-ideally when hopper volumes become low, and thus it may be beneficial to refill hoppers earlier when using this material.
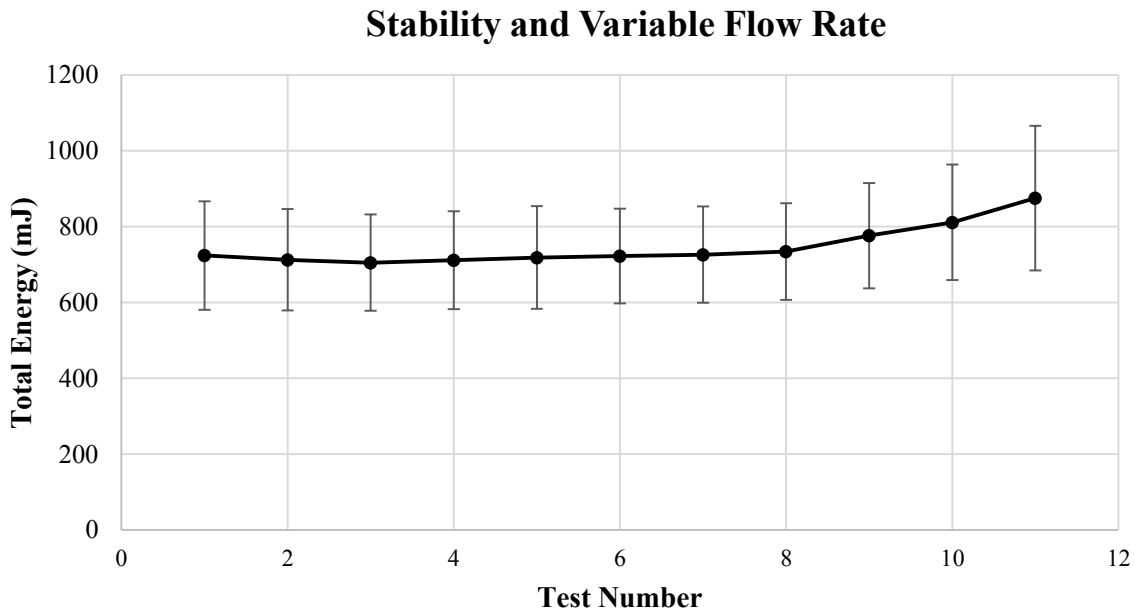
Figure 19. Measured results from the stability and volumetric flow rate testing. Error bars indicate one standard deviation from the mean. Test runs 1-7 show the stability testing, and test runs 8-12 show the variable flow rate testing.
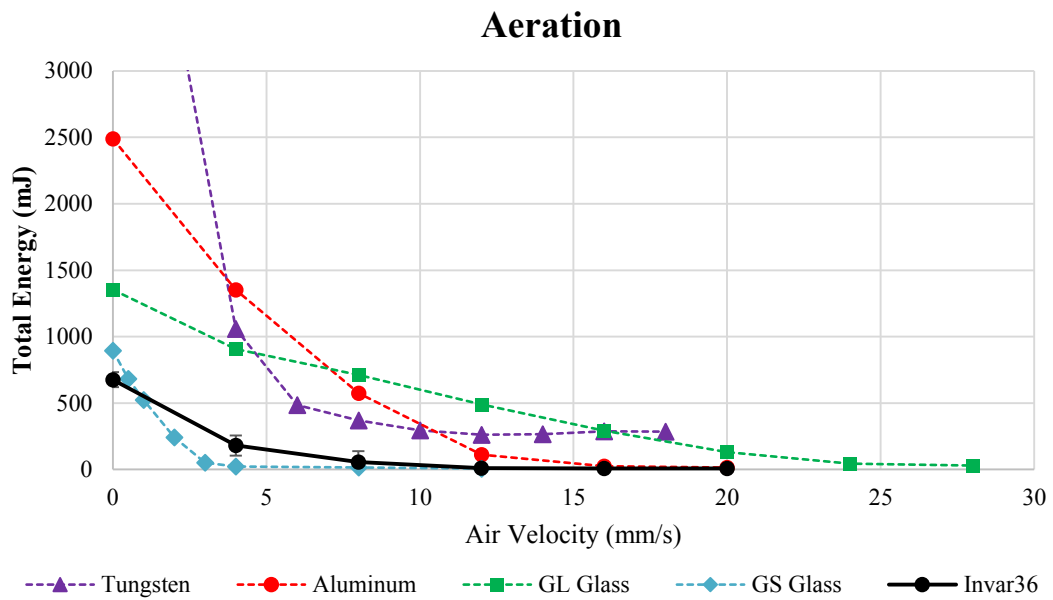
Figure 20. Measured results from the aeration testing. Error bars indicate one standard deviation from the mean. Dashed curves represent plots from literature [98].
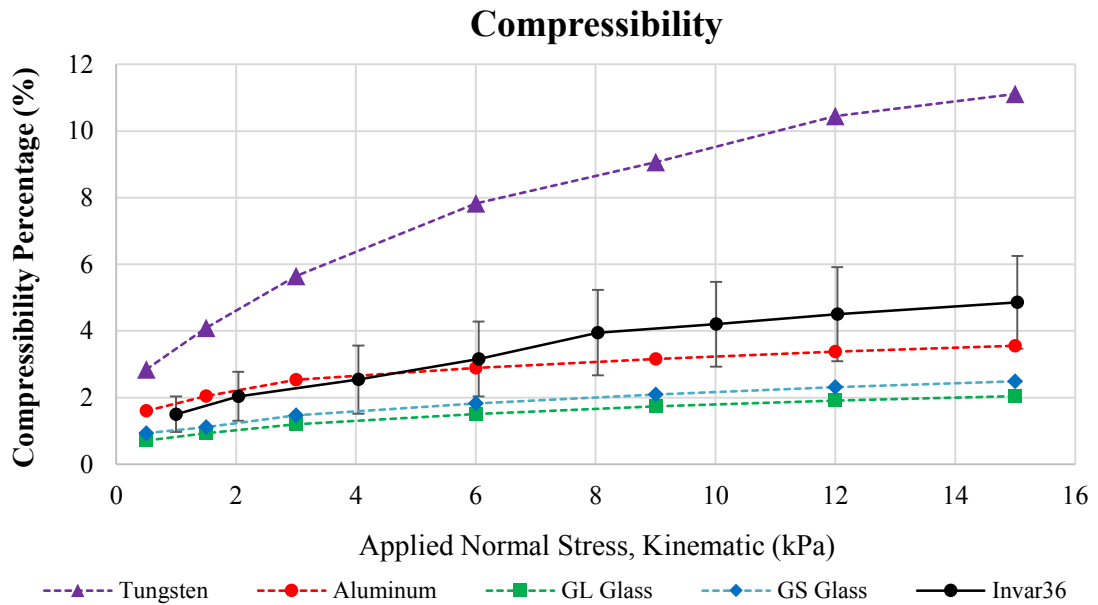
Figure 21. Measured results from the compressibility testing. Error bars indicate one standard deviation from the mean. Dashed curves represent plots from literature [98].
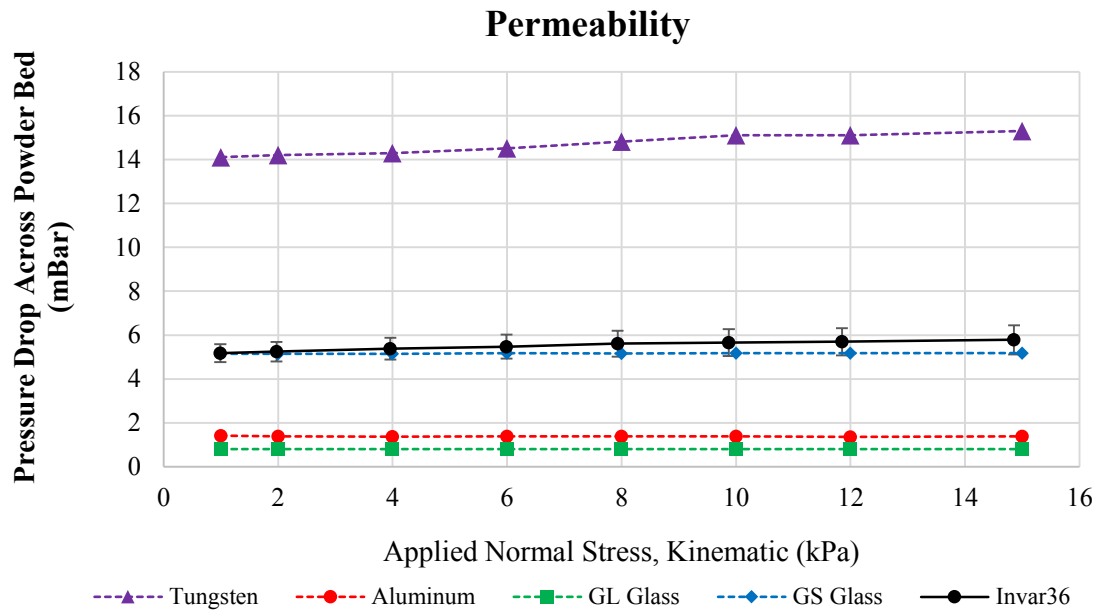
Figure 22. Measured results from the permeability testing. Error bars indicate one standard deviation from the mean. Dashed curves represent plots from literature [98].
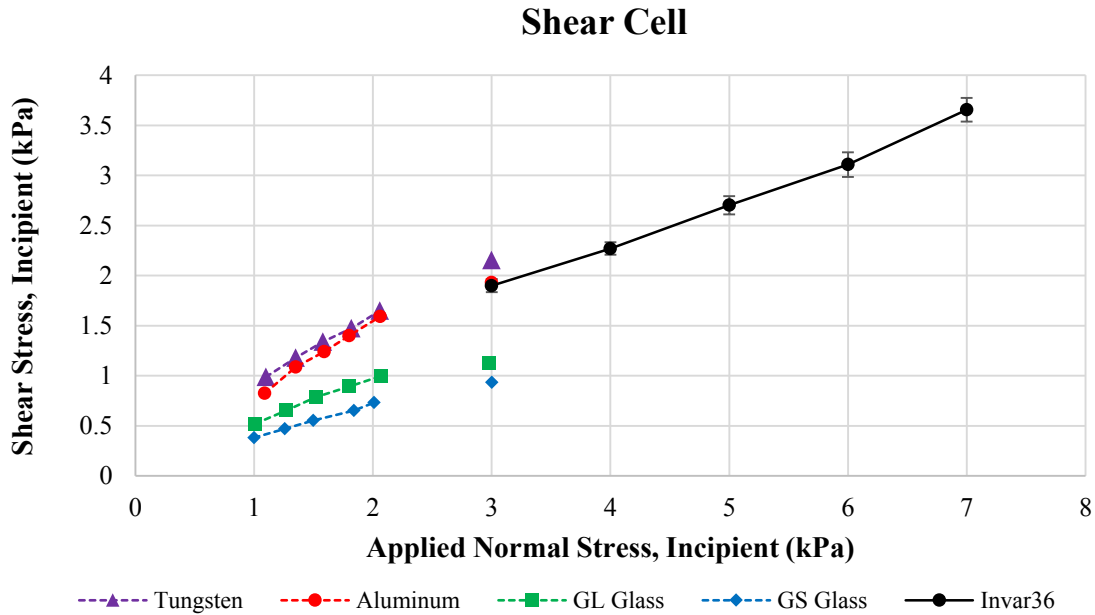
Figure 23. Measured results from the shear cell testing. Error bars indicate one standard deviation from the mean. Dashed curves represent plots from literature [98].

Chapter 4

Experiment 1: Process Mapping and Process Window Identification for Part Density and Coefficient of Thermal Expansion

The experimental work done for this thesis has been divided into two different experiments. The current experiment focuses on the development of a process map for the minimization of bulk porosity and thermal expansion characteristics of LPBF-built Invar36 parts. An energy density approach is used as a tool to translate and to select reasonable recipes from literature. Based on the best practices for LPBF, as discussed in section 2.1.1, a build is set up and then analyzed for porosity with computed tomography (CT) scanning, and for thermal expansion behaviour with thermo-mechanical analysis. Using statistical analysis techniques, an optimal process window is then identified from the generated process map.

4.1 Experimental Methods

Based on previous work performed by Qiu and by Harrison [59], [60], samples fabricated with volumetric energy densities in the range of $106.67 - 277.78 \left[\frac{J}{mm^3}\right]$ were found to produce samples with appreciably low porosities <0.5% [59], [60]. These two existing works on LPBF of Invar36 have been performed using continuous mode laser beams. In the context of this work, the energy density range from literature was used as guidance, and an experiment was designed with the goal of developing a process map for the modulated laser beam LPBF process, and furthermore, for finding an optimal process window for achieving fully dense parts. As previously mentioned, significant build variables that affect the energy input in a LPBF fusion process are power, speed, hatching distance, and layer thickness. For the Renishaw AM 400 system, the equivalent energy input parameters are power, exposure time, point distance, hatch distance, and layer thickness. By varying these build variables, a full factorial design was constructed to analyze their effects on part density and CTE. The chosen levels for the manufacturing plan are defined below in Table 13.

Table 13. Build variables that were modulated for the manufacturing plan.

Build Variable	Unit	Levels					
Power	[W]	250	275	300	350[A]	375[A]	400[A]
Grid distance	[μm]	60	70	80			
Exposure time	[μs]	60	70	80			
Layer thickness	[μm]	30					

[A] Corresponding to parts created in a second build

Build variables that are constant and that do not pertain to the volumetric energy density are not shown in the above table, but the entire set of possible build variables can be referenced in Appendix A. However, it should be noted that since the purpose of this initial build was to only investigate the effects of energy density on part density and coefficient of thermal expansion, build variables not pertaining to energy density were disabled when possible. With all five factors varied at multiple levels, the number of printed samples would have been unreasonable. For example, if all levels were excited at only two levels, the resulting experiment would have required $2^5 = 32$ samples. With three levels, the number would have increases to 243.

To reduce the number of samples to a more reasonable amount, the layer thickness was set to a constant value of 30 μm. The reasoning behind this is because the Renishaw AM 400 system is not capable of modifying layer thickness in-situ on a sample-by-sample basis. In terms of the selected value for the layer thickness, even though the supplier reported particle size was 44 μm, the 30 μm selection was deemed acceptable. This is due to the fact that, although the first layer may not be laid to the proper height (in terms of particle size), due to the inherent powder bed porosity, the effective layer thickness over time quickly becomes much larger than the original layer displacement. For example, based on the density of the laid powder bed, effective layer thickness can increase by 40%-150% [103], [104].

To further lessen the sample count, the hatch and point distance were linked 1:1. For example, when the hatch was set to 60 μm, the point distance was also set to a 60 μm. Unfortunately, because of this fact, the results presented in this work cannot separate the individual effects of these two build variables, and instead reports the combined effect (henceforth, referred to as 'grid distance'). Lastly, due to the amount of samples that were still required, a second build was printed to investigate the effects of higher power levels (denoted by superscript 'A' in Table 13). To close, the experiment required a total of 54 treatment combinations, and up to four replicates were fabricated for the analysis of part quality (216 total samples). Fractional factorial designs were considered as well to reduce sample count, but since the significance of interaction effects were unknown and only a limited number of builds were available for printing, the full factorial design was retained.

By giving a unique identification to each permutation of the build variables, Figure 24 is obtained. The detailed build variable table with accompanying identification labels are located in Appendix C, but the build variable levels can also be discerned from observation. Within the figure there are six

groups of nine points each; this corresponds to the six power levels. Each group contains three lines of adjacent points, which correspond to grid distance. Within each line, there are three points that correspond to exposure time. To clarify, the groups have increasing power from left-to-right, the lines correspond to increasing grid distance from top-to-bottom, and the points correspond to increasing exposure time from left-to-right. This is visualized by Figure 25. The upper and lower bound lines in Figure 24 illustrate the ranges of energy density found in literature to have low porosity (< 0.5%), and it can be seen that all sample points lie near or within this energy band.
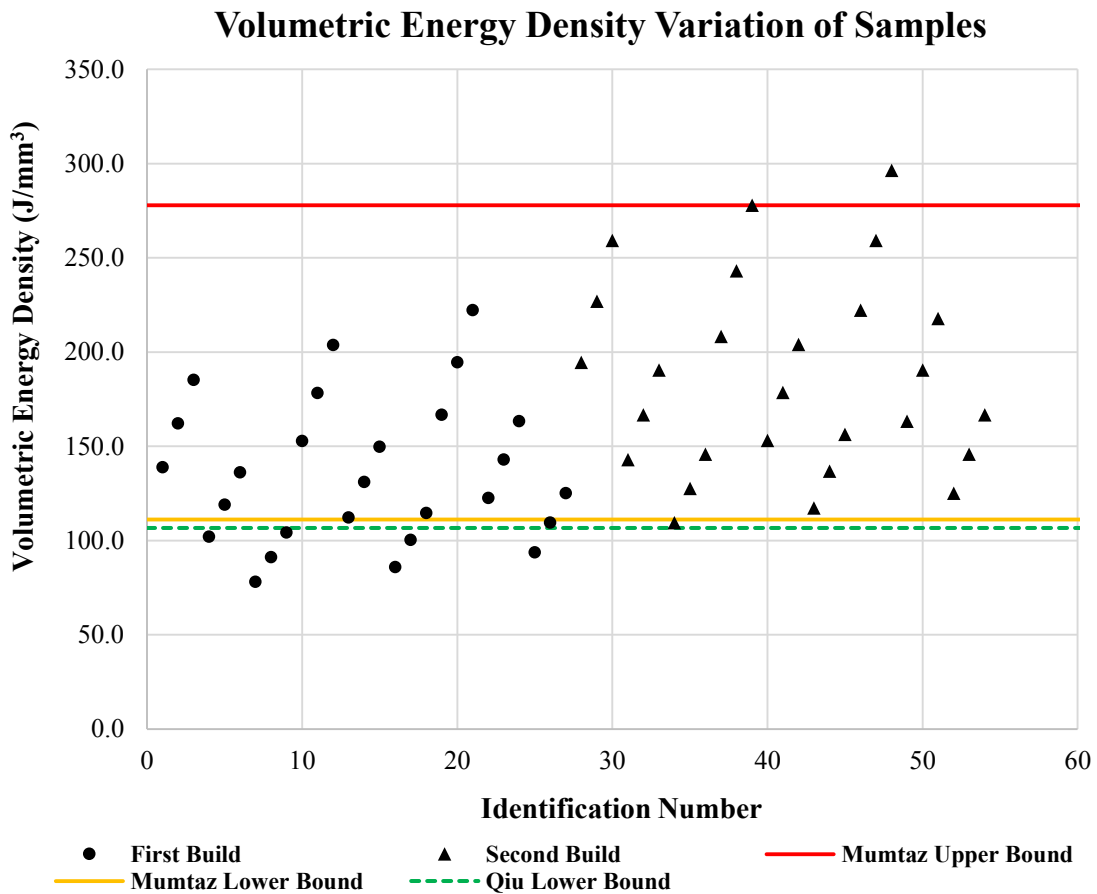
Figure 24. Variation of volumetric energy density across all permutations of variables.
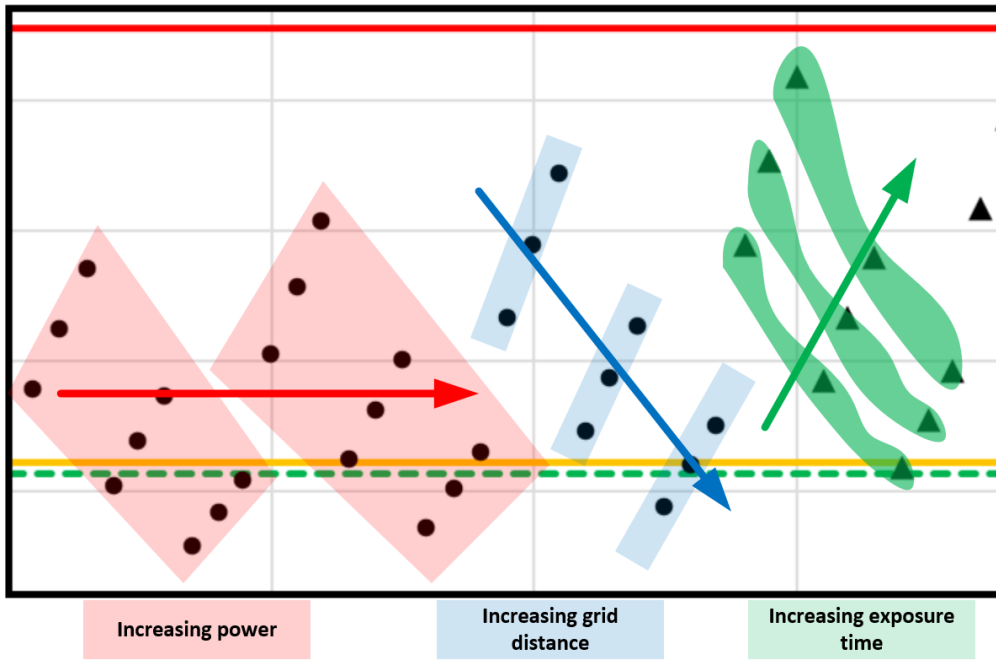
Figure 25. Explanatory figure showing influence of build variable choice on the point spread.

4.1.1 Selection of Standardized Artefacts

The selection of the standardized artefact was chosen to enable the possibility of fabricating the experiment in as little builds as possible, while still being flexible enough to analyze different process outcomes. The geometry of the artefact was selected was to enable both CT and thermo-mechanical analysis, and it can be referenced below in Figure 26.
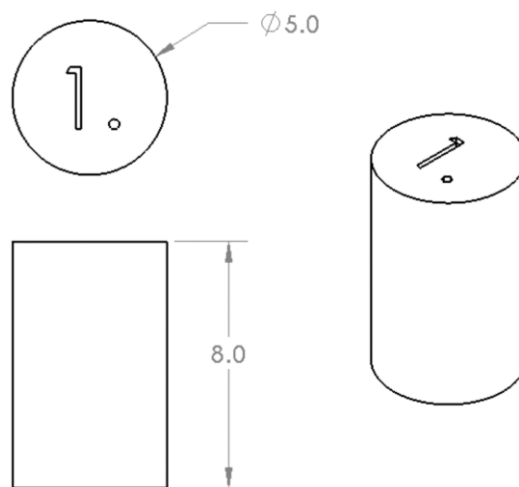
Figure 26. Sample geometry for measuring density and CTE (not to scale), with units in mm.

The dimensions of 5 mm diameter and 8 mm height were chosen such that the samples could be analyzed through CT imaging, as well as evaluated for their thermal expansion characteristics. According to ASTM E831-14, "Standard Test Method for Linear Thermal Expansion of Solid Materials by Thermomechanical Analysis", sample specimen geometry for thermal expansion measurements are required to be between 2 and 10 mm in length, not have lateral dimensions exceeding 10 mm, and have flat and parallel ends within $\pm$ 25 μm [105]. Deviations from the standard are reported to be acceptable, but may decrease the precision of measurements [105]. The limiting factor for CT scanning was with the overall sample thickness and volume. Thicker samples would have required longer exposure for X-ray penetration, and taller samples would have needed more images to be taken. Samples were therefore given a small footprint to expedite the CT scanning process. Lastly, samples were also given numeric identification labels for traceability purposes.

Supplementary standardized artefacts were also created for future study on the elastic properties, surface profile, and microstructure, but are not covered within the scope of work in this thesis. They are reported on in this work because of their influence on the build layout of the experiment. Figure 27 illustrates the geometries for the supplementary artefacts. A cubic geometry was chosen to be able to easily analyze the microstructure and surface profile along different directions. The dimensions were selected to be able to compare against similarly designed specimen in literature [59]. The large cylinders were created for the purposes of compression testing and conform to recommendations as per ASTM E9-09, "Standard Test Methods of Compression Testing of Metallic Materials at Room Temperature".
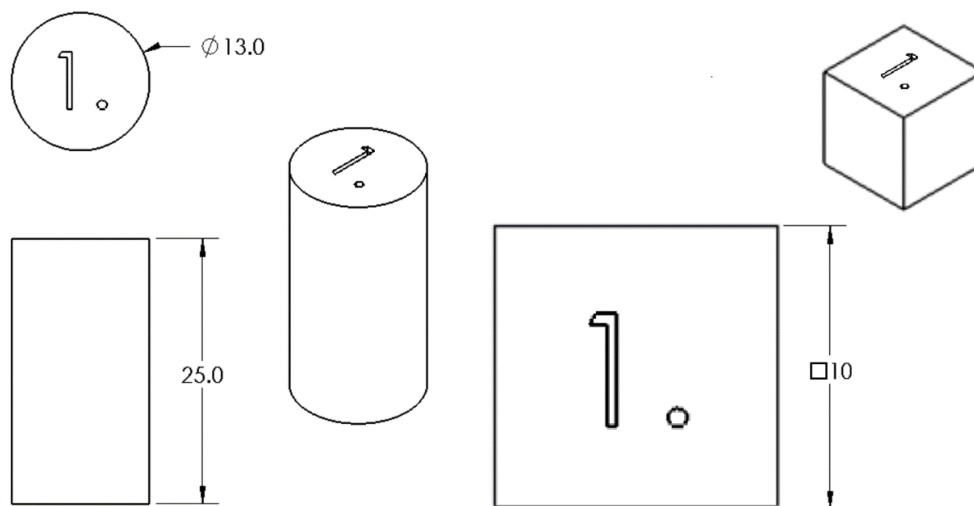
Figure 27. Additional artefact geometry for auxiliary studies (not to scale). Units are in mm.

For the density/CTE samples, four replicates were placed on the build to obtain a statistically relevant sample set. Due to their size, the larger compression testing cylinders were only given two replicates. Finally, since the microstructure cubes are largely for qualitative analysis, the microstructure cubes were only given one replicate. Although four replicates were stated to be printed for the density/CTE specimen, by the time the second build was ready to be printed, it became clear that CT analysis could only facilitate the imaging of one replicate, and thus the replicate count was reduced to two for the second build (in the event that a second replicate could be imaged in the future).

4.1.2 Build Layout

The build was laid out such that specimen of differing geometry types were grouped together if they had the same build variable combination, but between sets of build variable combinations, the locations were randomized. The entire layout was rotated by 5° clockwise to reduce the contact with the recoater blade during the spreading of new powder layers. Shown in Figure 28 and Figure 29 are the layouts for the first and second build, respectively. The green-shaded areas denote the layout for samples following the experiments described in this work, while red-shaded areas are samples that follow separate build variable combinations for auxiliary studies unrelated to this work. The second build was printed at the same time as the second experiment (will be further discussed in Chapter 5), and it is shaded in blue.
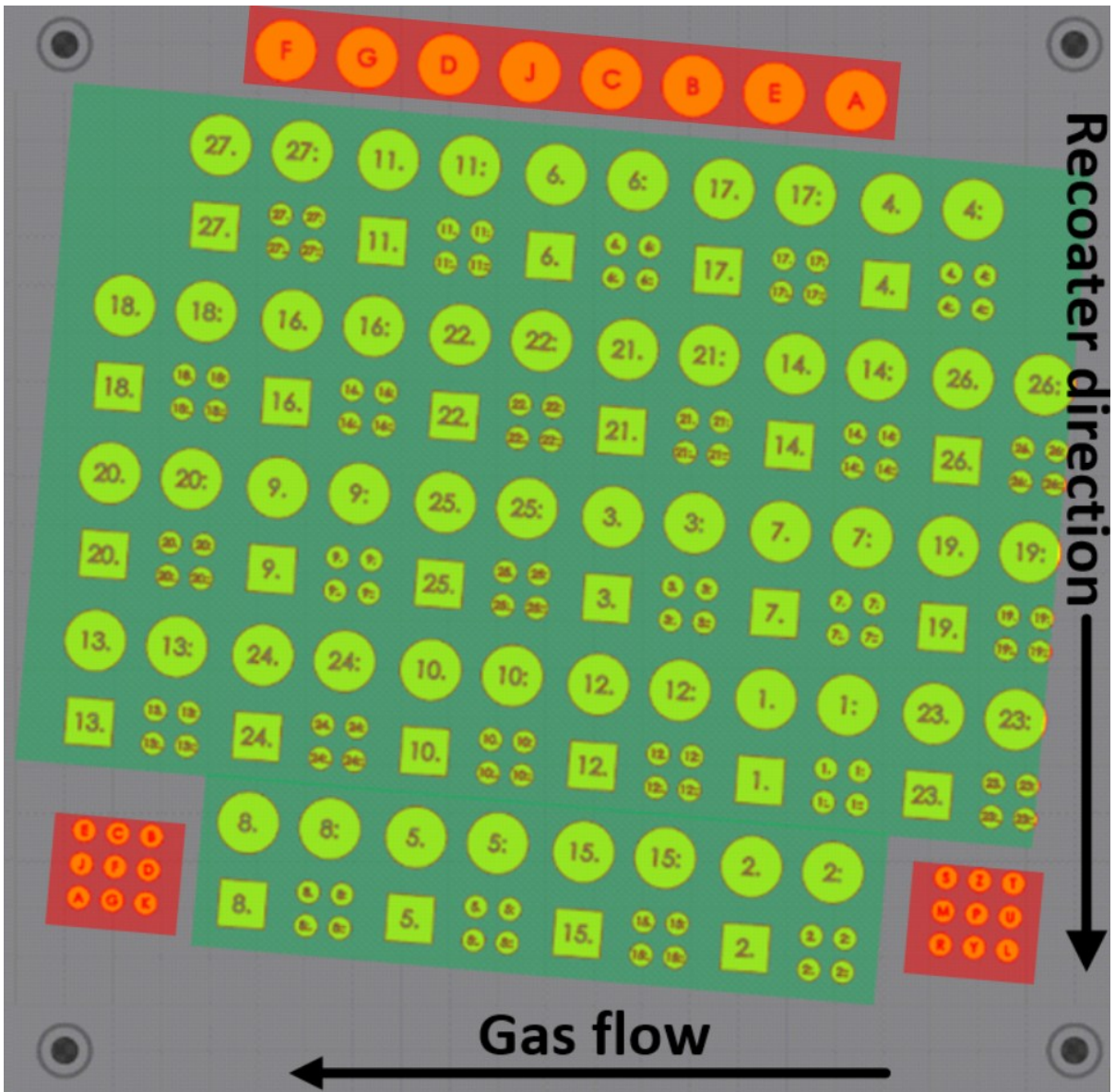
Figure 28. Layout for the first build with green-shaded areas denoting samples for the main experiment, and the red-shaded areas for auxiliary samples.
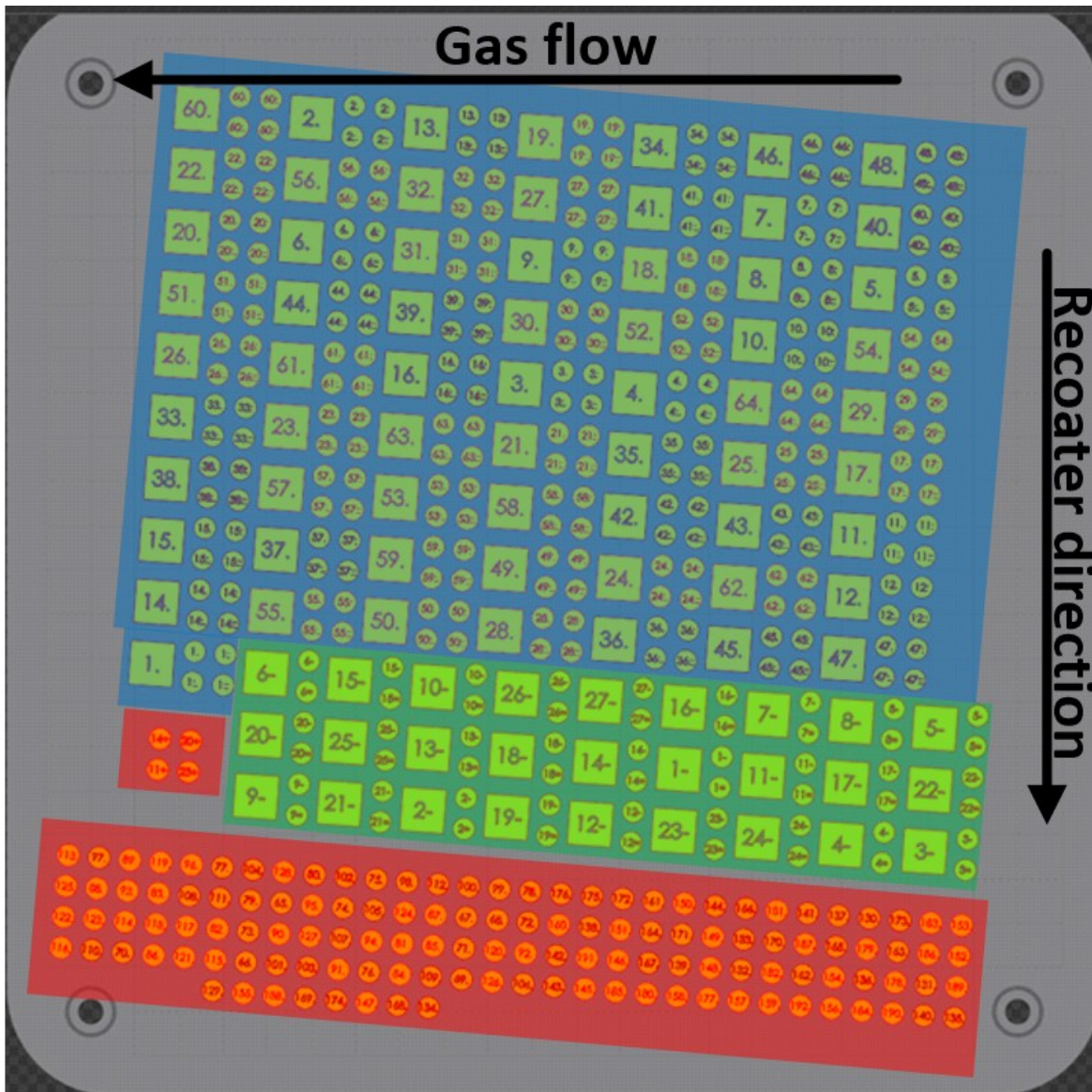
Figure 29. Layout for the second build with green-shaded areas denoting samples for the main experiment, red-shaded areas for the auxiliary samples, and blue-shaded areas for the second experiment.

4.1.3 Computed Tomography

The purpose of deploying computed tomography (CT) was to gain an in-depth visualization of the porous distribution within the printed samples. By quantifying the pore fractions within the sample volumes, it is possible to calculate the inverse (solid fraction), and thus effectively determine how dense parts became after solidification. Other methods to find part density were considered, such as

the application of Archimedes' principle through water displacement gravimetric analysis or gas displacement pycnometry, but were found to produce unreliable results. Specifically, for the water displacement gravimetry, the measurement scale used was not precise enough to capture the small differences between sample masses, and the temperature control for the water was not rigorous enough to capture differences in buoyancy. Moreover, the gas pycnometer failed to operate due to similar issues with temperature control. In addition to bulk density values for each sample studies, the CT data enabled a greater insight into the relationship between process parameters and pore size distribution, as well as spatially reconstructed pore location, pore morphology and pore orientation.

4.1.3.1 Image Acquisition

The imaging was performed by a Zeiss Xradia 520 Verse X-ray microscope, with the following Scout-and-Scan software settings applied for all sample analysis:

Table 14. Scout-and-scan settings for CT imaging.

Parameter	Unit	Value
Source power	[W]	10
X-ray energy	[kV]	140
Filter	-	HE4
X-ray optic	-	0.4× lens
Source position	[mm]	21.36
Detector position	[mm]	10.37
Exposure time	[s]	2.0
Number of projections	-	1001
Binning level	-	1
Voxel size	[μm]	12.0

The settings were chosen based on recommendations in the operating manual to obtain a strong enough signal, while still providing adequate contrast to distinguish features within the sample volume. A voxel (three-dimensional pixel) size of 12 μm was the smallest possible size chosen to be able to CT image all the samples within a reasonable amount of time. As mentioned in section 4.1, even with these settings, only one replicate of the experiment was able to be analyzed in this work. After scanning, images were automatically reconstructed into 16-bit greyscale .TIF for further processing.

4.1.3.2 Image Processing

A large volume of data was extracted from the CT imaging, which required the use of MATLab to automatically process the results. By using MATLab's built-in image processing capabilities, it was possible to quantify details regarding the pore size, shape, orientation, and location within the sample volume. Although the MATLab code detailing the exact procedure can be referenced to in Appendix D, the general methodology is described below to provide a basis of understanding for the results.

4.1.3.2.1 Image Contrasting

The first step for the analysis was to balance the contrast and brightness levels in the image to eliminate the background material and isolate the part volume. Figure 30, below, illustrates the image data before any processing. The light-grey areas correspond to the sample volume, while the darker grey area corresponds to the background material. The black areas are conversion artifacts from translating the cylindrical image space into images that have rectangular borders, and do not correspond to actual measured data.
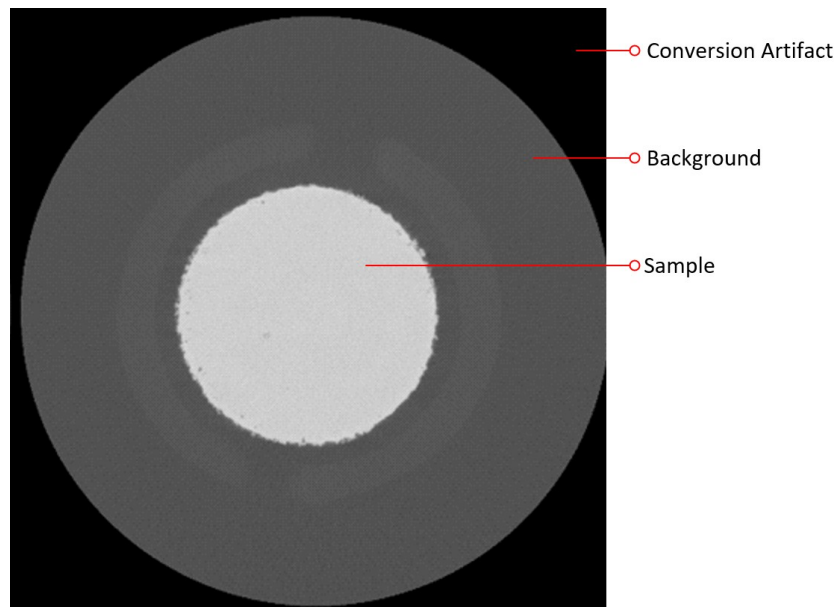
Figure 30. A single image slice of a CT scanned sample, showing unprocessed visualization of the image space.

To eliminate the background material, a threshold was set to truncate unwanted brightness intensity values. An example representing this procedure can be seen below in Figure 31. The image histogram is on the left, with intensity values ranging from 0 to 65535 (16-bit images have $2^{16}-1=65535$ levels of

brightness). Out of the two intensity distributions within the histogram, the lower intensity peak corresponds to the background noise from un-attenuated X-ray signals captured from the ambient environment. There is also a singularity at zero intensity because of the black borders of the image, which, to reiterate, is an artifact of converting a circular image space into a rectangular image. The corrected image contains values located within the red-shaded rectangular area, the limits of which have been defined through manual inspection as a right-tailed intensity drop-off to 0.5% from the nearest intensity peak. The limits within the red-shaded box were rescaled to fit an intensity distribution between 0 and 65535. The result of the contrasting procedure is shown on the right-hand side, showing that only the sample volume is present within the image space.
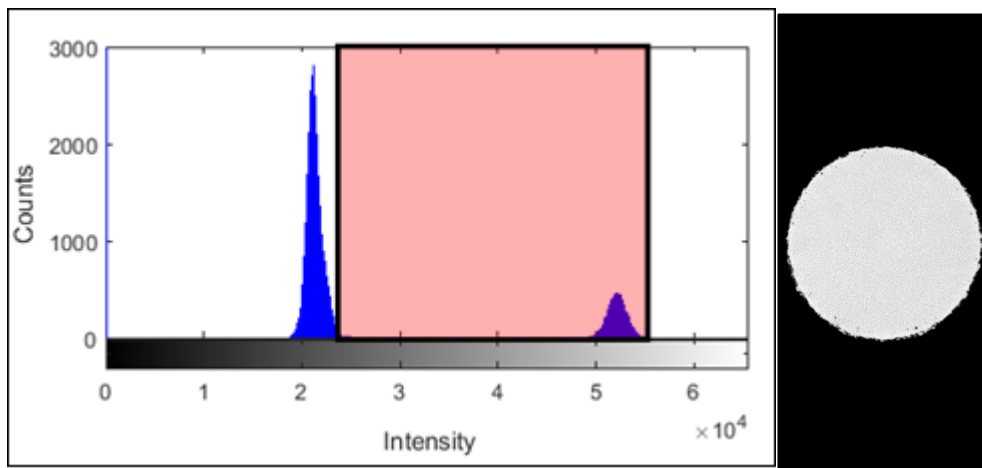
Figure 31. A typical image histogram on the left, illustrating the contrasting procedure with the selected rescaled values in red. The resulting contrasted image is shown on the right.

4.1.3.2.2 Image Segmentation

The next step for the image analysis was to isolate the intensities that corresponded to the porous defects from the bulk material, and similar to the previous step, an intensity threshold was defined (Figure 32). Through manual inspection of the pores, a left-tailed intensity drop-off to 1% of the peak value was found to adequately capture the edges of the pores. This is shown in the figure as a vertical red line. Instead of rescaling the image, the values were binarized with values of zero corresponding to pores and values of one corresponding to bulk material. As a noise reduction technique, the image was then dilated and eroded using a voxel connectivity of 26. Figure 33 demonstrates the geometric representation of different voxel connectivity values. The cube hidden in the center of these shapes represents the original voxel, and cubes surrounding the center are the 'connecting' voxels. The voxel

connectivity was aggressively chosen since the result from the contrasting often introduced a large amount of noise.
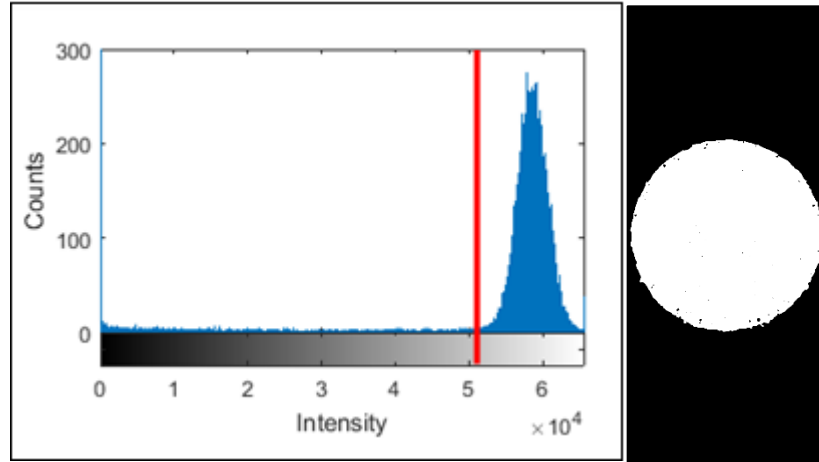
Figure 32. A typical image histogram on the left, illustrating the segmentation procedure. The set-point is defined by the red line. The resulting segmented image is shown in the right.
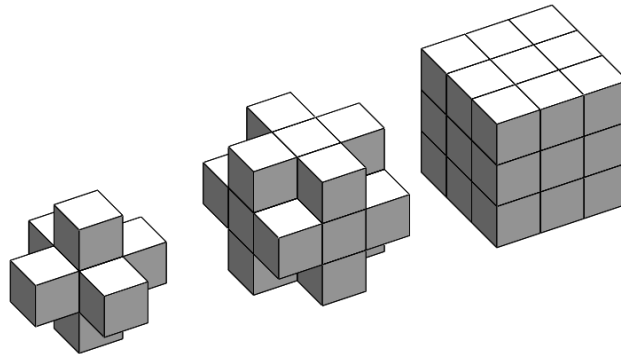
Figure 33. Sample image showing voxel connectivity. From left to right, the respective connectivity for each are 6, 18, and 26.

The dilation was performed to first grow the white sections of the image, where each white voxel expanded into its connectivity region. By performing this step, pores that were smaller than a 3×3 voxel cube were considered noise, and eliminated from the image space. To recover the lost pore volume from the dilation step, an erosion was performed to grow back the remaining black sections of the image to expand into its connectivity region. It should be noted that although this step reduces the amount of noise in the image, it also eliminates legitimate pores that were smaller than a 3×3 cube and also results in loss of fidelity for the pore geometry. Based on manual inspection, however, it was

found that the majority of pores within samples were much larger than 3×3 voxels and thus the loss of information for legitimately small pores was deemed acceptable. Additionally, since this research focuses mainly on the pore fraction and not the pore geometry, the loss of geometric information was also acceptable.

4.1.3.2.3 Pore Identification

To quantify the results, the fraction of zeros corresponding to pore volume needed to be isolated from the fraction of zeros that corresponded to background. To do so, an image masking operation was used to 'paint' the outside area and section it off from the 'zeros' corresponding to the inside. In two-dimensions, this step is similar to the use of 'fill' operations used in many graphics editors (Figure 34).
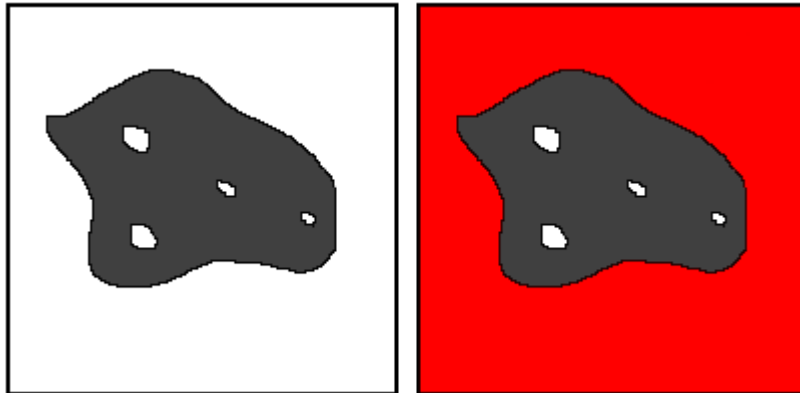
Figure 34. Schematic demonstrating fill operation in two-dimensional space. For illustration purposes, a red-colored fill operation is used to isolate the exterior from the interior of the part.

The threshold for voxel connectivity was chosen as 18, which is a more conservative approach taken such that more 'zeros' closer to the surface of the samples would be considered pores. This results in a slight overestimation of porosity, in comparison to smaller voxel connectivity values.

After masking, finding the pore fraction was a simple operation that involved quantifying the fraction of 'zeros' that corresponded to pores in the overall three-dimension image, from the fraction of 'ones' that corresponded to solid material. Furthermore, for additional analysis, MATLab's built-in function 'regionprops3' was used to extract the exact pore size, geometry, orientation, and location within the image space.

4.1.3.2.4 Image Output

To visualize the pore distribution within the sample, processed image outputs were also created. However, since the image data obtained from CT scanning was in a three-dimensional format, a two-dimensional representation was needed for presentation in this work. To do so, a minimum-intensity based projection method was employed. An explanation of the method is shown in Figure 35.
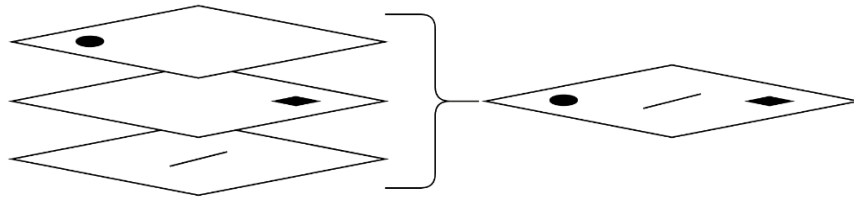
Figure 35. General schematic of the minimum intensity projection method, showing how the minimum intensities (colored black) become projected to the same plane.

Suppose that there are pores (colored black) along three different planes. Upon applying the minimum intensity projection, the dependency of the pores in one direction is eliminated by projecting the minimum values onto a single plane. As the figure shows, the in-plane orientation of the pores are preserved. This method of data visualization was applied to two different views of the samples (viewed from the top surface, and along the cylindrical section). It should be noted that since this method is only a projection of the pore distribution, it is not truly representative of the quantitative porosity within the samples; it does, however, serve as a good indication of the in-plane distribution of the pores.

4.1.3.2.5 Miscellaneous Steps

Aside from the techniques described above, the images were rotated using MATLab's 'imrotate' function with bilinear interpolation to align all samples alone the same global axes. Specifically, the images were rotated such that the cylinders were oriented as follows:
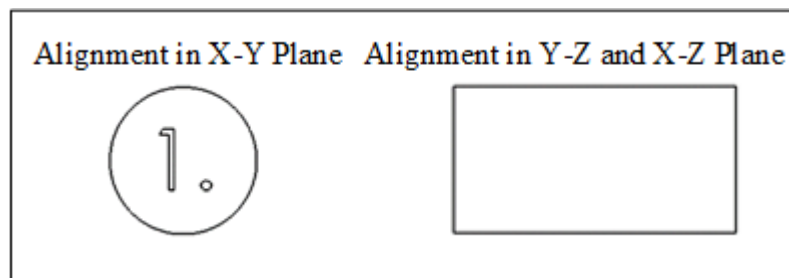
Figure 36. Schematic detailing the alignment of cylinders within CT images.

The alignment in the X-Y plane was chosen so the identification labels would be easily readable (parallel to English script orientation of left-to-right), and the orientation in the Y-Z and X-Z plane was chosen such that the projection of the cylinders into these planes resulted in an un-rotated cylinder from the axes directions. Continuing, due to interpolation defects from rotation, areas near the top and bottom tended to display artifacts, and thus had to be omitted from analysis. As well, near the top and bottom of samples the presence of X-ray related cone angle defects affected the visual clarity of the images and had to be omitted as well. Since cone angle defects can be detected by decreases in intensity, heights with >0.5% deviation from the average image intensity were considered affected by the cone angle defect, and removed. As a conservative estimate, additional 25 layers of cropping (with 12 μm voxel size, this results in 0.3 mm removed from analysis) was performed. In total, approximately 30% of the sample heights were not included in this analysis.

4.1.4 Thermal Expansion Measurements

The thermal expansion testing was facilitated by Dr. Geoffrey Rivers (University of Waterloo Advanced Composites and Adhesives Thermal Analysis Laboratory), with the analysis performed on a TMA Q400 thermo-mechanical analyzer by TA instruments. The testing was performed in accordance to ASTM Standard E831-14, "Standard Test Method for Linear Thermal Expansion of Solid Materials by Thermomechanical Analysis" [105].

The samples were placed on sample stages subjected to a nitrogen gas flow of 100 mL/min, and allowed to equilibrate at -70 °C for 10 minutes. A temperature ramp of 5 °C/min was then applied until samples reached 150 °C. Invar's constant thermal expansion properties break down as temperature increases to Invar's Curie temperature, and upon manual investigation, it was found that samples began to behave nonlinearly at temperature ranges of approximately 100 °C – 150 °C, and therefore the 150 °C was selected to reduce experiment run-time. The heating schedule for the samples is shown in Figure 37.

For the final calculation of the coefficient of thermal expansion, there was one deviation from the recommendations in the standards. According to the standards, the calculation for the linear CTE accounts for the change in length over temperature by taking the difference between the lengths and temperatures at two endpoints, as shown in Figure 38. In this work, the difference in length over time is instead found by constructing a line, through linear regression, between the two endpoints, and

taking the slope as the representative value. This deviation in standards is done because it better represents the behaviour of the material than by just averaging the measurements at two points.
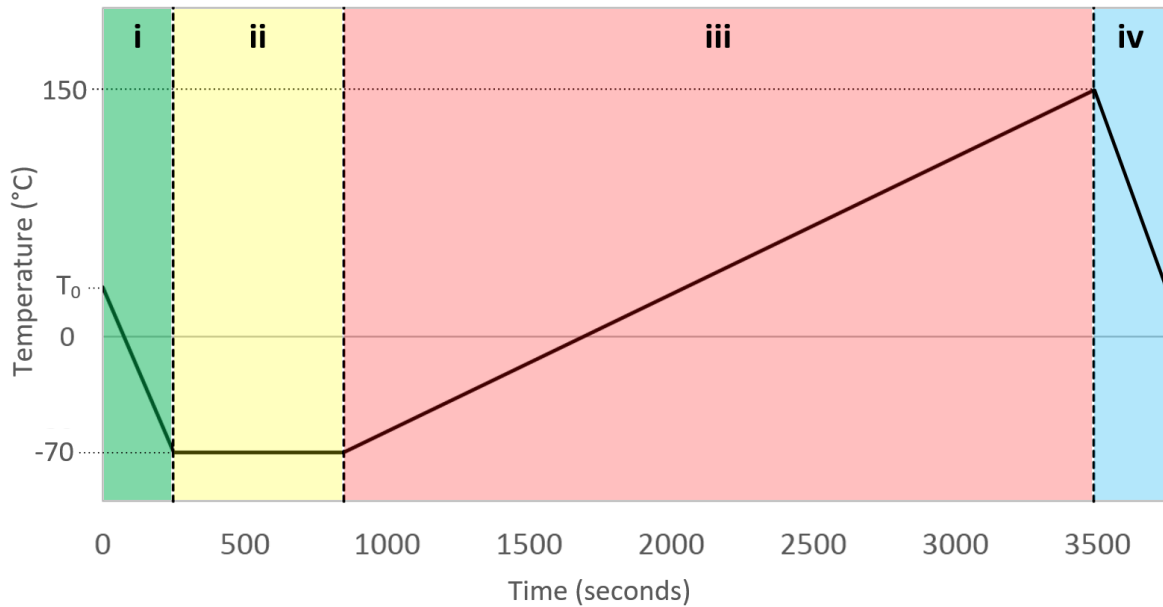
Figure 37. Schematic illustrating the heating schedule with (i) cooling to -70 °C, (ii) isothermal at -70 °C for 10 minutes, (iii) temperature ramp of 5 °C/min until 150 °C, and (iv) unload machine and return to room temperature.
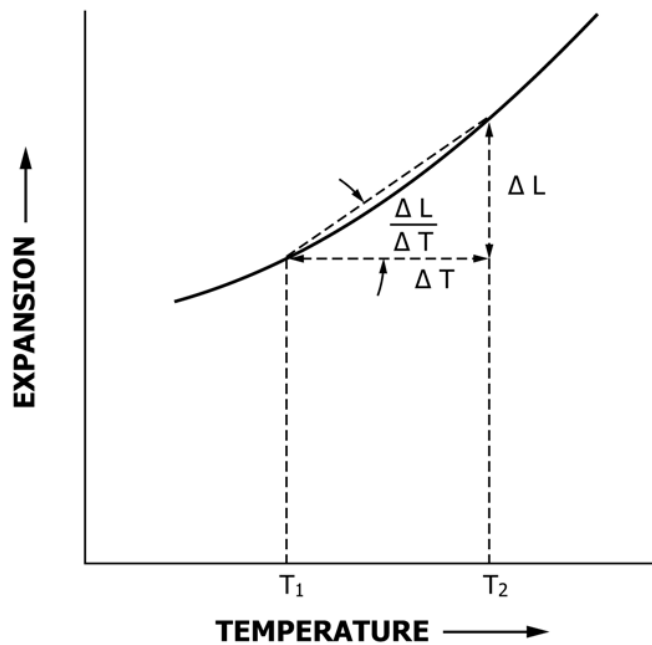
Figure 38. Calculation of change in length over time, as per ASTM Standard E831-14 [105].

4.1.5 Statistical Analysis of Results

In the manufacturing plan, four replicates of the density artefacts were planned for analysis, with the factors set up so that a full-factorial analysis of variance (ANOVA) would be possible to determine the effects of each build variable. Due to time and scheduling constraints, however, only a single replicate was able to be imaged for each sample.

With experiments that contain only one replicate, standard ANOVA of the full model is not normally possible because there is no way to measurably report on the error. However, there are ways to analyze single replicate experiments. By eliminating higher-order interactions from the model, one can effectively gain extra degrees of freedom in the model for estimating the error. The simplest method is to just assume that there are no higher order interactions. This is because in many systems, main effects and lower order interactions effects are significant, while higher-order interactions are negligible (known as the sparcity of effects principle) [95]. One can also use regression techniques to eliminate higher-order polynomials, or the Tukey test, which can be used to determine if there are interactions between parameters [95].

For this work, the application of Tukey's test is used to determine the effect of varying the parameter levels. Originally, the Tukey test developed in 1949 was used to determine if there are interactions between two factors, but it is also possible to extend the derivations to determine interactions for more complex designs [106]. This is shown by Yang in 2014, where they extended the Tukey test for three-factor experiments [106]. The derivations pertinent to the extended Tukey test can be referenced in Appendix E.

To implement the model, MATLab code was written and can be referenced in Appendix F and Appendix G. Aside from the results presented by the statistical analysis, the data is also shown using several different graphical formats to aid in results visualization.

4.1.6 Auxiliary Analysis

4.1.6.1 Chemical Composition Analysis

To observe the chemical composition evolution of the material as it solidified from powder into bulk material, chemical analysis was performed on parts from the experiment. The procedure for chemical composition analysis is followed as per the previous chapter, section 3.1.1.

However, the analysis for chemical composition is costly, due to the amount of preparation required, and thus only a small representative set of parts was selected. Particularly, the samples that

were tested were samples 5, 20, 23, 26, 32, and 50. Samples 5, 23, 32, and 50 were selected to have identical grid distance and exposure time and only had power modified at increased levels. The intention was to purely see the degree of material vaporization with energy density, and variation of power was the most convenient way of increasing the energy density without introducing too many samples that required to be tested. Samples 20 and 26 were selected such that they had comparable energy densities to the other selected samples, where sample 20 was comparable to sample 50 and sample 26 was comparable to sample 5, so that the differences in selecting identical energy densities but different recipes could be observed. A table detailing the samples and their build variable combinations are shown below.

Table 15. Samples selected to be analyzed for their chemical composition.

Build Variable	Unit	Sample Identification Number					
		5	20	23	26	32	50
Power	[W]	250	300	300	300	350	400
Grid distance	[μm]	70	60	70	80	70	70
Exposure time	[μs]	70	70	70	70	70	70
Energy Density	[J/mm^3]	119	194.4	142.9	109.4	166.7	190.5

4.1.6.2 Melt Pool Geometry

In addition to the chemical composition of the parts described in Table 15, optical microscopy was employed on the samples to observe the melt pool behaviour within each sample. Similarly, the small number of samples were selected because polishing and etching are time-consuming processes, and thus it was not feasible to be performed for an entire set of 54 samples.

Although this analysis was not part of the main goal of the experiment, the supplementary information provided important details about the melting modes during processing. For the artefact selection, the cubic samples were used, since the faces of the cube are aligned with the build and laser scanning directions. Also, prior to imaging the cube samples were polished and etched. This was provided by the service of Hamed Asgari Moslehabadi (Post-Doctoral Fellow, Multi-Scale Additive Manufacturing Lab), who also performed the optical imaging for all results presented in this work.

4.2 Results and Discussion

4.2.1 Chemical Composition Analysis

Shown below in Table 16 are the chemical composition results for the tested samples, 5, 20, 23, 26, 32, and 50. Based on the results here, the bulk samples appear to change composition slightly from the powder, but the overall compositions remain comparable and conform to the standards. As well, between all the samples there is a negligible difference in composition, which implies that the selected variations in build variables do not affect the chemical composition of the parts.

The stability of the materials' main constituents can be explained by observing the phase diagram (Figure 12, section 2.2) which shows that the liquidus and solidus for the alloy are at almost the exact same temperature. This means that upon melting and solidification, both the iron and nickel liquidate or solidify simultaneously and thus segregation of elements is not expected. Additionally, the vaporiz-

Table 16. Chemical composition of the measured samples, as compared with supplier and ASTM specifications.

Element	Sample wt. %							Supplier wt. %	ASTM wt. %
	Powder	5	20	23	26	32	50		
Iron	63.3	62.9	62.9	62.9	62.9	62.9	62.6	Remainder	Remainder
Nickel	35.6	36.0	36.0	36.0	36.0	36.1	36.1	36	36 nominal
Cobalt	< 0.01	0.01						0.01	0.50 max
Manganese	0.35	0.33	0.30	0.32	0.32	0.32	.32	0.44	0.60 max
Silicon	0.17	0.15						<0.01	0.40 max
Carbon	Not measured							0.010	0.05 max
Aluminum	<0.01							<0.01	0.10[A] max
Magnesium	Not measured							<0.01	0.10[A] max
Zirconium	Not measured							<0.01	0.10[A] max
Titanium	<0.01							<0.01	0.10[A] max
Chromium	< 0.01	0.01	0.01	0.01	0.01	0.06	0.16	0.12	0.25 max
Phosphorus	0.010	<0.010						0.02	0.015[B] max
Sulfur	<0.005							0.003	0.015[B] max
Copper	<0.01							<0.01	Not in standard
Molybdenum	<0.01						0.03	0.05	Not in standard
Selenium	Not measured							<0.003	Not in standard

[A] The total sum of aluminum, magnesium, titanium, and zirconium shall not exceed 0.20%
[B] The total sum of phosphorus and sulfur shall not exceed 0.025%

ation temperatures of both iron and nickel are very similar in temperature [107], [108]. Thus even upon material vaporization due to excessive laser input, the material is not expected to vary significantly in composition.

4.2.2 Melt Pool Geometry

Figure 39 illustrates the optical microscopy images of the samples that had identical grid distance and exposure times, but varying power. It can be seen that initially the melt pool is semi-circular in shape. As the laser power increases, the melt pools become deeper and wider, forming a shape reminiscent of a wine glass or "goblet". Similarly, Figure 40 shows the optical microscopy images with identical power and exposure time, but varying grid distance. From here it becomes very evident that the smaller grid distances result in a deeper penetrating melt, while longer grid distances result in shallower melts. This may be because the shorter grid distances causes an overall increase in heat input, and the overlap of laser scans may be prolonging the time the material stays melted, and thus allowing the liquid phase to penetrate deeper into the material. Overall, it appears that the increase of energy density, whether it is through laser power or exposure time, will result in deeper and wider melt pools as the laser heating mode transitions towards keyhole melting.

Sample 5	Sample 23
Energy density: 119.0 J/mm³	Energy density: 142.9 J/mm³
Sample 32	**Sample 50**
Energy density: 166.7 J/mm³	Energy density: 190.5 J/mm³
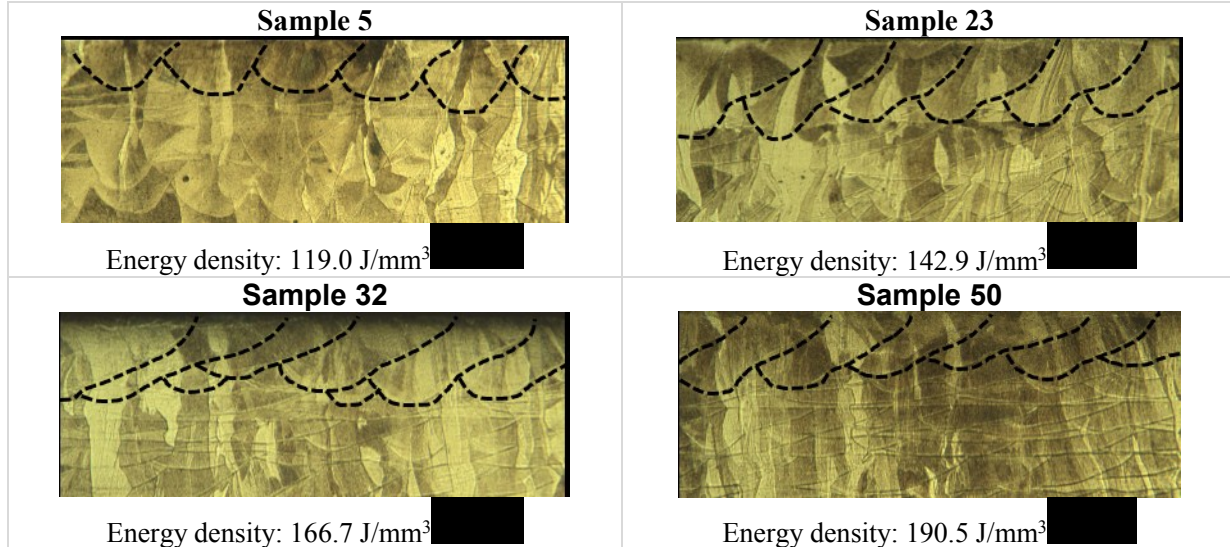
Figure 39. Optical microscopy images detailing the melt pool geometry within the LPBF parts with varying power. The dashed lines show the melt pools of the last deposited layers.
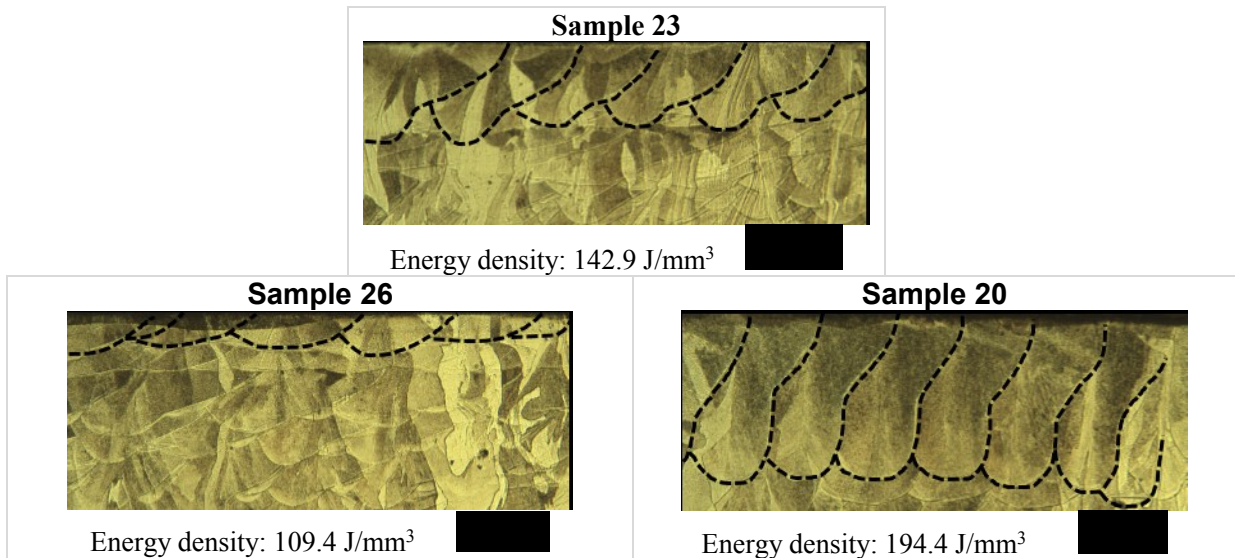
Figure 40. Optical microscopy images detailing the melt pool geometry within the LPBF parts with varying exposure time. Dashed lines show the melt pools of the last deposited layers.

4.2.3 Interpretation of CT Pore Space Data (Overall Part)

Two representative sample results are displayed below in Figure 41, where the lowest and highest quantified solid fractions are located on the volumetric energy density plot from Figure 24. As well, respective minimum intensity projection plots are displayed in Figure 42 and Figure 43. Figure 42 represents the part with the lowest quantified solid fraction of 99.72%, while Figure 43 represents the highest quantified solid fraction of 99.92%. The solid fraction is the inverse measure of pore fraction, and depending on the circumstances, either term will be used within this work. Ideally, the optimal process outcome will have higher solid fractions. The entire set of images can be referenced in Appendix H. As discussed previously in section 4.1.3.2.4, these images show a projection of the pores across the entire sample, and are more adequate measures of pore distribution and geometry than quantity.

When comparing the differences in build variables between the two, the best performing part has a relatively low power level, a large hatch spacing, and a low exposure time, while the worst performing part has the highest power level, the smallest hatch spacing, and the longest exposure time. When referring to Figure 24, the best performing part has one of the lowest energy densities and the worst performing part has the highest overall energy density.
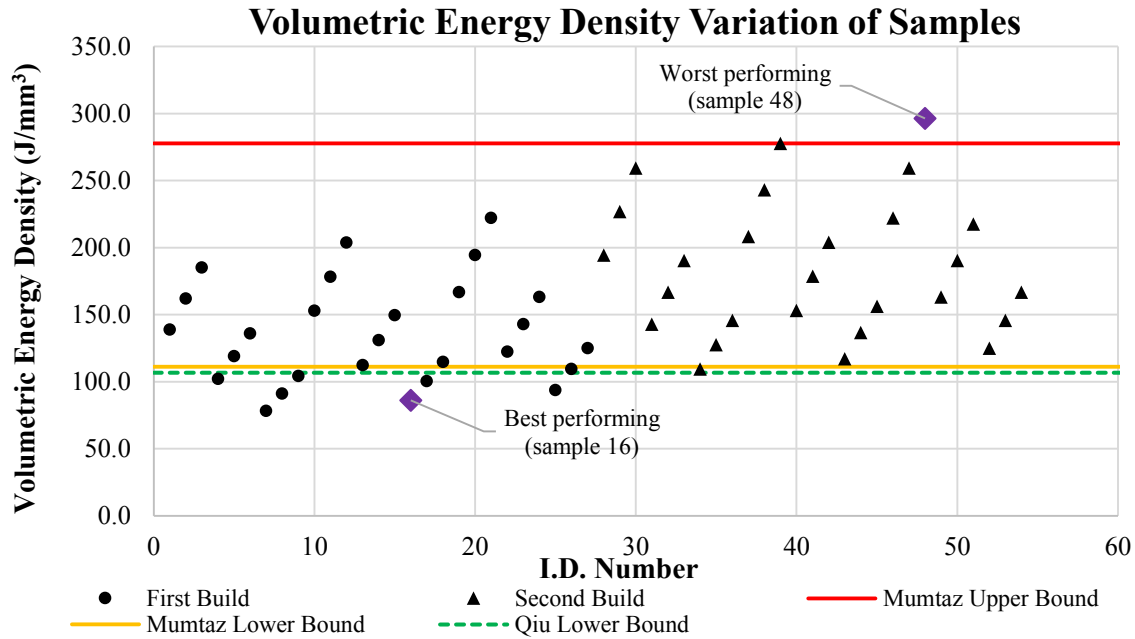
Figure 41. Variation of volumetric energy density across all permutations of variables, with the worst and best performing CT parts labelled.
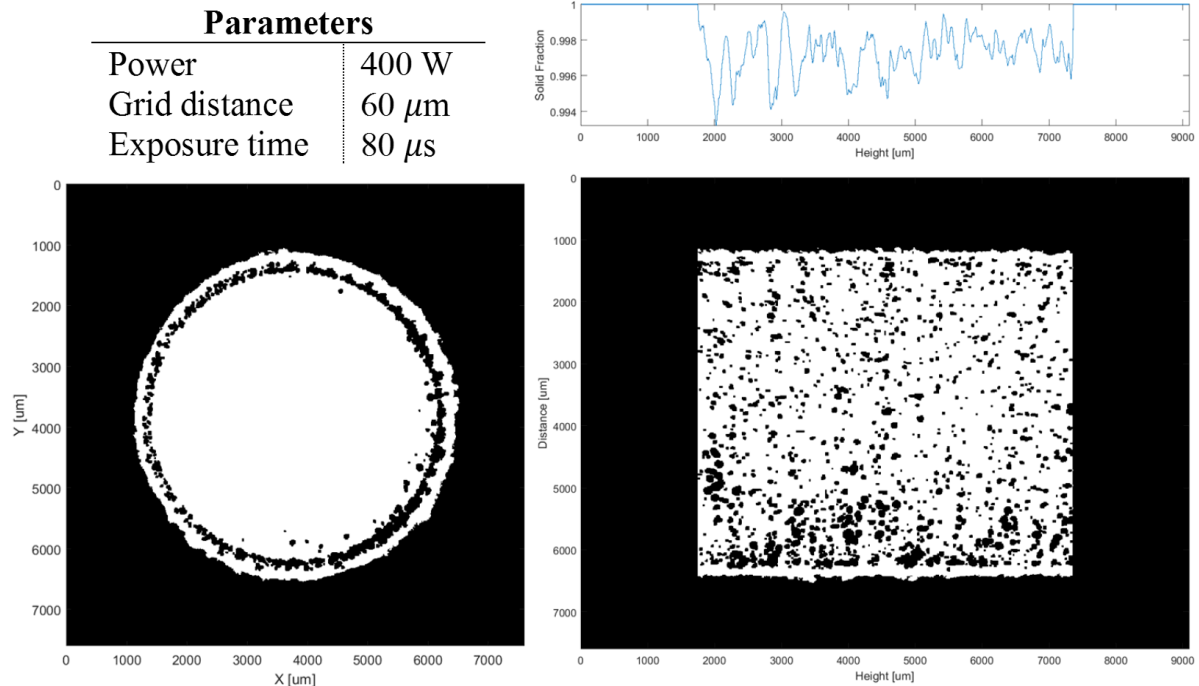
Figure 42. Worst overall performing part from the CT analysis, in terms of the overall porosity. The build variables for this sample correspond to sample 48.

Parameters	
Power	275 W
Grid distance	80 μm
Exposure time	60 μs
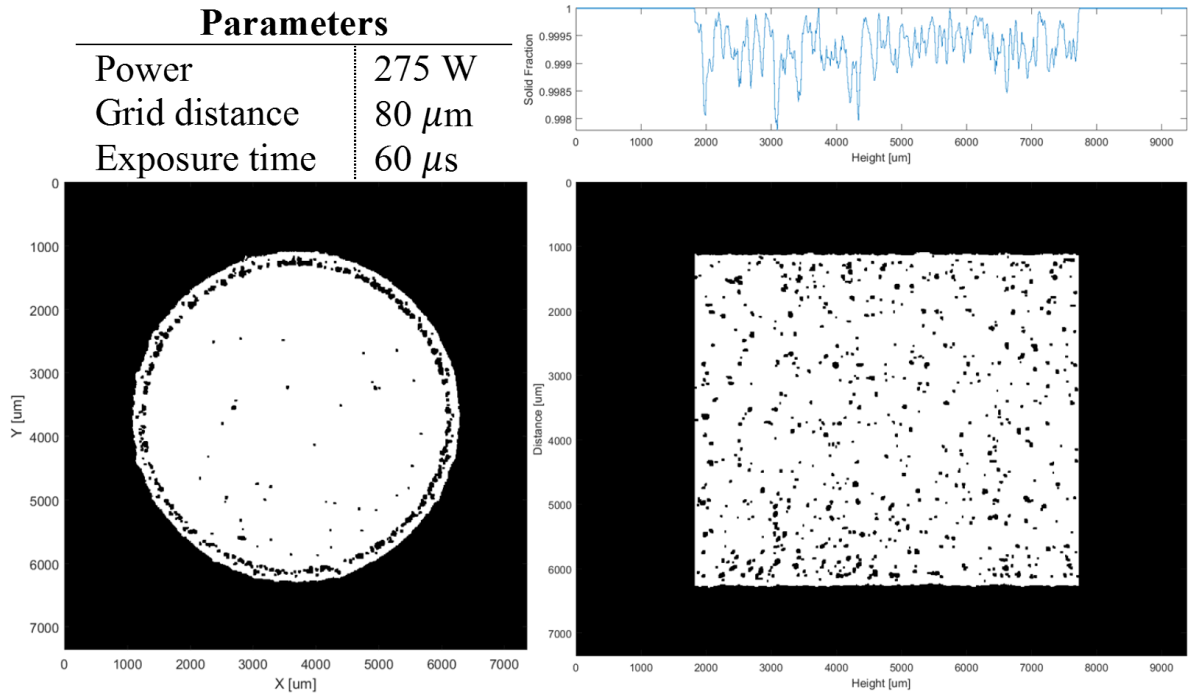
Figure 43. Best overall performing part from the CT analysis, in terms of the overall porosity. The build variables for this sample correspond to sample 16.

With these results in mind, it appears as though the minimum energy density bound (as specified by Qiu and Harrison) to achieve full melt is accurate, while deviations above the maximum energy bound transition to regions of over melt and increased porosity. The increased porosity may be due to material vaporization, specifically around the border region of parts, as well as the effect of pore entrapment as the melt pool transitions towards keyhole-mode laser melting (similar to conditions within laser welding) [109], [110].

Overall, in terms of the pore size and distribution, it appears as if the pores become larger and more numerous with transition from worst performing to the best performing parts (shown below in Figure 44). The pore sizes are described in voxels (three-dimensional pixel), where each voxel is a cube with a side length of 12 μm. This observation is understandable, since the transition from lower to higher energy density regimes will result in more material vaporization and increased heat input, which then leads to increased porosity. In addition to the observations on the total porosity and pore size distribution, there are other interesting phenomenon as well.
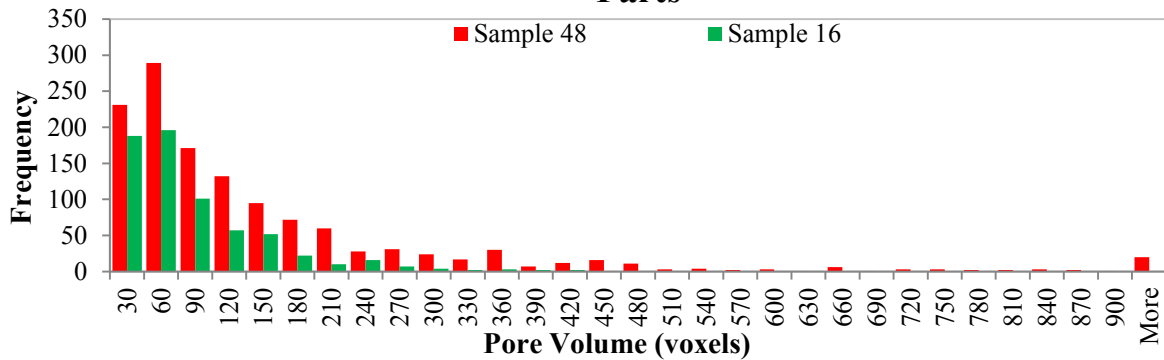
Figure 44. Pore size distribution plot highlighting the differences between the worst (sample 48) and best performing parts (16).

One interesting observation is that there is a heavy bias of pores towards the outer edges of the specimen. The cause of these defects is illuminated when the effect of the scan paths is considered. Figure 45, below, illustrates a single slice that is 171 out of 316 layers deep into the three-dimensional CT data, as viewed from the top of the cylinder. Additionally, the equivalent scanning pattern was extracted from Renishaw's build preparation software, QuantAM, and overlaid 1:1 to highlight the effects of the scanning strategy on the pores.
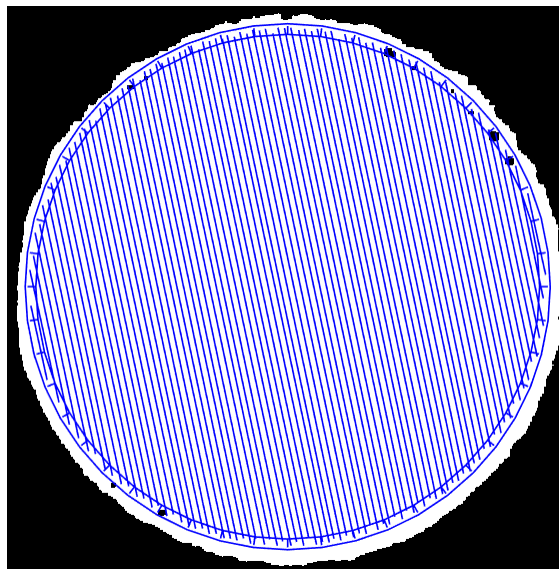
Figure 45. Single CT cross-section of a representative part section with the overlaid scan path. Build variables for this image correspond to sample 11, which was printed at 275 W power, 60 μm grid distance, and 70 μs exposure time.

70

Before continuing, terminology describing the scanning features must be introduced. In the figure above, there are three distinct types of scanning features present: the border lines, the hatch lines, and the block path lines. Figure 46, below, illustrates the differences. Within the default parameters for the build software, the parts built as part of this experiment had one border line, blocked path lines, hatch lines, and no contour lines.
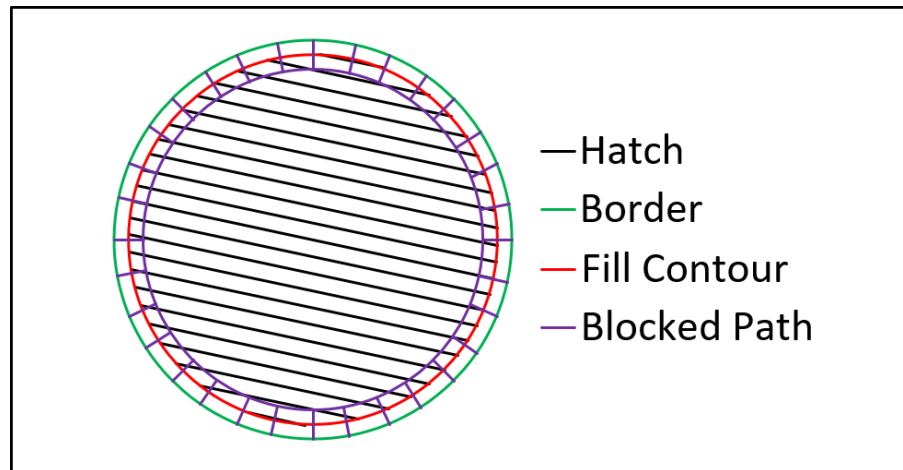
Figure 46. Schematic showing differences between different line types

The pores visible in the figure clearly occur in the areas subjected to circumferential border scans, and they appear to coincide with the ends of the hatch lines. It is hypothesized that this may be due to the fact that—unlike scan features more central to the part, the ends of hatch lines do not have the added benefit of re-melting from adjacent scan lines that may eliminate residual porosity. Additionally, there is another build variable in the build software, called 'hatch compensation' that was not modified for the experiment and it may contributed to the pores along the border region. By default, the hatch compensation build variable is set to 'off'. To explain the functionality of hatch compensation, consider a scenario where the hatch compensation build variable is off, a hatch line is 150 μm long, but the point distance is only 60 μm in length. As the hatch line becomes discretized into point laser scans, only three exposure points will be generated; one exposure at the beginning of the hatch line, another one displaced 60 μm away from the start, and a final one 120 μm from the start. Thus, there is a 30 μm gap that does not have any point exposures. This dilemma is demonstrated in Figure 47, showing how un-melted regions can occur if the hatch lines are not completely divisible by the point distances. To correct for these defects, turning on the hatch compensation may create a point at the end of the hatch lines, even if the remaining distance may be smaller than the point distance. An experiment further reviewing this is discussed in Chapter 5.
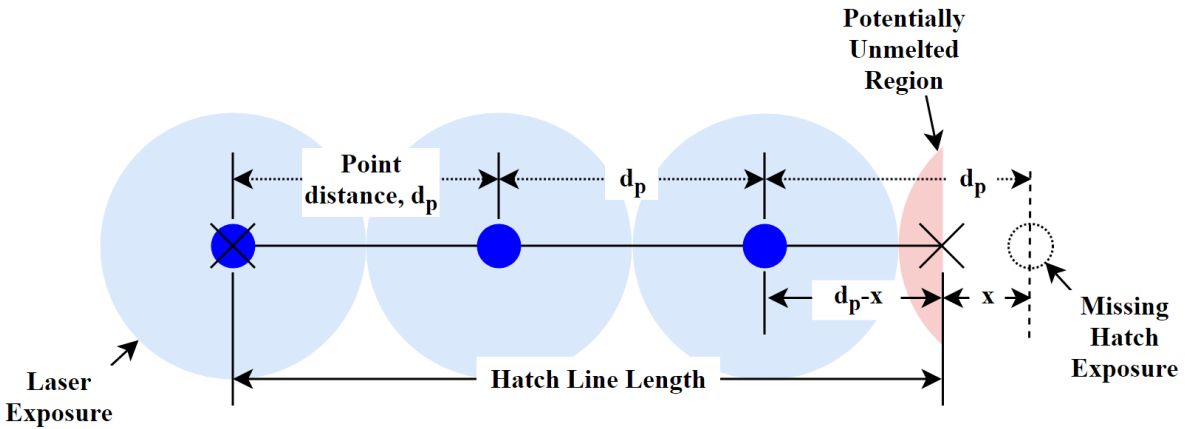
Figure 47. Figure illustrating the laser exposure with hatch line lengths indivisible by point distances, resulting in potential un-melted regions around the part perimeter.

Although it is not readily visible in Figure 42 or Figure 43, there appears to be an angular periodicity with the pores along the border. This behaviour can be better visualized within Figure 48, which shows three samples (correspond to samples part I.D.s 1, 2, and 3) that have the angular periodicity. It should be noted that this occurs across all samples that were tested, and the samples in Figure 48 were chosen purely for visualization purposes. From the figure, it appears that not only do the samples have angular periodicity, but the pores begin at the same locations and the angular periodicity occurs at the same frequency across all samples. To determine the cause of this periodicity, the scan paths for the parts can once again be reviewed (Figure 49). When observing the transition between three consecutive layers, the blocked path lines do not appear to be rotating between layers. Thus, the result of repeated scans focused on the same areas is hypothesized to produce the angular periodicity of the pores.
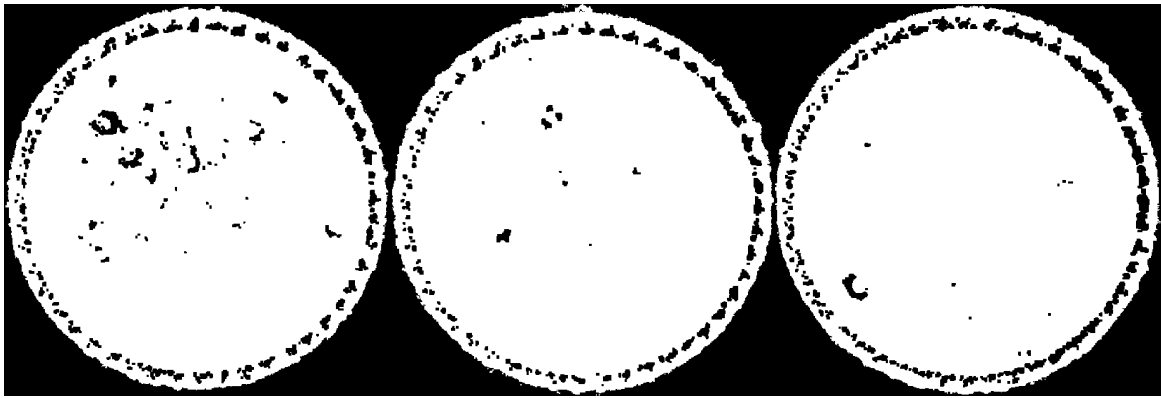
Figure 48. Representative figure showing the angular periodicity within the printed samples. From left-to-right are samples one, two, and three, which correspond to 250 W power; 60 μm grid distance; and 60, 70, and 80 μs exposure time.
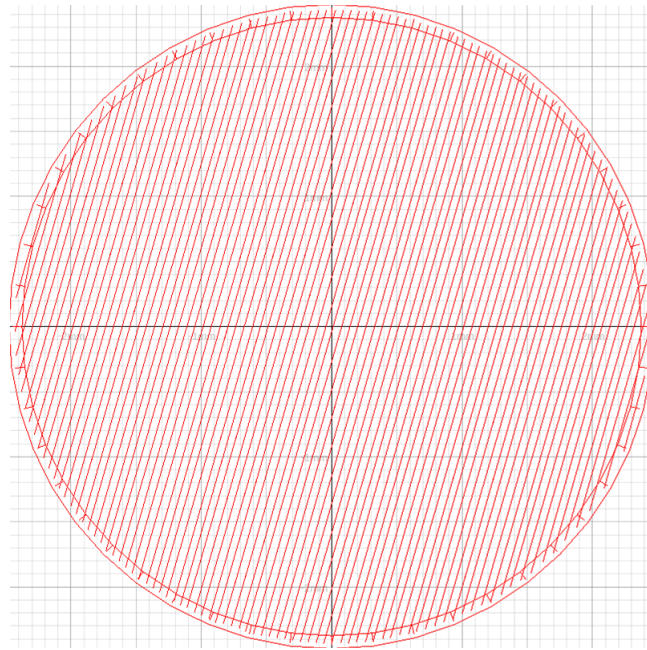
(a) Layer 213/300 of sample 1
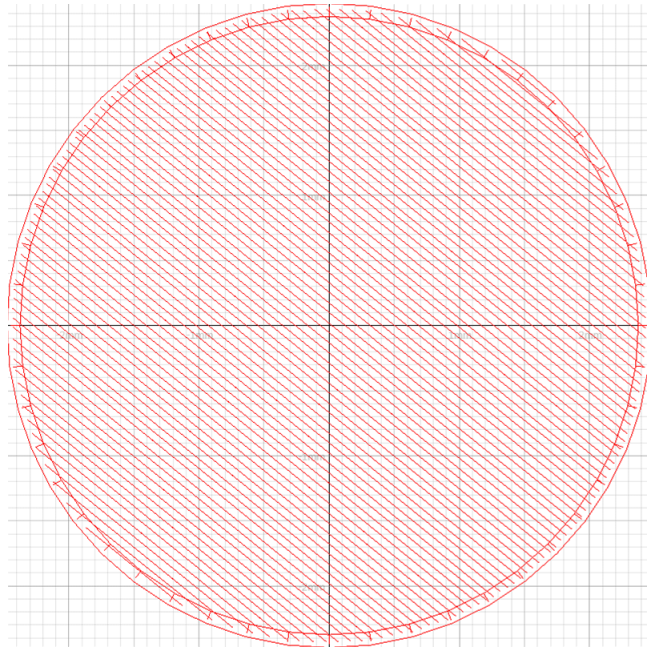
(b) Layer 214/300 of sample 1
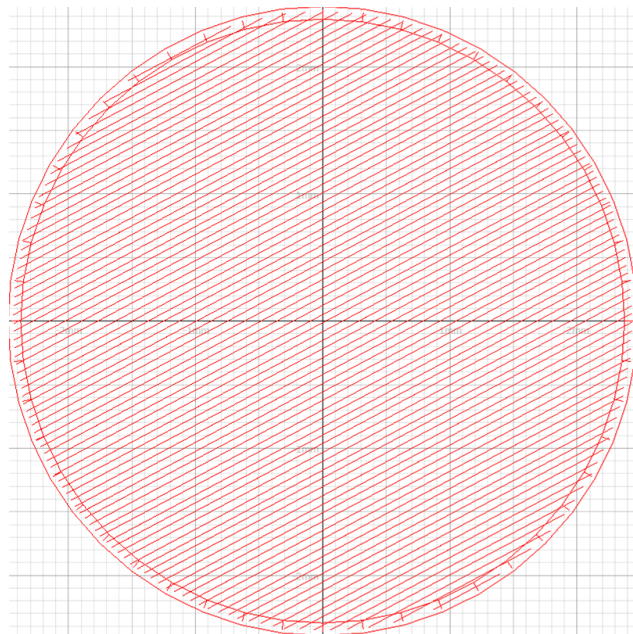
I Layer 215/300 of sample 1

Figure 49. Generated scan paths for sample 1, which corresponds to 250 W power, 60 µm grid distance, and 60 µs exposure time. Three consecutive layers are presented, where (a) – (c) are layers 213 – 215, respectively.

The effect of the blocked path on the angular periodicity becomes unmistakable when the scan path is overlaid on top of the minimum intensity projection of the CT data. Figure 50 shows layer 213 of the scan path for sample 1 laid upon the minimum intensity projection of sample 1. The sample bulk was dyed in orange to show the contrast between the pores, the scan-path, and the bulk material. As shown in the figure, the blocked paths are lined up 1:1 with the angular periodicity of the pores.
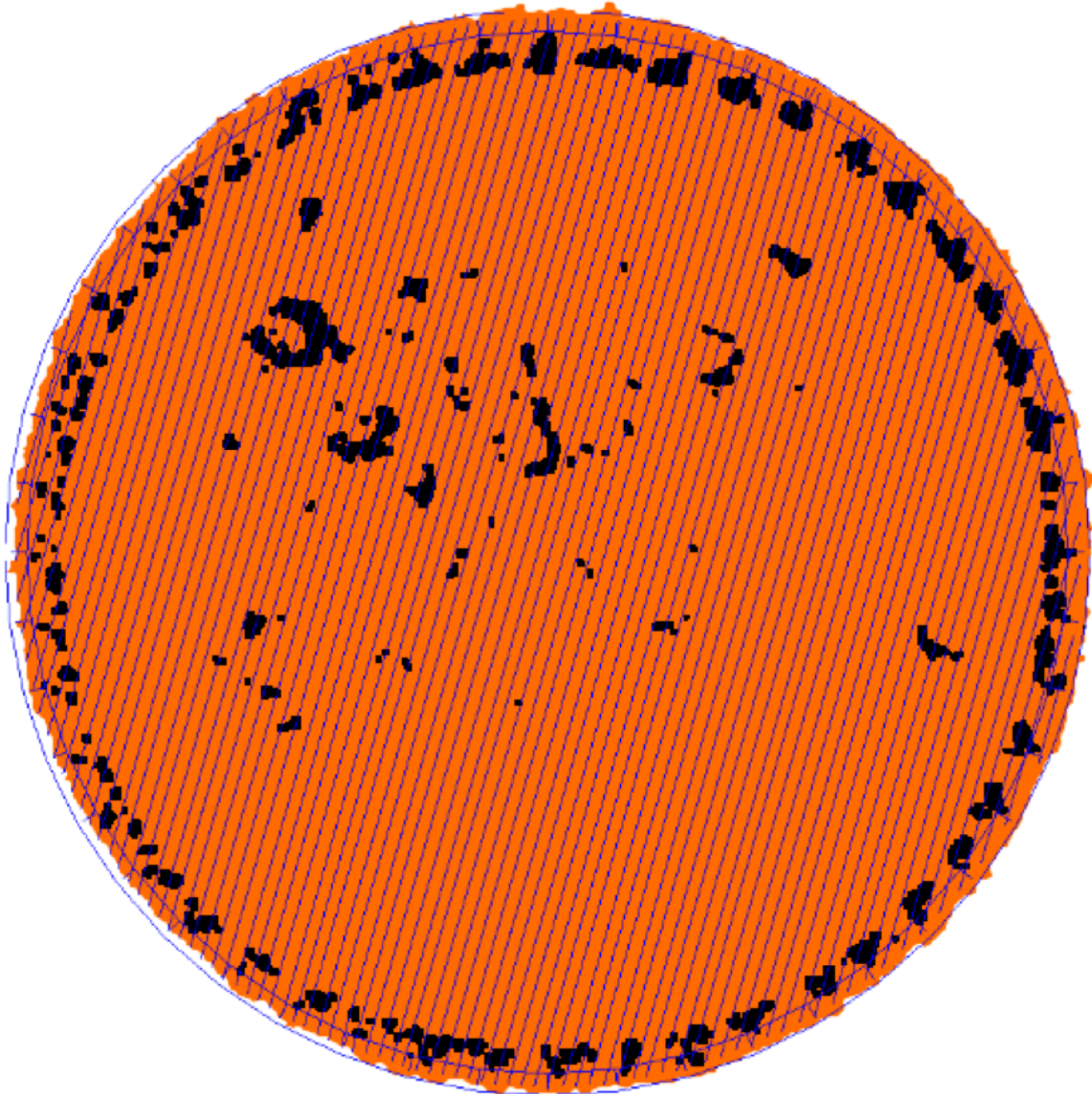
Figure 50. Scan path overlaid on the minimum intensity projection of sample 1, which corresponds to 250 W power, 60 μm grid distance, and 60 μs exposure time.

When observing the CT images, it is also apparent that the distribution of pores is biased towards the right side of samples. This is the most visually apparent with sample 20 (Figure 51, below), but it is also evident in the other samples as well.

When considering the fact that all the samples were oriented in the same direction across the build bed (refer to Figure 28, section 4.1.2), it becomes evident that a directional bias was introduced into the experiment. Particularly, it appears as if the gas flow may have been affectual, as it flows from right-to-left. As discussed in section 2.1.1, in addition to providing an inert atmosphere for processing, the role of gas flow is to disperse fumes and ejected particles from the build area.
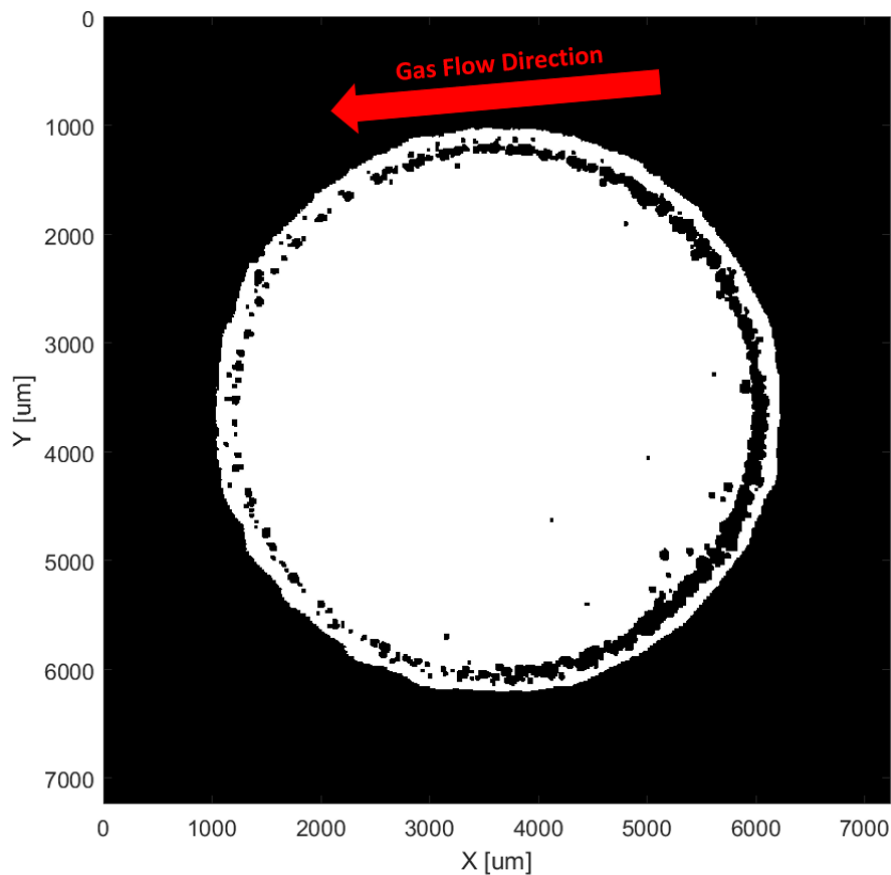
Figure 51. Representative part from the CT analysis showing the bias in spatial pore distribution. The build variables for this sample correspond to sample 20, which was printed at 300 W power, 60 μm grid distance, and 70 μs exposure time.

Upon consideration of this effect, it becomes reasonable to hypothesize that at the left edge of samples, the effect of gas flow results in the ejected particles being blown away and off of the

samples. For the right side of samples, however, the gas flow reintroduces the ejected particles into the sample, thus causing the opportunity for more defects. An example of this hypothesis is shown below in Figure 52. This effect seems to be diminished when a lower power was used, and is explored further in the next chapter.
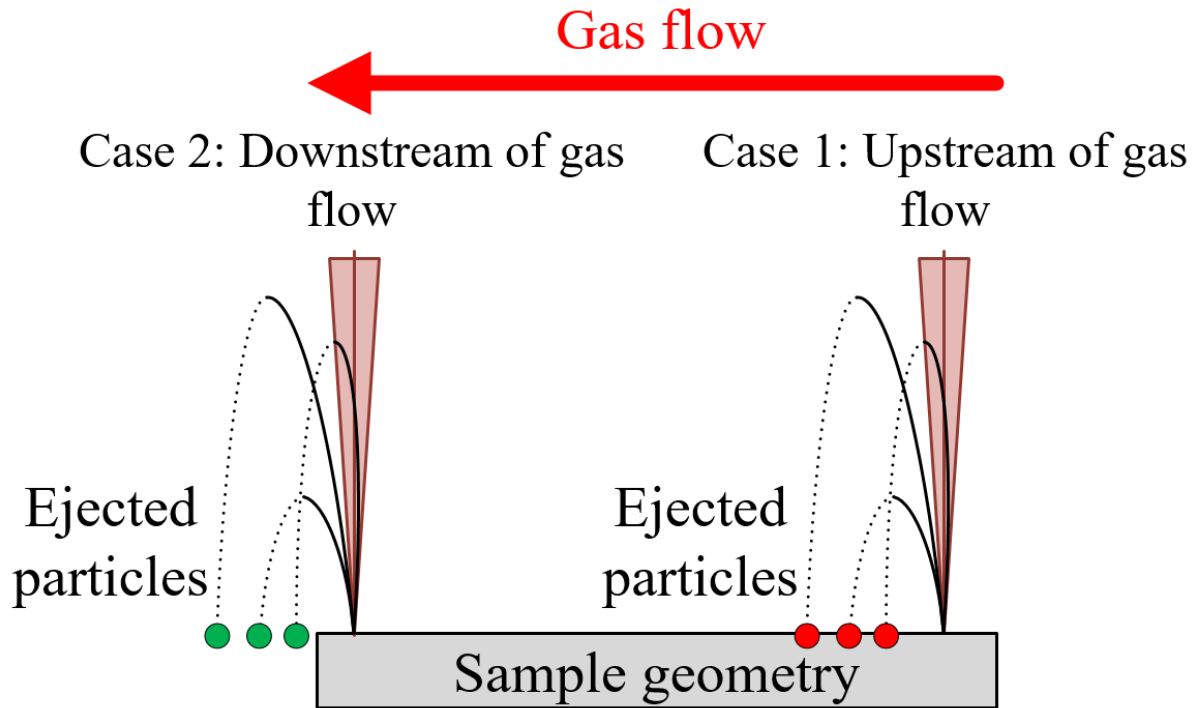
Figure 52. Hypothesized influence of gas flow on the porosities within the border regions.

All in all, the observations seem to show that the more energy dense parts have greater porosity than the less energy dense samples. Continued analysis into the distribution of the pores within the samples show that they are resultant of interactions between scan strategy build variables that involve areas near or at the border of the parts (for example the blocked paths and borders). For future study, the effects of these build variables are investigated in Chapter 5, but since the goal of the sets of experiment in this chapter is to investigate the effect of only the energy density related build variables on porosity, further analysis in this chapter will pertain only to the energy density related build variables. As well, since the pores near the border appears to be mainly affected by border-region build variables, the analysis also looks into the effect of energy density related parameters with the border region omitted in this chapter.

4.2.4 Process Mapping based on Solid Fraction (Overall Part)

To first visualize the effect of the build variables on the solid fraction of parts, a third data 'axis' was added to the energy density plot (Figure 24, from section 4.1) in the form of varying size circles (Figure 53). The sizes of the circles are relative to the solid fraction of the parts and only serve for comparative purposes.

From this visualization tool, it is difficult to tell the effect of build variables, because the differences of solid fraction between parts are very small. However, it appears as though there is a general trend of decreasing circle size with increasing power (refer to Figure 25, section 4.1, for explanation on deciphering sample I.D. to power, grid distance, and exposure time). It is more difficult to see any trends with increasing grid distance or exposure time.

Due to the difficulty with determining any significant trends, an alternative visualization method was used. Through the use of MATLab, a three-dimensional surface plot of the process map was constructed, where twenty surface plots of constant solid fraction were generated with respect to power, grid distance, and exposure time. After compiling the data focusing on the solid fraction of the samples, the following three-dimensional surface plot was created (Figure 54). The purpose of these surface plots is to provide an informed view into the process map, and describe the resulting part performance based on the build variable selection.

Variation of CT Solid Fraction with Part I.D and Energy Density
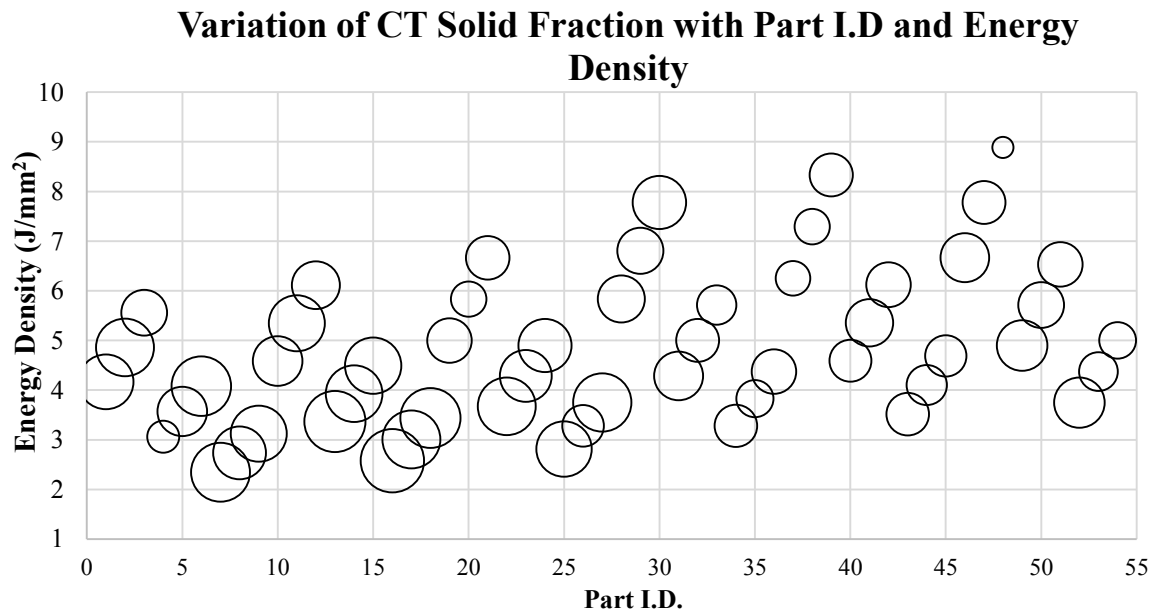
Figure 53. Variation of volumetric energy density across all permutations of variables, with an additional 'axis' describing solid fraction through the use of variable size circles.

78

To explain, the solid fraction of each part in terms of the power, grid distance, and exposure time, is plotted in a three-dimensional contour plot, where each contour corresponds to a constant solid fraction. The surfaces were generated using a 'scatteredinterpolant' function with natural neighbor interpolation. As such, the shape of the contours within the plot are not entirely representative of the true behaviour of the process map. However, they serve as a useful visualization tool for determining the overall behaviour within the process map.

Figure 54. Three-dimensional surface plot describing the effects of power, grid distance, and exposure time on the solid fraction of parts.

It is straightforward to see that there is a trend of increasing power with decreasing solid fraction, and this matches with previous observations of the CT images. As previously mentioned, this is likely due to the transition of the melting mode towards keyhole melting, causing material vaporization and pore entrapment. In terms of the effects of exposure time and grid distance, it is still difficult to ascertain any trends with varying those build variables. To further clarify, individual sectioned surface plots for the effect of grid distance and exposure time within each power level were created. Within the surface plots, the lowest and highest solid fraction parts for each power level are also

labelled with accompanying CT minimum intensity projection plots. Similarly, the curves within the plot are generated with interpolation and may not be entirely representative of the true process behaviour within those regions. These plots can be referred to below (Figure 55 – Figure 60).

However, once again, it is challenging to visually correlate any change in grid distance and exposure time with the solid fraction, however it appears that that within each power level there are multiple zones of good performance, and that overall the increase of power decreases performance. As well, the majority of well performing parts for each power level occur within mid-to-high levels of hatch distances, which suggest that larger hatch distances may play a beneficial role. It was previously mentioned that the overall pore sizes appeared to increase with energy density.

Figure 55. Two-dimensional surface plot describing the effects of grid distance and exposure time on the solid fraction of parts at a power of 250 W. Where the CT images describe (a) worst performing and (b) best performing parts.

Figure 56. Two-dimensional surface plot describing the effects of grid distance and exposure time on the solid fraction of parts at a power of 275 W. Where the CT images describe (a) worst performing and (b) best performing parts.

Figure 57. Two-dimensional surface plot describing the effects of grid distance and exposure time on the solid fraction of parts at a power of 300 W. Where the CT images describe (a) worst performing and (b) best performing parts.

Figure 58. Two-dimensional surface plot describing the effects of grid distance and exposure time on the solid fraction of parts at a power of 350 W. Where the CT images describe (a) worst performing and (b) best performing parts.

84

Figure 59. Two-dimensional surface plot describing the effects of grid distance and exposure time on the solid fraction of parts at a power of 375 W. Where the CT images describe (a) worst performing and (b) best performing parts.
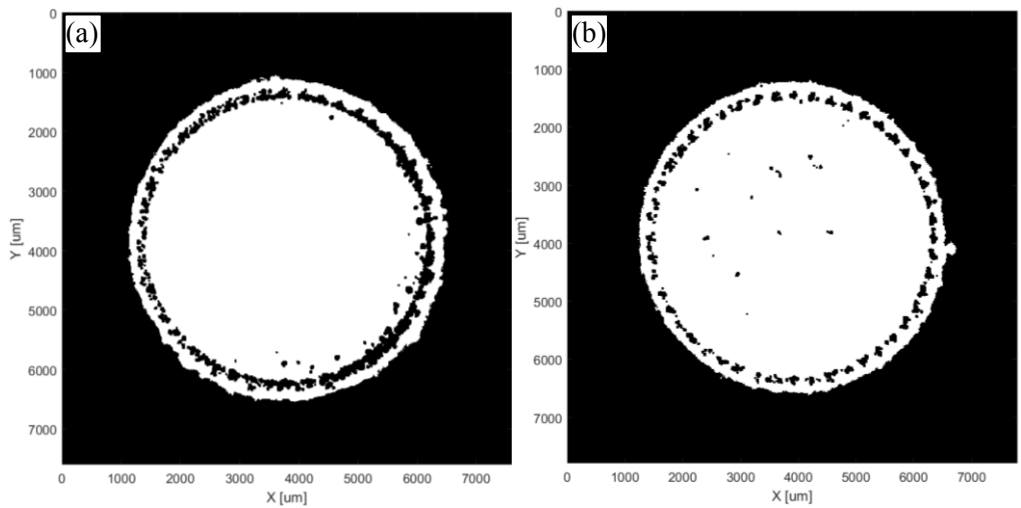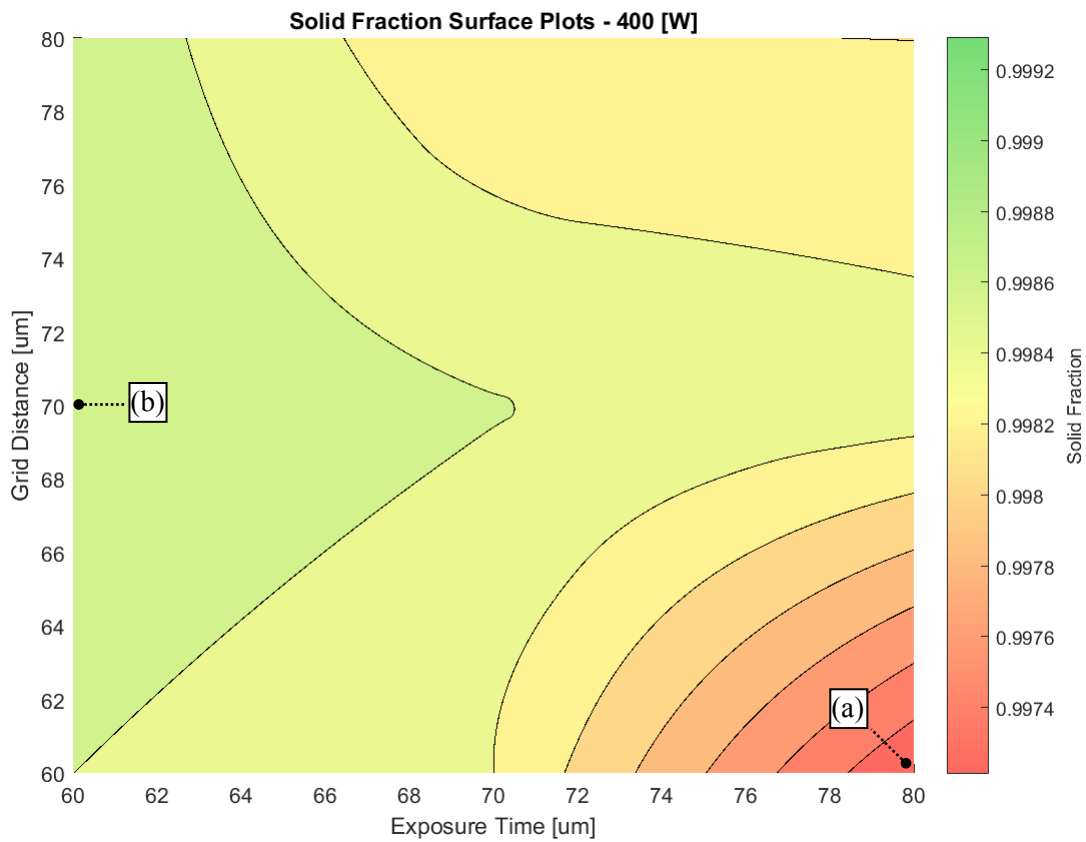
Figure 60. Two-dimensional surface plot describing the effects of grid distance and exposure time on the solid fraction of parts at a power of 400 W. Where the CT images describe (a) worst performing and (b) best performing parts.

4.2.5 Interpretation of CT Pore Space Data (Border Regions Removed)

To recall, the intention for this experiment was not to focus on the effect of border region build variables, but to purely focus on the effect of energy input build variables on the bulk part regions. This is because the effect of localized defects along the borders are due to border-region build variables only, and may contribute to erroneous conclusions. Thus, by truncating the radii of samples by 10% to omit the porosity defects along the borders, it was possible to obtain information about build variable modification within the core regions of the part (Figure 61).

| (a) Before truncating | (b) After truncating |
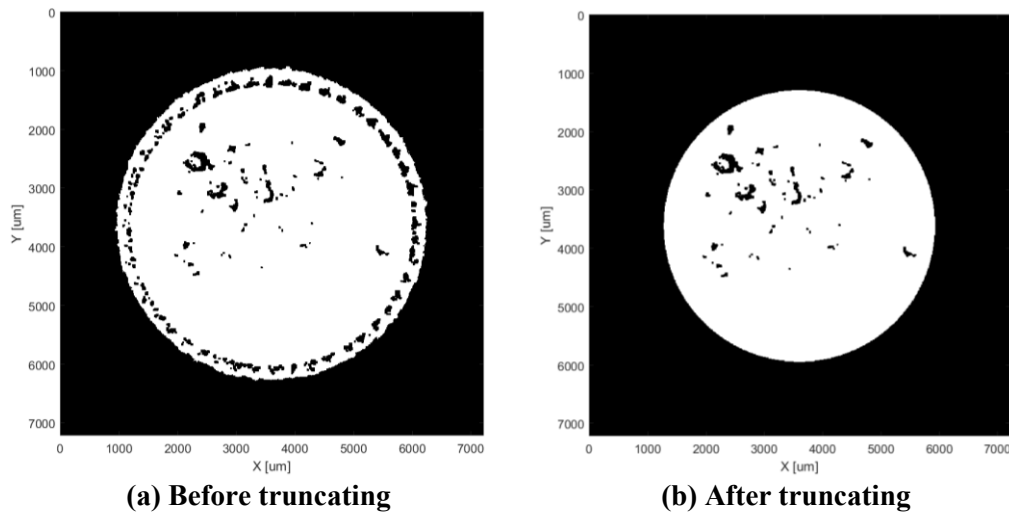
Figure 61. Example illustrating showing the CT data (a) before and (b) after truncating the radius to omit border-region porosity.

In a similar exercise to before, once the truncation was performed, the worst performing and best performing parts can be compared. The worst performing part had a solid fraction of ≈99.85%, while the best performing part had a solid fraction of ≈99.99%. Their respective locations on the energy density plot (as per Figure 41) are shown in Figure 62. The summary of the CT analysis can be observed in Figure 63 and Figure 64, and as before, the full set of images can be referenced in Appendix I.
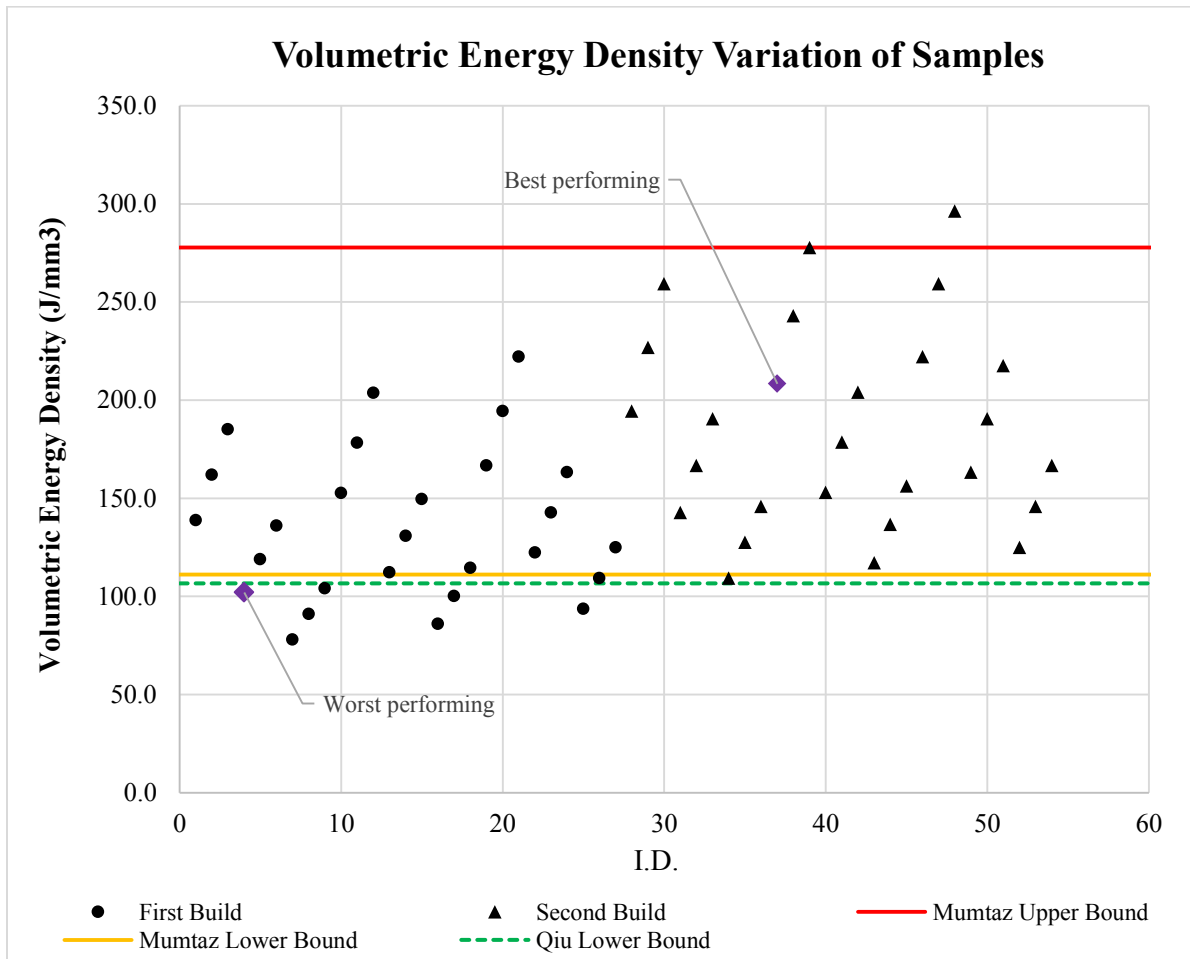
Figure 62. Variation of volumetric energy density across all permutations of variables, with the worst and best performing CT parts (with border regions removed) labelled.

Without the influence of the border region pores, it becomes evident that the porosity within the core regions are much more organized, with pores appearing to be structured on a per-layer basis. As well, the pores are much larger and less spherical, with some pores also appearing to have spherical material solidified in the center of the pores. This is attributed to the 'balling' phenomenon that occurs in LPBF, and is associated with melt pool instabilities that result in the material forming droplets to minimize surface tension in the melt pool. It is suggested that at lower energy density values, there may be insufficient energy input to form a stable melt pool. As well, at larger values of power, the re-melting effect across multiple layers may collapse some pores.
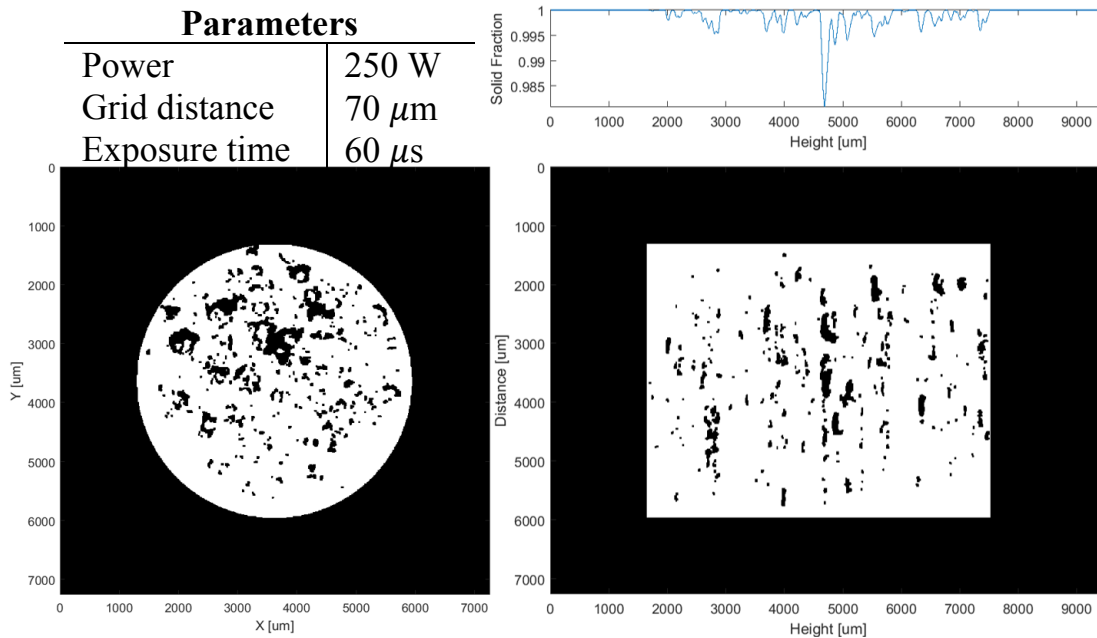
Figure 63. Worst performing part from the CT analysis, in terms of the porosity, with border regions removed. The build variables for this sample correspond to sample 4.
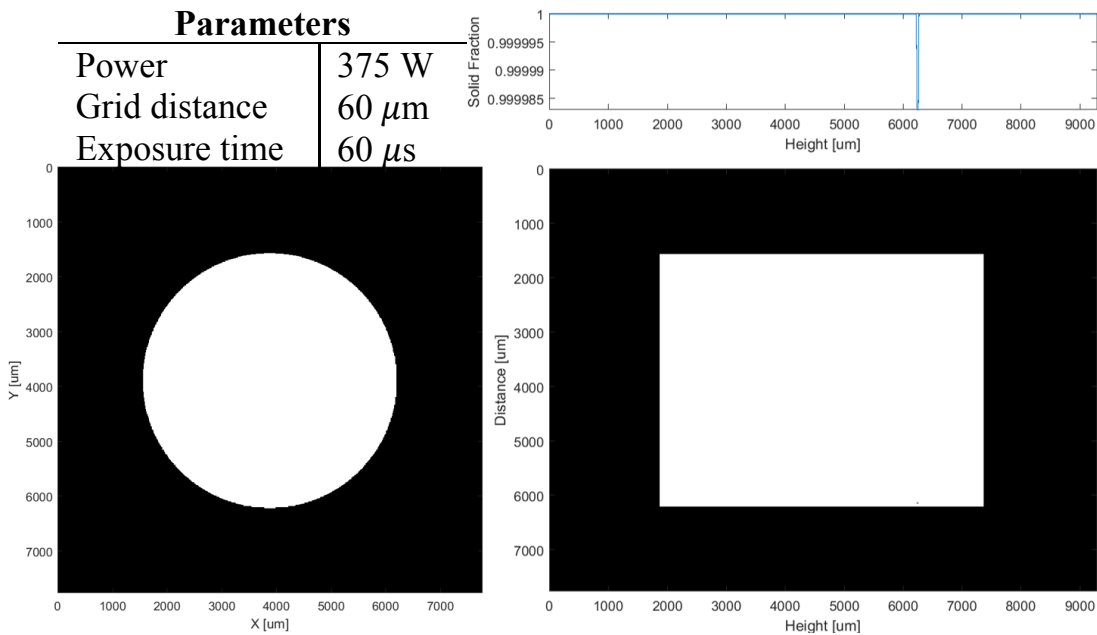
Figure 64. Best performing part from the CT analysis, in terms of the porosity, with border regions removed. The build variables for this sample correspond to sample 37.

4.2.6 Process Mapping based on Solid Fraction (Border Regions Removed)

Once again, quantifying the solid fraction and plotting it in terms of the energy input build variables results in a similar three-dimensional isosurface plot. The large volume of empty space inside the plot is due to the fact that there is very little variation in terms of solid fraction for the majority of the process map. Aside from the sharp decrease in solid fraction in the low power regions of the plot, the modification of build variables does not appear to change the solid fraction by any significant amount.
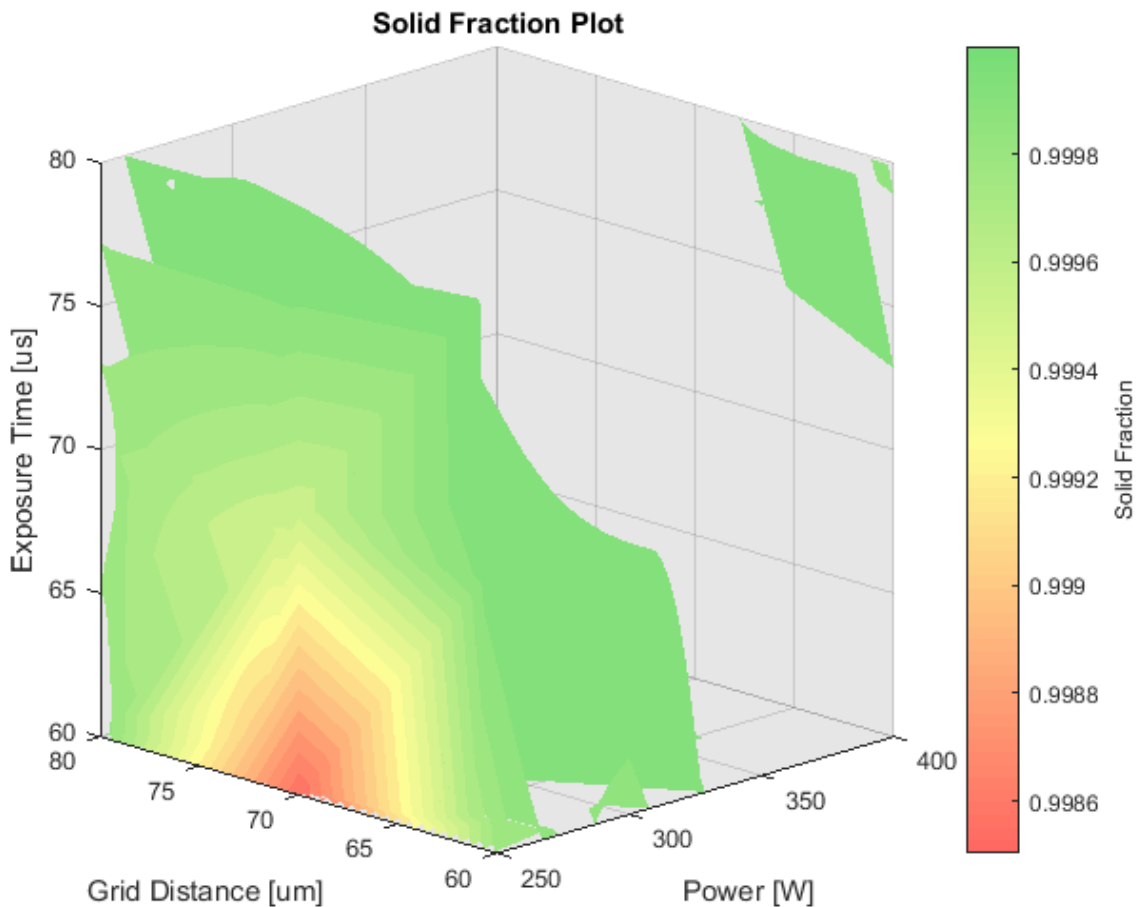
Figure 65. Three-dimensional surface plot describing the effects of power, grid distance, and exposure time on the solid fraction of parts, without the effect of the border regions.

As before, individual sectioned surface plots for the effect of grid distance and exposure time within each power level were created for further clarification. The worst and best performing parts for each power level are also labelled with accompanying CT minimum projection plots. These plots can be referred to below (Figure 66 – Figure 71).
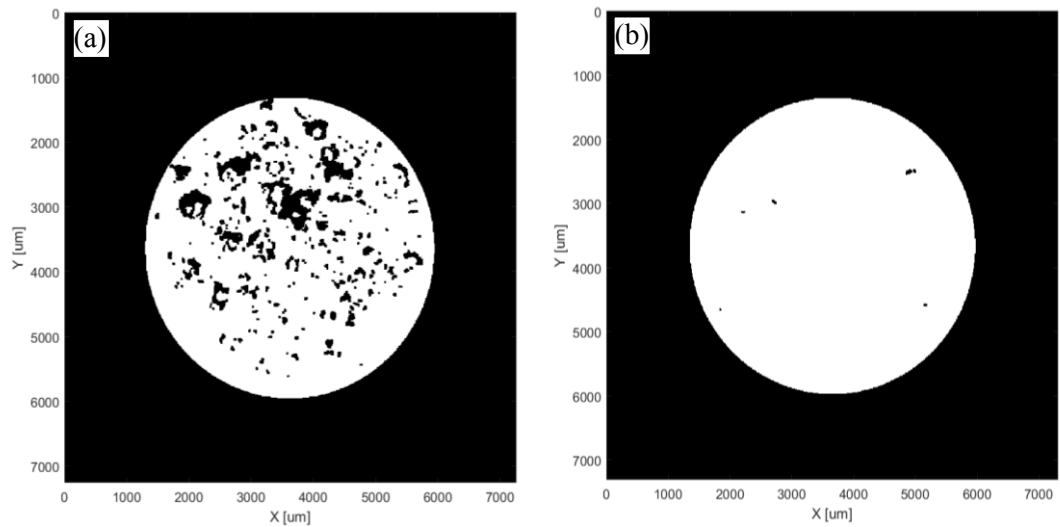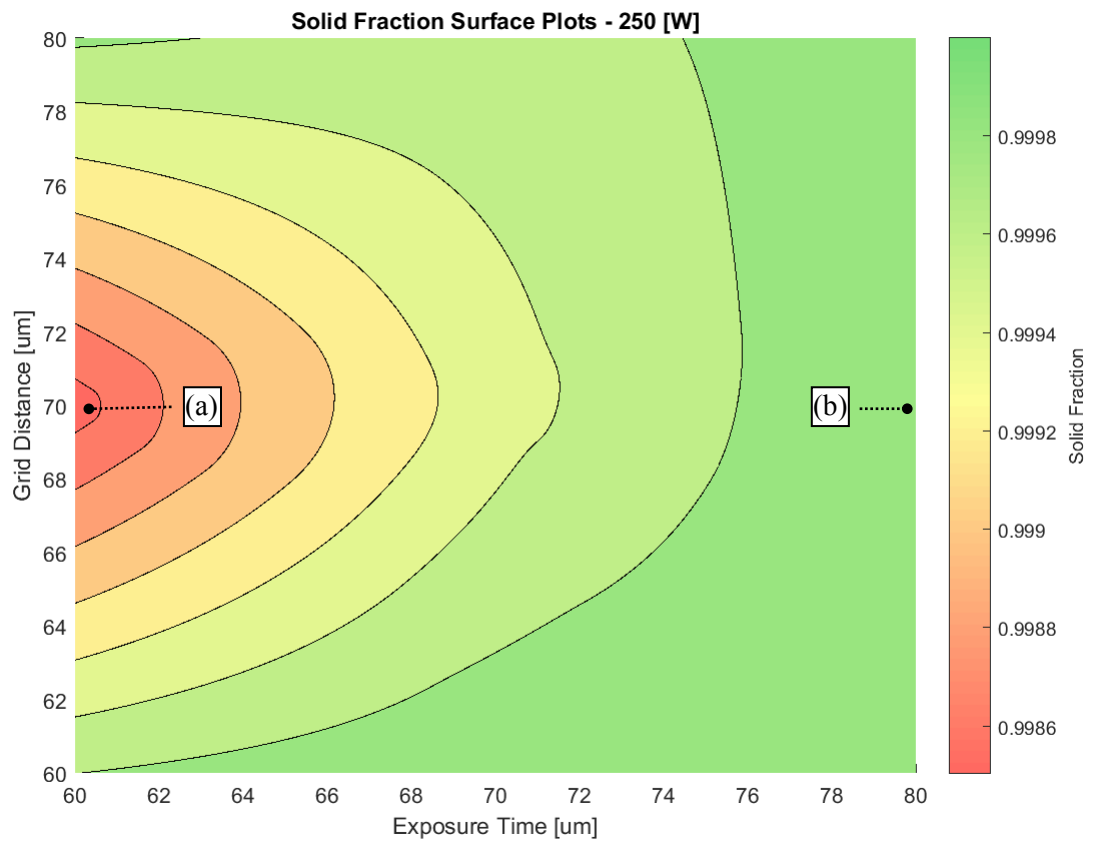
Figure 66. Two-dimensional surface plot describing the effects of grid distance and exposure time on the solid fraction of parts (without border regions) at a power of 250 W. Where the CT images describe (a) worst performing and (b) best performing parts.
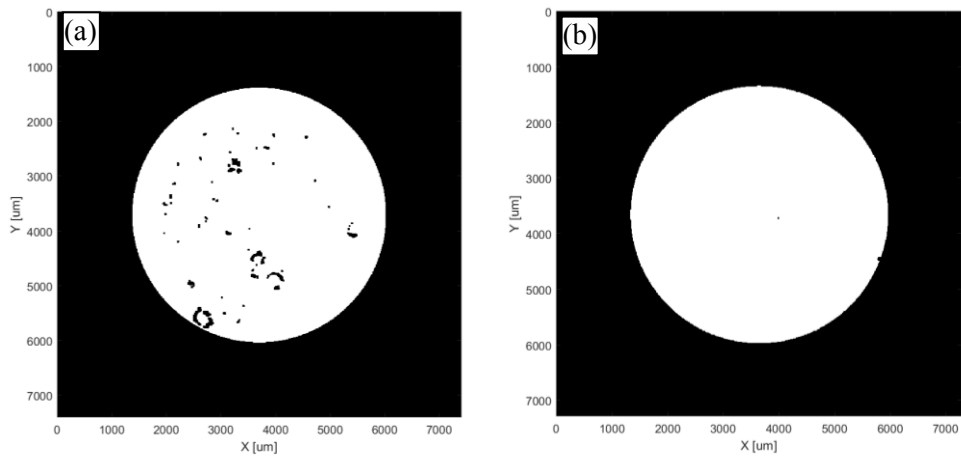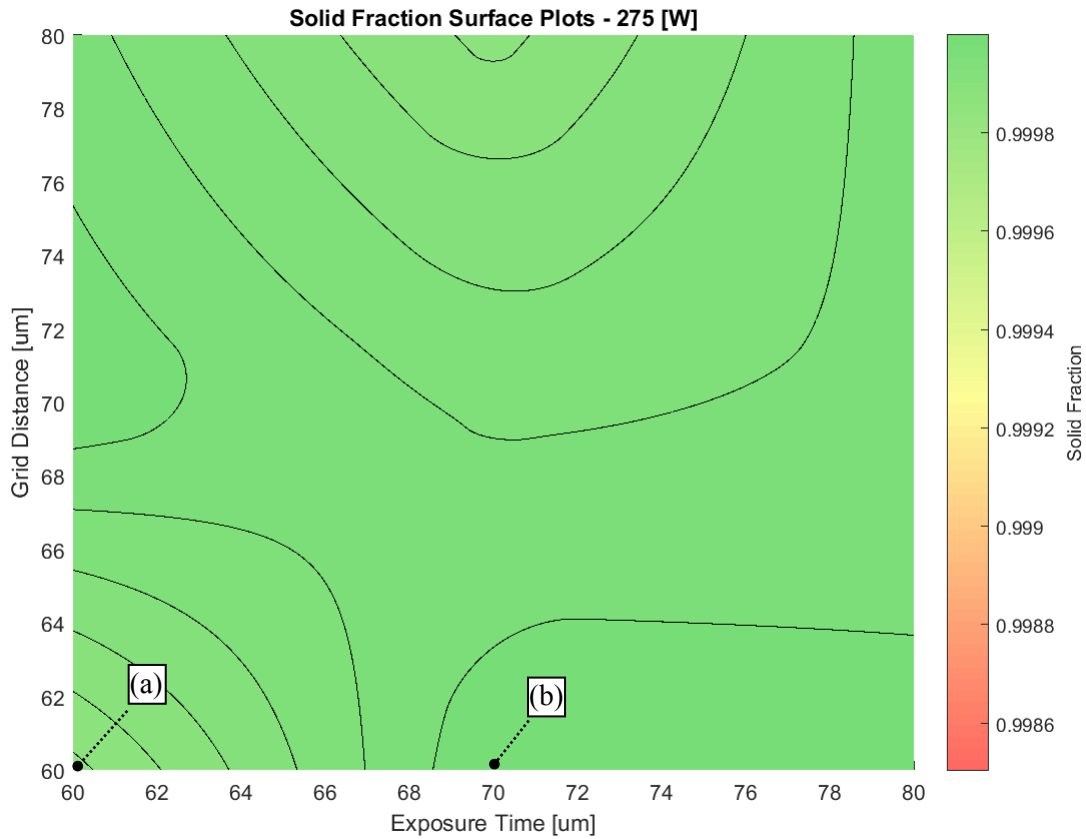
Figure 67. Two-dimensional surface plot describing the effects of grid distance and exposure time on the solid fraction of parts (without border regions) at a power of 275 W. Where the CT images describe (a) worst performing and (b) best performing parts.
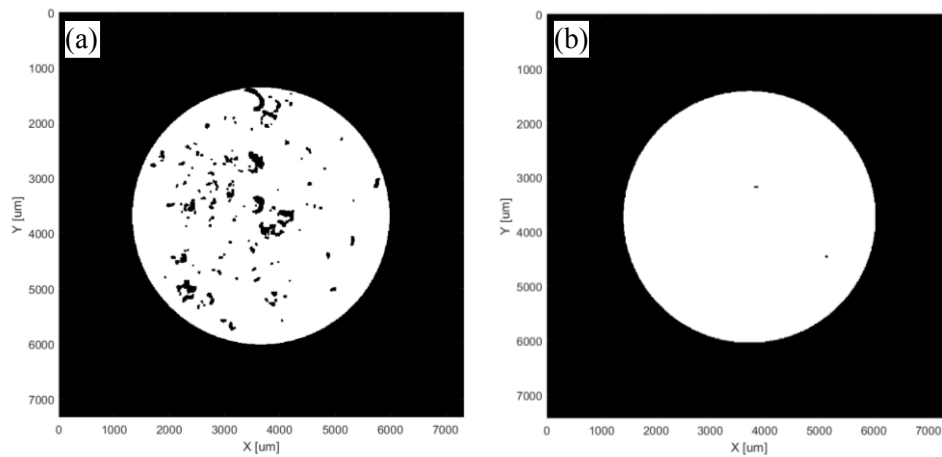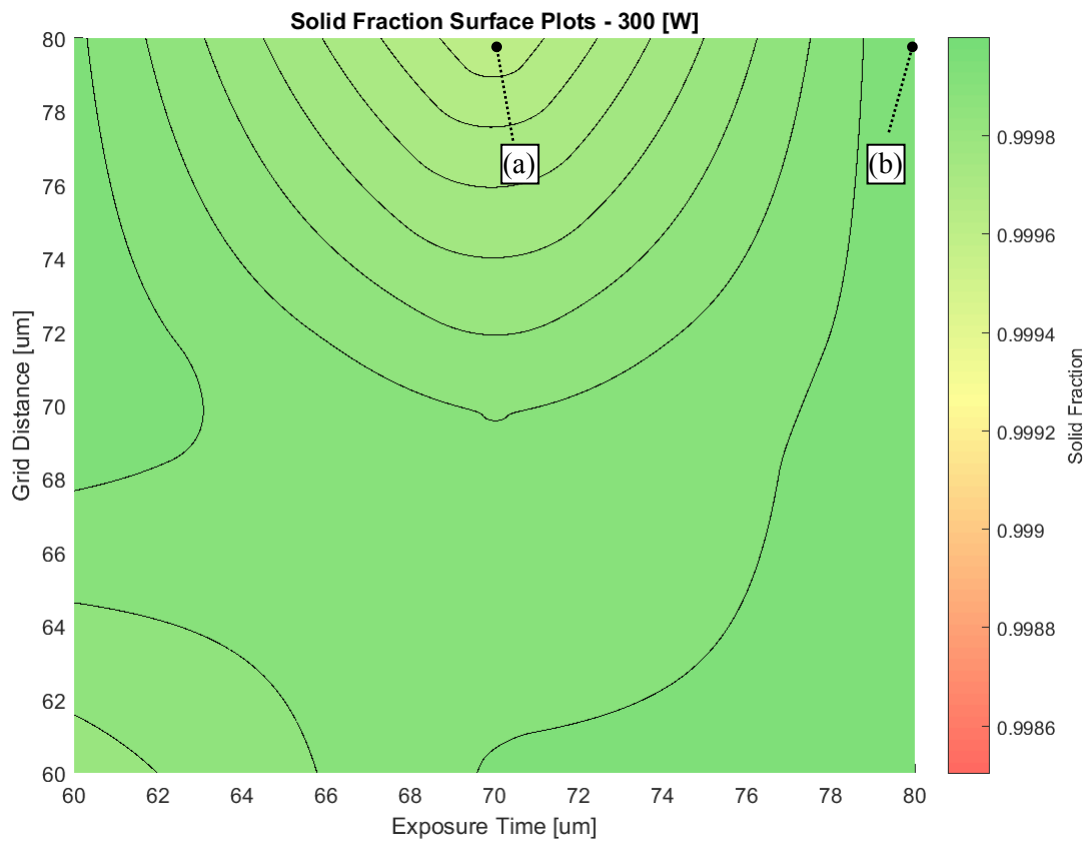
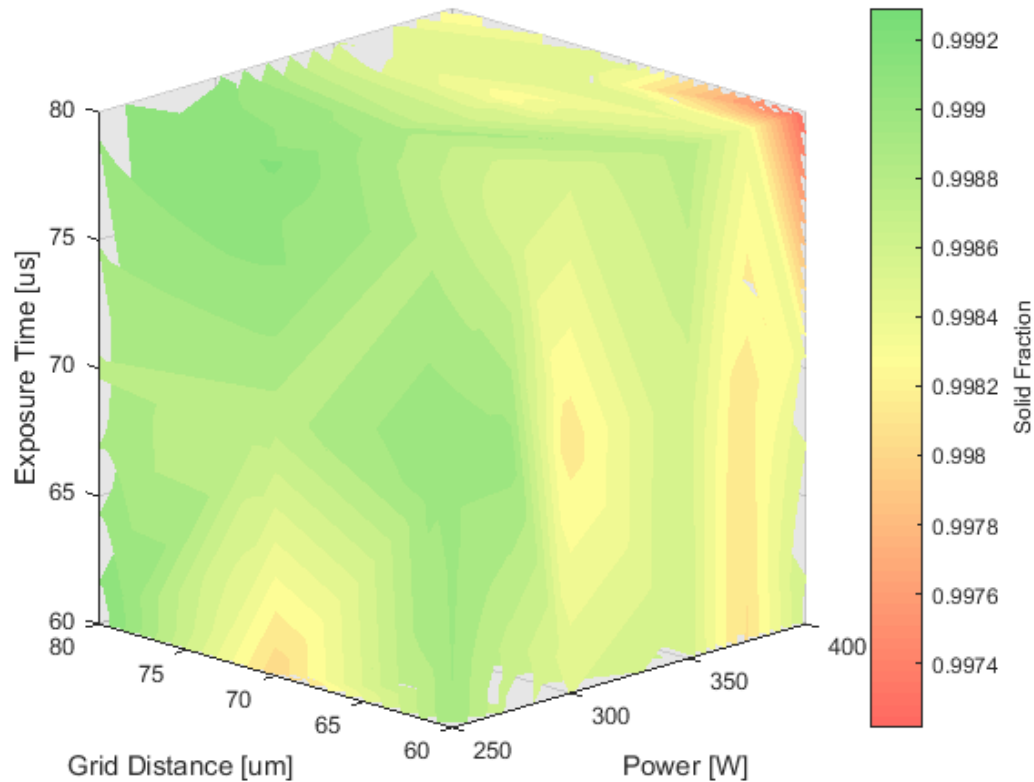**Figure 68. Two-dimensional surface plot describing the effects of grid distance and exposure time on the solid fraction of parts (without border regions) at a power of 300 W. Where the CT images describe (a) worst performing and (b) best performing parts.**
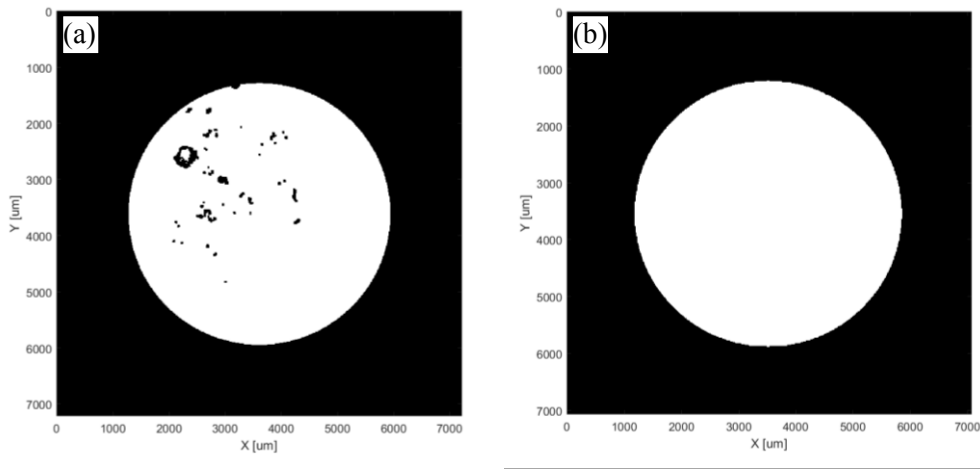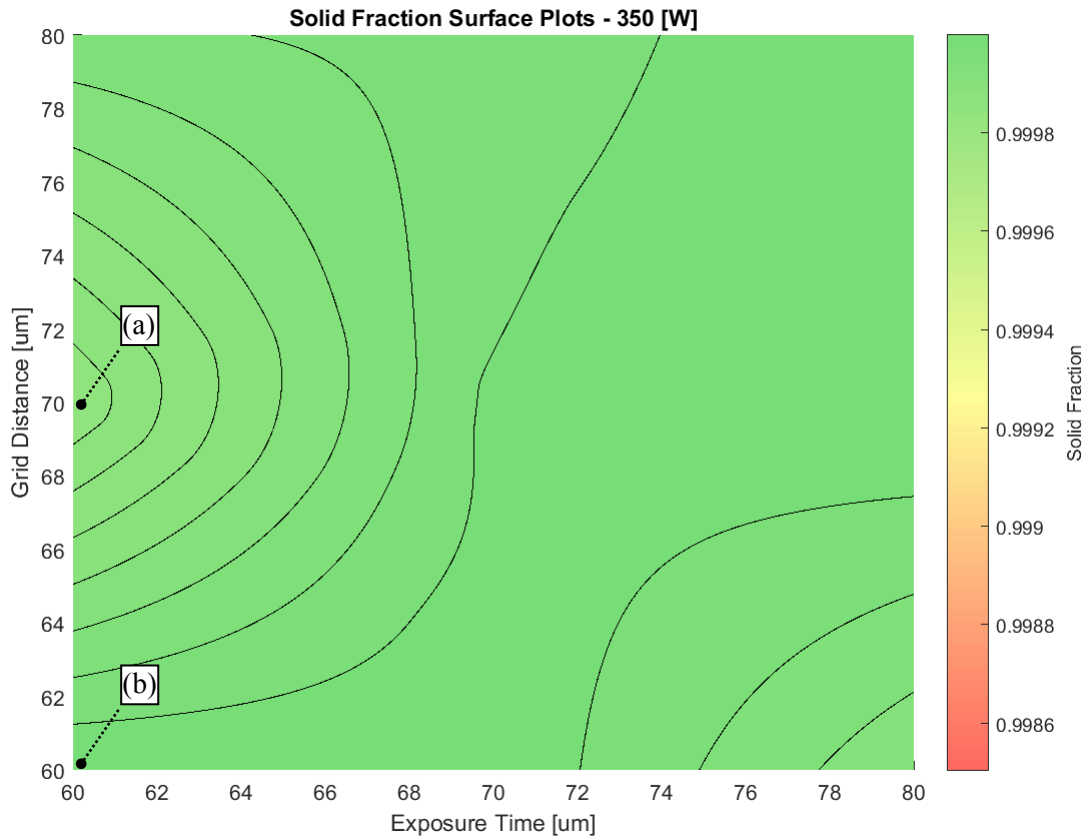
Figure 69. Two-dimensional surface plot describing the effects of grid distance and exposure time on the solid fraction of parts (without border regions) at a power of 350 W. Where the CT images describe (a) worst performing and (b) best performing parts.
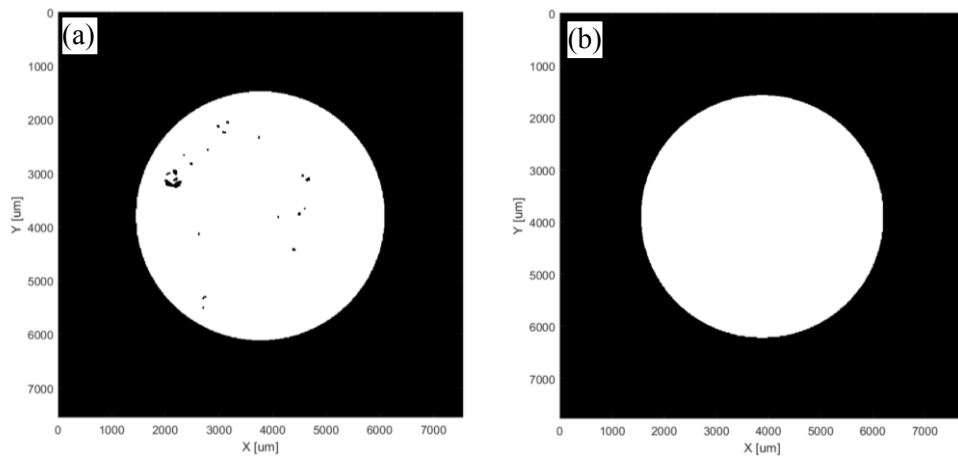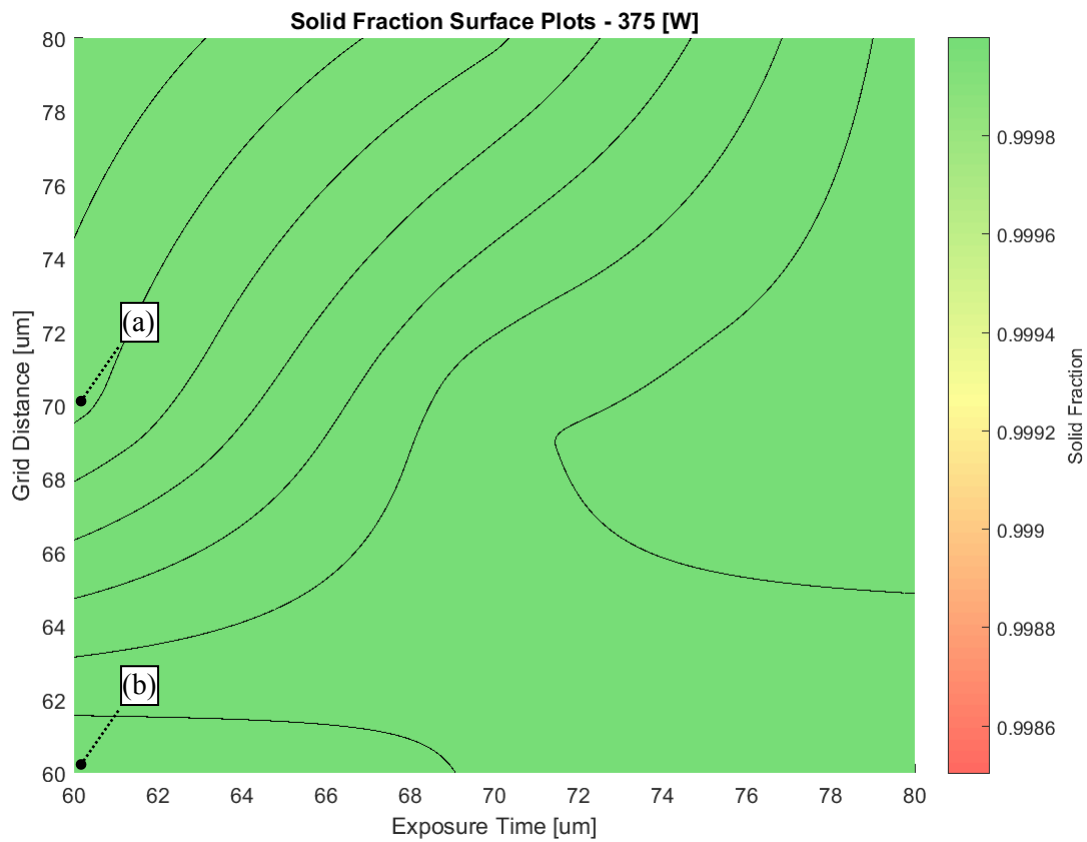
Figure 70. Two-dimensional surface plot describing the effects of grid distance and exposure time on the solid fraction of parts (without border regions) at a power of 375 W. Where the CT images describe (a) worst performing and (b) best performing parts.
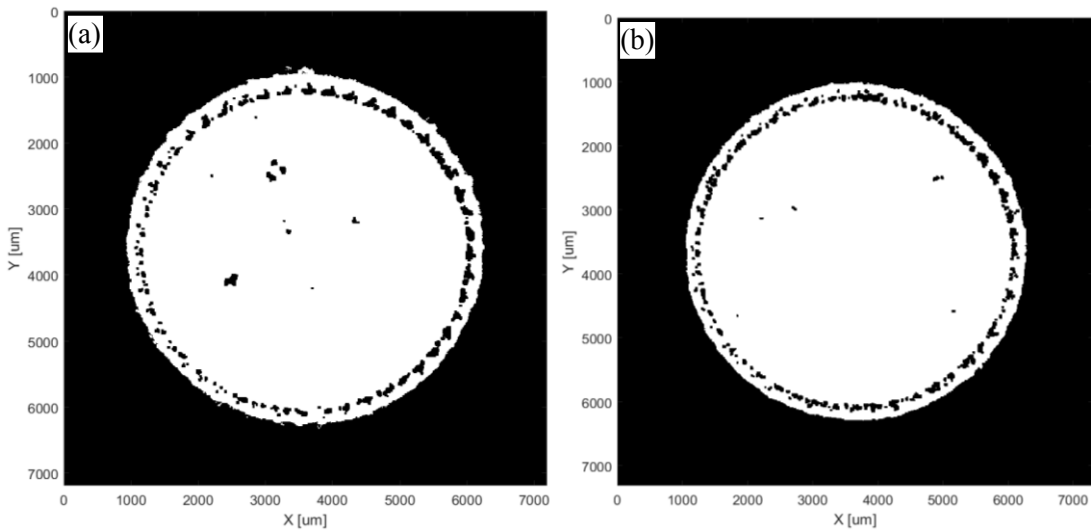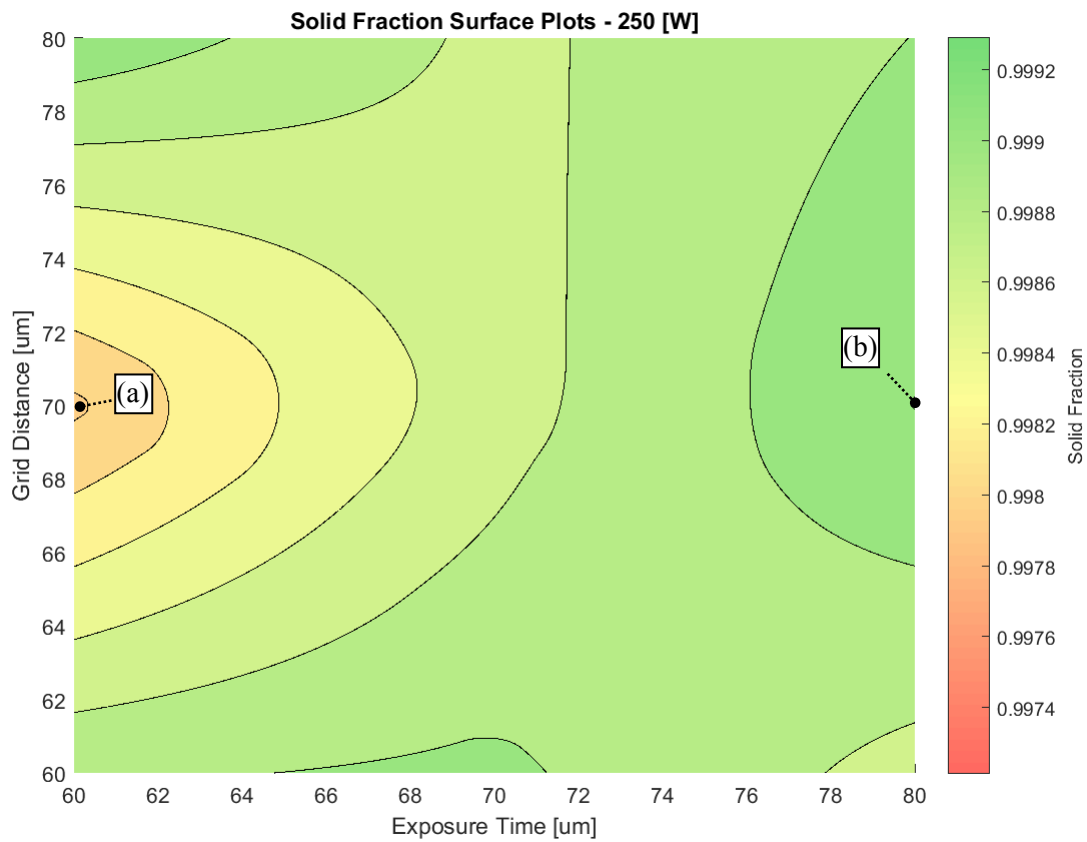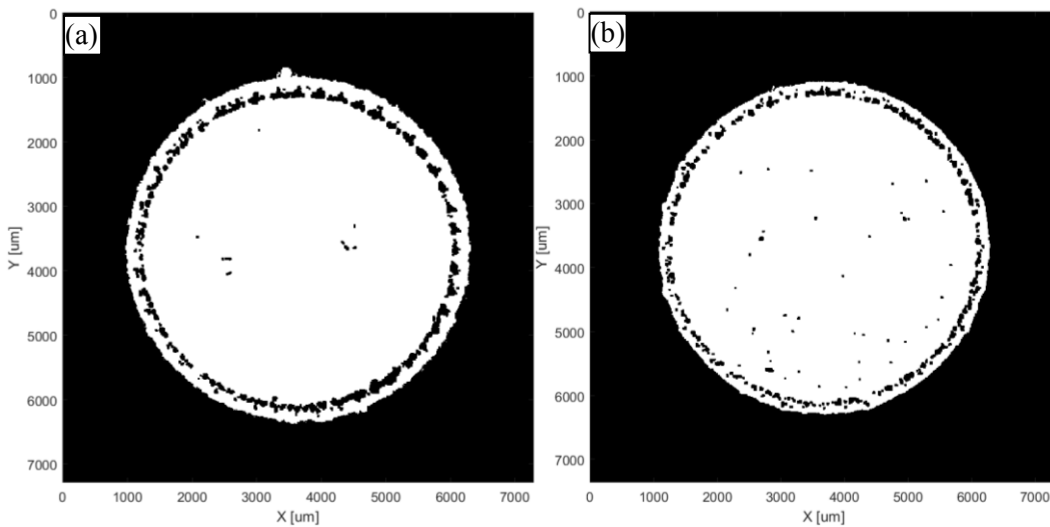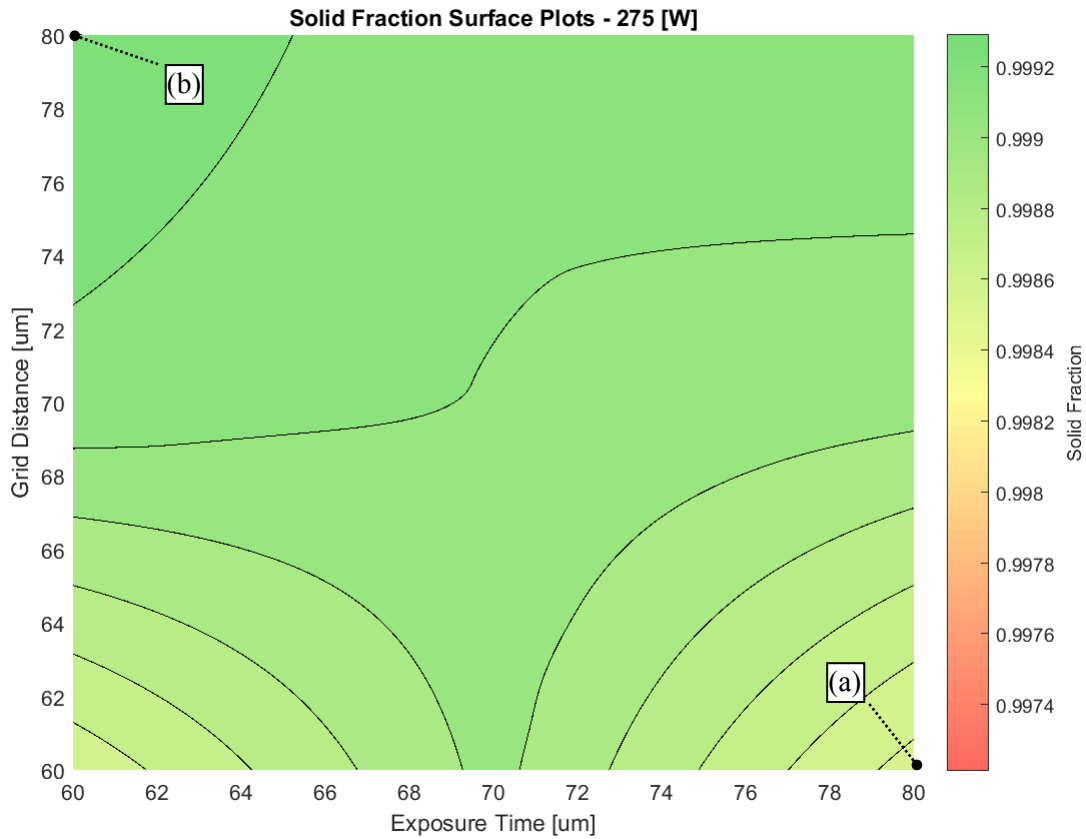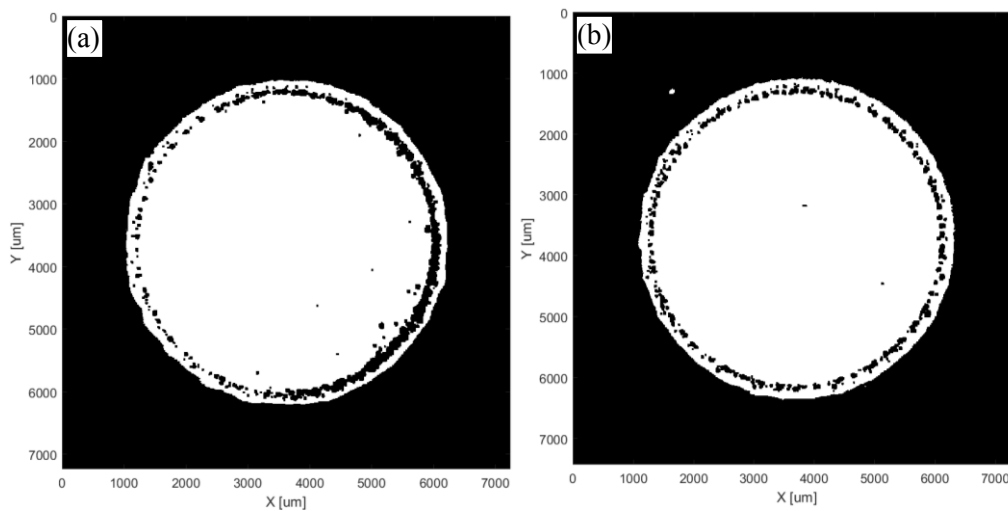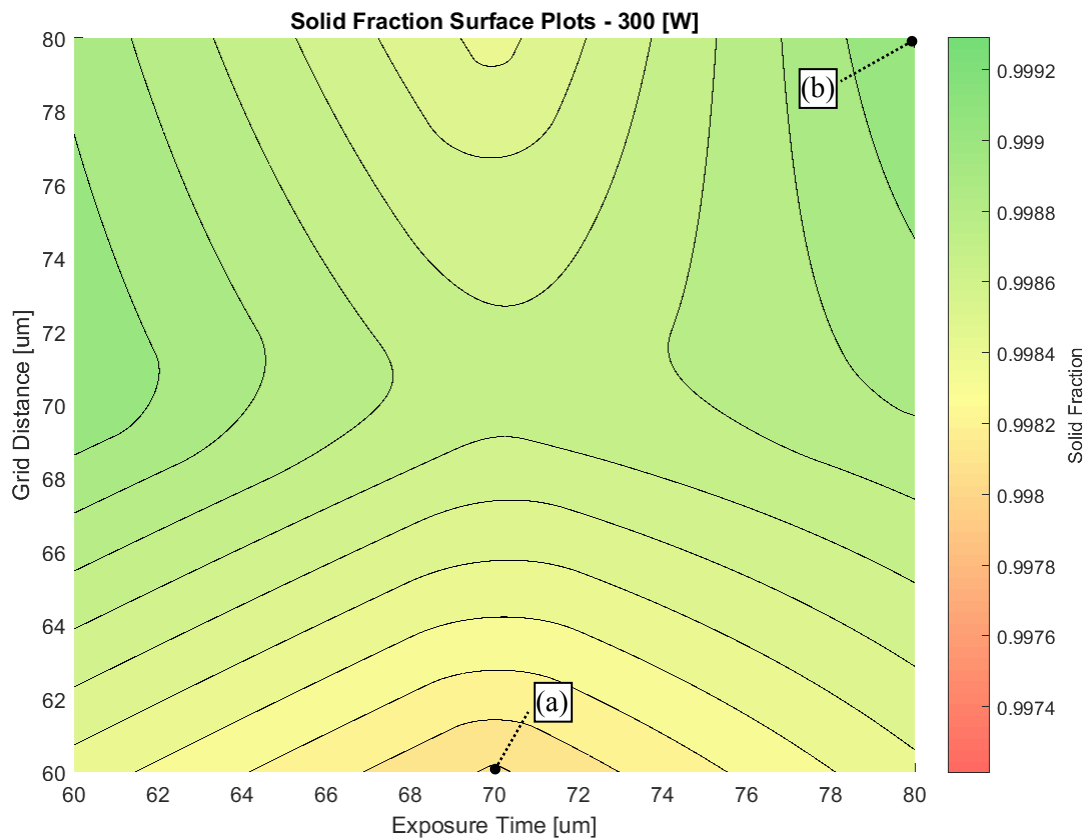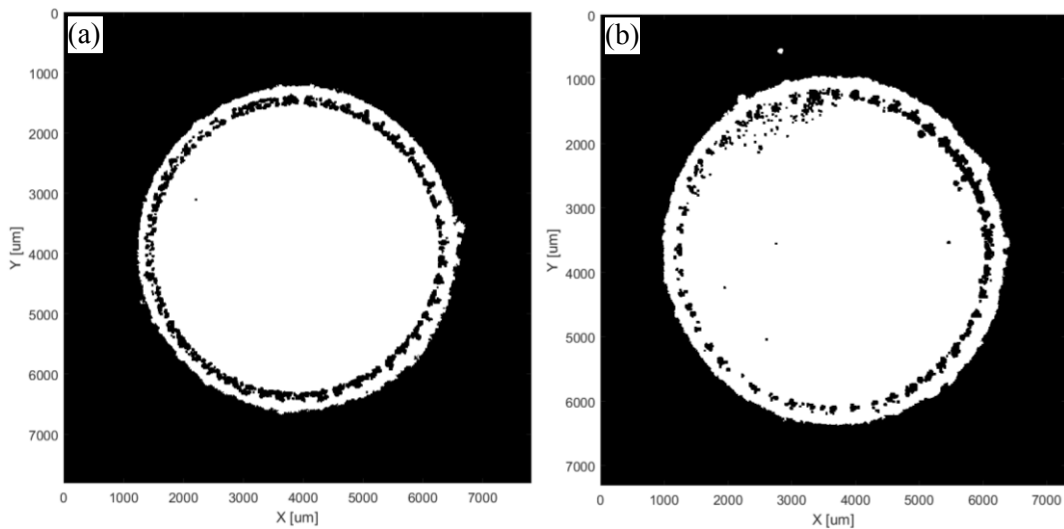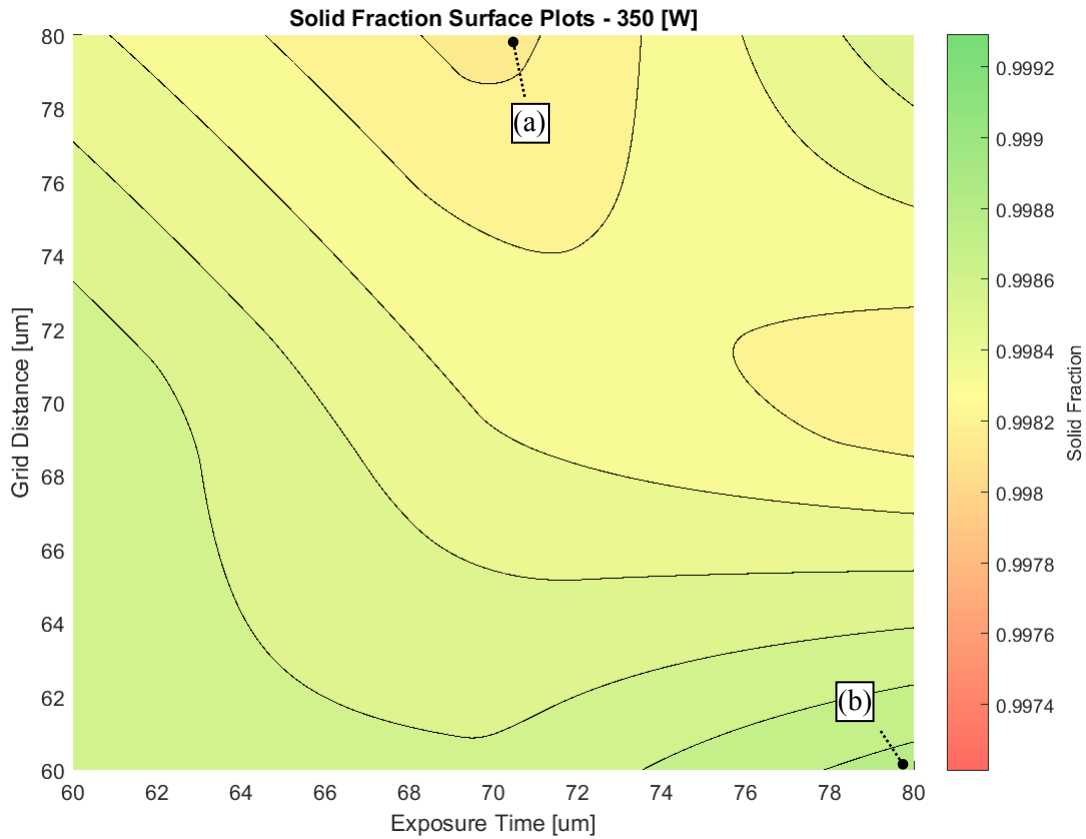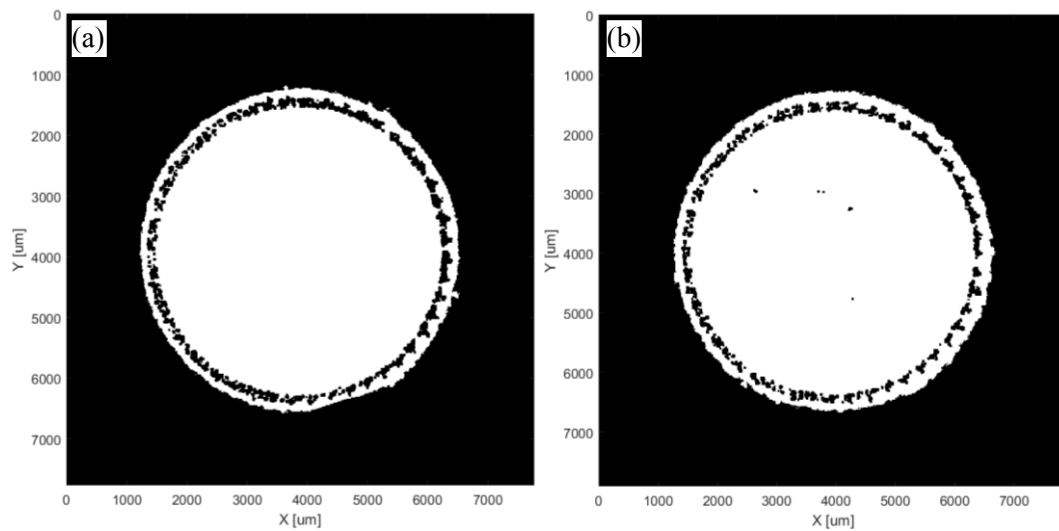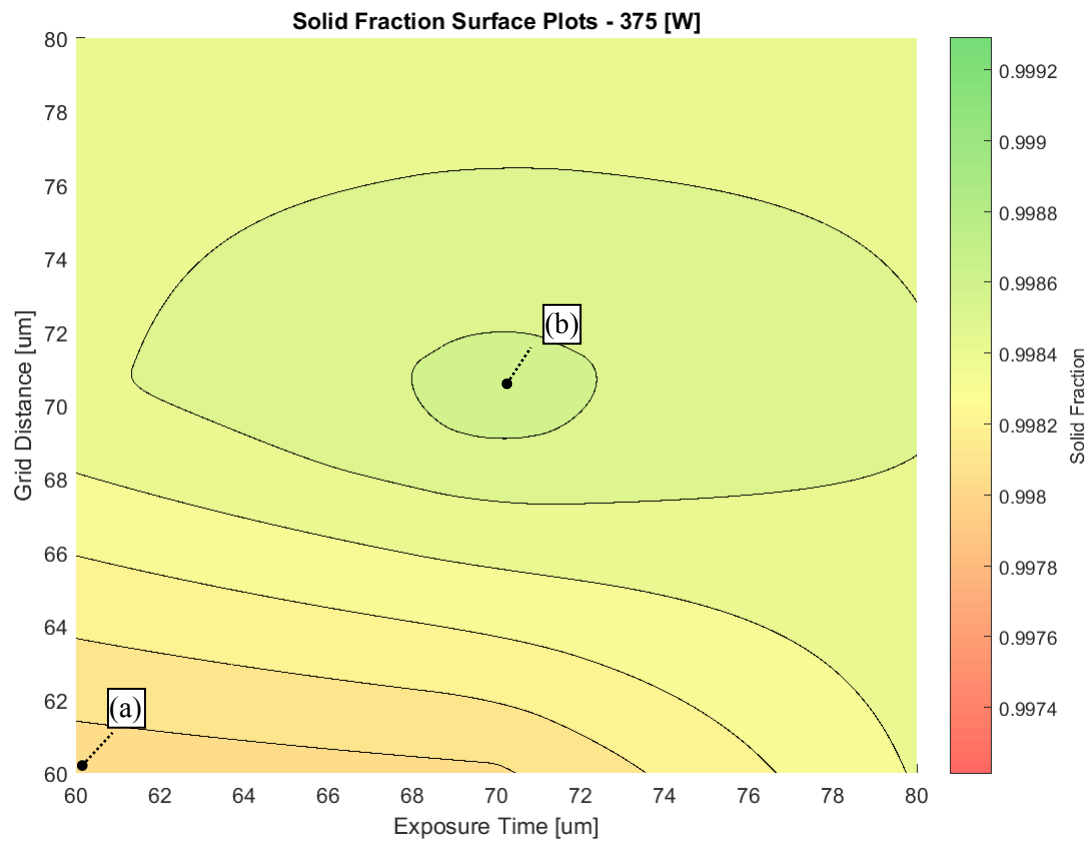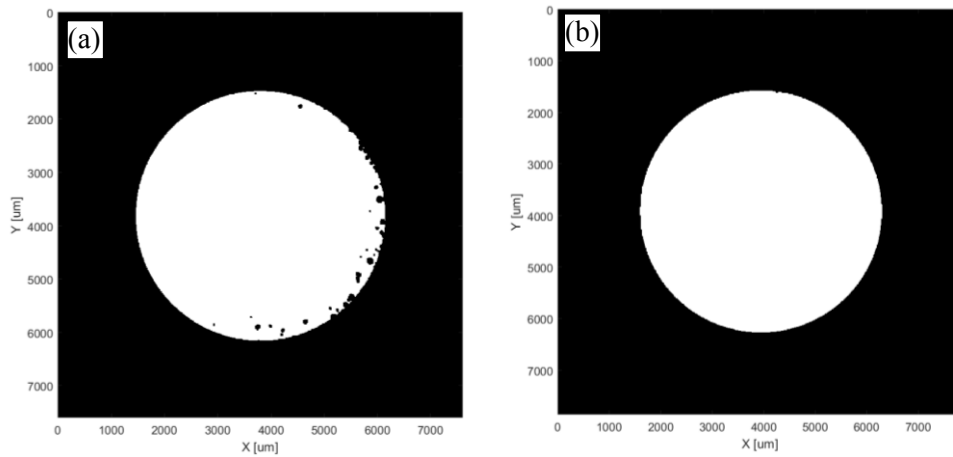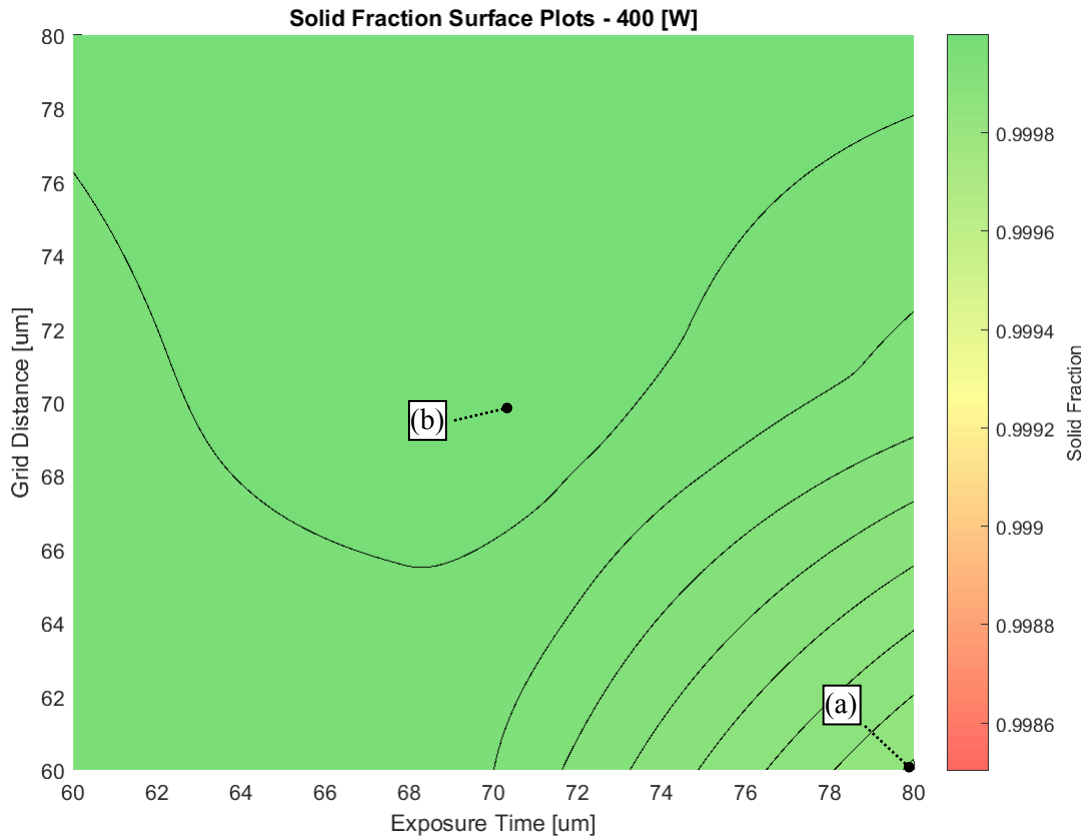
Figure 71. Two-dimensional surface plot describing the effects of grid distance and exposure time on the solid fraction of parts (without border regions) at a power of 400 W. Where the CT images describe (a) worst performing and (b) best performing parts.

It can be seen that the overall homogeneity of the solid fraction makes it difficult to discern the effects of grid distance or exposure time within each power level. Also, aside from the improvement in solid fraction between 250 W and 275 W of power, it is also difficult to see the effect of power. However, it is interesting to note that for virtually all power levels, the worst performing part always had a lower energy density than the best performing part. This may be due to localized optimizations within each power level, where at a certain energy density threshold, the effect of re-melting guarantees the elimination of pores within the sample. In particular, at power levels up to 300 W, increase of energy density due to exposure time is observed to be the most influential build variable between the worst- and best-performing parts. This may be because at lower power regimes, there is a minimum required exposure time at which re-melting is optimal. At power levels above 300 W, the extra energy input from higher power levels may have reduced this exposure time threshold and thus grid distance becomes more prominent, where the increase in grid distance allows for more overlap in re-melting. The exception is at the highest power level, where the best performing part had lower energy density than the worst performing part. From observation, it appears that the energy density was high enough for vaporization to occur and cause gas entrapment, as shown by the presence of spherical pores.

4.2.7 Statistical Analysis of Solid Fraction Results (Overall Part)

As mentioned previously, it was only possible to analyze a single replicate of the experiment, and thus a model based on Tukey's test was applied to free up degrees of freedom for the analysis. The result of the analysis is described below in Table 17 for the overall part (as per Figure 54). It can be seen that the laser power is shown to have a significant effect (at $\alpha = 0.05$) on the measured solid fraction of the parts, confirming the previous visual observation. Moreover, the interaction effects, the grid distance, and the exposure time are not determined to be significant build variables, which confirms the earlier observations.

Overall, the model has an adjusted R-squared value of 29.16%, which indicates that there are additional factors that may be unaccounted for in the model. In particular, the effect of gas flow, the un-optimized border region build variables, or the part layout may have added to the variability. It should be noted that the model used in Table 17 is best suited to determine the significance of build variables and not their functional relationship. Therefore, although the model does not very accurately explain all the variance in the model, obtaining 29.16% of all variance explained by the significant build variables is still a powerful conclusion. To ensure the validity of the ANOVA, several model

97

adequacy plots were constructed to verify the validity of the assumptions of normality and independence for the distribution of errors. These plots are shown below in Figure 72.

Table 17. ANOVA table showing the effects of the build variables on overall part solid fraction.

Source of Variation	Sum of Squares	Degrees of Freedom	Mean Square	F_0	p-value
Power	3.0315×10^{-6}	5	6.0630×10^{-7}	5.5315	0.00058003
Grid	5.6062×10^{-7}	2	2.8031×10^{-7}	2.5574	0.090123
Exposure Time	1.0936×10^{-7}	2	5.4679×10^{-8}	0.49885	0.61095
P/G	1.3571×10^{-10}	1	1.3571×10^{-10}	0.0012381	0.97211
P/E	9.7098×10^{-8}	1	9.7098×10^{-8}	0.88585	0.35225
G/E	1.0695×10^{-8}	1	1.0695×10^{-8}	0.097574	0.75638
P/G/E	6.8484×10^{-9}	1	6.8484×10^{-9}	0.06248	0.8039
Error	4.3844×10^{-6}	40	1.0961×10^{-7}		
Total	8.2006×10^{-6}	53			

Adjusted R-squared value: 0.2916
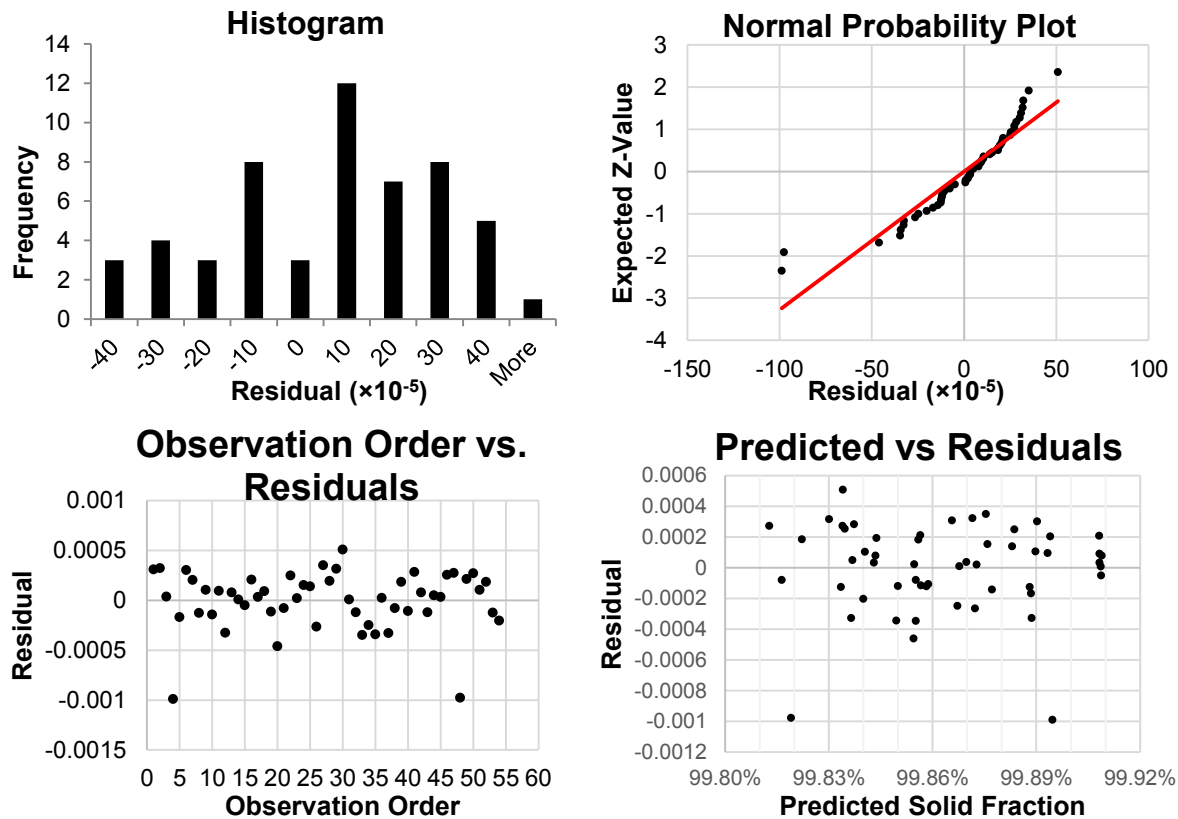
Figure 72. Model adequacy plots for the ANOVA model for assessing the normality and independence assumptions.

From the model adequacy plots, there are several observations. Firstly, the residuals do not appear to be following a normal distribution, based on the data shown in the histogram and the normal probability plot. Secondly, the residuals plotted against observation order and predicted solid fractions appear to show the presence of outliers, which may be affecting the model prediction. Because of these observations, it is not possible to confirm that the errors are normally and independently distributed for the model used to develop the ANOVA table, and thus the results obtained cannot be considered reliable. Thus, in order to analyze the results, an alternate procedure is used to analyze the single replicate measurements.

As discussed in section 4.1.5, dropping large order interactions are often feasible assumptions to make, due to the 'sparcity of effects' principle. Thus, by dropping the 'P/G/E' interaction effect from the model, enough degrees of freedom were recovered to run a reduced-model ANOVA. To confirm the viability of this assumption, model adequacy plots were plotted after analysis. The results are shown below in Table 18. The omission of the three-factor interaction results in a better fitting model than in Table 17, with 54.59% of the observed variance explained by Table 18. Similar to Table 17, the results here show power is a significant factor (at $\alpha = 0.05$), and as well, grid distance. This confirms the earlier observations of the effects of power and grid distance. Since the p-value of the grid distance is higher, the conclusions are not as powerful. This manifested itself earlier with the uncertainty in the prior observations. Another interesting observation is that the interaction between power and grid, although not considered significant, is at lower p-values than the other insignificant factors. Although the effect is not immediately discernible, additional measurements in the future may reveal the relationship between the build variables. It is hypothesized, however, that with increasing overlap the effect of power becomes more influential as multiple spots are being re-exposed before they can fully solidify, and similarly with decreasing overlap there may be cases where power provides insufficient melt.

Described below in Figure 73 are the model adequacy plots. From the plots, it appears as though the normality and independence assumptions are more valid than previously, with the residuals taking on a normal distribution, but appear to be slightly biased in the positive direction. This may be attributed to an outlier present in the data, as shown in the predicted vs residual plot, that may be influencing the model prediction. This residual corresponds with the sample with the worst solid fraction (sample 48). Since the sample point was placed within the extreme ranges of the experiment, it is expected that the solid fraction would dramatically decrease as the laser-material interaction

99

moves towards material vaporization. Thus, the sample point was not removed from analysis such that its influence on the results are relevant to the process outcome.

Table 18. ANOVA table showing the reduced model without the three-factor interactions.

Source of Variation	Sum of Squares	Degrees of Freedom	Mean Square	F_0	p-value
Power	3.0315×10^{-6}	5	6.0630×10^{-7}	8.6283	0.0002
Grid	5.6062×10^{-7}	2	2.8031×10^{-7}	3.9891	0.0348
Exposure Time	1.0936×10^{-7}	2	5.4679×10^{-8}	0.7781	0.4727
P/G	1.4582×10^{-6}	10	1.4582×10^{-7}	2.0752	0.0790
P/E	1.2899×10^{-6}	10	1.2899×10^{-7}	1.8357	0.1189
G/E	3.4565×10^{-7}	4	8.6413×10^{-8}	1.2297	0.3299
Error	1.4054×10^{-6}	20	7.0269×10^{-8}		
Total	8.2006×10^{-6}	53			

Adjusted R-squared value: 0.5340
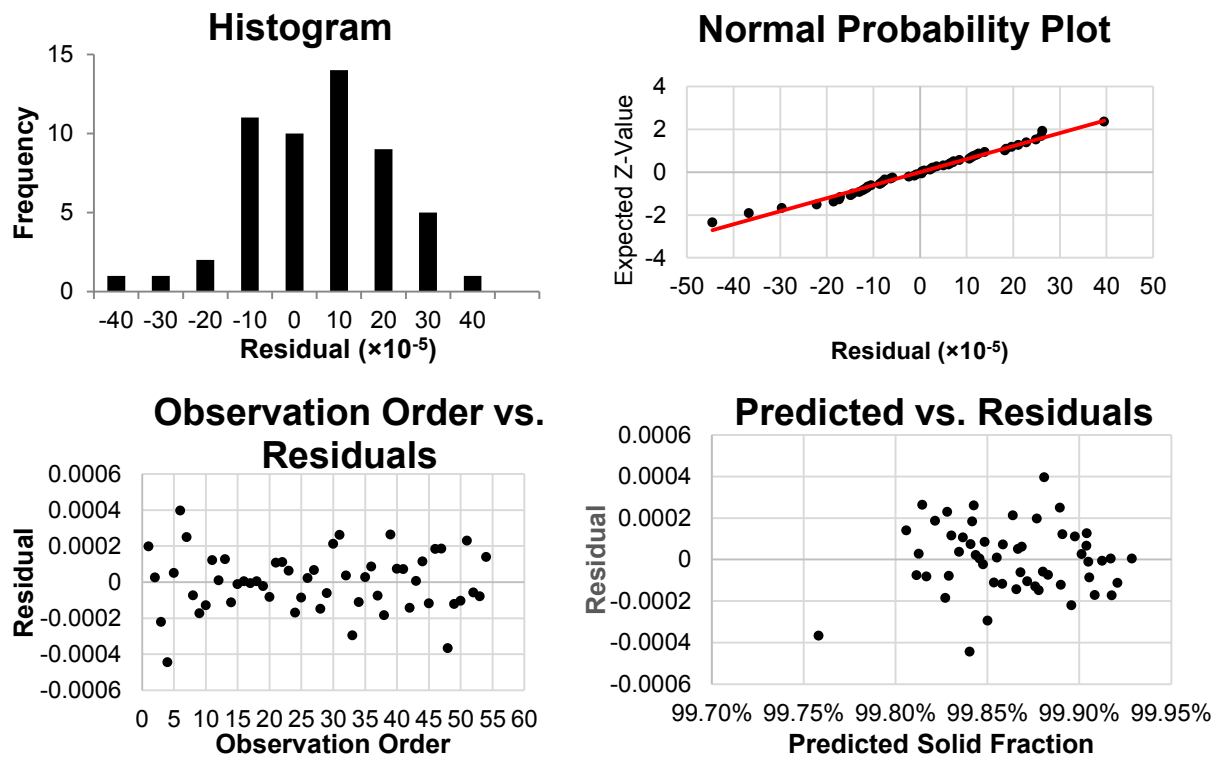
Figure 73. Model adequacy plots for the ANOVA reduced model, showing the validity of the normality and independence assumptions.

4.2.8 Statistical Analysis of Solid Fraction Results (Border Region Removed)

By applying the same statistical approach to the results that focus on the part with border region removed, Table 19 can be found. In this case, the model appears to show all build variables are significant in determining the solid fraction in the core, and that adjusted R-squared value appears to fit well with a value of 78.40%. However, the model adequacy plots need to be consulted as well, and are provided below in Figure 74.

Table 19. ANOVA table showing the effect of build variables on core region solid fraction.

Source of Variation	Sum of Squares	Degrees of Freedom	Mean Square	F_0	p-value
Power	5.6966×10^{-7}	5	1.1393×10^{-7}	11.14	9.1191×10^{-7}
Grid	6.9169×10^{-8}	2	3.4585×10^{-8}	3.3815	0.04397
Exposure Time	1.1075×10^{-7}	2	5.5377×10^{-8}	5.4145	0.0082982
P/G	4.4747×10^{-7}	1	4.4747×10^{-7}	43.751	6.4801×10^{-8}
P/E	3.7382×10^{-7}	1	3.7382×10^{-7}	36.55	4.0772×10^{-7}
G/E	1.0549×10^{-7}	1	1.0549×10^{-7}	10.315	0.0026057
P/G/E	4.2445×10^{-7}	1	4.2445×10^{-7}	41.501	1.1305×10^{-7}
Error	4.0910×10^{-7}	40	1.0228×10^{-8}		
Total	2.5099×10^{-6}	53			

R-squared value: 0.7840

Similar to the model adequacy plots in Figure 72, the residual plots in Figure 74 show significant deviations from ideal behaviour. From the histogram and normal probability plots, the residuals do not conform to a normal distribution, and appear to congregate near a single value. This is further shown in the plot describing residual vs. observation order, where the behaviour of the residuals appear to be structured, where they should be essentially random. There also appears to be the presence of an outlier in the residuals vs. predicted value plot. Unfortunately, the analysis cannot be re-run without the presence of an outlier, because only the minimal amount of samples were gathered for model viability. Therefore, because the errors in the model do not appear to be normally and independently distributed, the results concluded in Table 19 cannot be considered valid and dependable. In a similar exercise to the previous dataset, an alternate method was performed, by assuming higher-order interactions were negligible, and ANOVA was performed on the reduced model.
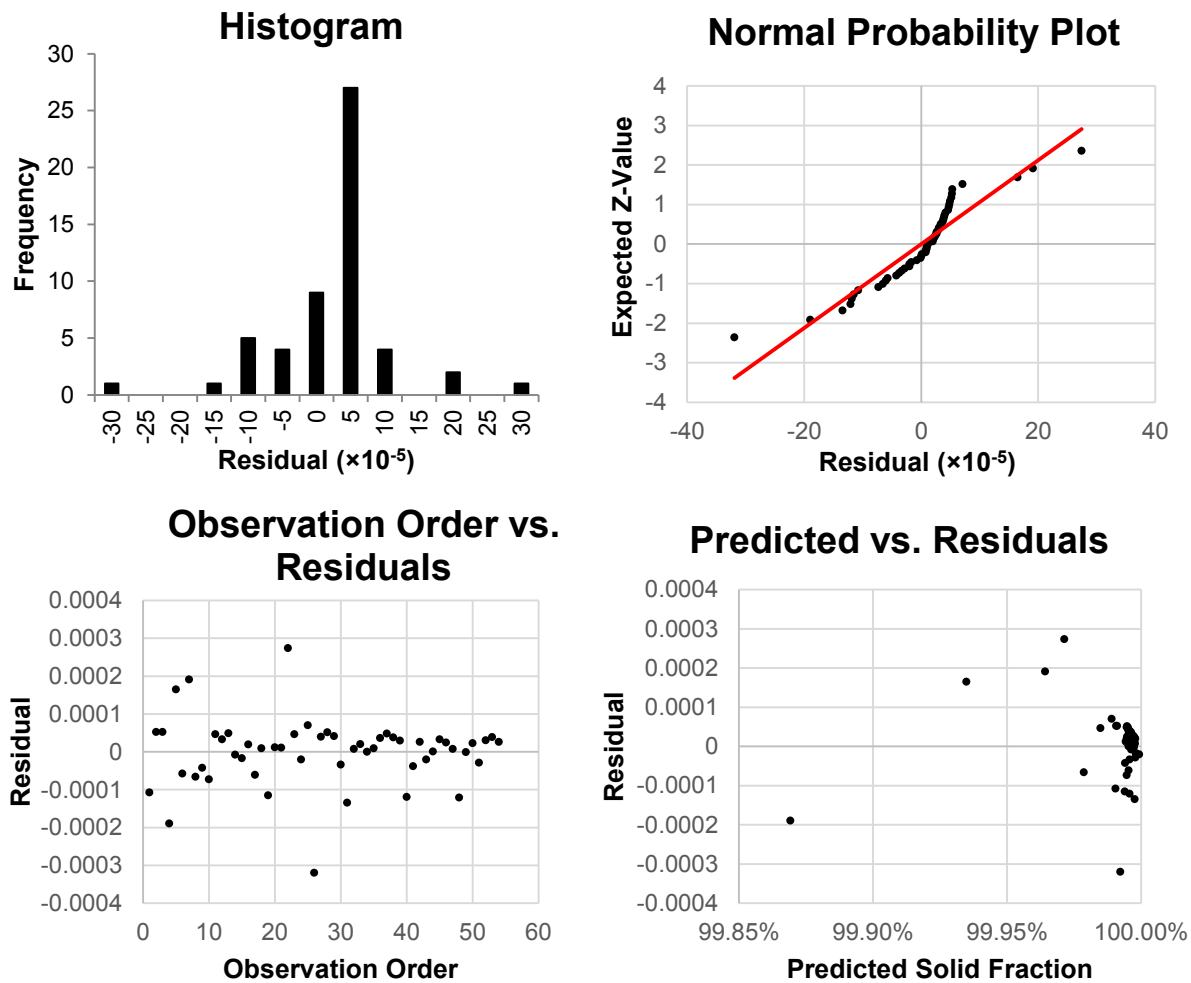
Figure 74. Model adequacy plots for the ANOVA model, describing CT data without border regions, for assessing the normality and independence assumptions.

Upon neglecting the three-factor interaction term, and running the ANOVA on the reduced model, Table 20 is generated. From the table, it appears as though only the influence of laser power is significant, and this is likely from the large increase in solid fraction as laser power moves from 250 W to higher levels. The overall model has an adjusted R-squared value fitting approximately 33.89%. Once again, model adequacy plots are constructed to verify the validity of the observations shown in Table 20. These plots can be referenced in Figure 75. By using the reduced model, it appears as though the residuals conform more closely to a normal distribution, as shown by the histogram and normal probability plot. However, there still appears to be the presence of outliers, and they may be affecting the model fit, because of the anomalous behaviour in the residual vs. run order plot, and the

102

predicted vs. residual plot. Particularly, there is a large imbalance in the x-axis for the predicted vs. residual plot. To attempt to correct for this anomaly, a final modification was made to the analysis by neglecting the outlier term from the analysis, and the result of which can be referred to in Table 21.

Table 20. ANOVA table for the reduced model without three factor interactions, showing the effect of build variables on core region solid fraction.

Source of Variation	Sum of Squares	Degrees of Freedom	Mean Square	F_0	p-value
Power	5.69657×10^{-7}	5	1.13931×10^{-7}	3.64	0.0167
Grid	6.91691×10^{-8}	2	3.45845×10^{-8}	1.10	0.3507
Exposure Time	1.10754×10^{-7}	2	5.53770×10^{-8}	1.77	0.1962
P/G	5.21603×10^{-7}	10	5.21603×10^{-8}	1.67	0.1589
P/E	4.43497×10^{-7}	10	4.43497×10^{-8}	1.42	0.2429
G/E	1.69112×10^{-7}	4	4.22780×10^{-8}	1.35	0.2862
Error	6.26125×10^{-7}	20	3.13063×10^{-8}		
Total	2.5099×10^{-6}	53			

R-squared value: 0.3389
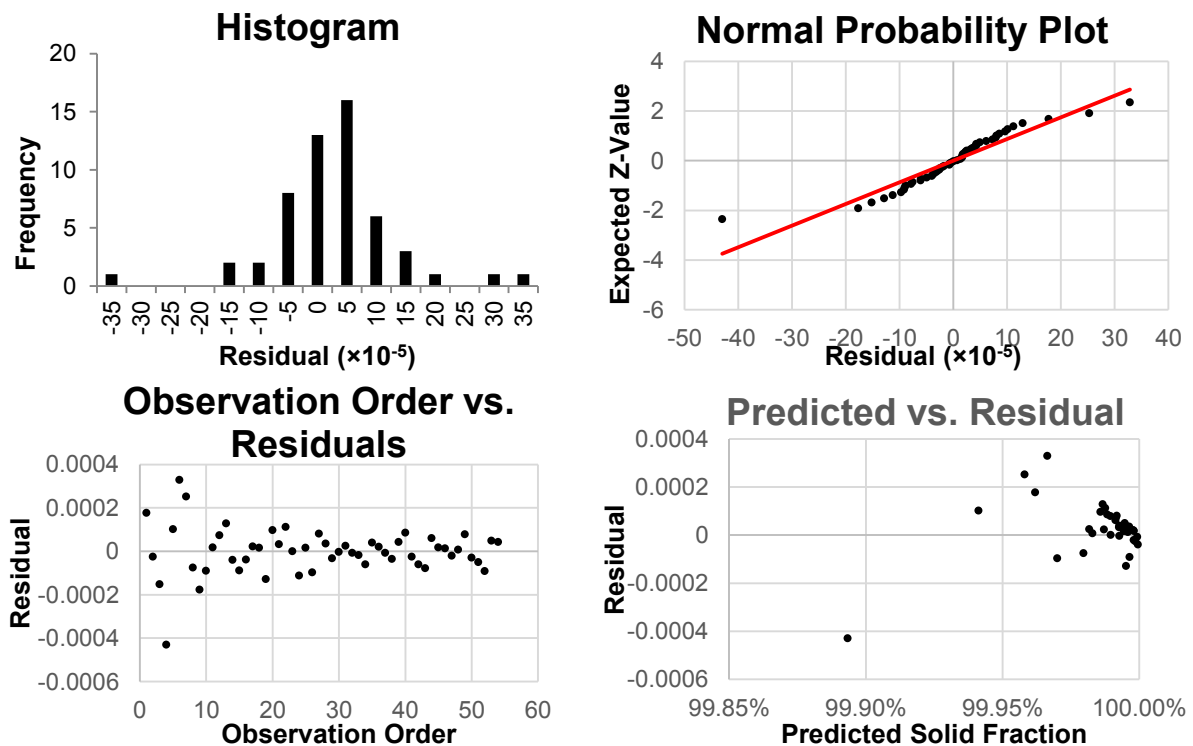
Figure 75. Model adequacy plots for the reduced ANOVA model, describing CT data without border regions, for assessing the normality and independence assumptions.

Table 21. ANOVA table for the reduced model without the outlier or three factor interactions, showing the effect of build variables on core region solid fraction.

Source of Variation	Sum of Squares	Degrees of Freedom	Mean Square	F_0	p-value
Power	1.47194×10^{-7}	5	2.94388×10^{-8}	4.39	0.0087
Grid	3.97752×10^{-8}	2	1.98876×10^{-9}	0.30	0.7467
Exposure Time	3.30355×10^{-7}	2	1.65177×10^{-8}	2.46	0.1118
P/G	5.87841×10^{-7}	10	5.87841×10^{-9}	0.88	0.5691
P/E	1.00191×10^{-7}	10	1.00191×10^{-8}	1.49	0.2163
G/E	5.01472×10^{-7}	4	1.25368×10^{-8}	1.87	0.1573
Error	1.27372×10^{-7}	19	6.70381×10^{-9}		
Total	4.9329910^{-6}	52			

R-squared value: 0.2933

As described by the ANOVA, laser power is once again the only significant factor, with the overall model fitting with an adjusted r-square value of 29.33%. The model adequacy plots show that the residuals conform well to a normal distribution, and appear to be generally randomly distributed based on the residuals vs run order plot. However, when looking at the predicted vs. residuals plot, it appears as though the residuals are still imbalanced, and this is also shown by a positive bias of the residuals in the histogram. It is hypothesized that the reason why the model is failing to adequately describe the solid fraction behaviour is because the performance of the parts is already nearing optimal densification. That is, the variation of the build variables may be improving on the density up to a certain plateau. After reaching this point, variations in the build variables may not be affecting the density whatsoever, and any measured changes in density are resultant of uncontrolled variations within the process. This behaviour is seen in the predicted vs actual plot in Figure 76, where the predicted values and actual values appear to be relatively well correlated until the actual values reach peak performance at $\approx100\%$, and the model predictions break down. Thus it is estimated that selecting any power level in the experiment region above the minimum 250 W will produce well performing solid fraction results in the core regions, regardless of the choice of exposure time or grid distance.
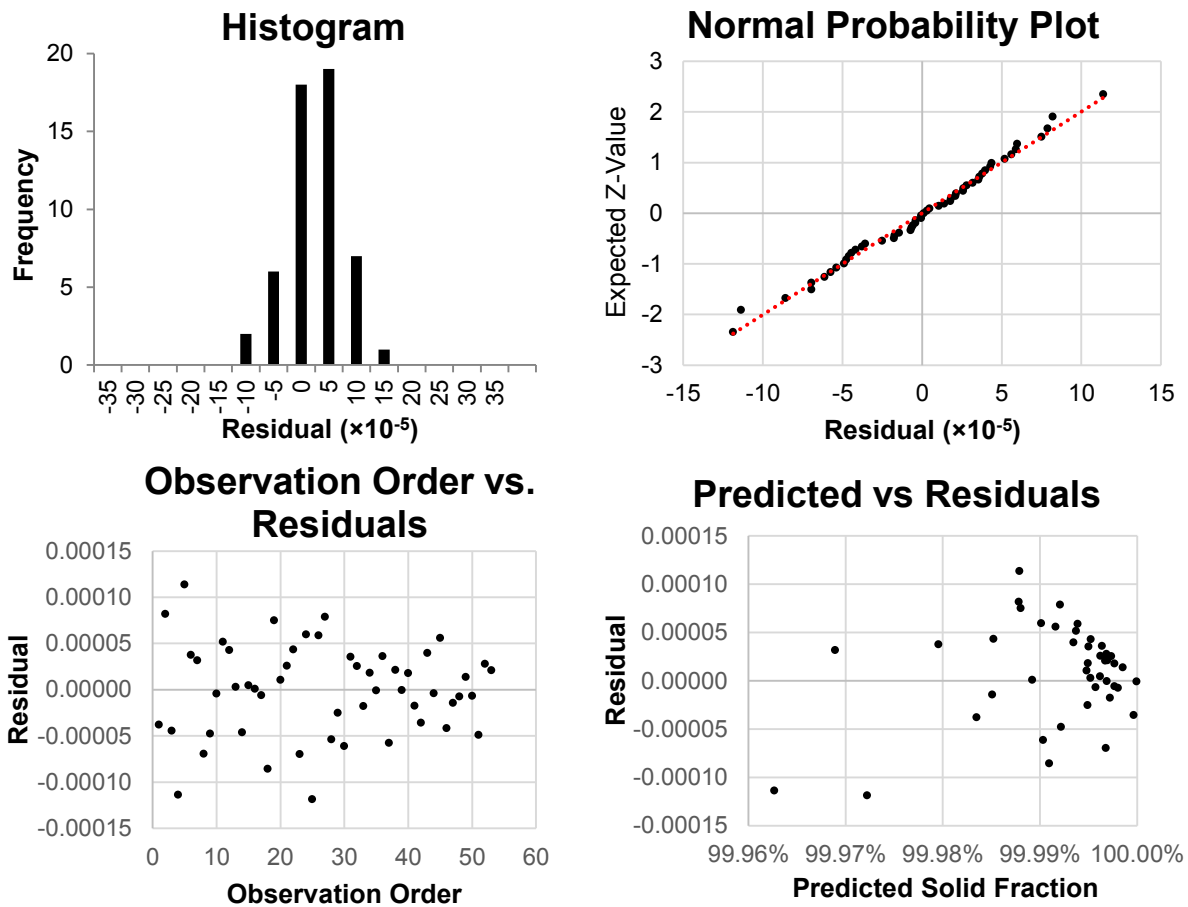
Figure 76. Model adequacy plots for the reduced ANOVA model, describing CT data without the outlier or border regions, for assessing the normality and independence assumptions.
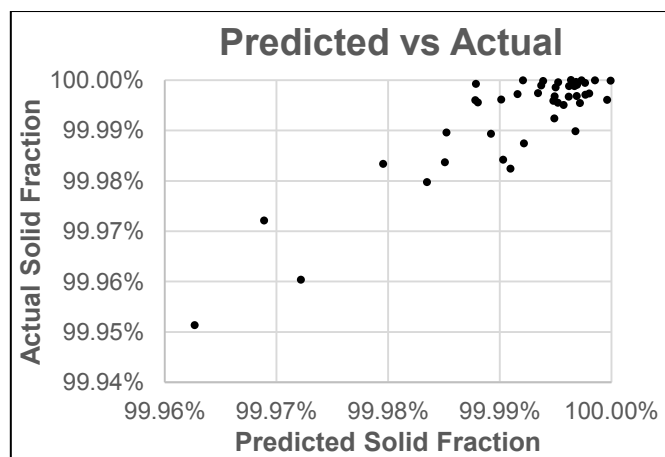
Figure 77. The plots for predicted solid fraction in comparison to the actual solid fraction for the reduced ANOVA model, describing CT data without the outlier or border regions.

To conclude, when considering the bulk part and the effect of the build variables on the border regions, it appears as though laser power and grid distance presents the only significant effects, with increasing power and generally decreasing grid distance correlated with increasing porosity. In terms of the solid fraction in the core regions, as long as the power level is higher than 250 W, the build variable selection is flexible with any selection of grid distance and exposure time within the experimental bounds. Therefore, it is suggested that the optimal values for laser power be above 250 W. The significance of the effect of grid distance, although not as powerful, suggests that larger grid distances may be beneficial. It is hypothesized that this decreases the occurrence of over-exposed points from overlapping scan exposures that may vaporize material. Since the effect of exposure time does not appear to have a significant effect, it is thus recommended that the most economical choice be selected, where low exposure times will result in faster builds.

Since the core region of parts are very well behaved, further experiments will be focusing on the effect of build variables on the border region of parts, and can be referenced in Chapter 5. However, the effect of density is not the only indicator of part quality for Invar36 specimen. Since thermal expansion is another critical aspect for Invar36 parts, the effect of build variable selection on thermal expansion must be considered as well and it will be discussed in the following section.

4.2.9 Process Mapping based on Thermal Expansion

To compare with conventional measurements for Invar36, the coefficient of thermal expansion (CTE) for all parts over a temperature range of 30 to 150 °C was measured and presented below in Figure 78. Overall, all measured thermal expansion values are lower than the values for conventional Invar36. According to ASTM F1684-06, the typical CTE for annealed Invar36 at temperature ranges between 30 °C and 150 °C lies within a range of 1.2 to 2.7 $\left[\frac{\mu m}{m°C}\right]$, while all measured values were lower than 1.0 $\left[\frac{\mu m}{m°C}\right]$. To explain this phenomenon, investigations by Harrison et al. found that the effect may be due to the buildup of residual stress, because upon heat-treatment the specimen regained CTE values closer to conventional values [60]. However, this phenomenon was found to be unique with Invar36, as other alloys did not show a decrease in CTE [60]. Thus it was suggested that the residual stress may be directly influencing the magneto-volume contraction of the material [60]. However there may be other factors, which will be discussed shortly.

In a similar exercise to section 4.2.4, a plot of the thermal expansion as a function of part I.D. and energy density was created, with the size of the circles corresponding to the measured thermal

106

expansion. However, similar difficulties with determining build variable effects were encountered within this plot. It does appear, however, that there is a trend of increasing size of the circles with larger sample I.D. Once again, the sample I.D. can be deciphered into the respective power, grid distance, and exposure time values using Figure 25 section 4.1.
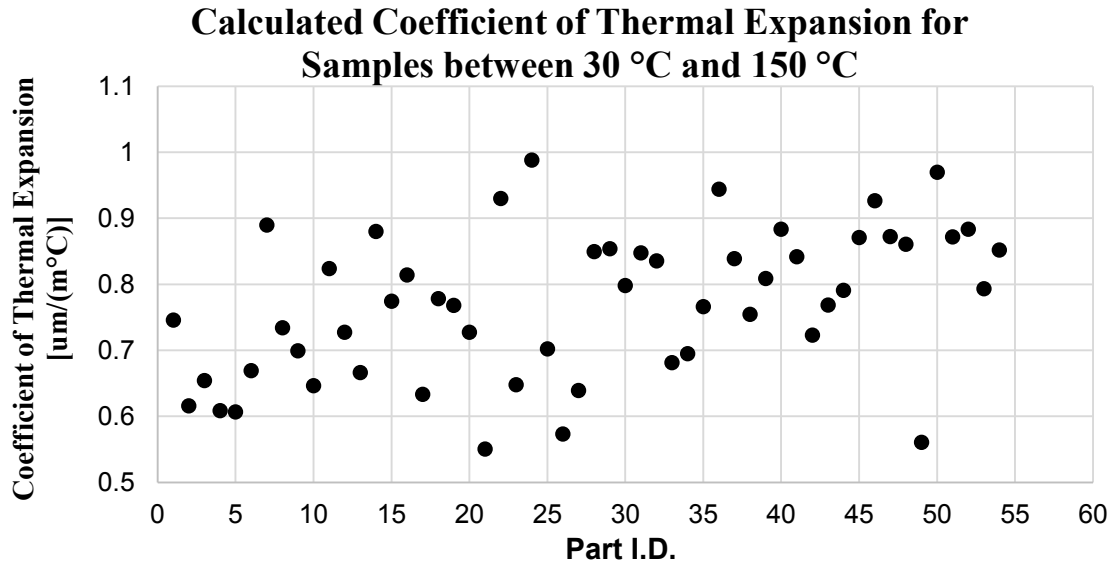
Figure 78. Measured CTE variation in terms of sample I.D. number.
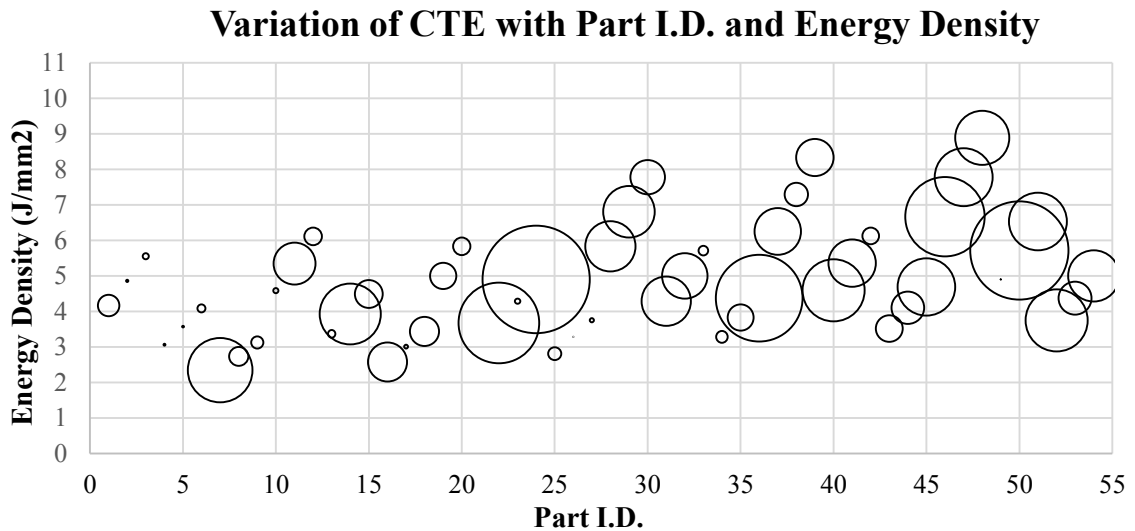
Figure 79. Variation of volumetric energy density across all permutations of build variables, with an additional 'axis' describing the coefficient of thermal expansion through the use of variable size circles.

Since the three-dimensional isosurface plot and two-dimensional surface plots are served to be more effective representations, the above plot is presented purely as a source for comparative observation. By plotting the results on a three-dimensional isosurface plot, it is possible to visualize the effects of each build variable on the thermal expansion (Figure 80).
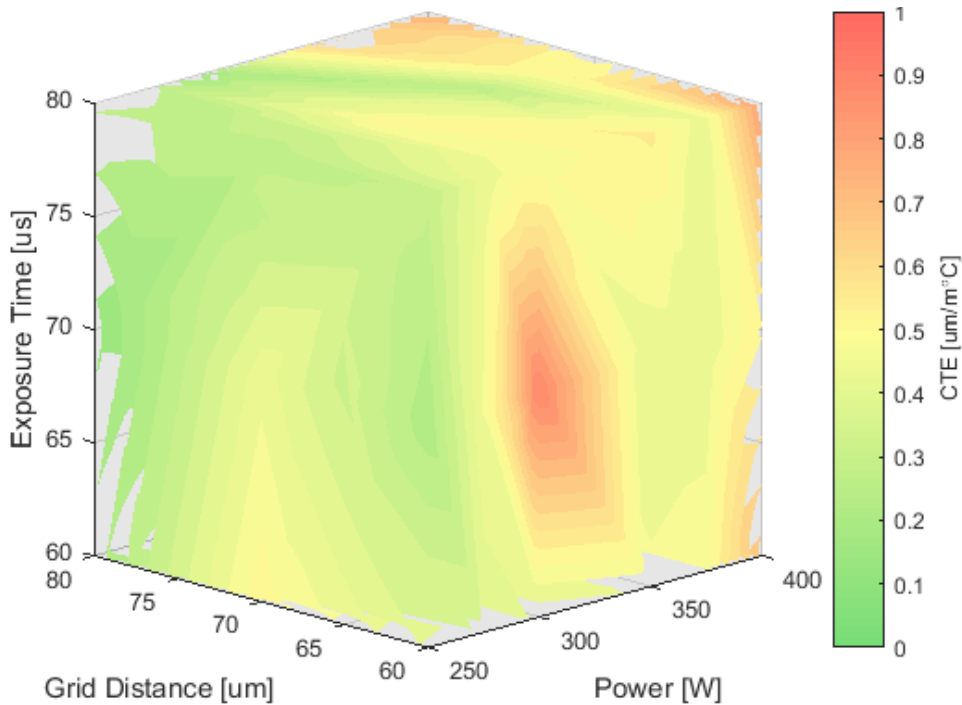
Figure 80. Three-dimensional surface plot describing the effects of power, grid distance, and exposure time on the coefficient of thermal expansion of parts.

In terms of the individual effects, it becomes clear that the increase of power appears to increase the thermal expansion coefficient, with the effects of grid distance and exposure time more difficult to ascertain. This may be explained by the microstructural evolution or chemical composition changes within the material during solidification. As mentioned in section 2.2, Invar36 is highly susceptible to CTE variation with chemical composition change, and this may have potentially been a factor as well. However, as discussed in section 4.2.1, the chemical composition did not change with any change in build variables, and thus the effect must be due to an alternate factor. Aside from residual stress, it has been shown in literature that other factors such as texture and grain sizes are correlated with variations in the CTE, In particular, certain crystal orientations are associated with lower CTE and likewise with larger grain sizes [111], [112].

As before, segregating the three-dimensional surface plot into individual surface plots elucidates the relationship between grid distance and exposure time at each power level (Figure 81 – Figure 86).

Figure 81. Two-dimensional surface plot describing the effects of grid distance and exposure time on the thermal expansion of parts at a power of 250 W.

Figure 82. Two-dimensional surface plot describing the effects of grid distance and exposure time on the thermal expansion of parts at a power of 275 W.

Figure 83. Two-dimensional surface plot describing the effects of grid distance and exposure time on the thermal expansion of parts at a power of 300 W.

Figure 84. Two-dimensional surface plot describing the effects of grid distance and exposure time on the thermal expansion of parts at a power of 350 W.

Figure 85. Two-dimensional surface plot describing the effects of grid distance and exposure time on the thermal expansion of parts at a power of 375 W.

Figure 86. Two-dimensional surface plot describing the effects of grid distance and exposure time on the thermal expansion of parts at a power of 400 W.

4.2.10 Statistical Analysis of Coefficient of Thermal Expansion Results

A statistical analysis similar to the previous section was also performed to determine the significance of the build variable effects on the thermal expansion coefficient, and Table 22 shows the findings.

Table 22. ANOVA table showing the effects of the build variables on CTE.

Source of Variation	Sum of Squares	Degrees of Freedom	Mean Square	F_0	p-value
Power	1.5232×10^{-1}	5	3.0465×10^{-2}	2.907963	0.02484
Grid	9.5649×10^{-4}	2	4.7824×10^{-4}	0.04565	0.955426
Exposure Time	2.5920×10^{-3}	2	1.2960×10^{-3}	0.123707	0.883976
P/H	7.0876×10^{-3}	1	7.0876×10^{-3}	0.676535	0.415659
P/E	3.0453×10^{-2}	1	3.0453×10^{-2}	2.906857	0.09596
H/E	1.7576×10^{-2}	1	1.7576×10^{-2}	1.677719	0.202654
P/H/E	1.6103×10^{-2}	1	1.6103×10^{-2}	1.537062	0.22228
Error	4.1905×10^{-1}	40	1.0476×10^{-2}		
Total	6.4614×10^{-1}	53			

R-squared value: 0.1407

As shown in the above table, only the power appears to be a significant factor, which confirms the prior observations. It should be noted, however, that the model fit for this analysis shows an adjusted R-squared value of only 14.07%. The measured results in general are very noisy, and as such a 14.07% fit is still an appreciable result. Particularly, it still demonstrates that the laser power is an influencing factor, although the trend is very slight. Factors that may have contributed to the noise in the measurements may include the fact that the sample ends were not of the same flatness and roughness. As well, when the samples were cut off of the build plate, they were not able to be cut at the same heights. To confirm the validity of the ANOVA analysis, model adequacy plots were constructed and can be referenced below in Figure 87. Overall the plots appear to confirm the normality and independence assumptions, and it does not appear that the residuals are behaving strangely.

To end, it appears as though the only effect on the CTE is laser power and that the increase in power results in larger CTE values. However, since the effect appears to be a minor contributor and since the CTE values are lower than conventional values, the build variable selection may be flexible if the requirements are to rival the properties of conventional parts. Therefore, similarly to the results in the previous section, it is suggested that the optimal selection of build variables be at lower power levels, for quality reasons, and longer grid distance and shorter exposure times, for economic reasons. Currently, additional work that is not covered within the scope of this thesis is being done to observe

influence of microstructural phenomenon on the CTE of Invar parts. For future experiments, it will be beneficial to further investigate the effect of heat treatment has on CTE. Although in this experiment the results for both part density and CTE are comparable, it is still imperative to outline a procedure that can quantitatively define a process map that considers both part density and CTE for future optimization processes. Thus, this concept will be discussed in the next section.
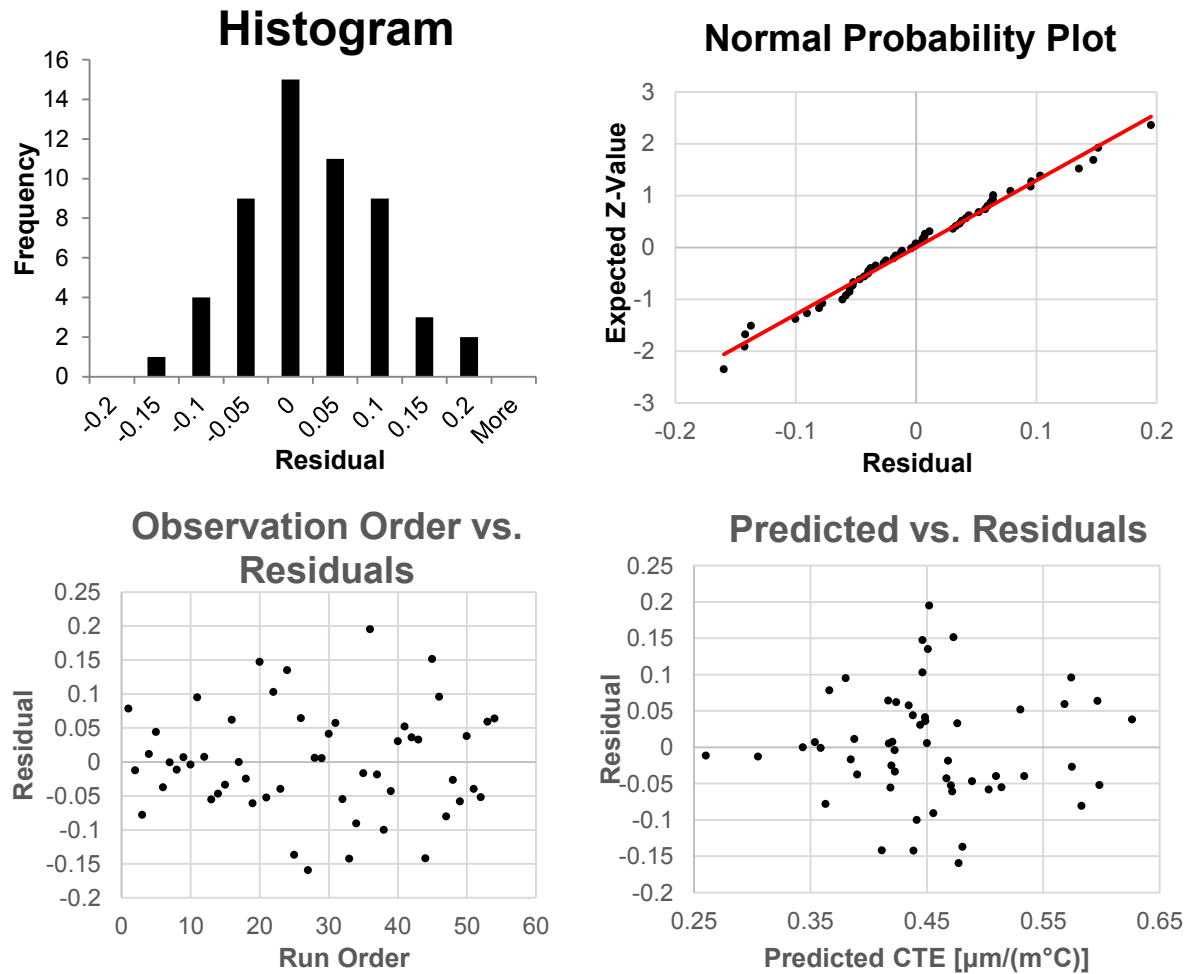
Figure 87. Model adequacy plot for the ANOVA model, describing CTE data, for assessing the normality and independence assumptions.

4.2.11 Process Mapping Considering both Part Density and Thermal Expansion

In this experiment, the analyses into both part density and thermal expansion shared the conclusion that lower power levels, larger grid distance, and shorter exposure times are the optimal build variable combinations for the process. However, these results may have been fortuitous, and a model that can

objectively take into account the effect of build variables on both process outcomes should be defined. For this work, a simple equation was used, which transforms each process outcome into a performance indicator valued between zero and one based on the respective minimum and maximum values. Then, the performance indicators for both are summed using weighted 'importance' factors. The equation is defined as follows:

$$W_\rho P_\rho + W_{CTE} P_{CTE} = P_{overall}$$

Where ρ and CTE are the indices for variables corresponding either to the part density or CTE process outcome. Continuing, W corresponds to the weighted importance of the process outcome, with ($W_\rho + W_{CTE} = 1$), while P corresponds to the performance of the remapped process outcome. Overall, a performance value of one was defined as an indicator of 'best' part quality, and a value of zero corresponds to 'worst' part quality. Within this work, an arbitrary weighting of 0.50 was selected for both process outcomes where equal importance was given to both process outcomes. Furthermore, since the CTE is a characteristic of the bulk part, only the bulk part density (not the density isolated to core region) was considered.

After calculating the overall performance, the worst performing and best performing parts were quantified to have performance values of 14.55% and 86.43%,. These parts correspond to sample 48 and sample 2, respectively. Their respective locations in the volumetric energy density plot (Figure 24) are described below in Figure 41. Similarly, an iso-surface plot was generated as per those in previous sections (Figure 89). Since the iso-surface plots in Figure 54 and Figure 80 suggest a shared conclusion, Figure 89 unsurprisingly also shows the same result. As seen in Figure 89, it appears as though there is an effect of increasing power with decreasing performance. Within each power level, it is difficult to tell the effect of grid distance and exposure time on the part performance. This is further shown by (Figure 90 – Figure 95), where there is a lack of consistency between worst and best parts within each power level.
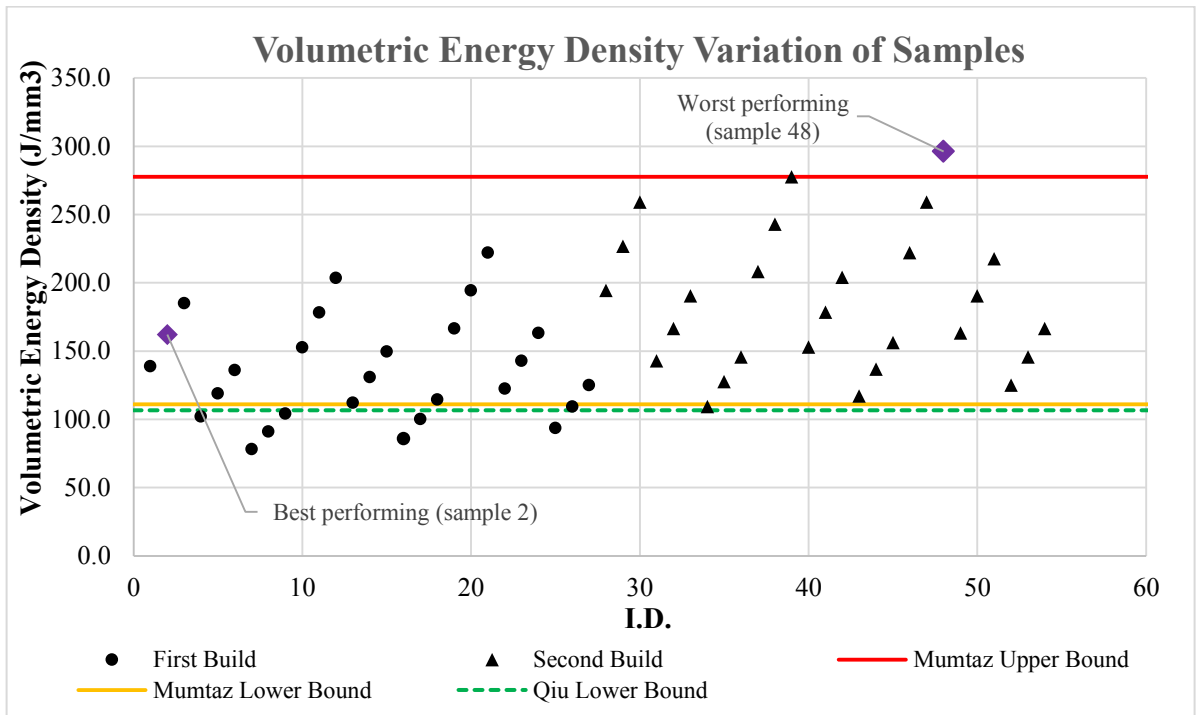
Figure 88. Variation of volumetric energy density across all permutations of variables, with the worst performing and best performing parts in terms of the generated 'performance factor'.
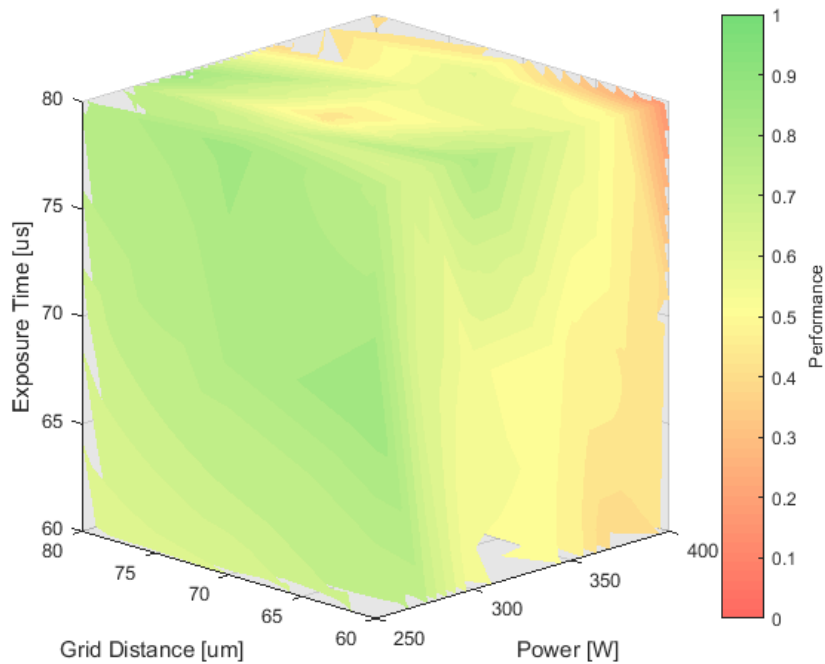
Figure 89. Iso-surface plot showing the effects of build variable levels on the combined performance of CTE and solid fraction.
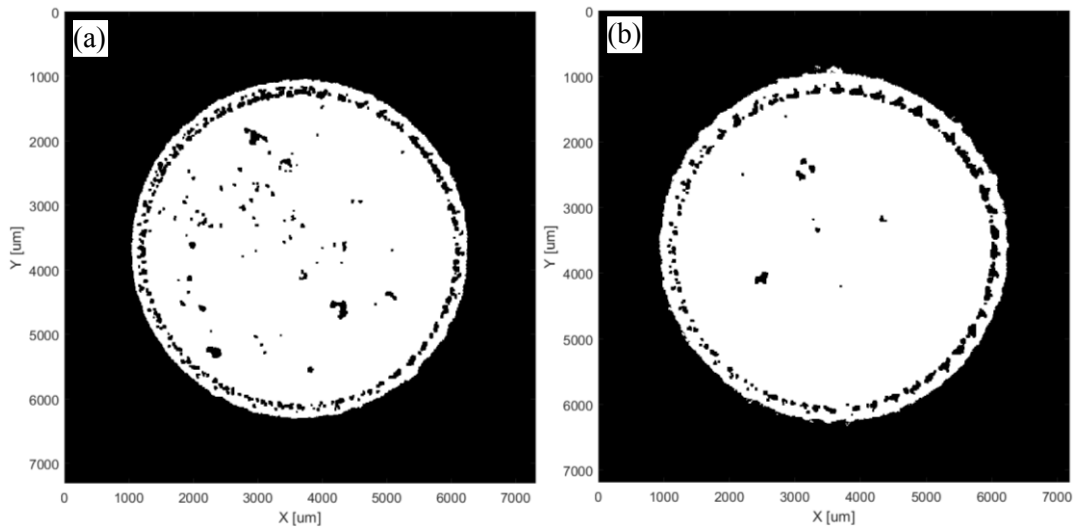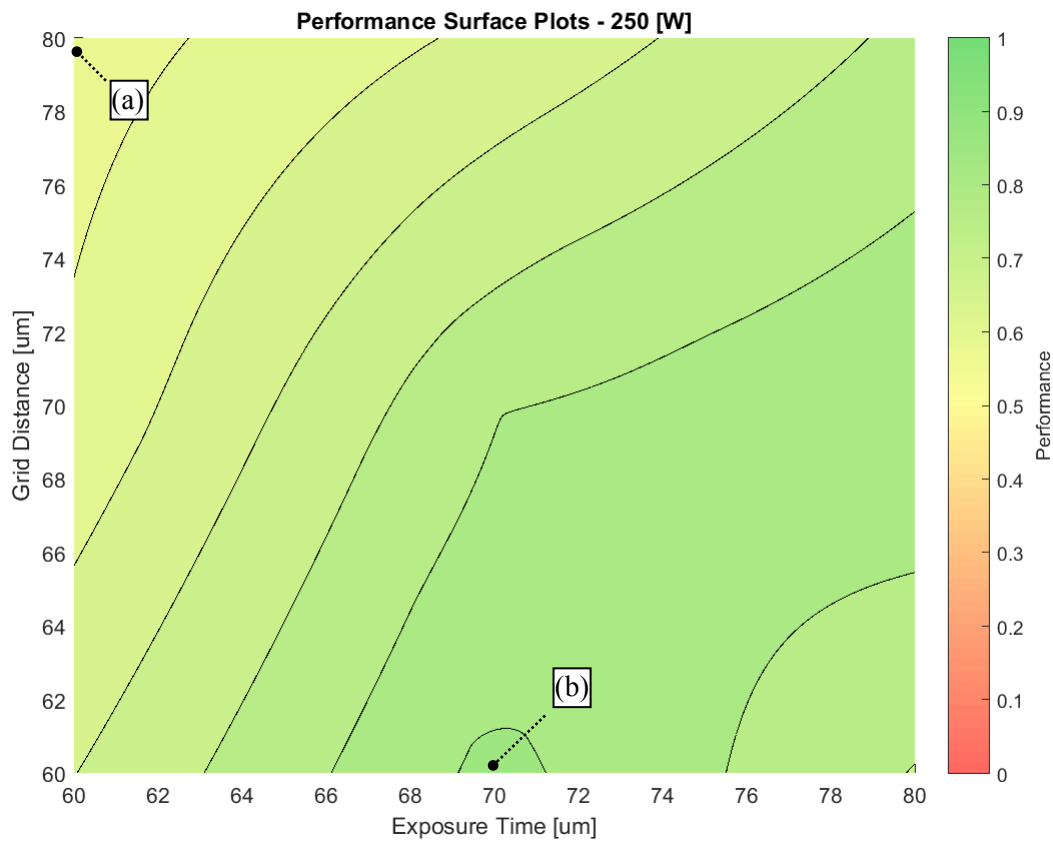
Figure 90. Two-dimensional surface plot describing the effects of grid distance and exposure time on part performance at a power of 250 W. Where the CT images describe (a) worst performing and (b) best performing parts.
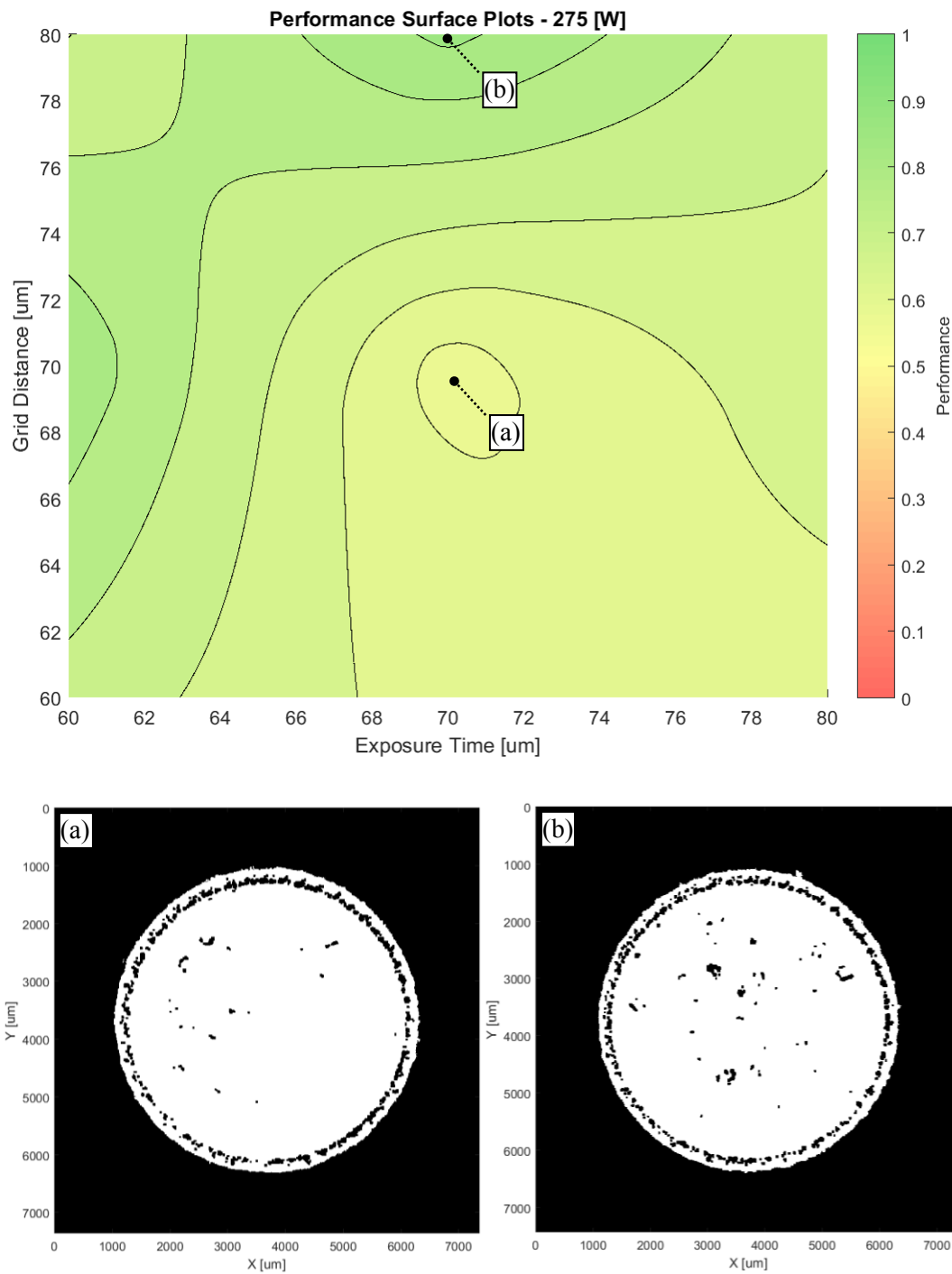
Figure 91. Two-dimensional surface plot describing the effects of grid distance and exposure time on part performance at a power of 275 W. Where the CT images describe (a) worst performing and (b) best performing parts.
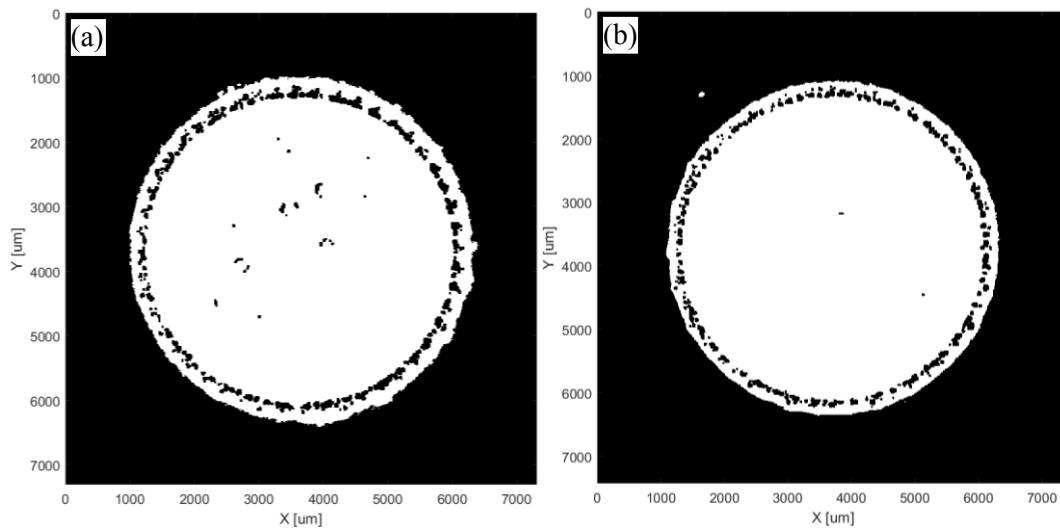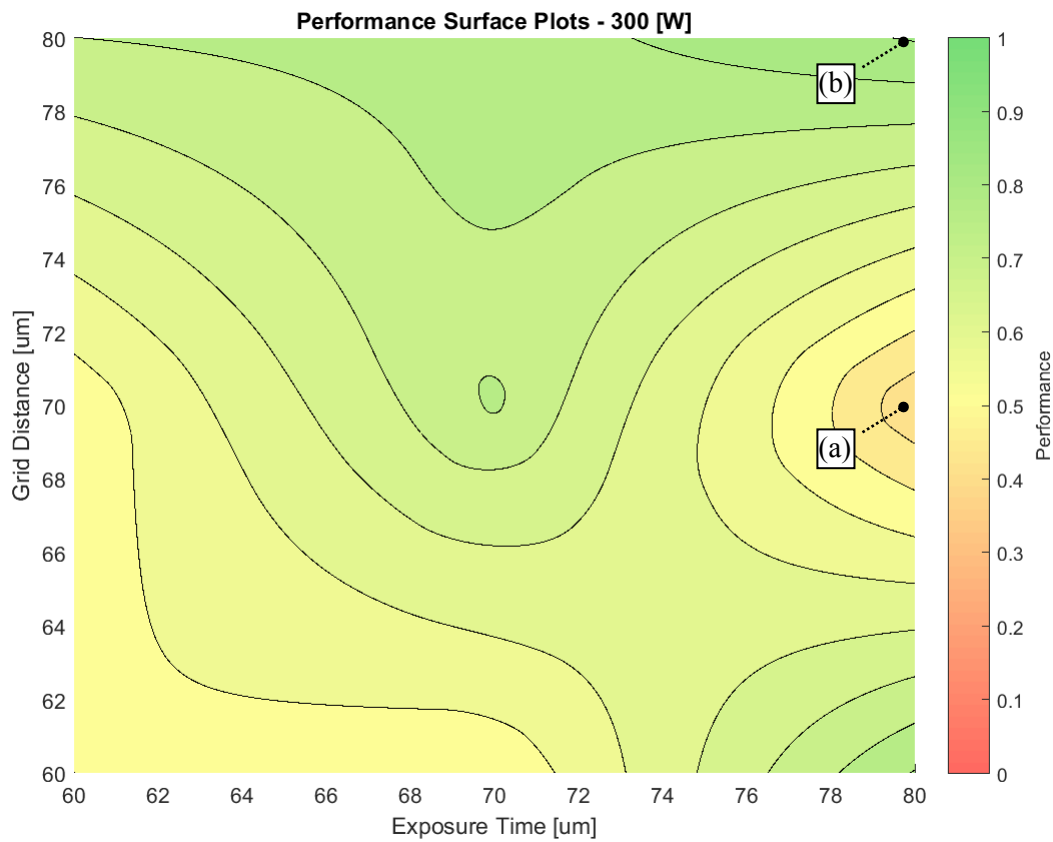
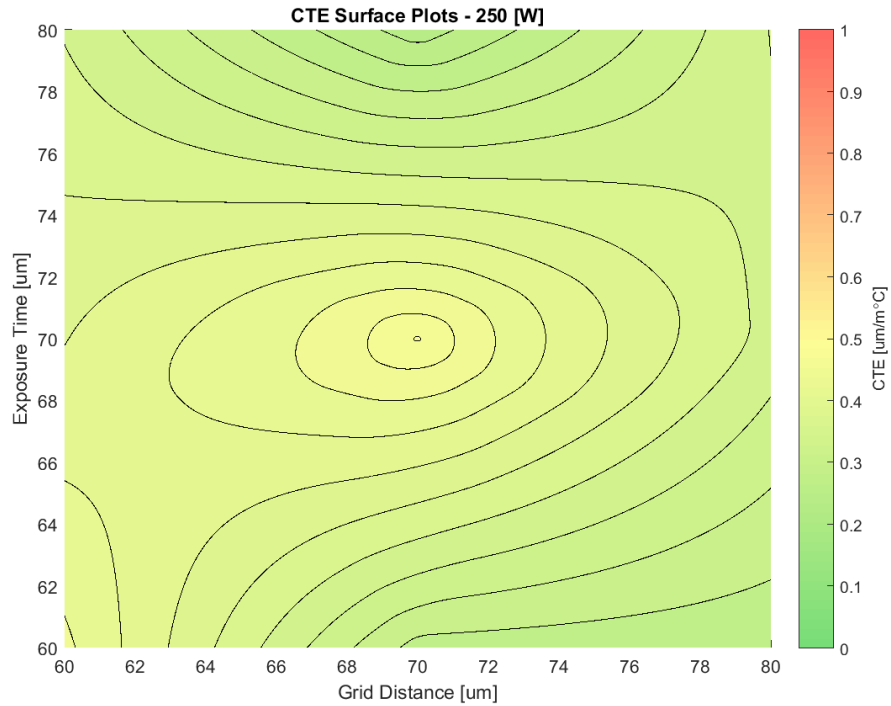**Figure 92. Two-dimensional surface plot describing the effects of grid distance and exposure time on part performance at a power of 300 W. Where the CT images describe (a) worst performing and (b) best performing parts.**
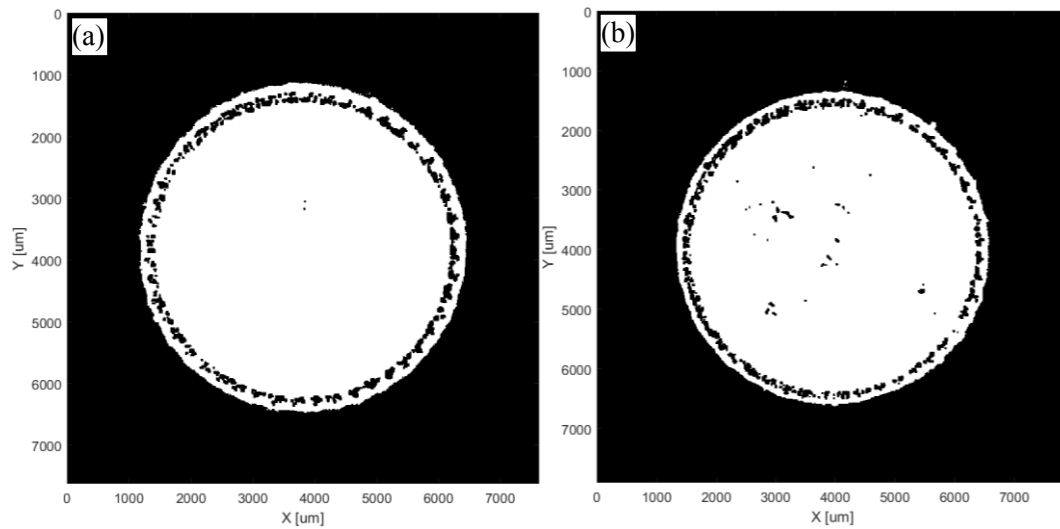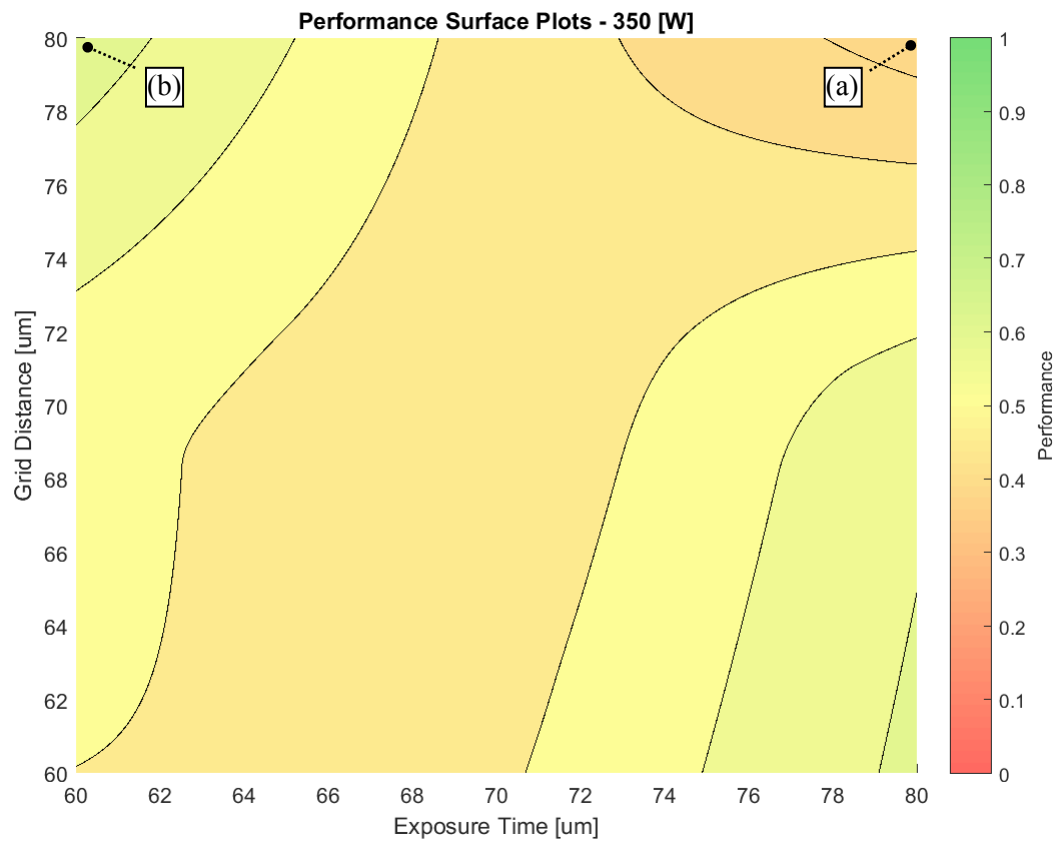
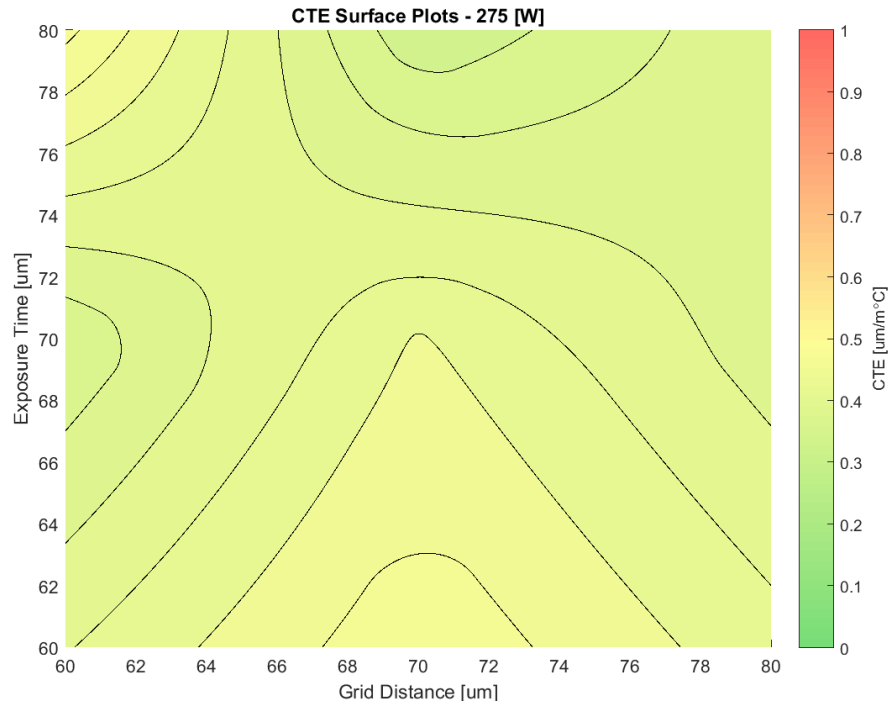**Figure 93. Two-dimensional surface plot describing the effects of grid distance and exposure time on part performance at a power of 350 W. Where the CT images describe (a) worst performing and (b) best performing parts.**
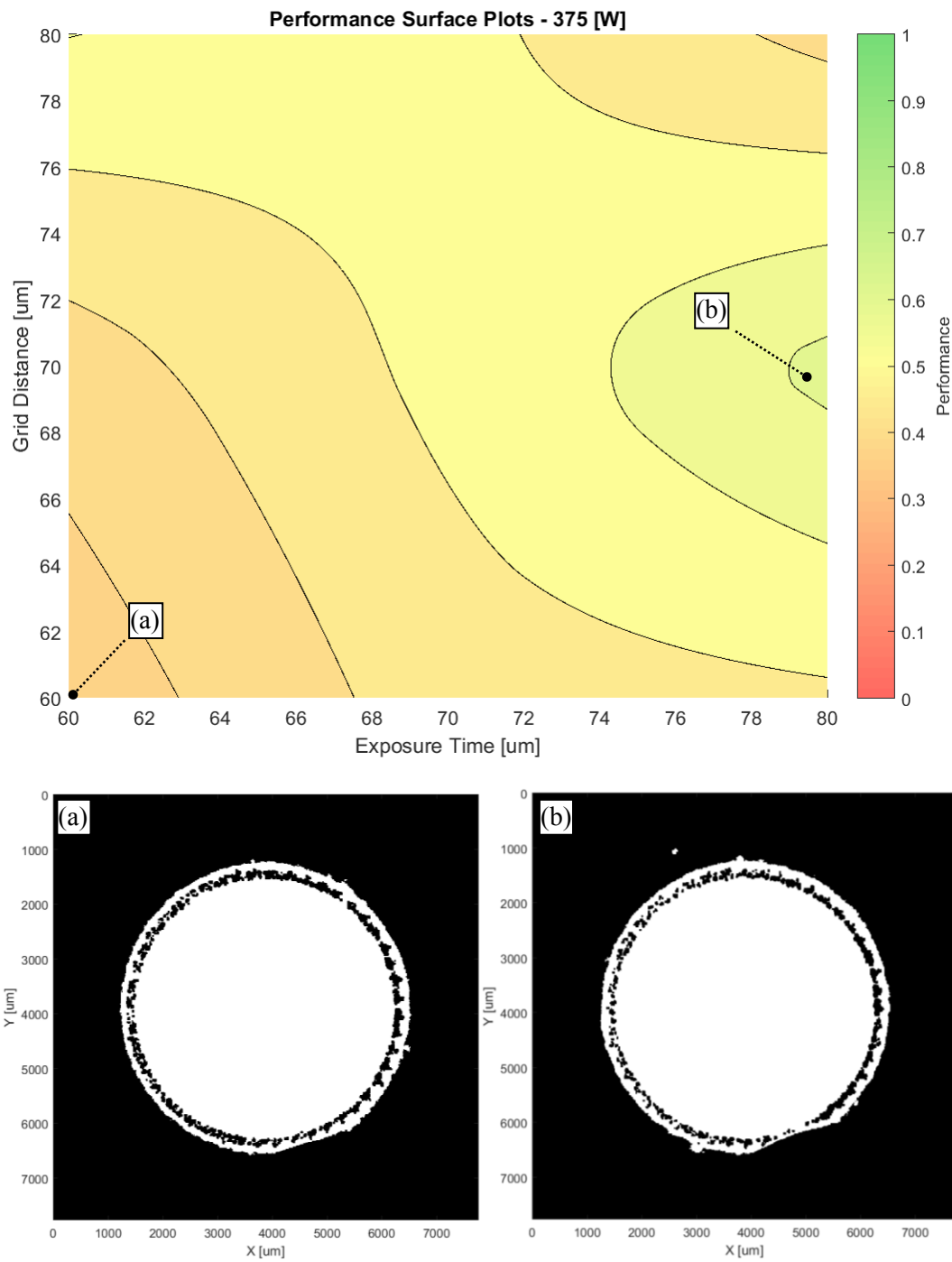
Figure 94. Two-dimensional surface plot describing the effects of grid distance and exposure time on part performance at a power of 375 W. Where the CT images describe (a) worst performing and (b) best performing parts.

120

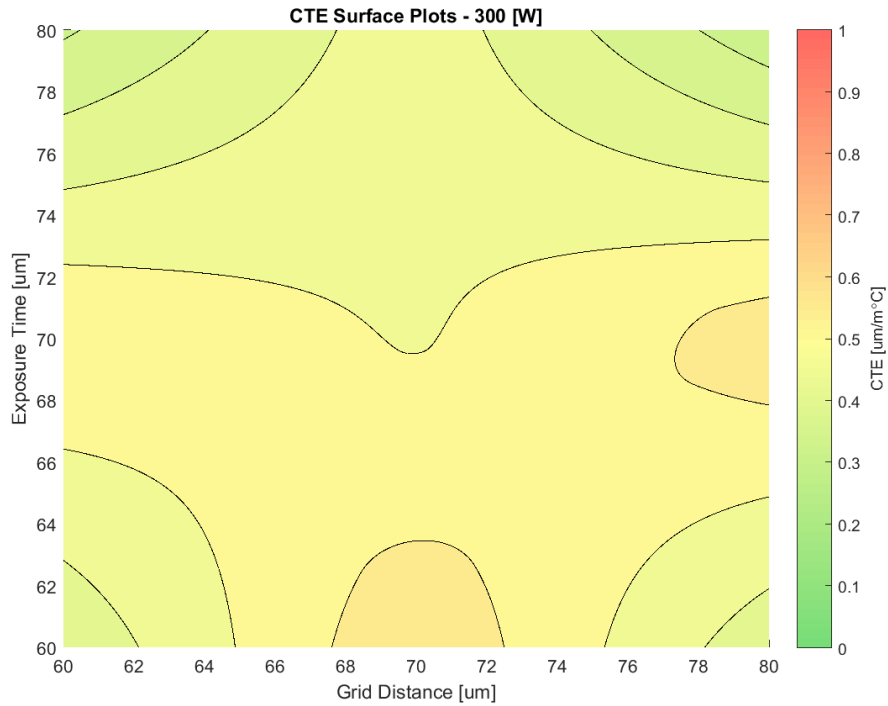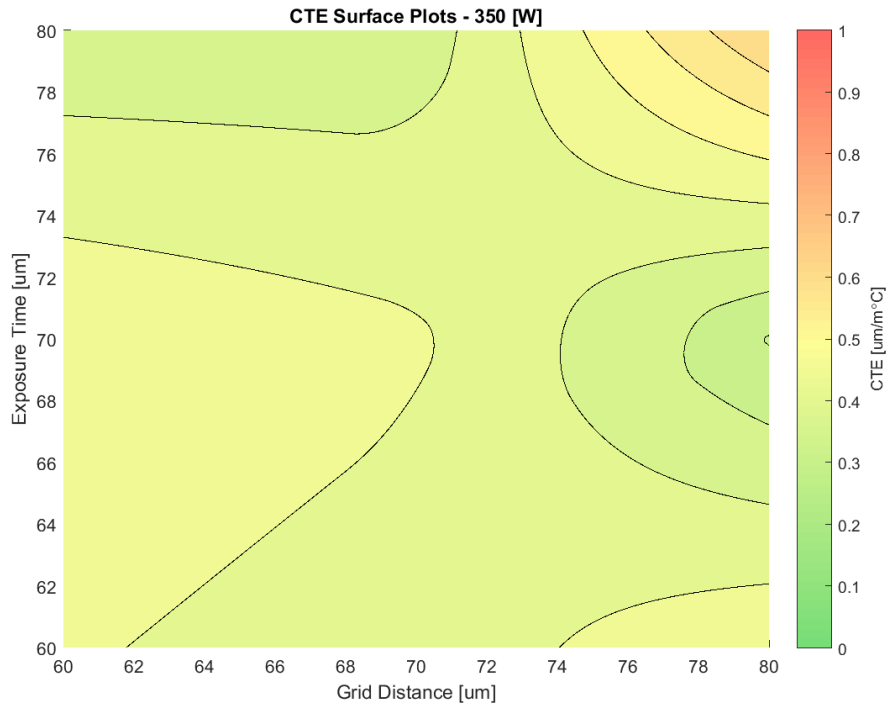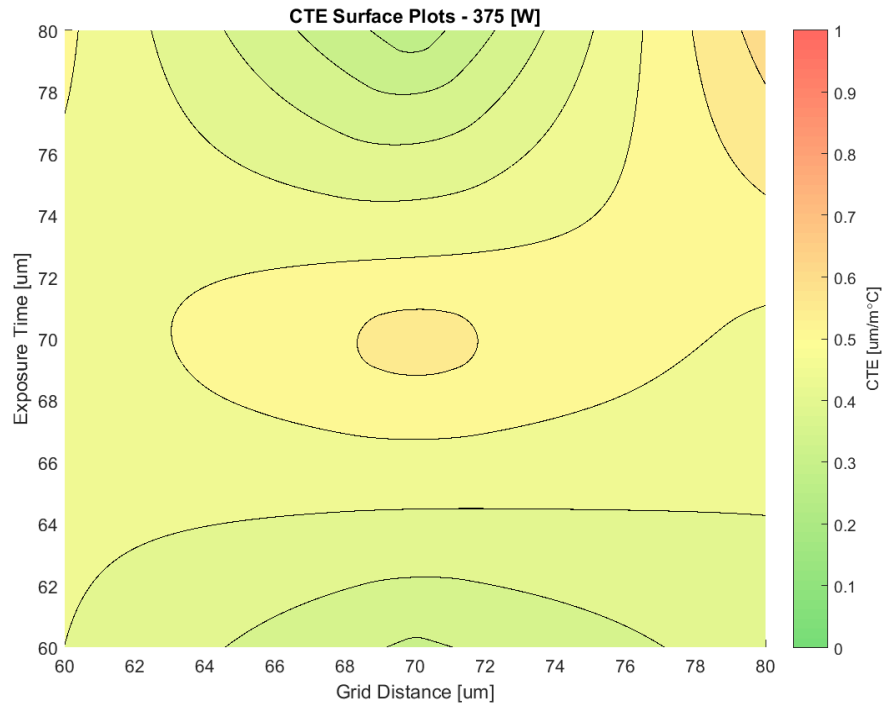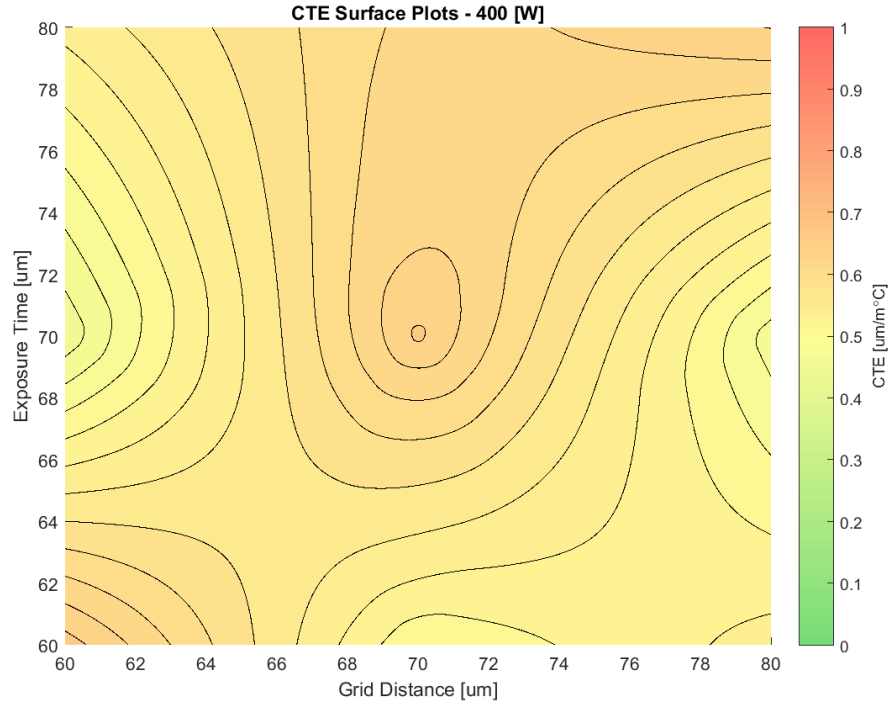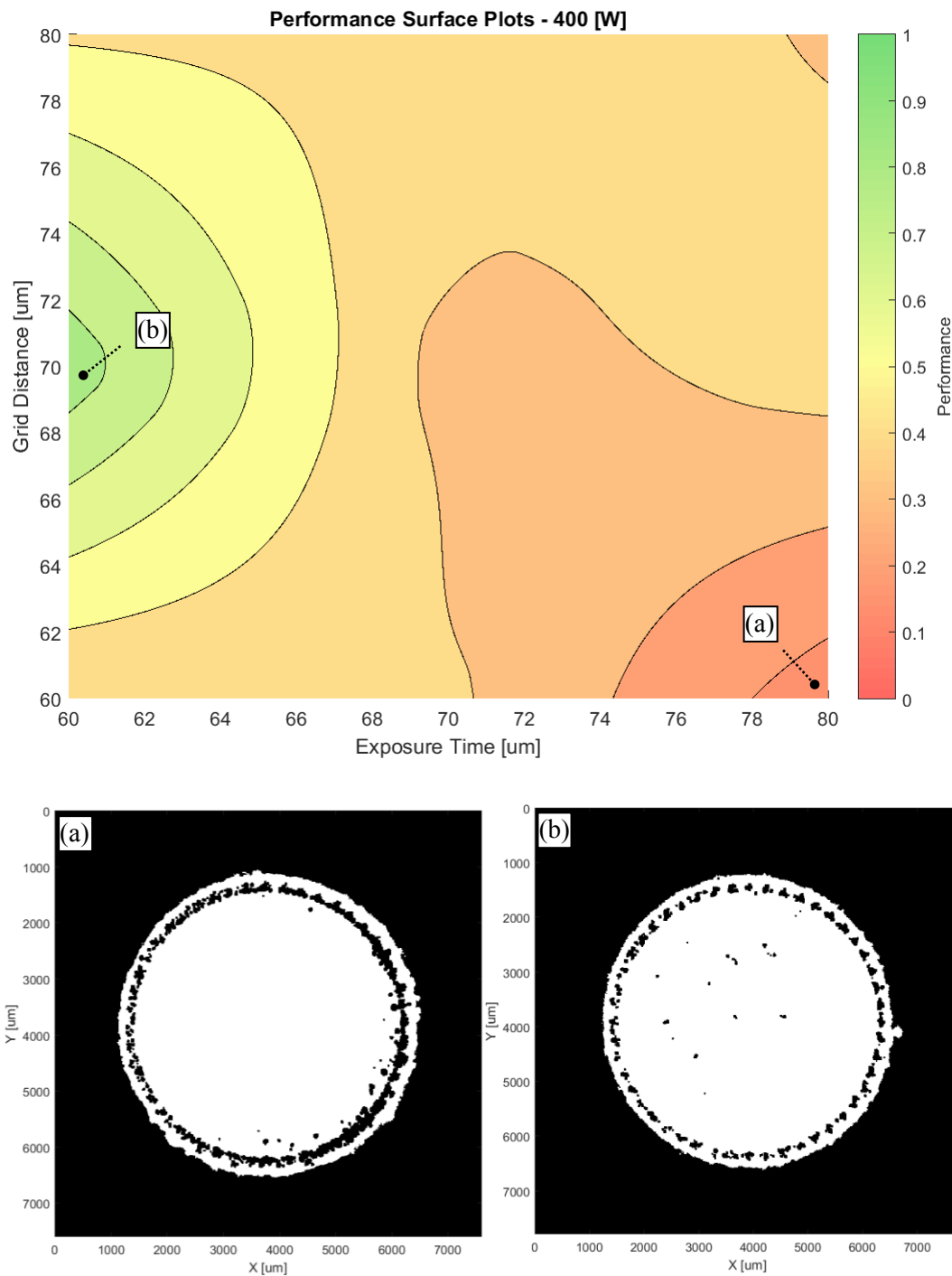**Figure 95. Two-dimensional surface plot describing the effects of grid distance and exposure time on part performance at a power of 400 W. Where the CT images describe (a) worst performing and (b) best performing parts.**

Upon construction of the ANOVA table, the results become more evident, with laser power showing a significantly lower p-value than for the analysis within previous sections, confirming that laser power is a significant factor (at $\alpha = 0.05$) in determining the performance of parts with other build variables showing no significance. Visual confirmations from Figure 89 point to the conclusion that lower powers result in better performing parts. Overall, the model fits at a 41.65% R-squared value, which is a better fit than previous models. This may be resultant of the effect of power becoming more prominent with the compounding of both process outcomes. The model adequacy plots are shown in Figure 96, and do not raise any concerns with the model assumptions.

Thus, when considering the effects of both solid fraction and coefficient of thermal expansion, a lower power level is ideal. The effects of the other factors are not as significant, and thus the most economical options should be selected, where processing speed would be the most desirable outcome.

Table 23. ANOVA table showing the effects of the build variables on the part performance process outcome.

Source of Variation	Sum of Squares	Degrees of Freedom	Mean Square	F_0	p-value
Power	0.67541	5	0.13508	8.6943	1.2049e-05
Grid	0.026929	2	0.013465	0.86663	0.42811
Exposure Time	0.00090286	2	0.00045143	0.029055	0.97138
P/G	0.014126	1	0.014126	0.90921	0.34605
P/E	0.056816	1	0.056816	3.6569	0.063018
G/E	0.006205	1	0.006205	0.39938	0.53101
P/G/E	0.0093542	1	0.0093542	0.60207	0.44235
Error	0.62147	40	0.015537		
Total	1.4112	53			

R-squared value: 0.4165
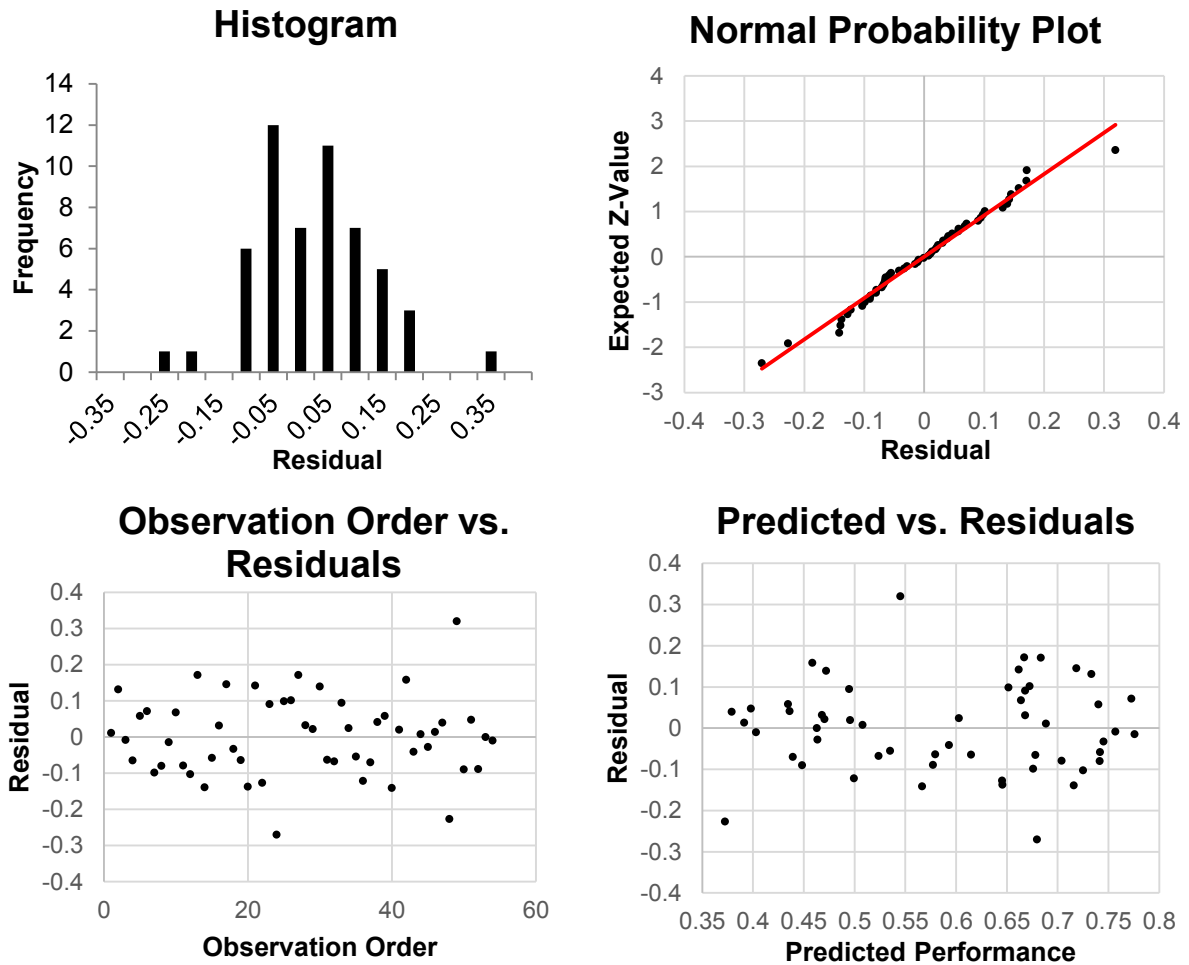
Figure 96. Model adequacy plots for the ANOVA model, describing part performance, for assessing the normality and independence assumptions.

4.3 Conclusion

For the experiment conducted in this chapter, the goal was to define a process map for the LPBF process of Invar36 parts. Through the use of statistical analysis techniques, process maps were defined for the experimental bounds in question, and then optimized process windows were selected based on the desired process outcome. In particular when considering only porosity as the process outcome, it was observed that lower powers would result in less porous parts, overall. A similar observation was made with larger grid distances. When considering the thermal expansion, the same conclusion was also achieved. Upon removal of the border regions of specimen, it was found that once a certain power threshold was attained, the material achieve essentially 99.99% density

throughout, and thus it was determined that the process window for the core regions is flexible. The overall conclusions can be generally seen below in Figure 97, when averaging the values for the process outcomes at each power level.

Average Solid Fraction and Coefficient of Thermal Expansion at each Power Level
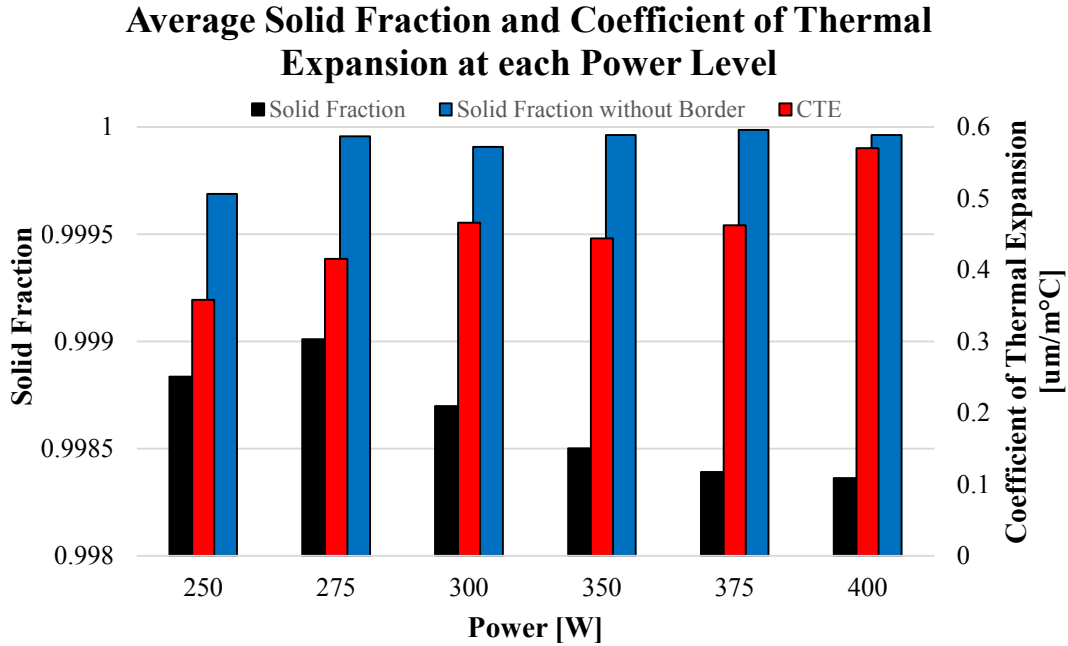
Figure 97. Average values for the process outcomes at each power level, showing the effect of power.

A weighted decision-making model was then proposed to assess the impact of both porosity and thermal expansion as an overall part quality indicator, and the results of the statistical analysis concurred with previous results.

Other observations with the experiment showed a bias of the pores towards the border region of parts, and it was hypothesized that this was due to the abrupt end of hatch scanning lines that cause instability in the melt pool. Additionally the endpoints of hatch lines do not achieve the benefit of re-melting from adjacent hatch lines. The effect of gas flow was also shown to affect the porosity, with a bias of pores upstream to the gas flow direction, which was attributed to the reintroduction of spatter into the material, causing additional porosity. Lastly, there was also a perceived angular periodicity in pores along the outside regions. The reasoning behind this type of defect was proven to be caused by blocked path lines. To investigate the effects of all these phenomena further, additional experimentation was performed and will be discussed in Chapter 5.

Outside of these main observations, it may also be valuable to analyze the influences of the build variables on the microstructural behaviour within LPBF-built parts, and subsequently the microstructural behaviour influences the CTE. Currently, ongoing work is being performed regarding this. Also, since it has been found that the residual stresses are an influencing factor on the thermal expansion behaviour of LPBF-built Invar36 parts, continued investigation on the effect of heat treatment should be performed as well.

Chapter 5

Experiment 2: Elimination of Border Region Porosity

The experimental work done for this thesis has been divided into two different experiments. The previous experiment focused on the development of a process map for the minimization of bulk porosity and thermal expansion characteristics of LPBF-built Invar36 parts. Based off of observations during CT analysis, it was found that there was a regional bias of defects towards the border region of parts. Thus this experiment was developed to focus on minimization of porous defects along the border region of parts. The QuantAM build variables affecting these regions were assessed, and then a build was set up to quantify the effects of these variables, similar to the previous chapter. The techniques used in this section include CT scanning for observing the porosity, and statistical analysis to determine the significance of the build variable variation.

5.1 Experimental Methods

As mentioned in Chapter 4, in the analysis of the CT pore space, it was observed that a large percentage of the pores occurred near the border regions of the parts. Figure 98 shows a minimum intensity projection of representative parts from the previous chapter, showing the defects of interest. Therefore, as a secondary step to further reduce porosity within a part, an experiment was designed to determine if the variation of build variables related to features in the neighborhood of the border regions could further reduce the porosity.

Figure 98. Representative figure showing the border region defects from Chapter 4. From left-to-right are samples one, two, and three, which correspond to 250 W power; 60 μm grid distance; and 60, 70, and 80 μs exposure time, respectively.

Upon inspection, out of all the build variables that can be modified within the build software (Appendix A), it was found that it is possible to directly adjust the settings for border scan lines and fill contour scan lines. Shown below in Figure 46 is a schematic that describes each type of scan line. This figure was presented earlier in Chapter 4, but is presented here again for clarity. For the experiment in Chapter 4, only the settings for fill hatch lines were varied.

For both the border and fill contour hatch lines, the build software is able to directly adjust settings involving the number of lines created, the offset between adjacent lines of the same time, the offset between lines of different types, and the energy input parameters. In addition to the types of scan lines, it is also possible to adjust the behaviour of fill hatch lines as they approach the border regions of parts with a variable known as hatch compensation.
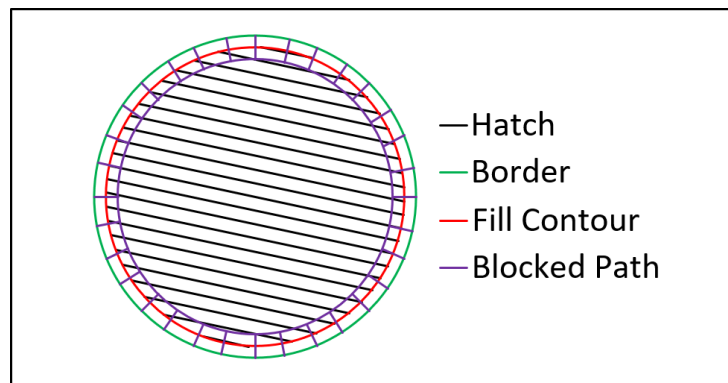
Figure 99. Schematic showing differences between different line types.

Particularly, the logic behind the creation of a point at the end of a hatch line with hatch compensation functions as follows:

$$(Hatch\ Compensation) \times d_p \geq (d_p - x)$$

Where hatch compensation is a percentage of $0 - 100\%$, d_p is the point distance, and x is the distance that the point distance is offset from the end of the hatch line (refer to Figure 47, section 4.2.3). If the hatch compensation build variable is turned on, and if the above inequality is valid, then the software generates an additional point at the end of the hatch line (Figure 100).

Based on observations of the generated scan paths, and the resulting porosities obtained in Chapter 4, several improvements are suggested and tested within this chapter to reduce the occurrence of pores within parts.
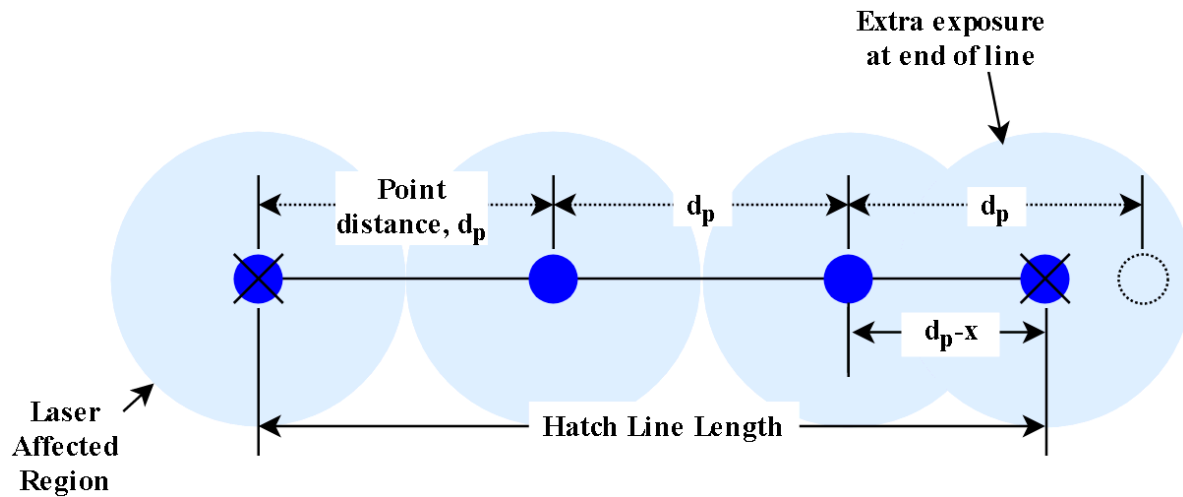
Figure 100. Figure illustrating a hatch line with an extra exposure point due to the effect of hatch compensation.

Firstly, since hatch compensation was not enabled in the first experiment, several scan lines did not have exposure points as they neared the border region of parts. As such, it is postulated that the absence of these laser exposures may have contributed to the porosity in the part.

Secondly, the border scan lines were not modified in the first experiment, and were therefore selected to have the same settings as the fill hatch lines. However, since the border lines do not do not solidify under the same conditions as the core regions, the settings for the border must be optimized separately from the fill hatch.

Thirdly, as shown in Figure 101, it appears that the most significant pores occur in the space between the end of a hatch lines and the border scan lines. This figure is identical to Figure 45, and has been presented again for readability. Within the build software, the fill contour build variable is typically used to this region between the hatch and borders, and for the experiment in Chapter 4, the fill contours were not enabled. Thus it is suggested that the re-enabling and control of the fill contour offset will aid in porosity reduction.

One last observation to restate is the presence of 'blocked path' lines in the analyzed samples in Chapter 4. It appears as if they did not function as intended, and instead resulted in repeated exposures at the same locations across many layers. These repeated exposures resulted in the observed angular periodicity of the pores.

128
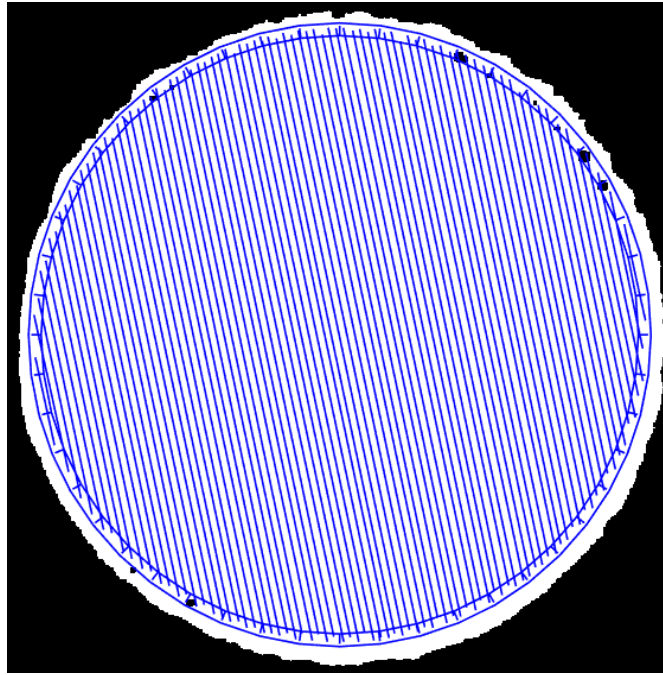
Figure 101. Single cross-section of a representative part section with the overlaid scan path. Build variables for this image correspond to sample 11, which was printed at 275 W power, 60 µm grid distance, and 70 µs exposure time.

By varying the aforementioned build variables, a factorial design was created, and the levels are reported in Table 24. For the core regions (corresponding to fill hatch lines), representative settings for well performing samples were selected from Chapter 4. For the borders, the only difference from the core settings was the modulation of the power between 250 W and 275 W (as opposed to 275 W and 300 W in the core). These settings were chosen because border regions encounter different solidification conditions (thermally insulating powder region on one side), and were also chosen to be equal to or less than the core power to reduce the melt pool size and possibly reducte the number of ejected particles due to excessive laser energy input. In terms of the fill contours, based on the laser spot diameter of 70 μm and the size of the pores occurring between the ends of hatch lines and the border lines (refer to Figure 45), a single fill contour line was found to be sufficient for melting the entire overlapping region. The power and point distance of the fill contours were cut in half to maintain the same energy density as the core, but to also effectively scan slower to give more time to collapse any pores that formed. The only varied build variables relating to the fill contour were the offset of the fill contour lines from the border and whether or not the fill contours were to be enabled. This was to see if the presence of fill contours would truly reduce the pores that occur between the

hatch and border lines. Based on the point distance, the upper value of the hatch compensation was varied such that an exposure point was guaranteed to be placed with end-point distances down to the laser spot radius (at maximum point distance of 70 μm and hatch compensation 50%). The lower end was selected mostly arbitrarily, but was selected to be more lenient and to add extra hatch lines for final endpoint distances of greater than 25% of the point distance. The effect of using different scan strategies was also of interest, since a strategy such as 'striped' would result in multiple instances where the ends of hatch lines could induce porosity.

Although many build variables near the border region were of interest to be varied, limitations of sample size and build layout clearance prevented a more thorough study to be performed. As such, many of the build variables described above only had a single selected level, and the rest were with levels varied at two levels. Overall with all the varied parameters at two levels, $2^7 = 128$ sample treatments were created as samples for analysis in current and future studies.

Table 24. Build variables that were modified for the manufacturing plan, and that were changed from default values.

Build variable	Unit	Levels	
Fill hatch (specimen core)			
Power	[μm]	275	300
Grid distance	[μm]	60	70
Exposure time	[μs]	70	
Border lines (specimen border)			
Power	[W]	250	275
Grid distance	[μm]	Same as core	
Exposure time	[μs]	Same as core	
# of borders	[-]	1	
Fill contour lines (specimen border)			
Power	[% of core]	50	
Grid distance	[% of core]	50	
Exposure time	[μs]	Same as core	
# of borders	[-]	1	
Contour offset	[% of grid distance]	50	100
Contour enabled	[-]	Yes	No
Scan strategy			
Type	[-]	Meander	Stripe
Width [stripe only]	[mm]	5	
Offset [stripe only]	[mm]	0	
Miscellaneous			
Hatch compensation	[%]	25	50
Blocked path	[-]	Off	

5.1.1 Selection of Standard Artefacts

The standard artefacts in this section are identical to those described in section 4.1.1. The only difference is with the numerical labelling scheme, which can be further referenced in Appendix J.

5.1.2 Build Layout

Using the same standard artefacts as in Chapter 4, the small cylindrical samples were fabricated with two replicates, while the cubes were fabricated with a single replicate. A similar methodology for the layout in section 4.1.2 was used. It should be noted that the build setup for this experiment was performed in parallel with the second build in Chapter 4, and thus they share the same build plate. An illustration of the build setup is described below in Figure 102, which is identical to Figure 29 presented in Chapter 4.
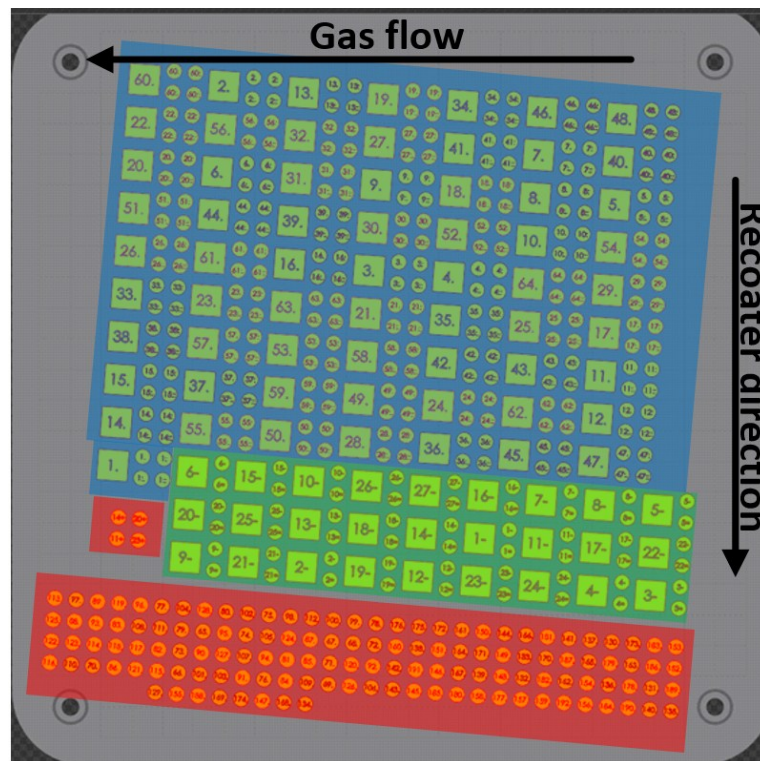
Figure 102. Layout for the second build with green-shaded areas denoting samples for the experiment in Chapter 4, red-shaded areas for the auxiliary samples, and blue-shaded areas for the second experiment.

The blue-shaded areas denote the layout for samples following the build variables combinations described in the chapter, while the red-shaded areas are samples that follow separate build variable

combinations sets for auxiliary studies unrelated to this work. The second build from Chapter 4, which was printed at the same time as the experiment in this chapter, is shaded in green.

5.1.3 Computed Tomography

The computed tomography of the samples was performed in accordance to the methods described in section 4.1.3.

5.1.4 Statistical Analysis of Results

Similar to the previous experiment, the large number of samples made it difficult to scan all replicates of all treatment levels. Instead of scanning only a single replicate of every treatment, a smaller subset of the experiment was selected, allowing both replicates to be scanned. This was in done order to get a better statistical representation of the results, with the remaining unanalyzed parts used to serve as additional sample points to be analyzed in the future. Thus, unlike the analysis performed in section 4.1.5, a full ANOVA was able to be performed similar to the process described in section 2.3.1. The subset of samples scanned adhere to the following build variable values:

Table 25. Design factor subset selected for statistical analysis

Build variable	Unit	Levels	
Fill hatch (specimen core)			
Power	[μm]	275	300
Grid distance	[μm]	60	
Exposure time	[μs]	70	
Border lines (specimen border)			
Power	[W]	250	275
Grid distance	[μm]	Same as core	
Exposure time	[μs]	Same as core	
# of borders	[-]	1	
Fill contour lines (specimen border)			
Power	[% of core]	50	
Grid distance	[% of core]	50	
Exposure time	[μs]	Same as core	
# of borders	[-]	1	
Contour offset	[% of grid distance]	50	100
Contour enabled	[-]	Yes	No
Scan strategy			
Type	[-]	Meander	
Miscellaneous			
Hatch compensation	[%]	25	50
Blocked path	[-]	Off	

The subset selection was chosen such that the most important aspect of the experiment remained intact, which is to study the effect of build variables on the border region of parts. Therefore, it was decided that variations in core grid distances and scan strategies were of a lower priority for analysis, and thus were not explored for the time being.

5.2 Results and Discussion

Before continuing, it should be noted that after printing the build and then having the samples removed from the build plate, a large number of the samples were lost during part removal. Because of this, the full factorial design specified in Table 25, was instead analyzed as an unbalanced design. This process was facilitated automatically within MATLab. However, because this approach was required to be taken, any presence of non-normality in the samples had a magnified effect and may have undermined the results of the statistical analysis (discussed further in section 5.2.2). The missing and measured sample results can be found in Appendix J. As well, there may have been biases introduced when the samples were removed from the build plate. Particularly, during part removal, the cutting equipment was slightly angled and resulted in samples on the right side of the build plate being much taller than samples on the left edge of the plate (refer to Figure 29, section 4.1.2 for the build layout). This can be seen in the resulting image data set in Appendix K.

5.2.1 Interpretation of CT Pore Space Data

Two representative sample results from this experiment are displayed below in Figure 103 and Figure 104. Figure 103 represents the part with the lowest quantified solid fraction of 99.94%, while Figure 104 represents the highest quantified solid fraction of 99.99%. To reiterate, the figures below show a projection of the pores across the entire sample dimensions, and are more adequate measures of pore distribution and geometry than quantity. Also, the entire image set and their resulting density values can be referenced in Appendix K.

In comparison, the samples in Chapter 4 with the same settings for the fill hatch (core settings) had solid fractions of 99.81% and 99.90%, respectively. Based on these values, it appears that there is an improvement in the enabling of the border region scan features. However, the density values calculated here consider the entire porosity throughout the part. Since the aim of this experiment is to minimize the porosity near the border region of the parts, calculation of the porosity without the consideration of the core will be more indicative.

133
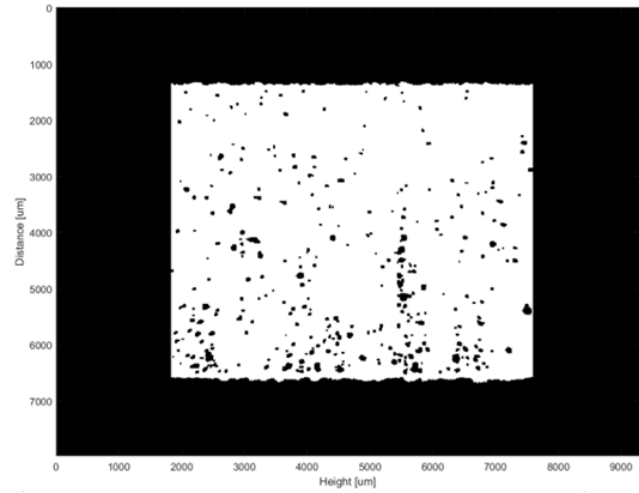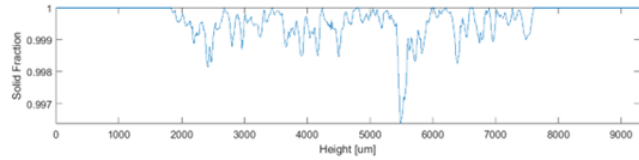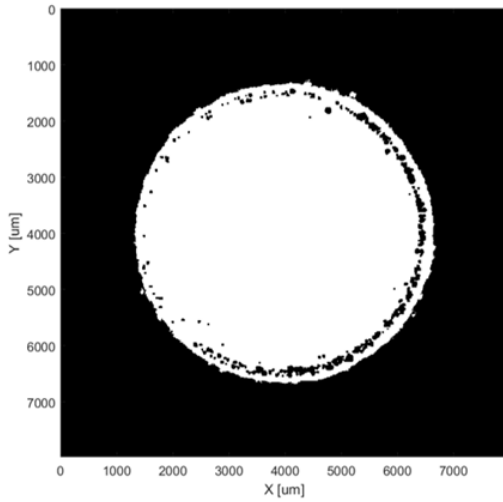
Figure 103. Worst overall performing part from the CT analysis, in terms of minimizing porosity. The build variables for this sample correspond to sample 15-4.
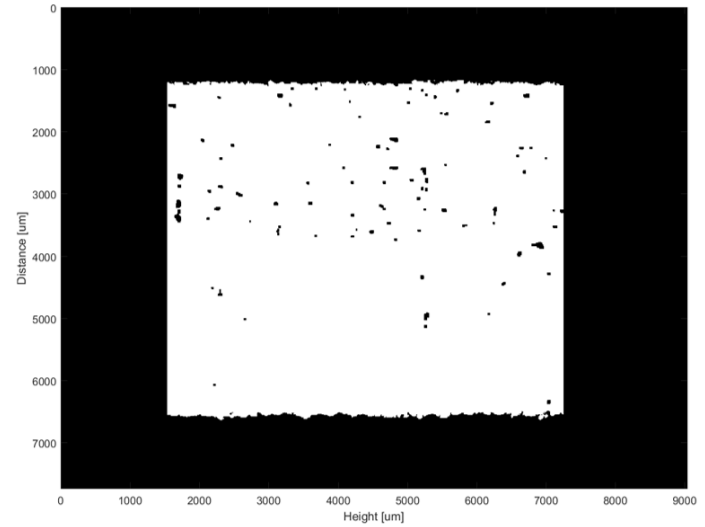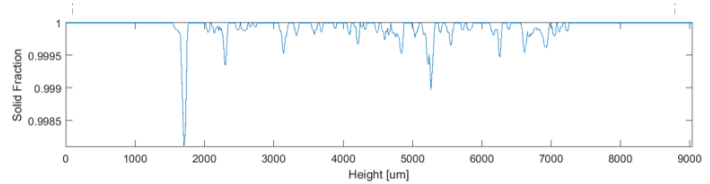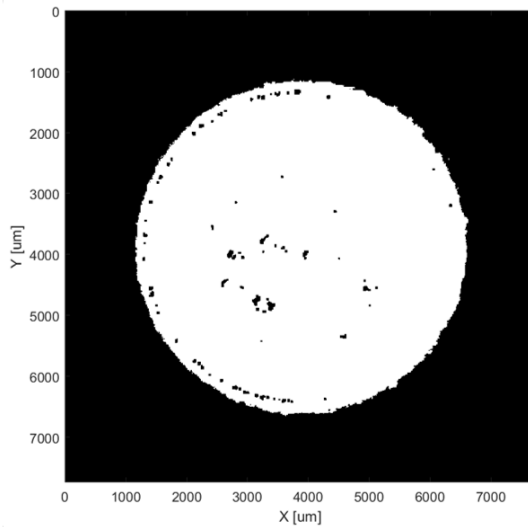
Figure 104. Best overall performing part from the CT analysis, in terms of minimizing porosity. The build variables for this sample correspond to sample 1-3.

By truncating the data in a similar fashion to Figure 61, except in this case, core regions are removed, it is possible to quantify the porosity within the border regions (Figure 105). Similarly, the 10% radius threshold was maintained. By applying this truncating process to the entire data set, it was found that the same samples remain as the worst and best performing. That is, Figure 103 and Figure 104 continue to represent the worst and best performing samples, overall.

(a) before truncating   **(b) after truncating**
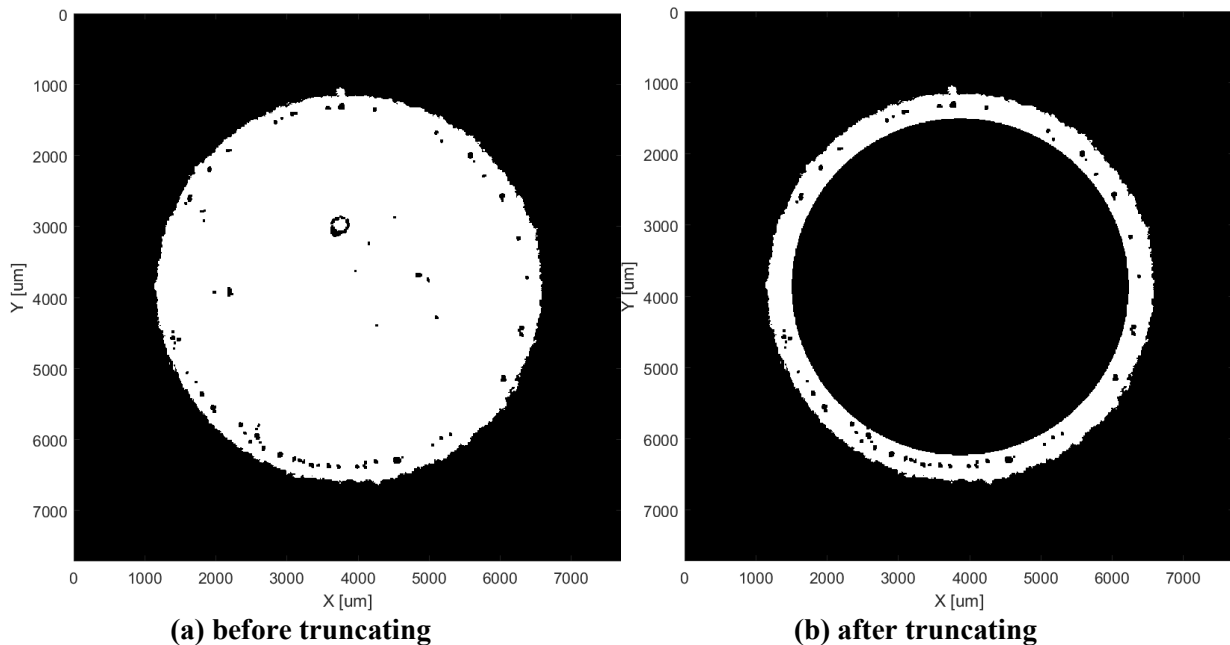
Figure 105. Example illustrating showing the CT data (a) before and (b) after truncating by radius to omit the core-region.

When comparing the differences between these two data sets, the better performing sample had a lower hatch compensation (25%, instead of 50%), lower fill contour offset (50% instead of 100%), lower border power (250 W instead of 275 W), and a lower overall power (275 W instead of 300 W). As it was shown in Chapter 4 Figure 44, samples with higher overall energy densities had larger and more numerous pores, and thus it is sensible that the same conclusion applies here for the overall power and border power. In terms of the benefits of using a lower hatch compensation, the earlier hypothesis that using a lower hatch compensation value would result in fewer absences of laser exposures, and thus reduce porosities, may be applicable as well. The increase in porosity associated with the fill contour offset at 100% in comparison to 50% is expected. This is because at a fill contour offset of 50%, the fill contour scan lines are well-centered between the border and hatch lines, and thus have a greater coverage to re-melt porous regions between the border and hatch lines

In addition to the results presented above, it appears that the directional bias of the pores towards one side of the parts still occurs. One interesting note is that the right-side bias of the gas flow does not exist in the best performing sample, and several other samples (Appendix K). It is speculated that as the effects of other influencing factors on the porosity are minimized with experimentation, such as the decrease of border power or the remelting of pores within the border region, the amount of ensuing pores related to material vaporization and ejection become eliminated. Thus, the right-hand side bias effect becomes negated within some samples. However, the effect of ejected particles may still be in place, as shown by the continued presence of pores on the left hand side.

In terms of other visualizations, unfortunately with four independent variables (instead of three, as is the case in the previous chapter), it is difficult to illustrate the results concisely with iso-surface plots. However, based on the results of the statistical analysis, it is still possible to clarify the effects and their significance.

5.2.2 Process Window Optimization of Border Region Porosity

Described in Table 26 are the results calculated from the ANOVA that show the effect of the build variables on overall solid fraction. To clarify, the source terms A, B, C, and D correspond to power, border power, fill contour offset, and hatch compensation. From the table, it can be seen that the parameters of significance (at $\alpha = 0.05$) are power, fill contour offset, and the interactions between fill contour offset and hatch compensation. This confirms the observations of the CT data in the previous section, and seems to suggest that there are additional effects from the interactions of build variables. However, before continuing to quantify the effects of the build variables, it should be noted that the ANOVA was performed on the overall part, and did not focus on the region of interest (the border region). Thus, the ANOVA was re-calculated for the solid fraction data, considering only the border region of parts and the results are shown in Table 27. In the results presented in Table 27, the p-value of the fill contour offset deviates away from significance (p-value 0.0501), but since it is barely away from the threshold, the effect of the fill contour offset will still be examined further. In addition, it appears as if the effect of the interactions between fill contour offset and hatch compensation become significant, as well as the effect of the interactions between power, border power, and fill contour offset; and power, border power, and hatch compensation. The reasoning for the shift in significance may be due to the fact that the border build variables only affect the border regions, and thus by excluding the core regions, the effects of these build variables become more prominent.

136

To assess the validity of the normality and independence assumptions for the ANOVA, model adequacy plots were constructed (Figure 96), similar to those in Chapter 4. The y-axis symmetry in the observation order vs residual and the predicted vs residual plots is because only two replicates were analysed in the experiment. Because of the model fitting procedure, the sum of residuals are deifned to equal zero, and for two replicate experiments, this results in symmetrical residuals.

From the plots, it appears that the data deviates from normality as well as independence. Because of this, the results from the ANOVA are not a reliable estimator of the true significance of the build parameter variation within the process. Because of these deviations, it is postulated that there may have been biases introduced when the samples were removed from the build plate. Particularly, during part removal, the cutting equipment was slightly angled and resulted in samples on the right side of the build plate being much taller than samples on the left edge of the plate (Appendix K). As a result, the calculated solid fraction of some samples may not be a complete representation of the overall solid fraction.

However, the most likely candidate for the invalidation of the normality assumption may be due to the missing samples that unbalanced the factorial design, as the missing samples result in a loss of orthogonality in the design. Due to this, it is not possible to completely decouple the variances of the build variable effects, which may give rise to errors that invalidate the independence assumption. As previously discussed, several samples were lost upon part removal from the build plate, and thus could not be accounted for during analysis. It is suggested that, given the resources, the build should be reprinted in order to obtain a statistically relevant set of measurements. Optimally, the entire build would be reprinted (Table 24), but given the time constraints, printing only the subset of build variable combinations in Table 25 is also suggested.

Table 26. ANOVA table describing the effects of the build variables on overall part solid fraction.

Source of Variation	Sum of Squares	Degrees of Freedom	Mean Square	F_0	p-value
A	2.67527×10^{-8}	1	2.67527×10^{-8}	5.53	**0.0366**
B	1.52186×10^{-8}	1	1.52186×10^{-8}	3.15	0.1014
C	2.75175×10^{-8}	1	2.75175×10^{-8}	5.69	**0.0344**
D	2.04006×10^{-8}	1	2.04006×10^{-8}	4.22	0.0624
A/B	3.39812×10^{-9}	1	3.39812×10^{-9}	0.70	0.4182
A/C	8.27138×10^{-11}	1	8.27138×10^{-11}	0.02	0.8981
A/D	4.09600×10^{-12}	1	4.09600×10^{-12}	0.00	0.9773
B/C	3.91169×10^{-9}	1	3.91169×10^{-9}	0.81	0.3861
B/D	1.48934×10^{-8}	1	1.48934×10^{-8}	3.08	0.1047
C/D	7.85492×10^{-8}	1	7.85492×10^{-8}	16.25	**0.0017**
A/B/C	1.94719×10^{-8}	1	1.94719×10^{-8}	4.03	0.0678
A/B/D	1.89599×10^{-8}	1	1.89599×10^{-8}	3.92	0.0711
A/C/D	1.50505×10^{-8}	1	1.50505×10^{-8}	3.11	0.1031
B/C/D	9.57345×10^{-9}	1	9.57345×10^{-9}	1.98	0.1848
A/B/C/D	5.85837×10^{-10}	1	5.85837×10^{-10}	0.12	0.7338
Error	5.80226×10^{-8}	12	4.83522×10^{-9}		
Total	3.58321×10^{-7}	27			

R-squared value: 0.6357

Table 27. ANOVA table with the effects of the build variables on border region solid fraction.

Source of Variation	Sum of Squares	Degrees of Freedom	Mean Square	F_0	p-value
A	4.49656×10^{-6}	1	4.49656×10^{-6}	9.11	**0.0107**
B	1.56773×10^{-7}	1	1.56773×10^{-7}	3.05	0.1064
C	2.19289×10^{-7}	1	2.19289×10^{-7}	4.74	0.0501
D	4.40148×10^{-7}	1	4.40148×10^{-7}	7.11	**0.0205**
A/B	2.07207×10^{-8}	1	2.07207×10^{-8}	0.49	0.4961
A/C	1.00940×10^{-8}	1	1.00940×10^{-8}	0.21	0.6570
A/D	3.60096×10^{-7}	1	3.60096×10^{-7}	0.98	0.3417
B/C	8.63208×10^{-8}	1	8.63208×10^{-8}	0.18	0.6883
B/D	3.22986×10^{-7}	1	3.22986×10^{-7}	4.44	0.0569
C/D	9.95333×10^{-6}	1	9.95333×10^{-6}	29.77	**0.0001**
A/B/C	4.88507×10^{-7}	1	4.88507×10^{-7}	5.22	**0.0413**
A/B/D	1.86167×10^{-7}	1	1.86167×10^{-7}	6.28	**0.0276**
A/C/D	1.49715×10^{-7}	1	1.49715×10^{-7}	2.70	0.1261
B/C/D	2.57333×10^{-7}	1	2.57333×10^{-7}	4.02	0.0682
A/B/C/D	4.71955×10^{-8}	1	4.71955×10^{-8}	0.65	0.4342
Error	5.05393×10^{-6}	12	1.15442×10^{-7}		
Total	5.17714×10^{-5}	27			

R-squared value: 0.7452
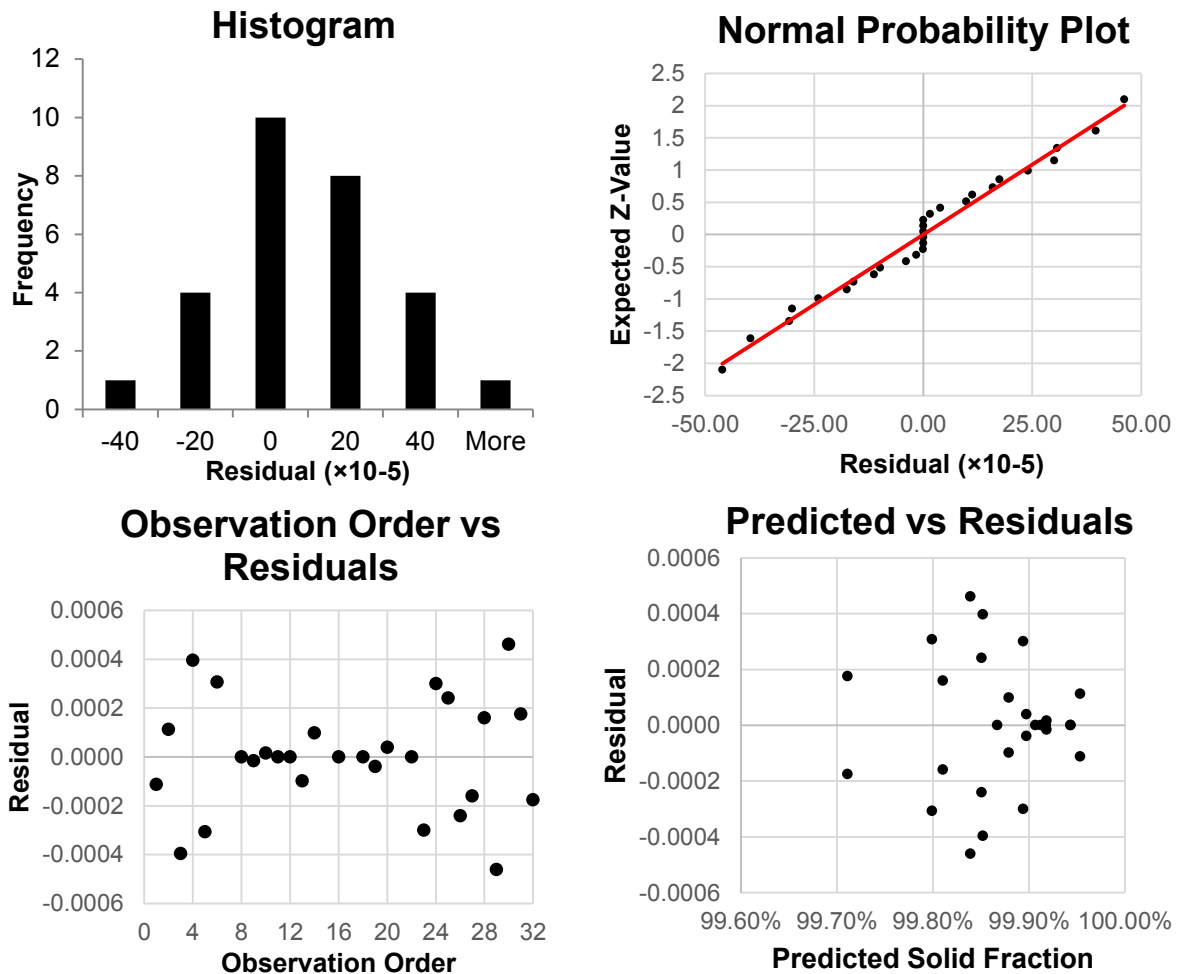
Figure 106. Model adequacy plots for the ANOVA model, describing part performance, for assessing the normality and independence assumptions.

Although the results of the ANOVA cannot be considered reliable at this time, the adjusted R-squared value of 74.52% means the effects are significant for the specific measured set of results. Although they may not be representative of the true process, the build variables can still be analyzed for their effect for this specific data set. As such, it may still serve useful to visualize the effects of the variation of build variables on the porosity within the samples. Thus, marginal means plots were constructed, which average all measurements at each level of the build variables. Figure 107 describes the plots for main effects, Figure 108 describes the plots for two-factor interaction effects, and Figure 109 and Figure 110 describe the plots for the three-factor interaction effects. The values that were inputted into these plots are the same values used in the ANOVA within Table 27.
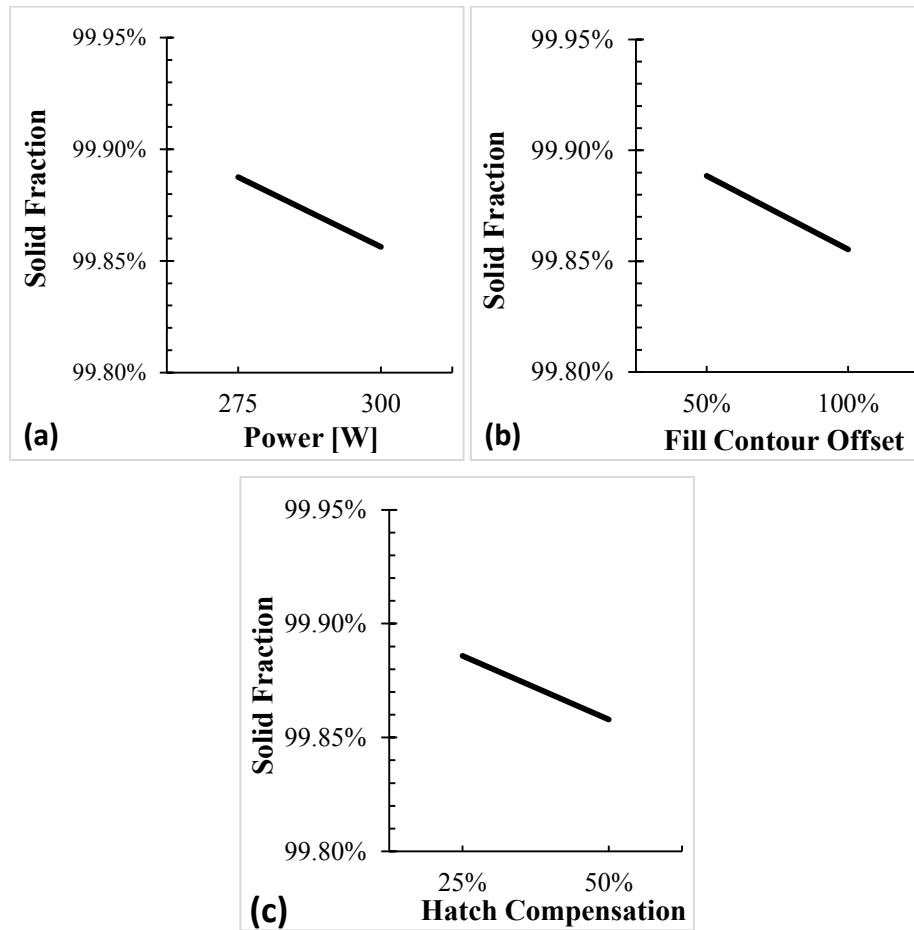
Figure 107. Marginal means plot for the main effects of (a) power, (b) fill contour offset, and (c) hatch compensation.

From the plots in Figure 107, the observed effects in section 5.2.1 are confirmed, showing that on average, the increase of power, fill contour offset, and hatch compensation all separately result in a decrease in solid fraction. Moving forward, when considering the interaction effects between fill contour offset and hatch compensation (Figure 108), the effect of fill contour offset appears to be vary depending on the hatch compensation, where at 25% hatch compensation the increase of fill contour offset decreases porosity, but the behaviour is opposite at 25% hatch compensation. The reasoning behind this behavior is currently up to speculation, but it may involve the fact that at higher hatch compensations the amount of fill hatch line endpoints being generated is less, and thus it would be more beneficial to have a fill contour offset that re-melts areas with absent laser exposures. This may be a delicate balance, where at a certain threshold, the re-exposure of areas with the fill contours may actually contribute to additional porosities, instead of eliminating them.
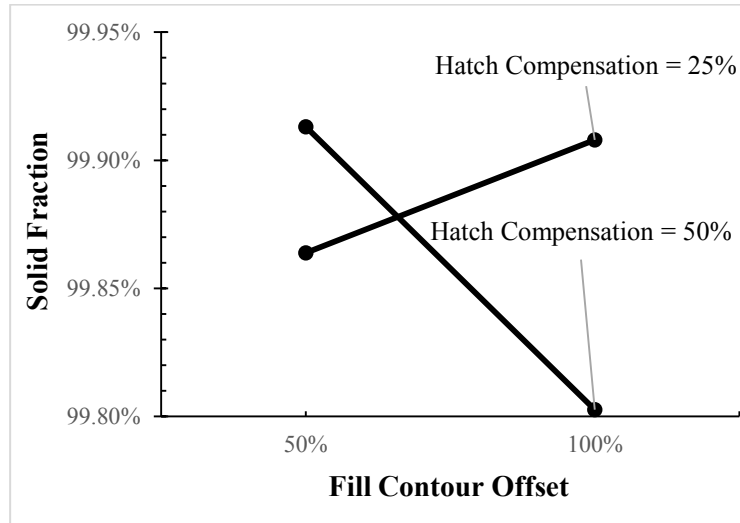
Figure 108. Marginal means plot for the interaction effects of fill contour offset and hatch compensation

Continuing, these interactions of hatch compensation and fill contour offset with the other build variables are further shown when looking at the three factor interactions for power, border power, and fill contour offset (Figure 109); and power, border power, and hatch compensation (Figure 110).
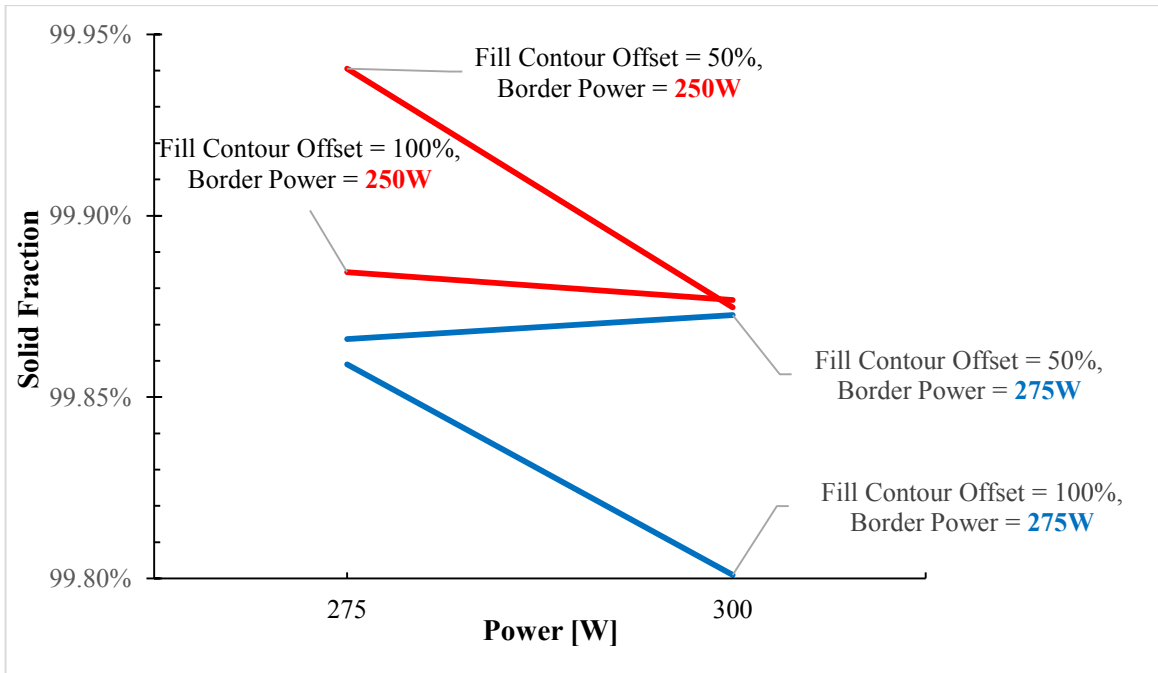
Figure 109. Marginal means plot for the interaction effects of power, border power, and fill contour offset.
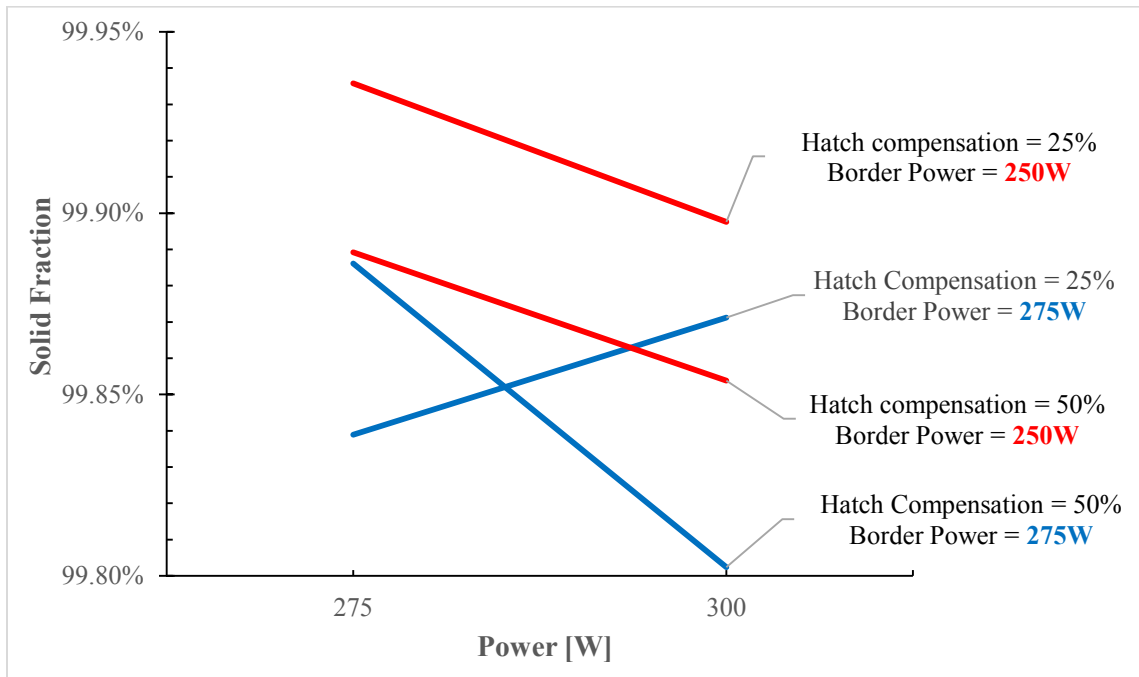
Figure 110. Marginal means plot for the interaction effects of border power, fill contour offset, and hatch compensation.

Although the interactions are complex and varied, there are several recurring trends that are seen between the results in Figure 107 - Figure 110. The decrease of both power and border power, for example, is found to increase the solid fraction in almost all situations. Thus, it is estimated that the lower power levels for power and border power may result in more stable melt pools, and thus would generally result in less porosity across the board, regardless of the amount of re-melting fill contours or additional hatch exposure points. Similarly, the lower values of fill contour offset is found to generally result in less porosity even when considering all of the other interaction effects. This may be because the majority of pores are occurring in the median area between the hatch and border lines (corresponding to 50% fill contour offset). Therefore, directly re-melting the area with fill contours will generally eliminate more pores than it generates. When considering the effect of hatch compensation, in almost all situations the selection of the lower hatch compensation values result in less porosities, which may be because having lower hatch compensation values guarantees the placement of additional exposure points, and limits the locations within a sample that do not receive laser exposure.

142

5.3 Conclusion

In conclusion, based on the results portrayed in this section, and within the selected experimental bounds, it appears as though selecting lower levels for power, fill contour offset, and hatch compensation will generally result in less porosity in the border regions. However, the statistical results imply that these conclusions may only be valid for this specific dataset and not the actual process. Thus, additional experimentation may be required in order to obtain statistically-robust conclusions. Specifically, it is suggested that continued measurements be found for the remaining and missing samples such that the concerns with the normality and independence assumptions of the statistical analysis are addressed. As well, outside of the general trends in build variable behaviour there are exceptions that should be further investigated. It is suggested that more detailed experimentation can be performed to clarify the behaviour within these process regions.

Chapter 6

Finite Element Modelling Approach to Simulate the Thermal History for Laser Powder Bed Fusion

Defining a modelling approach for the LPBF process is a difficult process because of the disparity in scale with defining the phenomenon during processing. As mentioned previously, LPBF parts are manufactured over time frames that span many hours, with laser speeds in the range of several meters per second, but the multi-physics phenomenon occurring during the process happens at time scales and geometric scales of microseconds and micrometers [7]. This chapter aims to familiarize the reader on the numerical simulation for LPBF and challenges associated with it. A simple finite element model is developed, based off of relations developed within literature, to assess the ability to predict melt pool depth as compared to experimental results.

6.1 Modelling Approach

The model was developed using the COMSOL 5.3 Multi-physics package. The basis of this modelling approach was founded on a solid-state heat conduction model, and thus the governing equation for the problem is defined as follows:

$$\rho C_p \frac{\partial T}{\partial t} + \nabla \cdot (-k\nabla T) = Q$$

Where C_p is the specific heat capacity $\left[\frac{J}{kg \cdot K}\right]$, ρ is the density of the material $\left[\frac{kg}{m^3}\right]$, k is the thermal conductivity $\left[\frac{W}{m \cdot K}\right]$, Q is a volumetric heat generation term $\left[\frac{W}{m^3}\right]$, t is time $[s]$, and T is temperature $[K]$. To take into account the latent heat of melting the following relation for heat capacity was first solved for heat capacity:

$$H = \int C_p dT \rightarrow \frac{dH}{dT} = C_p$$

Where H is the enthalpy $\left[\frac{J}{kg}\right]$. From the material properties data, the $\frac{dH}{dT}$ term was measured to be constant in the solid and liquid phases, but discontinuous during the phase transition. Thus, a linear approximation was made for this region, which essentially results in an artificial increase of specific heat capacity during the melting temperatures of the material. This approximation follows relations from literature as follows [113]:

$$C_p^* = \frac{\Delta H_m}{T_l - T_s} + C_{p,0}$$

Where C_p^* is the specific heat capacity $[\frac{J}{kg \cdot K}]$ in the melting region, T_l is the liquidus temperature $[K]$, T_s is the solidus temperature $[K]$, $C_{p,0}$ is the specific heat capacity in the solid phase $[\frac{J}{kg \cdot K}]$, and ΔH_m is the enthalpy change from material at the solidus temperature to material at the liquidus temperature $\left[\frac{J}{kg}\right]$. Referring back to the governing equation, it has been observed in literature that the thermal conductivity is affected by powder bed density and also by thermo-capillary (Marangoni convection) effects, where powder beds were found to reduce thermal conductivity to 1% of bulk, and Marangoni convection was found to increase thermal conductivity by $2\times$ in liquid phase [114], [115]. Although these interactions are complex phenomena, this model attempts to factor in these effects with the use of correction factors, as follows:

$$k_{eff}(T) = c \cdot (a + (b - a)\phi) \cdot k(T)$$

$$c = \begin{cases} 1, & T < T_l \\ c_0, & T \geq T_l \end{cases}$$

Where k_{eff} is the effective conductivity of the material $\left[\frac{W}{m \cdot K}\right]$, a is a fraction representing the conductivity of a porous powder bed, b is a fraction representing the conductivity of solidified material, c is the correction factor for Marangoni convection with a value of c_0 during the liquid phase, and ϕ is the densification ratio of the material. For the model, the densification ratio is defined as a non-decreasing piecewise function such that $0 \leq \phi \leq 1$. At temperatures below T_l, ϕ does not change in value, and at temperatures above T_l, ϕ is set to equal one. To implement this in the COMSOL 5.3 Multi-physics software package, the term was added as an additional ordinary differential equation (ODE) physics module which adhered to the following equation [116]:

$$e_a \frac{\partial^2 \phi}{\partial t^2} + d_a \frac{\partial \phi}{\partial t} = f$$

Where the mass and dampening coefficients e_a and d_a were set to equal zero, and the source term set to equal to $f = \phi - nojac(if(T > T_l, 1, \phi))$. The 'nojac' equation is a COMSOL expression used to omit a function from the Jacobian matrix, and was required because of the logical 'if' statement used within the equation. To account for the laser heat input into the system, the heat flux of the laser was defined as a Gaussian distribution as follows [113]:

$$I(r) = \frac{P}{\pi w^2} e^{-2\left(\frac{r(t)}{w}\right)^2}$$

Where $I(r)$ is the intensity of the laser $\left[\frac{W}{m^2}\right]$ at radius $[m]$, $r(t)$, from the laser center, P is the average power of the laser $[W]$, and w is the laser spot radius $[m]$. Since the laser position is dependent on time, $r(t)$ is defined as the following:

$$r(t) = \sqrt{(x - x_l + (y - y_l)^2}$$

Where the radius of any point from the laser center is dependent on the point's location (x [m], y [m]) and the current location of the laser ($x_l(t)$ [m], $y_l(t)$ [m]). For this model, a single line scan was modelled using the laser exposure scheme that the Renishaw AM 400 employs. As such, the resulting equation for the laser position is as follows:

$$x(t) = x_0 + d_p \times floor\left(\frac{t}{(t_e + t_d)}\right)$$

$$y(t) = y_0$$

Where (x_0 [m], y_0 [m]) is the initial position of the laser, d_p is the point distance of the laser [m], t_e is the laser exposure time [s], t_d is the drill delay of the laser [s], and t is the elapsed simulation time [s]. A flooring function 'floor()' is used to simulate the discontinuous behaviour of the laser exposures from the Renishaw AM 400 system, by enforcing the discretization of the laser position.

Because the powder bed is porous, the laser is absorbed volumetrically into the powder, and to address this, a laser absorption model developed by Gusarov has been employed [117]. Several simplifying assumptions were made, such as setting the particle size to a singular constant value, and assuming that the powders are arranged in cubic close packed structure. From these assumptions, the model derives a parametric equation for the laser absorption based off of the reflectivity of the material, the density in the powder bed, and the particle size of the powder. Afterwards, the model presents the overall laser input as a volumetric heat generation term as follows [117]:

$$U = -\beta Q_0 \frac{dq}{d\xi}$$

Where β is the extinction coefficient, $Q_0(r) = I(r)$ is the incident laser heat flux $\left[\frac{W}{m^2}\right]$, and q is the dimensionless absorptivity of the material at dimensionless depth of ξ. The relations defining β, q, and ξ are very involved, and thus are not defined here. However, they can be found in [117].

In terms of the boundary conditions for the model, a simplifying assumption was made that the boundaries were all thermally insulated such that at all boundaries $-\mathbf{n} \cdot \mathbf{q} = 0$. However, as discussed in section 2.1.1.3, the contributions of radiative and convective heat transfer are critical and thus should be considered in future modifications to the model. One exception to the boundary conditions

is that the model was given a symmetry condition along the X-Z plane at the origin (Figure 111), so that the amount of simulation time would be halved, in comparison to a full-size domain without the symmetry condition.

The geometry of the substrate is defined below in Figure 111. A rectangular domain of 1.50 mm in length along the x-axis, 0.5 mm in width along the y-axis, and 0.3 mm in height along the z-axis was chosen. A second rectangular block with dimensions of 1.05 mm along the x-axis, 140 μm along the y-axis, and 30 μm along the z-axis was embedded within the domain to act as the simulation area for the powder bed, and it was centered along the x-axis, and flush with the X-Z and X-Y plane. Figure 112 shows an isometric view of the model domain with the generated mesh as well.
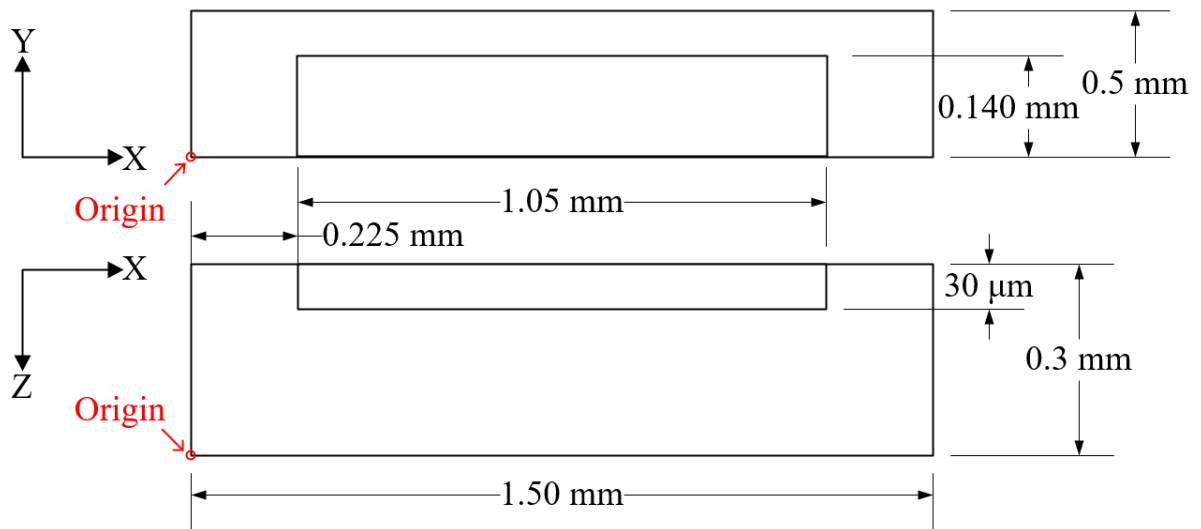
Figure 111. Schematic for the model domain used in the simulation. Displayed geometry is not to scale and unless otherwise specified, dimensions are in millimeters.
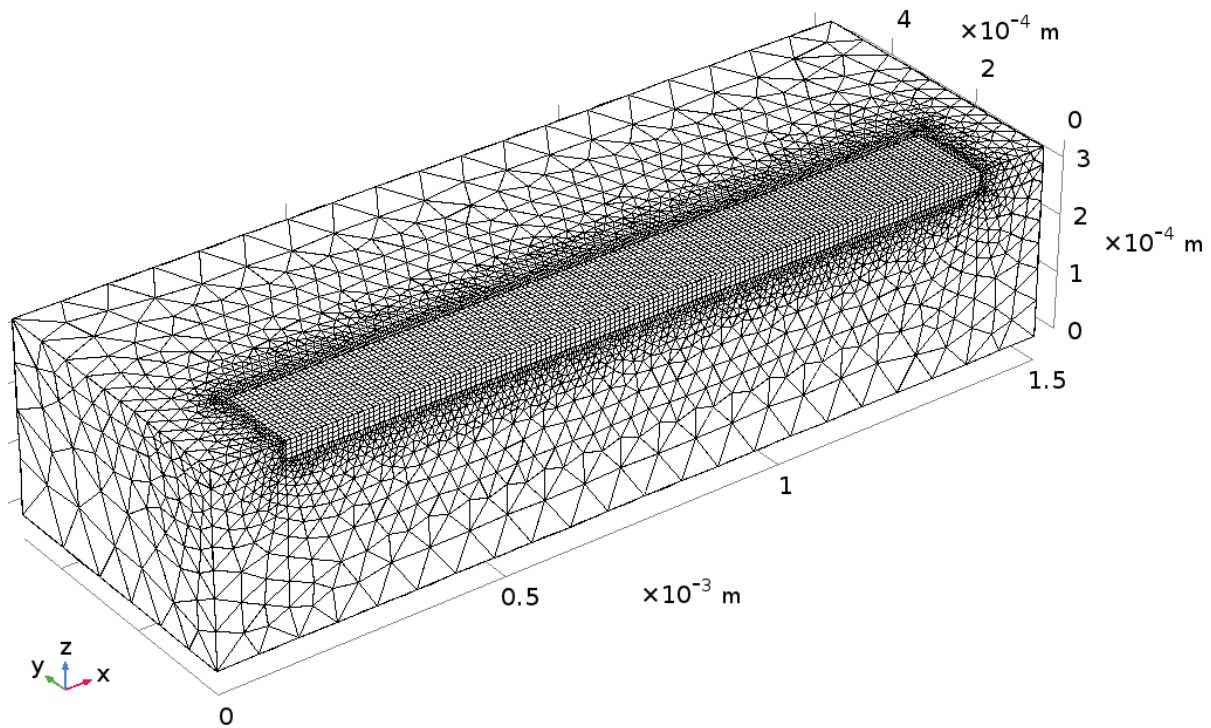
Figure 112. Visualization of model geometry for the simulation, with the generated mesh.

The mesh for the overall domain was selected to have free tetrahedrals automatically generated using the parameters defined in Table 28, while the embedded domain was generated such that only quadrilateral elements with equal side lengths of 8.75 μm were generated. This value corresponds to one quarter of the laser beam radius and was selected as an approximate baseline of the resolution required to simulate the melt pool behaviour.

Table 28. Mesh settings for the overall domain

Element Size Parameter	Unit	Value
Maximum element size	[m]	1.5×10^{-4}
Minimum element size	[m]	2.7×10^{-5}
Curvature factor	[-]	0.60
Resolution of narrow regions:	[-]	0.50

In terms of the simulation settings, a timeframe of 0 seconds to $(16 \times t_e)$ was selected so that 16 entire point exposures were observed during the simulation, where t_e corresponded to laser exposure time. In terms of the other energy input parameters, a parametric sweep was performed such that the results emulated the build variable selection of the components selected for melt pool analysis in

148

section 4.1.6.2. To reiterate, the build variables are described in Table 29 and it is identical to Table 15.

Table 29. Energy input parameters for the simulation

Build variable	Unit	Sample Identification Number					
		5	20	23	26	32	50
Power	[W]	250	300	300	300	350	400
Grid distance	[μm]	70	70	70	70	70	70
Exposure time	[μs]	70	60	70	80	70	70
Energy Density	[J/mm^3]	119	194.4	142.9	109.4	166.7	190.5

Any additional build variables that have not been discussed here can be found in Appendix O, where MATLab code is presented that can be executed in COMSOL with MATLab integration to import the model with all the defined build variables used in this work. The included MATLab code also generates all constants and material property tables used within this chapter. The thermophysical properties of Invar36 have been gathered from literature [118], [119].

For the initial conditions of the model, the temperature of the workpiece was set to initially begin at $T_o = 293.15$ K, and the densification ratio was set such that the initial powder layer (top-most 30 μm of material in the domain) had $\phi = 0$, and the substrate had $\phi = 1$. The distribution of solidification ratio in terms of domain height is shown below in Figure 113.
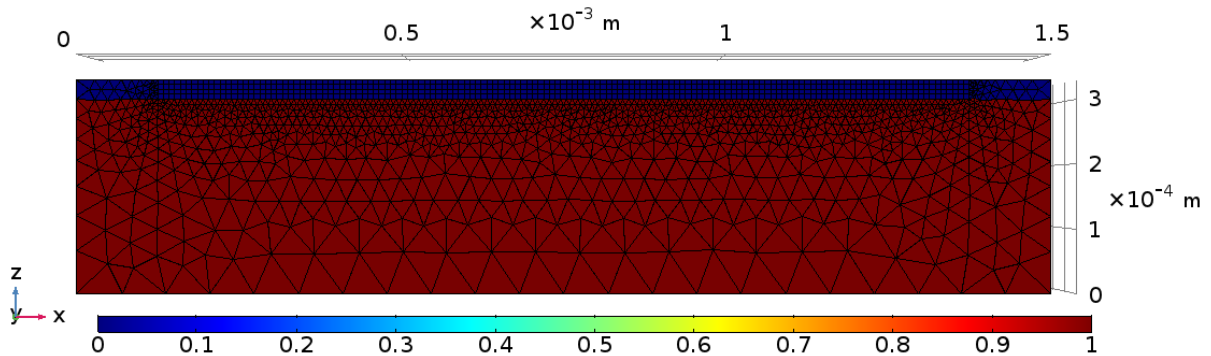
Figure 113. Initial distribution of the densification ratio in the simulation domain, where the value φ=1 corresponds to solidified substrate, and φ=0 corresponds to powder bed.

Once the simulations finished execution, the melt pool depths were extracted from the solution and tabulated for comparison with the experimental data.

6.2 Results

The computational time for each set of build parameter combinations (6 sets were simulated in total) required approximately 9.5 hours of computing time on a machine with the specifications shown below:

Table 30. Machine specifications for the model simulation

Specification	Value
Processor	Intel(R) Xeon(R) CPU E5-2680 v4 @2.40 GHz (56 CPUs)
Memory	256 GB DDR4-2133 MHz
Graphics	8 GB NVIDIA Quadro M5000

Based on these results, it can be seen that the amount of simulation time required to determine a single line scan may be prohibitive, and these results illustrate the challenges with simulating the LPBF process in a feasible scale.

Moving on, Figure 114 shows a representative result of the simulation for temperature with energy input parameters equal to those of sample 5, as described in Table 29. As well, Figure 115 illustrates the solidification history of the material. While representative images of every simulation result can be found in Appendix P, all simulation results look visually similar to the results presented in Figure 114 and Figure 115, except with deviations in melt pool length, width, and depth, and in solidification width. From observation, it appears as if the heat transfer in the z-direction is much greater than in the x- or y-direction. This is shown by the sharp boundary in temperature gradient in areas that have not been fully melted. This is due to the correctional factor in the model due to powder bed densities for thermal conductivity, and shows that it is behaving as intended. Additionally, it seems as if the melt pool edge extends further in the positive x-direction in the substrate than in the powder layer. Once again this may be a result of the increased thermal conductivity in the substrate, in comparison to the powder bed. Due to the decrease in conductivity in the powder bed, the melt pool width does not appear to extend much farther past the radius of the laser exposure.

To compare against the experimental results, the melt pool depths were found by inspecting the locations where the melt pool penetrated the deepest within the domain. To facilitate this measurement, the data within the temperature plot was truncated such that temperature below the solidus temperature of Invar36 ($T_{sol} = 1450\,°C$) were omitted from the results data set. A visualization of this process is shown below in Figure 116. For future experimentation, the melt pool

length was also measured. Likewise, to measure the melt pool width, a similar process to Figure 116 was performed, except by using data from the top view instead.

Afterwards, a plot was constructed to compare the differences between experimental melt pool depths and simulated melt pool depths, and this is shown in Figure 117. To clarify, the x-axis of the figure plots the volumetric energy density of the samples normalized with the measured enthalpy to melt the material. This provides an indication of the fraction of energy input that exceeded the minimum required energy to initiate melting. The y-axis of the figure describes the depth of melt normalized with the layer thickness of the build. Thus, a melt depth of one is the minimum required to ensure the powder layers are fully melted.
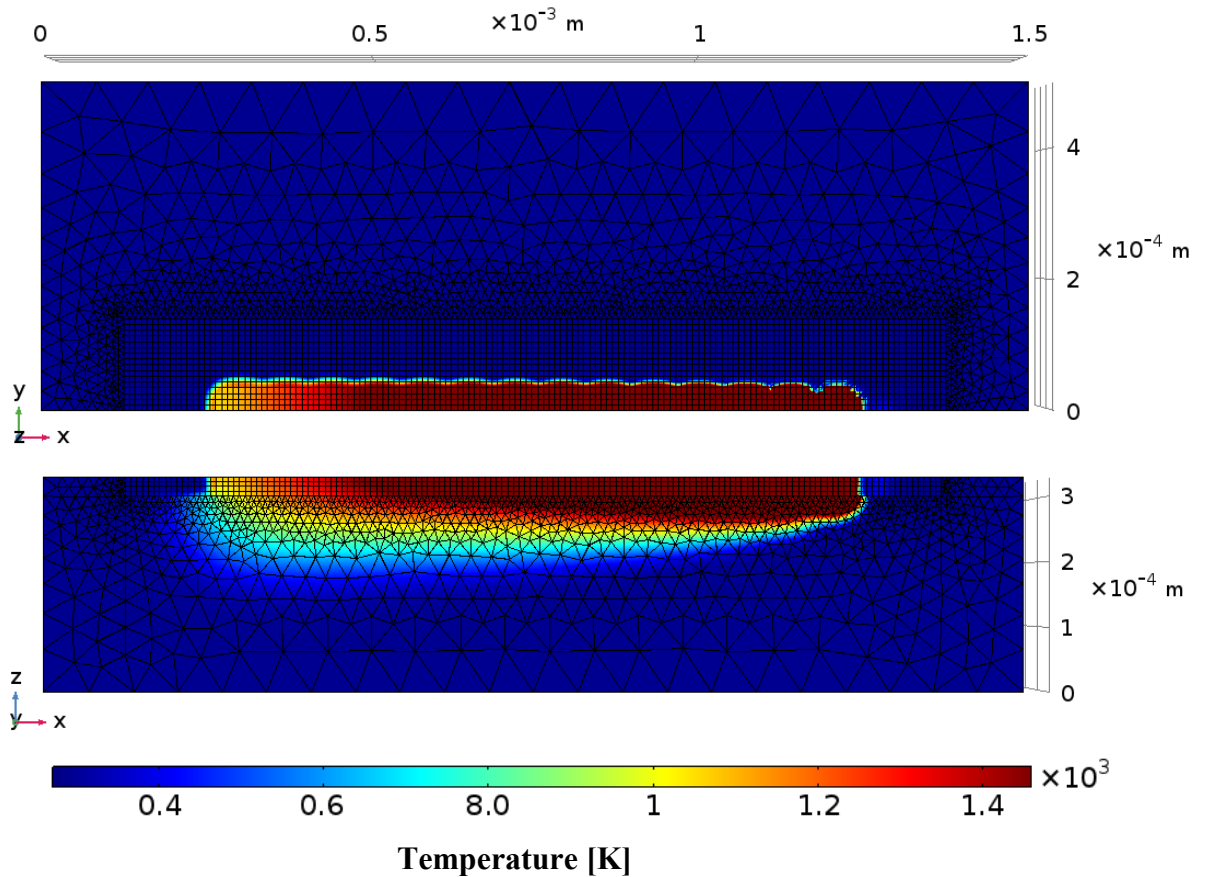
Figure 114. Top and side view of the results for temperature at a time equal to 16 exposure points (0.00112s). Simulation build variables equal those of sample 5 from Table 29.

151
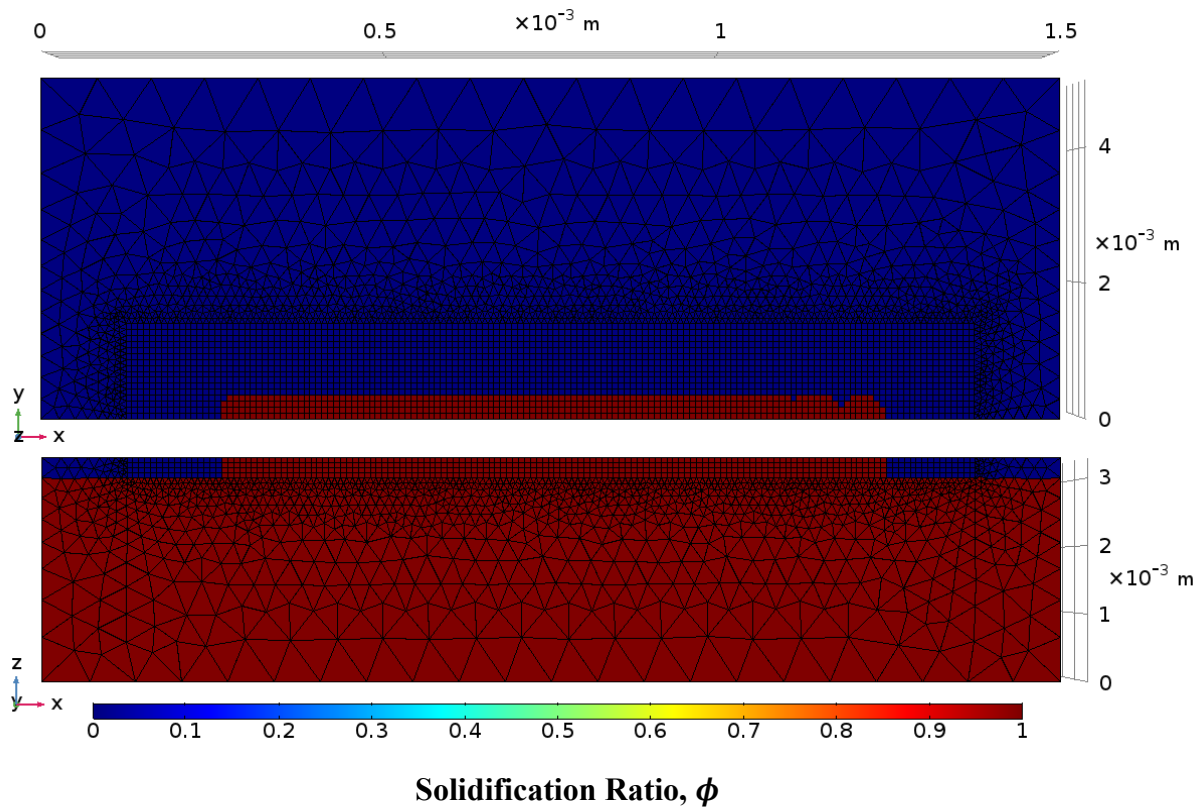
Figure 115. Top and side view of the solidification ratio at a time equal to 16 exposure points (0.00112s). Simulation build variable selection equal those of sample 5 from Table 29.
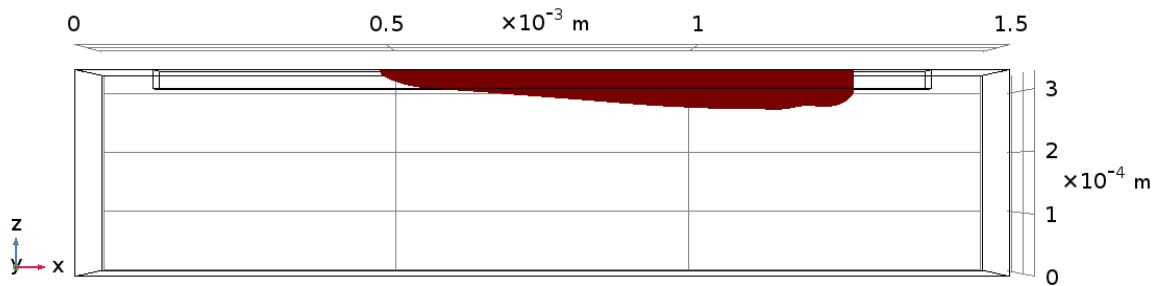
Figure 116. Side view showing only temperatures above melting temperature at a time of 16 exposure points (0.00112s). Simulation build variable selection equal to sample 5 from Table 29.
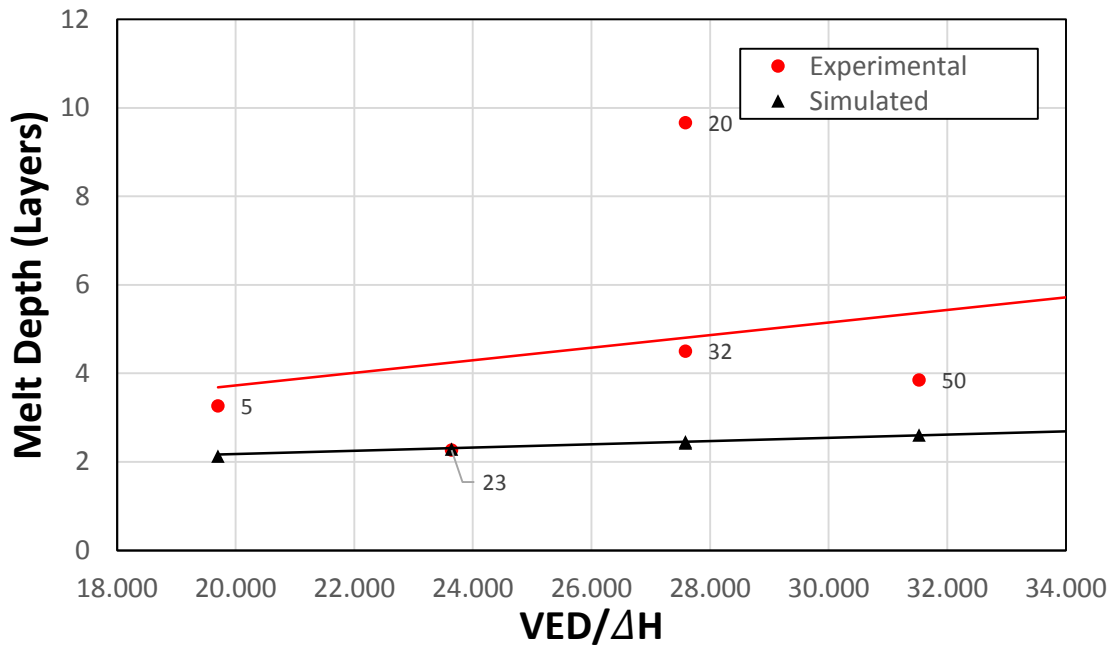
Figure 117. Simulated melt pool depths normalized by the layer thickness plotted against increase in volumetric energy density normalized by enthalpy to melt with the simulation and experimental results plotted for comparison.

As shown by the above figure, the simulated model appears to underpredict the melt depth during processing. Due to the amount of simplifying assumptions made in the model, this result is expected. For example, although the effect of thermocapillary action was included, it is only a constant correctional factor that does not account for full magnitude effects of melt convection, especially as the laser transitions towards keyhole melting regimes. Additionally, the laser absorption of the material was estimated assuming a constant particle size that is optimally packed. However, as mentioned in Chapter 2 and Chapter 3, the particle size distribution and packing state are crucial influencing factors to laser heat input. To relate, the supplied powder used in the experiments was a bimodal powder that was not perfectly spherical, and thus it is expected that the laser absorption within the experiments may have been much higher than simulated conditions. As well, the thermal conductivity within the build bed was approximately also simply, while the true conductivity within a build bed is much more complex. Lastly, the model only simulated a single line scan, and thus the melt pools did not have the benefit of increased heat input from adjacent hatch lines.

To more accurately predict the melt pool behaviour, it is possible to simulate the melt pool dynamics upon melt, as per King et al. [120], and also employ a more robust laser absorption model,

such as with Boley et al. and their ray tracing based absorption model [46]. However, the increase in fidelity with these approaches may also increase the computational cost for simulation. To address this issue, the use of entirely parametric models should be investigated as well, such as with Rubenchik et al. [121].

6.3 Conclusion

In this chapter, a simple finite element model was introduced with the aim of discussing the viability of numerical simulation for LPBF and also challenges associated with it. A comparative experiment was constructed, where the simulation results for melt pool depth using build variable combinations from Chapter 4 were compared against experimentally measured melt pool depths.

From the findings, it was observed that the simulation study required over 9.5 hours of simulation per sample set, for a solution time domain of 16 exposure points. The simulation results show a dominance in heat transfer through the sample height due to the modelled increase in thermal conductivity in the substrate compared to the powder bed. When compared to the experimental measurements, it appears that the model under-predicts the melt pool depth. This was attributed to the assumptions inadequately representing the true behaviour of the melt pool, especially upon transition towards keyhole melting modes, where convection heat transfer becomes more prominent.

For future considerations, mesh independency analyses need to be performed to ensure that the results are not dependent on the fineness of the mesh. As well, investigation into tuning the correctional factors within the model may result in better approximations of melt pool depth, compared to the experimental results. As well, alternative models also be considered, where more rigorous estimations of the melt pool behaviour can improve on model estimates. Overall, the exercise performed in this chapter shows the difficulties in adequately predicting the complex physics of LPBF, while still obtaining results in a feasible time frame. Even with the simplifying assumptions made, the amount of simulation time was extensive, and thus the development of more parametric models is also suggested for time efficiency reasons.

Chapter 7
Conclusions and Future Work

The focus within this thesis was to develop a strategy for process mapping and process window identification with the intent of lowering the barrier for adoption of the laser powder bed fusion (LPBF) technology. This thesis contributed to this through the optimization of process outcomes such as density and thermal expansion characteristics on a novel material for the LPBF process. The study of porous defect space within samples through computed tomography (CT) provided valuable insight on phenomena that occur during processing. Furthermore, the analyses of Invar36's thermal expansion behaviour show that it is possible to achieve and improve on the material's dimensional using LPBF processes. Through the use of statistical techniques, it was demonstrated that it is possible to optimize processes on a more refined level. These conclusions are elaborated upon below, and recommendations for future work are discussed as well.

7.1 Thesis Conclusions

Since the thesis was divided up into several distinct chapters, the following conclusions can be drawn from each:

The goal of Chapter 3 was to characterize the behaviour of the feedstock material due to its possible influences on the LPBF process in-situ. With this in mind, it was first determined that the chemical composition of the powder did not deviate beyond ASTM requirements for Invar36. This traceability in chemical composition confirmed that any deviation in chemical composition in bulk samples would be purely due to in-situ processing, and not issues with the feedstock material. In terms of the particle size distribution, it was found that the particle size conformed well to the supplier specifications of particle size, but analysis into the distribution found that the powder adhered to a bimodal distribution centered about 27 μm and 40 μm. This observation gave valuable insight for future recipe generation, due to the fact that bimodal powders have increased absorptivity. Thus, when translating this study to single mode powders, the lower absorptivity can be accounted for. Lastly, the rheology analysis found that the powder is expected to behave well in terms of its flow characteristics. However, because of the high shear cell measurements, the powder may behave poorly in hoppers at low volume, and thus it may be beneficial to refill hoppers earlier when using Invar36.

In Chapter 4, the objective was to develop a process map for process outcomes such as porosity and the coefficient of thermal expansion (CTE) for Invar36 parts for LPBF, with the ultimate goal of defining an optimized process window. After characterization of the solid fraction through CT analysis, a process map defining the solid fraction behaviour and thermal expansion behaviour was constructed within three-dimensional space, and within two-dimensional space at multiple power levels. By using statistical analysis techniques, an optimal process window was defined, showing that lower power, higher grid distances, and lower exposure times produced better process outcomes. Additional observations, however, showed that a majority of defects occurred near the border region of samples. As well, the pores displayed patterns of angular periodicity and a tendency towards the right side of parts. Thus the statistical analysis was re-run with those border regions removed. As a result, it showed that the optimal process window was large, with the samples achieving > 99.99% density once a certain power threshold of > 250 W was passed. Lastly, a weighted performance parameter was developed to assess the quality of parts with both process outcomes. Based on the statistical analysis, the optimal process window considering both process outcomes concurred with the earlier results for each process outcome separately.

An experiment was created in Chapter 5, based off of the observations in Chapter 4, to minimize the effect of border region porosity through the variation of power, border power, fill contour offset, and hatch compensation. According to the observations, it was found that the selection of lower levels for power, fill contour offset, and hatch compensation generally resulted in less porosity in the border regions. However, the statistical results implied that these conclusions may be valid only for the measured data set, and not the true process as a whole.

Within Chapter 6, a finite element modeling approach to simulating the LPBF process was introduced with the aim of discussing the viability and challenges associated with it. To compare against measured results, the model was simulated over a range of build variable combinations equal to the recipes observed in section 4.1.6.1. The validity of the modelling approach was verified by comparing the melt pool depths, and after simulation it was found that the model under-predicted the melt pool depth. This was attributed to the assumptions inadequately representing the true behaviour of the melt pool, especially upon transition towards keyhole melting modes, where convection heat transfer becomes more prominent.

7.2 Future Work

Within this thesis, several recommendations can be made, based on the observations within each chapter:

For the experiment described in Chapter 4, it is suggested additional measurements should be taken to verify and enrich the robustness of the statistical results. Since the model predictions trend towards lower energy density values, the model can also be further calibrated by exciting lower energy density process regions. It may also be beneficial to observe the influences of the build variables on the microstructural evolution in the material; ongoing experimentation is being performed regarding this. Since it was mentioned that residual stresses are an influencing factor on the thermal expansion behaviour of LPBF-built Invar36 parts, an investigation on the heat treatment effect should be performed as well.

Regarding Chapter 5, the veracity of the observed results should be confirmed by re-analyzing the experiment after either recovering missing samples, or reprinting the build. This is in order to address the concerns with the normality and independence assumptions of the experiment. As a result, the observations found would be more representative of the process. As well, outside of the general trends presented in the experiment, the process appeared to behave unexpectedly in certain exceptional cases. Due to this, it may be valuable to further investigate this behaviour with further experimentation into the affected process regions.

The results presented in the two aforementioned chapters also focus on a specific process region and for specific part geometries. Thus continued work is being done to validate the optimization results with differing geometries, and for differing LPBF systems.

Lastly, the finite element model presented in Chapter 6 requires additional work that should be performed in order to confirm mesh independency of results. As well, it is suggested that the tuning of the correctional factors in the model may improve on the accuracy of the model in comparison to the experimental results. It may also be possible to consider alternative models, where more rigorous estimations of the melt pool behaviour can improve on model estimates. Due to time inefficiencies from the numerical approach, it may also be more feasible to look into the development of parametric models.

References

[1]   T. Wohlers, *Wohler's Report 2016*. Wohlers Associates, Inc, 2016.

[2]   "ASTM ISO/ASTM52900-15 Standard Terminology for Additive Manufacturing – General Principles – Terminology." ASTM International, 2015.

[3]   T. Kellner, "An Epiphany Of Disruption: GE Additive Chief Explains How 3D Printing Will Upend Manufacturing," *GE Reports*, 13-Nov-2017. [Online]. Available: https://www.ge.com/reports/epiphany-disruption-ge-additive-chief-explains-3d-printing-will-upend-manufacturing/.

[4]   T. Kellner, "New One-Of-A-Kind Turboprop Engine Delivers Jet-Like Simplicity To Pilots," *GE Reports*, 12-Nov-2017. [Online]. Available: https://www.ge.com/reports/new-one-kind-turboprop-engine-delivers-jet-like-simplicity-pilots/.

[5]   I. Gibson, D. Rosen, and B. Stucker, *Additive Manufacturing Technologies*. New York, NY: Springer New York, 2015.

[6]   T. Wohlers, T. Caffrey, R. Campbell, O. Diegel, and Kowen, *Wohlers report 2018 3D printing and additive manufacturing state of the industry ; annual worldwide progress report*. Fort Collins, Colorado: Wohlers Associates, Inc, 2018.

[7]   W. E. King *et al.*, "Laser powder bed fusion additive manufacturing of metals; physics, computational, and materials challenges," *Appl. Phys. Rev.*, vol. 2, no. 4, p. 041304, Dec. 2015.

[8]   M. Mani, B. Lane, A. Donmez, S. Feng, S. Moylan, and R. Fesperman, "Measurement Science Needs for Real-time Control of Additive Manufacturing Powder Bed Fusion Processes," National Institute of Standards and Technology, NIST IR 8036, Feb. 2015.

[9]   T. G. Spears and S. A. Gold, "In-process sensing in selective laser melting (SLM) additive manufacturing," *Integrating Mater. Manuf. Innov.*, vol. 5, no. 1, Dec. 2016.

[10]   D. Gu, *Laser Additive Manufacturing of High-Performance Materials*. Berlin, Heidelberg: Springer Berlin Heidelberg, 2015.

[11]   B. Langefeld, "Additive Manufacturing – The Next Generation," *Roland Berger*, 2016. [Online]. Available: https://www.rolandberger.com/en/Publications/pub_additive_manufacturing.html. [Accessed: 05-Jul-2018].

[12]   M. Brandt, *Laser Additive Manufacturing: Materials, Design, Technologies, and Applications*. Kent: Elsevier Science, 2016.

[13]   M. Gouge, *Thermo-mechanical modeling of additive manufacturing*. Kidlington: Butterworth-Heinemann, 2018.

[14]   I. Yadroitsev, *Selective laser melting: Direct manufacturing of 3D-objects by selective laser melting of metal powders*. Lambert Academic Publishing, 2009.

[15]   W. J. Sames, F. A. List, S. Pannala, R. R. Dehoff, and S. S. Babu, "The metallurgy and processing science of metal additive manufacturing," *Int. Mater. Rev.*, vol. 61, no. 5, pp. 315–360, Jul. 2016.

[16]   W. T. Chen and C. W. Nelson, "Thermal Stress in Bonded Joints," vol. 23, no. 2, p. 10, 1979.

[17]   P. Mercelis and J. Kruth, "Residual stresses in selective laser sintering and selective laser melting," *Rapid Prototyp. J.*, vol. 12, no. 5, pp. 254–265, Oct. 2006.

[18]   J. A. Slotwinski, E. J. Garboczi, P. E. Stutzman, C. F. Ferraris, S. S. Watson, and M. A. Peltz, "Characterization of Metal Powders Used for Additive Manufacturing," *J. Res. Natl. Inst. Stand. Technol.*, vol. 119, p. 460, Oct. 2014.

[19]   H. P. Tang, M. Qian, N. Liu, X. Z. Zhang, G. Y. Yang, and J. Wang, "Effect of Powder Reuse Times on Additive Manufacturing of Ti-6Al-4V by Selective Electron Beam Melting," *JOM*, vol. 67, no. 3, pp. 555–563, Mar. 2015.

[20]   H. Lee, C. H. J. Lim, M. J. Low, N. Tham, V. M. Murukeshan, and Y.-J. Kim, "Lasers in additive manufacturing: A review," *Int. J. Precis. Eng. Manuf.-Green Technol.*, vol. 4, no. 3, pp. 307–322, Jul. 2017.

[21]   J. R. Tredicce *et al.*, "Spatial and temporal instabilities in a CO 2 laser," *Phys. Rev. Lett.*, vol. 62, no. 11, pp. 1274–1277, Mar. 1989.

[22]   W. L. Nighan, W. J. Wiegand, and R. A. Haas, "Ionization instability in CO $_2$ laser discharges," *Appl. Phys. Lett.*, vol. 22, no. 11, pp. 579–582, Jun. 1973.

[23]   J. Stone, C. A. Burrus, A. G. Dentai, and B. I. Miller, "Nd:YAG single-crystal fiber laser: Room-temperature cw operation using a single LED as an end pump," *Appl. Phys. Lett.*, vol. 29, no. 1, pp. 37–39, Jul. 1976.

[24]   R. Weber, B. Neuenschwander, and H. P. Weber, "Thermal effects in solid-state laser materials," *Opt. Mater.*, p. 10, 1999.

[25]   J. Berger *et al.*, "Fiber-bundle coupled, diode end-pumped Nd:YAG laser," *Opt. Lett.*, vol. 13, no. 4, p. 306, Apr. 1988.

[26]   B. Zhou, T. J. Kane, G. J. Dixon, and R. L. Byer, "Efficient, frequency-stable laser-diode-pumped Nd:YAGlaser," p. 3.

[27]   L. Lazov and N. Angelov, "PHYSICAL MODEL ABOUT LASER IMPACT ON METALS AND ALLOYS," 2010, pp. 124–128.

[28]   J. C. Ion, *Laser processing of engineering materials: principles, procedure and industrial application*. Amsterdam: Boston : Elsevier/Butterworth-Heinemann, 2005.

[29]   A. G. Demir, P. Colombo, and B. Previtali, "From pulsed to continuous wave emission in SLM with contemporary fiber laser sources: effect of temporal and spatial pulse overlap in part quality," *Int. J. Adv. Manuf. Technol.*, vol. 91, no. 5–8, pp. 2701–2714, Jul. 2017.

[30]   T.-Y. Kuo and Y.-D. Lin, "Effects of Different Shielding Gases and Power Waveforms on Penetration Characteristics and Porosity Formation in Laser Welding of Inconel 690 Alloy," *Mater. Trans.*, vol. 48, no. 2, pp. 219–226, 2007.

[31]   B. Zhou, J. Zhou, H. Li, and F. Lin, "A study of the microstructures and mechanical properties of Ti6Al4V fabricated by SLM under vacuum," *Mater. Sci. Eng. A*, vol. 724, pp. 1–10, May 2018.

[32]   D. D. Gu, W. Meiners, K. Wissenbach, and R. Poprawe, "Laser additive manufacturing of metallic components: materials, processes and mechanisms," *Int. Mater. Rev.*, vol. 57, no. 3, pp. 133–164, May 2012.

[33]   "Materials laser melting - Concept laser," *Concept Laser - Metal 3D printers for parts*, Jul-2018. [Online]. Available: https://www.concept-laser.de/en/products/materials.html.

[34]   "EOS Metal Materials for Additive Manufacturing," *EOS Electro Optical Systems: Industrial 3D Printing*, Jul-2018. [Online]. Available: https://www.eos.info/material-m.

[35]   "Renishaw: enhancing efficiency in manufacturing and healthcare," *Renishaw: enhancing efficiency in manufacturing and healthcare*, Jul-2018. [Online]. Available: http://www.renishaw.com/en/additive-manufacturing-systems--15239.

[36]   "TRUMPF GmbH + Co. KG," *Metal powder for additive manufacturing*, Jul-2018. [Online]. Available: https://www.trumpf.com/en_INT/products/machines-systems/3d-printing-systems/truservices-powder/.

[37]   J. Dawes, R. Bowerman, and R. Trepleton, "Introduction to the Additive Manufacturing Powder Metallurgy Supply Chain," *Johns. Matthey Technol. Rev.*, vol. 59, no. 3, pp. 243–256, Jul. 2015.

[38]   T. DebRoy *et al.*, "Additive manufacturing of metallic components – Process, structure and properties," *Prog. Mater. Sci.*, vol. 92, pp. 112–224, Mar. 2018.

[39]   S. Hoeges, C. T. Schade, and R. Causton, "DEVELOPMENT OF A MARAGING STEEL POWDER FOR ADDITIVE MANUFACTURING," p. 10.

[40]   P. Sun, Z. Z. Fang, Y. Zhang, and Y. Xia, "Review of the Methods for Production of Spherical Ti and Ti Alloy Powder," *JOM*, vol. 69, no. 10, pp. 1853–1860, Oct. 2017.

[41]   P. Vora, R. Martinez, N. Hopkinson, I. Todd, and K. Mumtaz, "Customized Alloy belnds for in-situ formation.pdf," *Technologies*, vol. 5, no. 2, p. 24, May 2017.

[42]   A. Donev, "Improving the Density of Jammed Disordered Packings Using Ellipsoids," *Science*, vol. 303, no. 5660, pp. 990–993, Feb. 2004.

[43]   R. P. Zou and A. B. Yu, "Evaluation of the packing characteristics of mono-sized non-spherical particles," *Powder Technol.*, vol. 88, no. 1, pp. 71–79, Jul. 1996.

[44]   G. H. Ristow, "Dynamics of granular materials in a rotating drum," *Europhys. Lett. EPL*, vol. 34, no. 4, pp. 263–268, May 1996.

[45]   L. C. Y. Chan and N. W. Page, "Particle fractal and load effects on internal friction in powders," *Powder Technol.*, vol. 90, no. 3, pp. 259–266, Mar. 1997.

[46]   C. D. Boley, S. A. Khairallah, and A. M. Rubenchik, "Calculation of laser absorption by metal powders in additive manufacturing," *Appl. Opt.*, vol. 54, no. 9, p. 2477, Mar. 2015.

[47]   A. Manthiram, D. L. Bourell, and H. L. Marcus, "Nanophase materials in solid freeform fabrication," *JOM*, vol. 45, no. 11, pp. 66–70, Nov. 1993.

[48]   Y. Kizaki, H. Azuma, S. Yamazaki, H. Sugimoto, and S. Takagi, "Phenomenological Studies in Laser Cladding. Part I. Time-Resolved Measurements of the Absorptivity of Metal Powder," *Jpn. J. Appl. Phys.*, vol. 32, no. Part 1, No. 1A, pp. 205–212, Jan. 1993.

[49]   A. Simchi, "The role of particle size on the laser sintering of iron powder," *Metall. Mater. Trans. B*, vol. 35, no. 5, pp. 937–948, Oct. 2004.

[50]   R. M. German, "Prediction of sintered density for bimodal powder mixtures," *Metall. Trans. A*, vol. 23, no. 5, pp. 1455–1465, May 1992.

[51]   S. Moylan, J. Slotwinski, A. Cooke, K. Jurrens, and M. A. Donmez, "Lessons learned in establishing the NIST metal additive manufacturing laboratory," National Institute of Standards and Technology, NIST TN 1801, Jun. 2013.

[52]   J. Kranz, D. Herzog, and C. Emmelmann, "Design guidelines for laser additive manufacturing of lightweight structures in TiAl6V4," *J. Laser Appl.*, vol. 27, no. S1, p. S14001, Feb. 2015.

[53]   A. A. Popovich, V. S. Sufiiarov, E. V. Borisov, I. A. Polozov, D. V. Masaylo, and A. V. Grigoriev, "Anisotropy of mechanical properties of products manufactured using selective laser melting of powdered materials," *Russ. J. Non-Ferr. Met.*, vol. 58, no. 4, pp. 389–395, Jul. 2017.

[54]   K. Guan, Z. Wang, M. Gao, X. Li, and X. Zeng, "Effects of processing parameters on tensile properties of selective laser melted 304 stainless steel," *Mater. Des.*, vol. 50, pp. 581–586, Sep. 2013.

[55]   P. Hanzl, M. Zetek, T. Bakša, and T. Kroupa, "The Influence of Processing Parameters on the Mechanical Properties of SLM Parts," *Procedia Eng.*, vol. 100, pp. 1405–1413, 2015.

[56]   N. Hrabe and T. Quinn, "Effects of processing on microstructure and mechanical properties of a titanium alloy (Ti–6Al–4V) fabricated using electron beam melting (EBM), Part 2: Energy input, orientation, and location," *Mater. Sci. Eng. A*, vol. 573, pp. 271–277, Jun. 2013.

[57]   E. Yasa, J. Deckers, T. Craeghs, M. Badrossamay, and J.-P. Kruth, "INVESTIGATION ON OCCURRENCE OF ELEVATED EDGES IN SELECTIVE LASER MELTING," p. 13.

[58]   M. van Elsen, F. Al-Bender, and J. Kruth, "Application of dimensional analysis to selective laser melting," *Rapid Prototyp. J.*, vol. 14, no. 1, pp. 15–22, Jan. 2008.

[59]   C. Qiu, N. J. E. Adkins, and M. M. Attallah, "Selective laser melting of Invar 36: Microstructure and properties," *Acta Mater.*, vol. 103, pp. 382–395, Jan. 2016.

[60]   N. J. Harrison, I. Todd, and K. Mumtaz, "Thermal expansion coefficients in Invar processed by selective laser melting," *J. Mater. Sci.*, vol. 52, no. 17, pp. 10517–10525, Sep. 2017.

[61]   L. N. Carter *et al.*, "Process optimisation of selective laser melting using energy density model for nickel based superalloys," *Mater. Sci. Technol.*, pp. 1–5, Feb. 2016.

[62]   H. Gong, K. Rafi, H. Gu, T. Starr, and B. Stucker, "Analysis of defect generation in Ti–6Al–4V parts made using powder bed fusion additive manufacturing processes," *Addit. Manuf.*, vol. 1–4, pp. 87–98, Oct. 2014.

[63]   T. Nakamoto, N. Shirakawa, Y. Miyata, and H. Inui, "Selective laser sintering of high carbon steel powders studied as a function of carbon content," *J. Mater. Process. Technol.*, vol. 209, no. 15–16, pp. 5653–5660, Aug. 2009.

[64]   J. J. S. Dilip, G. D. J. Ram, T. L. Starr, and B. Stucker, "Selective laser melting of HY100 steel: Process parameters, microstructure and mechanical properties," *Addit. Manuf.*, vol. 13, pp. 49–60, Jan. 2017.

[65]   A. Simchi, "Direct laser sintering of metal powders: Mechanism, kinetics and microstructural features," *Mater. Sci. Eng. A*, vol. 428, no. 1–2, pp. 148–158, Jul. 2006.

[66]   K. G. Prashanth, S. Scudino, T. Maity, J. Das, and J. Eckert, "Is the energy density a reliable parameter for materials synthesis by selective laser melting?," *Mater. Res. Lett.*, vol. 5, no. 6, pp. 386–390, Nov. 2017.

[67]   N. J. Harrison, I. Todd, and K. Mumtaz, "Reduction of micro-cracking in nickel superalloys processed by Selective Laser Melting: A fundamental alloy design approach," *Acta Mater.*, vol. 94, pp. 59–68, Aug. 2015.

163

[68]   C. E. Guillaume, "The Anomaly of Nickel-Steels," *Proc. Phys. Soc. Lond.*, vol. 32, p. 374, 1919.

[69]   H. Saito, *Physics and Applications of Invar Alloys*. Maruzen, 1978.

[70]   E. Kneller, A. Seeger, and H. Kronmüller, "Quantentheorie und Elektronentheorie des Ferromagnetismus," in *Ferromagnetismus*, Berlin, Heidelberg: Springer Berlin Heidelberg, 1962, pp. 734–771.

[71]   D. G. Rancourt and M.-Z. Dang, "Relation between anomalous magnetovolume behavior and magnetic frustration in Invar alloys," *Phys. Rev. B*, vol. 54, no. 17, p. 12225, 1996.

[72]   W. Martienssen and H. Warlimont, Eds., *Springer handbook of condensed matter and materials data*. Heidelberg ; New York: Springer, 2005.

[73]   L. J. Swartzendruber, "The Fe-Ni (iron-nickel) system," vol. 12, no. 3, p. 25, 1991.

[74]   C. E. Guillaume, "Action des additions métallurgiques sur l'anomalie de dilatabilité des aciers au nickel," *Comptes Rendus Hebd. Séances Académie Sci.*, vol. 170, pp. 1433–1435, 1920.

[75]   "ASTM F1684-06, Standard Specification for Iron-Nickel and Iron-Nickel-Cobalt Alloys for Low Thermal Expansion Applications." ASTM International, May-2016.

[76]   J. R. Davis, Ed., *Alloying: understanding the basics*. Materials Park, OH: ASM International, 2001.

[77]   "304 Stainless Steel," *Online Materials Information Resource - Matweb*. [Online]. Available: http://www.matweb.com/search/datasheetText.aspx?bassnum=MQ304A. [Accessed: 07-Jul-2018].

[78]   W. S. McCain, "MECHANICAL AND PHYSICAL PROPERTIES OF INVAR AND INVAR-TYPE ALLOYS," p. 78.

[79]   T. Stephenson, D. Tricker, A. Tarrant, R. Michel, and J. Clune, "Physical and Mechanical Properties of LoVAR: a new lightweight particle-reinforced Fe-36Ni alloy," in *SPIE Optical Engineering+ Applications*, 2015.

[80]   S. K. Kim, Y. D. Lee, K. Hansson, and H. Fredriksson, "Influence of Cooling Rate on the Hot Cracking Formation of Nickel Rich Alloys.," *ISIJ Int.*, vol. 42, no. 5, pp. 512–519, 2002.

[81]   A. Vinogradov, S. Hashimoto, and V. I. Kopylov, "Enhanced strength and fatigue life of ultra-fine grain Fe–36Ni Invar alloy," *Mater. Sci. Eng. A*, vol. 355, no. 1–2, pp. 277–285, Aug. 2003.

[82]   B. Mills and A. H. Redford, *Machinability of Engineering Materials*. Dordrecht: Springer Netherlands, 2013.

[83]   W. S. Park, M. S. Chun, M. S. Han, M. H. Kim, and J. M. Lee, "Comparative study on mechanical behavior of low temperature application materials for ships and offshore structures: Part I—Experimental investigations," *Mater. Sci. Eng. A*, vol. 528, no. 18, pp. 5790–5803, Jul. 2011.

[84]   B. Zalba, B. Sánchez-valverde, and J. M. Marín, "An experimental study of thermal energy storage with phase change materials by design of experiments," *J. Appl. Stat.*, vol. 32, no. 4, pp. 321–332, Jun. 2005.

[85]   A. Y. T. Sun, S. Anand, and J. S. Y. Tang, "Comprehensive design of experiments-based framework for optimal CMM inspection and uncertainty analysis of form tolerances," *Int. J. Prod. Res.*, vol. 40, no. 9, pp. 2097–2123, Jan. 2002.

[86]   N. Alagumurthi, K. Palaniradja, and V. Soundararajan, "Optimization of Grinding Process Through Design of Experiment (DOE)—A Comparative Study," *Mater. Manuf. Process.*, vol. 21, no. 1, pp. 19–21, Jan. 2006.

[87]   V. Nekkanti, T. Muniyappan, P. Karatgi, M. S. Hari, S. Marella, and R. Pillai, "Spray-drying process optimization for manufacture of drug–cyclodextrin complex powder using design of experiments," *Drug Dev. Ind. Pharm.*, vol. 35, no. 10, pp. 1219–1229, Oct. 2009.

[88]   E. Brandl, U. Heckenberger, V. Holzinger, and D. Buchbinder, "Additive manufactured AlSi10Mg samples using Selective Laser Melting (SLM): Microstructure, high cycle fatigue, and fracture behavior," *Mater. Des.*, vol. 34, pp. 159–169, Feb. 2012.

[89]   H. Liao and J. Shie, "Optimization on selective laser sintering of metallic powder via design of experiments method," *Rapid Prototyp. J.*, vol. 13, no. 3, pp. 156–162, Jun. 2007.

[90]   K. A. Mumtaz, P. Erasenthiran, and N. Hopkinson, "High density selective laser melting of Waspaloy®," *J. Mater. Process. Technol.*, vol. 195, no. 1–3, pp. 77–87, Jan. 2008.

[91]   K. Mumtaz and N. Hopkinson, "Top surface and side roughness of Inconel 625 parts processed using selective laser melting," *Rapid Prototyp. J.*, vol. 15, no. 2, pp. 96–103, 2009.

[92]   J. H. Oh and S. Y. Lim, "Precise size control of inkjet-printed droplets on a flexible polymer substrate using plasma surface treatment," *J. Micromechanics Microengineering*, vol. 20, no. 1, p. 015030, Jan. 2010.

[93]   J. Kechagias, "Investigation of LOM process quality using design of experiments approach," *Rapid Prototyp. J.*, vol. 13, no. 5, pp. 316–323, Oct. 2007.

[94]   M. Averyanova, E. Cicala, P. Bertrand, and D. Grevey, "Experimental design approach to optimize selective laser melting of martensitic 17-4 PH powder: part I–single laser tracks and first layer," *Rapid Prototyp. J.*, vol. 18, no. 1, pp. 28–37, 2012.

[95]   D. C. Montgomery, *Design and Analysis of Experiments*, 8th ed. Chihester, United Kingdom: John Wiley and Sons, 2013.

[96]   "CAMSIZER X2 - particle size & shape analyzer," *Particle Analysis Instruments - Retsch Technology*. [Online]. Available: https://www.retsch-technology.com/. [Accessed: 01-Jul-2018].

[97]   "Powder Testing with the FT4 Powder Rheometer," *Freeman Technology: a micromeritics company*. [Online]. Available: http://www.freemantech.co.uk/_powders/ft4-powder-rheometer-universal-powder-tester. [Accessed: 10-Jul-2018].

[98]   R. Freeman and X. Fu, "Characterisation of powder bulk, dynamic flow and shear properties in relation to die filling," *Powder Metall.*, vol. 51, no. 3, pp. 196–201, Sep. 2008.

[99]   R. Freeman, "Measuring the flow properties of consolidated, conditioned and aerated powders — A comparative study using a powder rheometer and a rotational shear cell," *Powder Technol.*, vol. 174, no. 1–2, pp. 25–33, May 2007.

[100]   J. Clayton, D. Millington-Smith, and B. Armstrong, "The Application of Powder Rheology in Additive Manufacturing," *JOM*, vol. 67, no. 3, pp. 544–548, Mar. 2015.

[101]   X. Fu, D. Huck, L. Makein, B. Armstrong, U. Willen, and T. Freeman, "Effect of particle shape and size on flow properties of lactose powders," *Particuology*, vol. 10, no. 2, pp. 203–208, Apr. 2012.

[102]   "ASTM B527-15, Standard Test Method for Tap Density of Metal Powders and Compounds." ASTM International, Apr-2015.

[103]   H. W. Mindt, M. Megahed, N. P. Lavery, M. A. Holmes, and S. G. R. Brown, "Powder Bed Layer Characteristics: The Overseen First-Order Process Input," *Metall. Mater. Trans. A*, vol. 47, no. 8, pp. 3811–3822, Aug. 2016.

[104]   A. Spierings and G. Levy, "Comparison of density of stainless steel 316L parts produced with Selective Laser Melting using different powder grades," in *20th Annual International Solid Freeform Fabrication Symposium,* Austin, Texas, 2009.

[105]   "ASTM E831-14, Standard Test Method for Linear Thermal Expansion of Solid Materials by Thermomechanical Analysis." ASTM International, 01-Aug-2014.

[106]   M. Yang, "Statistical Analysis of Unreplicated Factorial Designs Using Contrasts," Electronic Theses & Dissertations, Georgia Southern University, 2014.

[107]   "Material Safety Data Sheet for Iron." Fisher Scientific, 06-Nov-2007.

[108]   "Material Safety Data Sheet for Nickel." Fisher Scientific, 24-Jun-2015.

[109]   W. E. King *et al.*, "Observation of keyhole-mode laser melting in laser powder-bed fusion additive manufacturing," *J. Mater. Process. Technol.*, vol. 214, no. 12, pp. 2915–2925, Dec. 2014.

[110]   S. A. Khairallah, A. T. Anderson, A. Rubenchik, and W. E. King, "Laser powder-bed fusion additive manufacturing: Physics of complex melt flow and formation mechanisms of pores, spatter, and denudation zones," *Acta Mater.*, vol. 108, pp. 36–45, Apr. 2016.

[111]   D. P. Jones, D. H. MacKerron, and S. V. Norval, "Effect of crystal texture on the anisotropy of thermal expansion in polyethylene naphthalate: measurements and modelling," *Plast. Rubber Compos.*, vol. 42, no. 2, pp. 66–74, Mar. 2013.

[112]   F. J. Parker and R. W. Rice, "Correlation between Grain Size and Thermal Expansion for Aluminum Titanate Materials," *J. Am. Ceram. Soc.*, vol. 72, no. 12, pp. 2364–2366, Dec. 1989.

[113]   W. M. Steen and J. Mazumder, *Laser Material Processing*. London: Springer London, 2010.

[114]   J. Xing, W. Sun, and R. S. Rana, "3D modeling and testing of transient temperature in selective laser sintering (SLS) process," *Opt. - Int. J. Light Electron Opt.*, vol. 124, no. 4, pp. 301–304, Feb. 2013.

[115]   S. Kolossov, E. Boillat, R. Glardon, P. Fischer, and M. Locher, "3D FE simulation for temperature evolution in the selective laser sintering process," *Int. J. Mach. Tools Manuf.*, vol. 44, no. 2–3, pp. 117–123, Feb. 2004.

[116]   W. Frei, "Using the Previous Solution Operator in Transient Modeling," *COMSOL Blog*, 25-Jun-2015. .

[117]   A. V. Gusarov, I. Yadroitsev, P. Bertrand, and I. Smurov, "Model of Radiation and Heat Transfer in Laser-Powder Interaction Zone at Selective Laser Melting," *J. Heat Transf.*, vol. 131, no. 7, p. 072101, 2009.

[118]   A. Seifter, G. Pottlacher, H. Jäger, G. Groboth, and E. Kaschnitz, "Measurements of thermophysical properties of solid and liquid Fe-Ni alloys," *Berichte Bunsenges. Für Phys. Chem.*, vol. 102, no. 9, pp. 1266–1271, 1998.

[119]   A. Seifter, K. Boboridis, B. Didoukh, G. Pottlacher, and H. Jager, "Thermophysical properties of Fe64/Ni36 (Invar) above the melting region," *High Temp.-High Press.*, vol. 29, no. 4, pp. 411–415, Jan. 1997.

[120]   W. King, A. T. Anderson, R. M. Ferencz, N. E. Hodge, C. Kamath, and S. A. Khairallah, "Overview of modelling and simulation of metal powder bed fusion process at Lawrence Livermore National Laboratory," *Mater. Sci. Technol.*, vol. 31, no. 8, pp. 957–968, Jun. 2015.

[121]   A. M. Rubenchik, W. E. King, and S. S. Wu, "Scaling laws for the additive manufacturing," *J. Mater. Process. Technol.*, vol. 257, pp. 234–243, Jul. 2018.

Appendix A:

Renishaw AM 400 System Build Parameters

Table A 1. General parameters for the Renishaw AM 400.

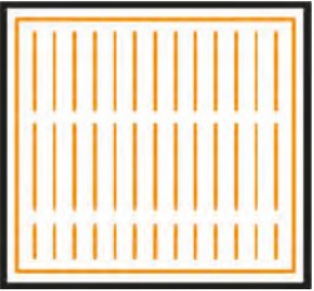| Parameter	Parameter description
Layer thickness	Layer thickness in unit of measure.
Pos X	Position in X (left-right) measured form the build plate centre.
Pos Y	Position in Y (wipe axis) measured from build plate centre.
Layers count	Total number of layers.

Table A 2. Strategy parameters for the Renishaw AM 400.

Parameter	Parameter description
Hatch pattern strategy	This gives you a choice of hatch pattern for your component. Each hatch pattern had advantages and disadvantages, depending upon the characteristics of the component being built. Meander　　　Chessboard　　　Stripe
Field size	The field size is the size of each area in a chessboard hatch pattern.
Field offset	Field offset is used to overlap the fields, to prevent porosity in the component being built.
Minimal field size	The minimal field size is the smallest size a field can be in a chessboard hatch pattern.
Stripe size	In a stripe hatch pattern, each layer is cut into strips at a user defined width. The stripe size is commonly 5 mm. This allows constant time between each successive stripe and therefore maintains a more consistent temperature throughout.
Stripe offset	A stripe offset is used to overlap the stripes, to prevent porosity. Negative offsets indicate higher overlap.
Merge vector length	Minimum length a stripe must have. Stripes with lengths lower than this are merged with another co-linear line.
Merge vector	Toggle if you want to enable "merge vector" or not. (1/0 is ON/OFF)
Block sort/sort optimized	Laser path will move in a continuous movement around holes. It will then return and fill in any missing gaps.

Table A 3. Control parameters for the Renishaw AM 400.

Parameter	Parameter description
Total fill	Fills the layers with only additional border lines, without doing any hatch filling.
Volume fill contours	Similar to borders, but is used to fill the area between fill hatching and borders.
Volume hatch	Volume hatching is the hatching that forms the vast majority of layer areas within a component. (1/0 is ON/OFF)
Volume jump optimisation	Laser path will move in a continuous movement around holes. It will then return and fill in any missing gaps.
Upskin	Enable the rescanning of top surfaces of the build.
Downskin	Enables reduction of energy, or increased speeds in areas that are facing downwards.
Upskin border	Toggles the ability to have borders for upskin layers. (1/0 is ON/OFF)
Blocked path	Reduces the number of scans in thin areas to a single scan.
Hatch compensation	Allows the creation of additional hatch exposures at the end of hatch lines.

Table A 4. Order parameters for the Renishaw AM 400.

Parameter	Parameter description
Scan order 1 to 9	Changes the order of each type of scan line.
Volume border inout	When scan settings permit multiple borders, can enable to scan the border from the inside-out, or outside-in. (1/0 is inout/outin)
Volume fill contour inout	When scan settings permit multiple fill contours, can enable to scan the border from the inside-out, or outside-in. (1/0 is inout/outin)

Types of scan lines include: Volume hatch, downskin hatch, upskin hatch, volume border, downskin border, upskin border, downskin contour, upskin contour, volume contour

Table A 5. Volume parameters for the Renishaw AM 400.

Parameter	Parameter description
Beam compensation	Offset the laser from the edge of the .STL boundary.
Border count	Number of borders.
Border distance	Offset between borders.
Fill contour offset	Offset of the fill contours from the outermost border.
Number of fill contours	The number of fill contours. The fill contours will be generated outside-in, and will overlap with the fill hatch.
Fill contour distance	Offset between fill contours.
Hatch distance	Offset between adjacent scan lines.
Hatch offset	The offset between hatch fill and the innermost border (negative value means overlap).
Hatch start angle	The angle at which the hatch starts.
Hatch increment angle	Increment angle between layers of hatch.
Filter length	Scan lines smaller than this number will not be created. For example, you don't need to scan lines smaller than spot size.
Blocked path resolution	Controls the smoothness of the blocked path.
Blocked path trim distance	Controls the trimming of the blocked path (in mm).
Blocked path filter length	Controls removal of tiny segments (in mm).
Hatch compensation threshold	Percentage of the point distance where distances greater than the hatch compensation will result in addition exposure points.

Table A 6. Upskin/downskin parameters for the Renishaw AM 400.

Parameter	Parameter description
Use start angle	Starts scan direction at a user specified angle, or continue from the last angle in the volume hatch. (1/0 is yes/no)
Keep additional borders	Enables you to keep additional upskin borders. (1/0 is yes/no)
Border offset	The distance between upskin border and upskin hatches.
Number of exposures	The number of times the upskin is scanned.
Number of layers	The number of layers on which the upskin hatching is applied.
Skin area tolerance	The minimal area width on which the upskin is applied.
Hatch offset	The offset between hatch fill and the innermost border (negative value means overlap).
Hatch distance	Offset between adjacent scan lines.
Filter length	Scan lines smaller than this number will not be created. For example, you don't need to scan lines smaller than spot size.
Rotation increment angle	Increment angle between layers of hatch in the upskin layers.
Rotation start angle	The angle at which the upskin fill hatch starts.

Table A 7. Scan volume/upskin/downskin parameters for the Renishaw AM 400.

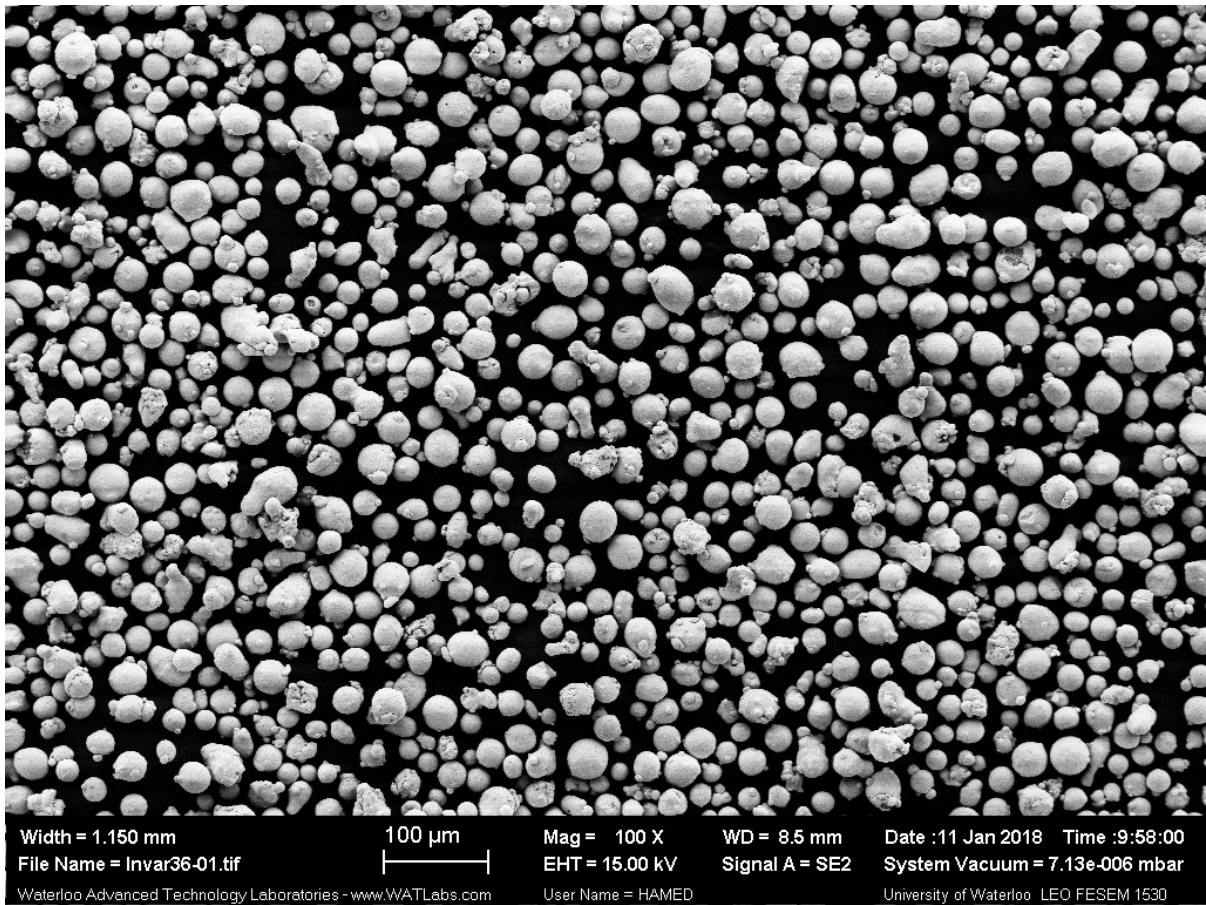| Parameter	Parameter description
Border power	Power of the laser when scanning the borders.
Border focus	The focal plane of the laser (in mm) when scanning borders.
Border point distance	The distance between point exposures for the borders (in μm)
Border exposure time	The length of time the laser is on per point exposure for the borders (in μs).
Hatches power	Power of the laser when hatching.
Hatches focus	The focal plane of the laser (in mm) when hatching.
Hatches point distance	The distance between point exposures for hatching (in μm).
Hatches exposure time	The length of time the laser is on per point exposure for hatching (in μs).
Fill contours power	Power of the laser when scanning the fill contours.
Fill contours focus	The focal plane of the laser (in mm) when scanning fill contours.
Fill contours point distance	The distance between point exposures for the fill contours (in μm).
Fill contours exposure time	The length of time the laser is on per point exposure for the fill contours (in μs).
Additional border power	Power of the laser when scanning additional borders.
Additional border focus	The focal plane of the laser (in mm) when scanning additional borders.
Additional border point distance	The distance between point exposures for additional borders (in μm).
Additional border exposure time	The length of time the laser is on per point exposure for additional borders (in μs).
Border block path power	Power of the laser when scanning the blocked paths.
Border block path focus	The focal plane of the laser (in mm) when scanning blocked paths.
Border block path point distance	The distance between point exposures for the blocked paths (in μm).
Border block path exposure time	The length of time the laser is on per point exposure for the fill contours (in μs).
Additional blocked path power	Power of the laser when scanning additional blocked path.
Additional blocked path focus	The focal plane of the laser (in mm) when scanning additional blocked path.
Additional blocked path point distance	The distance between point exposures for additional blocked path (in μm).
Additional blocked path exposure time	The length of time the laser is on per point exposure for additional blocked path (in μs).

Appendix B:

Scanning Microscopy Images

Width = 1.150 mm	100 µm	Mag = 100 X	WD = 8.5 mm	Date :11 Jan 2018 Time :9:58:00
File Name = Invar36-01.tif		EHT = 15.00 kV	Signal A = SE2	System Vacuum = 7.13e-006 mbar
Waterloo Advanced Technology Laboratories - www.WATLabs.com		User Name = HAMED		University of Waterloo LEO FESEM 1530

Figure B 1. SEM image 1 of powder particle distribution

Width = 1.139 mm	100 µm	Mag = 100 X	WD = 8.5 mm	Date :11 Jan 2018 Time :9:59:53
File Name = Invar36-02.tif		EHT = 15.00 kV	Signal A = SE2	System Vacuum = 5.80e-006 mbar
Waterloo Advanced Technology Laboratories - www.WATLabs.com		User Name = HAMED		University of Waterloo LEO FESEM 1530
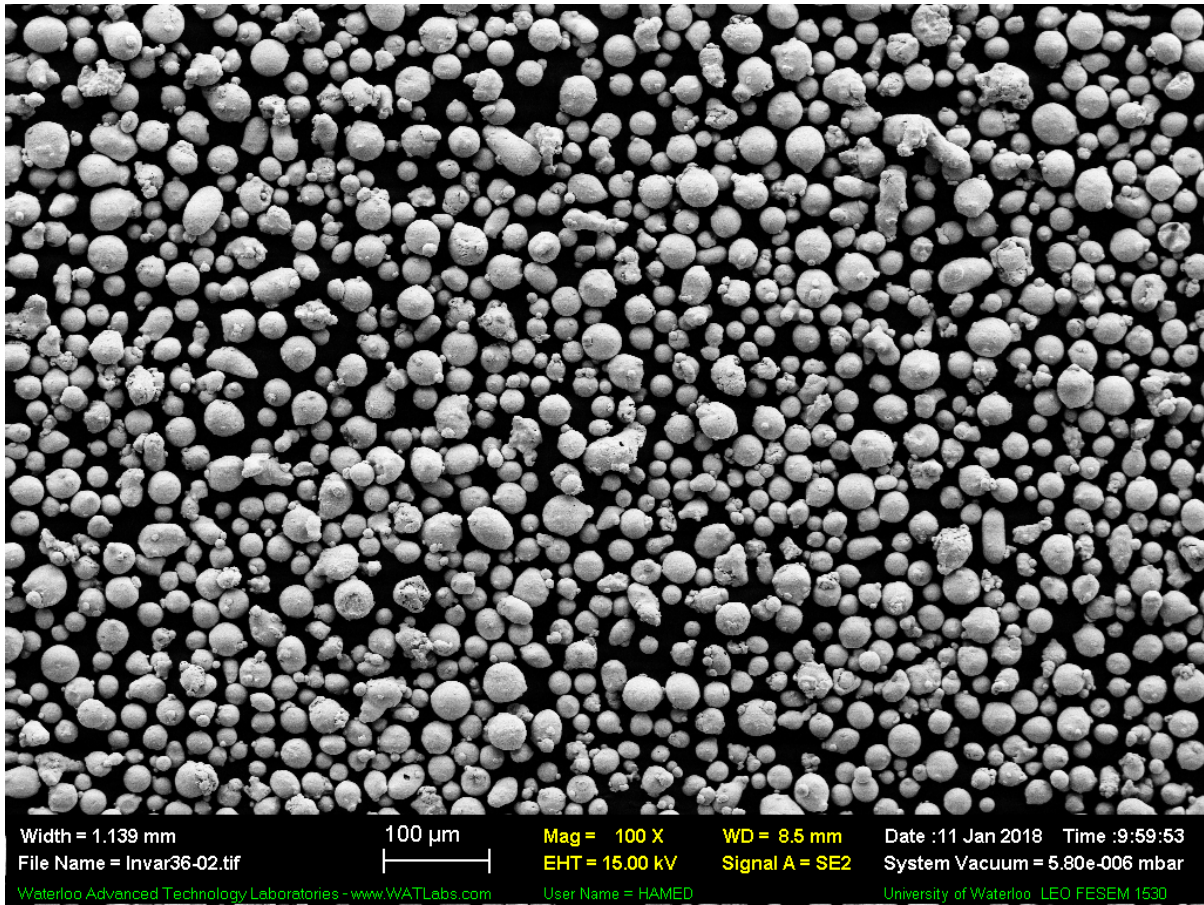
Figure B 2. SEM image 2 of powder particle distribution

Width = 1.139 mm
File Name = Invar36-03.tif
Waterloo Advanced Technology Laboratories - www.WATLabs.com

100 µm

Mag = 100 X
EHT = 15.00 kV
User Name = HAMED

WD = 8.6 mm
Signal A = SE2

Date :11 Jan 2018   Time :10:00:57
System Vacuum = 5.23e-006 mbar
University of Waterloo LEO FESEM 1530
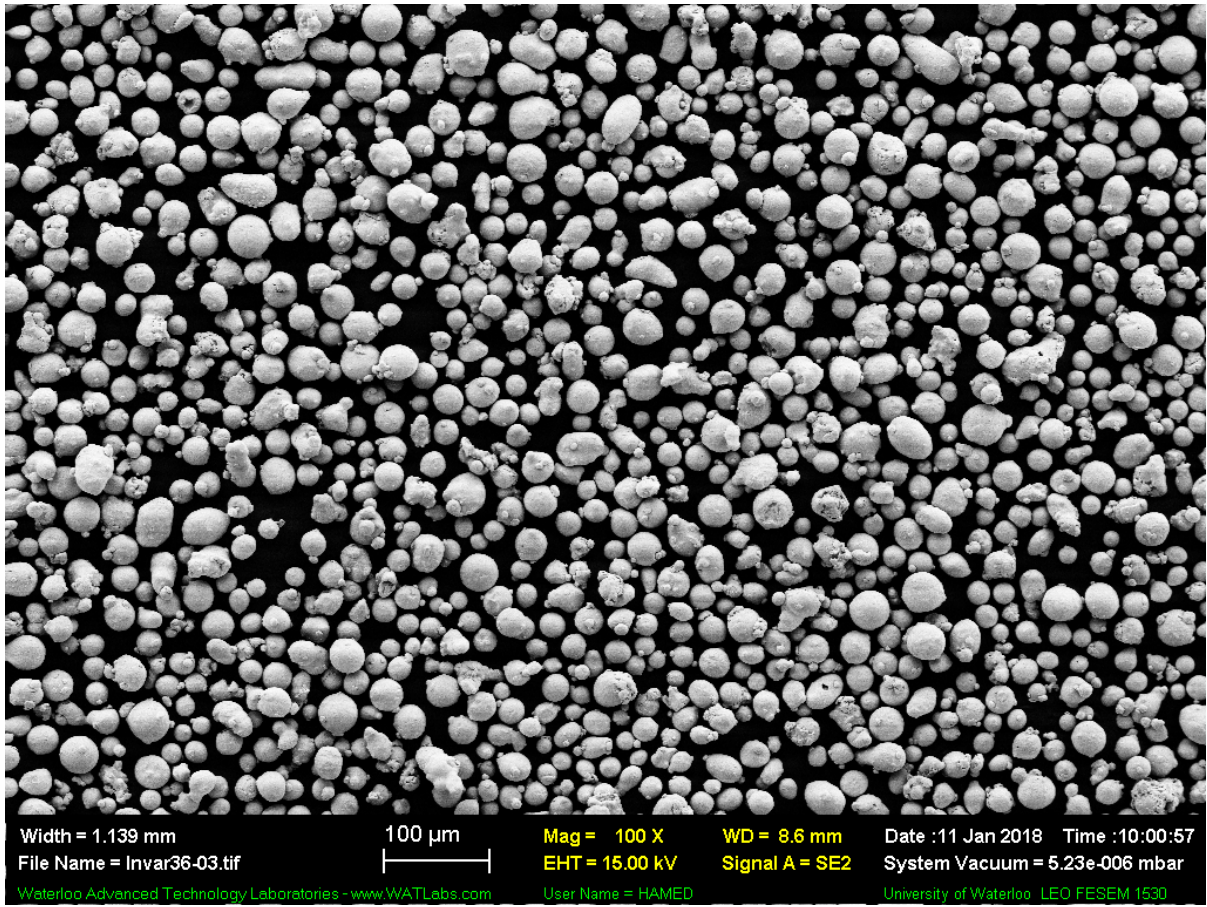
Figure B 3. SEM image 3 of powder particle distribution
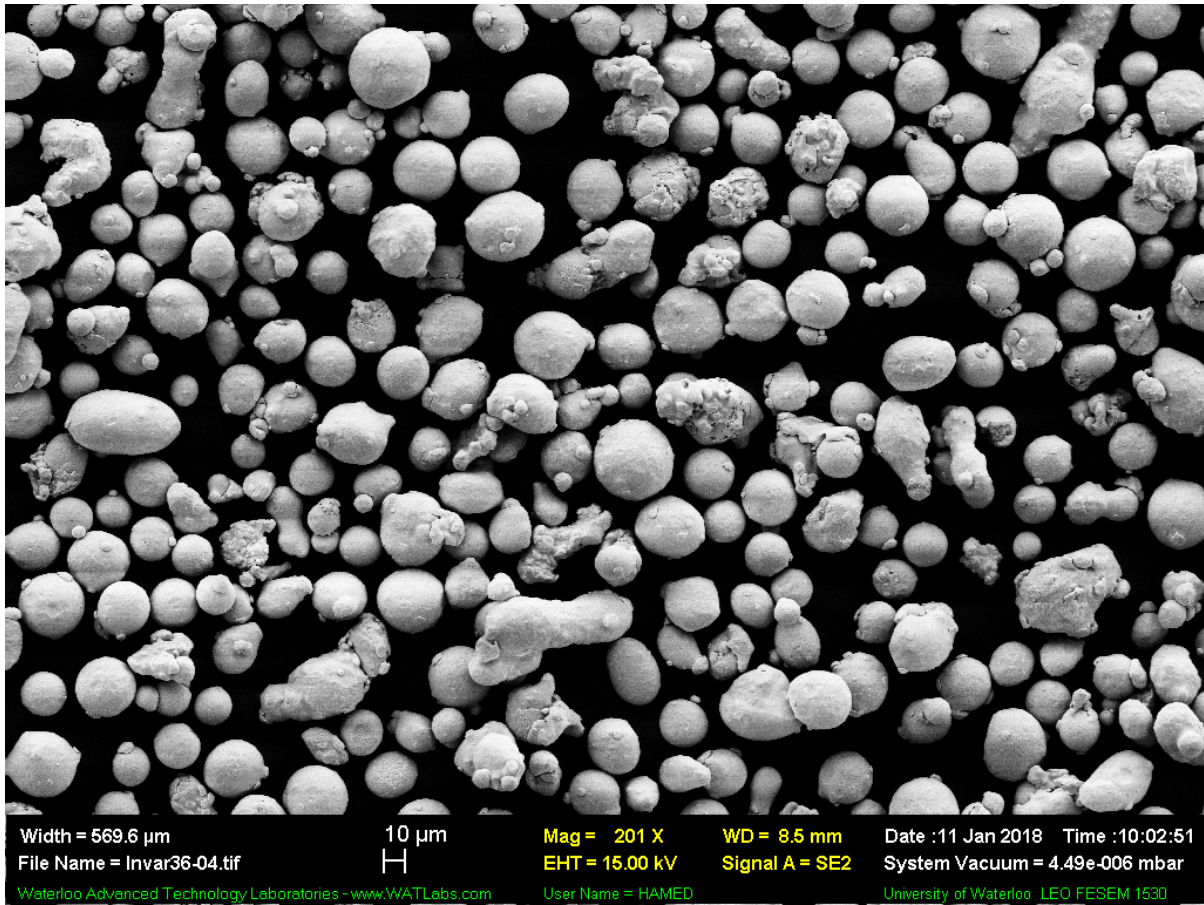
Figure B 4. SEM image 4 of powder particle distribution

Width = 569.6 µm
File Name = Invar36-05.tif
20 µm
Mag = 201 X
EHT = 15.00 kV
WD = 8.5 mm
Signal A = SE2
Date :11 Jan 2018   Time :10:04:08
System Vacuum = 4.05e-006 mbar
Waterloo Advanced Technology Laboratories - www.WATLabs.com
User Name = HAMED
University of Waterloo LEO FESEM 1530
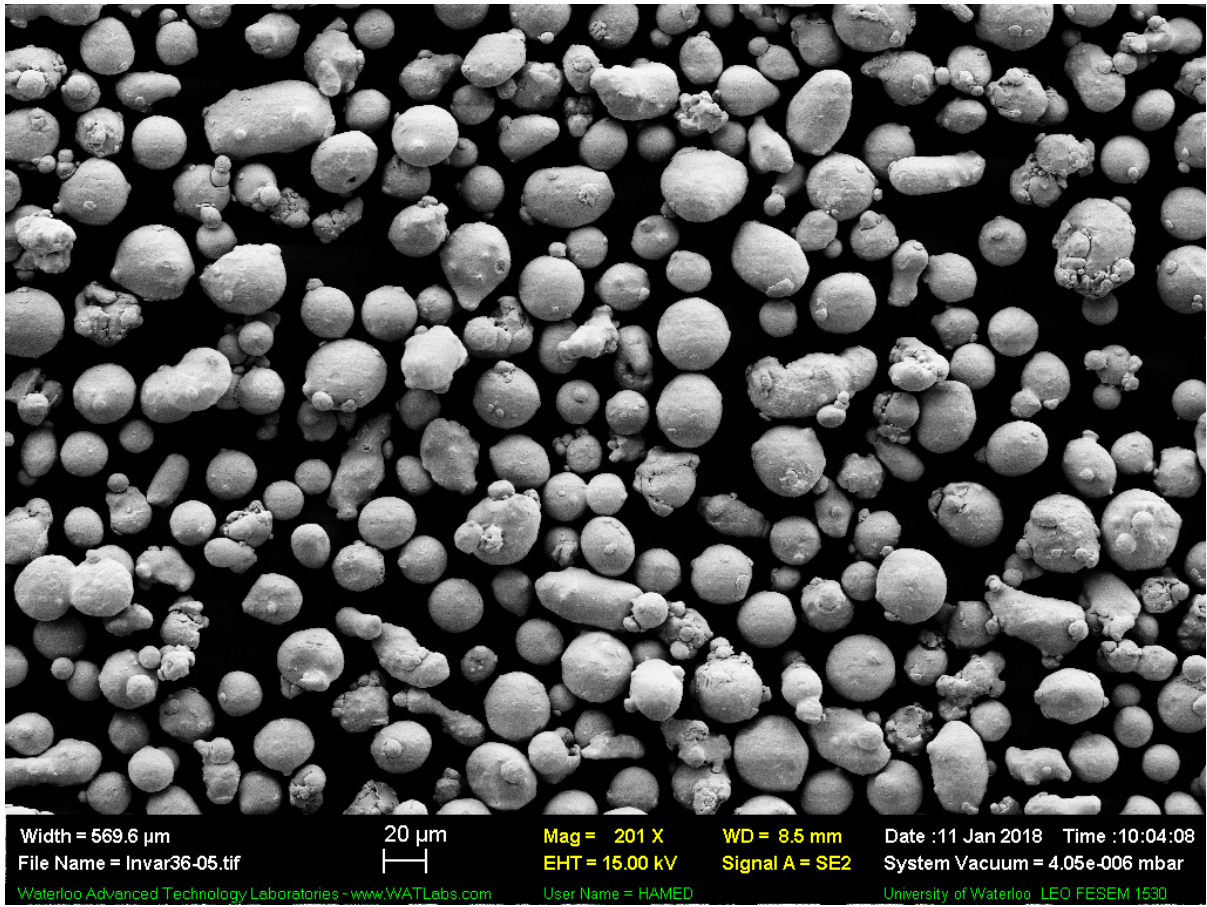
Figure B 5. SEM image 5 of powder particle distribution
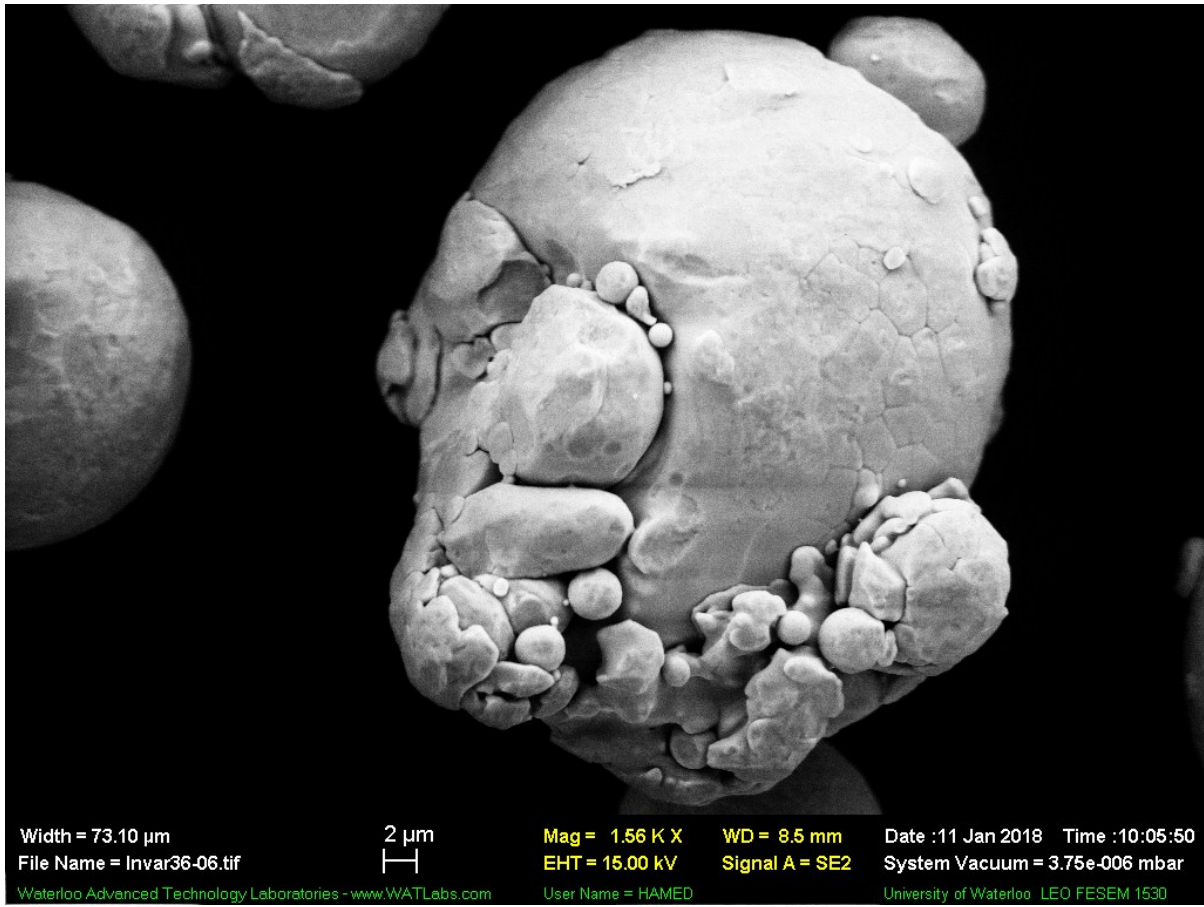
Figure B 6. SEM image 1 of particle of interest
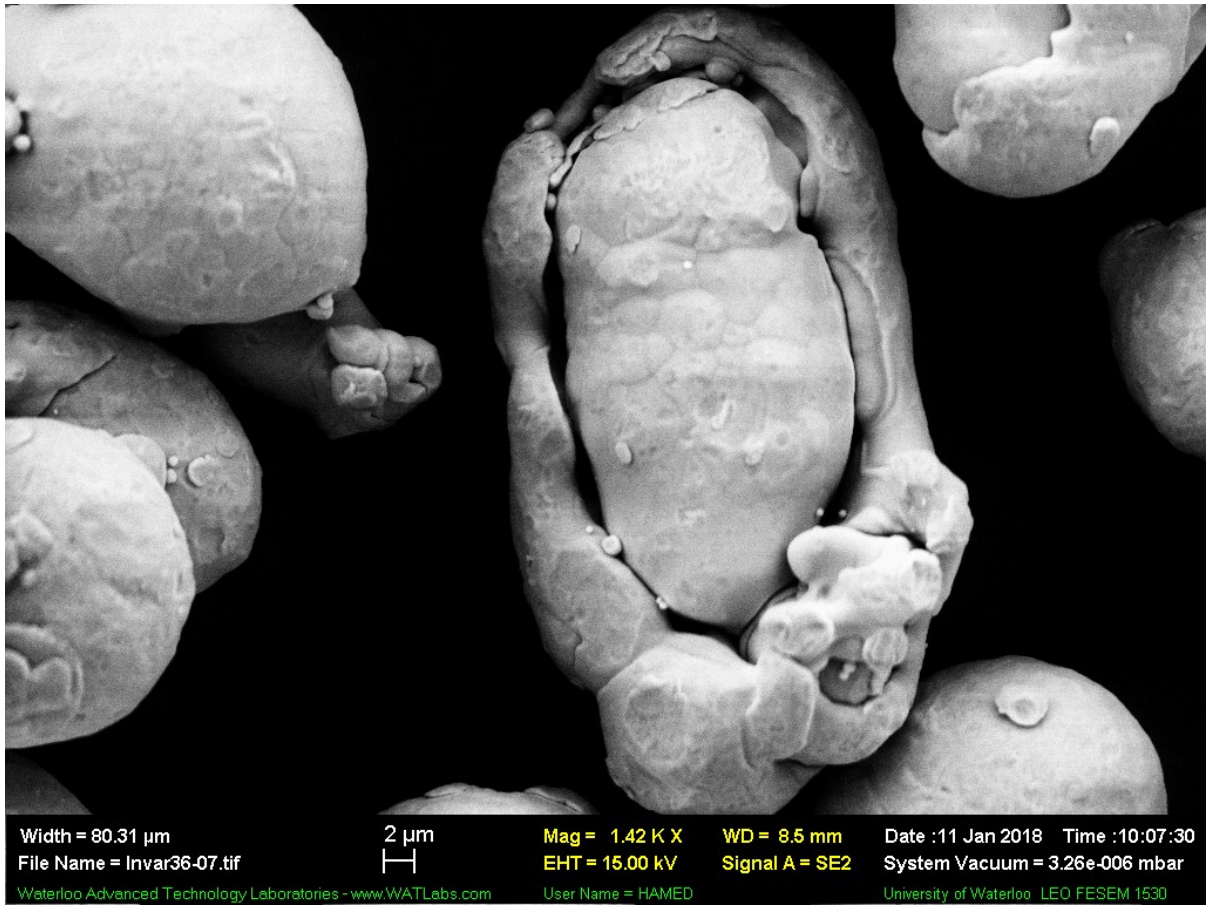
Figure B 7. SEM image 2 of particle of interest

179
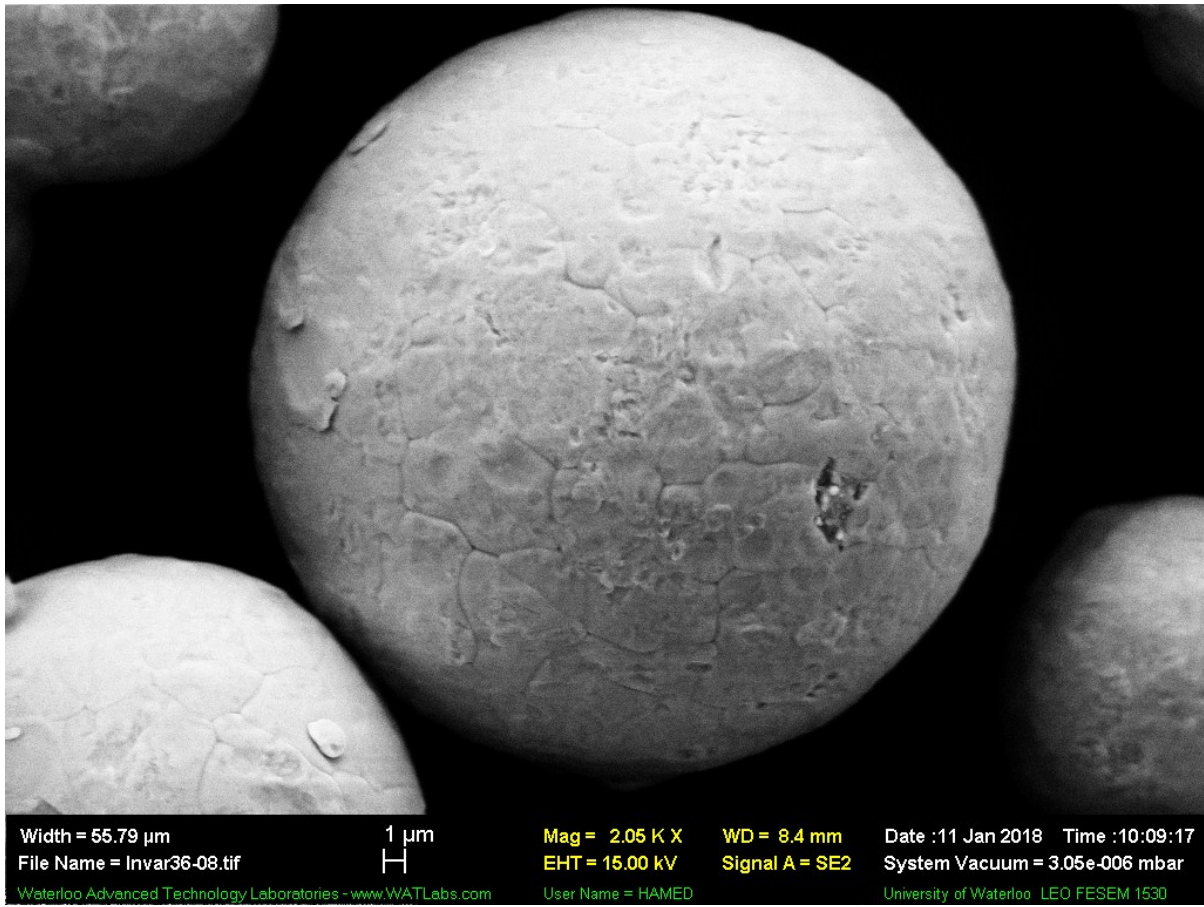
Figure B 8. SEM image 3 of particle of interest
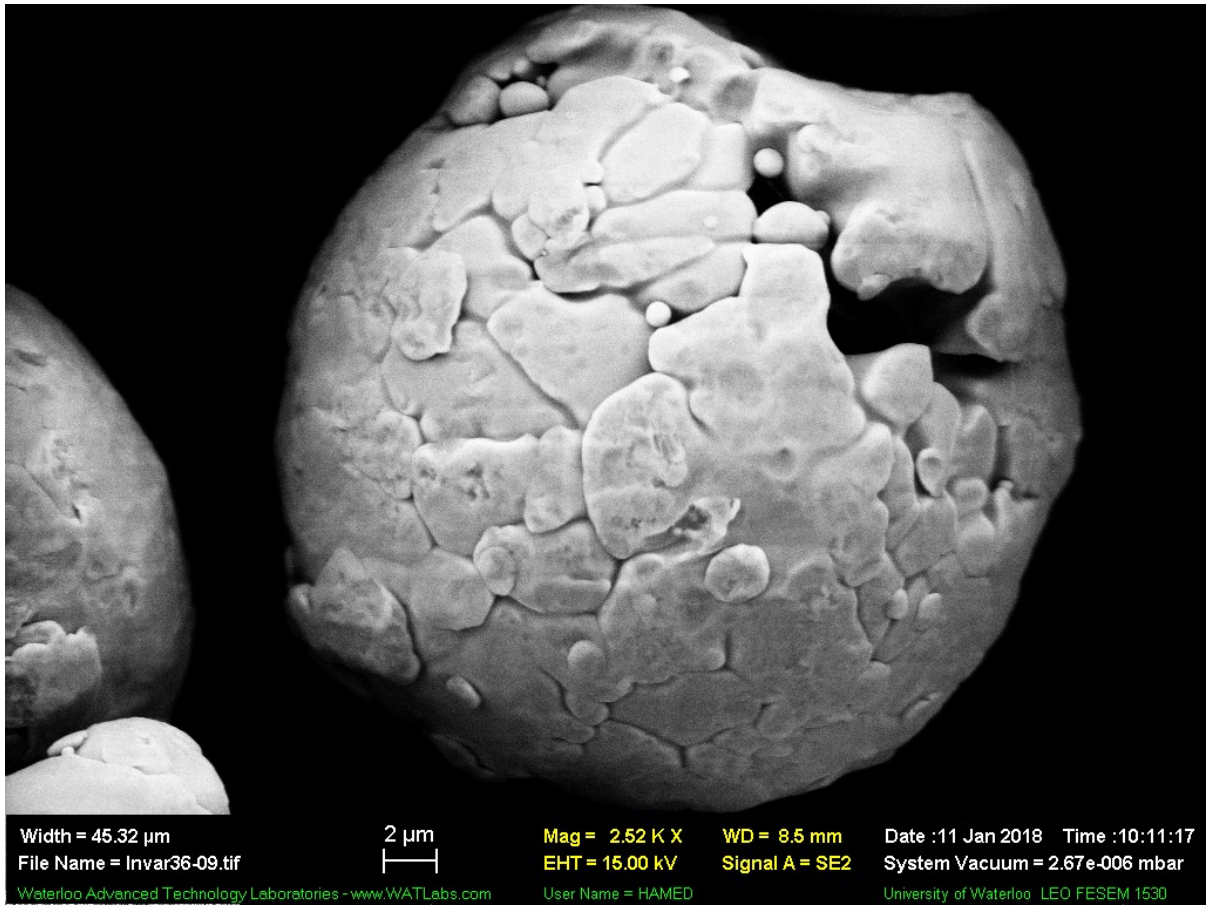
Figure B 9. SEM image 4 of particle of interest
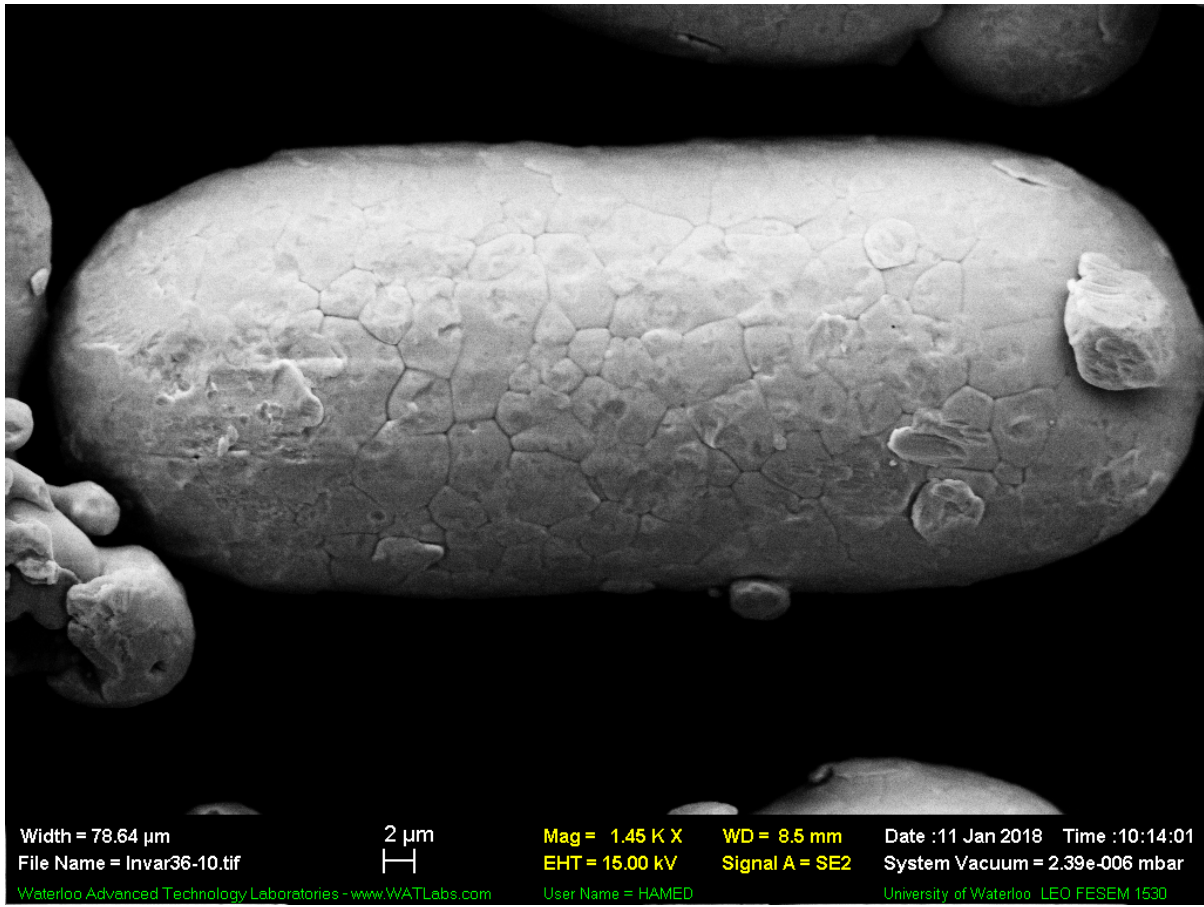
Figure B 10. SEM image 5 of particle of interest

Width = 61.92 μm   2 μm   Mag = 1.84 K X   WD = 8.5 mm   Date :11 Jan 2018   Time :10:18:48
File Name = Invar36-11.tif   ⊢―⊣   EHT = 15.00 kV   Signal A = SE2   System Vacuum = 2.07e-006 mbar
Waterloo Advanced Technology Laboratories - www.WATLabs.com   User Name = HAMED   University of Waterloo LEO FESEM 1530
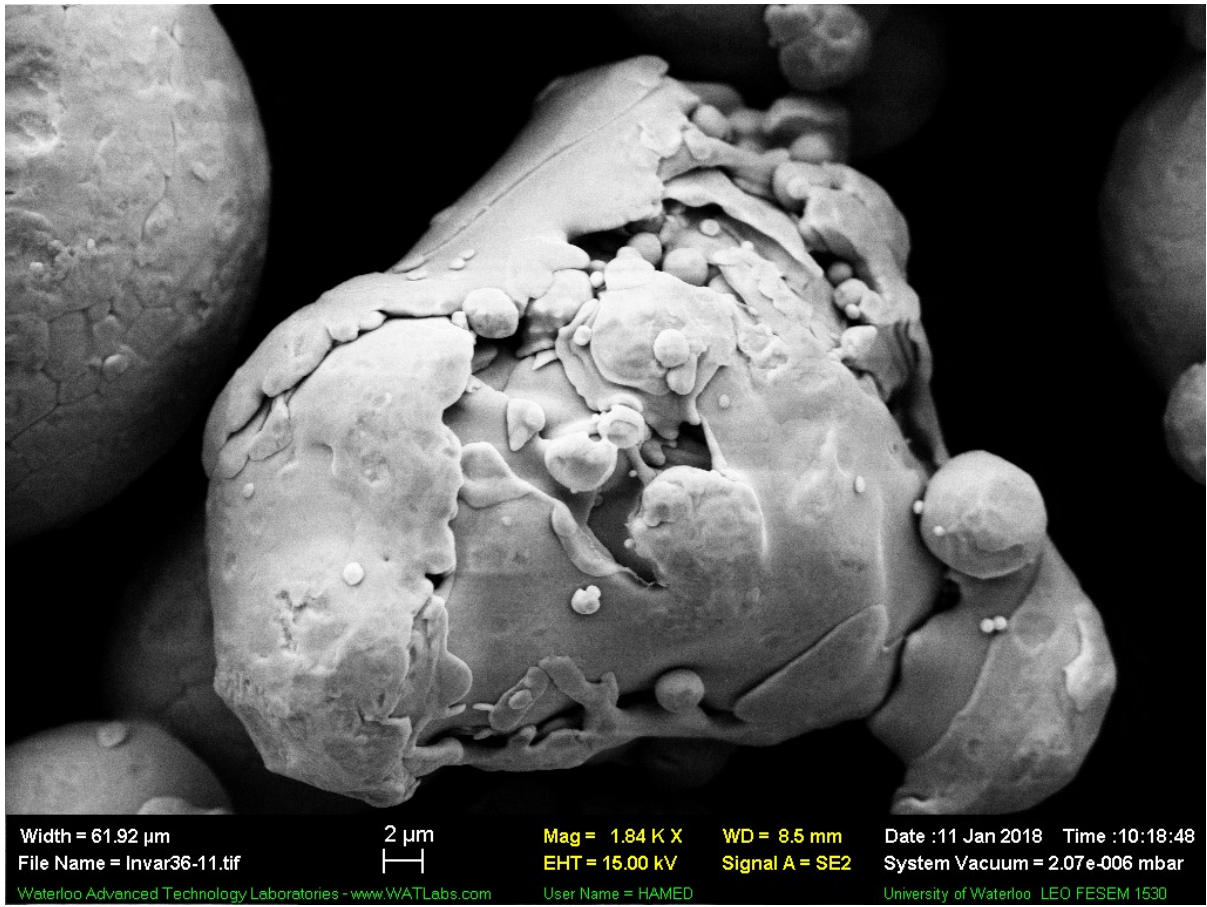
Figure B 11. SEM image 6 of particle of interest

Width = 54.65 µm   1 µm   Mag = 2.09 K X   WD = 8.5 mm   Date :11 Jan 2018   Time :10:21:04
File Name = Invar36-12.tif   EHT = 15.00 kV   Signal A = SE2   System Vacuum = 1.83e-006 mbar
Waterloo Advanced Technology Laboratories - www.WATLabs.com   User Name = HAMED   University of Waterloo   LEO FESEM 1530
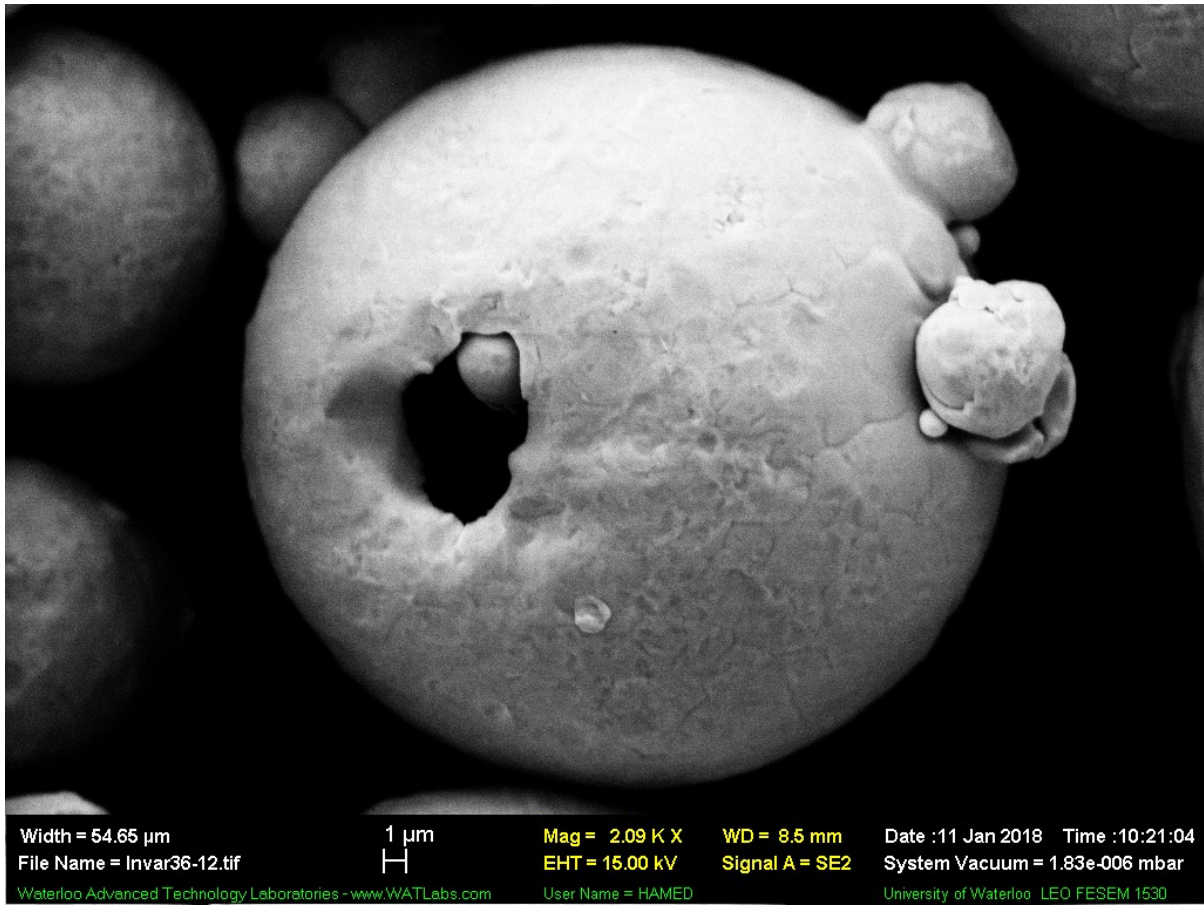
Figure B 12. SEM image 7 of particle of interest
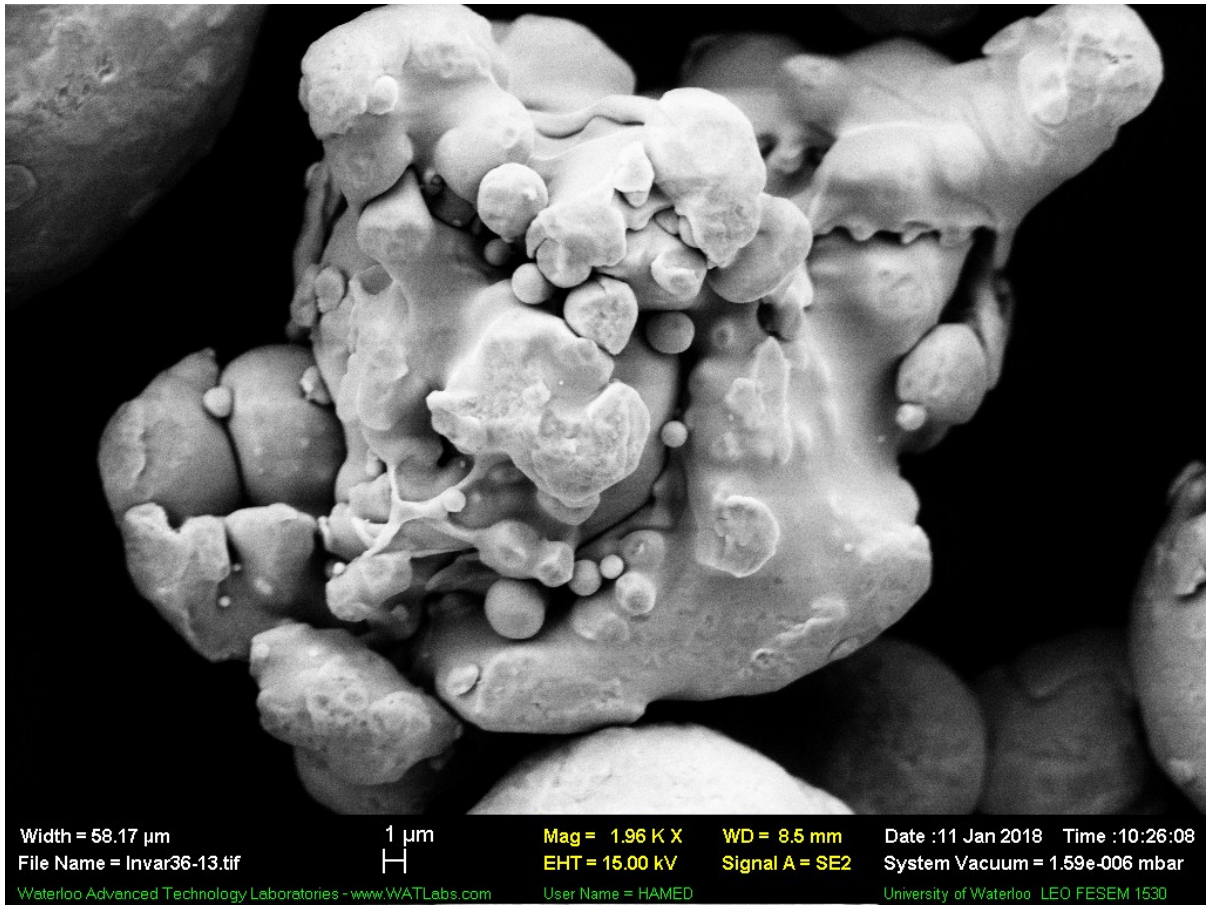
Figure B 13. SEM image 9 of particle of interest

185
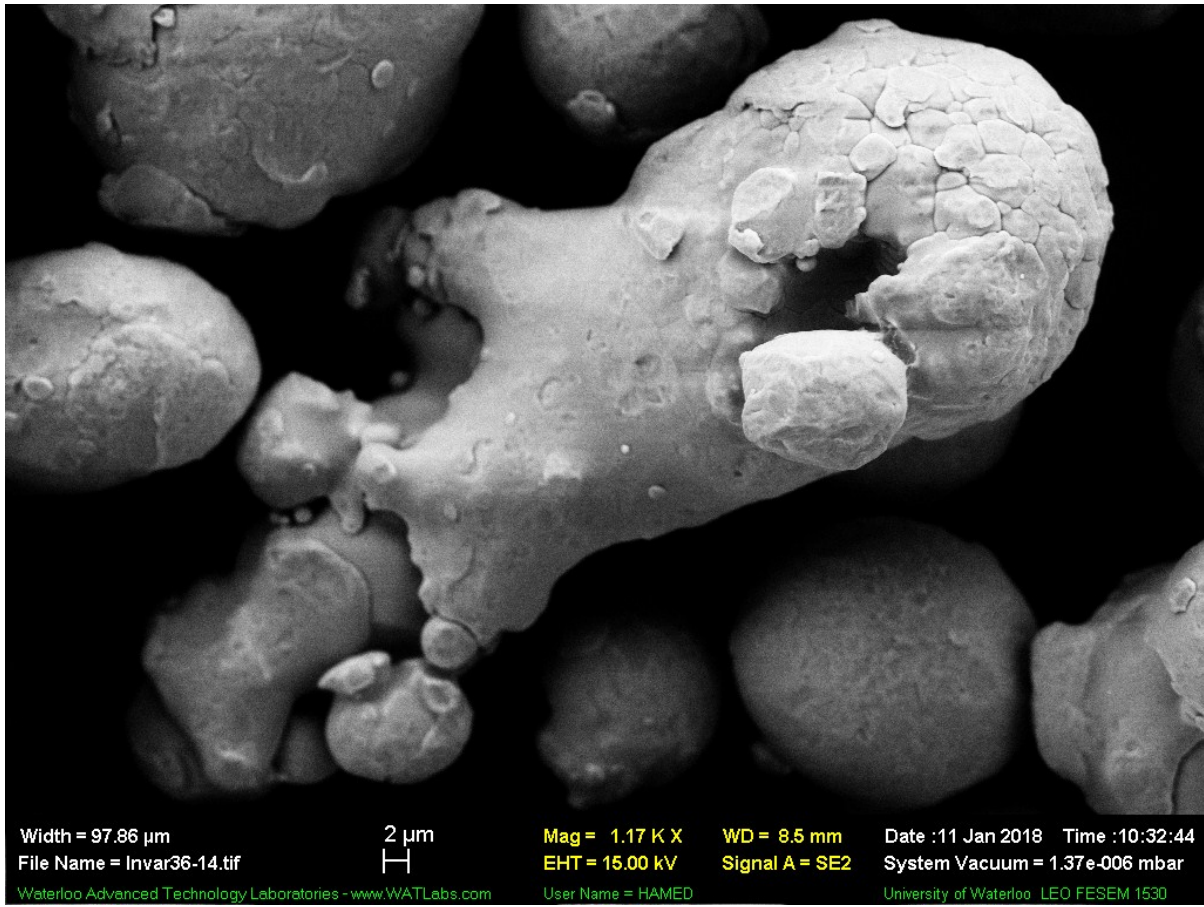
Figure B 14. SEM image 10 of particle of interest
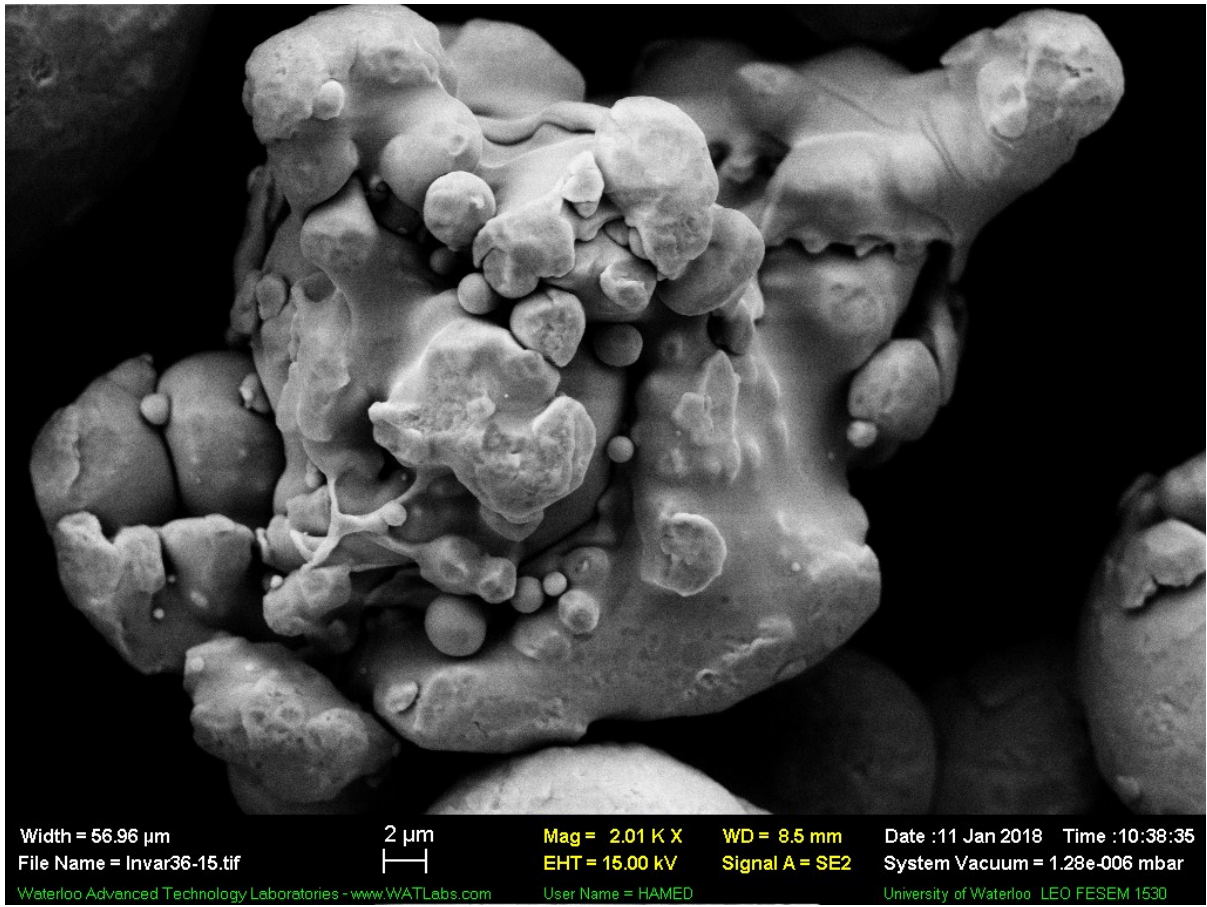
Figure B 15. SEM image 11 of particle of interest

Width = 72.38 μm
File Name = Invar36-16.tif
2 μm
Mag = 1.58 K X **WD = 8.5 mm** Date :11 Jan 2018 Time :10:44:27
EHT = 15.00 kV **Signal A = SE2** System Vacuum = 1.13e-006 mbar
Waterloo Advanced Technology Laboratories - www.WATLabs.com User Name = HAMED University of Waterloo LEO FESEM 1530
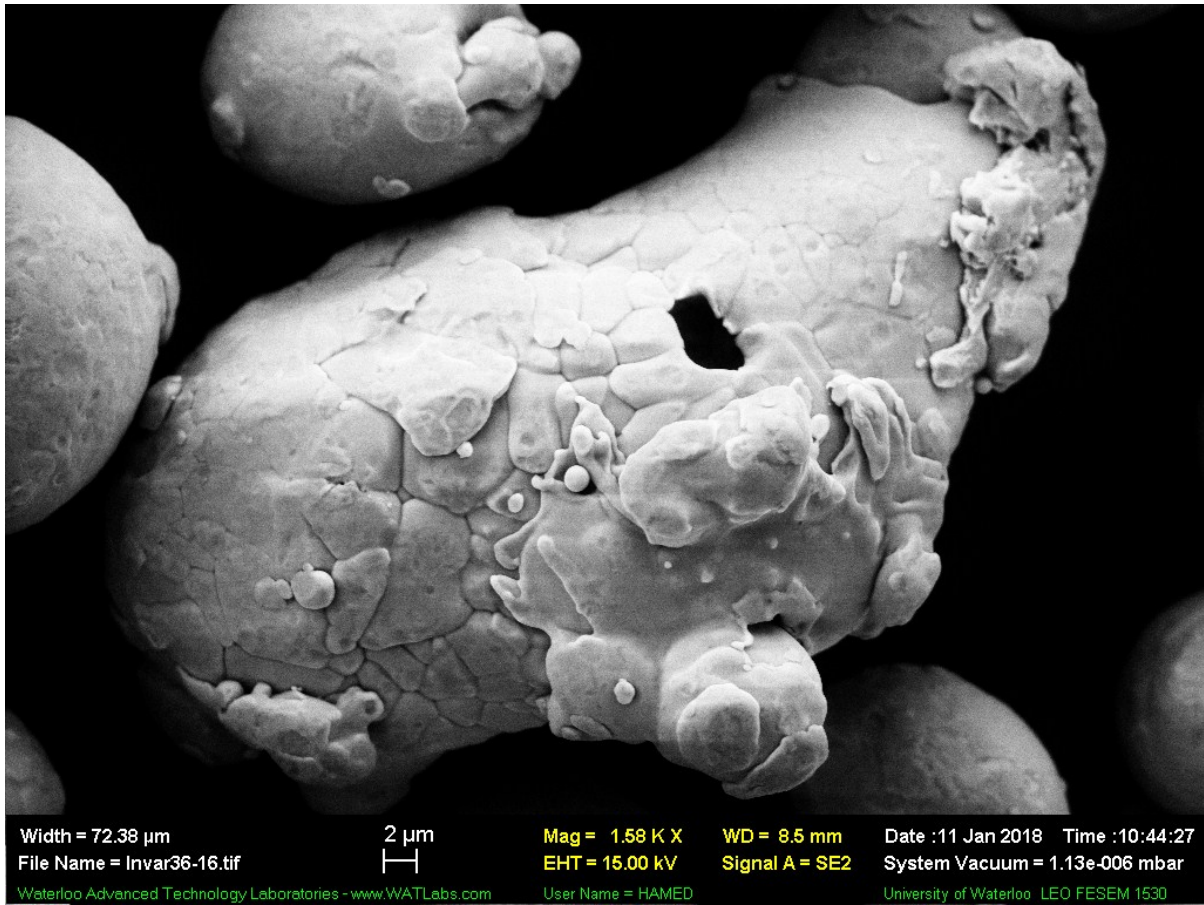
Figure B 16. SEM image 12 of particle of interest

188

Appendix C:

Recipe for Experiment in Chapter 4, with All Build Variable Combinations and Identifications

Table C 1. Build variable table for the experiment in Chapter 4, showing all build variable combinations within the build recipe. Part labels not necessarily equal to Part I.D.

Part Label	Part I.D.	Power [W]	Grid Distance [μm]	Exposure Time [μs]	Equivalent Velocity [mm/s]	Energy Density (Surface) [J/mm²]	Energy Density (Volumetric) [J/mm³]
1	1	250	60	60	1000	4.17	138.9
2	2	250	60	70	857	4.86	162.0
3	3	250	60	80	750	5.56	185.2
4	4	250	70	60	1167	3.06	102.0
5	5	250	70	70	1000	3.57	119.0
6	6	250	70	80	875	4.08	136.1
7	7	250	80	60	1333	2.34	78.1
8	8	250	80	70	1143	2.73	91.1
9	9	250	80	80	1000	3.13	104.2
10	10	275	60	60	1000	4.58	152.8
11	11	275	60	70	857	5.35	178.2
12	12	275	60	80	750	6.11	203.7
13	13	275	70	60	1167	3.37	112.2
14	14	275	70	70	1000	3.93	131.0
15	15	275	70	80	875	4.49	149.7
16	16	275	80	60	1333	2.58	85.9
17	17	275	80	70	1143	3.01	100.3
18	18	275	80	80	1000	3.44	114.6
19	19	300	60	60	1000	5.00	166.7
20	20	300	60	70	857	5.83	194.4
21	21	300	60	80	750	6.67	222.2
22	22	300	70	60	1167	3.67	122.4
23	23	300	70	70	1000	4.29	142.9
24	24	300	70	80	875	4.90	163.3
25	25	300	80	60	1333	2.81	93.8
26	26	300	80	70	1143	3.28	109.4
27	27	300	80	80	1000	3.75	125.0

Table C 1 (cont'd). Build variable table for the experiment in Chapter 4, showing all build variable combinations within the build recipe. Part labels not necessarily equal to Part I.D.

Part Label	Part I.D.	Power [W]	Grid Distance [μm]	Exposure Time [μs]	Equivalent Velocity [mm/s]	Energy Density (Surface) [J/mm^2]	Energy Density (Volumetric) [J/mm^3]
1- and 1=	28	350	60	60	1000	5.83	194.4
2- and 2=	29	350	60	70	857	6.81	226.9
3- and 3=	30	350	60	80	750	7.78	259.3
4- and 4=	31	350	70	60	1167	4.29	142.9
5- and 5=	32	350	70	70	1000	5.00	166.7
6- and 6=	33	350	70	80	875	5.71	190.5
7- and 7=	34	350	80	60	1333	3.28	109.4
8- and 8=	35	350	80	70	1143	3.83	127.6
9- and 9=	36	350	80	80	1000	4.38	145.8
10- and 10=	37	375	60	60	1000	6.25	208.3
11- and 11=	38	375	60	70	857	7.29	243.1
12- and 12=	39	375	60	80	750	8.33	277.8
13- and 13=	40	375	70	60	1167	4.59	153.1
14- and 14=	41	375	70	70	1000	5.36	178.6
15- and 15=	42	375	70	80	875	6.12	204.1
16- and 16=	43	375	80	60	1333	3.52	117.2
17- and 17=	44	375	80	70	1143	4.10	136.7
18- and 18=	45	375	80	80	1000	4.69	156.3
19- and 19=	46	400	60	60	1000	6.67	222.2
20- and 20=	47	400	60	70	857	7.78	259.3
21- and 21=	48	400	60	80	750	8.89	296.3
22- and 22=	49	400	70	60	1167	4.90	163.3
23- and 23=	50	400	70	70	1000	5.71	190.5
24- and 24=	51	400	70	80	875	6.53	217.7
25- and 25=	52	400	80	60	1333	3.75	125.0
26- and 26=	53	400	80	70	1143	4.38	145.8
27- and 27=	54	400	80	80	1000	5.00	166.7

Table C 2. Auxiliary study studying effect of scan strategy (not within scope of thesis).

ID	Scan Strategy	Field Size [mm]	Field Overlap [mm]
A	Chessboard	2.5	0
B	Chessboard	2.5	-0.06
C	Chessboard	5	0
D	Chessboard	5	-0.06
E	Stripe	2.5	0
F	Stripe	2.5	-0.06
G	Stripe	5	0
J	Stripe	5	-0.06

Table C 3. Auxiliary study studying effect of hatch offset (not within scope of thesis).

ID	Power [W]	Hatch Offset [mm]
A	0.75	-0.7
B	0.75	0
C	0.75	0.7
D	0.5	-0.7
E	0.5	0
F	0.5	0.7
G	0.25	-0.7
J	0.25	0
K	0.25	0.7
L	0.75	-0.7
M	0.75	0
P	0.75	0.7
Q	0.5	-0.7
S	0.5	0
T	0.5	0.7
U	0.25	-0.7
Y	0.25	0
Z	0.25	0.7

Appendix D:

MATLab Code and Accompanying Functions for the CT Analyses

```
%% ----------------CT Image Data Processing Script-------------------- %%
% ASSUMPTIONS
% - Images are inputted as 16-bit unsigned data type
% - Images have the same dimensions (width, height)
% - The alignment algorithm assumes that the part is a perfect cylinder,
%   ande therefore tries to rotate the part to be a perfect cylinder.
% - Brightness/contrasting settings are done based on chracterics of
%   a single slice taken from the middle of the image stack.
%   Refer to [N#] for more details
%
% Required functions
% - 'Slider', 'nhood3', 'partalign', 'SliderScan', 'SliderScanComb',
% 'SlideStack', 'getPath'

%% -------------------------- [STARTUP] ------------------------------- %%

close all; clear all; clc; %#ok<*CLALL>

%-----------------User defined variables-------------------------------%
%Modify these variables to tune how the script processes the data

%Output structure
%'OUTPUT' folder will always be put in the root folder of where the image stack
% was originally located
USER_DIR = char({ ...
'OUTPUT\SCANPATH\';              %Scan-path overlay plots
'OUTPUT\PORES\';                 %Pore size/shape/orientation/distribution
'OUTPUT\FULLPART\ALIGNED\';      %Aligned image Stack
'OUTPUT\FULLPART\BINARY\';       %Segmented image
'OUTPUT\FULLPART\PORE_ONLY\';    %Segented image with only pores
'OUTPUT\FULLPART\RESULTS\';      %Summary reports
'OUTPUT\TRUNCATE\BINARY\';       %Without truncated data, segmented image
'OUTPUT\TRUNCATE\PORE_ONLY\';    %Without truncated data, segmented with only pores
'OUTPUT\TRUNCATE\RESULTS\';      %Without truncated data, summary reports
});

%If the image stacks have the part flipped about the vertical axis,
%(i.e, letters are backwards) set this variable to  '1', and the code will
%automatically 'unmirror' the image. By default, assumes image stack input has
%correct orientation
USER_DATA_FLIP = 1;

%Chooses which regions to truncate, 1 = remove borders, -1 = remove core
USER_TRUNC = 1;

%The binwidth affects the resolution of the outputted histogram. Smaller bins
%increases the precision, but may hinder peak finding functionality. I try to
%set it to be as low as possible without breaking the script.
USER_BINWIDTH_CONTRAST = 4;  %Width of bins, for histogram (max 65535)
USER_BINWIDTH_PORES = 8;

%Minimum peak width is used to ignore large singular points of data in the
%histogram. I try to set it as low as possible without breaking the script
USER_PWIDTH_CONTRAST = 125;  %During brightness/contrast setting
USER_PWIDTH_PORES    = 100;  %During pore threshholding

%I assume the histogram only has two peaks, one for the 'background' and one
%for the 'foreground' information. For the pore threshholding, it is assumed
%that I have already removed one of the peaks in a previous step
USER_NPEAK_CONTRAST  = 2;    %Maximum number of peaks
```

```matlab
USER_NPEAK_PORES = 1;

%Some images may have the ends of other parts visible. This offset is used to
%ensure that the script starts indexing from white space. Set this to zero if
%you are expecting to see your part up to the boundaries of the image
USER_INDEX_OFFSET = 75;

%Intensity scale factors to help the script decide when to Z-crop the images,
%and to set the threshholding values.

%Scale of intensity that indicates part is no longer visible
USER_CROP_INTENSITY_SCALE = 0.25;

%Scale of peak intensity that indicates the tail end
USER_CONTRAST_INTENSITY_SCALE = 0.005;
USER_CONTRAST_THRESHOLD = 0.01;
USER_BINARYMASK_INTENSITY_SCALE = 0.01;

%Crop is performed by cropping anything outside of a certain radius. By default,
%the algorithm sets the radius equal to the radius of the part. This buffer
%artificially increases the radius to be more conservative with cropping.
USER_XYCROP_BUFFER = 1.25;

%Indicates where along the histogram to set the threshold for the binary mask.
%Anything above this value is considered '1' and anything below is considered
%'0'. By default I set it to '1' because I assume the earlier steps did the
%threshholding properly.
USER_BINARY_MASK_INTENSITY_THRESHHOLD = 1; % Minimum: 1 , Maximum: 65535

%Fitting method during the part alignment. Refer to 'help robustfit' for more
%details on the available methods
USER_FIT_TUNE = 1.25; %Tuning parameter used for the brightness/contrast section
USER_FIT_METHOD  = 'bisquare';

%The layer thickness used for the part (to align the scan path).
%Specify in millimeters [mm]
USER_LAYER_THICKNESS = 30/1000;
USER_POINT_DISTANCE = 70;

%When cropping the stack to eliminate areas affected by the cone angle, what is
%the tolerance of the fitting error
USER_CONE_ANGLE_TOLERANCE = 0.005;

%Extra layers to crop from both ends when removing the cone angle, to be
%conservative.
USER_CONE_ANGLE_EXTRACROP = 25;

%When performing the flood fill, indicates where to place the initial seed
USER_X = 1; %Absolute position in X, with '1' = left most
USER_Y = 1; %Absolute position in Y, with '1' = top most
USER_Z = 0.5; %Relative position in Z, with '0.5' = 50% up the stack

%Variables to define the 'connected neighbourhood' for the floodfill and noise
%pore finding operations. https://en.wikipedia.org/wiki/Pixel_connectivity
USER_NEIGHBOUR_FLOOD = 6;
USER_NEIGHBOUR_NOISE = 24;
USER_NEIGHBOUR_PORE = 18;

%---------Global Variables (Accessible in all sections of the script)----------%
%Enable if I want to also align scan paths as well
%Only enable if you have the required .SSL scan paths
GLOBAL_SCAN = 0;

%Allows user interaction even when input box is open
GLOBAL_OPTIONS.WindowStyle='normal';

GLOBAL_GRANDTOTALPORE = []; %Total solid fraction, between stacks
```

```matlab
GLOBAL_VSIZE = [];          %Voxel Size
GLOBAL_AUTO = questdlg...    %Automatic processing mode
        ('Would you like to automatically process the data?', ...
        'Automatic Processing','Yes','No','Yes');
%Converts 'GLOBAL_AUTO' into boolean so its easier to write 'if' statements
if strcmp(GLOBAL_AUTO,'Yes')
    GLOBAL_AUTO = true;
else
    GLOBAL_AUTO = false;
end

%% -------------------------[IMAGE IMPORTING]------------------------- %%

%Initializing important variables
again = 'Yes'; %Variable to see if another stack should be processed
GLOBAL_PATH = [];     %Directory to look for .CSV files
GLOBAL_FILENAME = []; %What to name the files when outputting
same = '-';    %Variable to indicate if all stacks have same voxel size

%Gathering directories of all the .TIF stacks
while(strcmp(again,'Yes'))
    %Directory of selected .TIF file
    [file, temppath] = uigetfile('*.*','Select an image from stack');
    tempname = strsplit(temppath,'\');

    %Append the current directory to the array
    GLOBAL_PATH = char(GLOBAL_PATH,temppath);
    GLOBAL_FILENAME = char(GLOBAL_FILENAME,char(tempname(end-1)));

    %Get voxel size of the stack
    %Default value is set to the value for previous stack
    if isempty(GLOBAL_VSIZE)
        default = '';
    else
        default = num2str(GLOBAL_VSIZE(end));
    end

    %If stacks all have the same voxel size, skip the user input dialog
    if (strcmp(same,'Yes'))
        GLOBAL_VSIZE = [GLOBAL_VSIZE; str2double(default)]; %#ok<*AGROW>
    else
        GLOBAL_VSIZE= [GLOBAL_VSIZE; str2double(inputdlg(...
                        'Voxel size: ','Input',1,{default}))];
    end

    %Check if user wants to add another stack to process
    again = questdlg('Would you like to select another stack to process?', ...
                    'Multiple Stack Processing','Yes','No','Yes');

    %Check if voxel size is same for every stack
    if strcmp(again,'Yes') && strcmp(same,'-')
        same = questdlg('Will the voxel size be the same for every stack?', ...
                'Voxel Size','Yes','No','Yes');
    end
end
GLOBAL_ITERATION = 2; %Redundant code. Only used for debugging purposes
%% Iterating through every single .TIF Stack
for GLOBAL_ITERATION = 2:size(GLOBAL_PATH,1)
    %Getting all images in directory
    srcfiles = dir(strcat(GLOBAL_PATH(GLOBAL_ITERATION,:),'*.tif*'));

    %Height of the stack
    stackheight = size(srcfiles,1);

    %Filepath of all images
    InfoImage = imfinfo(strcat(GLOBAL_PATH(GLOBAL_ITERATION,:),...
                srcfiles(1).name));
```

194

```matlab
    mImage = InfoImage.Width; %Width of images, in pixels
    nImage = InfoImage.Height;%Height of images, in pixels

    %Initializing the MATLAB Variable that stores the images
    tifstack = uint16(zeros(nImage,mImage,stackheight));

    %Importing the .TIFF files to MATLAB
    h = waitbar(0,'Importing Images:');
    for i =1:stackheight
        tifstack(:,:,i) = imread(strcat(GLOBAL_PATH(GLOBAL_ITERATION,:),...
                          srcfiles(i).name),'Info',InfoImage);
        waitbar(i/stackheight,h,strcat('Importing images: ',num2str(i),'/', ...
                num2str(stackheight)));
    end
    close(h);

    %Clearing variables to save memory
    clearvars -except tifstack stackheight GLOBAL_* USER_*
%-------------------------------------------------------------------------
    %% --------------------- [CROP SETTINGS]  ------------------------------%%
    %Finds the average intensity across all layers
    iavg = mean(squeeze(mean(tifstack)))'; %average intensity per layer
    iAVG = mean(iavg); %total max intensity

    %Finding the upper range that is considered part
    j = floor(stackheight/2); %Starting at middle of stack
    checkup = min(iavg(j:end))+(max(iavg(j:end))-min(iavg(j:end)))*...
              (USER_CROP_INTENSITY_SCALE);
    while(iavg(j)>=checkup)
        j=j+1;%Increases until check is satisfied
    end
    top = j; %Sets the upper range

    %Finding the lower range that is considered part
    j = floor(stackheight/2); %Starting at middle of stack
    checkdown = min(iavg(1:j))+(max(iavg(1:j))-min(iavg(1:j)))*...
              (USER_CROP_INTENSITY_SCALE);
    while(iavg(j)>=checkdown)
        j=j-1;%Decrease until check is satisfied
    end
    bot = j; %Sets the upper range

    %Debug code (plots the results from above to troubleshoot how
    %well the algorithm finds the part)
    %{
        ifit = flipud(robustfit(1:length(iavg),iavg, ...
               USER_FIT_METHOD,USER_FIT_TUNE));
        esti = polyval(ifit,1:length(iavg));
        figure
        hold on
        plot(1:length(iavg), iavg)
        plot(1:length(iavg), esti)
        plot(bot, iavg(bot),'o')
        plot(top,iavg(top),'o')
    %}

    %If automatic mode is off, prompt the user for ranges for the crop
    if ~GLOBAL_AUTO
        Slider(tifstack);
        h = msgbox('Please select lower and upper layers for the part');
        waitfor(h);
        bot = str2double(inputdlg('Lower: ','Input',1, ...
                        {num2str(bot)},GLOBAL_OPTIONS));
        top = str2double(inputdlg('Upper: ','Input',1, ...
                        {num2str(top)},GLOBAL_OPTIONS));
    end
```

195

```matlab
    %Performing the height crop
    h = waitbar(1,'Cropping the image along the Z-axis');
    tifstack = tifstack(:,:,bot:top); %Height cropping
    stackheight = top-bot;
    close(h);

    %If automatic mode is off, close all figures after crop is finished
    if ~GLOBAL_AUTO
        close();
        Slider(tifstack);
        pause;
        close();
    end

    %Clearing variables to save memory
    clearvars -except tifstack stackheight GLOBAL_* USER_*

%% ------------------ [BRIGHTNESS / CONTRAST SETTINGS] ------------------ %%

    %Finds the average intensity across all layers
    iavg = mean(squeeze(mean(tifstack)))'; %Average intensity per layer
    iAVG = mean(iavg); %Average intensity across entire image stack

    %Determining the intensity that corresponds to part
    ifit = flipud(robustfit(1:length(iavg),iavg,USER_FIT_METHOD,USER_FIT_TUNE));


    %Below, if the average intensity of a layer is outside of the error
    %threshold defined by USER_CONTRAST_THRESHOLD, then that layer is no longer
    %considered part of the specimen

    %Finding the upper range
    j = floor(stackheight/2); %Starting at middle of stack
    while(abs(iavg(j)-polyval(ifit,j))/polyval(ifit,j) <= USER_CONTRAST_THRESHOLD)
        j=j+1;%Increases until check is satisfied
    end
    top = j; %Sets the upper range

    %Finding the lower range
    j = floor(stackheight/2); %Starting at middle of stack
    while(abs(iavg(j)-polyval(ifit,j))/polyval(ifit,j) <= USER_CONTRAST_THRESHOLD)
        j=j-1;%Decrease until check is satisfied
    end
    bot = j; %Sets the upper range

    %Debug code to plot how well the algorithm finds the part
    %{
        esti = polyval(ifit,1:length(iavg));
        figure
        hold on
        plot(1:length(iavg), iavg)
        plot(1:length(iavg), esti)
        plot(bot, iavg(bot),'o')
        plot(top,iavg(top),'o')
    %}

    %Extracting the histogram from the images, using the ranges specified above
    bincount = floor(65535/USER_BINWIDTH_CONTRAST);
    [counts, bin] = histcounts(tifstack(:,:,bot:top), bincount);
    bincenters = (bin(1:end-1) + bin(2:end))/2;

    %Peak finding based on peak widths and expected number of peaks
    [pks, locs] = findpeaks(counts,'MinPeakWidth',USER_PWIDTH_CONTRAST, ...
                    'NPeaks',USER_NPEAK_CONTRAST);

    %Determining threshholding values
    for i = 1:length(pks)
```

196

```matlab
        %Picks the upper/lower ends by finding intensity drop-off by a
        %scale of CONTRAST_INTENSITY)SCALE.
        check = pks(i)*USER_CONTRAST_INTENSITY_SCALE;
        j = locs(i); %The drop-off check is relative to the current highest peak
        while(counts(j)>=check  && j<length(counts))
            j=j+1; %Incrementally move farther away from peak until the
                   %threshhold is satisfied
        end
        range(i) = ceil(bincenters(j)); %Makes note of the location on histogram
    end

    %Apply automatic thresholding values (unless 'auto mode' turned off)
    if  (GLOBAL_AUTO)
        mini = range(1);
        maxi = range(2);
    else
        img = imtool(tifstack(:,:,floor(stackheight/2)));
        imgc = imcontrast(img);
        h = msgbox('Please determine minimum and maximum levels.');
        waitfor(h);
        mini = str2double(inputdlg('Minimum intensity: ','Input',1, ...
                        {num2str(range(1))},GLOBAL_OPTIONS));
        maxi = str2double(inputdlg('Maximum intensity: ','Input',1, ...
                        {num2str(range(2))},GLOBAL_OPTIONS));
        delete(imgc);
    end

    %Performing the brightness/contrast scaling
    h = waitbar(1,('Adjusting brightness/contrast levels...'));
    tifstack = uint16((double(tifstack)-mini)/(maxi-mini)*65535);
    tifstack(tifstack<0)=0;
    tifstack(tifstack>65535)=65535;
    close(h);
    close all hidden

    %Clearing variables to save memory
    clearvars -except tifstack stackheight GLOBAL_* USER_*
%% -----------------------[PART ALIGNMENT SETTINGS] -----------------------%%
%----------------------- Determining Misalignment --------------------------%

%Alignment is based on assumption that the parts have cylindrical cross sections

    %Prompts for user input, unless 'auto mode' is turned on
    if GLOBAL_AUTO
        intensity = USER_BINARY_MASK_INTENSITY_THRESHHOLD;
    else
        img = imtool(tifstack(:,:,floor(stackheight/2)));
        imcontrast(img);
        h = msgbox('Please specify threshold for binary mask');
        waitfor(h);
        intensity = str2double(inputdlg('Minimum Threshold: ','Input', ...
                                1,{'1'},GLOBAL_OPTIONS));
    end

    %Creates the binary mask
    h = waitbar(1,'Creating binary mask');
    bwtif = mat2gray(tifstack, [intensity-1 intensity]);
    close(h);

    %If 'auto mode' is off, close all figures
    if ~(GLOBAL_AUTO)
        close('all');
        Slider(bwtif);
        pause;
        close();
    end
```

```matlab
    %Determining part alignment
    [truecenter, truediameter] = partalign(bwtif); %#ok<ASGLU>

    %Debug code to see how well the part aligns
    %{
    for i = 1 : length(bwtif(1,1,:))
        imshow(bwtif(:,:,i));
        viscircles(truecenter(i,1:2),truediameter(i)/2);
        xlim([0 1000])
        ylim([0 1000])
        pause(0.01)
        cla
    end
    %}

    %Allows user to select the layer range to align the part. Can be used to
    %avoid regions where the data is not uniform, but the robustfit algorithm in
    %MATLAB should be able to account for most circumstance. By default, the
    %code considers that the entire part is valid
    if GLOBAL_AUTO
        bot = 1;
        top = stackheight;
    else
        h = msgbox('Please determine layer range for alignment');
        waitfor(h);
        img = figure;
        for i = 1:3
            img = subplot(3,1,i);
            plot(truecenter(:,i))
        end
        bot = str2double(inputdlg('Minimum: ','Input',1,{'1'},...
            GLOBAL_OPTIONS));
        top = str2double(inputdlg('Maximum: ','Input',1, ...
            {num2str(stackheight+1)},GLOBAL_OPTIONS));

        close();
    end

    clear bwtif

%--------------------------- Rotating the Part -------------------------------%

    %Finding misalignment angle and part center by fitting a line
    alignROW = flipud(robustfit(truecenter(bot:top,3),truecenter(bot:top,2), ...
            USER_FIT_METHOD,USER_FIT_TUNE));
    alignCOL = flipud(robustfit(truecenter(bot:top,3),truecenter(bot:top,1),...
            USER_FIT_METHOD,USER_FIT_TUNE));

    %The angle is defined by the inverse tangent of the slope
    angleROW = rad2deg(atan(alignROW(1)));
    angleCOL = rad2deg(atan(alignCOL(1)));

    %Preview alignment results
    if ~GLOBAL_AUTO
        estROW = polyval(alignROW,truecenter(:,3));
        estCOL = polyval(alignCOL,truecenter(:,3));

        figure
        subplot(3,1,1)
        hold on
        plot(truecenter(:,3), truecenter(:,2))
        plot(truecenter(:,3), estROW)

        subplot(3,1,2)
        hold on
        plot(truecenter(:,3), truecenter(:,1))
        plot(truecenter(:,3), estCOL)
```

198

```matlab
        pause();
        close();
    end

    %Taking the X-Z slice.
    h = waitbar(1,'Aligning part about Y');
    yzslice = permute(tifstack,[3 1 2]); %Same as 'left slice' in ImageJ
    yzslice = imrotate(yzslice,-angleROW,'crop'); %Counter-clockwise is positive
    close(h);
    if ~GLOBAL_AUTO %Display the results, if 'auto mode' is turned off
        Slider(yzslice);
        pause;
        close();
    end
    clear tifstack %Clearing variables to save memory

    %Taking the Y-Z slice
    h = waitbar(1,'Aligning part about X');
    xzslice = permute(yzslice,[3 1 2]); %Same as 'left slice' in ImageJ
    xzslice = imrotate(xzslice,angleCOL,'crop');
    close(h);
    if ~GLOBAL_AUTO %Display the results, if 'auto mode' is turned off
        Slider(xzslice);
        pause;
        close();
    end
    clear yzslice %Clearing variable to save memory

    %Returning to original orientation
    h = waitbar(1,'Returning to original orientation');

    %Sometimes TIFStacks are exported with the images mirrored
    %(letters look backwards); This code, below fixes that issue.
    if (USER_DATA_FLIP == 1)
        aligned = permute(xzslice, [1 3 2]);
    else
        aligned = permute(xzslice, [3 1 2]);
    end
    close(h);

    if ~GLOBAL_AUTO %Display the results, if 'auto mode' is turned off
        Slider(aligned);
        pause;
        close();
    end
    clear xzslice


%% ------------------ Cropping parts X-Y direction -------------------------%

%----------------------Finding center of the part----------------------------%

    %Creates the binary mask
    h = waitbar(1,'Creating binary mask');
    bwtif = mat2gray(aligned, [intensity-1 intensity]);
    close(h);

    %Determining part alignment
    [truecenter, truediameter] = partalign(bwtif);

    clear bwtif

    %Finding alignment angle and true part center by fitting a line
    alignROW = flipud(robustfit(truecenter(bot:top,3),truecenter(bot:top,2), ...
            USER_FIT_METHOD,USER_FIT_TUNE));
    alignCOL = flipud(robustfit(truecenter(bot:top,3),truecenter(bot:top,1), ...
```

199

```
                    USER_FIT_METHOD,USER_FIT_TUNE));

    centerROW = alignROW(2); %Center along horizontal
    centerCOL = alignCOL(2); %Center along vertical
    circleRAD = nanmean(truediameter)/2;

    %Debug code to see how well the images are aligned
    %{
    figure
    for i = 1 : length(aligned(1,1,:))
        imshow(bwtif(:,:,i));
        viscircles(truecenter(i,1:2),truediameter(i)/2);
        xlim([0 1000])
        ylim([0 1000])
        pause(0.01)
        cla
    end
    %}

    %Determining the crop limits for the image
    cropRAD = floor(circleRAD*USER_XYCROP_BUFFER);

    %Relating center locations to image indices
    cropROW = floor(centerROW);
    cropCOL = floor(centerCOL);

    %Performing the crop
    h = waitbar(0,'Cropping X-Y boundaries...');
    aligned = aligned(cropROW-cropRAD:cropROW+cropRAD, ...
            cropCOL-cropRAD:cropCOL+cropRAD,:); %Cropping
    close(h);

    %New center, after cropping
    centerROW = size(aligned,2)/2; %Center along horizontal
    centerCOL = size(aligned,1)/2; %Center along vertical

    if ~GLOBAL_AUTO %Display the results, if 'auto mode' is turned off
        Slider(aligned);
        pause;
        close();
    end

%% ----------------[Rotate to align top surface labels] --------------------%%

    %This section requires extensive user input, and therefore is disabled for automatic
processing
    if ~(GLOBAL_AUTO)

        %Selecting layers to use to align the scan paths together
            %-CT Images
                Slider(aligned);
                h = msgbox('Please specify a layer showing features that can help rotate align
the cylinders');
                waitfor(h);
                imageref = str2double(inputdlg('Matching layer: ','Input',1,...
                        {'1'},GLOBAL_OPTIONS));
                close();

            %Aligning the image to fit the scan-path
            lastrotate = 0; %Current rotation of image
            lastcol = 0;    %X-translation of image
            lastrow = 0;    %Y-translation of image
            alignokay = 0;  %Variable to check if image is properly aligned
            figure
            while ~alignokay
                %Showing the last rotated image
                imshow(imrotate(aligned(:,:,imageref),lastrotate,'crop'));
```

200

```matlab
                %Checking if the rotation is satisfactory
                check = questdlg(...
                'Is the image aligned correctly to the scan path?', ...
                'Image Alignment','Yes','No','Yes');
                if strcmp(check,'No')
                    input = inputdlg({'Rotate: '},...
                        'Input', 1,{num2str(lastrotate)}, GLOBAL_OPTIONS);
                    lastrotate = str2double(input(1));
                    hold off;
                else
                    alignokay = 1;
                    aligned = imrotate(aligned,lastrotate,'crop');
                    close();
                end
            end
        end
%% ------------------[SCAN PATH SUPERIMPOSITION ] -------------------- %
%%{
%This section requires extensive user input, and therefore is disabled for
%automatic processing
if ~(GLOBAL_AUTO) && (GLOBAL_SCAN)

    %Output directory for superimposed images
    output_directory = strcat(GLOBAL_PATH(GLOBAL_ITERATION,:),USER_DIR(1,:));
    if(~exist(output_directory,'dir'))
        [status, msg, msgid] = mkdir(output_directory);
    end

    %Reorienting so that the top of the part starts at beginning of stack
    Slider(aligned);
    h = msgbox('Scroll through the figure and determine if first image corresponds to the top
or bottom of the part. Press [OK] once you find out.');
    waitfor(h);
    flipimage = questdlg...
            ('Does the first image in the stack correspond to the top or bottom of your
part?', ...
            'Stack Orientation','Top','Bottom','Top');
    if strcmp(flipimage,'Bottom')
        aligned = flip(aligned,3);
    end
    close();

    %Importing the scan path into memory
    [scanfile, scanpath] = uigetfile('*.*','Select the scan path file');
    scanfilepath = [scanpath scanfile];
    GLOBAL_scancloud = getPath(scanfilepath, USER_LAYER_THICKNESS,...
    USER_POINT_DISTANCE,GLOBAL_VSIZE(GLOBAL_ITERATION-1),centerCOL,centerROW);

    %Debug code to preview all scan paths
    %{
        figure
        hold on
        uniquelayer = flip(unique(GLOBAL_scancloud(:,1)),1);
        for layer = 1:length(uniquelayer)
            for contour = 1:max(GLOBAL_scancloud(:,2))
                B = GLOBAL_scancloud(GLOBAL_scancloud(:,1)==uniquelayer(layer)...
                    & GLOBAL_scancloud(:,2)==contour,:);
                SCANPLOT = plot(B(:,3),B(:,4), '.r');

                contour
                pause
            end
            pause;
            %pause(0.001);
            cla;
        end
```

201

```matlab
    pause;
    close(h);
%}

%Selecting layers to use to align the scan paths together
%-Scan Path
  SliderScan(GLOBAL_scancloud);
  h = msgbox('Please specify a reference layer to align with the CT image.');
  waitfor(h);
  slideref = str2double(inputdlg('Reference layer: ','Input',1,{'1'}, ...
            GLOBAL_OPTIONS));
  close();
%-CT Images
  SlideScanComb(aligned,GLOBAL_scancloud,slideref);
  h = msgbox('Please specify a layer with similar features.');
  waitfor(h);
  imageref = str2double(inputdlg('Matching layer: ','Input',1,{'1'}, ...
            GLOBAL_OPTIONS));
  close();

%Selecting the layer to use to anchor the scan paths
%-Scan Path
  SliderScan(GLOBAL_scancloud);
  h = msgbox('Please specify which layer to anchor to the CT Image');
  waitfor(h);
  GLOBAL_slidealign = str2double(inputdlg('Reference layer: ','Input',1, ...
                      {'1'},GLOBAL_OPTIONS));
  close();
%-CT Image stack
  SlideScanComb(aligned,GLOBAL_scancloud,GLOBAL_slidealign);
  h = msgbox('Please select the layer to anchor the scan path to.');
  waitfor(h);
  GLOBAL_imagealign = str2double(inputdlg('Matching layer: ','Input',1,...
                      {'1'},GLOBAL_OPTIONS));
  close();

%Aligning the image to fit the scan-path
lastrotate = 0; %Current rotation of image
lastcol = 0;    %X-translation of image
lastrow = 0;    %Y-translation of image
alignokay = 0;  %Variable to check if image is properly aligned
figure
while ~alignokay
    %Showing the last rotated image
    imshow(imrotate(aligned(:,:,imageref),lastrotate,'crop'));
    hold on;
    %Overlay scan path on top
    uniquelayer = flip(unique(GLOBAL_scancloud(:,1)),1);
    for contour = 1:max(GLOBAL_scancloud(GLOBAL_scancloud(:,1)==uniquelayer(slideref),2))
        A = GLOBAL_scancloud(GLOBAL_scancloud(:,1)==uniquelayer(slideref)...
            & GLOBAL_scancloud(:,2)==contour,:);
        plot(A(:,3)+lastcol,A(:,4)-lastrow, 'b');
    end

    %Checking if the rotation is satisfactory
    check = questdlg('Is the image aligned correctly to the scan path?', ...
    'Image Alignment','Yes','No','Yes');
    if strcmp(check,'No')
        input = inputdlg({'Move X: ','Move Y: ','Rotate: '},...
          'Input', [1; 1; 1],{num2str(lastcol), num2str(lastrow), ...
          num2str(lastrotate)}, GLOBAL_OPTIONS);
        lastcol = str2double(input(1));
        lastrow = str2double(input(2));
        lastrotate = str2double(input(3));
        hold off;
    else
        alignokay = 1;
```

202

```matlab
                GLOBAL_scancloud(:,3) = GLOBAL_scancloud(:,3)+lastcol;
                GLOBAL_scancloud(:,4) = GLOBAL_scancloud(:,4)-lastrow;
                aligned = imrotate(aligned,lastrotate,'crop');
                close();
            end
        end

        %Plotting and saving all values
        SCANPLOT = figure;
        set(SCANPLOT,'Visible','off');
        h = waitbar(0, 'Exporting overlaid images:');
        vsize = GLOBAL_VSIZE(GLOBAL_ITERATION-1)/1000; %Changing units of GLOBAL_VSIZE
        temparray = [];
        for i = 1:length(aligned(1,1,:))
            %Absolute distance away from the anchor CT image
            dist = abs(GLOBAL_imagealign-i)*vsize;

            if (i > GLOBAL_imagealign)
                %Number of indexes away from the anchor
                dist = floor(dist/USER_LAYER_THICKNESS);
                index = GLOBAL_slidealign + dist;
            elseif (i < GLOBAL_imagealign)
                %Number of indexes away from the anchor
                dist = ceil(dist/USER_LAYER_THICKNESS);
                index = GLOBAL_slidealign - dist;
            else
                index = GLOBAL_slidealign;
            end

            %If the indexes are within the range, plot both the scan and the part
            SCANPLOT = imshow(aligned(:,:,i));
            hold on;
            if ~(index<1 || index > length(uniquelayer))
                for                           contour                          =
1:max(GLOBAL_scancloud(GLOBAL_scancloud(:,1)==uniquelayer(index),2))
                    A = GLOBAL_scancloud(GLOBAL_scancloud(:,1)==uniquelayer(index)...
                        & GLOBAL_scancloud(:,2)==contour,:);
                    SCANPLOT = plot(A(:,3),A(:,4), 'b');
                    dlmwrite(strcat(GLOBAL_PATH(GLOBAL_ITERATION,:),...
                        USER_DIR(1,:),'VolumetricContour-', ...
                        GLOBAL_FILENAME(GLOBAL_ITERATION,:),'.txt'),...
                        [temparray ; i*ones(size(A,1),1) A],'-append');
                end
            end
            hold off
            saveas(SCANPLOT,strcat(GLOBAL_PATH(GLOBAL_ITERATION,:),USER_DIR(1,:),...
                'Scanpath-',GLOBAL_FILENAME(GLOBAL_ITERATION,:),'-',num2str(i),...
                '.png'));
            waitbar(i/length(aligned(1,1,:)),h,strcat('Exporting          overlaid          images:
',num2str(i),'/',num2str(length(aligned(1,1,:)))));
        end

    close(h);
end
  %}
%% ------------------------------ [CONE ANGLE REMOVAL] ----------------------%%

% This part of the code is intended to remove areas affected by cone angle.
% It does so by looking at the alignment (from previous section) and chooses
% areas where the data becomes consistent. This assumes that the sample are
% uniform in cross section

% Currently using XY slices, but I should probably use XZ slices to determine
% where cone angle defect ends
% I should probably also change it based on average intensity per layer

    %Fitted values (Y-hat)
```

```matlab
COLhat = polyval(alignCOL,truecenter(:,3));
ROWhat = polyval(alignROW,truecenter(:,3));

%True Values
COLt = truecenter(:,1);
ROWt = truecenter(:,2);

%Error (% Difference)
ECOL = abs(COLhat - COLt)./COLt;
EROW = abs(ROWhat - ROWt)./ROWt;

%Height cropping is set for when error drops below CONE_ANGLE_TOLERANCE
check = USER_CONE_ANGLE_TOLERANCE;

%Determining the cropping off the bottom
j = floor(stackheight/2); %Indexing starts at the middle of the stack
while (ECOL(j) <= check && EROW(j) <= check && j > 0)
    j=j-1;%Decrement until error is really bad
end
bot = j;

%Applying the extra cropping to be conservative
if (j + USER_CONE_ANGLE_EXTRACROP) < length(ECOL)
    bot = j + USER_CONE_ANGLE_EXTRACROP;
    j = bot;
else
    bot = j;
end

%Determining the cropping off the top
j = floor(stackheight/2); %Indexing starts at the middle of the stack
while (ECOL(j) <= check && EROW(j) <= check) && j < length(ECOL)
    j=j+1;%Increase until error is really bad
end
top = j;

%Applying the extra cropping
if (j - USER_CONE_ANGLE_EXTRACROP) > bot
    top = j - USER_CONE_ANGLE_EXTRACROP;
else
    top = j;
end

%If 'auto mode' is off, prompt the user for ranges for the crop
if ~GLOBAL_AUTO
    Slider(aligned);
    h = msgbox('Please select lower and upper layers for cone angle removal');
    waitfor(h);
    bot = str2double(inputdlg('Lower: ','Input',1,{num2str(bot)},GLOBAL_OPTIONS));
    top = str2double(inputdlg('Upper: ','Input',1,{num2str(top)},GLOBAL_OPTIONS));
    close();
end

%Performing the height crop
h = waitbar(1,'Removing cone angle effected areas');
aligned(:,:,1:bot-1) = 0;
aligned(:,:,top+1:end) = 0;
%aligned = aligned(:,:,bot:top); %Height cropping
close(h);

%If automatic mode is off, Output result and close all figures after
%User presses a button
if ~GLOBAL_AUTO
    close();
    Slider(aligned);
    pause;
    close();
```

```matlab
    end

    clearvars -except aligned bwtif intensity GLOBAL_* USER_*

%% --------------------------[SEGMENTATION] ------------------------------- %%

    h = waitbar(1,'Segmenting image...');
    %Height of stack (need to find again because stackheight has changed)
    stackheight = length(aligned(1,1,:));

    %Peak identification (refer to previous section for explanation)
    bincount = floor(65535/USER_BINWIDTH_PORES);

    %Histograph extraction
    [counts, bin] = histcounts(aligned(:,:,:), bincount);
    bincenters = (bin(1:end-1) + bin(2:end))/2;

    %Removes the first and last entry (these two limits have absurdly high bin
    %counts because of cylindrical space translation to rectangular, as well as
    %from previous operations). Removing this doesn't improve peak
    %identification by much, but helps with debugging
    counts(1) = 0;
    counts(length(counts)) = 0;

    %Peak finding (used to threshhold the pores)
    [pks, locs] = findpeaks(counts,'MinPeakWidth',USER_PWIDTH_PORES,'NPeaks',...
        USER_NPEAK_PORES);

    %Determining threshholding values
    check = int16(pks*USER_BINARYMASK_INTENSITY_SCALE);
    j = locs; %Indexing starts at current peak
    while(counts(j)>check  && j>1)
        j=j-1;%Incrementally decreases (looks at left tail of histogram)
    end
    range = ceil(bincenters(j)); %Makes note of the threshhold on histogram

    %Adjusts the contrast/brightness and creates a binary image
    bwtif = aligned;
    bwtif(bwtif<range)=0;
    bwtif(bwtif>=range)=1;
    bwtif = logical(bwtif);

    %3D Array representing how the flood grows (3D Cross)
    FloodFilter = nhood3(USER_NEIGHBOUR_FLOOD);

    %3D Array representing how the noise is reduced
    NoiseFilter = nhood3(USER_NEIGHBOUR_NOISE);

    %Starting point of the flood fill
    x = USER_X;
    y = USER_Y;
    z = floor(length(aligned(1,1,:))*USER_Z);
    loc = [y x z];

    %Masking the cone-angle removed regions
    range = squeeze(mean(mean(aligned)));
    first = find(range~=0,1,'first');
    last = find(range~=0,1,'last');
    bwtif(:,:,1:first-1) = 1;
    bwtif(:,:,last+1:end) = 1;

    %Performing the flood fill, and other stuff
    waitbar(0.25,h,'Removing noise...')
    bwtif = ~imopen(~bwtif,NoiseFilter);   %Removes noise
    waitbar(0.5,h,'Finding pores using flood-fill... (may take some time!)')
    bwtif2 = ~imfill(bwtif,loc);               %Pores
```

```matlab
%Unmasking...
bwtif(:,:,1:first-1) = 0;
bwtif(:,:,last+1:end) = 0;

%Miscellaneous operations
waitbar(0.75,h,'Determining total volume...')
bwtif3 = logical(bwtif2+bwtif);          %Part with pores filled
waitbar(0.95,h,'Isolating background...')
bwtif4 = ~bwtif3;                         %Background only
close(h);

clearvars -except aligned intensity ...
      bwtif bwtif2 bwtif3 bwtif4 ...
      stackheight GLOBAL_* USER_*


%% --------------------- [PORE STATISTICS] ------------------------ %%

%Output directory for pore data
%Fully aligned part
output_directory = strcat(GLOBAL_PATH(GLOBAL_ITERATION,:),USER_DIR(2,:));
if(~exist(output_directory,'dir'))
    [status, msg, msgid] = mkdir(output_directory);
end

%Finding all the pores, and labelling each with a unique number
pdistr = bwconncomp(bwtif2,USER_NEIGHBOUR_PORE);
pdistr_labelled = labelmatrix(pdistr);

%Finding location and volume of each pore (centroid)
poredata = regionprops(pdistr,'Centroid','Area','Image');
%pcentroid = cat(1,poredata.Centroid);

%Finding orientation of each pore
%Extracted from regionprops3 by Chaoyuan Yeh
%https://www.mathworks.com/MATLabcentral/fileexchange/47578-regionprops3
pixList = regionprops(pdistr, 'PixelList');
for i = 1:length(pixList)
    pixs = struct2array(pixList(i));
    covmat = cov(pixs);
    [eVectors, eValues] = eig(covmat);
    eValues = diag(eValues);
    [eValues, idx] = sort(eValues,'descend');

    pores(i).FirstAxis = eVectors(:,idx(1))'; %#ok<*SAGROW>
    pores(i).SecondAxis = eVectors(:,idx(2))';
    pores(i).ThirdAxis = eVectors(:,idx(3))';
    pores(i).EigenValues = eValues';
    distMat = sum(pixs.*repmat(eVectors(:,idx(1))',size(pixs,1),1),2);
    pores(i).FirstAxisLength = range(distMat);
    distMat = sum(pixs.*repmat(eVectors(:,idx(2))',size(pixs,1),1),2);
    pores(i).SecondAxisLength = range(distMat);
    distMat = sum(pixs.*repmat(eVectors(:,idx(3))',size(pixs,1),1),2);
    pores(i).ThirdAxisLength = range(distMat);
    pores(i).Centroid = mean(pixs,1);
    pores(i).MeridionalEccentricity = sqrt(1-(eValues(3)/eValues(1))^2);
    pores(i).EquatorialEccentricity = sqrt(1-(eValues(3)/eValues(2))^2);
    pores(i).Volume = poredata(i).Area;
end
writetable(struct2table(pores), strcat(GLOBAL_PATH(GLOBAL_ITERATION,:),...
          USER_DIR(2,:),'PoreData-',...
          GLOBAL_FILENAME(GLOBAL_ITERATION,:),'.txt'))

%Pore size distribution
pvolume = cat(1,pores.Volume);
[N, edges] = histcounts(pvolume);
 %Converting voxel^3 to um^3
```

```
    edgesu = edges(2:length(edges))*GLOBAL_VSIZE(GLOBAL_ITERATION-1)^3;
    bplot = bar(edgesu,N);
    xlabel('Volume [um^3]');
    ylabel('Count');
    saveas(bplot,strcat(GLOBAL_PATH(GLOBAL_ITERATION,:),USER_DIR(2,:),...
            'PoreSizeDistribution-',...
            GLOBAL_FILENAME(GLOBAL_ITERATION,:),'.png'));
    delete(bplot);
    close();

%% -----------------------[OUTPUT SECTION]-------------------------------%%

%Output structure for the entire part
    p = strcat(GLOBAL_PATH(GLOBAL_ITERATION,:),USER_DIR(3,:)); %Fully aligned part
    p = char(p,strcat(GLOBAL_PATH(GLOBAL_ITERATION,:),USER_DIR(4,:))); %Segmented part
    p = char(p,strcat(GLOBAL_PATH(GLOBAL_ITERATION,:),USER_DIR(5,:))); %Pore only
    p = char(p,strcat(GLOBAL_PATH(GLOBAL_ITERATION,:),USER_DIR(6,:))); %Result Summary
    for i = 1:length(p(:,1))
        if(~exist(p(i,:),'dir'))
            [status, msg, msgid] = mkdir(p(i,:));
        end
    end

    h = waitbar(0,'Getting porosity as a function of radius...');
    %Plotting as a function of radius-------------------------------------
    %Flattening pores across all Z-values
    rad1 = (~squeeze(max(permute(bwtif3, [3 1 2]))));
    rad2 = (squeeze(max(permute(bwtif2, [3 1 2]))));
    rad3 = ~logical(rad1 + rad2);
    %Plotting the result, scaling, and labelling the figure
    XYplot = image(imresize(rad3,[GLOBAL_VSIZE(GLOBAL_ITERATION-1)*...
        (length(bwtif(:,1,1))) ...
        GLOBAL_VSIZE(GLOBAL_ITERATION-1)*length(bwtif(1,:,1))]));
    colormap(gray(2));
    axis([0 GLOBAL_VSIZE(GLOBAL_ITERATION-1)*(length(bwtif(1,:,1))) 0 ...
         GLOBAL_VSIZE(GLOBAL_ITERATION-1)*...
         length(bwtif(:,1,1))]);
    xlabel('X [um]');
    ylabel('Y [um]');
    set(gcf,'Position', [0.13 0.11 600 600]);
    pbaspect([1 1 1])
    %Exporting figure to file
    saveas(XYplot,strcat(GLOBAL_PATH(GLOBAL_ITERATION,:),USER_DIR(6,:), ...
            'XYgraph-',GLOBAL_FILENAME(GLOBAL_ITERATION,:),'.png'));
    delete(XYplot);
    close();

    waitbar(0.5,h,'Getting porosity as a function of Z...');
    %Plotting and saving porosity as a function of Z
    %Flattening pores across all Y-Values
    Zmask  = squeeze(max(bwtif2));
    Zmask2 = ~squeeze(max(~bwtif4));
    Zmask3 = ~(Zmask2+Zmask);
    %Calculating porosity as as function of Z
    Zpore = zeros(stackheight,1);
    for i = 1:stackheight
        d2pore = sum(sum(bwtif2(:,:,i)));
        d2part = sum(sum(bwtif3(:,:,i)));
        if d2part == 0
            Zpore(i) = 1;
        else
            Zpore(i) = 1-d2pore/d2part;
        end
    end
    %Plotting, labelling, and scaling all the figures
    Zplot = figure('Position',[0.13 0.11 1000 1000]);
    subplot(4,1,1);
```

207

```matlab
plot(GLOBAL_VSIZE(GLOBAL_ITERATION-1)*(1:length(bwtif(1,1,:))),Zpore);
axis([0 GLOBAL_VSIZE(GLOBAL_ITERATION-1)*(length(bwtif(1,1,:))) ...
    min(Zpore) max(Zpore)]);
xlabel('Height [um]');
ylabel('Solid Fraction');
subplot(4,1,2:4);
image(imresize(Zmask3,[GLOBAL_VSIZE(GLOBAL_ITERATION-1)*length(bwtif(1,:,1)) ...
     GLOBAL_VSIZE(GLOBAL_ITERATION-1)*length(bwtif(1,1,:))]));
axis([0 GLOBAL_VSIZE(GLOBAL_ITERATION-1)*(length(bwtif(1,1,:))) 0 ...
    GLOBAL_VSIZE(GLOBAL_ITERATION-1)*length(bwtif(1,:,1))]);
colormap(gray(2));
xlabel('Height [um]');
ylabel('Distance [um]');
Zplot.PaperPositionMode = 'auto';
%Exporting image to file
saveas(Zplot,strcat(GLOBAL_PATH(GLOBAL_ITERATION,:),USER_DIR(6,:), ...
    'Zgraph-',GLOBAL_FILENAME(GLOBAL_ITERATION,:),'.png'));

%Saving data as a plot
Zpore = [ (1:stackheight)' Zpore(:) ]; %#ok<*NASGU>
save(strcat(GLOBAL_PATH(GLOBAL_ITERATION,:),USER_DIR(6,:),'Zdata-', ...
    GLOBAL_FILENAME(GLOBAL_ITERATION,:),'.txt'),'Zpore', '-ascii');
delete(Zplot);

waitbar(0.95,h,'Getting total porosity as a function of Z...');
%Total Porosity-----------------------------------------------------E--
totalpore = 1-sum(sum(sum(bwtif2)))/sum(sum(sum(bwtif3)));
save(strcat(GLOBAL_PATH(GLOBAL_ITERATION,:),USER_DIR(6,:),...
    'Porosity-',GLOBAL_FILENAME(GLOBAL_ITERATION,:),'.txt'),...
    'totalpore', '-ascii');

%Saving the total porosity to compare with all other analyzed
%filestacks
GLOBAL_GRANDTOTALPORE = [GLOBAL_GRANDTOTALPORE ; ...
                        [totalpore GLOBAL_ITERATION-1]];

waitbar(0,h,'Writing images (Full): ');
%Writing images
for i = 1:stackheight
    imwrite(aligned(:,:,i),strcat(GLOBAL_PATH(GLOBAL_ITERATION,:), ...
        USER_DIR(3,:),num2str(i),'.tiff'),'Compression' ,'none');
    imwrite(bwtif(:,:,i),strcat(GLOBAL_PATH(GLOBAL_ITERATION,:),...
        USER_DIR(4,:),num2str(i),'.tiff'),'tiff','Compression', 'none');
    imwrite(bwtif2(:,:,i),strcat(GLOBAL_PATH(GLOBAL_ITERATION,:),...
        USER_DIR(5,:),num2str(i),'.tiff'),'tiff','Compression', 'none');
    waitbar(i/stackheight,h,strcat('Writing images (Full): ',...
        num2str(i),'/',num2str(stackheight)));
end
close(h);


%clearvars -except path GLOBAL_* USER_*

%% -----Truncating the data to look at specific regions-------------------%%

%Refinding the center (because part was cropped)
[truecenter, truediameter] = partalign(bwtif);

centerX = nanmean(truecenter(:,1)); %Center along horizontal
centerY = nanmean(truecenter(:,2)); %Center along vertical
circleRAD = nanmean(truediameter)/2;

h = waitbar(0,'Removing truncated regions: ');
%Removing the truncated region
PERCENTREMOVE = 0.10; %Truncate 10%
for i = 1:length(bwtif(1,:,1))
    for j = 1:length(bwtif(:,1,1))
```

```matlab
        tempradius = sqrt((i - centerX)^2 + (j - centerY)^2);
        if USER_TRUNC
            if tempradius > (1-PERCENTREMOVE)*circleRAD
                bwtif(j,i,:) = 0;
                bwtif2(j,i,:) = 0;
                bwtif3(j,i,:) = 0;
                bwtif4(j,i,:) = 1;
            end
        else
            if tempradius < (1-PERCENTREMOVE)*circleRAD
                bwtif(j,i,:) = 0;
                bwtif2(j,i,:) = 0;
                bwtif3(j,i,:) = 0;
                bwtif4(j,i,:) = 1;
            end
        end
    end
    waitbar(i/length(bwtif(1,:,1)),h,strcat(...
        'Removing truncated region: ',num2str(i),'/',...
        num2str(length(bwtif(1,:,1)))));
end
close(h);


%% -------Outputting again, but this time without truncated region--------%%

p = strcat(GLOBAL_PATH(GLOBAL_ITERATION,:),USER_DIR(7,:));
p = char(p,strcat(GLOBAL_PATH(GLOBAL_ITERATION,:),USER_DIR(8,:)));
p = char(p,strcat(GLOBAL_PATH(GLOBAL_ITERATION,:),USER_DIR(9,:)));
for i = 1:length(p(:,1))
    if(~exist(p(i,:),'dir'))
        [status, msg, msgid] = mkdir(p(i,:));
    end
end

%--------------------------------------------------%
%Finding all the pores, and labelling each with a unique number

clear pdistr pdistr_labelled poredata pores pixList

pdistr = bwconncomp(bwtif2,USER_NEIGHBOUR_PORE);
pdistr_labelled = labelmatrix(pdistr);

%Finding location and volume of each pore (centroid)
poredata = regionprops(pdistr,'Centroid','Area','Image');
%pcentroid = cat(1,poredata.Centroid);

%Finding orientation of each pore
%Extracted from regionprops3 by Chaoyuan Yeh
%https://www.mathworks.com/MATLabcentral/fileexchange/47578-regionprops3
pixList = regionprops(pdistr, 'PixelList');
for i = 1:length(pixList)
    pixs = struct2array(pixList(i));
    covmat = cov(pixs);
    [eVectors, eValues] = eig(covmat);
    eValues = diag(eValues);
    [eValues, idx] = sort(eValues,'descend');

    pores(i).FirstAxis = eVectors(:,idx(1))'; %#ok<*SAGROW>
    pores(i).SecondAxis = eVectors(:,idx(2))';
    pores(i).ThirdAxis = eVectors(:,idx(3))';
    pores(i).EigenValues = eValues';
    distMat = sum(pixs.*repmat(eVectors(:,idx(1))',size(pixs,1),1),2);
    pores(i).FirstAxisLength = range(distMat);
    distMat = sum(pixs.*repmat(eVectors(:,idx(2))',size(pixs,1),1),2);
    pores(i).SecondAxisLength = range(distMat);
    distMat = sum(pixs.*repmat(eVectors(:,idx(3))',size(pixs,1),1),2);
```

209

```matlab
        pores(i).ThirdAxisLength = range(distMat);
        pores(i).Centroid = mean(pixs,1);
        pores(i).MeridionalEccentricity = sqrt(1-(eValues(3)/eValues(1))^2);
        pores(i).EquatorialEccentricity = sqrt(1-(eValues(3)/eValues(2))^2);
        pores(i).Volume = poredata(i).Area;
end
if exist('pores')
    writetable(struct2table(pores), strcat(GLOBAL_PATH(...
        GLOBAL_ITERATION,:),USER_DIR(2,:),'PoreDataTrunc-',...
        GLOBAL_FILENAME(GLOBAL_ITERATION,:),'.txt'))
else
    fileid = strcat(GLOBAL_PATH(GLOBAL_ITERATION,:),USER_DIR(2,:),...
        'PoreDataTrunc-',GLOBAL_FILENAME(GLOBAL_ITERATION,:),'.txt');
    ftemp = fopen(fileid,'w');
    fprintf(ftemp,'No pores found')
    fclose('all');
end
%-----------------------------------------------------------------%

h = waitbar(0,'Getting porosity as a function of radius...');
%Plotting as a function of radius-------------------------------------
%Flattening pores across all Z-values
rad1 = (~squeeze(max(permute(bwtif3, [3 1 2]))));
rad2 = (squeeze(max(permute(bwtif2, [3 1 2]))));
rad3 = ~logical(rad1 + rad2);
%Plotting the result, scaling, and labelling the figure
XYplot = image(imresize(rad3,[GLOBAL_VSIZE(GLOBAL_ITERATION-1)*...
    (length(bwtif(:,1,1)))  ...
            GLOBAL_VSIZE(GLOBAL_ITERATION-1)*length(bwtif(1,:,1))]));
colormap(gray(2));
axis([0 GLOBAL_VSIZE(GLOBAL_ITERATION-1)*(length(bwtif(1,:,1))) 0 ...
    GLOBAL_VSIZE(GLOBAL_ITERATION-1)*...
      length(bwtif(:,1,1))]);
xlabel('X [um]');
ylabel('Y [um]');
set(gcf,'Position', [0.13 0.11 600 600]);
pbaspect([1 1 1])
%Exporting figure to file
saveas(XYplot,strcat(GLOBAL_PATH(GLOBAL_ITERATION,:),USER_DIR(9,:),...
    'XYgraph-', ...
        GLOBAL_FILENAME(GLOBAL_ITERATION,:),'.png'));
delete(XYplot);
close();

waitbar(0.5,h,'Getting porosity as a function of Z...');
%Plotting and saving porosity as a function of Z----------------------
%Flattening pores across all Y-Values
Zmask  = squeeze(max(bwtif2));
Zmask2 = ~squeeze(max(~bwtif4));
Zmask3 = ~(Zmask2+Zmask);
%Calculating porosity as as function of Z
Zpore = zeros(stackheight,1);
for i = 1:stackheight
    d2pore = sum(sum(bwtif2(:,:,i)));
    d2part = sum(sum(bwtif3(:,:,i)));
    if d2part == 0
        Zpore(i) = 1;
    else
        Zpore(i) = 1-d2pore/d2part;
    end
end

%Plotting, labelling, and scaling all the figures
Zplot = figure('Position',[0.13 0.11 700 700]);
h = subplot(4,1,1);
if min(Zpore) == max(Zpore)
   out = min(Zpore)*0.99 ;
```

```matlab
    else
        out = min(Zpore);
    end
    plot(GLOBAL_VSIZE(GLOBAL_ITERATION-1)*(1:length(bwtif(1,1,:))),Zpore);
    axis([0 GLOBAL_VSIZE(GLOBAL_ITERATION-1)*(length(bwtif(1,1,:))) out max(Zpore)]);
    xlabel('Height [um]');
    ylabel('Solid Fraction');
    g = subplot(4,1,2:4);
    image(imresize(Zmask3,[GLOBAL_VSIZE(GLOBAL_ITERATION-1)*length(bwtif(1,:,1)) ...
            GLOBAL_VSIZE(GLOBAL_ITERATION-1)*length(bwtif(1,1,:))]));
    axis([0 GLOBAL_VSIZE(GLOBAL_ITERATION-1)*(length(bwtif(1,1,:))) 0 ...
            GLOBAL_VSIZE(GLOBAL_ITERATION-1)*length(bwtif(1,:,1))]);
    colormap(gray(2));
    xlabel('Height [um]');
    ylabel('Distance [um]');
    Zplot.PaperPositionMode = 'auto';
    %Exporting image to file
    saveas(Zplot,strcat(GLOBAL_PATH(GLOBAL_ITERATION,:),USER_DIR(9,:),...
            'Zgraph-',GLOBAL_FILENAME(GLOBAL_ITERATION,:),'.png'));
    delete(Zplot);

    h = waitbar(0.95,'Getting total porosity as a function of Z...');
    %Total Porosity-----------------------------------------------------E--
    totalpore = 1-sum(sum(sum(bwtif2)))/sum(sum(sum(bwtif3)));
    save(strcat(GLOBAL_PATH(GLOBAL_ITERATION,:),USER_DIR(9,:),'Porosity-',...
            GLOBAL_FILENAME(GLOBAL_ITERATION,:),'.txt'),'totalpore', '-ascii');

    %Saving the total porosity to compare with all other analyzed
    %filestacks
    GLOBAL_GRANDTOTALPORE = [GLOBAL_GRANDTOTALPORE ; [totalpore ...
            GLOBAL_ITERATION-1]];


    waitbar(0,h,'Writing images (with truncation): ');
    %Writing images
    for i = 1:stackheight
        imwrite(bwtif(:,:,i),strcat(GLOBAL_PATH(GLOBAL_ITERATION,:),...
            USER_DIR(7,:),num2str(i),...
                '.tiff'),'tiff','Compression', 'none');
        imwrite(bwtif2(:,:,i),strcat(GLOBAL_PATH(GLOBAL_ITERATION,:),...
            USER_DIR(8,:),num2str(i),'.tiff'),...
                'tiff','Compression', 'none');
        waitbar(i/stackheight,h,strcat('Writing images (Core): ',num2str(i),...
            '/',num2str(stackheight)));
    end
    close(h);

    disp(strcat('Image Stacks Completed: ',num2str(GLOBAL_ITERATION-1),'/',...
        num2str(length(GLOBAL_PATH(:,1))-1)));

    clearvars -except path GLOBAL_* USER_*


end
%% ------------------------------------------------------------------------ %%
completed = questdlg(...
'Completed! Would you like to save a file detailing the total porosity between parts?', ...
                'Voxel Size','Yes','No','Yes');
if strcmp(completed,'Yes')
    directory = uigetdir('*.*','Select a directory');
    save(strcat(directory,'\totalporosity.txt'),'GLOBAL_GRANDTOTALPORE', '-ascii');
end

%Removes all variables from memory
clear all ; close all; clc;
```

```matlab
function Slider(image)

NumFrames = length(image(1,1,:)); %// Check below for dummy 4D matrix/image sequence
hFig = figure('Position',[100 100 500 500],'Units','normalized');

handles.axes1 = axes('Units','normalized','Position',[0 .2 1 .75]);

%// Create slider and listener object for smooth visualization
handles.SliderFrame = uicontrol('Style','slider','Position',[60 20 400 25],...
    'Min',1,'Max',NumFrames,'Value',1,'SliderStep',[1/NumFrames 2/NumFrames],...
    'Callback',@XSliderCallback);
handles.SliderxListener = addlistener(handles.SliderFrame,'Value','PostSet',...
    @(s,e) XListenerCallBack);

handles.Text1 = uicontrol('Style','Text','Position',[150 55 60 25],'String',...
    'Current frame');
handles.Edit1 = uicontrol('Style','Edit','Position',[200 55 100 25],'String',...
    '1');

%// Use setappdata to store the image stack and in callbacks, use getappdata to
%retrieve it and use it. Check the docs for the calling syntax.

setappdata(hFig,'image',image); %// You could use %//setappdata
%(0,'MyMatrix',MyMatrix) to store in the base workspace.

%// Display 1st frame
imshow(image(:,:,1))

%// IMPORTANT. Update handles structure.
guidata(hFig,handles);

%// Listener callback, executed when you drag the slider.

    function XListenerCallBack

        %// Retrieve handles structure. Used to let MATLAB recognize the
        %// edit box, slider and all UI components.
        handles = guidata(gcf);

%// Here retrieve MyMatrix using getappdata.
MyMatrix = getappdata(hFig,'image');

        %// Get current frame
        CurrentFrame = round((get(handles.SliderFrame,'Value')));
        set(handles.Edit1,'String',num2str(CurrentFrame));

        %// Display appropriate frame.
        imshow(image(:,:,CurrentFrame),'Parent',handles.axes1);

        guidata(hFig,handles);
    end


%// Slider callback; executed when the slider is release or you press
%// the arrows.
    function XSliderCallback(~,~)

        handles = guidata(gcf);

%// Here retrieve MyMatrix using getappdata.
    MyMatrix = getappdata(hFig,'image');

        CurrentFrame = round((get(handles.SliderFrame,'Value')));
        set(handles.Edit1,'String',num2str(CurrentFrame));
```

```matlab
        imshow(MyMatrix(:,:,CurrentFrame),'Parent',handles.axes1);

        guidata(hFig,handles);
    end

end
```

```matlab
function SliderScan(scanpath)

%Modified 'Slider.m' function to display scan paths

uniquelayer = flip(unique(scanpath(:,1)),1);

NumFrames = length(uniquelayer); %// Check below for dummy 4D matrix/image
%sequence
hFig = figure('Position',[100 100 500 500],'Units','normalized');

%handles.axes1 = axes('Units','normalized','Position',[0 .2 1 .75]);
handles.axes1 = axes('Units','normalized','Position',[0.15 0.2 .75 .75]);

%// Create slider and listener object for smooth visualization
handles.SliderFrame = uicontrol('Style','slider','Position',[60 20 400 25],...
    'Min',1,'Max',NumFrames,'Value',1,'SliderStep',[1/NumFrames 2/NumFrames],...
    'Callback',@XSliderCallback);
handles.SliderxListener = addlistener(handles.SliderFrame,'Value','PostSet',...
    @(s,e) XListenerCallBack);

handles.Text1 = uicontrol('Style','Text','Position',[150 55 60 25],'String',...
    'Current frame');
handles.Edit1 = uicontrol('Style','Edit','Position',[200 55 100 25],'String',...
    '1');

%// Use setappdata to store the image stack and in callbacks, use getappdata to
%retrieve it and use it. Check the docs for the calling syntax.

setappdata(hFig,'image',scanpath); %// You could use %//setappdata(0,'MyMatrix',
%MyMatrix) to store in the base workspace.

%// Display 1st frame
%imshow(scanpath(:,:,1))
for contour = 1:max(scanpath(:,2))
    A = scanpath(scanpath(:,1)==uniquelayer(1) & scanpath(:,2)==contour,:);
    plot(A(:,3),-A(:,4), 'b');
    hold on
end
hold off
set(gca,'xtick',[],'ytick',[])

%// IMPORTANT. Update handles structure.
guidata(hFig,handles);

%// Listener callback, executed when you drag the slider.

    function XListenerCallBack

        %// Retrieve handles structure. Used to let MATLAB recognize the
        %// edit box, slider and all UI components.
        handles = guidata(gcf);

%// Here retrieve MyMatrix using getappdata.
MyMatrix = getappdata(hFig,'image');

        %// Get current frame
```

```matlab
        CurrentFrame = round((get(handles.SliderFrame,'Value')));
        set(handles.Edit1,'String',num2str(CurrentFrame));

        %// Display appropriate frame.
        %imshow(scanpath(:,CurrentFrame),'Parent',handles.axes1);

        for contour = 1:max(scanpath(:,2))
            A = scanpath(scanpath(:,1)==uniquelayer(CurrentFrame) & ...
                scanpath(:,2)==contour,:);
            plot(A(:,3),-A(:,4), 'b', 'Parent', handles.axes1);
            hold on
        end
        hold off
        set(gca,'xtick',[],'ytick',[])

        guidata(hFig,handles);
    end


%// Slider callback; executed when the slider is release or you press
%// the arrows.
    function XSliderCallback(~,~)

        handles = guidata(gcf);

%// Here retrieve MyMatrix using getappdata.
    MyMatrix = getappdata(hFig,'image');

        CurrentFrame = round((get(handles.SliderFrame,'Value')));
        set(handles.Edit1,'String',num2str(CurrentFrame));

        %imshow(MyMatrix(:,:,CurrentFrame),'Parent',handles.axes1);

            for contour = 1:max(scanpath(:,2))
                A = scanpath(scanpath(:,1)==uniquelayer(CurrentFrame) & ...
                    scanpath(:,2)==contour,:);
                plot(A(:,3),-A(:,4), 'b','Parent',handles.axes1);
                hold on
            end
        hold off
        set(gca,'xtick',[],'ytick',[])

        guidata(hFig,handles);
    end

end
```

```matlab
function SlideScanComb(CTimage,scanpath,sliderref)

%Modified 'Slider.m' function to display scan paths

uniquelayer = flip(unique(scanpath(:,1)),1);

NumFrames = length(CTimage(1,1,:)); %// Check below for dummy 4D matrix/image
%sequence
hFig = figure('Position',[100 100 500 500],'Units','normalized');

%handles.axes1 = axes('Units','normalized','Position',[0 .2 1 .75]);
handles.axes1 = axes('Units','normalized','Position',[0.15 0.2 .75 .75]);

%// Create slider and listener object for smooth visualization
handles.SliderFrame = uicontrol('Style','slider','Position',[60 20 400 25],...
    'Min',1,'Max',NumFrames,'Value',1,'SliderStep',[1/NumFrames 2/NumFrames],...
    'Callback',@XSliderCallback);
```

214

```matlab
handles.SliderxListener = addlistener(handles.SliderFrame,'Value','PostSet',...
    @(s,e) XListenerCallBack);

handles.Text1 = uicontrol('Style','Text','Position',[150 55 60 25],'String',...
    'Current frame');
handles.Edit1 = uicontrol('Style','Edit','Position',[200 55 100 25],'String',...
    '1');

%// Use setappdata to store the image stack and in callbacks, use getappdata to retrieve it
%// and use it. Check the docs for the calling syntax.

setappdata(hFig,'image',scanpath); %// You could use %//setappdata(0,'MyMatrix',MyMatrix) to
%// store in the base workspace.

%// Display 1st frame
%imshow(scanpath(:,:,1))
imshow(CTimage(:,:,1));
hold on;
for contour = 1:max(scanpath(:,2))
    A = scanpath(scanpath(:,1)==uniquelayer(slideref) & scanpath(:,2)==contour,...
        :);
    plot(A(:,3),A(:,4), 'b');
end
hold off
set(gca,'xtick',[],'ytick',[])

%// IMPORTANT. Update handles structure.
guidata(hFig,handles);

%// Listener callback, executed when you drag the slider.

    function XListenerCallBack

        %// Retrieve handles structure. Used to let MATLAB recognize the
        %// edit box, slider and all UI components.
        handles = guidata(gcf);

%// Here retrieve MyMatrix using getappdata.
MyMatrix = getappdata(hFig,'image');

        %// Get current frame
        CurrentFrame = round((get(handles.SliderFrame,'Value')));
        set(handles.Edit1,'String',num2str(CurrentFrame));

        %// Display appropriate frame.
        %imshow(scanpath(:,CurrentFrame),'Parent',handles.axes1);
        imshow(CTimage(:,:,CurrentFrame));
        hold on;
        for contour = 1:max(scanpath(:,2))
            A = scanpath(scanpath(:,1)==uniquelayer(slideref) &...
                scanpath(:,2)==contour,:);
            plot(A(:,3),A(:,4), 'b', 'Parent', handles.axes1);
            hold on
        end
        hold off
        set(gca,'xtick',[],'ytick',[])

        guidata(hFig,handles);
    end


%// Slider callback; executed when the slider is release or you press
%// the arrows.
    function XSliderCallback(~,~)

        handles = guidata(gcf);
```

215

```matlab
%// Here retrieve MyMatrix using getappdata.
    MyMatrix = getappdata(hFig,'image');

        CurrentFrame = round((get(handles.SliderFrame,'Value')));
        set(handles.Edit1,'String',num2str(CurrentFrame));

        %imshow(MyMatrix(:,:,CurrentFrame),'Parent',handles.axes1);
        imshow(CTimage(:,:,CurrentFrame));
        hold on;
        for contour = 1:max(scanpath(:,2))
            A = scanpath(scanpath(:,1)==uniquelayer(slideref) &...
                scanpath(:,2)==contour,:);
            plot(A(:,3),A(:,4), 'b', 'Parent', handles.axes1);
            hold on
        end
        hold off
        set(gca,'xtick',[],'ytick',[])

        guidata(hFig,handles);
    end

end
```

```matlab
function SlideStack(CTimage,scanpath,slideref)


if nargin == 1
    error('SlideStack: You require at least one input');
elseif nargin == 3
    error('SlideStack:');
end


NumFrames = length(image(1,1,:)); %// Check below for dummy 4D matrix/image
%sequence
hFig = figure('Position',[100 100 500 500],'Units','normalized');

handles.axes1 = axes('Units','normalized','Position',[0 .2 1 .75]);

%// Create slider and listener object for smooth visualization
handles.SliderFrame = uicontrol('Style','slider','Position',[60 20 400 25],...
    'Min',1,'Max',NumFrames,'Value',1,'SliderStep',[1/NumFrames 2/NumFrames],...
    'Callback',@XSliderCallback);
handles.SliderxListener = addlistener(handles.SliderFrame,'Value','PostSet',...
    @(s,e) XListenerCallBack);

handles.Text1 = uicontrol('Style','Text','Position',[150 55 60 25],'String',...
    'Current frame');
handles.Edit1 = uicontrol('Style','Edit','Position',[200 55 100 25],'String',...
    '1');

%// Use setappdata to store the image stack and in callbacks, use getappdata to
%retrieve it and use it. Check the docs for the calling syntax.

setappdata(hFig,'image',image); %// You could use %//setappdata(0,'MyMatrix',
%MyMatrix) to store in the base workspace.

%// Display 1st frame
imshow(image(:,:,1))

%// IMPORTANT. Update handles structure.
guidata(hFig,handles);
```

```matlab
%// Listener callback, executed when you drag the slider.

    function XListenerCallBack

        %// Retrieve handles structure. Used to let MATLAB recognize the
        %// edit box, slider and all UI components.
        handles = guidata(gcf);

%// Here retrieve MyMatrix using getappdata.
MyMatrix = getappdata(hFig,'image');

        %// Get current frame
        CurrentFrame = round((get(handles.SliderFrame,'Value')));
        set(handles.Edit1,'String',num2str(CurrentFrame));

        %// Display appropriate frame.
        imshow(image(:,:,CurrentFrame),'Parent',handles.axes1);

        guidata(hFig,handles);
    end


%// Slider callback; executed when the slider is release or you press
%// the arrows.
    function XSliderCallback(~,~)

        handles = guidata(gcf);

%// Here retrieve MyMatrix using getappdata.
    MyMatrix = getappdata(hFig,'image');

        CurrentFrame = round((get(handles.SliderFrame,'Value')));
        set(handles.Edit1,'String',num2str(CurrentFrame));

        imshow(MyMatrix(:,:,CurrentFrame),'Parent',handles.axes1);

        guidata(hFig,handles);
    end

end


function [ truecenter, truediameter ] = partalign(array)
    %Determines part alignment by fitting circles to every slice
    h = waitbar(0,'Determining Alignment: ');
    %Initializing variables...
    arraylength = length(array(1,1,:));
    truecenter = zeros(arraylength,3);
    truediameter = zeros(arraylength,1);
    for i = 1:arraylength

        %Fitting circles using MATLAB's 'regionprops' function
        stats = regionprops('table', array(:,:,i),'centroid',...
            'MajorAxisLength','MinorAxisLength');
        centers = stats.Centroid; %[column_center row_center]
        diameters = mean([stats.MajorAxisLength stats.MinorAxisLength],2);

        %Since MATLab might find several circles per slice,
        %Pick only the largest circle
        if isempty(centers) == 0
            truecenter(i,1) = centers(diameters == max(diameters),1);
            truecenter(i,2) = centers(diameters == max(diameters),2);
            truediameter(i) = diameters(diameters == max(diameters));
        else
        %If no circles are found, set the results equal to 0 (nothing)
            truecenter(i,1) = NaN;
            truecenter(i,2) = NaN;
```

217

```
            truediameter(i) = NaN;
        end
        %Make note of the layer for each circle
        truecenter(i,3) = i;
        waitbar(i/arraylength,h,strcat('Determining Alignment: ',num2str(i),...
            '/',num2str(arraylength)));
    end
    close(h);

end


function [ output ] = nhood3( A )
%Creates a matrix defining the pixel connectivity in 3D Space
%Refer to https://en.wikipedia.org/wiki/Pixel_connectivity

output = zeros(3,3,3);

    switch A
        case 6
            output =          [0 0 0 ; 0 1 0 ; 0 0 0];
            output(:,:,2) = [0 1 0 ; 1 1 1 ; 0 1 0];
            output(:,:,3) = [0 0 0 ; 0 1 0 ; 0 0 0];
        case 18
            output =          [0 1 0 ; 1 1 1 ; 0 1 0];
            output(:,:,2) = [1 1 1 ; 1 1 1 ; 1 1 1];
            output(:,:,3) = [0 1 0 ; 1 1 1 ; 0 1 0];
        case 24
            output =          [1 1 1 ; 1 1 1 ; 1 1 1];
            output(:,:,2) = [1 1 1 ; 1 1 1 ; 1 1 1];
            output(:,:,3) = [1 1 1 ; 1 1 1 ; 1 1 1];
        otherwise

    end


end


function [ output ] = getPath(filepath, layerthickness, pointdistance, ...
    voxelsize,centerx,centery)

%filepath = scanfilepath;
%layerthickness = USER_LAYER_THICKNESS;
%pointdistance = USER_POINT_DISTANCE;
%voxelsize = GLOBAL_VSIZE(GLOBAL_ITERATION-1);
%centerx = centerCOL;
%centery = centerROW;

DEBUG_LENGTH = 30;

%-----------------------------------------------------------------------
%This function converts a scan path to point cloud

%Assumes that the file format is a Stratasys Layer File V0 (.SSL)
%Assumes input units are in INCHES
%Assumes input part is centered along origin, with
%increasing Z = increasing height

%The function reads the input file as follows:
% Z   -> Start a new layer and resets the contour.
% C   -> End the previous contour and start a new contour
% END -> End of file
% ### ### -> If it is a number, add the cooridnate to the current contour

%Note, the .SSL only shows the points associated with the complete line
%vector, and does not calculate individual exposure points
```

218

```
%-------------------------------------------------------------------------
%Layer thickness, voxelsizecenterx, and centery are inputs to help align scan.
%Input units are in [mm], except voxelsize, which is in [um]

%Output format is:
% [ layer contour x y]
% Where layer = current layer
% Where contour = current contour
% Where [x y] = x,y coordinates for a point that belongs to the contour

%-------------------------------------------------------------------------

%[NOTE]: Fix the spaghetti code later. It's really messy right now and hard
%to read

h = waitbar(0, 'Importing scan path');

%Converting voxelsize from [um] to [mm]
voxelsize=voxelsize*1E-3;

%Loading the file into memory
fileImport = importdata(filepath);
lineCount = length(fileImport);

%Reading the file and labelling layers, contours, and coordinates
waitbar(0.33,h,'Segregating layers');
partition = cell2mat(cellfun(@(x) ...
    ~isnan(str2double(x(1:((length(x)>4)*4+1))))+... Co-ords labelled as '1'
    strcmp(x(1),'Z')*2 + ...                         New layers labelled as '2'
    strcmp(x(1),'C')*3 , ...                         New contours labelled as '3'
    fileImport,'UniformOutput',false));

%Finding the location of all the spaces between lines
%Used when we output coordinates because X-Y components are separated by a
%space. ex: '-0.093 0.483'
temp = cellfun(@(x) find(x==' ',1),fileImport,'UniformOutput',false);
temp(cellfun('isempty',temp))= {0};

%Segregating the different labels
layerlocation = find(partition==2);
contourlocation = find(partition==3);
xylocation = find(partition==1);


waitbar(0.66,h,'Populating array');
%Labels every line in the file with the current layer and contour number
%It is a bit convoluted, but the most time-efficient way I found to do it

%Initializing the layer and contour count as 0
layer = 1;
layerarray = zeros(lineCount,1);
contourarray = zeros(lineCount,1);

%For all of the layers
for i = 2:length(layerlocation) %layerlocation(i) represents the index
    %where next layer begins

    %Set all lines in the file between two layers equal to the current layer count
    layerarray(layerlocation(i-1)+1:layerlocation(i)) = layer*...
                ones(layerlocation(i)-layerlocation(i-1),1);
    layer = layer+1;

    %For all contours
    contour = 2;

    %For current layer, find the indices where there are contours
```

```matlab
    cmin = find(contourlocation == min(...
        contourlocation(contourlocation>layerlocation(i-1) &...
        contourlocation<layerlocation(i))),1,'first');
    cmax = find(contourlocation == max(...
        contourlocation(contourlocation>layerlocation(i-1) &...
        contourlocation<layerlocation(i))),1,'last');

    %Set all lines in the file beteen two contours, but within the current
    %layer equal to the current contour count
    contourarray(layerlocation(i-1)+1:contourlocation(cmin)) = ones(...
        contourlocation(cmin)-layerlocation(i-1),1);
    for j = cmin:cmax-1
        contourarray(contourlocation(j)+1:contourlocation(j+1)) = contour*...
            ones(contourlocation(j+1)-contourlocation(j),1);
        contour=contour+1;
    end
    %Between the last contour and the next layer is technically another
    %contour
    contourarray(contourlocation(j+1)+1) = contour*ones(layerlocation(i)-...
        contourlocation(j+1),1);
end

%Between the last layer and 'End of File' there is technically one more
%contour
layerarray(layerlocation(i)+1:lineCount) = layer*ones(lineCount-layerlocation(i),1);
%Same for Contours
contour = 2;
cmin = find(contourlocation == min(contourlocation(...
    contourlocation>layerlocation(i) & contourlocation<lineCount)),1,'first');
cmax = find(contourlocation == max(contourlocation(...
    contourlocation>layerlocation(i) & contourlocation<lineCount)),1,'last');
contourarray(layerlocation(i)+1:contourlocation(cmin)) = ones(...
    contourlocation(cmin)-layerlocation(i),1);
for j = cmin:cmax-1
    contourarray(contourlocation(j)+1:contourlocation(j+1)) = contour*ones(...
        contourlocation(j+1)-contourlocation(j),1);
    contour=contour+1;

end
contourarray(contourlocation(j+1)+1) = contour*ones(...
    lineCount-contourlocation(j+1),1);

%Populating array with the correct co-ordinates
coords = cell2mat(cellfun(@(y) y',cellfun(@(x) textscan(x,'%f'),fileImport(...
    xylocation)),'UniformOutput',false));
xyarray = NaN(lineCount,2);
xout = coords(:,1)*25.4/voxelsize+centerx;
yout = -coords(:,2)*25.4/voxelsize+centery;
xyarray(xylocation,:)=[xout yout];

waitbar(0.99,h,'Compiling Output...');

%Compiling the output matrix
output = [layerarray*layerthickness contourarray xyarray];
output(any(isnan(output),2),:)=[];

waitbar(0,h,'Redefining endpoints')
%Getting exact points
%Converting point distance to voxels
    pointdistance = pointdistance/(voxelsize*1000);
    %Gets the number of points per contour
    uniquelayer = flip(unique(output(:,1)),1);
    for i = 1:length(uniquelayer)
        temp1 = output(output(:,1)==uniquelayer(i),2);
        [counts,~] = histc(temp1, unique(temp1));

        for j = 1:length(counts)
```
220

```matlab
                %If the count is 2, we know its just a straight line (i.e hatch)
                if counts(j) == 2
                    %Getting the two points of the line..
                    t_points = output(output(:,1)==uniquelayer(i) &...
                        output(:,2) == j,3:4);

                    %Total length of the line [in mm]
                    t_d = diff(t_points);
                    t_length = sum(sqrt(sum(t_d.*t_d,2)));

                    if t_length > DEBUG_LENGTH
                        %Finding how many point exposures fit in the line
                        t_num = floor(t_length / pointdistance);

                        %Reshaping
                        t_vec = (t_points(2,:) - t_points(1,:))/t_length;
                        t_add = t_vec*(t_num*(pointdistance));
                        %[t_points(1,:) t_points(1,:) + t_add]
                        t_newpoint = t_points(1,:) + t_add;

                        %Updating
                        t_points(2,:) = t_newpoint;
                        output(output(:,1)==uniquelayer(i) &...
                            output(:,2) == j,3:4) = t_points;
                    end
                end
            end
            waitbar(i/length(uniquelayer),h,'Redefining endpoints')
        end

        close(h);

%Debug code to visualize the scan path for one layer
%{
uniquelayer = unique(output(:,1));
for layer = uniquelayer(1):uniquelayer(2)-uniquelayer(1): max(output(:,1))
    figure;
    set(gca,'color','none')
    hold on;
    for contour = 1:max(output(:,2))
        A = output(output(:,1)==layer & output(:,2)==contour,:);
        plot(A(:,3),A(:,4), 'b');

    end
    pause;
    close();
end
%}

%-----------------------------------------------------------------------
End
```

221

Appendix E:
Extended Tukey's Test for Three-Factor Experiments

To restate the derivations of Yang , by using Tukey method the following model is assumed [106]:

$$(\tau_{12})_{ij} = \lambda_{12}(\tau_1)_i(\tau_2)_j; \ (\tau_{13})_{ik} = \lambda_{13}(\tau_1)_i(\tau_3)_k; (\tau_{23})_{jk} = \lambda_{23}(\tau_2)_j(\tau_3)_k;$$

$$(\tau_{123})_{ijk} = \lambda_{123}(\tau_1)_i(\tau_2)_j(\tau_3)_k$$

Which states that the effect, τ, due the interactions between parameters, is because of the combined main effects and a linear constant, λ.

Moving on, there is a total of $a + b + c + 5$ parameters plus the common variance in the model, where a, b, c are the number of varied levels for each parameter [106]. For the least squares estimation, a function is then defined as follows [106]:

$$Q = Q(\mu, (\tau_1)_1, \dots, (\tau_1)_a, (\tau_2)_1, \dots, (\tau_2)_b, (\tau_3)_1, \dots, (\tau_3)_c, \lambda_{12}, \lambda_{13}, \lambda_{23}, \lambda_{123})$$

$$Q = \sum_{i=1}^{a}\sum_{j=1}^{b}\sum_{k=1}^{c}\big(Y_{ijk} - \mu - (\tau_1)_i - (\tau_2)_j - (\tau_3)_k - \lambda_{12}(\tau_1)_i(\tau_2)_j - \lambda_{13}(\tau_1)_i(\tau_3)_k$$

$$- \lambda_{23}(\tau_2)_j(\tau_3)_k - -\lambda_{123}(\tau_1)_i(\tau_2)_j(\tau_3)_k\big)^2$$

Where μ represents the overall mean and Y_{ijk} the response variable. With the following conditions applied [106],

$$\frac{\partial Q}{\partial \mu} = 0; \frac{\partial Q}{\partial (\tau_1)_i} = 0; \frac{\partial Q}{\partial (\tau_2)_j} = 0; \frac{\partial Q}{\partial (\tau_3)_k} = 0; \frac{\partial Q}{\partial \lambda_{12}} = 0; \frac{\partial Q}{\partial \lambda_{13}} = 0; \frac{\partial Q}{\partial \lambda_{23}} = 0; \frac{\partial Q}{\partial \lambda_{123}} = 0;$$

The least squares estimators can then be found as [106]:

$$(\widehat{\tau_1})_i = \bar{Y}_{i..} - \bar{Y}_{...} \ ;$$

$$(\widehat{\tau_2})_j = \bar{Y}_{.j.} - \bar{Y}_{...} \ ;$$

$$(\widehat{\tau_3})_k = \bar{Y}_{..k} - \bar{Y}_{...} \ ;$$

$$\widehat{\lambda_{12}} = \frac{\sum_{i=1}^{a}\sum_{j=1}^{b}\sum_{k=1}^{c}(\bar{Y}_{i..} - \bar{Y}_{...})(\bar{Y}_{.j.} - \bar{Y}_{...})Y_{ijk}}{c\sum_{i=1}^{a}\sum_{j=1}^{b}(\bar{Y}_{i..} - \bar{Y}_{...})^2(\bar{Y}_{.j.} - \bar{Y}_{...})^2}$$

$$\widehat{\lambda_{13}} = \frac{\sum_{i=1}^{a}\sum_{j=1}^{b}\sum_{k=1}^{c}(\bar{Y}_{i..} - \bar{Y}_{...})(\bar{Y}_{..k} - \bar{Y}_{...})Y_{ijk}}{b\sum_{i=1}^{a}\sum_{k=1}^{c}(\bar{Y}_{i..} - \bar{Y}_{...})^2(\bar{Y}_{..k} - \bar{Y}_{...})^2}$$

$$\widehat{\lambda_{23}} = \frac{\sum_{i=1}^{a}\sum_{j=1}^{b}\sum_{k=1}^{c}(\bar{Y}_{.j.} - \bar{Y}_{...})(\bar{Y}_{..k} - \bar{Y}_{...})Y_{ijk}}{a\sum_{j=1}^{b}\sum_{k=1}^{c}(\bar{Y}_{.j.} - \bar{Y}_{...})^2(\bar{Y}_{..k} - \bar{Y}_{...})^2}$$

$$\widehat{\lambda_{123}} = \frac{\sum_{i=1}^{a}\sum_{j=1}^{b}\sum_{k=1}^{c}(\bar{Y}_{i..} - \bar{Y}_{...})(\bar{Y}_{.j.} - \bar{Y}_{...})(\bar{Y}_{..k} - \bar{Y}_{...})Y_{ijk}}{\sum_{i=1}^{a}\sum_{j=1}^{b}\sum_{k=1}^{c}(\bar{Y}_{i..} - \bar{Y}_{...})^2(\bar{Y}_{.j.} - \bar{Y}_{...})^2(\bar{Y}_{..k} - \bar{Y}_{...})^2}$$

With these estimators, we can find $\widehat{Y_{ijk}}$ as [106],

$$\widehat{Y_{ijk}} = \bar{Y}_{...} + (\bar{Y}_{i..} - \bar{Y}_{...}) + (\bar{Y}_{.j.} - \bar{Y}_{...}) + (\bar{Y}_{..k} - \bar{Y}_{...}) + \widehat{\lambda_{12}}(\bar{Y}_{i..} - \bar{Y}_{...})(\bar{Y}_{.j.} - \bar{Y}_{...})$$
$$+ \widehat{\lambda_{13}}(\bar{Y}_{i..} - \bar{Y}_{...})(\bar{Y}_{..k} - \bar{Y}_{...}) + \widehat{\lambda_{23}}(\bar{Y}_{.j.} - \bar{Y}_{...})(\bar{Y}_{..k} - \bar{Y}_{...}) + \widehat{\lambda_{123}}(\bar{Y}_{i..} - \bar{Y}_{...})(\bar{Y}_{.j.} - \bar{Y}_{...})(\bar{Y}_{..k} - \bar{Y}_{...})$$

Also the error is assumed to be an independent and identically distributed variable that follows a normally distribution $N(0, \sigma^2)$, and it can be expressed as [106],

$$\widehat{\epsilon_{ijk}} = Y_{ijk} - \widehat{Y_{ijk}}$$

The total sum of squares, SST, for the model is then defined as [106],

$$SST = \sum_{i=1}^{a}\sum_{j=1}^{b}\sum_{k=1}^{c}(Y_{ijk} - \bar{Y}_{...})^2$$

To analyze the significance of the parameters, the SST requires to be partitioned as follows [106]:

$$SSA = bc\sum_{i=1}^{a}(\bar{Y}_{i..} - \bar{Y}_{...})^2 \text{, with degrees of freedom}, df_{SSA} = a - 1;$$

$$SSB = ac\sum_{j=1}^{b}(\bar{Y}_{.j.} - \bar{Y}_{...})^2, df_{SSB} = b - 1;$$

$$SSC = ab\sum_{k=1}^{c}(\bar{Y}_{..k} - \bar{Y}_{...})^2, df_{SSC} = c - 1;$$

$$SSAB^* = c\sum_{i=1}^{a}\sum_{j=1}^{b}\widehat{\lambda_{12}}^2(\bar{Y}_{i..} - \bar{Y}_{...})^2(\bar{Y}_{.j.} - \bar{Y}_{...})^2, df_{SSAB^*} = 1;$$

$$SSAC^* = b\sum_{i=1}^{a}\sum_{k=1}^{c}\widehat{\lambda_{13}}^2(\bar{Y}_{i..} - \bar{Y}_{...})^2(\bar{Y}_{..k} - \bar{Y}_{...})^2, df_{SSAC^*} = 1;$$

$$SSBC^* = a\sum_{j=1}^{b}\sum_{k=1}^{c}\widehat{\lambda_{23}}^2(\bar{Y}_{.j.} - \bar{Y}_{...})^2(\bar{Y}_{..k} - \bar{Y}_{...})^2, df_{SSBC^*} = 1;$$

$$SSABC^* = \sum_{i=1}^{a}\sum_{j=1}^{b}\sum_{k=1}^{c}\widehat{\lambda_{123}}^2(\bar{Y}_{i..} - \bar{Y}_{...})^2(\bar{Y}_{.j.} - \bar{Y}_{...})^2(\bar{Y}_{..k} - \bar{Y}_{...})^2, df_{SSABC^*} = 1;$$

$$SSE^* = SST - SSA - SSB - SSC - SSAB^* - SSAC^* - SSBC^* - SSABC^*$$

Where the star notation (e.g. $SSAB^*$ instead of $SSAB$) is used to differentiate the sum of squares based off of Tukey's method from the true sum of squares, if a full ANOVA was performed.

Since it can be derived that the sum of squares interactions and the error have the following distributions [106]:

$$\frac{SSAB^*}{\sigma^2} \sim \chi_1^2, \frac{SSAC^*}{\sigma^2} \sim \chi_1^2, \frac{SSBC^*}{\sigma^2} \sim \chi_1^2, \frac{SSABC^*}{\sigma^2} \sim \chi_1^2, \frac{SSE^*}{\sigma^2} \sim \chi_{abc-a-b-c-2}^2$$

The significance levels (p-values) can be found as [106],

$$SL_{12} = P\left(F_{1,abc-a-b-c-2} \geq \frac{abc - a - b - c - 2}{1} \times \frac{SSAB^*}{SSE^*}\right);$$

223

$$SL_{13} = P\left(F_{1,abc-a-b-c-2} \geq \frac{abc-a-b-c-2}{1} \times \frac{SSAC^*}{SSE^*}\right);$$

$$SL_{23} = P\left(F_{1,abc-a-b-c-2} \geq \frac{abc-a-b-c-2}{1} \times \frac{SSBC^*}{SSE^*}\right);$$

$$SL_{123} = P\left(F_{1,abc-a-b-c-2} \geq \frac{abc-a-b-c-2}{1} \times \frac{SSABC^*}{SSE^*}\right);$$

These values can then be used to determine if there is evidence to reject the null hypotheses by setting up the following hypotheses [106]:

$$H_0 : \lambda_{12} = 0, H_0 : \lambda_{13} = 0, H_0 : \lambda_{23} = 0, H_0 : \lambda_{123} = 0$$

To test for non-additivity, the null and alternative hypothesis are [106],

$$H_0 : \lambda_{12} = \lambda_{13} = \lambda_{23} = \lambda_{123} \text{ and } H_1 : {\sim}H_0$$

To reject the null hypothesis, the statistical test is [106],

$$\frac{MSAB^*}{MSE^*} \geq c_{AB} \ \lor \ \frac{MSAC^*}{MSE^*} \geq c_{AC} \ \lor \ \frac{MSBC^*}{MSE^*} \geq c_{BC} \ \lor \ \frac{MSABC^*}{MSE^*} \geq c_{ABC},$$

Where the mean square values are found by [106],

$$MSAB^* = \frac{SSAB^*}{1}, MSAC^* = \frac{SSAC^*}{1}, MSBC^* = \frac{SSBC^*}{1}$$

$$MSABC^* = \frac{SSABC^*}{1}, MSE^* = \frac{SSE^*}{abc-a-b-c-2}$$

The significance of the test, α, is defined by [106],

$$\alpha = P\left(\frac{MSAB^*}{MSE^*} \geq c_{AB}\right) + P\left(\frac{MSAC^*}{MSE^*} \geq c_{AC}\right) + P\left(\frac{MSBC^*}{MSE^*} \geq c_{BC}\right) + P\left(\frac{MSABC^*}{MSE^*} \geq c_{ABC}\right)$$

If one takes the critical values to be the same, such that $c_{AB} = c_{AC} = c_{BC} = c_{ABC}$ for all the tests, and sets the value to be the $100(1-\gamma)$th percentile of their appropriate F-distribution, then [106],

$$\alpha = 4\gamma$$

Appendix F:

Raw Data for Statistical Analysis of Chapter 4

Table F 1. Raw data input for the MATLab code. Values correspond to the variable 'perf' within the code.

Power (coded)	Grid distance (coded)	Exposure time (coded)	Batch	Solid fraction (overall)	Solid fraction (no border)	CTE $\left[\frac{\mu m}{m \cdot C}\right]$	Performance Parameter
-1	-1	-1	1	0.998966	0.999797	0.444642	0.698743
-1	-1	0	1	0.999038	0.99996	0.292439	0.864264
-1	-1	1	1	0.998736	0.999964	0.285181	0.74762
-1	0	-1	1	0.997958	0.998503	0.399013	0.612327
-1	0	0	1	0.998717	0.999513	0.481964	0.797389
-1	0	1	1	0.999205	0.999993	0.352671	0.843635
-1	1	-1	1	0.999144	0.999834	0.358037	0.577079
-1	1	0	1	0.998755	0.999721	0.248478	0.661151
-1	1	1	1	0.999004	0.999899	0.360675	0.761003
-0.66667	-1	-1	1	0.998631	0.999874	0.418506	0.731357
-0.66667	-1	0	1	0.999029	0.999998	0.475465	0.624554
-0.66667	-1	1	1	0.99856	0.999989	0.427753	0.62184
-0.66667	0	-1	1	0.999167	0.999995	0.363574	0.838106
-0.66667	0	0	1	0.999095	0.999955	0.442099	0.576411
-0.66667	0	1	1	0.999037	0.999964	0.389056	0.683155
-0.66667	1	-1	1	0.999291	0.999967	0.485725	0.698732
-0.66667	1	0	1	0.999117	0.999893	0.343429	0.863644
-0.66667	1	1	1	0.999174	0.999971	0.394615	0.711677
-0.33333	-1	-1	1	0.998454	0.999824	0.410971	0.550097
-0.33333	-1	0	1	0.998085	0.999956	0.593801	0.50757
-0.33333	-1	1	1	0.998474	0.999959	0.418001	0.803308
-0.33333	0	-1	1	0.999087	0.999988	0.549546	0.517422
-0.33333	0	0	1	0.998748	0.999896	0.493871	0.758072
-0.33333	0	1	1	0.998913	0.999973	0.586181	0.409058
-0.33333	1	-1	1	0.998969	0.999961	0.343538	0.749484
-0.33333	1	0	1	0.998459	0.999603	0.481018	0.773653
-0.33333	1	1	1	0.999105	0.999998	0.317616	0.854143
0.33	-1	-1	1	0.998632	1	0.455947	0.499722
0.33	-1	0	1	0.998618	0.999995	0.422596	0.49177
0.33	-1	1	1	0.998849	0.999924	0.490052	0.610729

Table F 1 (cont'd). Raw data input for the MATLab code. Values correspond to the variable 'perf' within the code.

Power (coded)	Grid distance (coded)	Exposure time (coded)	Batch	Solid fraction (overall)	Solid fraction (no border)	CTE $\left[\frac{\mu m}{m^\circ C}\right]$	Performance Parameter
0.33	0	-1	1	0.998687	0.999842	0.491795	0.51544
0.33	0	0	1	0.998382	0.999986	0.459025	0.45594
0.33	0	1	1	0.998205	0.999999	0.295997	0.588874
0.33	1	-1	1	0.998424	0.999954	0.364951	0.626325
0.33	1	0	1	0.998153	0.999968	0.367793	0.479768
0.33	1	1	1	0.998571	0.999999	0.64719	0.377428
0.666667	-1	-1	1	0.998037	1	0.449783	0.36871
0.666667	-1	0	1	0.998085	0.999995	0.341194	0.476725
0.666667	-1	1	1	0.998408	0.999991	0.423933	0.492417
0.666667	0	-1	1	0.998482	0.999969	0.474937	0.42503
0.666667	0	0	1	0.998656	0.999994	0.58249	0.514787
0.666667	0	1	1	0.998514	0.999999	0.48497	0.616185
0.666667	1	-1	1	0.998461	0.999961	0.509238	0.551302
0.666667	1	0	1	0.998419	0.999974	0.269394	0.515218
0.666667	1	1	1	0.998463	0.999997	0.624369	0.435025
1	-1	-1	1	0.998601	0.999972	0.670033	0.404214
1	-1	0	1	0.998401	0.99996	0.502389	0.418096
1	-1	1	1	0.997214	0.999837	0.547862	0.145516
1	0	-1	1	0.998777	0.999973	0.445062	0.864259
1	0	0	1	0.998613	0.999999	0.664529	0.358196
1	0	1	1	0.998509	0.999951	0.469874	0.444808
1	1	-1	1	0.998743	0.999984	0.54609	0.48784
1	1	0	1	0.998211	0.999997	0.627492	0.462534
1	1	1	1	0.998198	0.999988	0.660634	0.392349

MATLab Code for Statistical Analysis in Chapter 4

```matlab
% Based on Tukey`s Method Extended for 3 Factors
% Example of this is shown in
%
https://digitalcommons.georgiasouthern.edu/cgi/viewcontent.cgi?article=2193&context
=etd
% page 39


%% Initializing


clear all; close all; clc;


%Loading perf table
%Format is POWER | HATCH | EXPOSURE TIME | BATCH | ... | PERF
% WHERE '...' can be any other unused miscellaneous columns


%Loading the raw data
load('MATLab.mat');


%%
%Required constants
a = (unique(perf(:,1)));      % Number of power levels
b = (unique(perf(:,2)));      % Number of hatching levels
c = (unique(perf(:,3)));      % Number of exposure times


%%Process outcome
index = 5; % Column number of the outcome of interest


%% -----------Finding Least Squares Estimators of all Effects------------------%


% Definitions
%{
A = effect of power
B = effect of hatch
C = effect of exposure time
AB =  Linear Parameter. Effect of power and hatch interaction = AB*A*B
AC =  Linear Parameter. Effect of power and hatch interaction = AC*A*C
BC =  Linear Parameter. Effect of power and hatch interaction = BC*B*C
ABC = Linear Parameter. Effect of power and hatch interaction = ABC*A*B*C
%}


y = mean(perf(:, index)); %Grand Average


%Average across each main effect
y_i = []; y_j = []; y_k = [];
for i = a', y_i = [y_i ; mean(perf(perf(:,1)==i,end))]; end %#ok<*AGROW>
for j = b', y_j = [y_j ; mean(perf(perf(:,2)==j,end))]; end %#ok<*AGROW>
for k = c', y_k = [y_k ; mean(perf(perf(:,3)==k,end))]; end %#ok<*AGROW>


%Main effects
A = y_i - y;
```

```matlab
B = y_j - y;
C = y_k - y;

%Finding interaction effects
num = 0; den = 0;
for i = 1:length(a)
    for j = 1:length(b)
        for k = 1:length(c)
            num = num + (y_i(i)-y)*(y_j(j)-y)*perf(perf(:,1)==a(i) & ...
                perf(:,2)==b(j) & perf(:,3)==c(k),end);
        end
            den = den + (y_i(i)-y)^2 * (y_j(j)-y)^2;
    end
end
AB = num/(length(c)*den); %Effect of AB

num = 0; den = 0;
for i = 1:length(a)
    for j = 1:length(b)
        for k = 1:length(c)
            num = num + (y_i(i)-y)*(y_k(k)-y)*perf(perf(:,1)==a(i) & ....
                perf(:,2)==b(j) & perf(:,3)==c(k),end);
            if j == 1
                den = den + (y_i(i)-y)^2 * (y_k(k)-y)^2;
            end
        end
    end
end
AC = num/(length(b)*den); %Effect of AC

num = 0; den = 0;
for i = 1:length(a)
    for j = 1:length(b)
        for k = 1:length(c)
            num = num + (y_j(j)-y)*(y_k(k)-y)*perf(perf(:,1)==a(i) & ...
                perf(:,2)==b(j) & perf(:,3)==c(k),end);
            if i == 1
                den = den + (y_j(j)-y)^2 * (y_k(k)-y)^2;
            end
        end
    end
end
BC = num/(length(a)*den); %Effect of BC

num = 0; den = 0;
for i = 1:length(a)
    for j = 1:length(b)
        for k = 1:length(c)
            num = num + (y_i(i)-y)*(y_j(j)-y)*(y_k(k)-y)*perf(perf(:,1)==a(i)...
                & perf(:,2)==b(j) & perf(:,3)==c(k),end);
            den = den + (y_i(i)-y)^2 * (y_j(j)-y)^2*(y_k(k)-y)^2 ;
        end
    end
end
ABC = num/den;%Effect of ABC
```

```matlab
%Finding residuals
for i = a', y_i = [y_i ; mean(perf(perf(:,1)==i,end))]; end %#ok<*AGROW>
for j = b', y_j = [y_j ; mean(perf(perf(:,2)==j,end))]; end %#ok<*AGROW>
for k = c', y_k = [y_k ; mean(perf(perf(:,3)==k,end))]; end %#ok<*AGROW>
residual = [];
for i = 1:length(a)
    for j = 1:length(b)
        for k = 1:length(c)
            %Residual of y-hat(i,j,k)
            localresidual = perf(perf(:,1)==a(i) & perf(:,2)==b(j) &...
                            perf(:,3)==c(k),end) - y ...
                            -(y_i(i)-y) - (y_j(j)-y) - (y_k(k)-y) - ...
                            AB*(y_i(i)-y)*(y_j(j)-y) - AC*(y_i(i)-y)* ...
                            (y_k(k)-y) - BC*(y_j(j)-y)*(y_k(k)-y) - ...
                            ABC*(y_i(i)-y)*(y_j(j)-y)*(y_k(k)-y);
            tempindex = [ a(i) b(j) c(k) 1 localresidual];

            %Adding residual to the matrix
            residual = [residual ; tempindex];
        end
    end
end
residuals = residual(:,end);
plot(residuals);


%%
% --------------------------------ANOVA-------------------------------------

%Initializing
SST = 0; SSA = 0; SSB = 0; SSC = 0; SSAB = 0; SSAC = 0; SSBC = 0; SSABC = 0;

for i = 1:length(a)
    for j = 1:length(b)
        for k = 1:length(c)
            SST = SST + (perf(perf(:,1)==a(i) & perf(:,2)==b(j) &...
                perf(:,3)==c(k),end)-y)^2;
        end
    end
end

%Sum of Squares of A
for i = 1:length(a)
    SSA = SSA + (y_i(i)-y)^2;
end
SSA = SSA*length(b)*length(c);

%Sum of Squares of B
for j = 1:length(b)
    SSB = SSB + (y_j(j)-y)^2;
end
SSB = SSB*length(a)*length(c);

%Sum of Squares of C
for k = 1:length(c)
    SSC = SSC + (y_k(k)-y)^2;
end
SSC = SSC*length(a)*length(b);
```

229

```matlab
%Sum of Squares of AB (with Tukeys model)
for i = 1:length(a)
    for j = 1:length(b)
        SSAB = SSAB + (y_i(i)-y)^2 * (y_j(j)-y)^2;
    end
end
SSAB = length(c)*SSAB*AB^2;

%Sum of Squares of AC (with Tukeys model)
for i = 1:length(a)
    for k = 1:length(c)
        SSAC = SSAC + (y_i(i)-y)^2 * (y_k(k)-y)^2;
    end
end
SSAC = length(b)*SSAC*AC^2;

%Sum of Squares of BC (with Tukeys model)
for j = 1:length(b)
    for k = 1:length(c)
        SSBC = SSBC + (y_j(j)-y)^2 * (y_k(k)-y)^2;
    end
end
SSBC = length(a)*SSBC*BC^2;

%Sum of Squares of ABC (with Tukeys model)
for i = 1:length(a)
    for j = 1:length(b)
        for k = 1:length(c)
            SSABC = SSABC + (y_i(i)-y)^2*(y_j(j)-y)^2 * (y_k(k)-y)^2;
        end
    end
end
SSABC = SSABC*ABC^2;

%Sum of Squares of Error
SSE = SST - SSA - SSB - SSC - SSAB - SSAC - SSBC - SSABC;

%Degrees of Freedom
dofa = length(a)-1;
dofb = length(b)-1;
dofc = length(c)-1;
dofab = 1;
dofac = 1;
dofbc = 1;
dofabc = 1;
dofe = (length(a)*length(b)*length(c)-length(a)-length(b)-length(c)-2);
doft=dofa+dofb+dofc+dofab+dofac+dofbc+dofabc+dofe;

%Mean Square
MSA = SSA/dofa;
MSB = SSB/dofb;
MSC = SSC/dofc;
MSAB = SSAB/dofab;
MSAC = SSAC/dofac;
MSBC = SSBC/dofbc;
MSABC = SSABC/dofabc;
```

```matlab
MSE = SSE/dofe;


%F observed
FA  = MSA/MSE;
FB  = MSB/MSE;
FC  = MSC/MSE;
FAB = MSAB/MSE;
FAC = MSAC/MSE;
FBC = MSBC/MSE;
FABC = MSABC/MSE;


%P value
PA = 1-fcdf(FA,dofa,dofe);
PB = 1-fcdf(FB,dofb,dofe);
PC = 1-fcdf(FC,dofc,dofe);
PAB = 1-fcdf(FAB,dofab,dofe);
PAC = 1-fcdf(FAC,dofac,dofe);
PBC = 1-fcdf(FBC,dofbc,dofe);
PABC = 1-fcdf(FABC,dofabc,dofe);
P_total = [PA; PB ; PC; PAB; PAC; PBC; PABC];


%Making note of all the sum of squares
Transition = [SSA;SSB;SSC;SSAB;SSAC;SSBC;SSABC;SSE;SST]


%Constructing the ANOVA table
names = table(...
    {'Power', 'Hatch', 'Exposure Time', 'P/H', 'P/E', 'H/E','P/H/E',
'Error','Total'}',...
     Transition, ...
    [dofa;dofb;dofc;dofab;dofac;dofbc;dofabc;dofe;doft], ...
    [MSA;MSB;MSC;MSAB;MSAC;MSBC;MSABC;MSE;NaN],...
    [FA;FB;FC;FAB;FAC;FBC;FABC;NaN;NaN],...
    [PA;PB;PC;PAB;PAC;PBC;PABC;NaN;NaN]...
    );
names.Properties.VariableNames={'Source_of_Variation',...
                                'Sum_of_Squares','Degrees_of_Freedom',...
                                'Mean_Square','F0','P_Value'};
%Displaying the ANOVA table
disp(names);


%Calculating the adjusted R-square value
Rsq = 1 - (SSE/dofe)/(SST/doft)

%% ----------------------------MATLAB ANOVA----------------------------------
%Use MATLAB's built in ANOVA if omitted higher order interactions

A = perf(:,1);
B = perf(:,2);
C = perf(:,3);
N = perf(:,4);


denn = perf(:,length(perf(1,:)));


%Reduced model ANOVA table
[p, t, stats,terms] = anovan(denn,{A B C},'model',[ 1 0 0 ; 0 1 0; 0 0 1 ;...
                                        1 1 0 ; 1 0 1 ; 0 1 1],...
```

```matlab
                                                       'varnames',{'A', 'B', 'C'}, 'alpha', .05);

alpha = 0.05;

%Checking if significant
significance = p < alpha;
t(1,8) = cellstr(strcat('Significant at alpha =',num2str(alpha),'?'));
t(2:length(significance)+1,8) = num2cell(significance);
cell2table(t)

%Residuals
residuals = stats.resid;

%Adjusted R-square
Rsq = 1-(cell2mat(t(end-1,2))/cell2mat(t(end-1,3)))/...
      (cell2mat(t(end,2))/cell2mat(t(end,3)))
```

Appendix H:
CT Image Analysis Results for Chapter 4

Parameters for sample I.D. 1

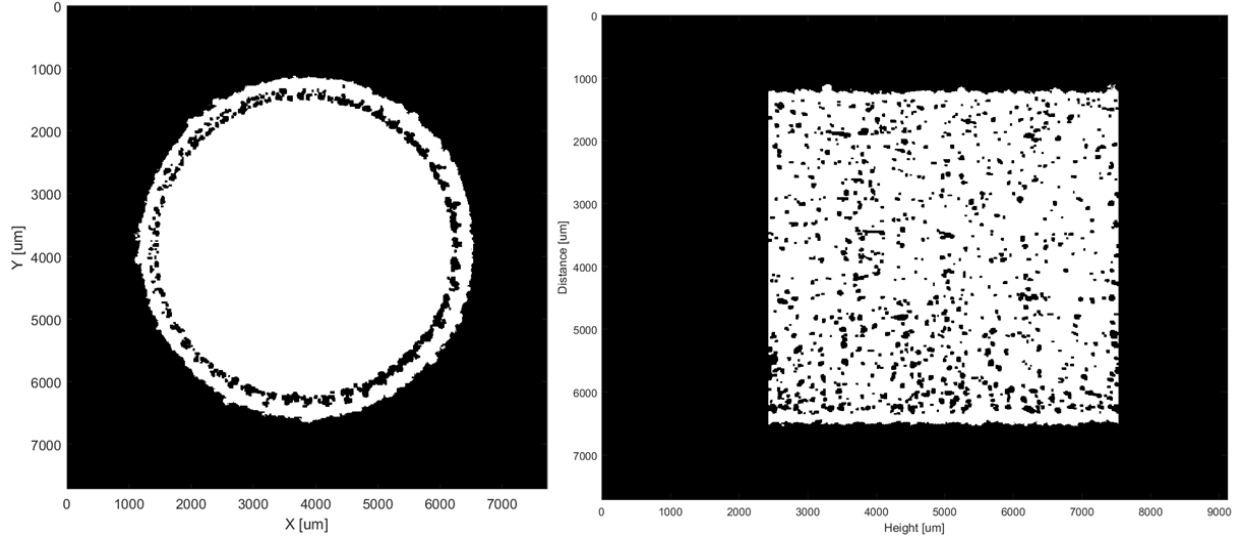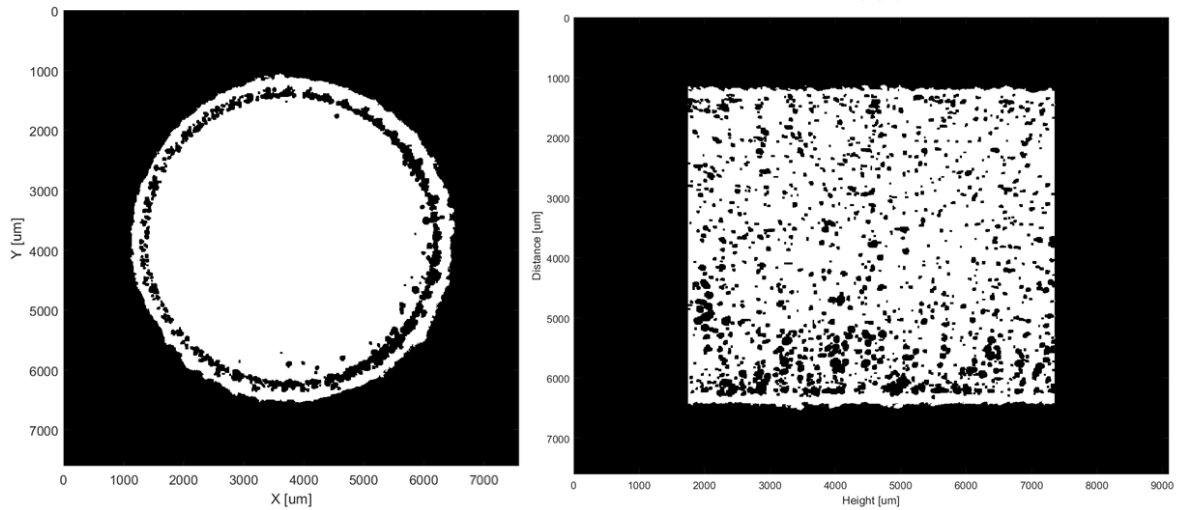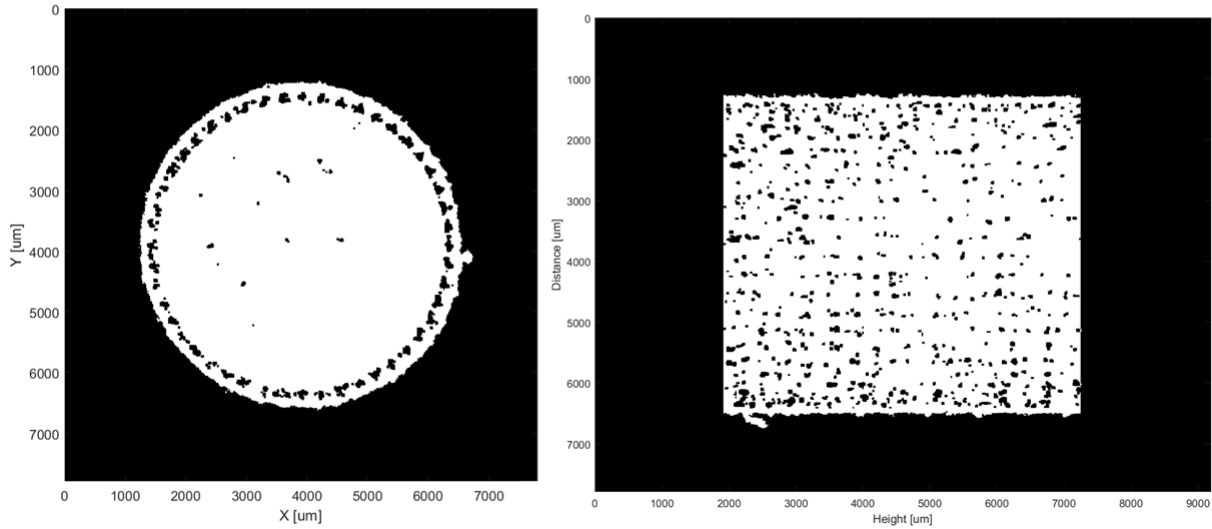| Power	250 W
Grid distance	60 μm
Exposure time	60 μm

Total solid fraction: 0.9989658
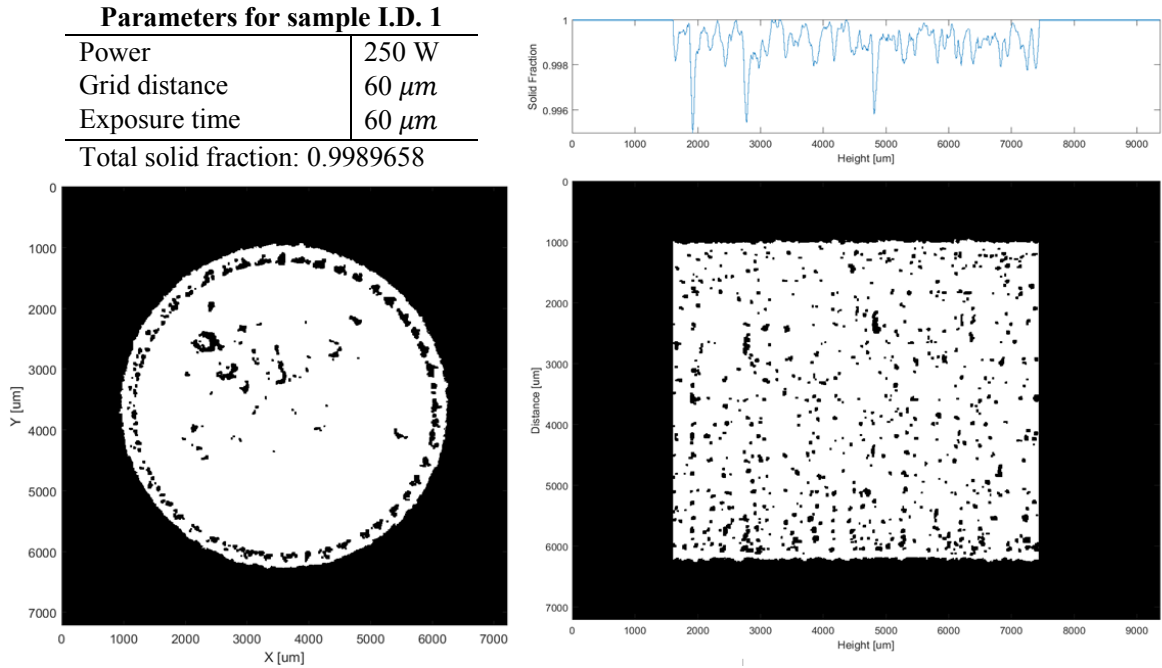
Figure H 1. Minimum intensity projection images from CT analysis. Build variables correspond to sample I.D. 1.

Parameters for sample I.D. 2

Power	250 W
Grid distance	60 μm
Exposure time	70 μm

Total solid fraction: 0.9990375
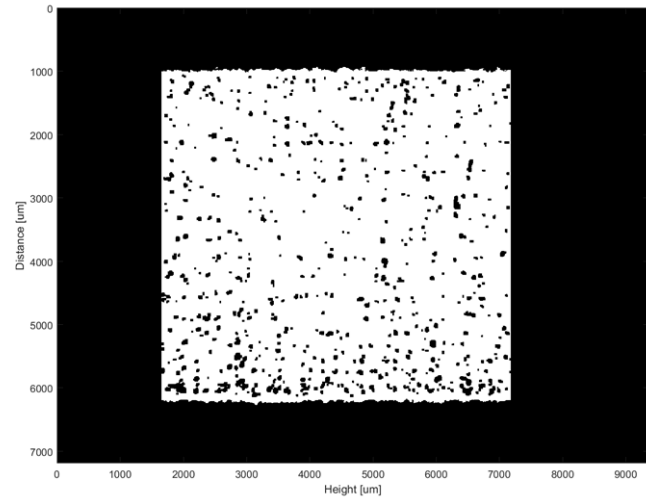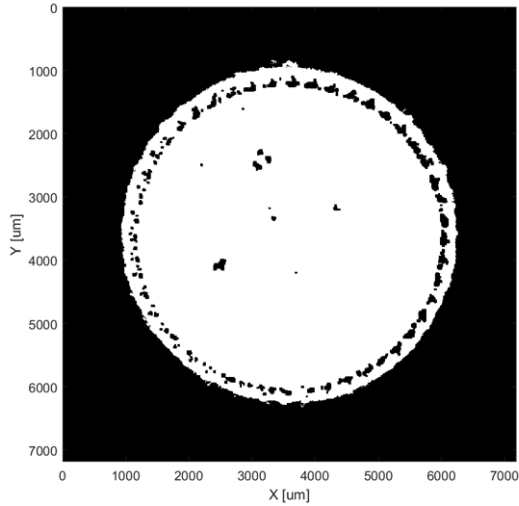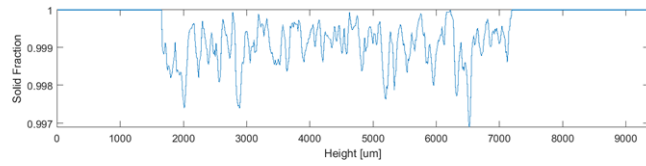
Figure H 2. Minimum intensity projection images from CT analysis. Build variables correspond to sample I.D. 2.

Parameters for sample I.D. 3

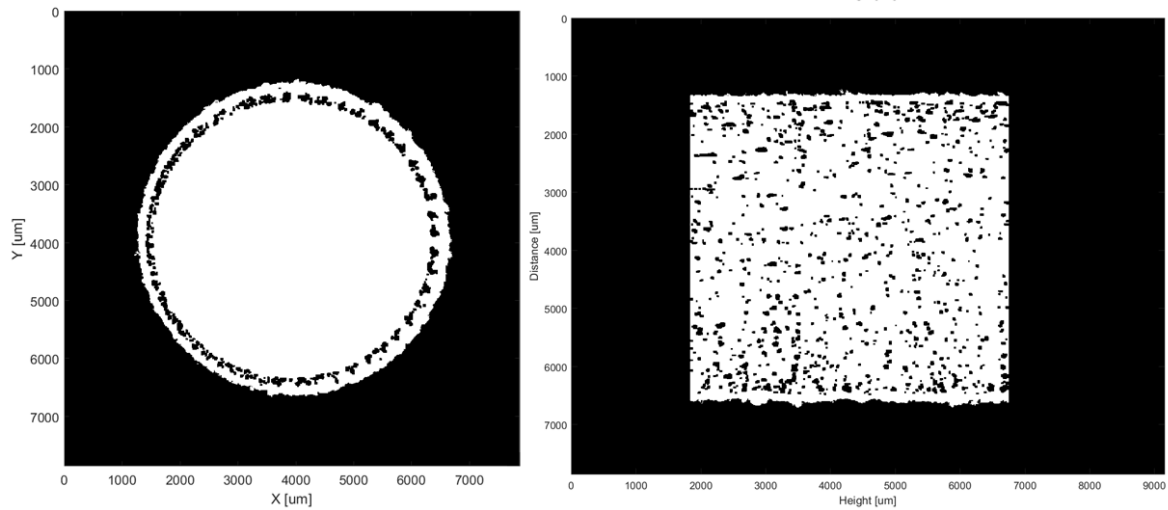| Power	250 W
Grid distance	60 μm
Exposure time	80 μm

Total solid fraction: 0.9987358

Figure H 3. Minimum intensity projection images from CT analysis. Build variables correspond to sample I.D. 3

234

Parameters for sample I.D. 4

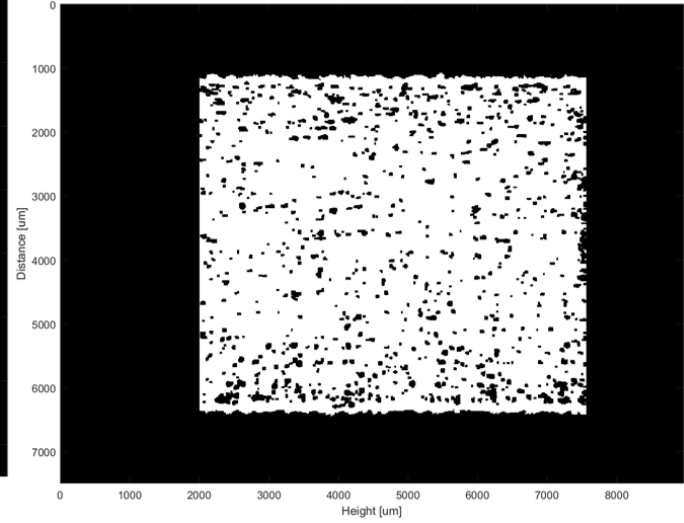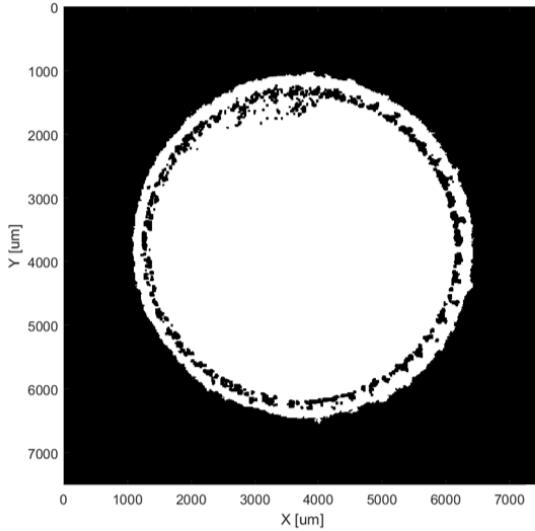| Power	250 W
Grid distance	70 μm
Exposure time	60 μm

Total solid fraction: 0.9979579
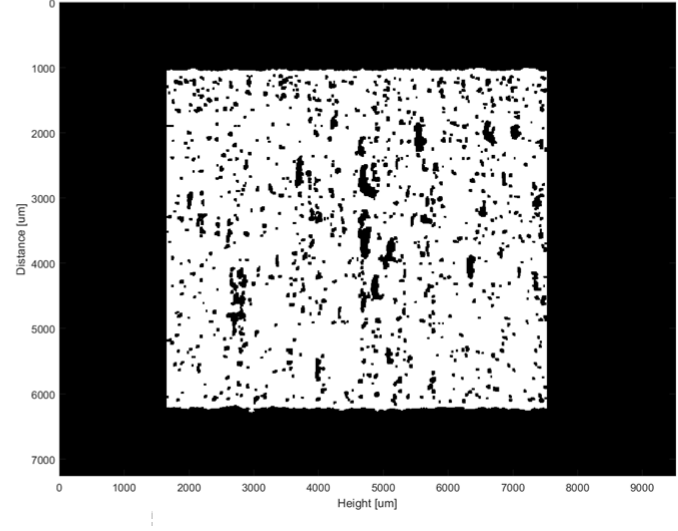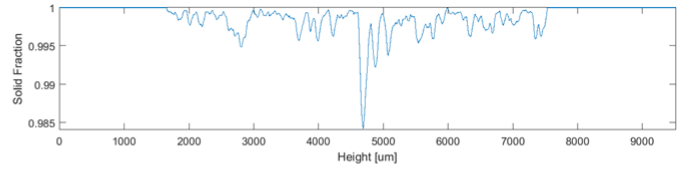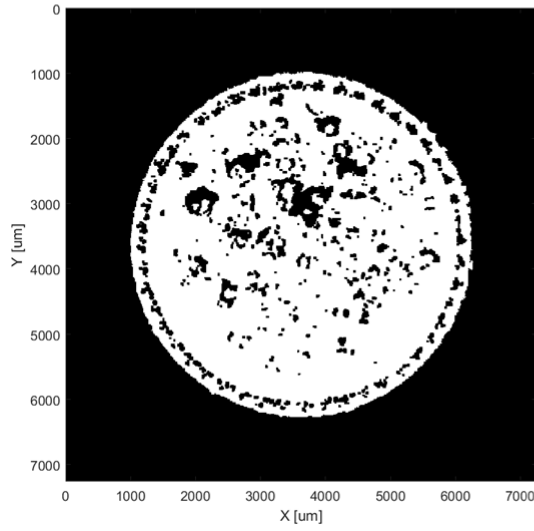
Figure H 4. Minimum intensity projection images from CT analysis. Build variables correspond to sample I.D. 4.

Parameters for sample I.D. 5

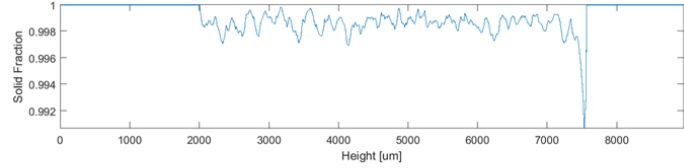| Power	250 W
Grid distance	70 μm
Exposure time	70 μm
Total solid fraction: 0.9987173	
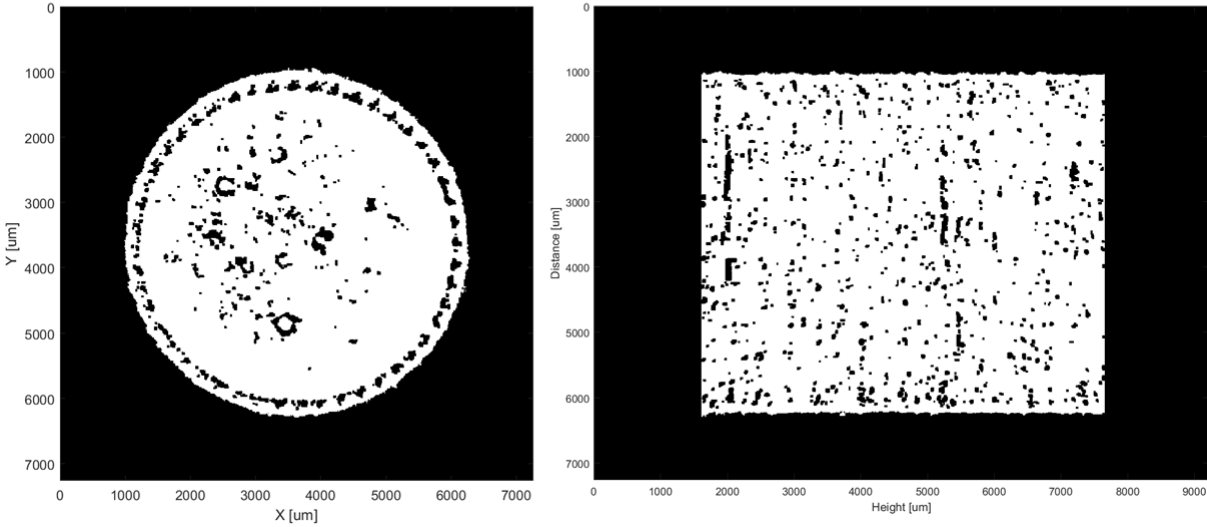
Figure H 5. Minimum intensity projection images from CT analysis. Build variables correspond to sample I.D. 5.

Parameters for sample I.D. 6

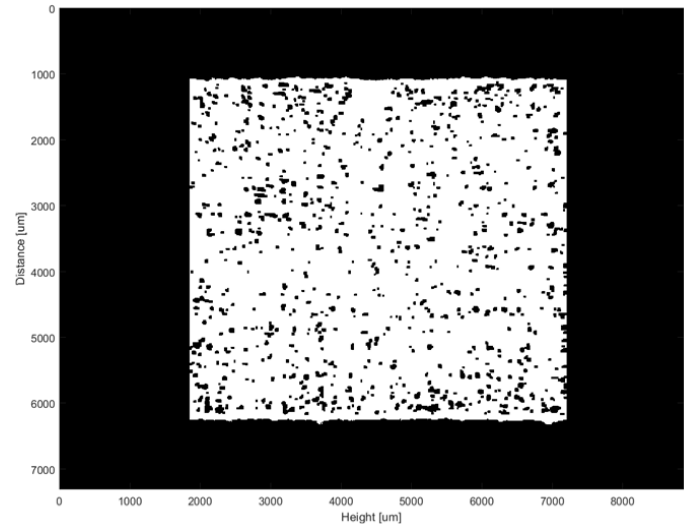| Power	250 W
Grid distance	70 μm
Exposure time	80 μm
Total solid fraction: 0.9992050	
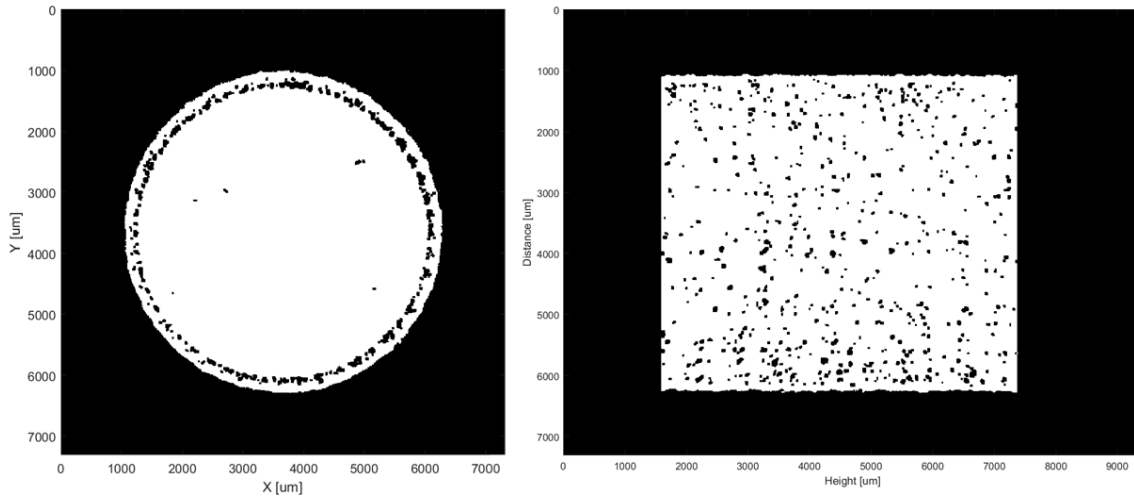
Figure H 6. Minimum intensity projection images from CT analysis. Build variables correspond to sample I.D. 6.

Parameters for sample I.D. 7

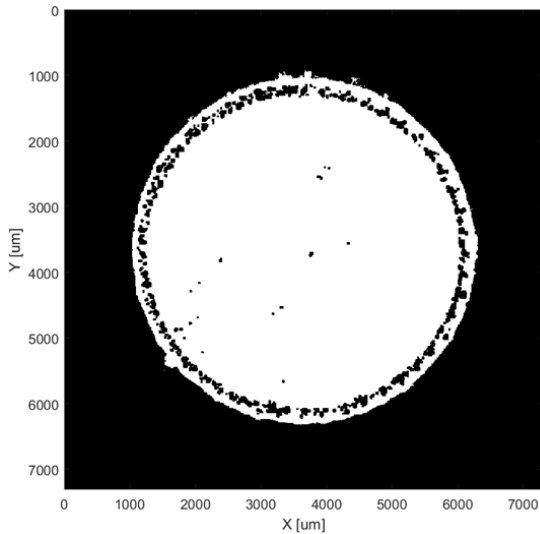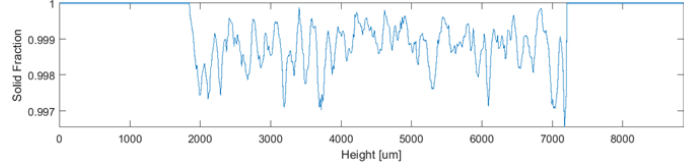| Power	250 W
Grid distance	80 μm
Exposure time	60 μm

Total solid fraction: 0.9991439
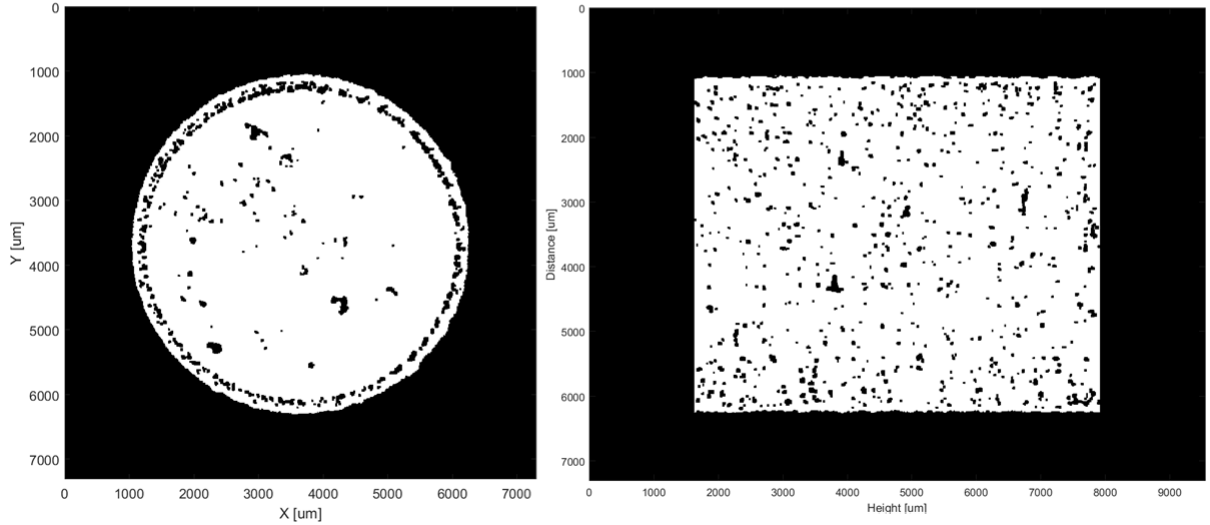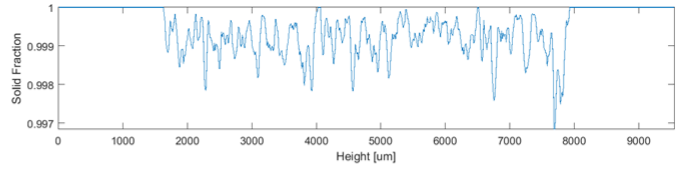
Figure H 7. Minimum intensity projection images from CT analysis. Build variables correspond to sample I.D. 7.

Parameters for sample I.D. 8

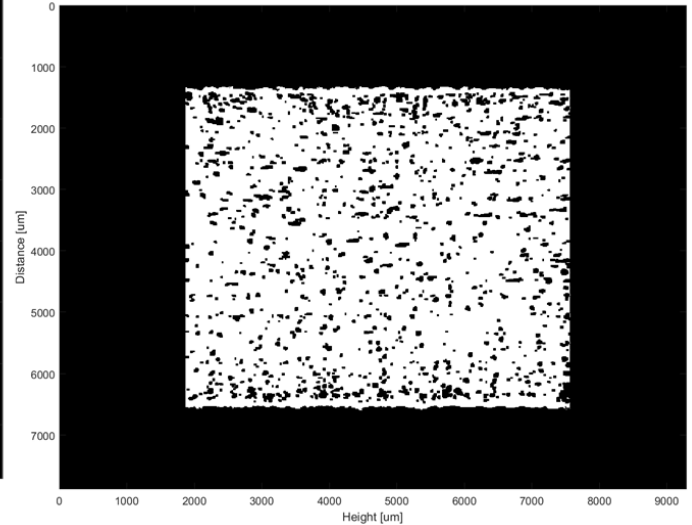| Power	250 W
Grid distance	80 μm
Exposure time	70 μm

Total solid fraction: 0.9987552
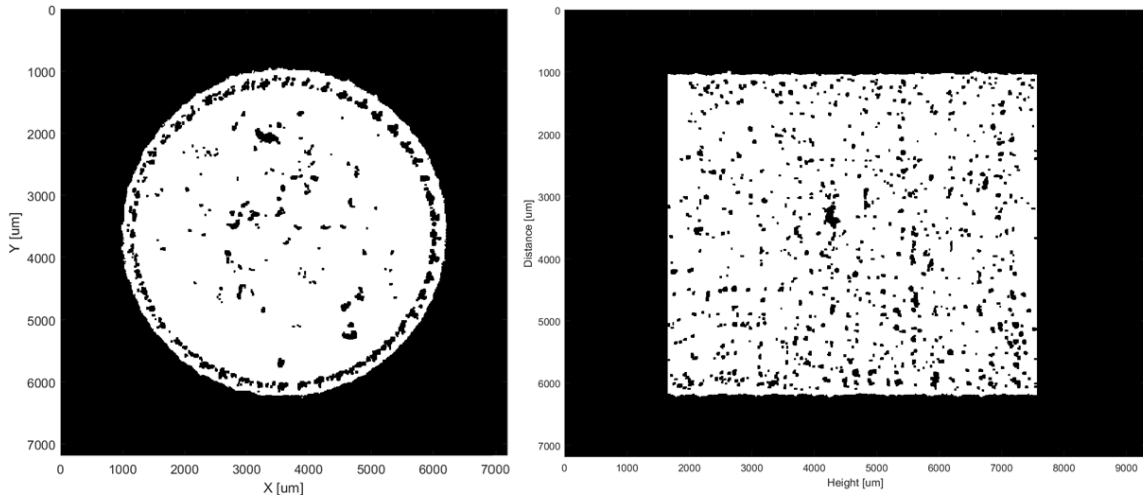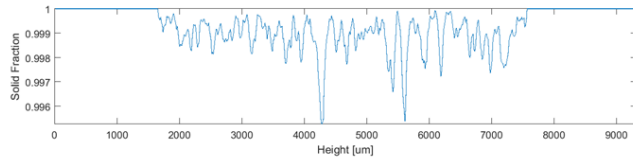
Figure H 8. Minimum intensity projection images from CT analysis. Build variables correspond to sample I.D. 8.

Parameters for sample I.D. 9

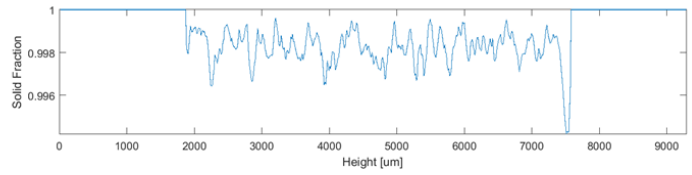| Power	250 W
Grid distance	80 μm
Exposure time	80 μm

Total solid fraction: 0.9990039

Figure H 9. Minimum intensity projection images from CT analysis. Build variables correspond to sample I.D. 9.

Parameters for sample I.D. 10

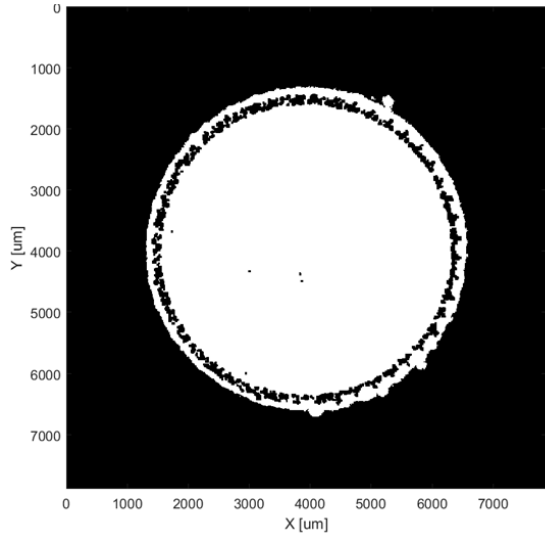| Power	275 W
Grid distance	60 μm
Exposure time	60 μm

Total solid fraction: 0.9986307
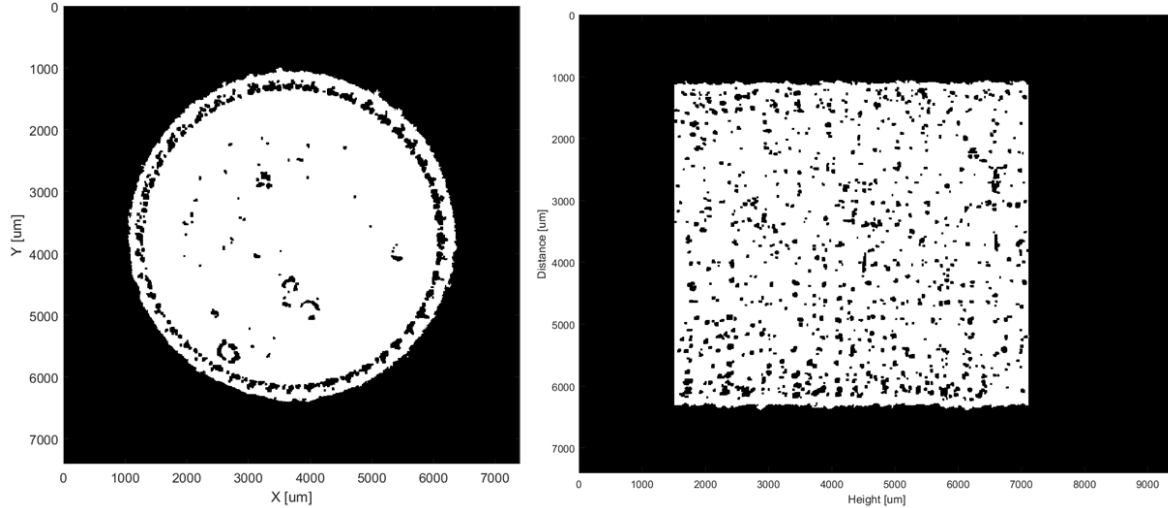
Figure H 10. Minimum intensity projection images from CT analysis. Build variables correspond to sample I.D. 10.

238

Parameters for sample I.D. 11

Power	275 W
Grid distance	60 μm
Exposure time	70 μm

Total solid fraction: 0.9990291
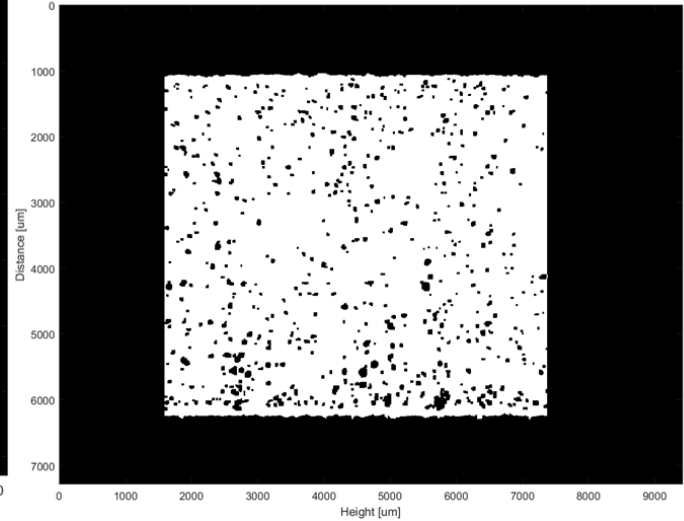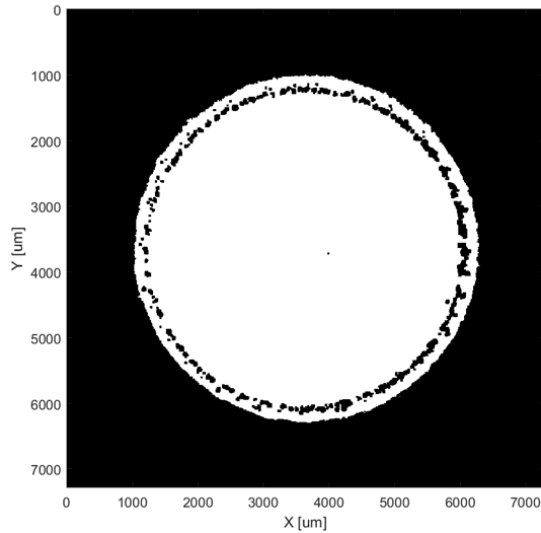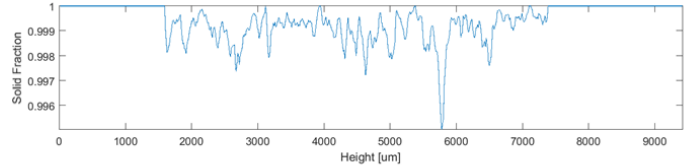
Figure H 11. Minimum intensity projection images from CT analysis. Build variables correspond to sample I.D. 11.

Parameters for sample I.D. 12

Power	275 W
Grid distance	60 μm
Exposure time	80 μm

Total solid fraction: 0.9985601

Figure H 12. Minimum intensity projection images from CT analysis. Build variables correspond to sample I.D. 12.

Parameters for sample I.D. 13

Power	275 W
Grid distance	70 μm
Exposure time	60 μm

Total solid fraction: 0.9991673
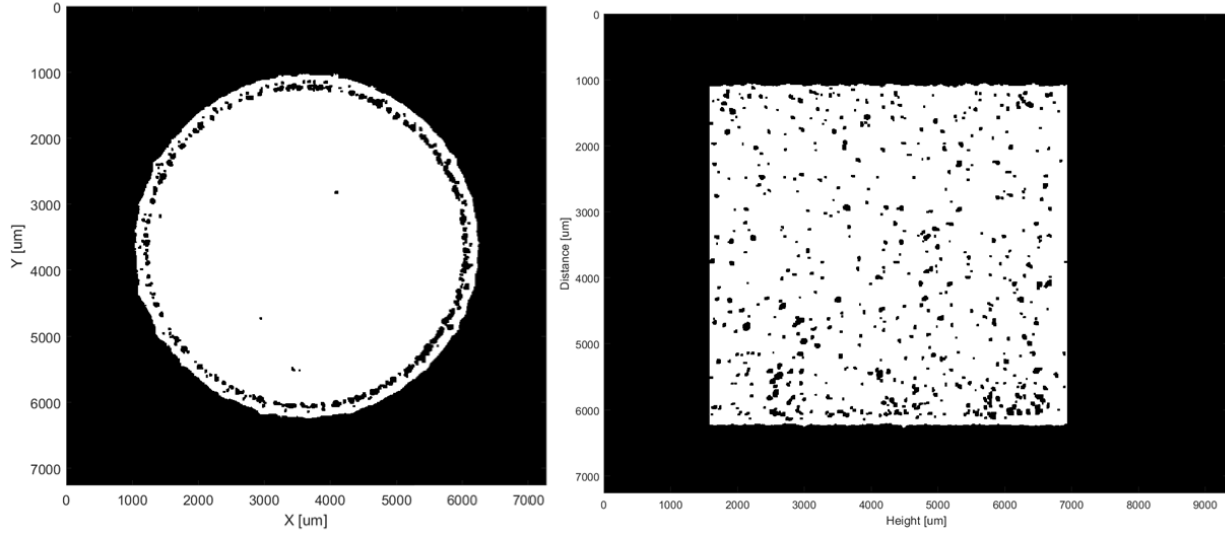
Figure H 13. Minimum intensity projection images from CT analysis. Build variables correspond to sample I.D. 13.

Parameters for sample I.D. 14

Power	275 W
Grid distance	70 μm
Exposure time	70 μm

Total solid fraction: 0.9990948
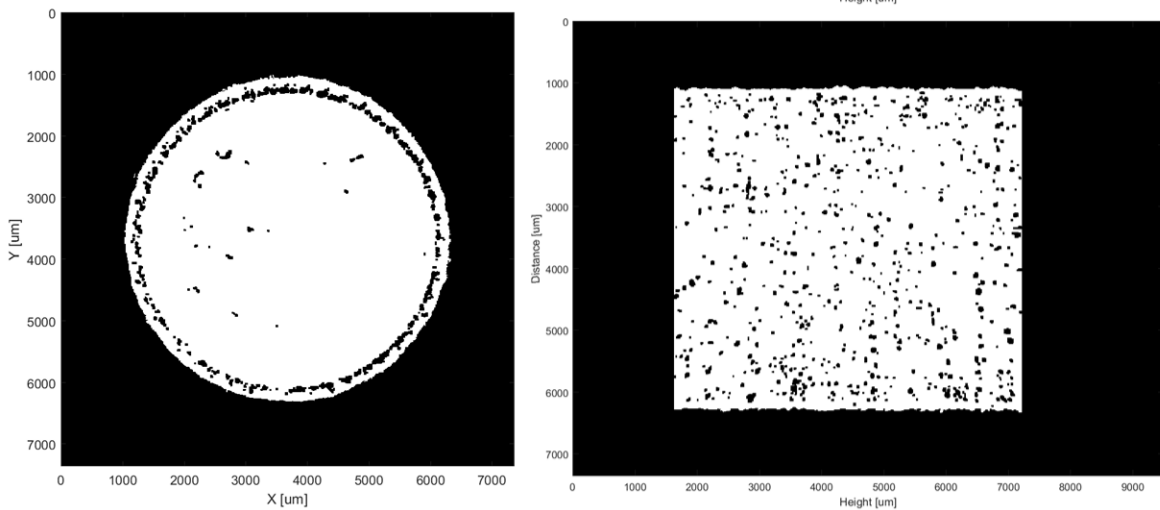
Figure H 14. Minimum intensity projection images from CT analysis. Build variables correspond to sample I.D. 14.

240

Parameters for sample I.D. 15

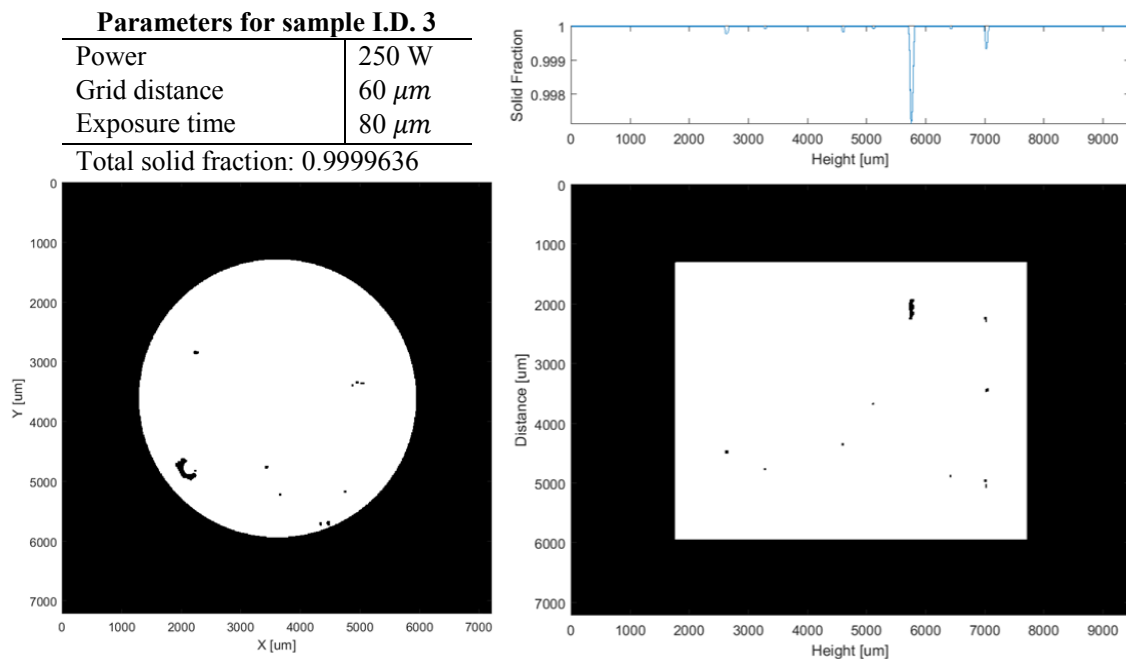| Power	275 W
Grid distance	70 μm
Exposure time	80 μm

Total solid fraction: 0.9990371

Figure H 15. Minimum intensity projection images from CT analysis. Build variables correspond to sample I.D. 15.

Parameters for sample I.D. 16

Power	275 W
Grid distance	80 μm
Exposure time	60 μm

Total solid fraction: 0.9992905
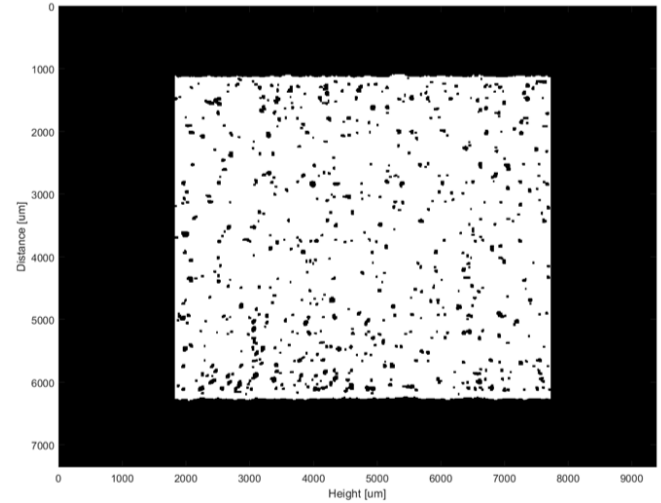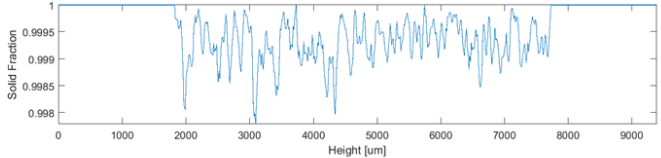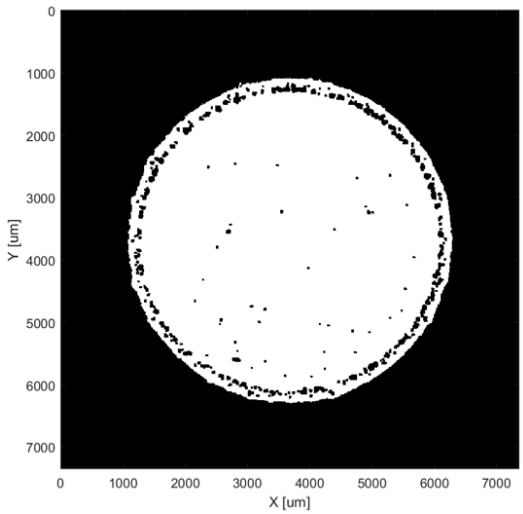
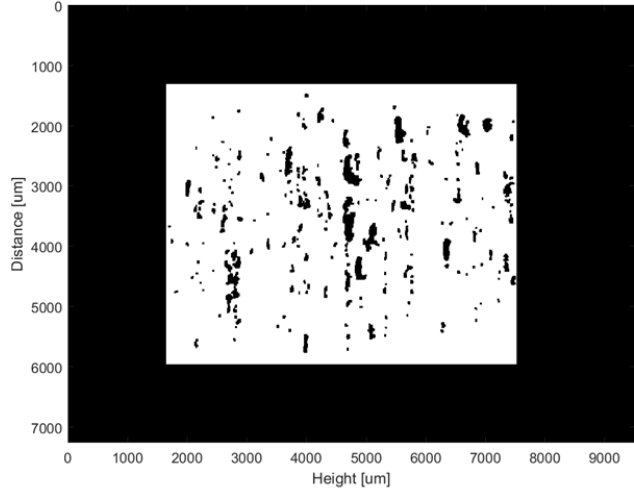**Figure H 16. Minimum intensity projection images from CT analysis. Build variables correspond to sample I.D. 16.**

Parameters for sample I.D. 17

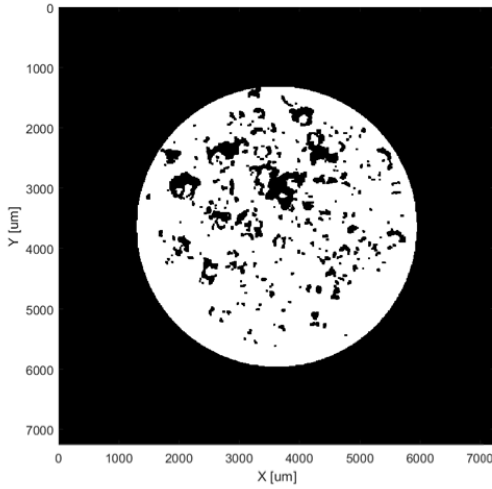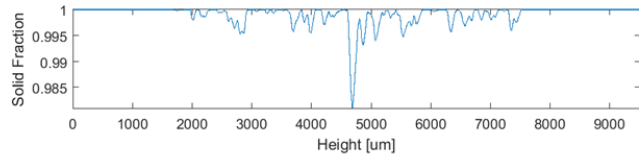| Power	275 W
Grid distance	80 μm
Exposure time	70 μm

Total solid fraction: 0.9991174
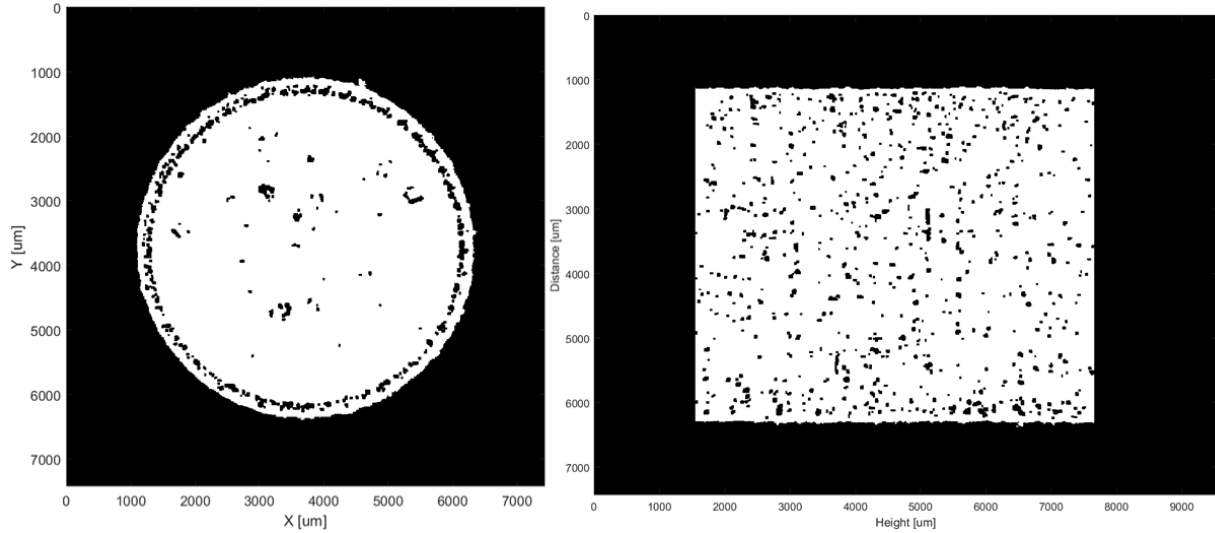
Figure H 17. Minimum intensity projection images from CT analysis. Build variables correspond to sample I.D. 17.

Parameters for sample I.D. 18

Power	275 W
Grid distance	80 μm
Exposure time	80 μm

Total solid fraction: 0.9991743

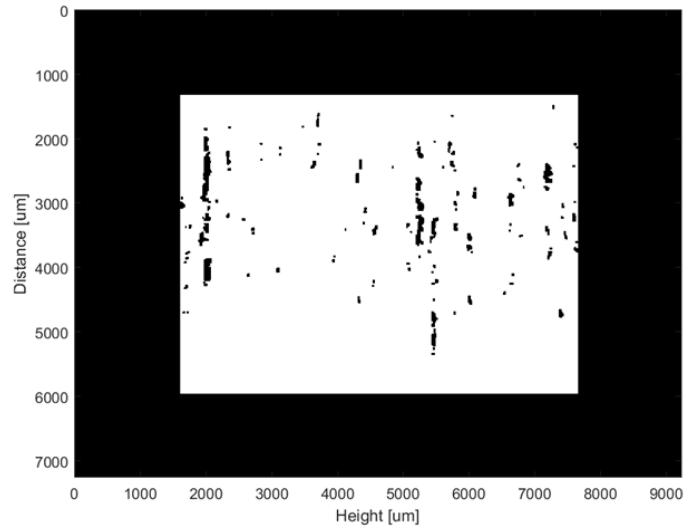**Figure H 18. Minimum intensity projection images from CT analysis. Build variables correspond to sample I.D. 18.**

Parameters for sample I.D. 19

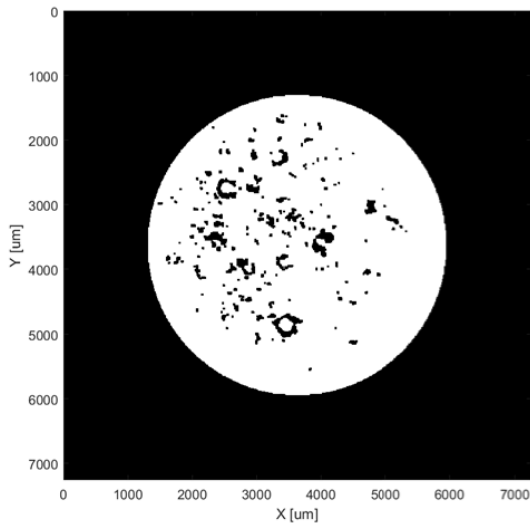| Power	300 W
Grid distance	60 μm
Exposure time	60 μm

Total solid fraction: 0.9984535
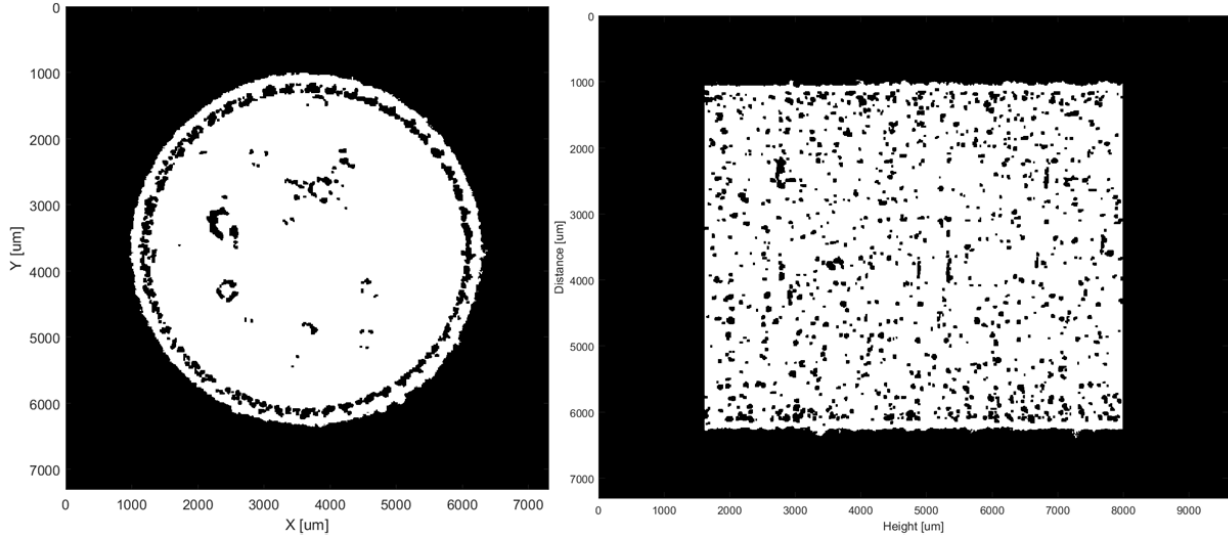
Figure H 19. Minimum intensity projection images from CT analysis. Build variables correspond to sample I.D. 19.

Parameters for sample I.D. 20

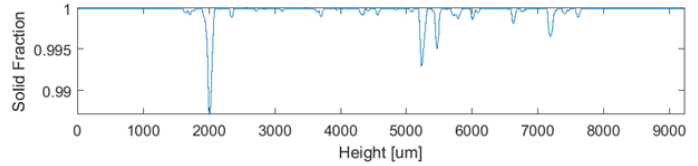| Power	300 W
Grid distance	60 μm
Exposure time	70 μm

Total solid fraction: 0.9980849
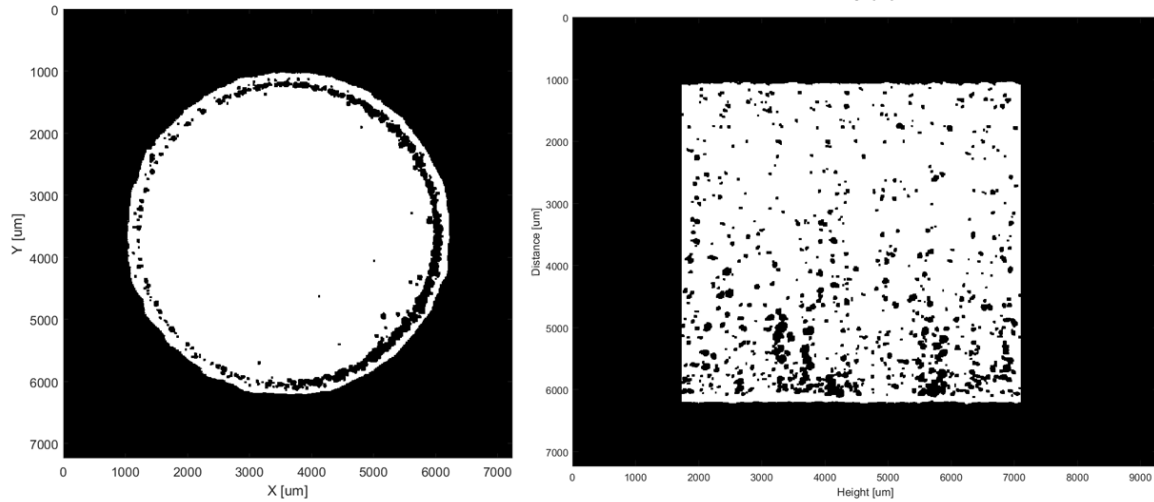
Figure H 20. Minimum intensity projection images from CT analysis. Build variables correspond to sample I.D. 20.

Parameters for sample I.D. 21

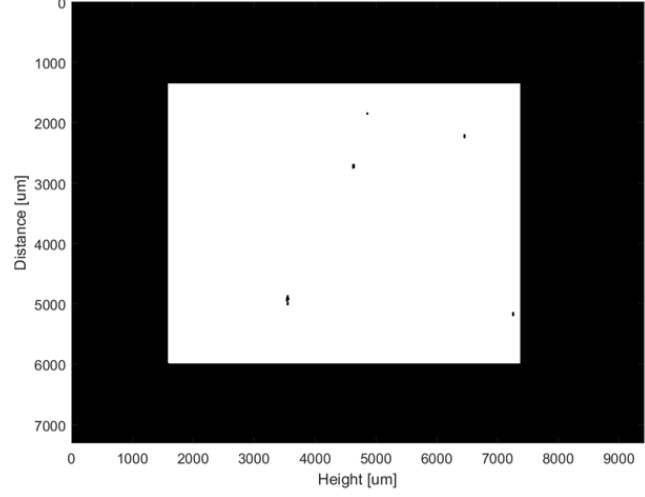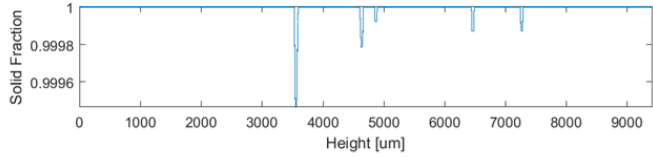| Power	300 W
Grid distance	60 μm
Exposure time	80 μm

Total solid fraction: 0.9984736

Figure H 21. Minimum intensity projection images from CT analysis. Build variables correspond to sample I.D. 21.

Parameters for sample I.D. 22

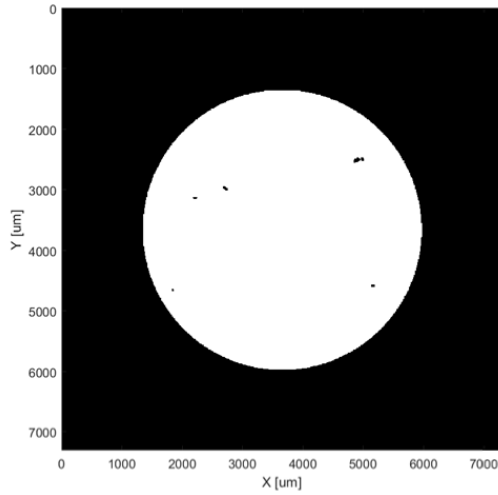| Power	300 W
Grid distance	70 μm
Exposure time	60 μm

Total solid fraction: 0.9990865
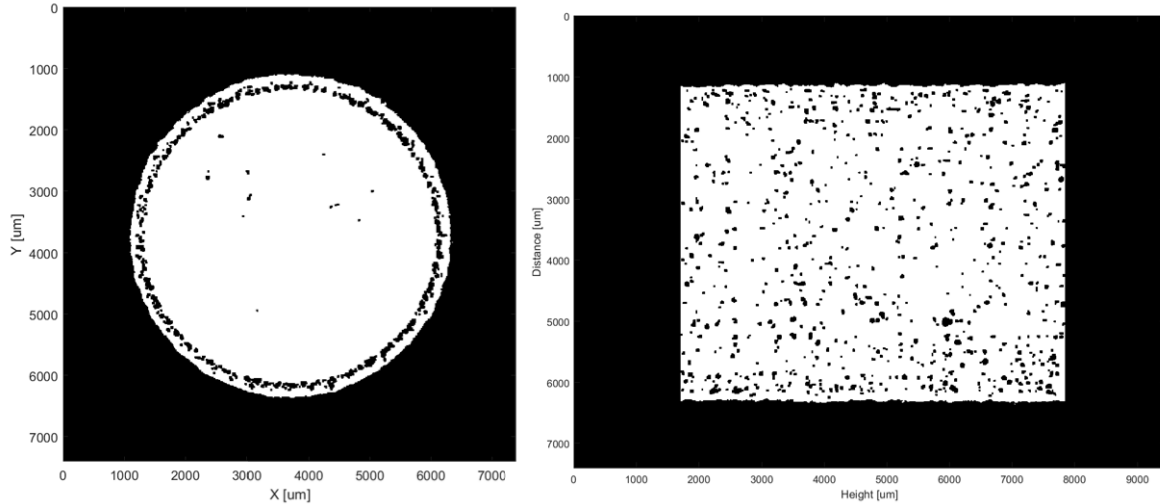
Figure H 22. Minimum intensity projection images from CT analysis. Build variables correspond to sample I.D. 22.

Parameters for sample I.D. 23

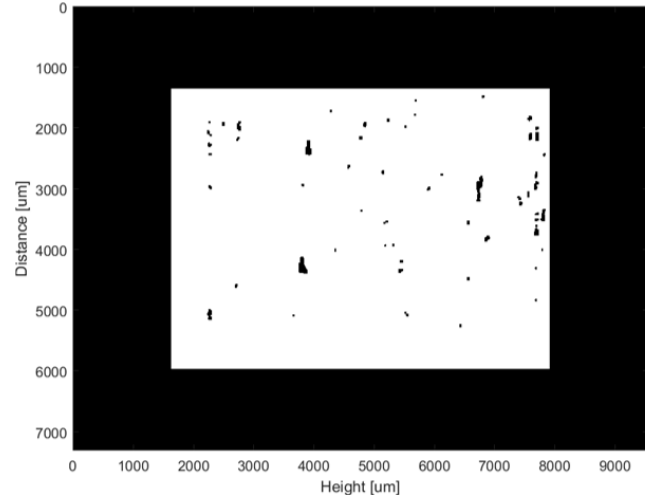| Power	300 W
Grid distance	70 μm
Exposure time	70 μm

Total solid fraction: 0.9987481
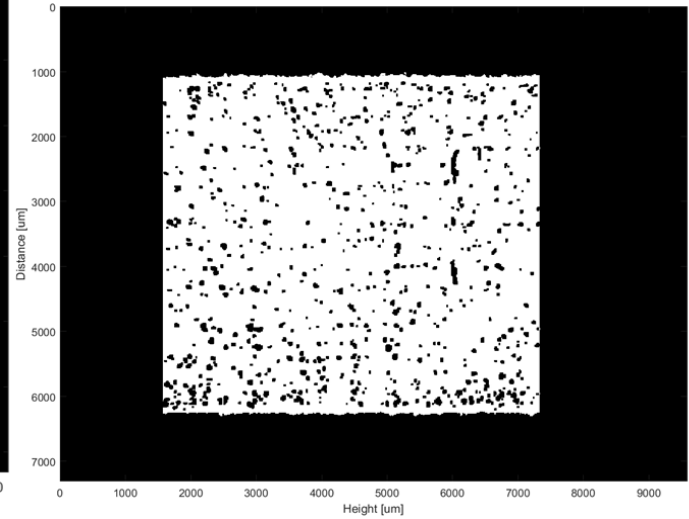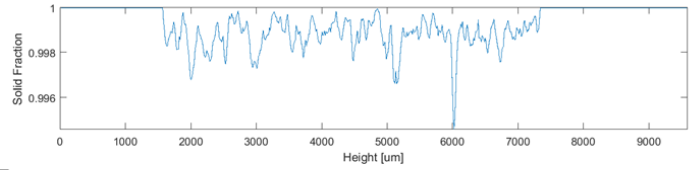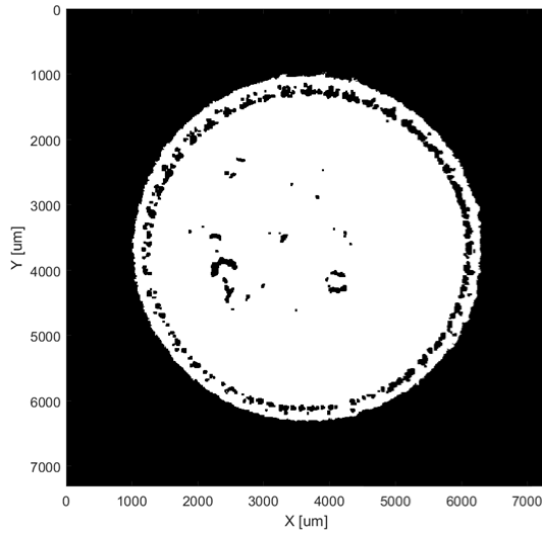
Figure H 23. Minimum intensity projection images from CT analysis. Build variables correspond to sample I.D. 23.

Parameters for sample I.D. 24

Power	300 W
Grid distance	70 μm
Exposure time	80 μm

Total solid fraction: 0.9989128
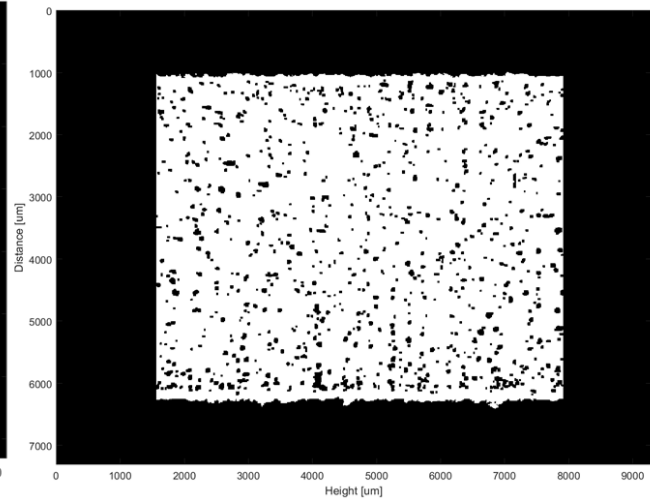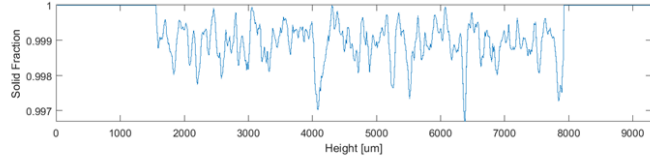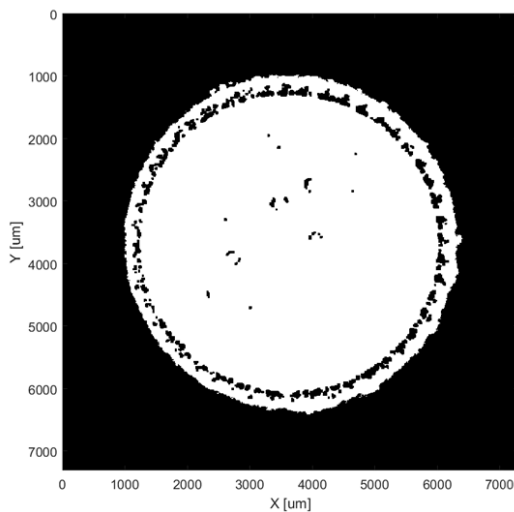
Figure H 24. Minimum intensity projection images from CT analysis. Build variables correspond to sample I.D. 24.

Parameters for sample I.D. 25

Power	300 W
Grid distance	80 μm
Exposure time	60 μm

Total solid fraction: 0.9989693
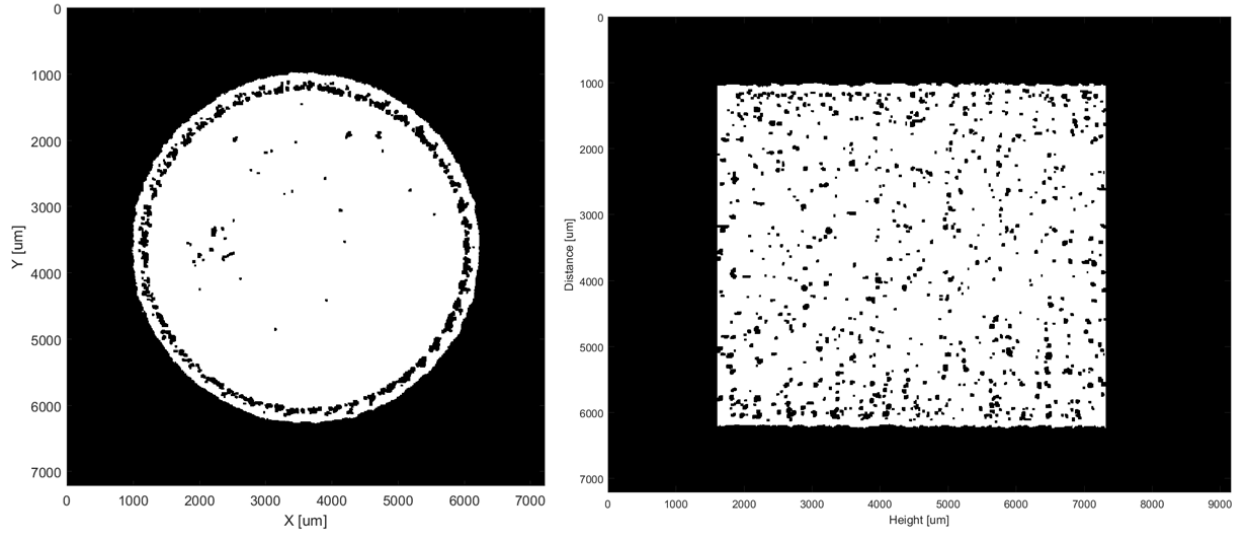
Figure H 25. Minimum intensity projection images from CT analysis. Build variables correspond to sample I.D. 25.

Parameters for sample I.D. 26

Power	300 W
Grid distance	80 μm
Exposure time	70 μm

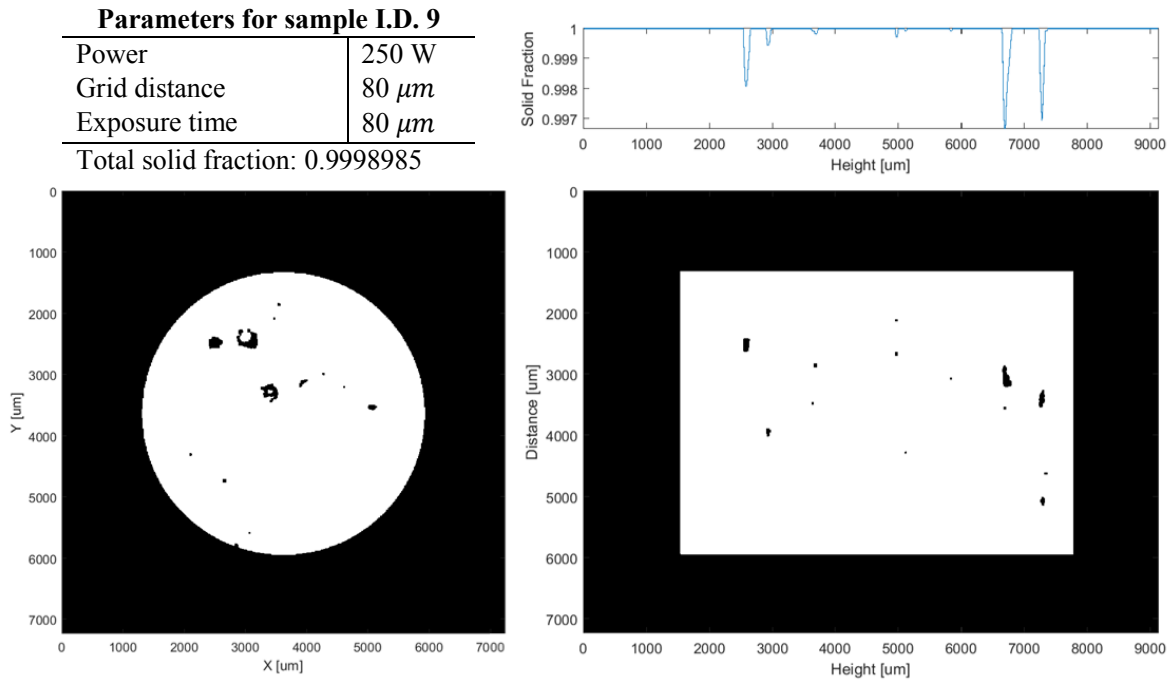Total solid fraction: 0.9984588
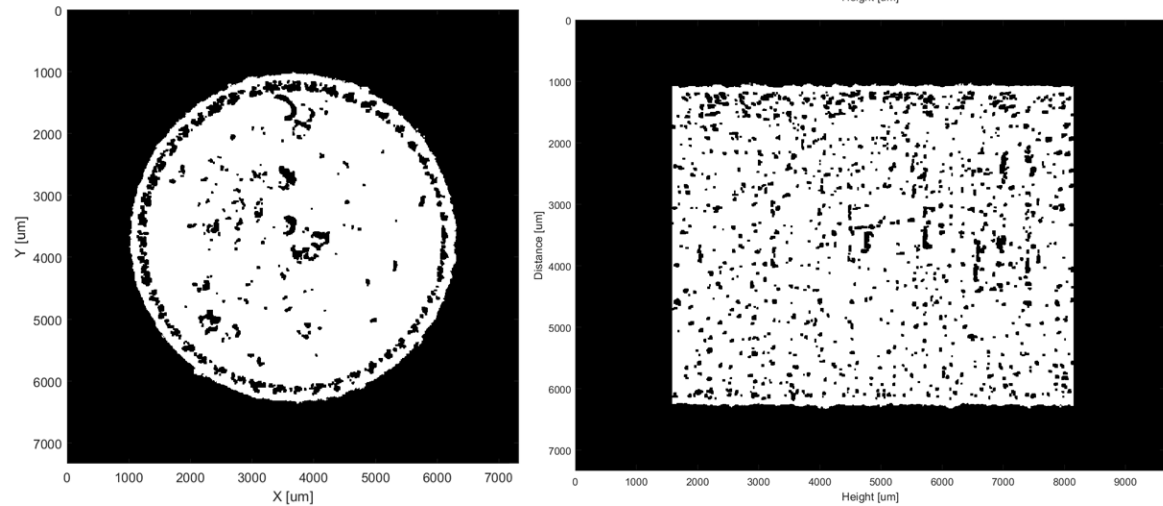
Figure H 26. Minimum intensity projection images from CT analysis. Build variables correspond to sample I.D. 26.

246

Parameters for sample I.D. 27

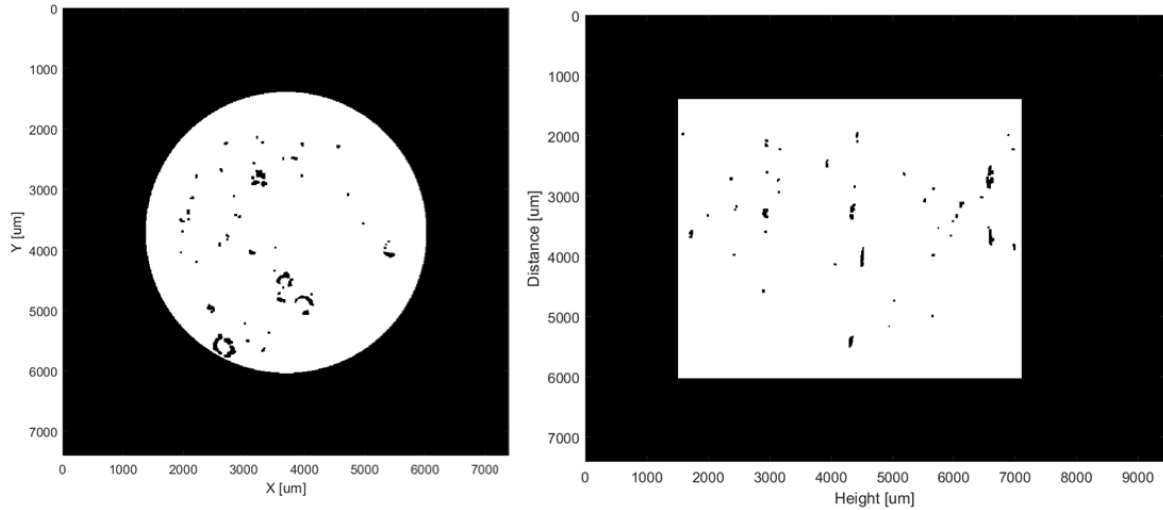| Power	300 W
Grid distance	80 μm
Exposure time	80 μm

Total solid fraction: 0.9991051

Figure H 27. Minimum intensity projection images from CT analysis. Build variables correspond to sample I.D. 27.

Parameters for sample I.D. 28

Power	350 W
Grid distance	60 μm
Exposure time	60 μm

Total solid fraction: 0.9986319
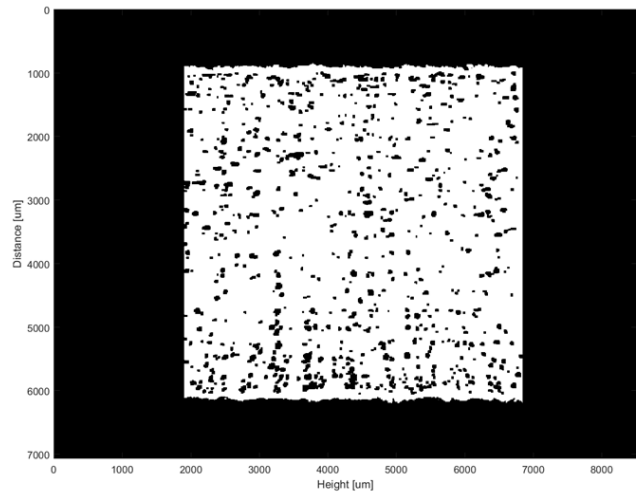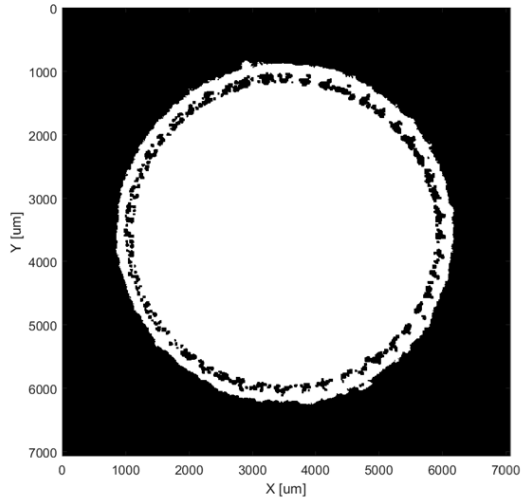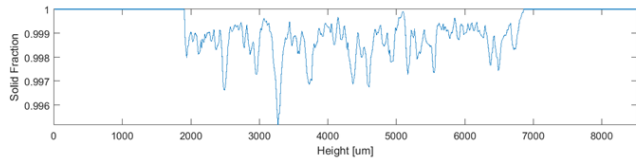
Figure H 28. Minimum intensity projection images from CT analysis. Build variables correspond to sample I.D. 28.

Parameters for sample I.D. 29

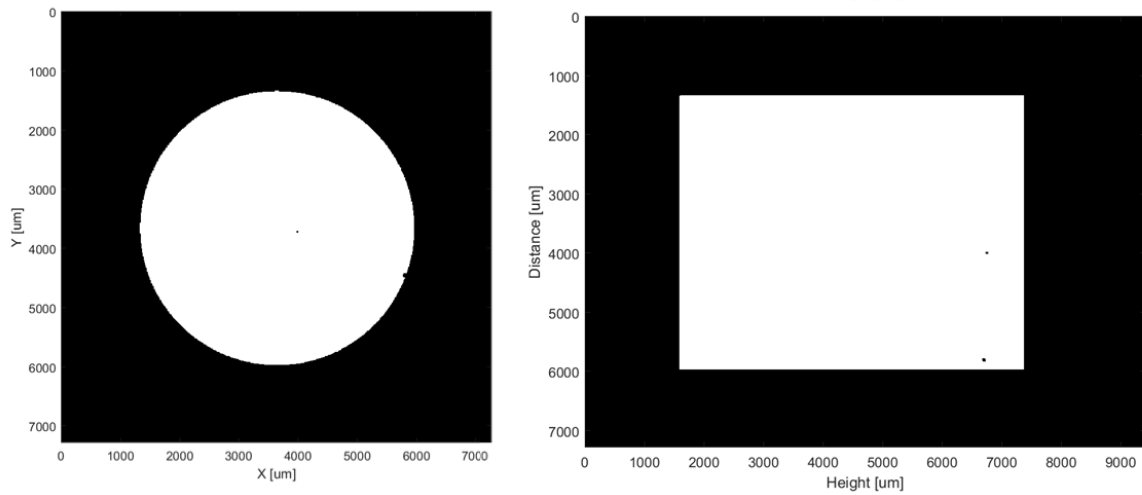| Power	350 W
Grid distance	60 μm
Exposure time	70 μm

Total solid fraction: 0.9986181
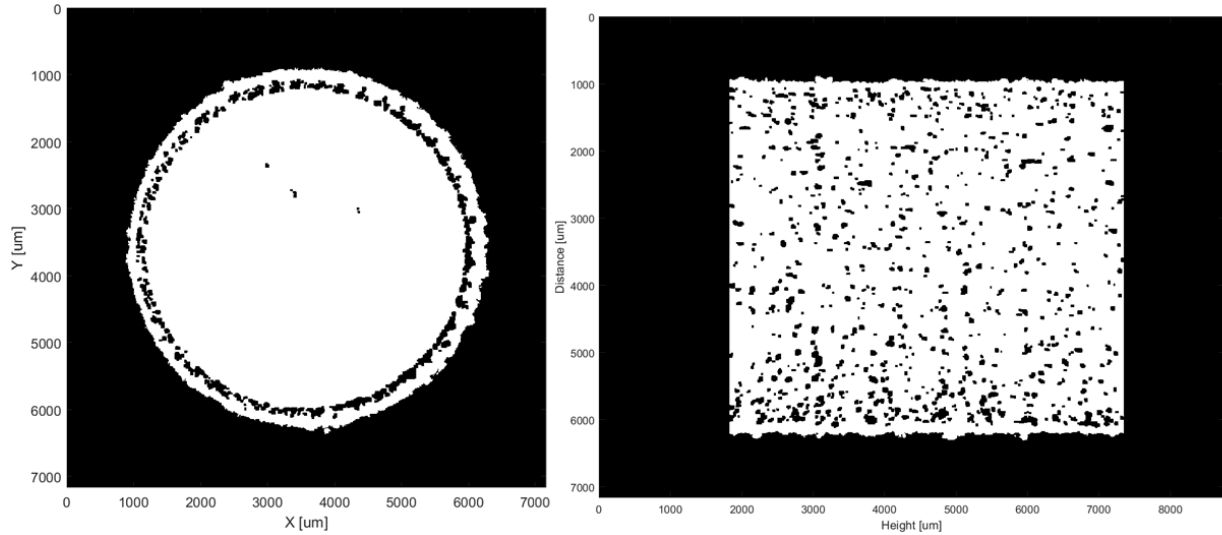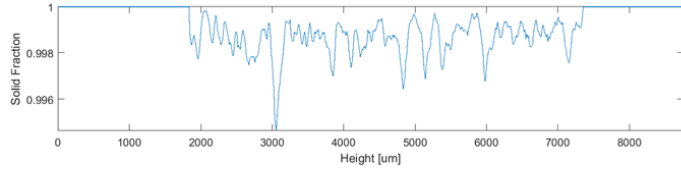
Figure H 29. Minimum intensity projection images from CT analysis. Build variables correspond to sample I.D. 29.

Parameters for sample I.D. 30

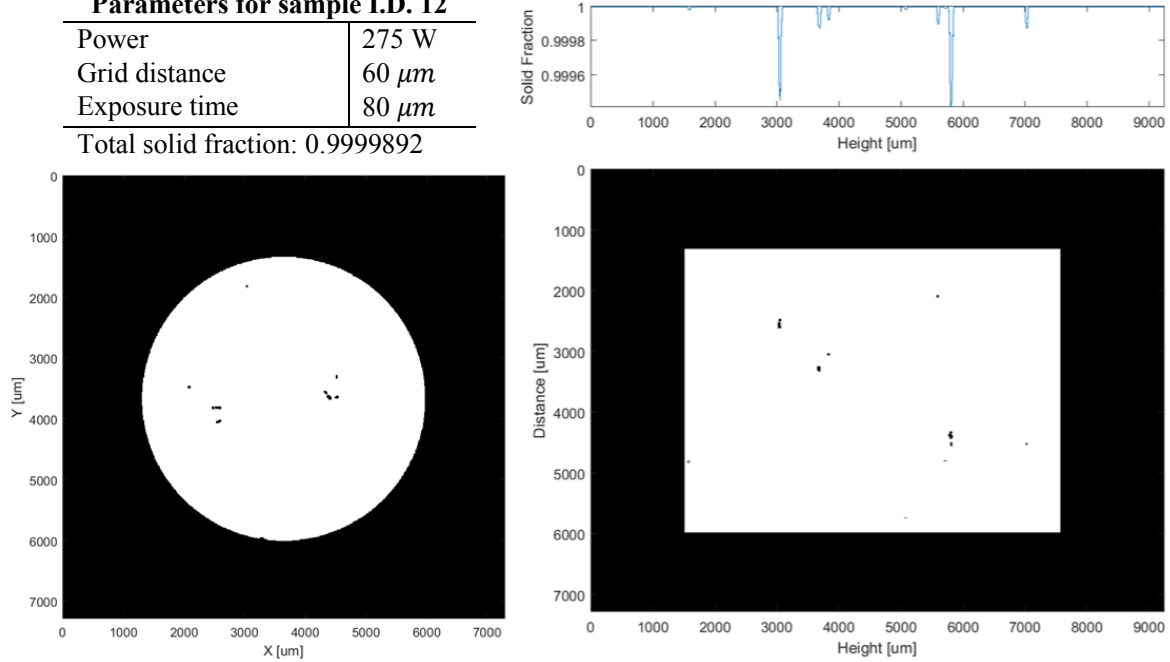| Power	350 W
Grid distance	60 μm
Exposure time	80 μm

Total solid fraction: 0.9988493

Figure H 30. Minimum intensity projection images from CT analysis. Build variables correspond to sample I.D. 30.

248

Parameters for sample I.D. 31

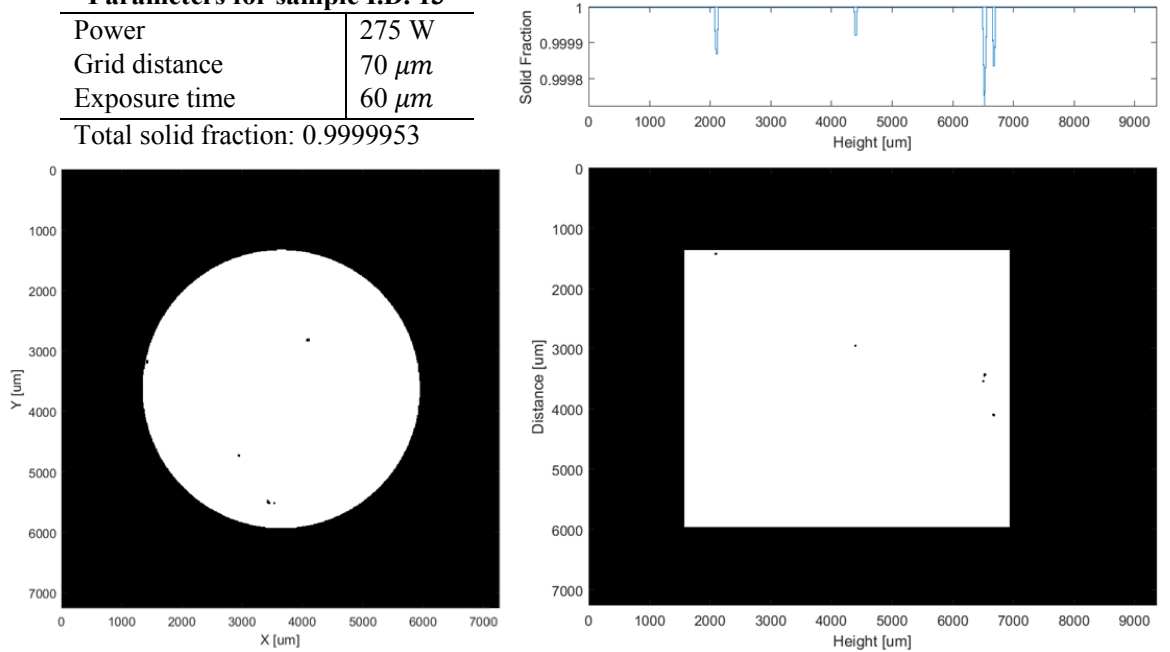| Power	350 W
Grid distance	70 μm
Exposure time	60 μm

Total solid fraction: 0.9986867
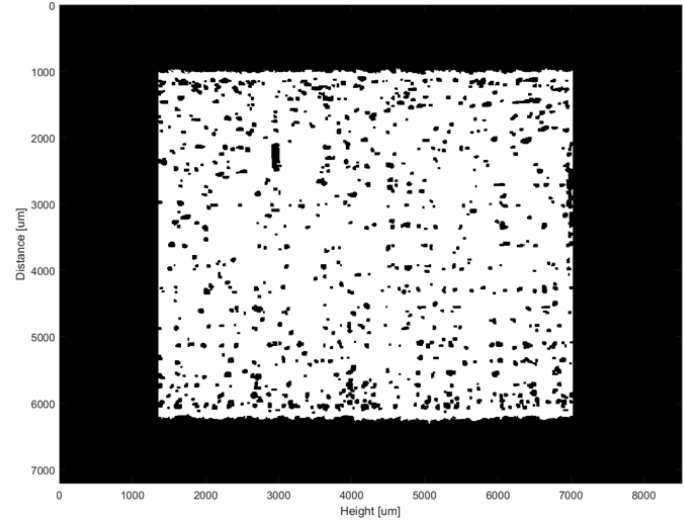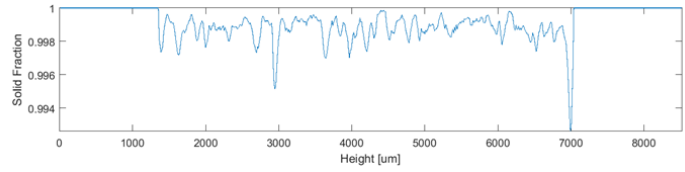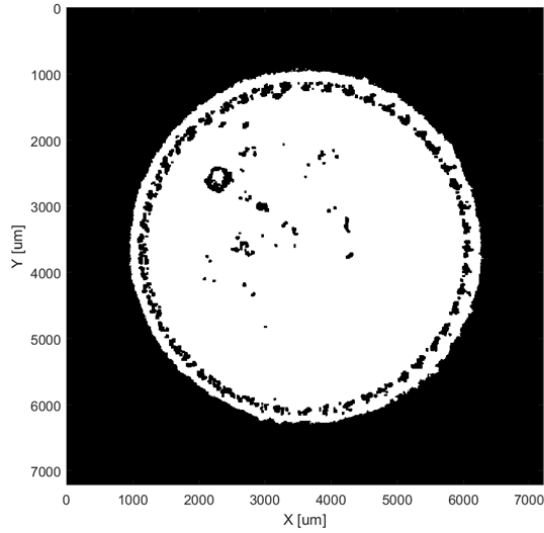
Figure H 31. Minimum intensity projection images from CT analysis. Build variables correspond to sample I.D. 31.

Parameters for sample I.D. 32

Power	350 W
Grid distance	70 μm
Exposure time	70 μm

Total solid fraction: 0.9983819
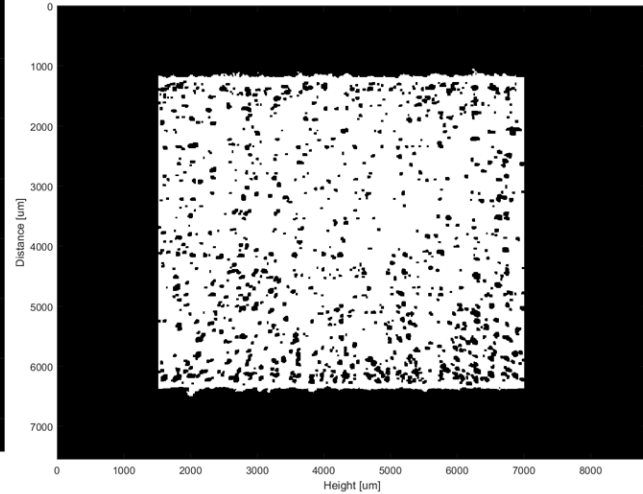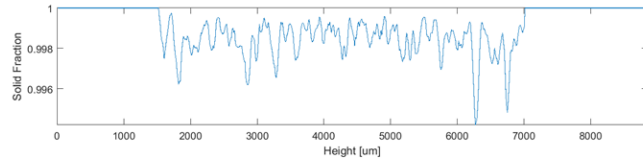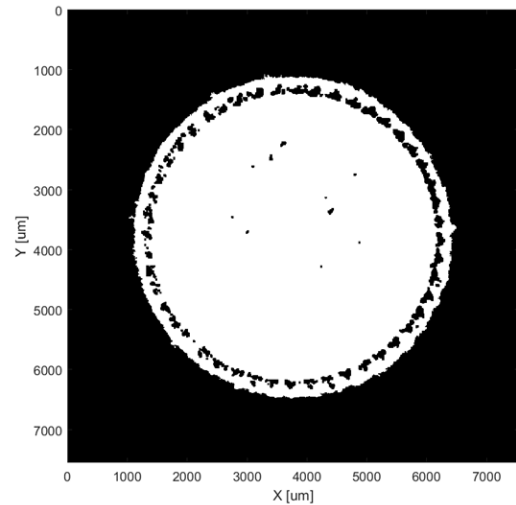
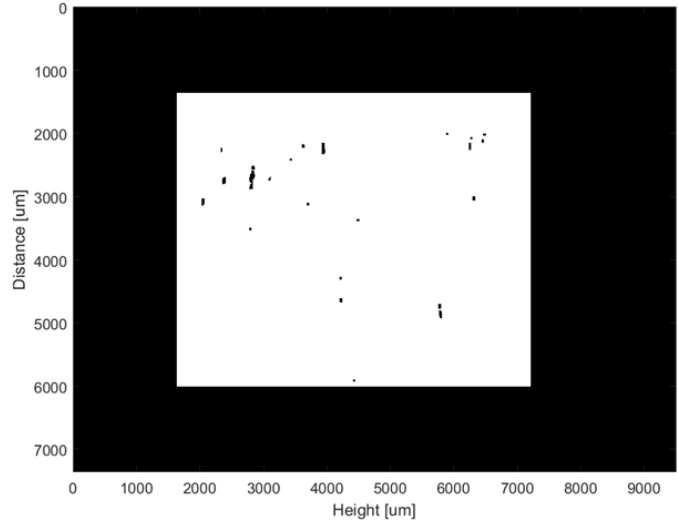**Figure H 32. Minimum intensity projection images from CT analysis. Build variables correspond to sample I.D. 32.**

Parameters for sample I.D. 33

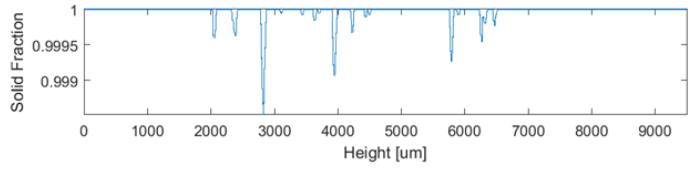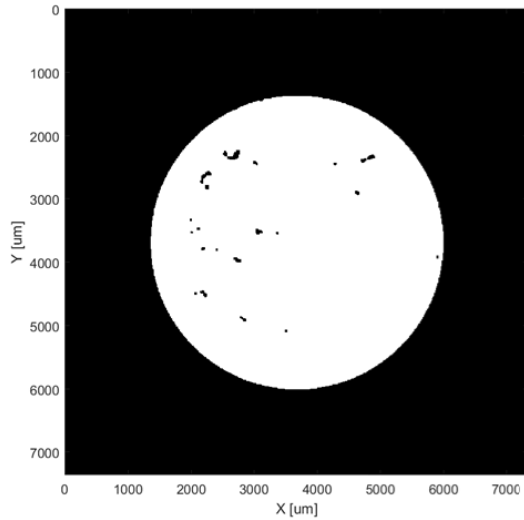| Power	350 W
Grid distance	70 μm
Exposure time	80 μm

Total solid fraction: 0.9982051

Figure H 33. Minimum intensity projection images from CT analysis. Build variables correspond to sample I.D. 33.

Parameters for sample I.D. 34

Power	350 W
Grid distance	80 μm
Exposure time	60 μm

Total solid fraction: 0.9984235
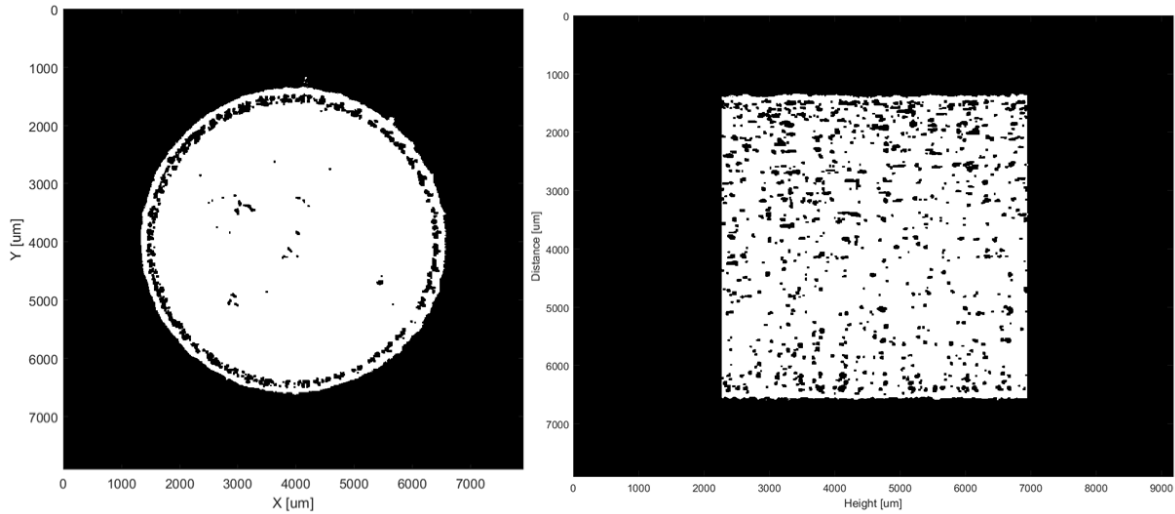
Figure H 34. Minimum intensity projection images from CT analysis. Build variables correspond to sample I.D. 34.

250

Parameters for sample I.D. 35

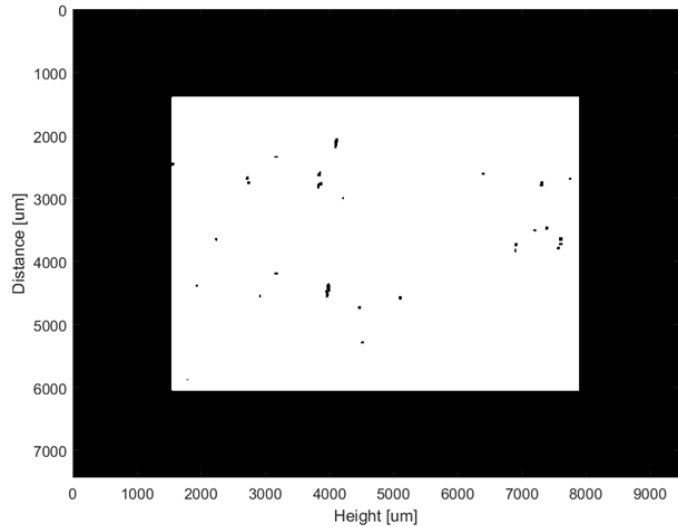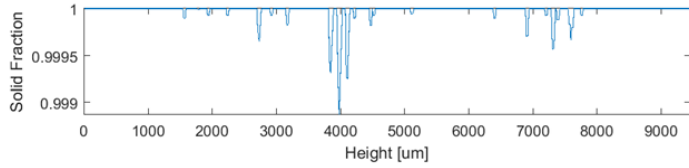| Power	350 W
Grid distance	80 μm
Exposure time	70 μm

Total solid fraction: 0.9981532
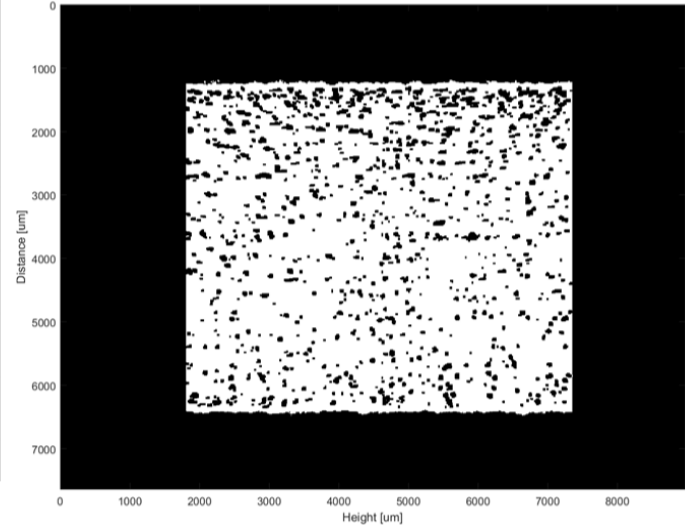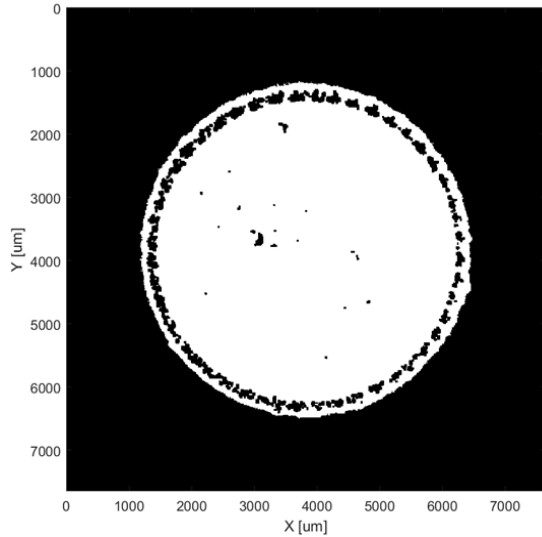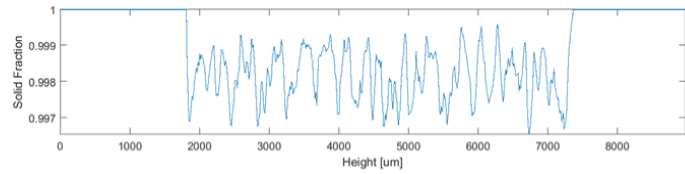
Figure H 35. Minimum intensity projection images from CT analysis. Build variables correspond to sample I.D. 35.

Parameters for sample I.D. 36

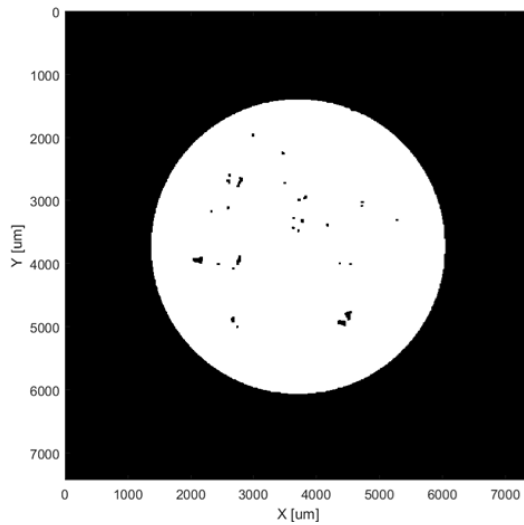| Power	350 W
Grid distance	80 μm
Exposure time	80 μm

Total solid fraction: 0.9985708

Figure H 36. Minimum intensity projection images from CT analysis. Build variables correspond to sample I.D. 36.

251

Parameters for sample I.D. 37

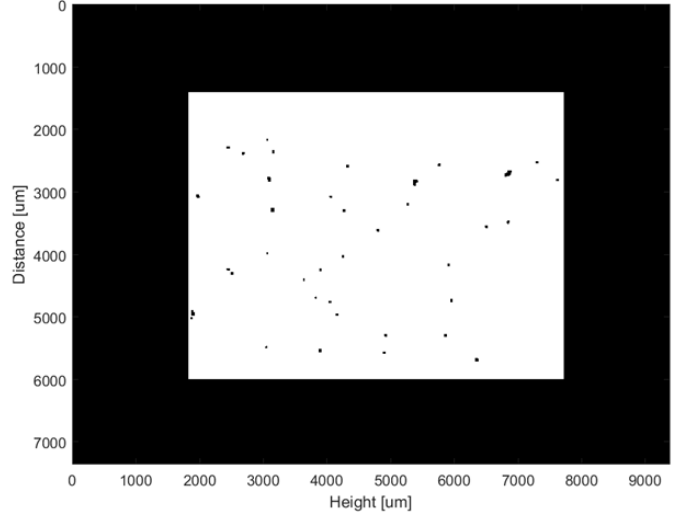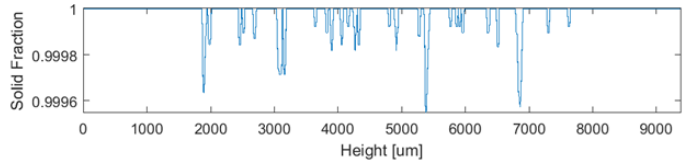| Power	375 W
Grid distance	60 μm
Exposure time	60 μm

Total solid fraction: 0.9980374
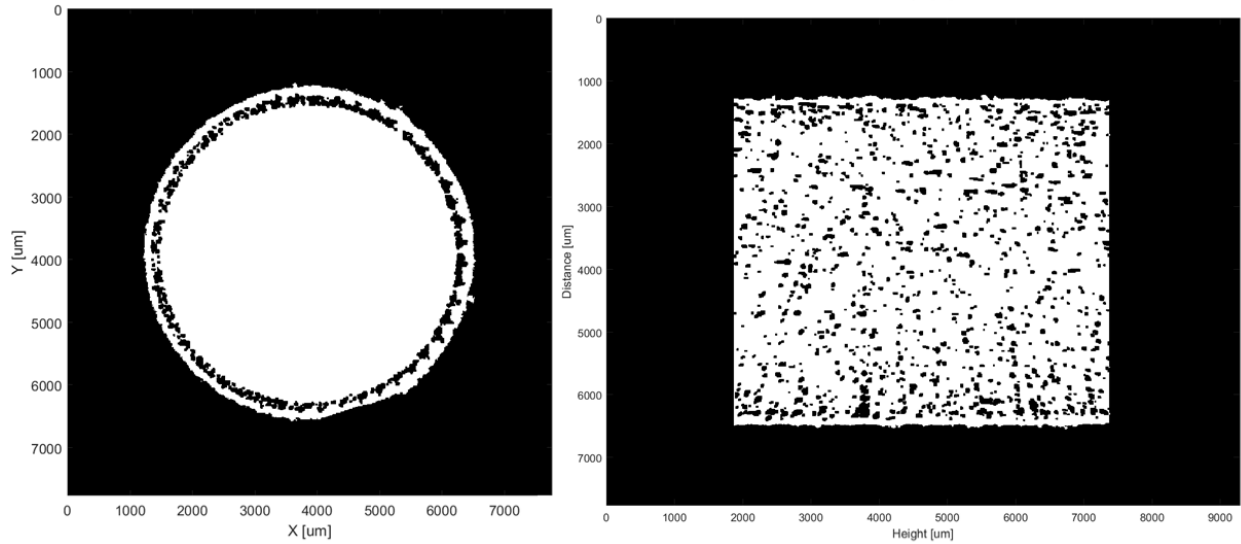
Figure H 37. Minimum intensity projection images from CT analysis. Build variables correspond to sample I.D. 37.

Parameters for sample I.D. 38

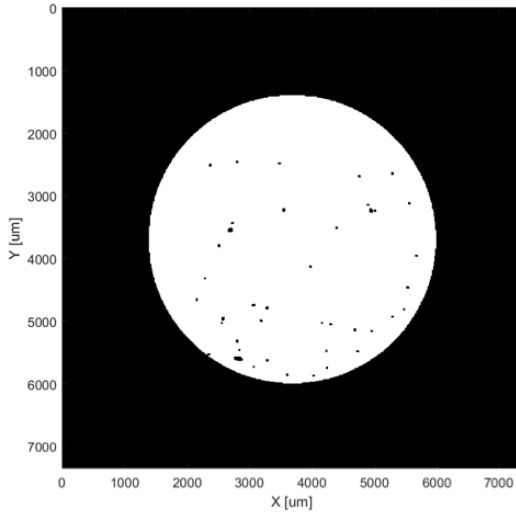| Power	375 W
Grid distance	60 μm
Exposure time	70 μm

Total solid fraction: 0.9980852
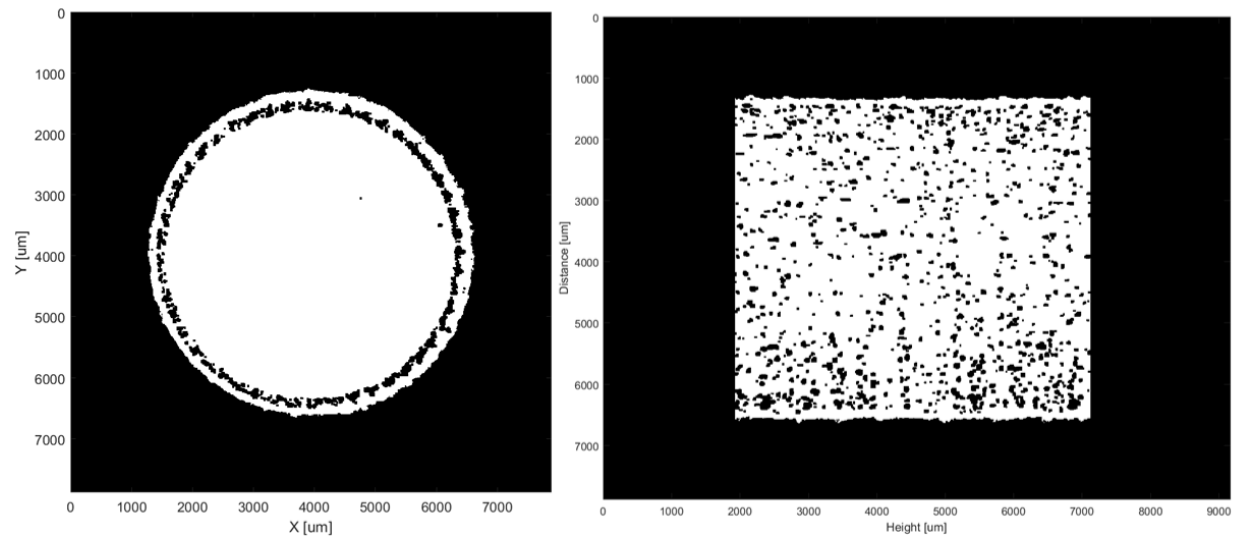
Figure H 38. Minimum intensity projection images from CT analysis. Build variables correspond to sample I.D. 38.

252

Parameters for sample I.D. 39

Power	375 W
Grid distance	60 μm
Exposure time	80 μm

Total solid fraction: 0.9984082

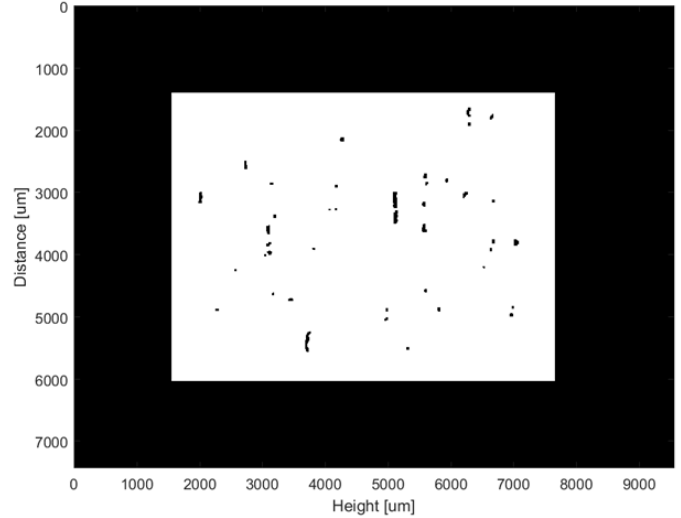**Figure H 39. Minimum intensity projection images from CT analysis. Build variables correspond to sample I.D. 39.**

Parameters for sample I.D. 40

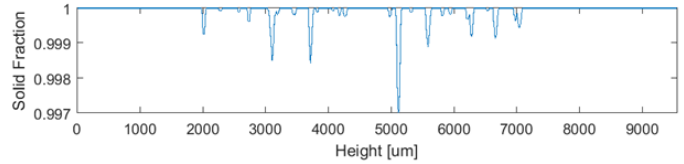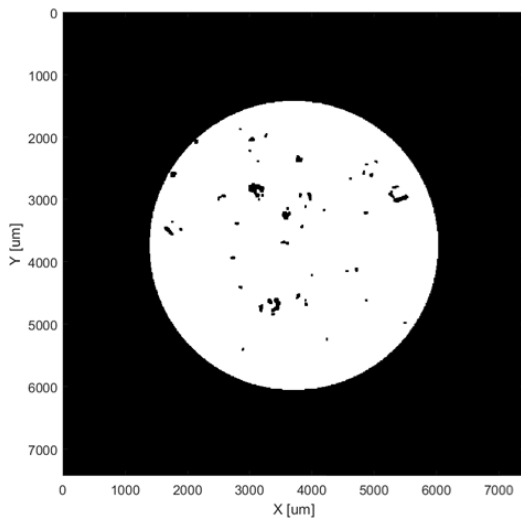|	
Power	375 W
Grid distance	70 μm
Exposure time	60 μm

Total solid fraction: 0.9984817
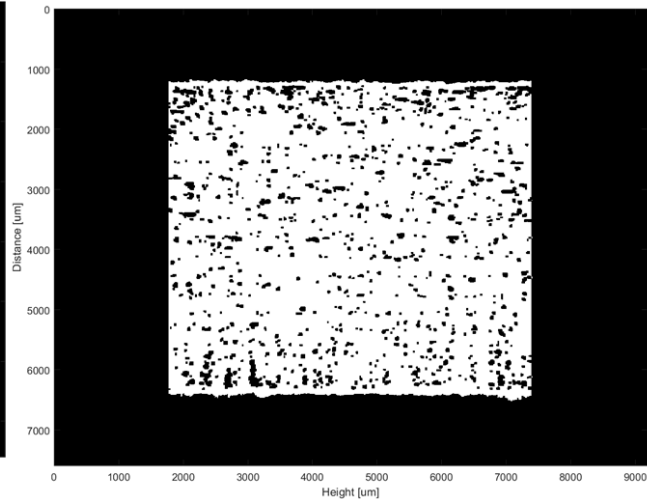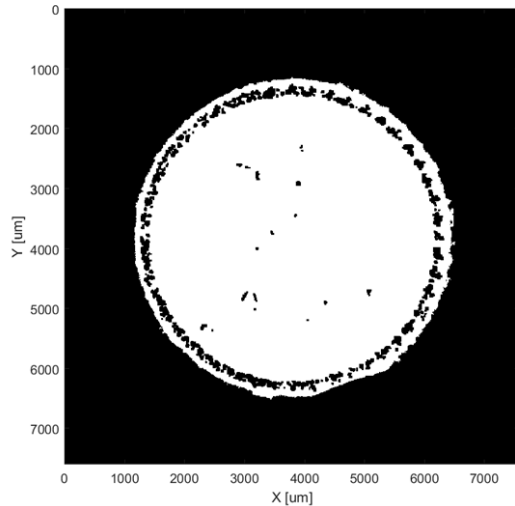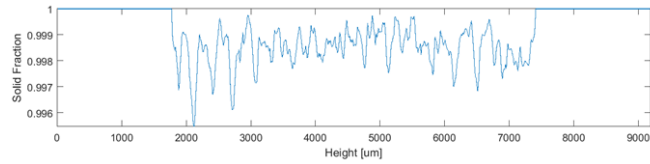
Figure H 40. Minimum intensity projection images from CT analysis. Build variables correspond to sample I.D. 40.

Parameters for sample I.D. 41

Power	375 W
Grid distance	70 μm
Exposure time	70 μm

Total solid fraction: 0.9986562
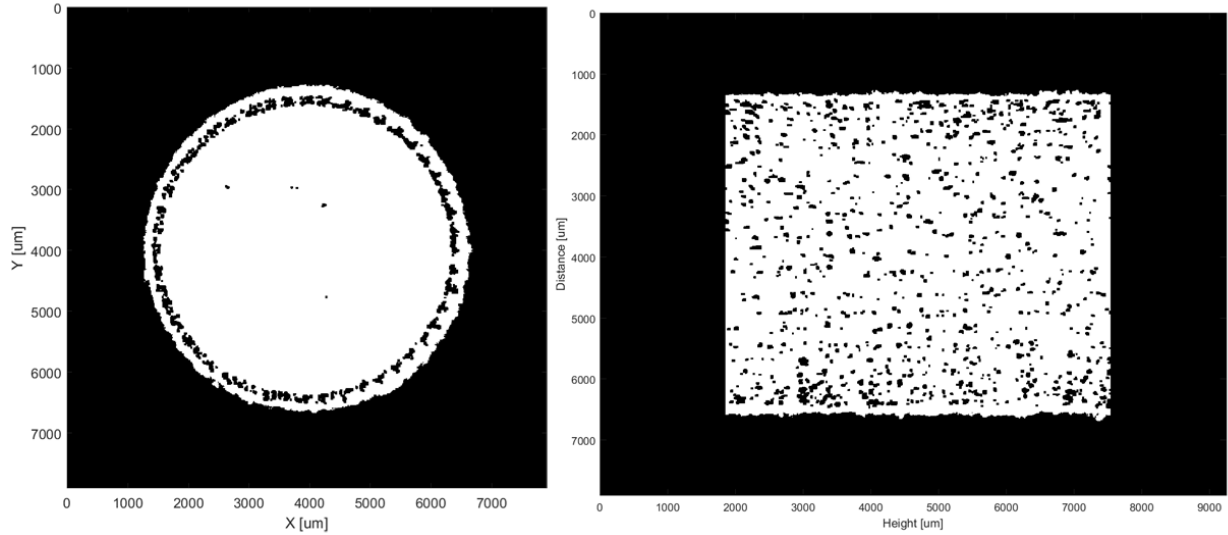
Figure H 41. Minimum intensity projection images from CT analysis. Build variables correspond to sample I.D. 41.

Parameters for sample I.D. 42

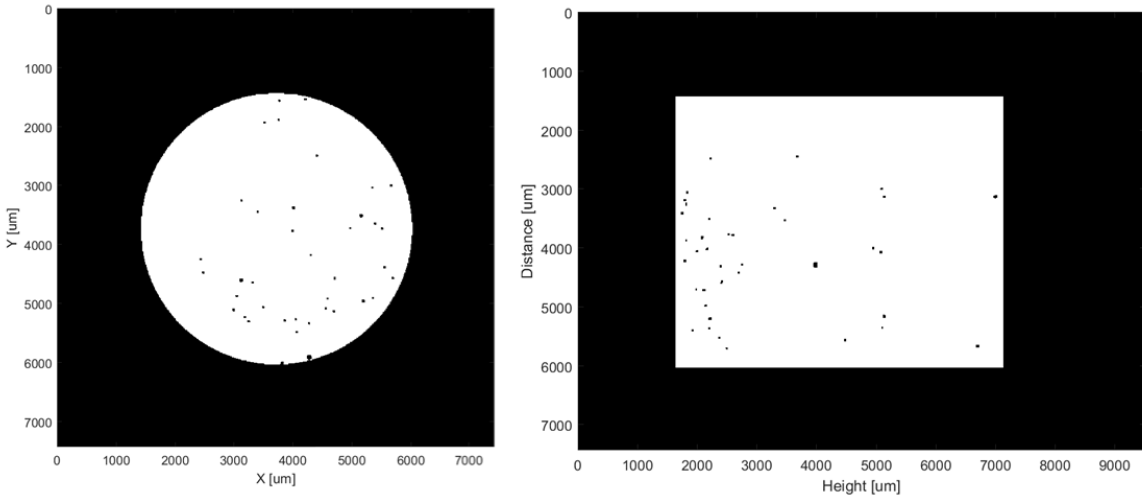| Power	375 W
Grid distance	70 μm
Exposure time	80 μm

Total solid fraction: 0.9985144

Figure H 42. Minimum intensity projection images from CT analysis. Build variables correspond to sample I.D. 42.

Parameters for sample I.D. 43

Power	375 W
Grid distance	80 μm
Exposure time	60 μm
Total solid fraction: 0.9984613	
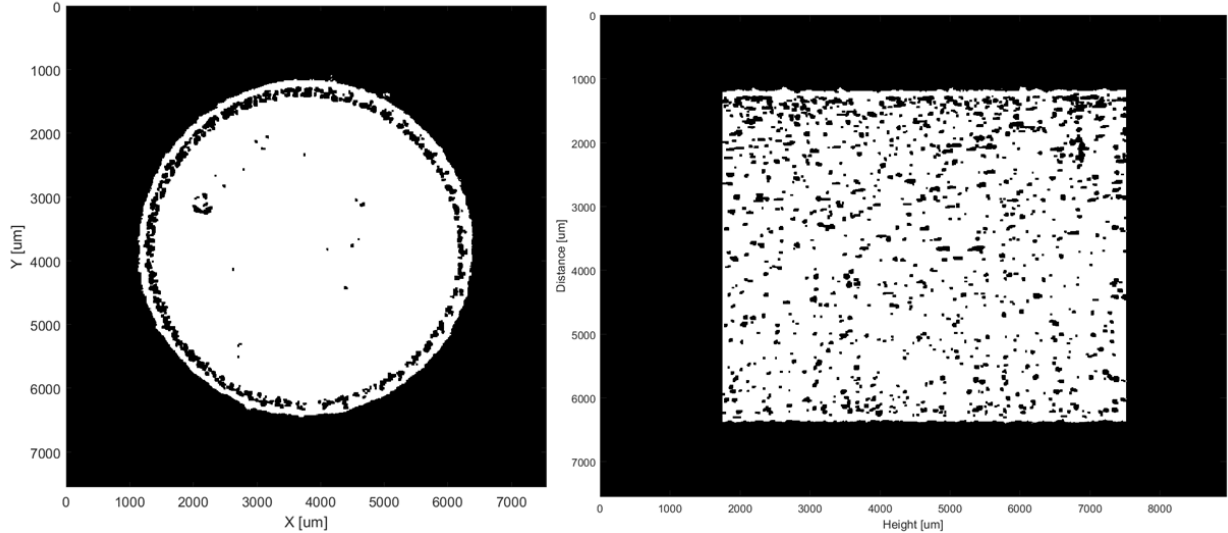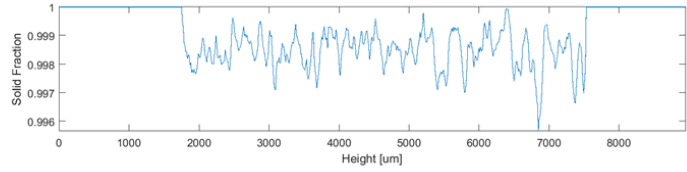
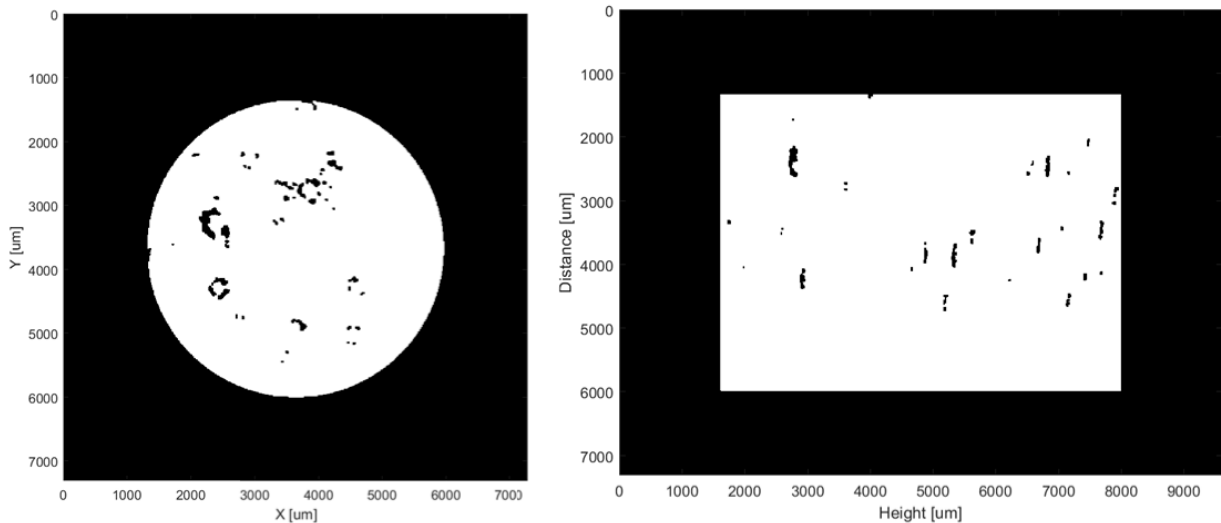**Figure H 43. Minimum intensity projection images from CT analysis. Build variables correspond to sample I.D. 43.**

Parameters for sample I.D. 44

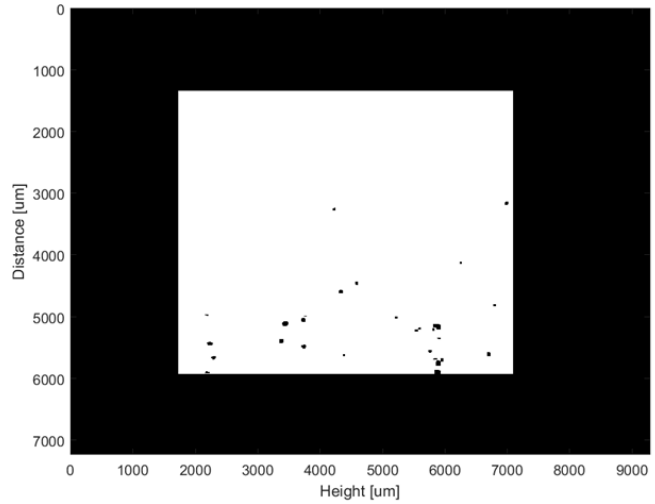| Power	375 W
Grid distance	80 μm
Exposure time	70 μm
Total solid fraction: 0.9984186	
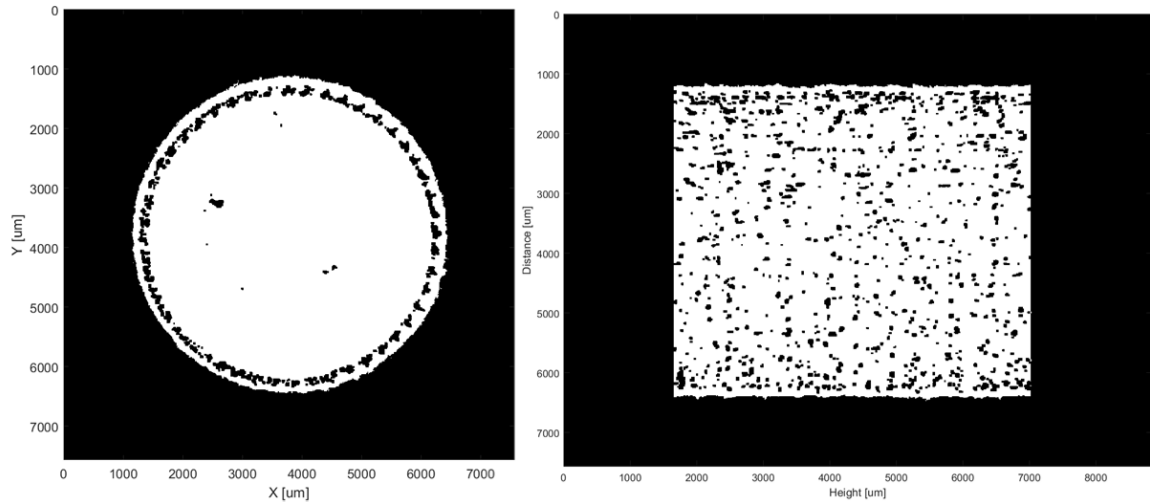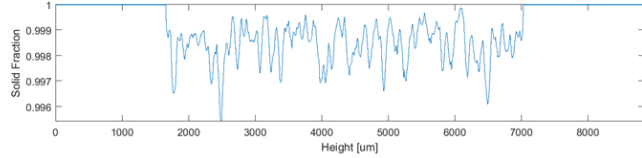
Figure H 44. Minimum intensity projection images from CT analysis. Build variables correspond to sample I.D. 44.

255

Parameters for sample I.D. 45

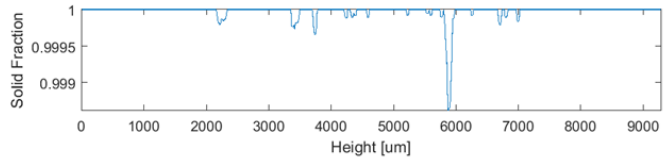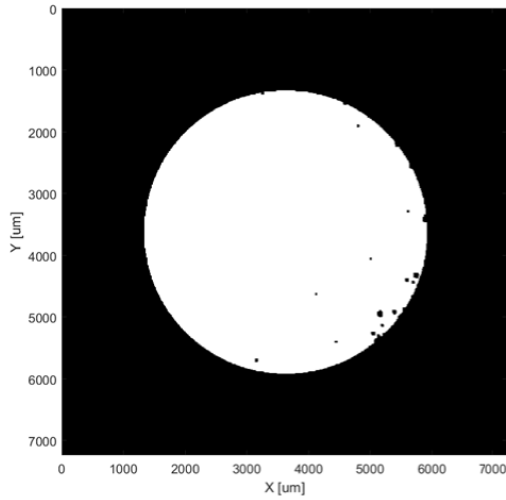| Power	375 W
Grid distance	80 μm
Exposure time	80 μm

Total solid fraction: 0.9984633

Figure H 45. Minimum intensity projection images from CT analysis. Build variables correspond to sample I.D. 45.

Parameters for sample I.D. 46

Power	400 W
Grid distance	60 μm
Exposure time	60 μm

Total solid fraction: 0.9986005
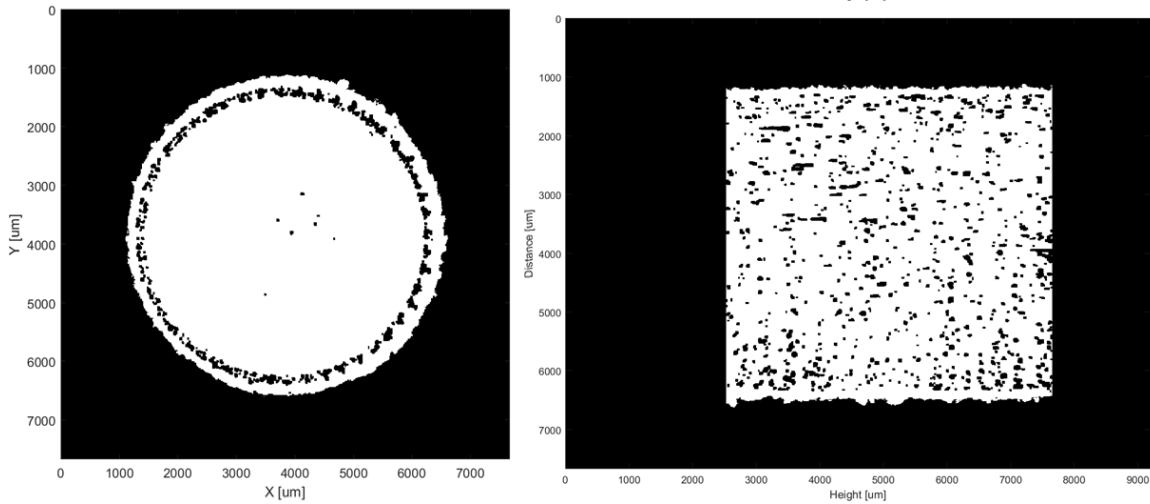
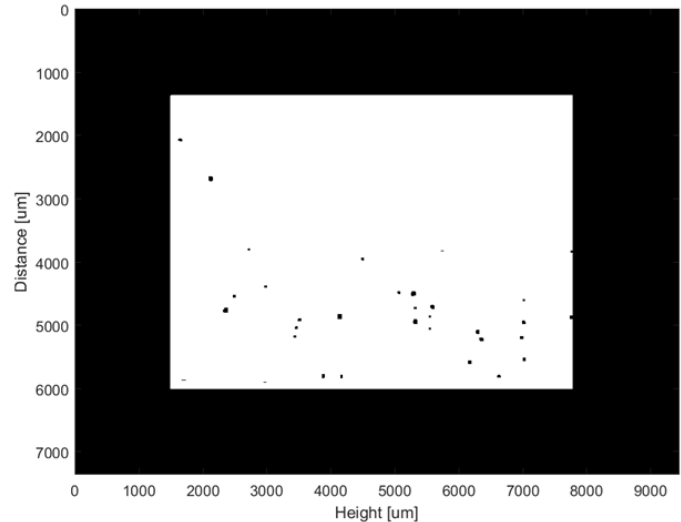**Figure H 46. Minimum intensity projection images from CT analysis. Build variables correspond to sample I.D. 46.**

Parameters for sample I.D. 47

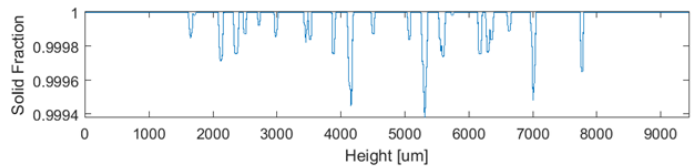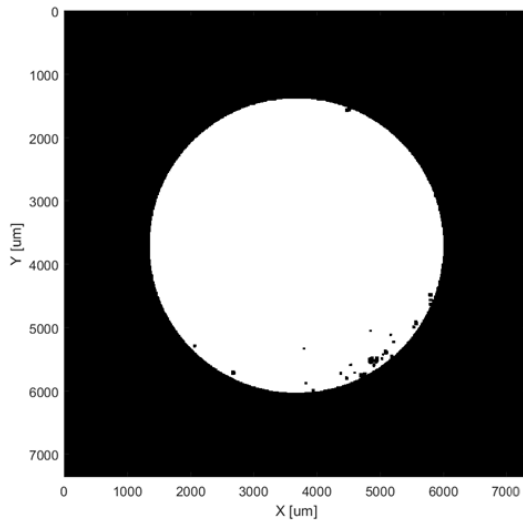| Power	400 W
Grid distance	60 μm
Exposure time	70 μm

Total solid fraction: 0.9984008

Figure H 47. Minimum intensity projection images from CT analysis. Build variables correspond to sample I.D. 47.

Parameters for sample I.D. 48

Power	400 W
Grid distance	60 μm
Exposure time	80 μm

Total solid fraction: 0.9972139

Figure H 48. Minimum intensity projection images from CT analysis. Build variables correspond to sample I.D. 48.

257

Parameters for sample I.D. 49

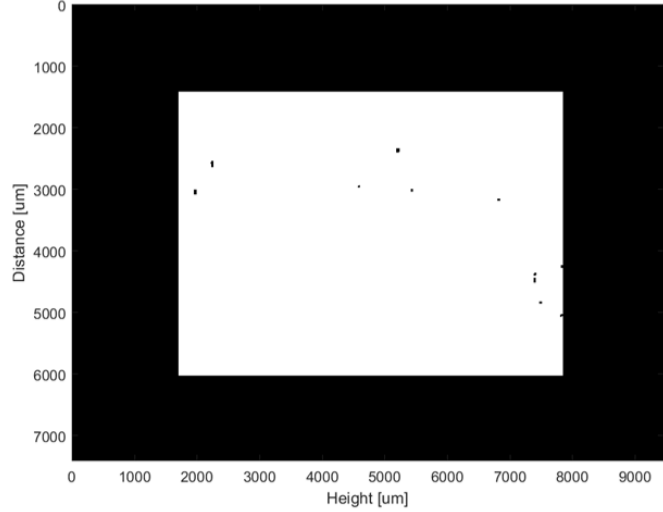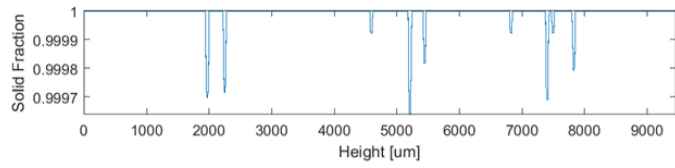| Power	400 W
Grid distance	70 μm
Exposure time	60 μm

Total solid fraction: 0.9987771

Figure H 49. Minimum intensity projection images from CT analysis. Build variables correspond to sample I.D. 49.

Parameters for sample I.D. 50

Power	400 W
Grid distance	70 μm
Exposure time	70 μm

Total solid fraction: 0.9986126

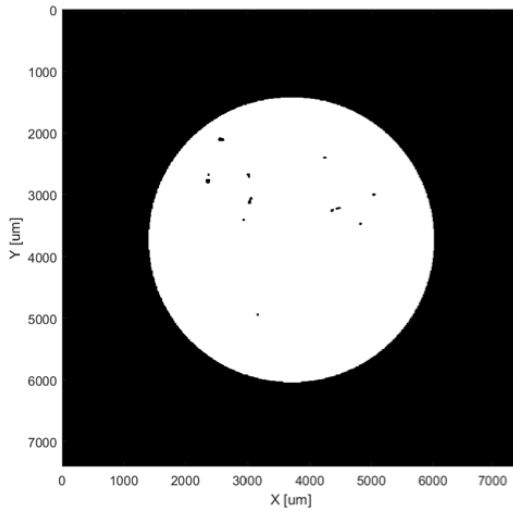**Figure H 50. Minimum intensity projection images from CT analysis. Build variables correspond to sample I.D. 50.**

Parameters for sample I.D. 51

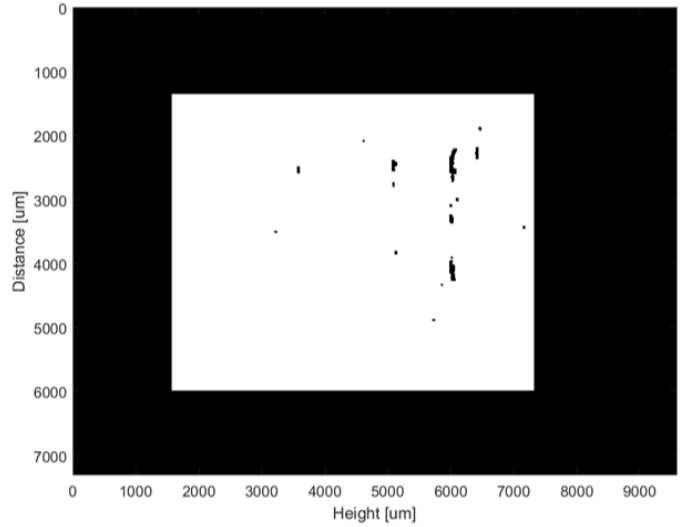| Power	400 W
Grid distance	70 μm
Exposure time	80 μm

Total solid fraction: 0.9985091

Figure H 51. Minimum intensity projection images from CT analysis. Build variables correspond to sample I.D. 51.

Parameters for sample I.D. 52

Power	400 W
Grid distance	80 μm
Exposure time	60 μm

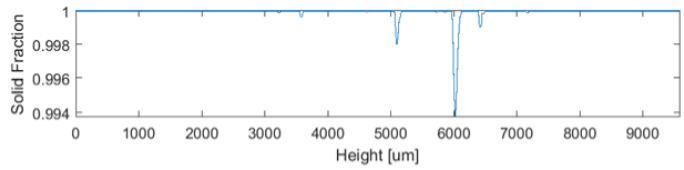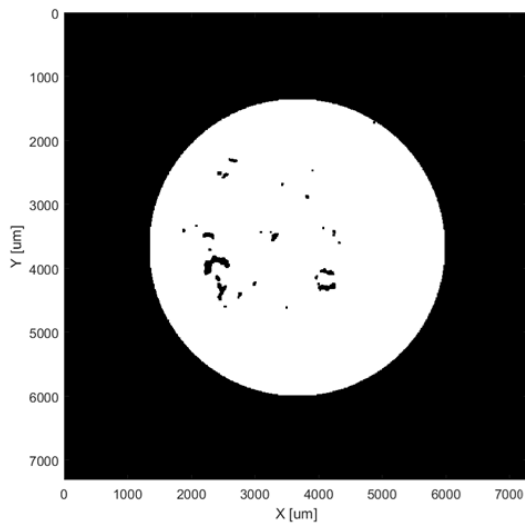Total solid fraction: 0.9987431

Figure H 52. Minimum intensity projection images from CT analysis. Build variables correspond to sample I.D. 52.

259

Parameters for sample I.D. 53

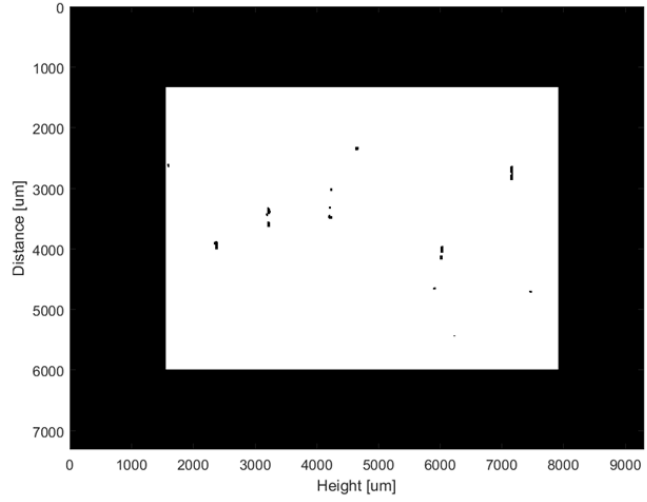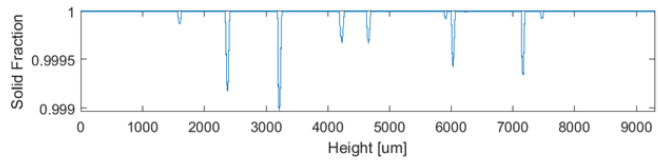| Power	400 W
Grid distance	80 μm
Exposure time	70 μm

Total solid fraction: 0.9982106

Figure H 53. Minimum intensity projection images from CT analysis. Build variables correspond to sample I.D. 53.

Parameters for sample I.D. 54

Power	400 W
Grid distance	80 μm
Exposure time	80 μm

Total solid fraction: 0.9981978

Figure H 54. Minimum intensity projection images from CT analysis. Build variables correspond to sample I.D. 54.

260

Appendix I:

CT Analysis Results (Border Regions Removed) for Chapter 4

Parameters for sample I.D. 1

Power	250 W
Grid distance	60 μm
Exposure time	60 μm

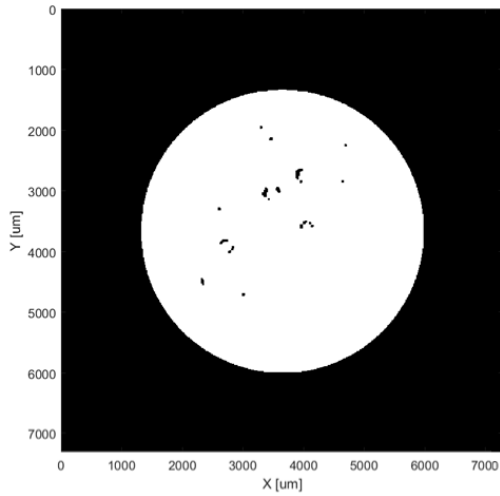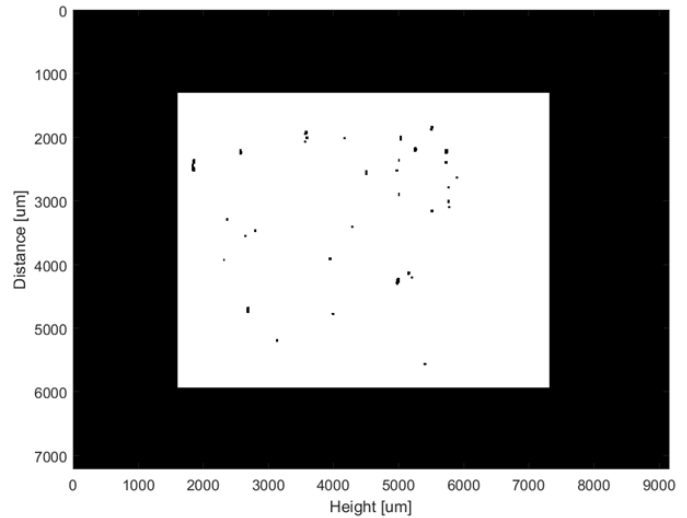Total solid fraction: 0.9997971
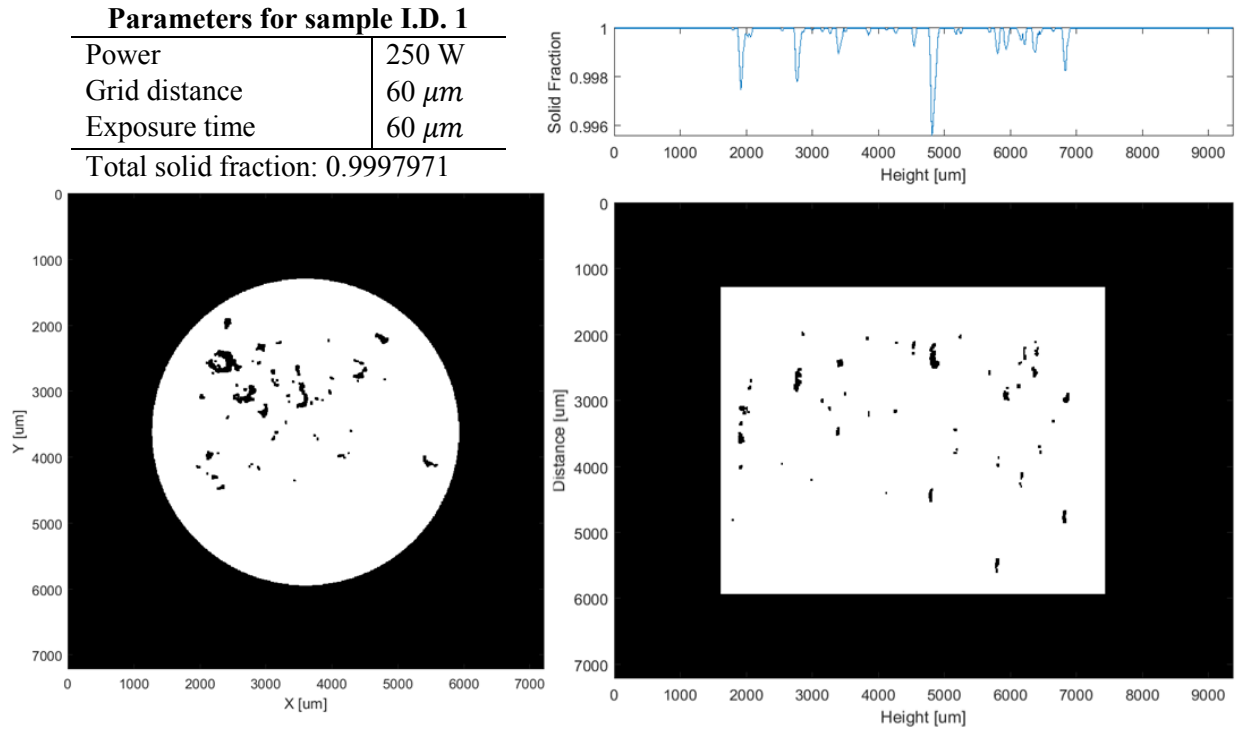
Figure I 1. Minimum intensity projection images from CT analysis. Build variables correspond to sample I.D. 1.

Parameters for sample I.D. 2

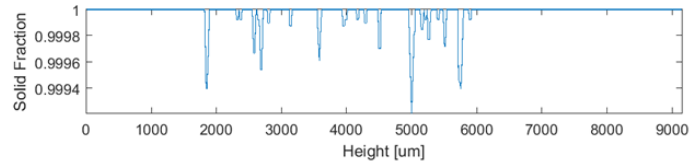| Power	250 W
Grid distance	60 μm
Exposure time	70 μm
Total solid fraction: 0.9999603	
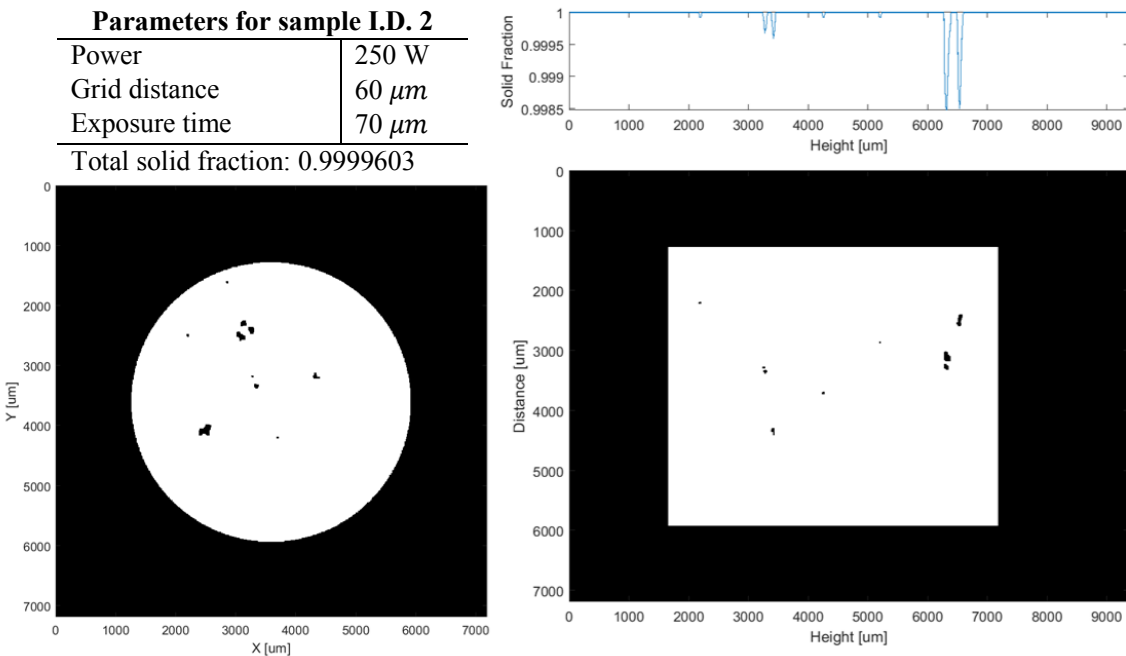
Figure I 2. Minimum intensity projection images from CT analysis. Build variables correspond to sample I.D. 2.

Parameters for sample I.D. 3

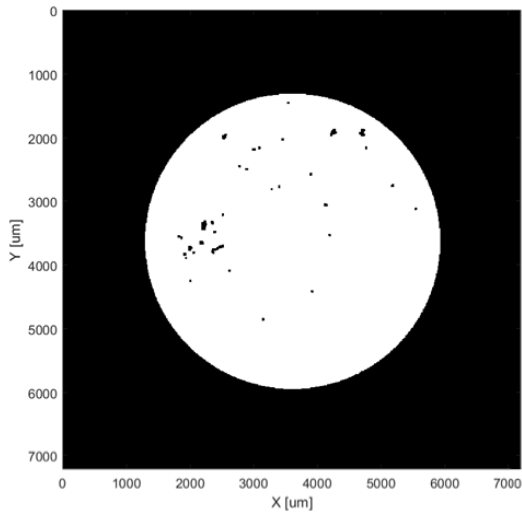| Power	250 W
Grid distance	60 μm
Exposure time	80 μm
Total solid fraction: 0.9999636	

Figure I 3. Minimum intensity projection images from CT analysis. Build variables correspond to sample I.D. 3.

262

Parameters for sample I.D. 4

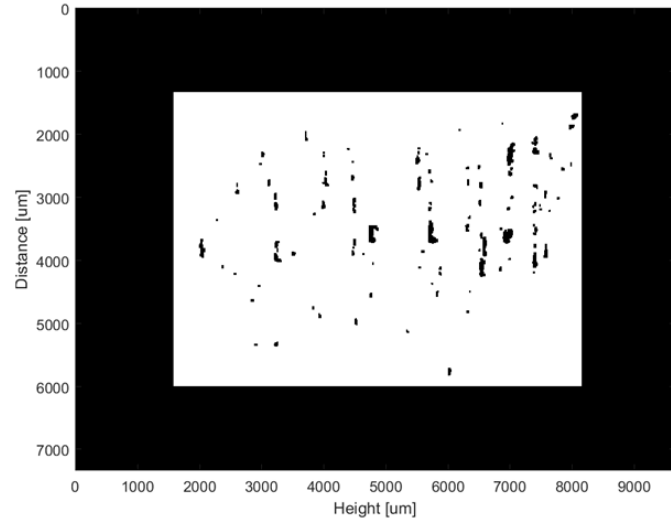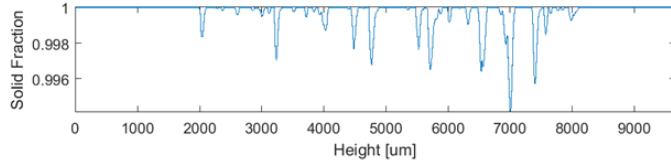| Power	250 W
Grid distance	70 μm
Exposure time	60 μm

Total solid fraction: 0.9985034

Figure I 4. Minimum intensity projection images from CT analysis. Build variables correspond to sample I.D. 4.

Parameters for sample I.D. 5

Power	250 W
Grid distance	70 μm
Exposure time	70 μm

Total solid fraction: 0.9995131

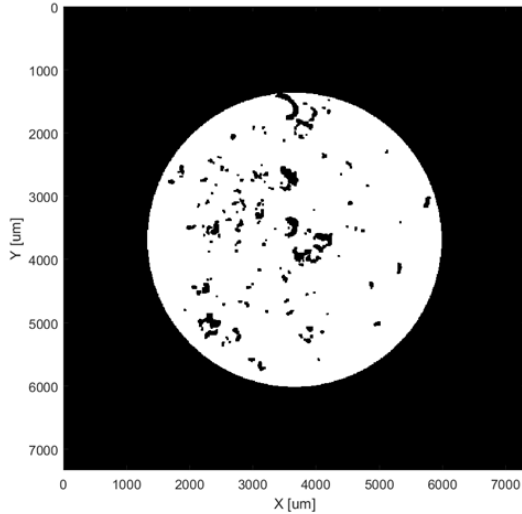**Figure I 5. Minimum intensity projection images from CT analysis. Build variables correspond to sample I.D. 5.**

263

Parameters for sample I.D. 6

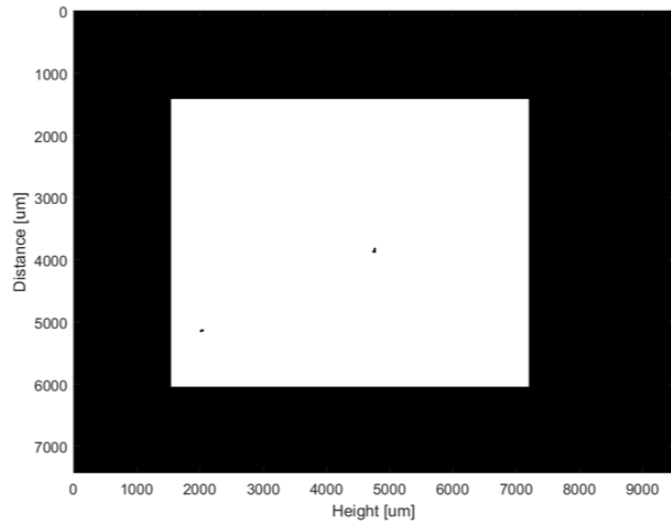| Power	250 W
Grid distance	70 μm
Exposure time	80 μm

Total solid fraction: 0.9999926

Figure I 6. Minimum intensity projection images from CT analysis. Build variables correspond to sample I.D. 6.

Parameters for sample I.D. 7

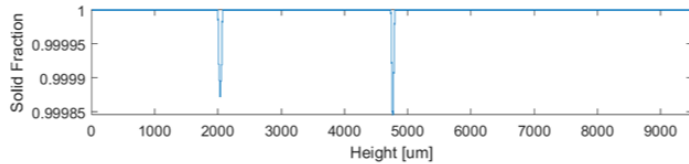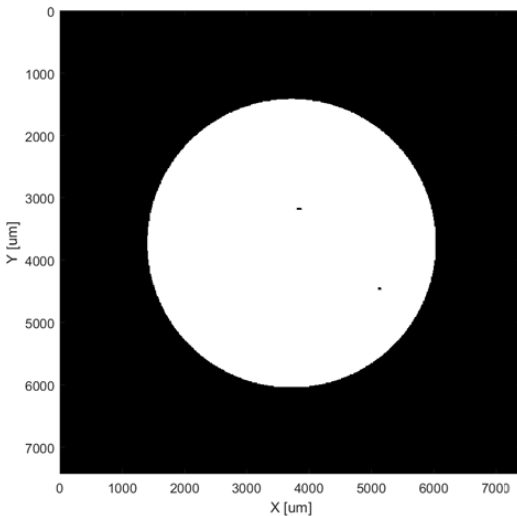| Power	250 W
Grid distance	80 μm
Exposure time	60 μm

Total solid fraction: 0.9998335
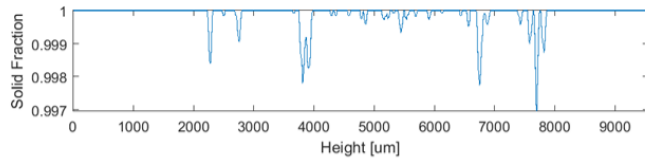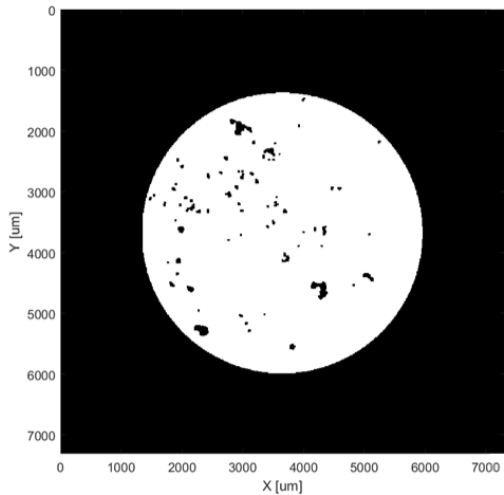
Figure I 7. Minimum intensity projection images from CT analysis. Build variables correspond to sample I.D. 7.

264

Parameters for sample I.D. 8

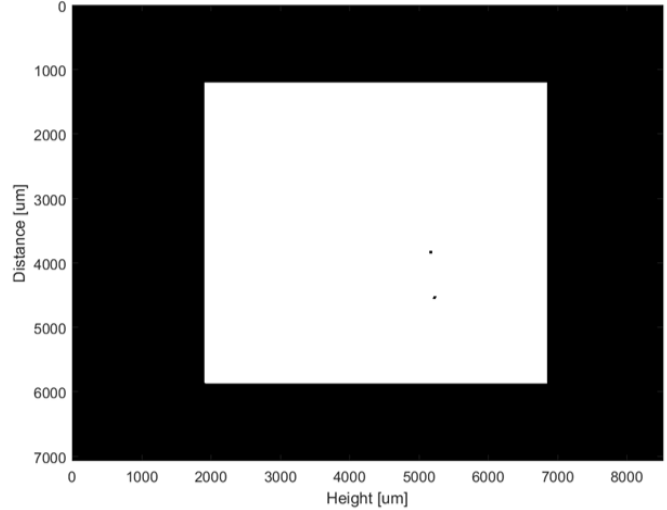| Power	250 W
Grid distance	80 μm
Exposure time	70 μm

Total solid fraction: 0.9997209
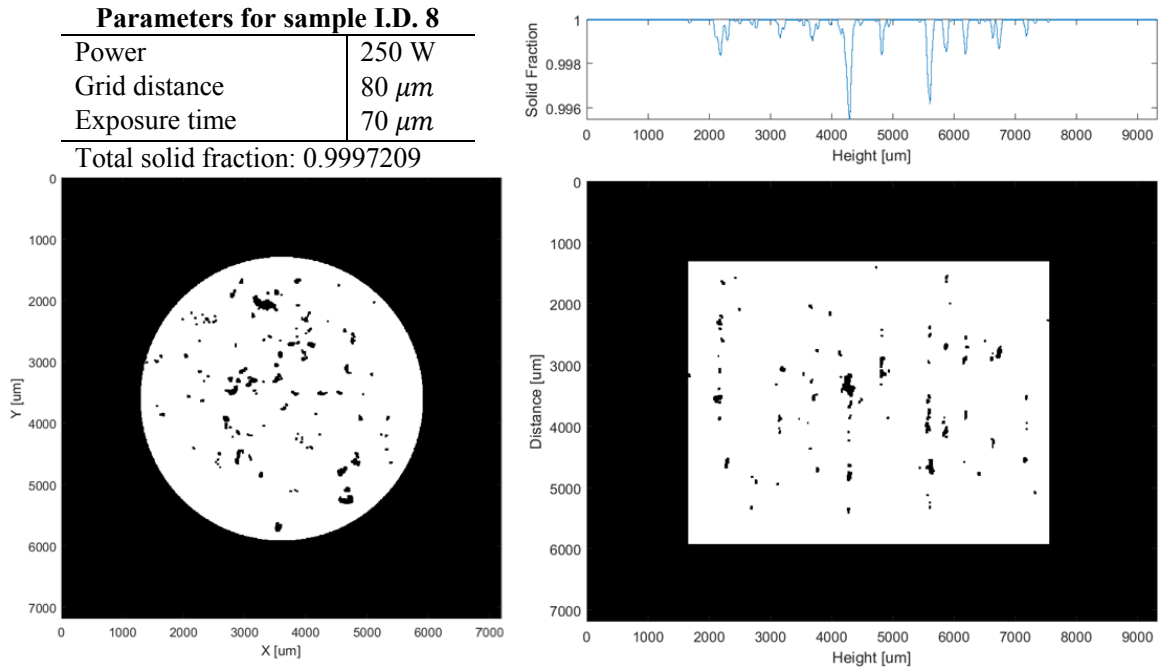
Figure I 8. Minimum intensity projection images from CT analysis. Build variables correspond to sample I.D. 8.

Parameters for sample I.D. 9

Power	250 W
Grid distance	80 μm
Exposure time	80 μm

Total solid fraction: 0.9998985

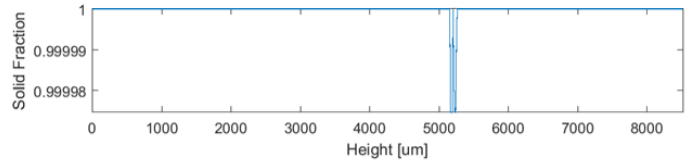**Figure I 9. Minimum intensity projection images from CT analysis. Build variables correspond to sample I.D. 9.**

Parameters for sample I.D. 10

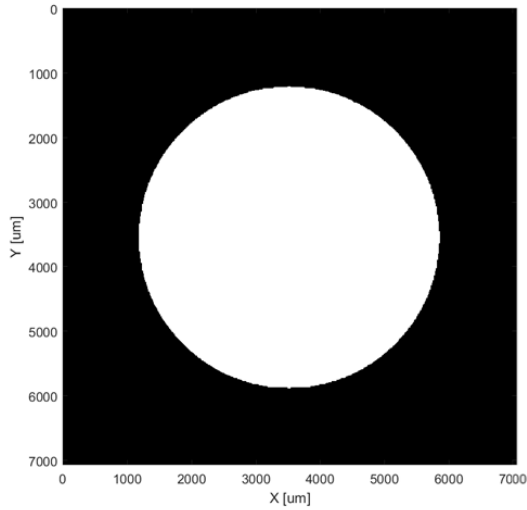| Power	275 W
Grid distance	60 μm
Exposure time	60 μm

Total solid fraction: 0.9998741

Figure I 10. Minimum intensity projection images from CT analysis. Build variables correspond to sample I.D. 10.

Parameters for sample I.D. 11

Power	275 W
Grid distance	60 μm
Exposure time	70 μm

Total solid fraction: 0.9999978

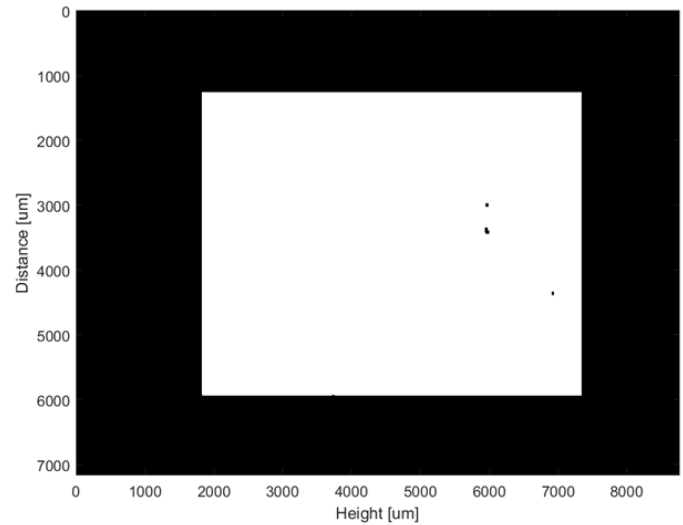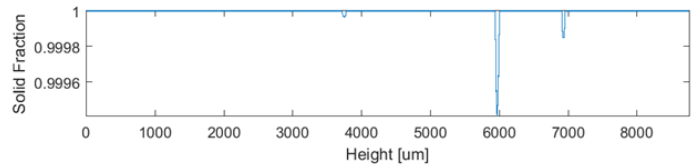**Figure I 11. Minimum intensity projection images from CT analysis. Build variables correspond to sample I.D. 11.**

Parameters for sample I.D. 12

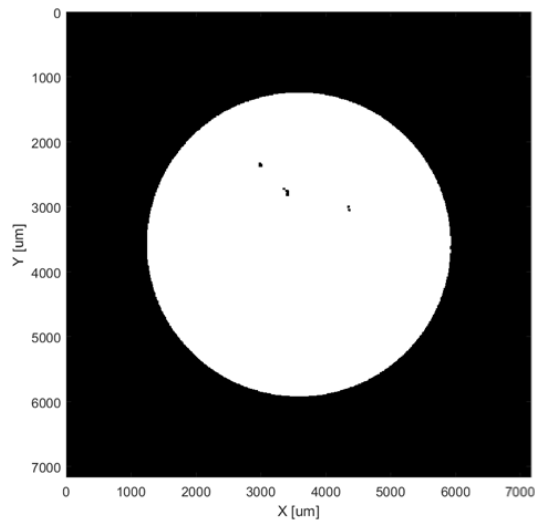| Power	275 W
Grid distance	60 μm
Exposure time	80 μm

Total solid fraction: 0.9999892

Figure I 12. Minimum intensity projection images from CT analysis. Build variables correspond to sample I.D. 12.

Parameters for sample I.D. 13

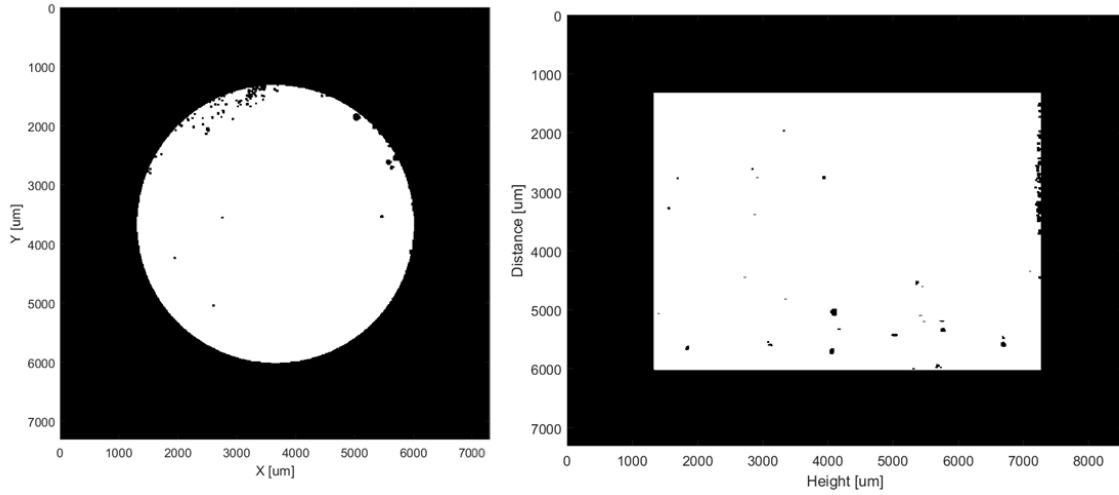| Power	275 W
Grid distance	70 μm
Exposure time	60 μm

Total solid fraction: 0.9999953

Figure I 13. Minimum intensity projection images from CT analysis. Build variables correspond to sample I.D. 13.

Parameters for sample I.D. 14

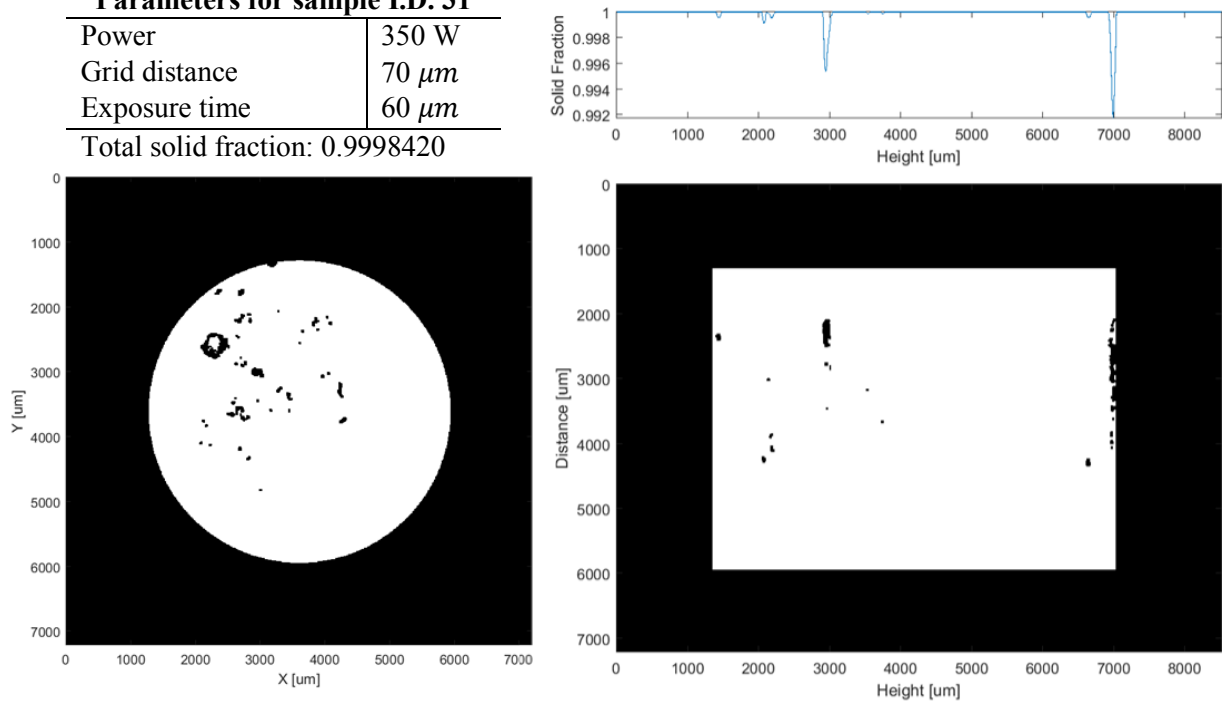| Power	275 W
Grid distance	70 μm
Exposure time	70 μm

Total solid fraction: 0.9999552

Figure I 14. Minimum intensity projection images from CT analysis. Build variables correspond to sample I.D. 14.

Parameters for sample I.D. 15

Power	275 W
Grid distance	70 μm
Exposure time	80 μm

Total solid fraction: 0.9999641

Figure I 15. Minimum intensity projection images from CT analysis. Build variables correspond to sample I.D. 15.

Parameters for sample I.D. 16

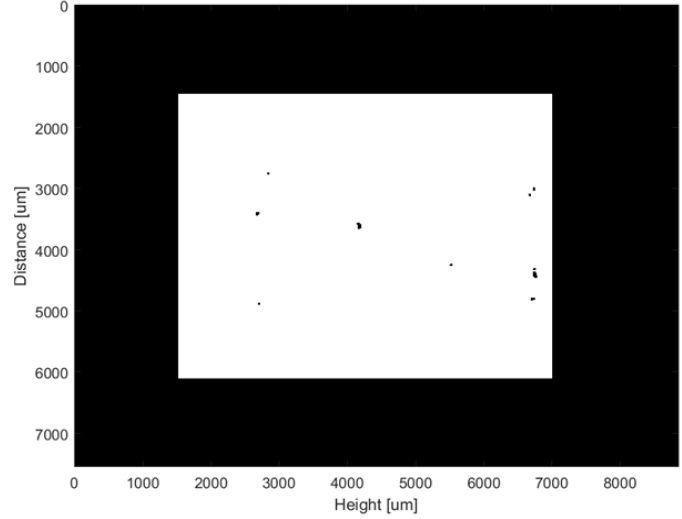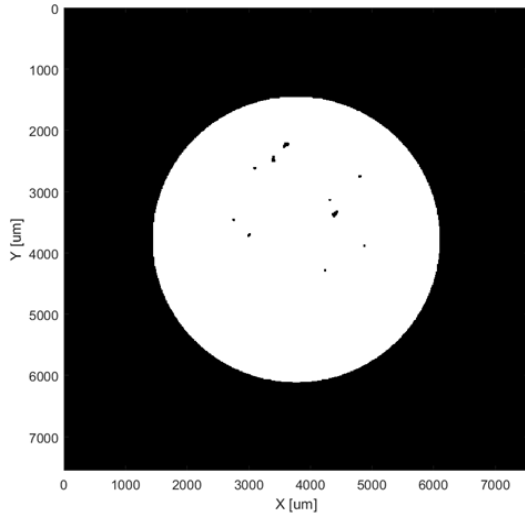| Power	275 W
Grid distance	80 μm
Exposure time	60 μm

Total solid fraction: 0.9999667

Figure I 16. Minimum intensity projection images from CT analysis. Build variables correspond to sample I.D. 16.

Parameters for sample I.D. 17

Power	275 W
Grid distance	80 μm
Exposure time	70 μm

Total solid fraction: 0.9998933

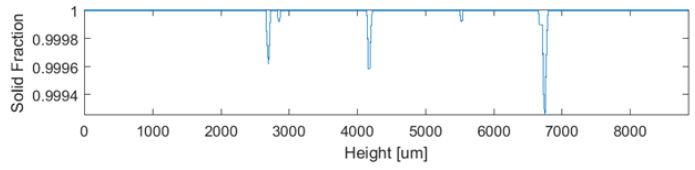**Figure I 17. Minimum intensity projection images from CT analysis. Build variables correspond to sample I.D. 17.**

Parameters for sample I.D. 18

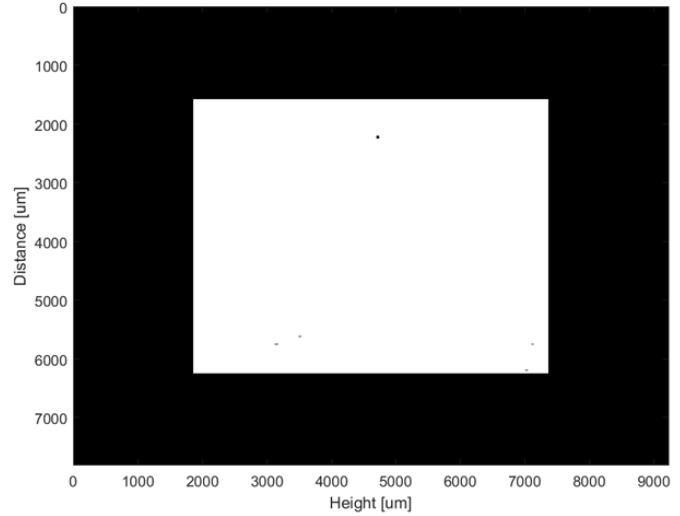| Power	275 W
Grid distance	80 μm
Exposure time	80 μm

Total solid fraction: 0.9999711

Figure I 18. Minimum intensity projection images from CT analysis. Build variables correspond to sample I.D. 18.

Parameters for sample I.D. 19

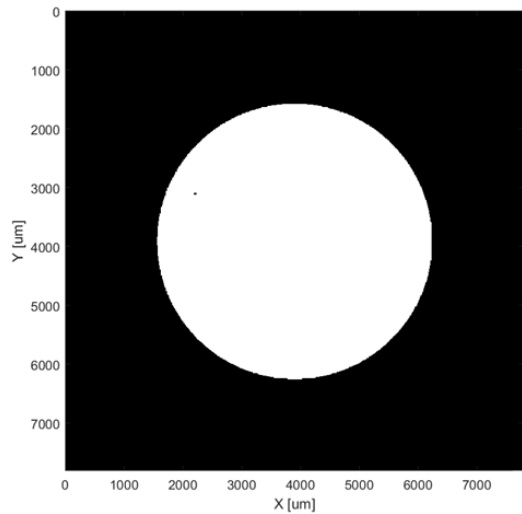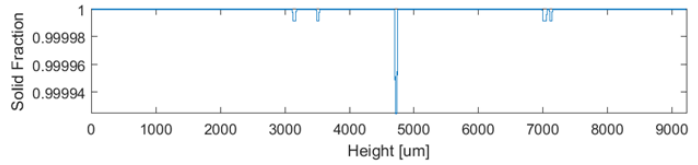| Power	300 W
Grid distance	60 μm
Exposure time	60 μm

Total solid fraction: 0.9998240

Figure I 19. Minimum intensity projection images from CT analysis. Build variables correspond to sample I.D. 19.

270

Parameters for sample I.D. 20

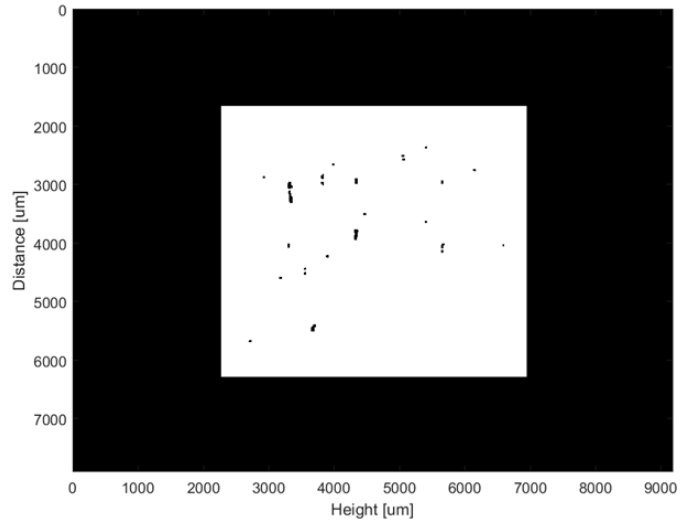| Power	300 W
Grid distance	60 μm
Exposure time	70 μm

Total solid fraction: 0.9999555

Figure I 20. Minimum intensity projection images from CT analysis. Build variables correspond to sample I.D. 20.

Parameters for sample I.D. 21

Power	300 W
Grid distance	60 μm
Exposure time	80 μm

Total solid fraction: 0.9999587

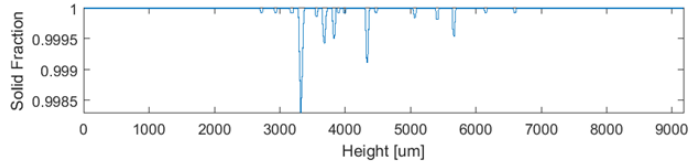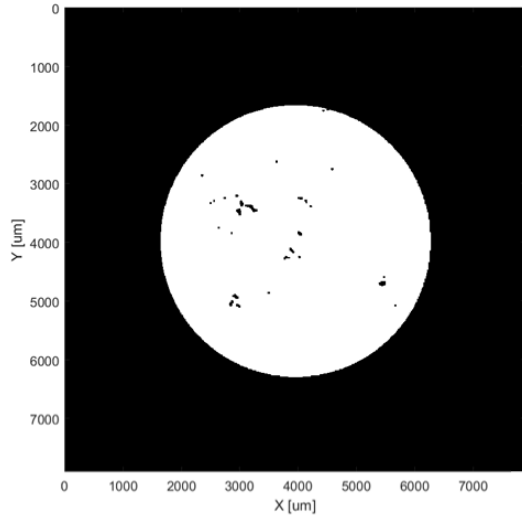**Figure I 21. Minimum intensity projection images from CT analysis. Build variables correspond to sample I.D. 21.**

Parameters for sample I.D. 22

Power	300 W
Grid distance	70 μm
Exposure time	60 μm

Total solid fraction: 0.9999881

Figure I 22. Minimum intensity projection images from CT analysis. Build variables correspond to sample I.D. 22.

Parameters for sample I.D. 23

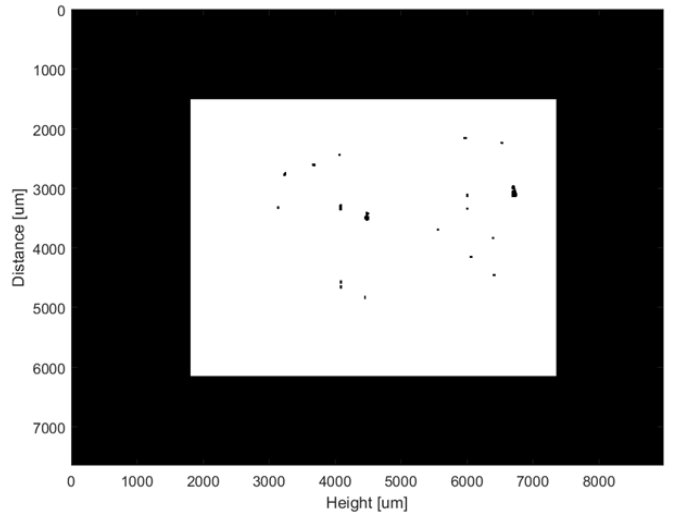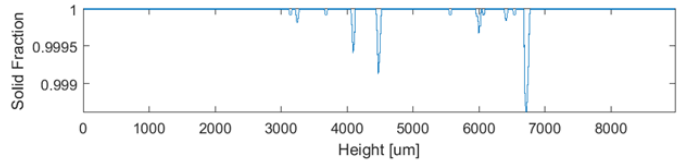| Power	300 W
Grid distance	70 μm
Exposure time	70 μm

Total solid fraction: 0.9998960

Figure I 23. Minimum intensity projection images from CT analysis. Build variables correspond to sample I.D. 23.

272

Parameters for sample I.D. 24

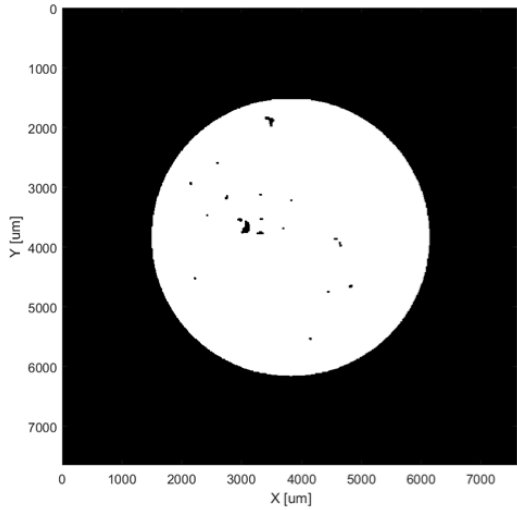| Power	300 W
Grid distance	70 μm
Exposure time	80 μm

Total solid fraction: 0.9999732

Figure I 24. Minimum intensity projection images from CT analysis. Build variables correspond to sample I.D. 24.

Parameters for sample I.D. 25

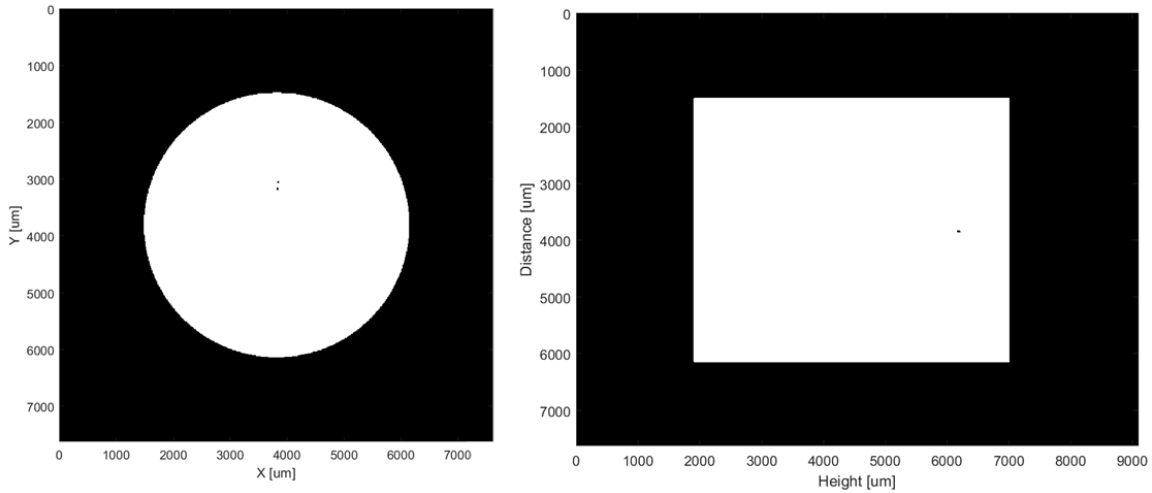| Power	300 W
Grid distance	80 μm
Exposure time	60 μm

Total solid fraction: 0.9999610

Figure I 25. Minimum intensity projection images from CT analysis. Build variables correspond to sample I.D. 25.

273

Parameters for sample I.D. 26

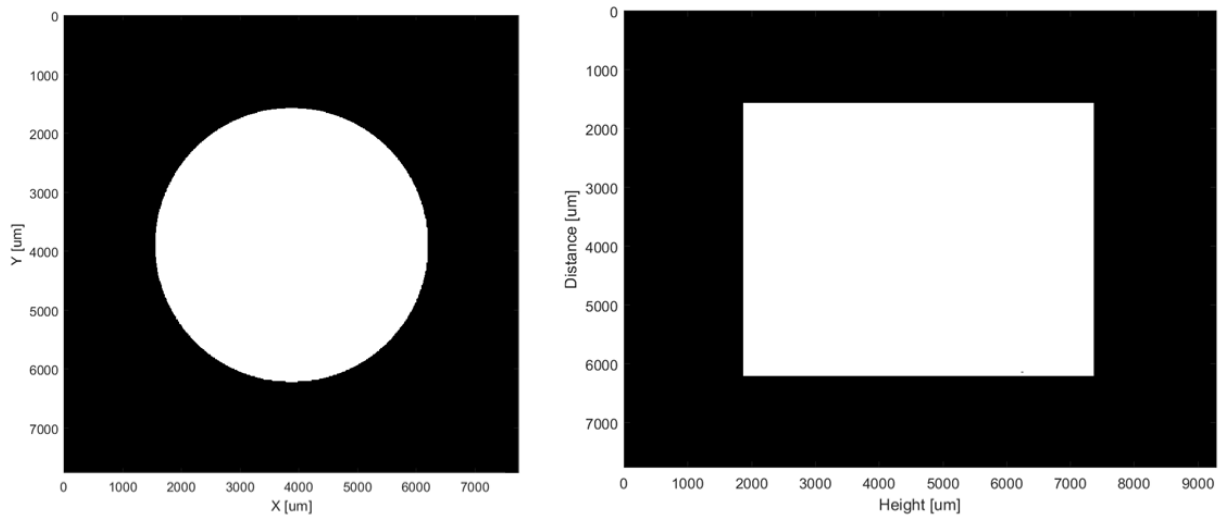| Power	300 W
Grid distance	80 μm
Exposure time	70 μm

Total solid fraction: 0.9996034

Figure I 26. Minimum intensity projection images from CT analysis. Build variables correspond to sample I.D. 26.

Parameters for sample I.D. 27

Power	300 W
Grid distance	80 μm
Exposure time	80 μm

Total solid fraction: 0.9999980

Figure I 27. Minimum intensity projection images from CT analysis. Build variables correspond to sample I.D. 27.

274

Parameters for sample I.D. 28

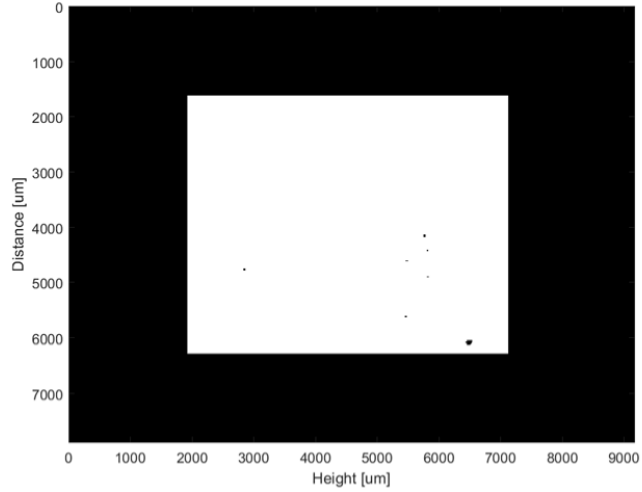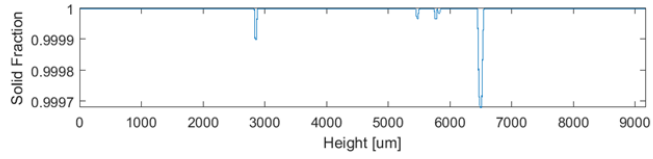| Power	350 W
Grid distance	60 μm
Exposure time	60 μm

Total solid fraction: 0.9999996

Figure I 28. Minimum intensity projection images from CT analysis. Build variables correspond to sample I.D. 28.

Parameters for sample I.D. 29

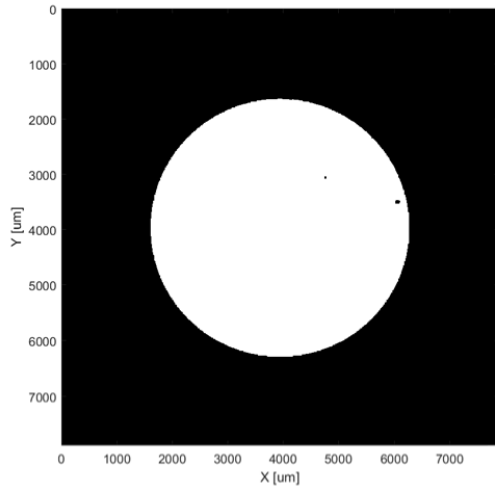| Power	350 W
Grid distance	60 μm
Exposure time	70 μm

Total solid fraction: 0.9999945

Figure I 29. Minimum intensity projection images from CT analysis. Build variables correspond to sample I.D. 29.

Parameters for sample I.D. 30

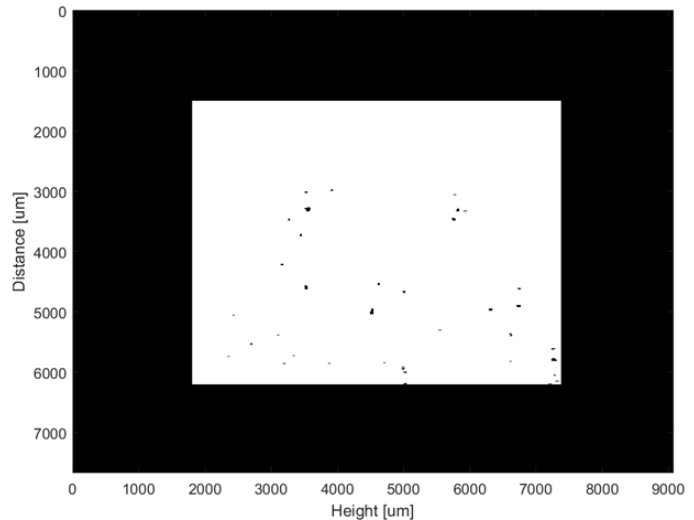| Power	350 W
Grid distance	60 μm
Exposure time	80 μm

Total solid fraction: 0.9999241

Figure I 30. Minimum intensity projection images from CT analysis. Build variables correspond to sample I.D. 30.

Parameters for sample I.D. 31

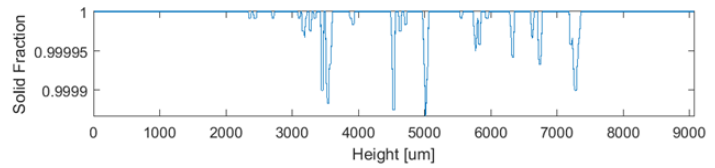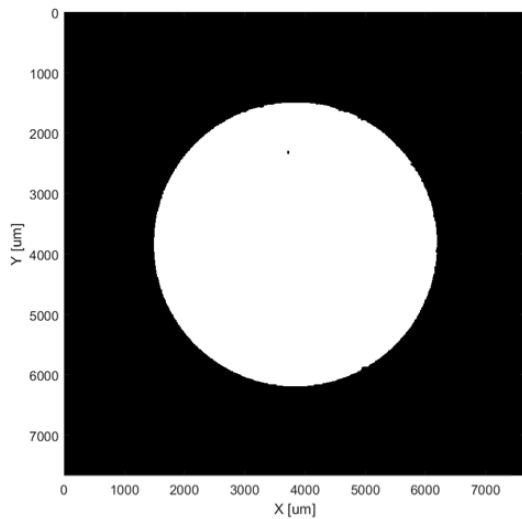| Power	350 W
Grid distance	70 μm
Exposure time	60 μm

Total solid fraction: 0.9998420

Figure I 31. Minimum intensity projection images from CT analysis. Build variables correspond to sample I.D. 31.

276

Parameters for sample I.D. 32

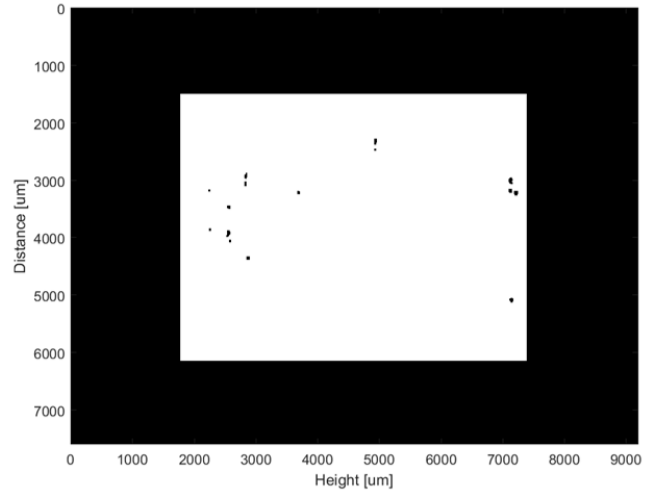| Power	350 W
Grid distance	70 μm
Exposure time	70 μm

Total solid fraction: 0.9999856

Figure I 32. Minimum intensity projection images from CT analysis. Build variables correspond to sample I.D. 32.

Parameters for sample I.D. 33

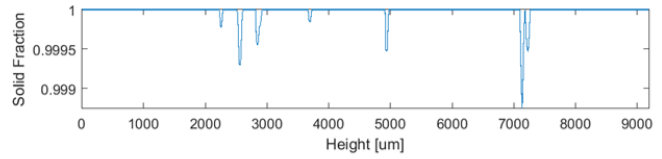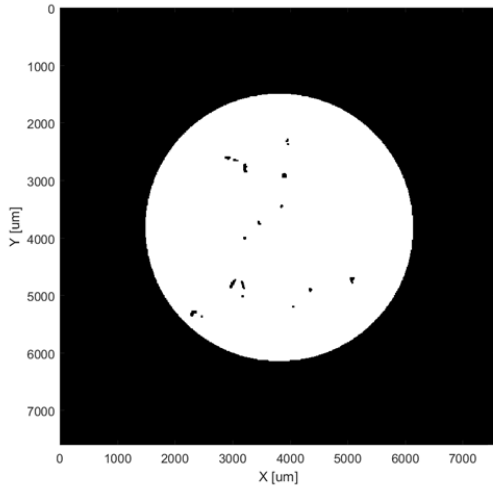| Power	350 W
Grid distance	70 μm
Exposure time	80 μm

Total solid fraction: 0.9999992

Figure I 33. Minimum intensity projection images from CT analysis. Build variables correspond to sample I.D. 33.

Parameters for sample I.D. 34

Power	350 W
Grid distance	80 μm
Exposure time	60 μm

Total solid fraction: 0.9999544

Figure I 34. Minimum intensity projection images from CT analysis. Build variables correspond to sample I.D. 34.

Parameters for sample I.D. 35

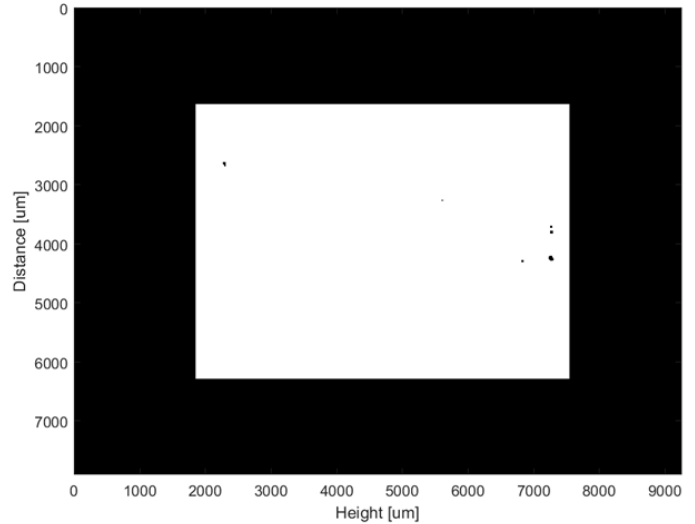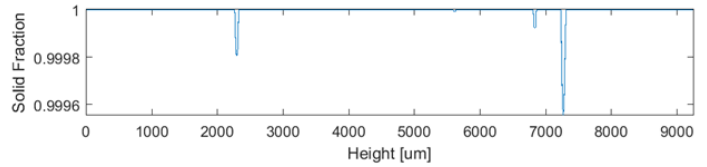| Power	350 W
Grid distance	80 μm
Exposure time	70 μm

Total solid fraction: 0.9999676

Figure I 35. Minimum intensity projection images from CT analysis. Build variables correspond to sample I.D. 35.

Parameters for sample I.D. 36

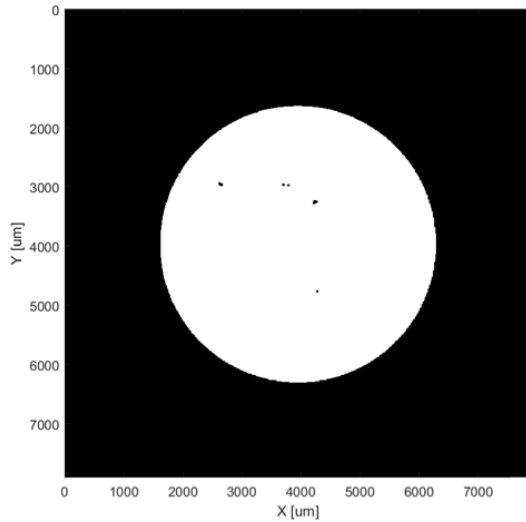| Power	350 W
Grid distance	80 μm
Exposure time	80 μm

Total solid fraction: 0.9999989

Figure I 36. Minimum intensity projection images from CT analysis. Build variables correspond to sample I.D. 36.

Parameters for sample I.D. 37

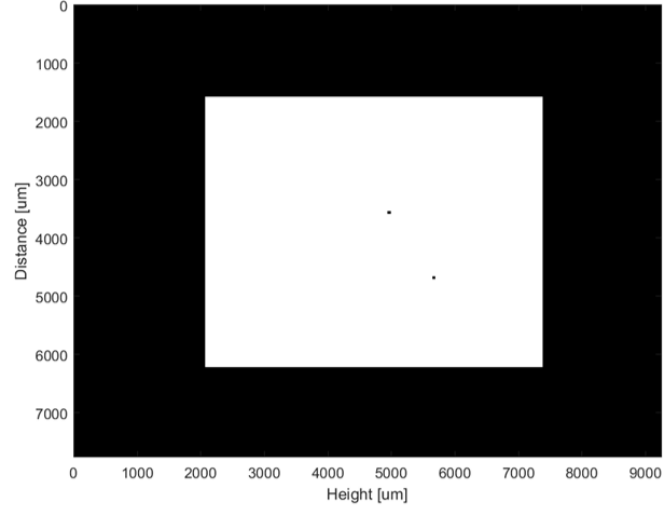| Power	375 W
Grid distance	60 μm
Exposure time	60 μm

Total solid fraction: 0.9999999

Figure I 37. Minimum intensity projection images from CT analysis. Build variables correspond to sample I.D. 37.

Parameters for sample I.D. 38

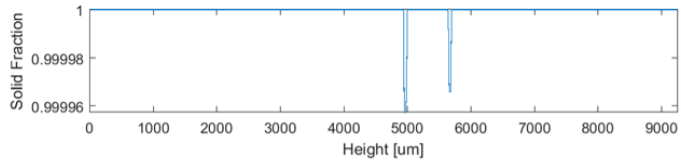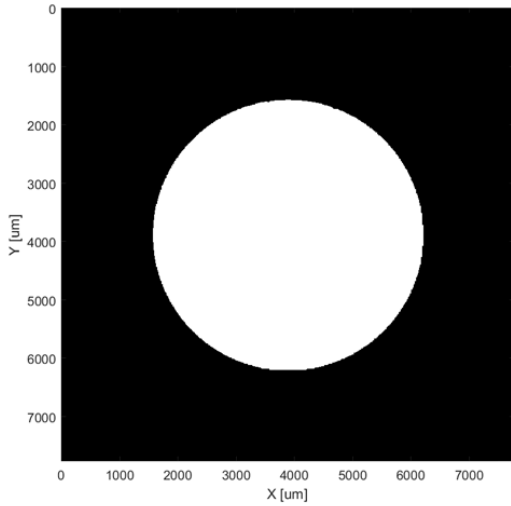| Power	375 W
Grid distance	$60 \ \mu m$
Exposure time	$70 \ \mu m$

Total solid fraction: 0.9999945

Figure I 38. Minimum intensity projection images from CT analysis. Build variables correspond to sample I.D. 38.

Parameters for sample I.D. 39

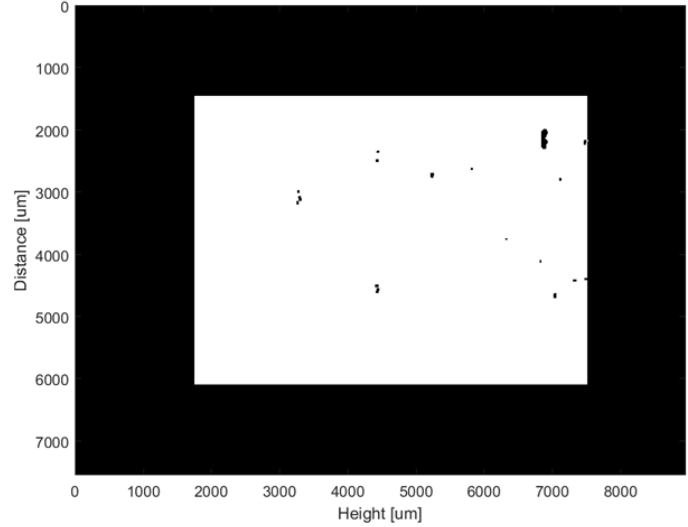| Power	375 W
Grid distance	$60 \ \mu m$
Exposure time	$80 \ \mu m$

Total solid fraction: 0.9999908

Figure I 39. Minimum intensity projection images from CT analysis. Build variables correspond to sample I.D. 39.

Parameters for sample I.D. 40

Power	375 W
Grid distance	70 μm
Exposure time	60 μm

Total solid fraction: 0.9999685

Figure I 40. Minimum intensity projection images from CT analysis. Build variables correspond to sample I.D. 40.

Parameters for sample I.D. 41

Power	375 W
Grid distance	70 μm
Exposure time	70 μm

Total solid fraction: 0.9999944

Figure I 41. Minimum intensity projection images from CT analysis. Build variables correspond to sample I.D. 41.

Parameters for sample I.D. 42

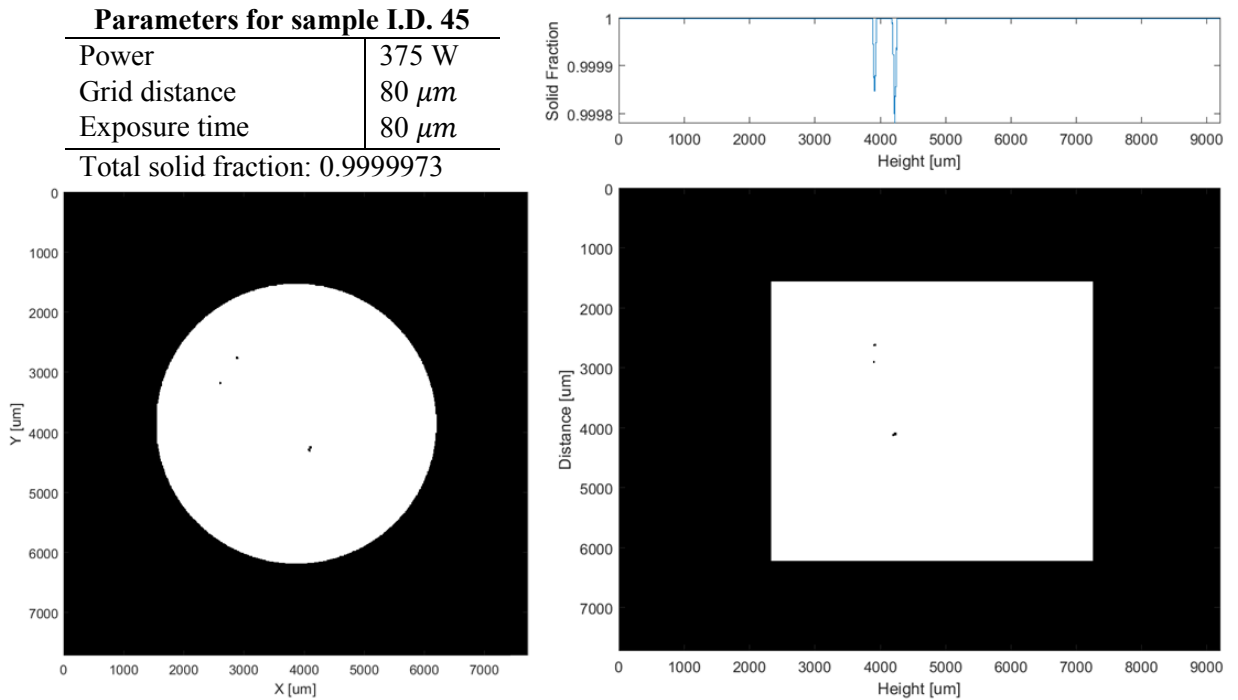| Power	375 W
Grid distance	70 μm
Exposure time	80 μm

Total solid fraction: 0.9999994

Figure I 42. Minimum intensity projection images from CT analysis. Build variables correspond to sample I.D. 42.

Parameters for sample I.D. 43

Power	375 W
Grid distance	80 μm
Exposure time	60 μm

Total solid fraction: 0.9999608
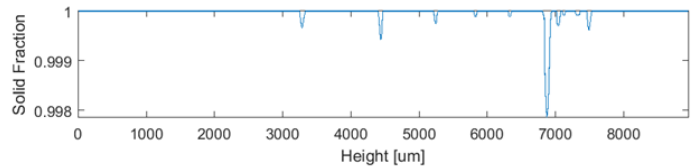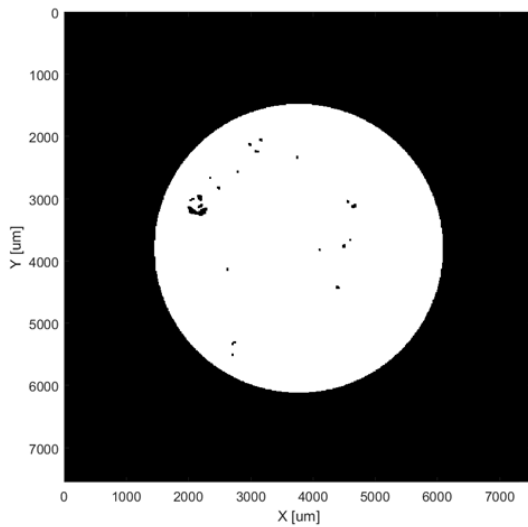
Figure I 43. Minimum intensity projection images from CT analysis. Build variables correspond to sample I.D. 43.

Parameters for sample I.D. 44

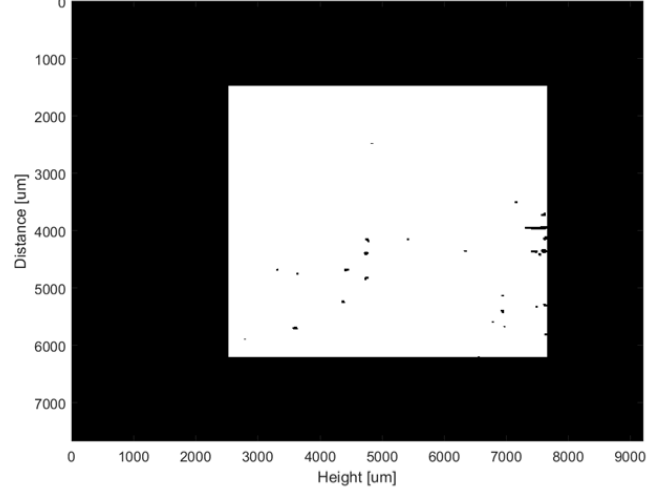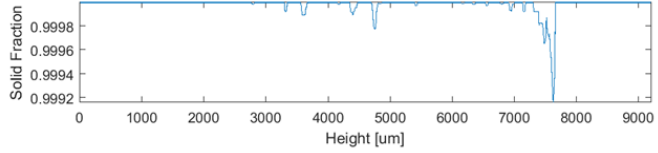| Power	375 W
Grid distance	80 μm
Exposure time	70 μm

Total solid fraction: 0.9999742
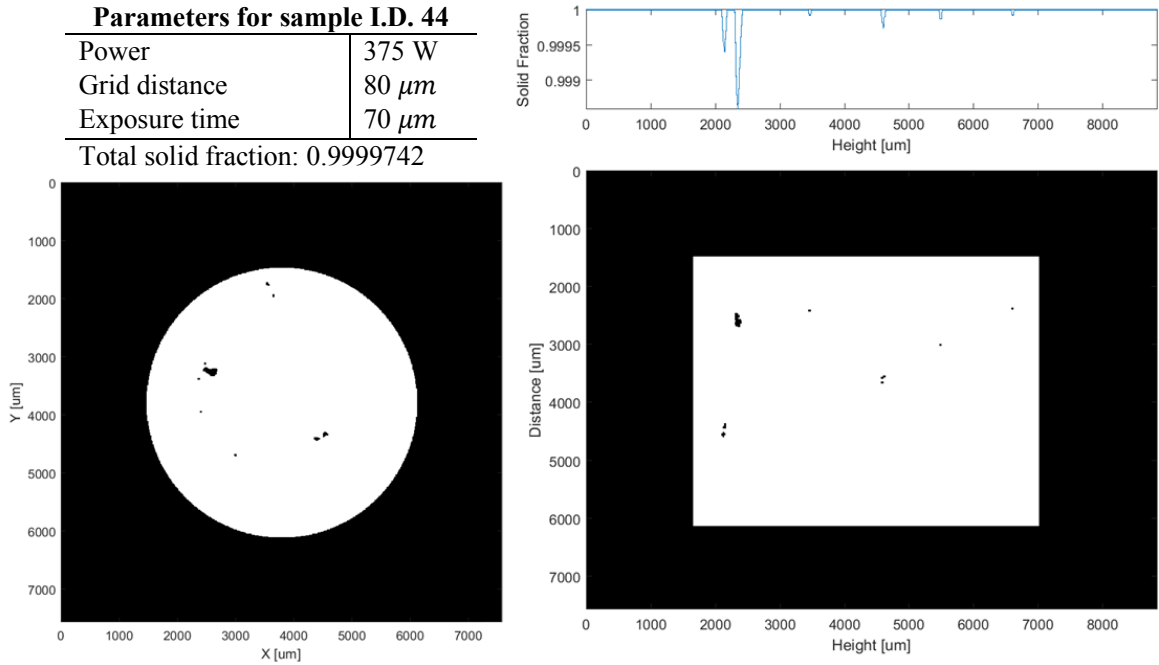
Figure I 44. Minimum intensity projection images from CT analysis. Build variables correspond to sample I.D. 44.

Parameters for sample I.D. 45

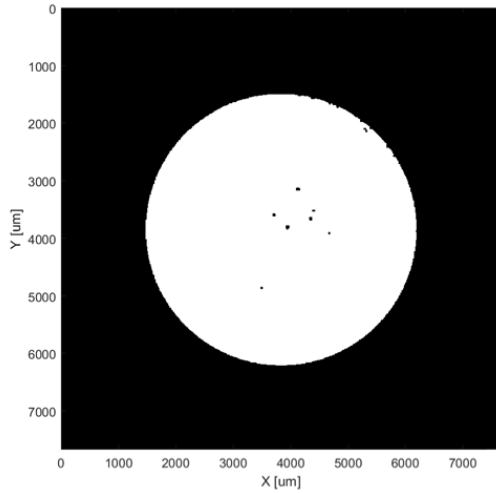| Power	375 W
Grid distance	80 μm
Exposure time	80 μm

Total solid fraction: 0.9999973

Figure I 45. Minimum intensity projection images from CT analysis. Build variables correspond to sample I.D. 45.

Parameters for sample I.D. 46

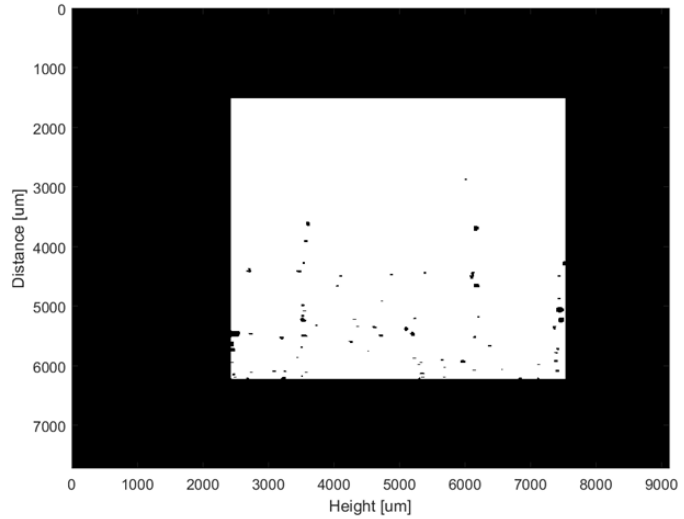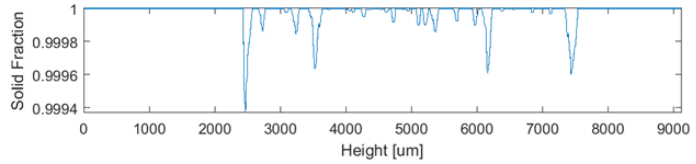| Power	400 W
Grid distance	60 μm
Exposure time	60 μm

Total solid fraction: 0.9999723

Figure I 46. Minimum intensity projection images from CT analysis. Build variables correspond to sample I.D. 46.

Parameters for sample I.D. 47

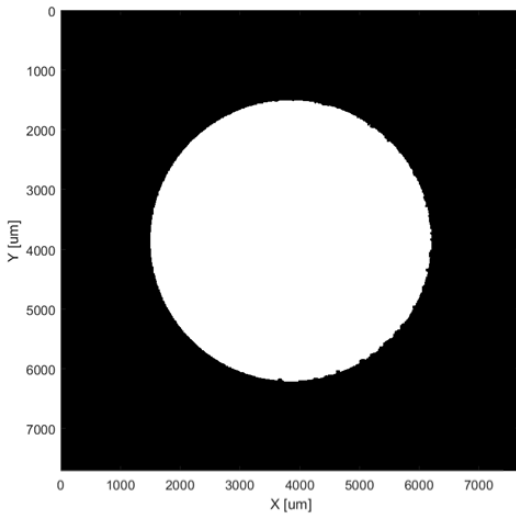| Power	400 W
Grid distance	60 μm
Exposure time	70 μm

Total solid fraction: 0.9999601

Figure I 47. Minimum intensity projection images from CT analysis. Build variables correspond to sample I.D. 47.

Parameters for sample I.D. 48

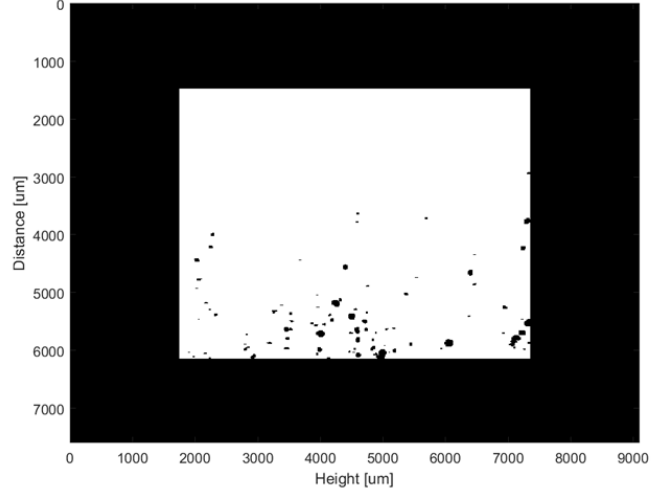| Power	400 W
Grid distance	60 μm
Exposure time	80 μm

Total solid fraction: 0.9998367

Figure I 48. Minimum intensity projection images from CT analysis. Build variables correspond to sample I.D. 48.

Parameters for sample I.D. 49

Power	400 W
Grid distance	70 μm
Exposure time	60 μm

Total solid fraction: 0.9999731

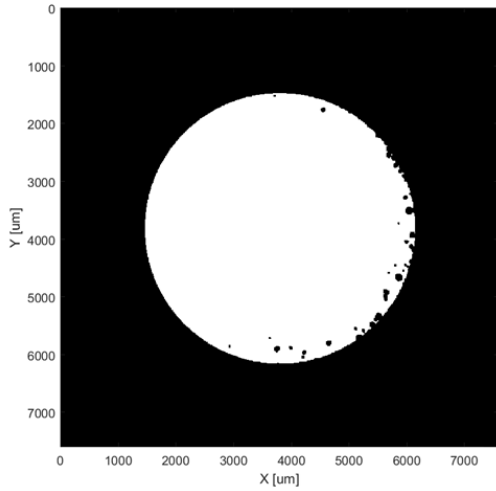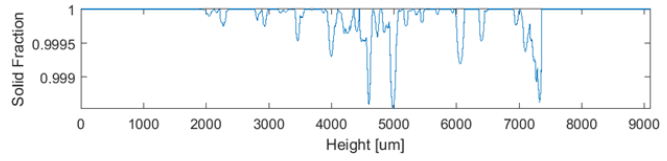**Figure I 49. Minimum intensity projection images from CT analysis. Build variables correspond to sample I.D. 49.**

Parameters for sample I.D. 50

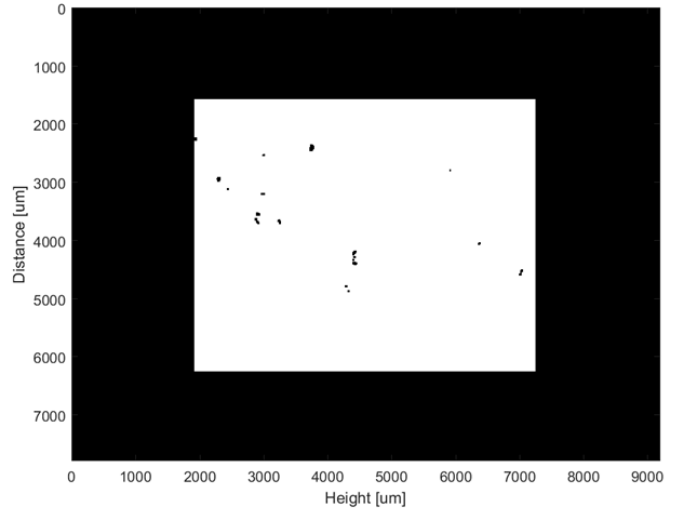| Power	400 W
Grid distance	70 μm
Exposure time	70 μm

Total solid fraction: 0.9999993

Figure I 50. Minimum intensity projection images from CT analysis. Build variables correspond to sample I.D. 50.

Parameters for sample I.D. 51

Power	400 W
Grid distance	70 μm
Exposure time	80 μm

Total solid fraction: 0.9999507

Figure I 51. Minimum intensity projection images from CT analysis. Build variables correspond to sample I.D. 51.

286

Parameters for sample I.D. 52

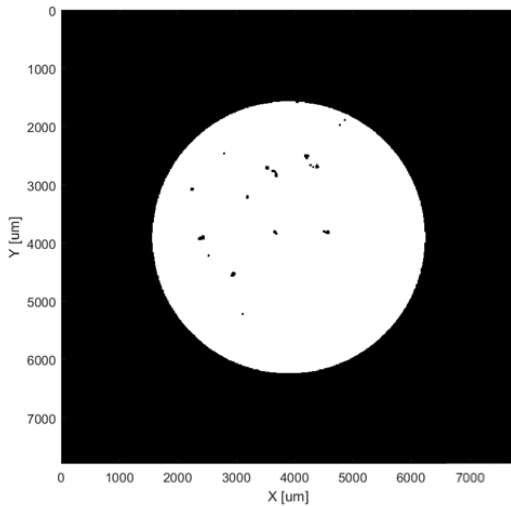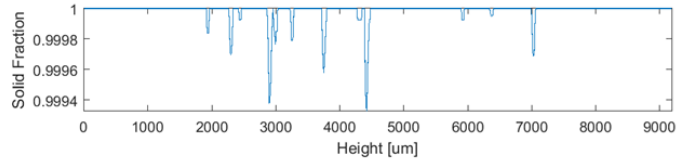| Power	400 W
Grid distance	80 μm
Exposure time	60 μm

Total solid fraction: 0.9999841

Figure I 52. Minimum intensity projection images from CT analysis. Build variables correspond to sample I.D. 52.

Parameters for sample I.D. 53

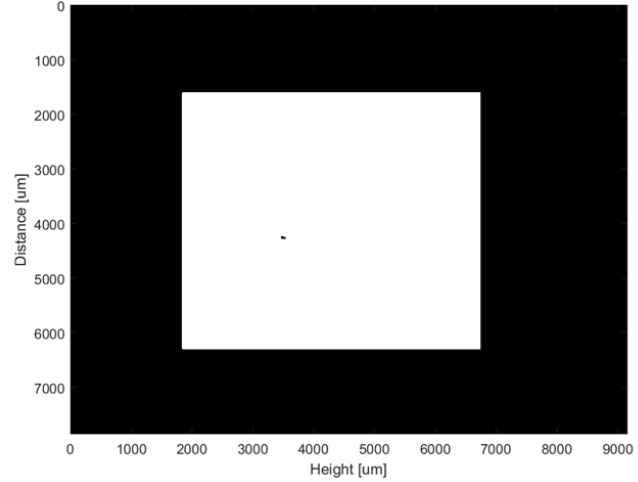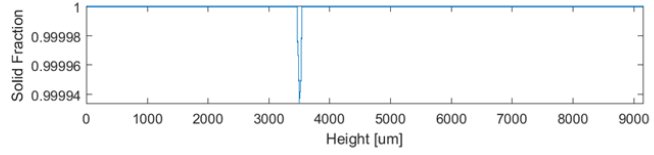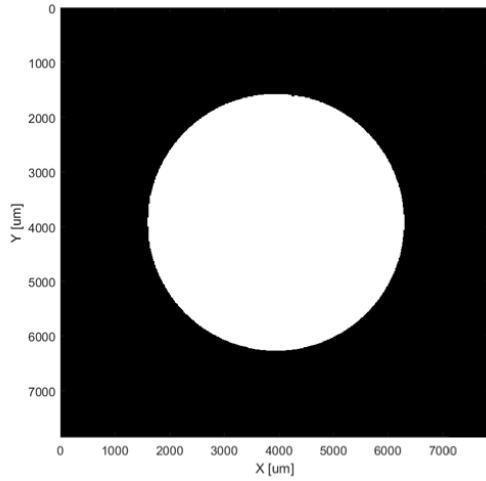| Power	400 W
Grid distance	80 μm
Exposure time	70 μm

Total solid fraction: 0.9999965

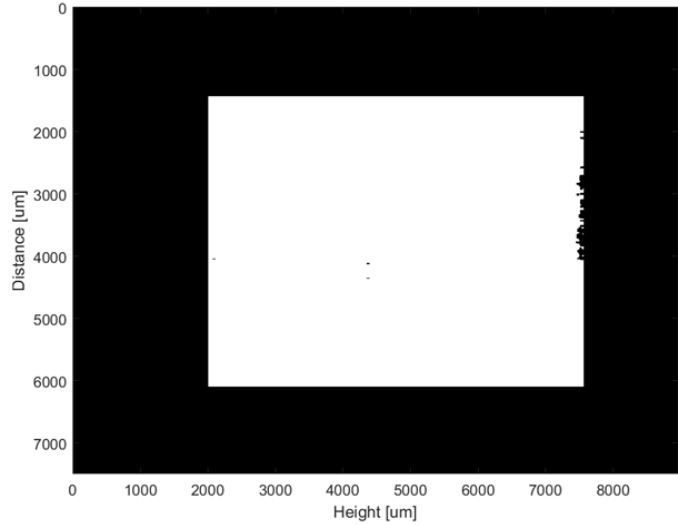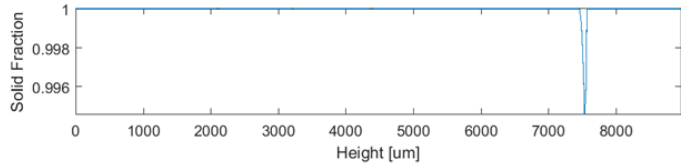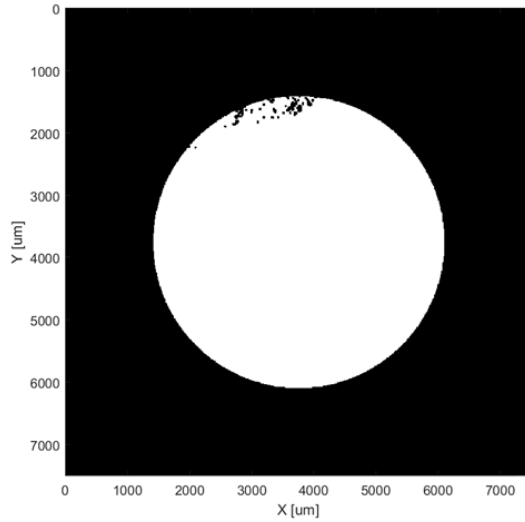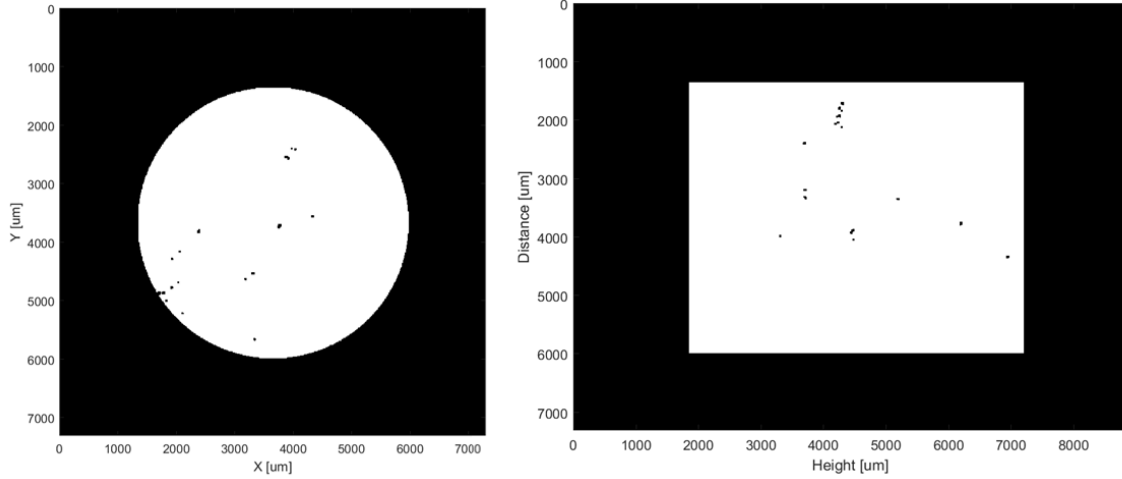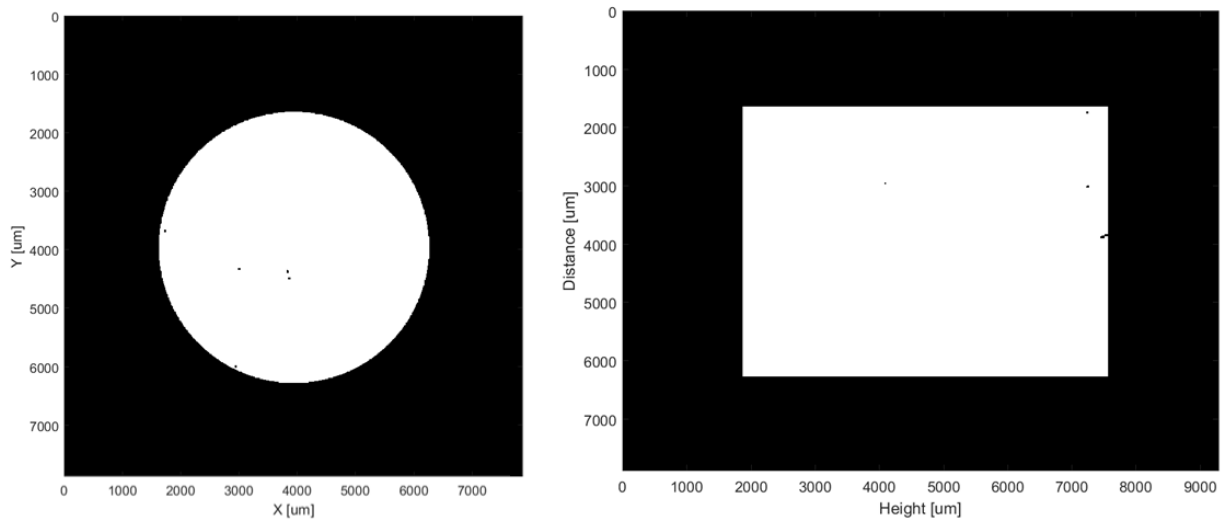**Figure I 53. Minimum intensity projection images from CT analysis. Build variables correspond to sample I.D. 53.**

Parameters for sample I.D. 54

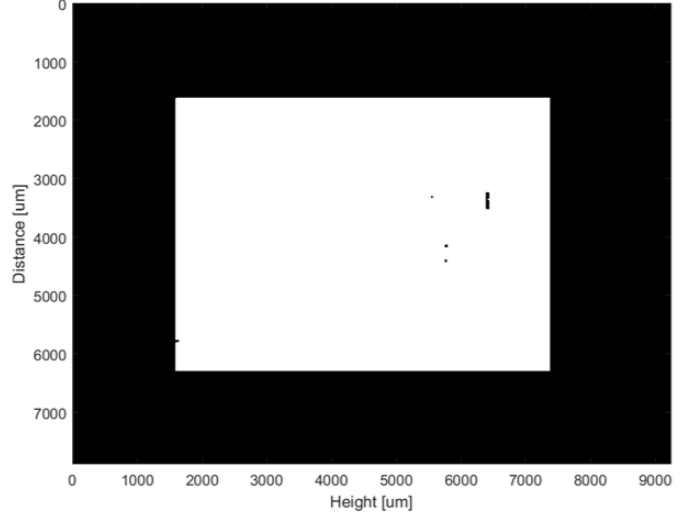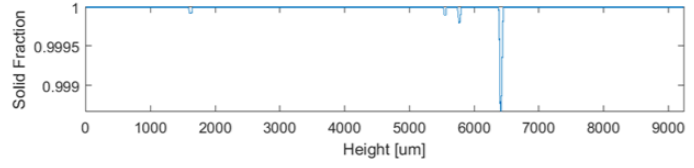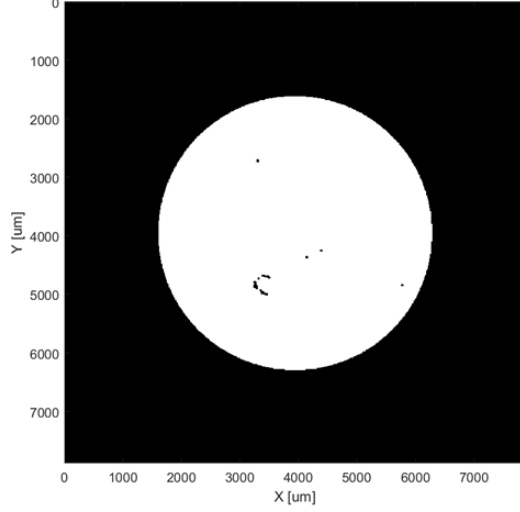| Power	400 W
Grid distance	80 μm
Exposure time	80 μm

Total solid fraction: 0.9999882

Figure I 54. Minimum intensity projection images from CT analysis. Build variables correspond to sample I.D. 54.

Appendix J:

Recipe for Experiment in Chapter 5, with All Build Variable Combinations and Identifications

Table J 1. Build variable table for the experiment in Chapter 5, showing all build variable combinations within the build recipe. Green-shaded rows indicate samples that were CT scanned. White-shaded rows indicate un-scanned samples for future analysis. Red-shaded rows indicate missing samples.

I.D.	Batch	Scan Strategy	Order	Hatch Compensation [%]	Fill Contour Offset [%]	Power [W]	Grid Distance [μm]	Border Power [W]
1	1	Meander	1	25	50	275	60	250
1	2	Meander	1	25	50	275	60	275
1	3	Meander	1	25	50	275	60	250
1	4	Meander	1	25	50	275	60	275
2	1	Meander	1	25	50	275	70	250
2	2	Meander	1	25	50	275	70	275
2	3	Meander	1	25	50	275	70	250
2	4	Meander	1	25	50	275	70	275
3	1	Meander	1	25	50	300	60	250
3	2	Meander	1	25	50	300	60	275
3	3	Meander	1	25	50	300	60	250
3	4	Meander	1	25	50	300	60	275
4	1	Meander	1	25	50	300	70	250
4	2	Meander	1	25	50	300	70	275
4	3	Meander	1	25	50	300	70	250
4	4	Meander	1	25	50	300	70	275
5	1	Meander	1	25	100	275	60	250
5	2	Meander	1	25	100	275	60	275
5	3	Meander	1	25	100	275	60	250
5	4	Meander	1	25	100	275	60	275
6	1	Meander	1	25	100	275	70	250
6	2	Meander	1	25	100	275	70	275
6	3	Meander	1	25	100	275	70	250
6	4	Meander	1	25	100	275	70	275
7	1	Meander	1	25	100	300	60	250

Table J 1 (cont'd, 1). Build variable table for the experiment in Chapter 5, showing all build variable combinations within the build recipe. Green-shaded rows indicate samples that were CT scanned. White-shaded rows indicate un-scanned samples for future analysis. Red-shaded rows indicate missing samples.

I.D.	Batch	Scan Strategy	Order	Hatch Compensation [%]	Fill Contour Offset [%]	Power [W]	Grid Distance [μm]	Border Power [W]
7	2	Meander	1	25	100	300	60	275
7	3	Meander	1	25	100	300	60	250
7	4	Meander	1	25	100	300	60	275
8	1	Meander	1	25	100	300	70	250
8	2	Meander	1	25	100	300	70	275
8	3	Meander	1	25	100	300	70	250
8	4	Meander	1	25	100	300	70	275
9	1	Meander	1	50	50	275	60	250
9	2	Meander	1	50	50	275	60	275
9	3	Meander	1	50	50	275	60	250
9	4	Meander	1	50	50	275	60	275
10	1	Meander	1	50	50	275	70	250
10	2	Meander	1	50	50	275	70	275
10	3	Meander	1	50	50	275	70	250
10	4	Meander	1	50	50	275	70	275
11	1	Meander	1	50	50	300	60	250
11	2	Meander	1	50	50	300	60	275
11	3	Meander	1	50	50	300	60	250
11	4	Meander	1	50	50	300	60	275
12	1	Meander	1	50	50	300	70	250
12	2	Meander	1	50	50	300	70	275
12	3	Meander	1	50	50	300	70	250
12	4	Meander	1	50	50	300	70	275
13	1	Meander	1	50	100	275	60	250
13	2	Meander	1	50	100	275	60	275
13	3	Meander	1	50	100	275	60	250
13	4	Meander	1	50	100	275	60	275
14	1	Meander	1	50	100	275	70	250
14	2	Meander	1	50	100	275	70	275
14	3	Meander	1	50	100	275	70	250

Table J 1 (cont'd, 2). Build variable table for the experiment in Chapter 5, showing all build variable combinations within the build recipe. Green-shaded rows indicate samples that were CT scanned. White-shaded rows indicate un-scanned samples for future analysis. Red-shaded rows indicate missing samples.

I.D.	Batch	Scan Strategy	Order	Hatch Compensation [%]	Fill Contour Offset [%]	Power [W]	Grid Distance [μm]	Border Power [W]
14	4	Meander	1	50	100	275	70	275
15	1	Meander	1	50	100	300	60	250
15	2	Meander	1	50	100	300	60	275
15	3	Meander	1	50	100	300	60	250
15	4	Meander	1	50	100	300	60	275
16	1	Meander	1	50	100	300	70	250
16	2	Meander	1	50	100	300	70	275
16	3	Meander	1	50	100	300	70	250
16	4	Meander	1	50	100	300	70	275
17	1	Meander	2	25	50	275	60	250
17	2	Meander	2	25	50	275	60	275
17	3	Meander	2	25	50	275	60	250
17	4	Meander	2	25	50	275	60	275
18	1	Meander	2	25	50	275	70	250
18	2	Meander	2	25	50	275	70	275
18	3	Meander	2	25	50	275	70	250
18	4	Meander	2	25	50	275	70	275
19	1	Meander	2	25	50	300	60	250
19	2	Meander	2	25	50	300	60	275
19	3	Meander	2	25	50	300	60	250
19	4	Meander	2	25	50	300	60	275
20	1	Meander	2	25	50	300	70	250
20	2	Meander	2	25	50	300	70	275
20	3	Meander	2	25	50	300	70	250
20	4	Meander	2	25	50	300	70	275
21	1	Meander	2	25	100	275	60	250
21	2	Meander	2	25	100	275	60	275
21	3	Meander	2	25	100	275	60	250
21	4	Meander	2	25	100	275	60	275
22	1	Meander	2	25	100	275	70	250

Table J 1 (cont'd, 3). Build variable table for the experiment in Chapter 5, showing all build variable combinations within the build recipe. Green-shaded rows indicate samples that were CT scanned. White-shaded rows indicate un-scanned samples for future analysis. Red-shaded rows indicate missing samples.

I.D.	Batch	Scan Strategy	Order	Hatch Compensation [%]	Fill Contour Offset [%]	Power [W]	Grid Distance [μm]	Border Power [W]
22	2	Meander	2	25	100	275	70	275
22	3	Meander	2	25	100	275	70	250
22	4	Meander	2	25	100	275	70	275
23	1	Meander	2	25	100	300	60	250
23	2	Meander	2	25	100	300	60	275
23	3	Meander	2	25	100	300	60	250
23	4	Meander	2	25	100	300	60	275
24	1	Meander	2	25	100	300	70	250
24	2	Meander	2	25	100	300	70	275
24	3	Meander	2	25	100	300	70	250
24	4	Meander	2	25	100	300	70	275
25	1	Meander	2	50	50	275	60	250
25	2	Meander	2	50	50	275	60	275
25	3	Meander	2	50	50	275	60	250
25	4	Meander	2	50	50	275	60	275
26	1	Meander	2	50	50	275	70	250
26	2	Meander	2	50	50	275	70	275
26	3	Meander	2	50	50	275	70	250
26	4	Meander	2	50	50	275	70	275
27	1	Meander	2	50	50	300	60	250
27	2	Meander	2	50	50	300	60	275
27	3	Meander	2	50	50	300	60	250
27	4	Meander	2	50	50	300	60	275
28	1	Meander	2	50	50	300	70	250
28	2	Meander	2	50	50	300	70	275
28	3	Meander	2	50	50	300	70	250
28	4	Meander	2	50	50	300	70	275
29	1	Meander	2	50	100	275	60	250
29	2	Meander	2	50	100	275	60	275
29	3	Meander	2	50	100	275	60	250
29	4	Meander	2	50	100	275	60	275

Table J 1 (cont'd, 4). Build variable table for the experiment in Chapter 5, showing all build variable combinations within the build recipe. Green-shaded rows indicate samples that were CT scanned. White-shaded rows indicate un-scanned samples for future analysis. Red-shaded rows indicate missing samples.

I.D.	Batch	Scan Strategy	Order	Hatch Compensation [%]	Fill Contour Offset [%]	Power [W]	Grid Distance [μm]	Border Power [W]
30	1	Meander	2	50	100	275	70	250
30	2	Meander	2	50	100	275	70	275
30	3	Meander	2	50	100	275	70	250
30	4	Meander	2	50	100	275	70	275
31	1	Meander	2	50	100	300	60	250
31	2	Meander	2	50	100	300	60	275
31	3	Meander	2	50	100	300	60	250
31	4	Meander	2	50	100	300	60	275
32	1	Meander	2	50	100	300	70	250
32	2	Meander	2	50	100	300	70	275
32	3	Meander	2	50	100	300	70	250
32	4	Meander	2	50	100	300	70	275
33	1	Stripe	1	25	50	275	60	250
33	2	Stripe	1	25	50	275	60	275
33	3	Stripe	1	25	50	275	60	250
33	4	Stripe	1	25	50	275	60	275
34	1	Stripe	1	25	50	275	70	250
34	2	Stripe	1	25	50	275	70	275
34	3	Stripe	1	25	50	275	70	250
34	4	Stripe	1	25	50	275	70	275
35	1	Stripe	1	25	50	300	60	250
35	2	Stripe	1	25	50	300	60	275
35	3	Stripe	1	25	50	300	60	250
35	4	Stripe	1	25	50	300	60	275
36	1	Stripe	1	25	50	300	70	250
36	2	Stripe	1	25	50	300	70	275
36	3	Stripe	1	25	50	300	70	250
36	4	Stripe	1	25	50	300	70	275
37	1	Stripe	1	25	100	275	60	250
37	2	Stripe	1	25	100	275	60	275
37	3	Stripe	1	25	100	275	60	250

Table J 1 (cont'd, 5). Build variable table for the experiment in Chapter 5, showing all build variable combinations within the build recipe. Green-shaded rows indicate samples that were CT scanned. White-shaded rows indicate un-scanned samples for future

I.D.	Batch	Scan Strategy	Order	Hatch Compensation [%]	Fill Contour Offset [%]	Power [W]	Grid Distance [μm]	Border Power [W]
37	4	Stripe	1	25	100	275	60	275
38	1	Stripe	1	25	100	275	70	250
38	2	Stripe	1	25	100	275	70	275
38	3	Stripe	1	25	100	275	70	250
38	4	Stripe	1	25	100	275	70	275
39	1	Stripe	1	25	100	300	60	250
39	2	Stripe	1	25	100	300	60	275
39	3	Stripe	1	25	100	300	60	250
39	4	Stripe	1	25	100	300	60	275
40	1	Stripe	1	25	100	300	70	250
40	2	Stripe	1	25	100	300	70	275
40	3	Stripe	1	25	100	300	70	250
40	4	Stripe	1	25	100	300	70	275
41	1	Stripe	1	50	50	275	60	250
41	2	Stripe	1	50	50	275	60	275
41	3	Stripe	1	50	50	275	60	250
41	4	Stripe	1	50	50	275	60	275
42	1	Stripe	1	50	50	275	70	250
42	2	Stripe	1	50	50	275	70	275
42	3	Stripe	1	50	50	275	70	250
42	4	Stripe	1	50	50	275	70	275
43	1	Stripe	1	50	50	300	60	250
43	2	Stripe	1	50	50	300	60	275
43	3	Stripe	1	50	50	300	60	250
43	4	Stripe	1	50	50	300	60	275
44	1	Stripe	1	50	50	300	70	250
44	2	Stripe	1	50	50	300	70	275
44	3	Stripe	1	50	50	300	70	250
44	4	Stripe	1	50	50	300	70	275
45	1	Stripe	1	50	100	275	60	250
45	2	Stripe	1	50	100	275	60	275
45	3	Stripe	1	50	100	275	60	250

Table J 1 (cont'd, 6). Build variable table for the experiment in Chapter 5, showing all build variable combinations within the build recipe. Green-shaded rows indicate samples that were CT scanned. White-shaded rows indicate un-scanned samples for future

I.D.	Batch	Scan Strategy	Order	Hatch Compensation [%]	Fill Contour Offset [%]	Power [W]	Grid Distance [μm]	Border Power [W]
45	4	Stripe	1	50	100	275	60	275
46	1	Stripe	1	50	100	275	70	250
46	2	Stripe	1	50	100	275	70	275
46	3	Stripe	1	50	100	275	70	250
46	4	Stripe	1	50	100	275	70	275
47	1	Stripe	1	50	100	300	60	250
47	2	Stripe	1	50	100	300	60	275
47	3	Stripe	1	50	100	300	60	250
47	4	Stripe	1	50	100	300	60	275
48	1	Stripe	1	50	100	300	70	250
48	2	Stripe	1	50	100	300	70	275
48	3	Stripe	1	50	100	300	70	250
48	4	Stripe	1	50	100	300	70	275
49	1	Stripe	2	25	50	275	60	250
49	2	Stripe	2	25	50	275	60	275
49	3	Stripe	2	25	50	275	60	250
49	4	Stripe	2	25	50	275	60	275
50	1	Stripe	2	25	50	275	70	250
50	2	Stripe	2	25	50	275	70	275
50	3	Stripe	2	25	50	275	70	250
50	4	Stripe	2	25	50	275	70	275
51	1	Stripe	2	25	50	300	60	250
51	2	Stripe	2	25	50	300	60	275
51	3	Stripe	2	25	50	300	60	250
51	4	Stripe	2	25	50	300	60	275
52	1	Stripe	2	25	50	300	70	250
52	2	Stripe	2	25	50	300	70	275
52	3	Stripe	2	25	50	300	70	250
52	4	Stripe	2	25	50	300	70	275
53	1	Stripe	2	25	100	275	60	250
53	2	Stripe	2	25	100	275	60	275
53	3	Stripe	2	25	100	275	60	250

Table J 1 (cont'd, 7). Build variable table for the experiment in Chapter 5, showing all build variable combinations within the build recipe. Green-shaded rows indicate samples that were CT scanned. White-shaded rows indicate un-scanned samples for future

I.D.	Batch	Scan Strategy	Order	Hatch Compensation [%]	Fill Contour Offset [%]	Power [W]	Grid Distance [μm]	Border Power [W]
53	4	Stripe	2	25	100	275	60	275
54	1	Stripe	2	25	100	275	70	250
54	2	Stripe	2	25	100	275	70	275
54	3	Stripe	2	25	100	275	70	250
54	4	Stripe	2	25	100	275	70	275
55	1	Stripe	2	25	100	300	60	250
55	2	Stripe	2	25	100	300	60	275
55	3	Stripe	2	25	100	300	60	250
55	4	Stripe	2	25	100	300	60	275
56	1	Stripe	2	25	100	300	70	250
56	2	Stripe	2	25	100	300	70	275
56	3	Stripe	2	25	100	300	70	250
56	4	Stripe	2	25	100	300	70	275
57	1	Stripe	2	50	50	275	60	250
57	2	Stripe	2	50	50	275	60	275
57	3	Stripe	2	50	50	275	60	250
57	4	Stripe	2	50	50	275	60	275
58	1	Stripe	2	50	50	275	70	250
58	2	Stripe	2	50	50	275	70	275
58	3	Stripe	2	50	50	275	70	250
58	4	Stripe	2	50	50	275	70	275
59	1	Stripe	2	50	50	300	60	250
59	2	Stripe	2	50	50	300	60	275
59	3	Stripe	2	50	50	300	60	250
59	4	Stripe	2	50	50	300	60	275
60	1	Stripe	2	50	50	300	70	250
60	2	Stripe	2	50	50	300	70	275
60	3	Stripe	2	50	50	300	70	250
60	4	Stripe	2	50	50	300	70	275
61	1	Stripe	2	50	100	275	60	250
61	2	Stripe	2	50	100	275	60	275
61	3	Stripe	2	50	100	275	60	250

Table J 1 (cont'd, 8). Build variable table for the experiment in Chapter 5, showing all build variable combinations within the build recipe. Green-shaded rows indicate samples that were CT scanned. White-shaded rows indicate un-scanned samples for future

I.D.	Batch	Scan Strategy	Order	Hatch Compensation [%]	Fill Contour Offset [%]	Power [W]	Grid Distance [μm]	Border Power [W]
61	4	Stripe	2	50	100	275	60	275
62	1	Stripe	2	50	100	275	70	250
62	2	Stripe	2	50	100	275	70	275
62	3	Stripe	2	50	100	275	70	250
62	4	Stripe	2	50	100	275	70	275
63	1	Stripe	2	50	100	300	60	250
63	2	Stripe	2	50	100	300	60	275
63	3	Stripe	2	50	100	300	60	250
63	4	Stripe	2	50	100	300	60	275
64	1	Stripe	2	50	100	300	70	250
64	2	Stripe	2	50	100	300	70	275
64	3	Stripe	2	50	100	300	70	250
64	4	Stripe	2	50	100	300	70	275

Appendix K:

CT Analysis Results for Chapter 5

Parameters for sample I.D. 1-1

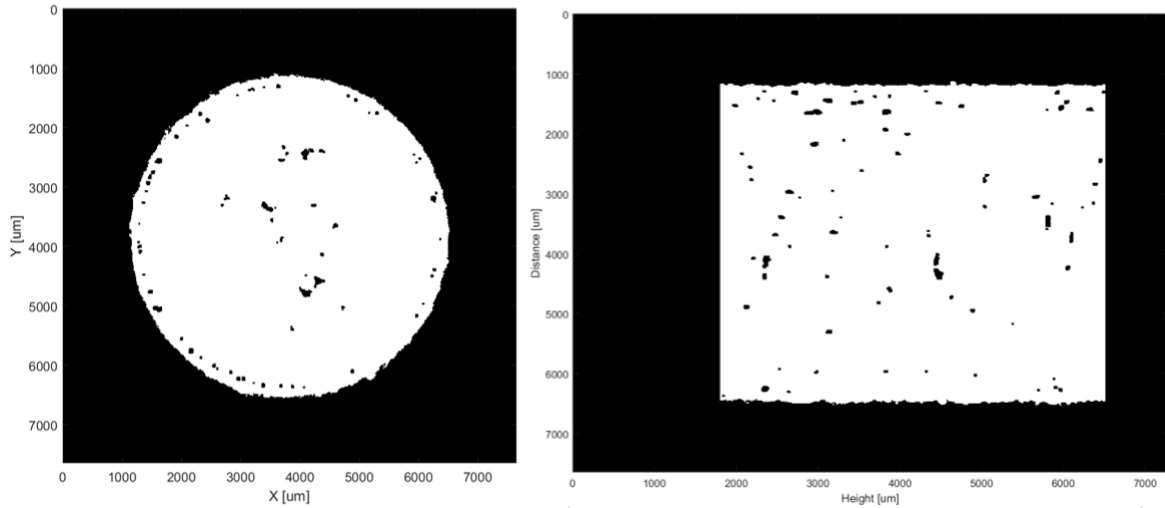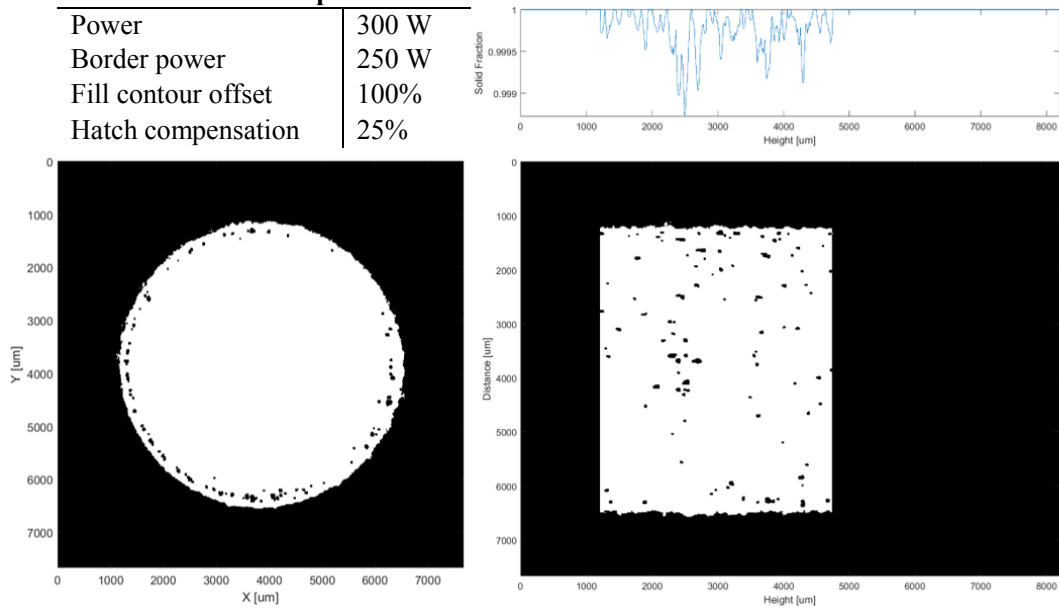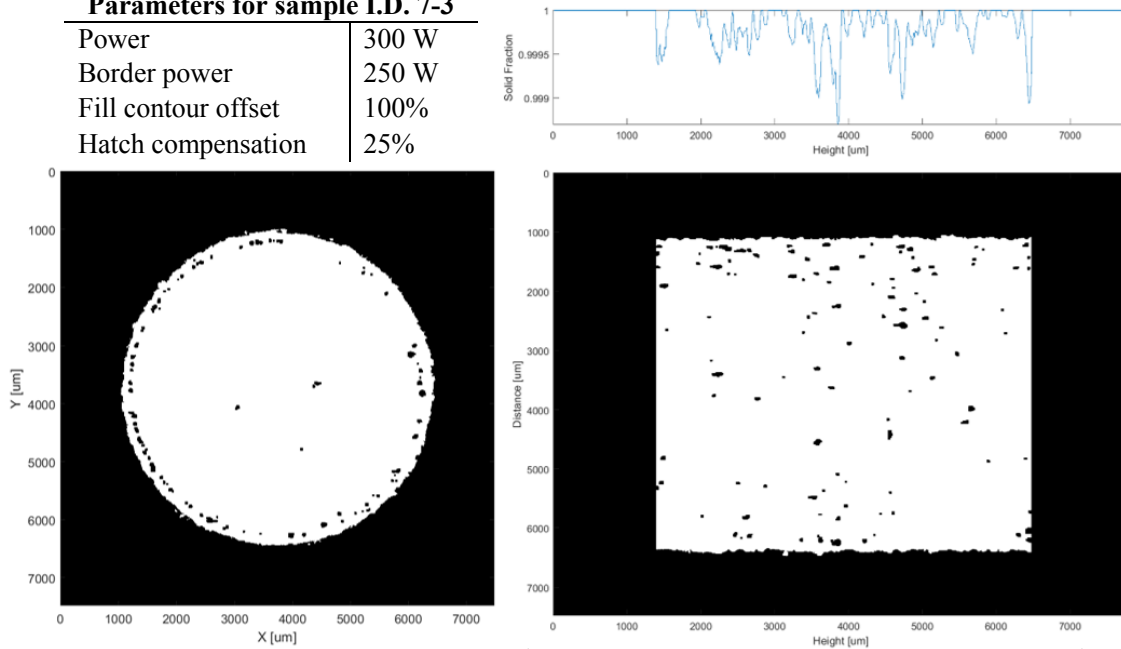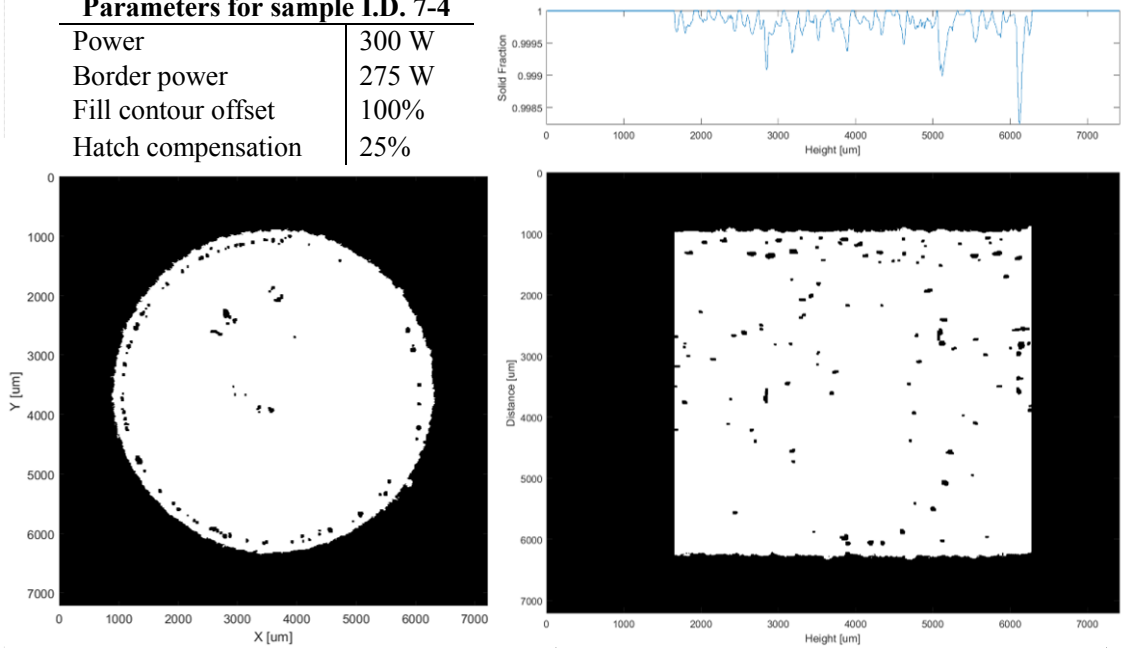| Power	275 W
Border power	250 W
Fill contour offset	50%
Hatch compensation	25%
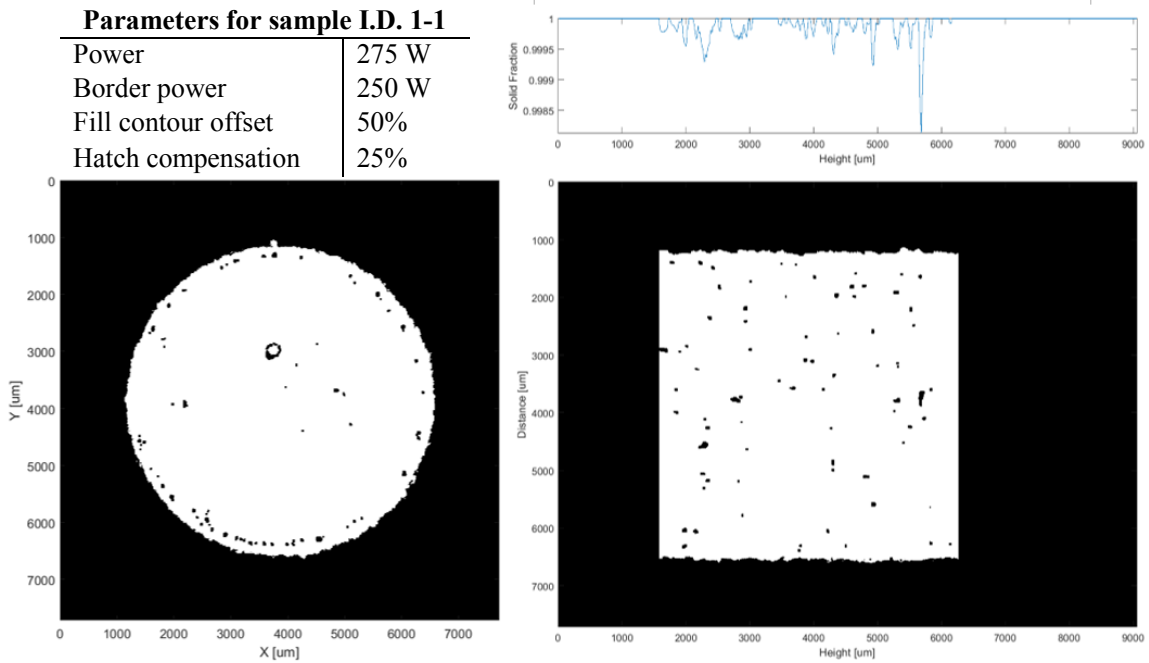
Figure K 1. Minimum intensity projection images from CT analysis. Build variables correspond to sample I.D. 1-1.

Parameters for sample I.D. 1-2

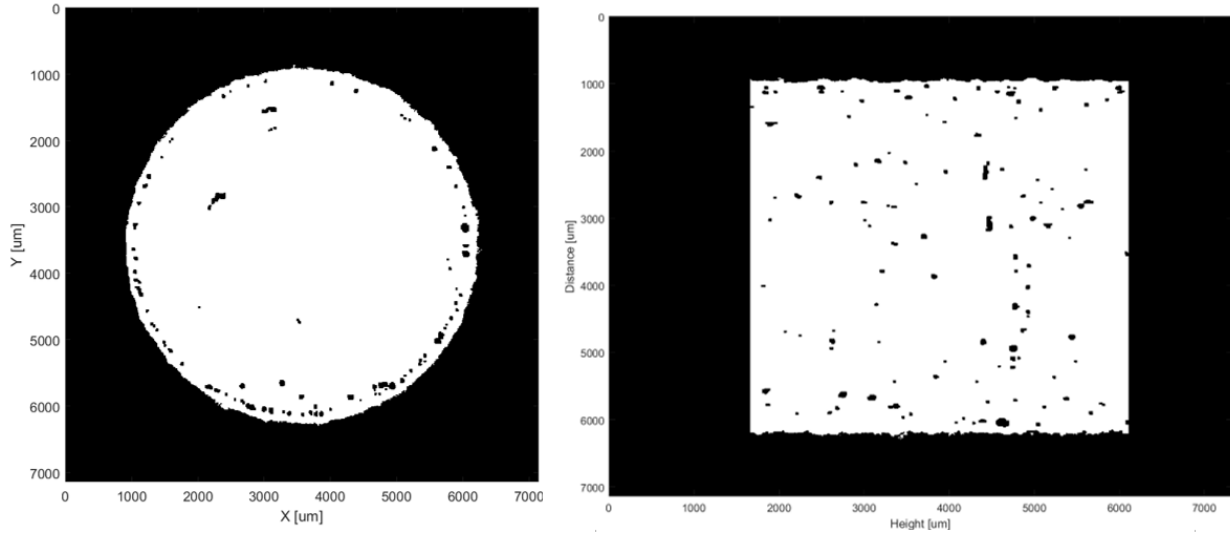|	
Power	275 W
Border power	275 W
Fill contour offset	50%
Hatch compensation	25%
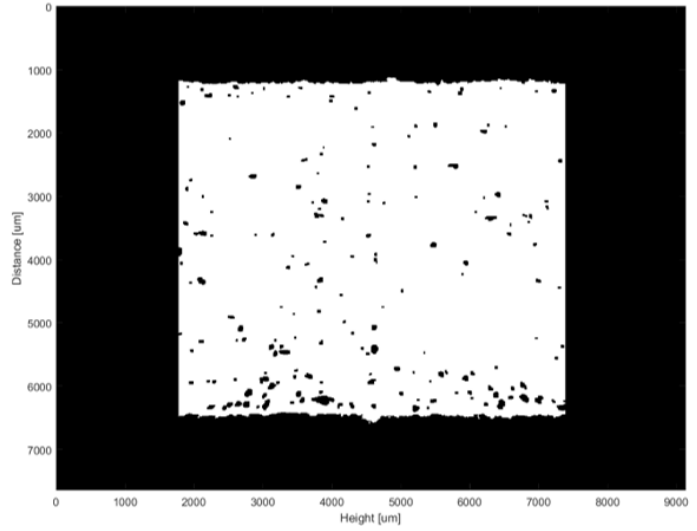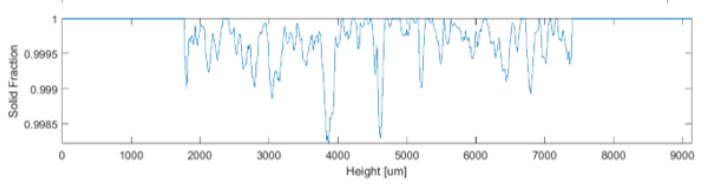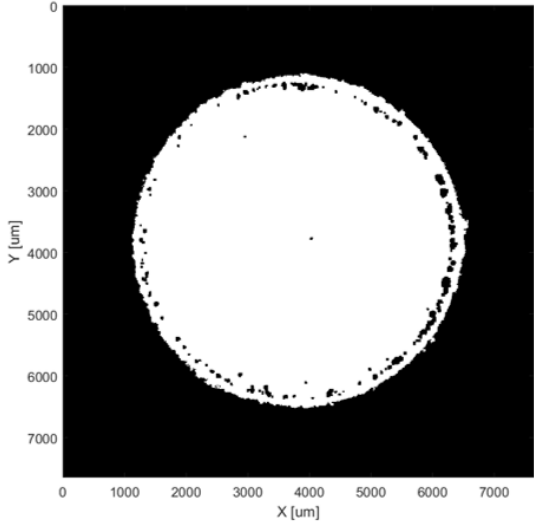
Figure K 2. Minimum intensity projection images from CT analysis. Build variables correspond to sample I.D. 1-2.

Parameters for sample I.D. 1-3

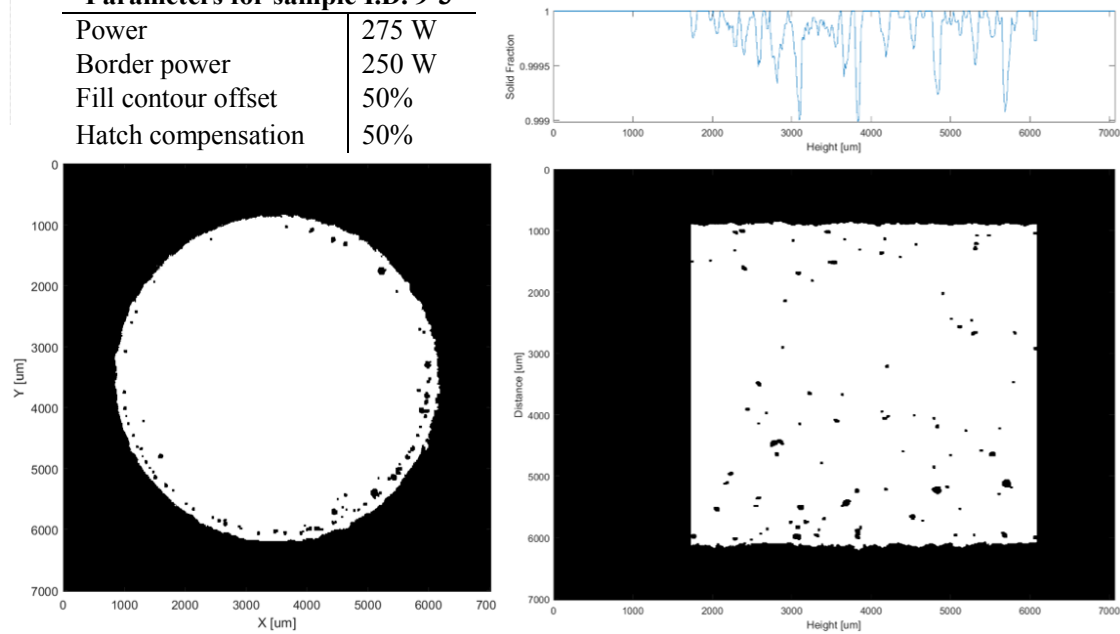| Power	275 W
Border power	250 W
Fill contour offset	50%
Hatch compensation	25%
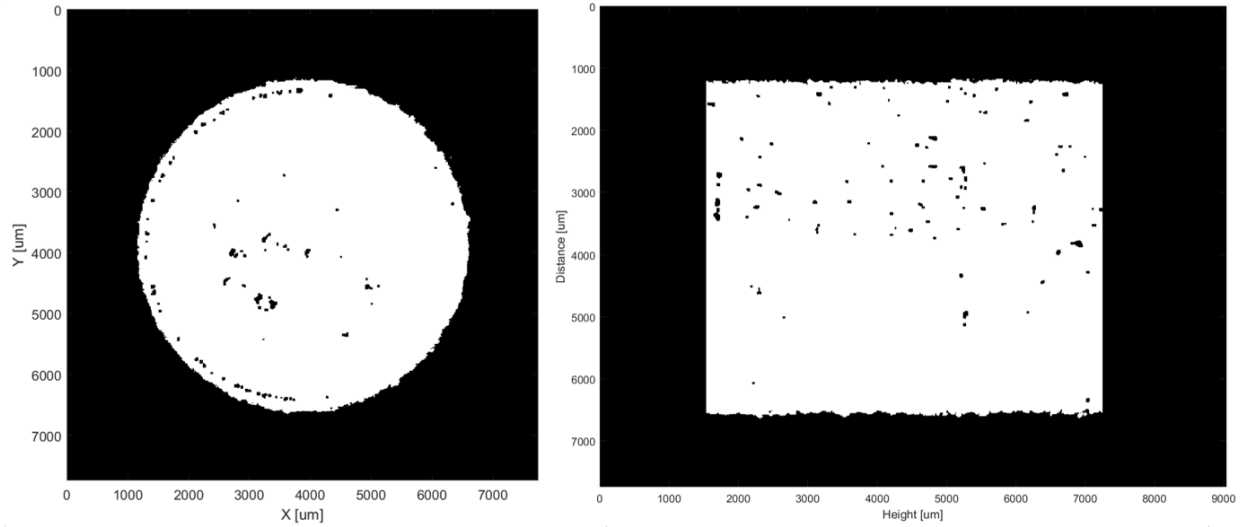
Figure K 3. Minimum intensity projection images from CT analysis. Build variables correspond to sample I.D. 1-3.

Parameters for sample I.D. 1-4

Power	275 W
Border power	275 W
Fill contour offset	50%
Hatch compensation	25%
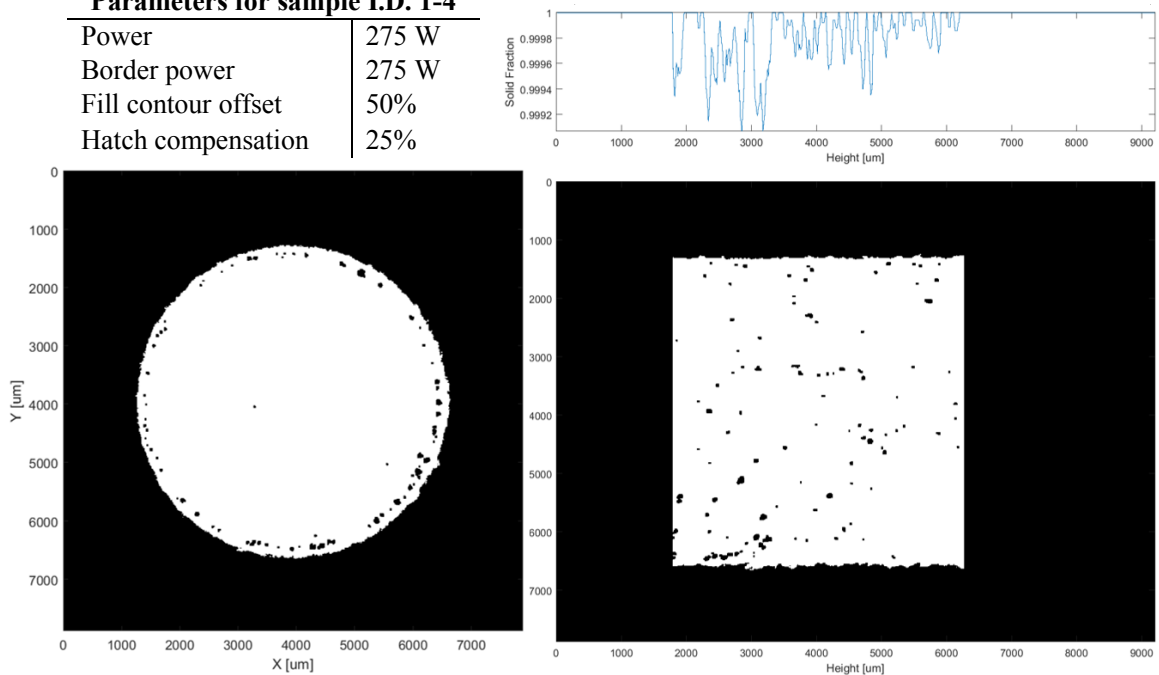
Figure K 4. Minimum intensity projection images from CT analysis. Build variables correspond to sample I.D. 1-4.

Parameters for sample I.D. 3-1

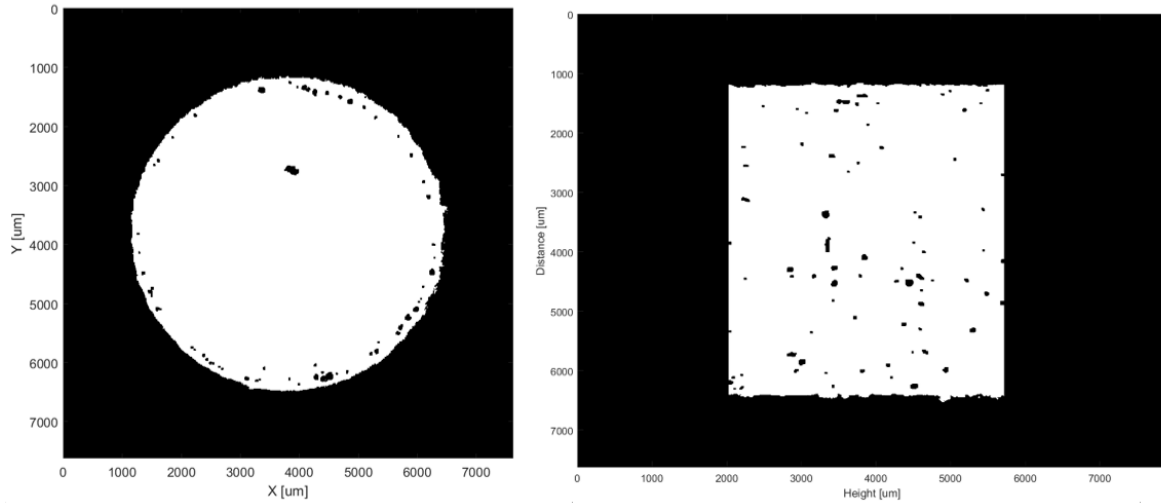| Power	300 W
Border power	250 W
Fill contour offset	50%
Hatch compensation	25%
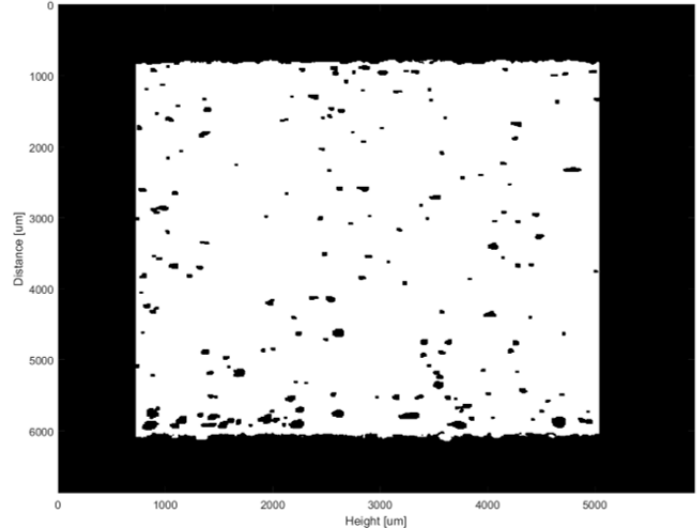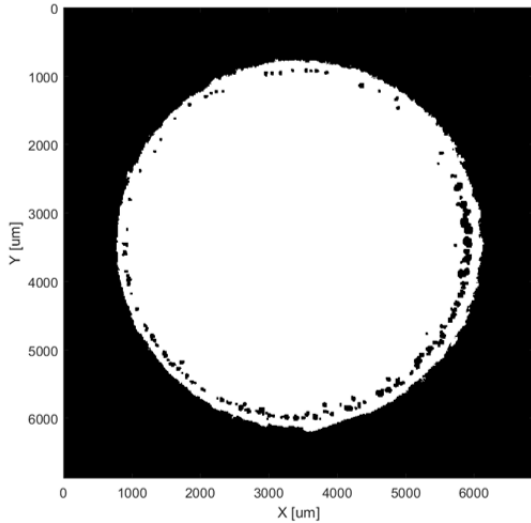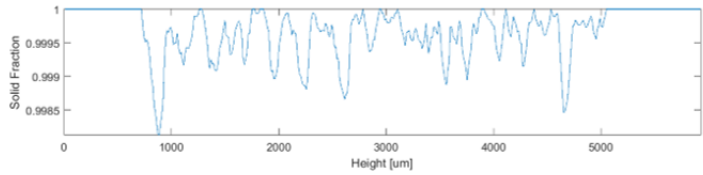
Figure K 5. Minimum intensity projection images from CT analysis. Build variables correspond to sample I.D. 3-1.

Parameters for sample I.D. 3-3

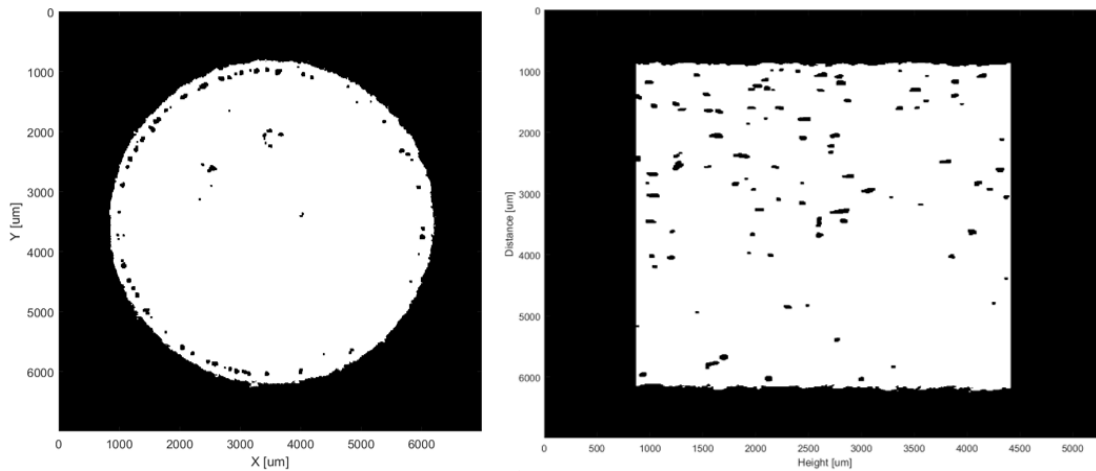| Power	300 W
Border power	250 W
Fill contour offset	50%
Hatch compensation	25%
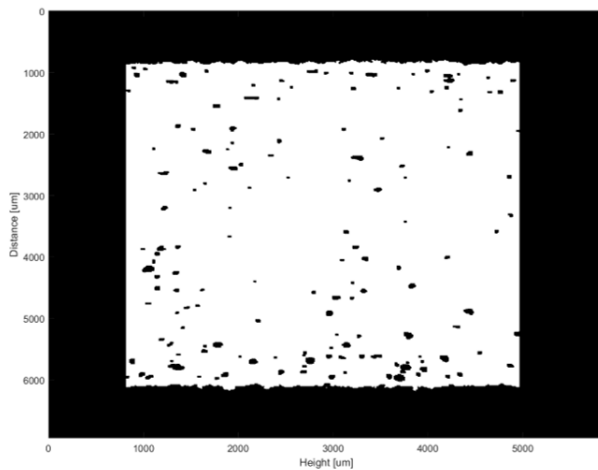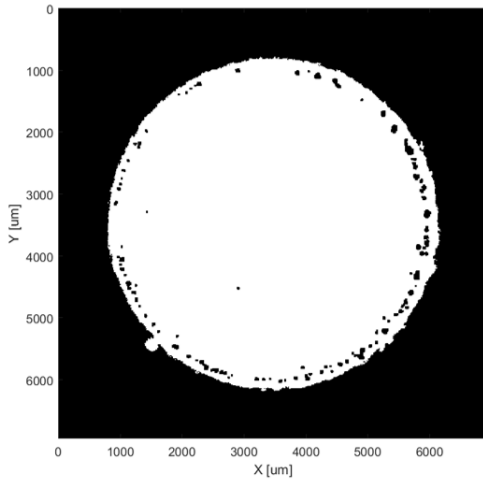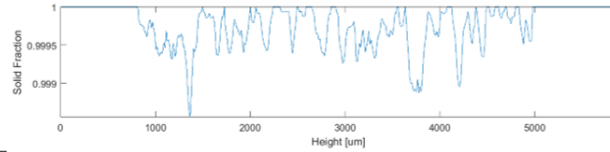
Figure K 6. Minimum intensity projection images from CT analysis. Build variables correspond to sample I.D. 3-3.

Parameters for sample I.D. 3-4

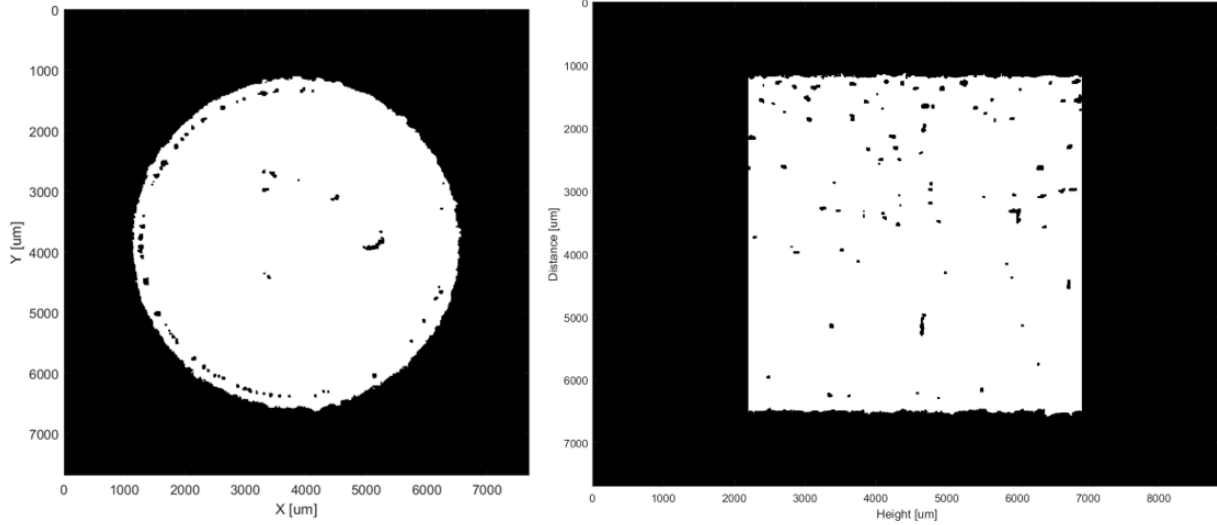| Power	300 W
Border power	275 W
Fill contour offset	50%
Hatch compensation	25%
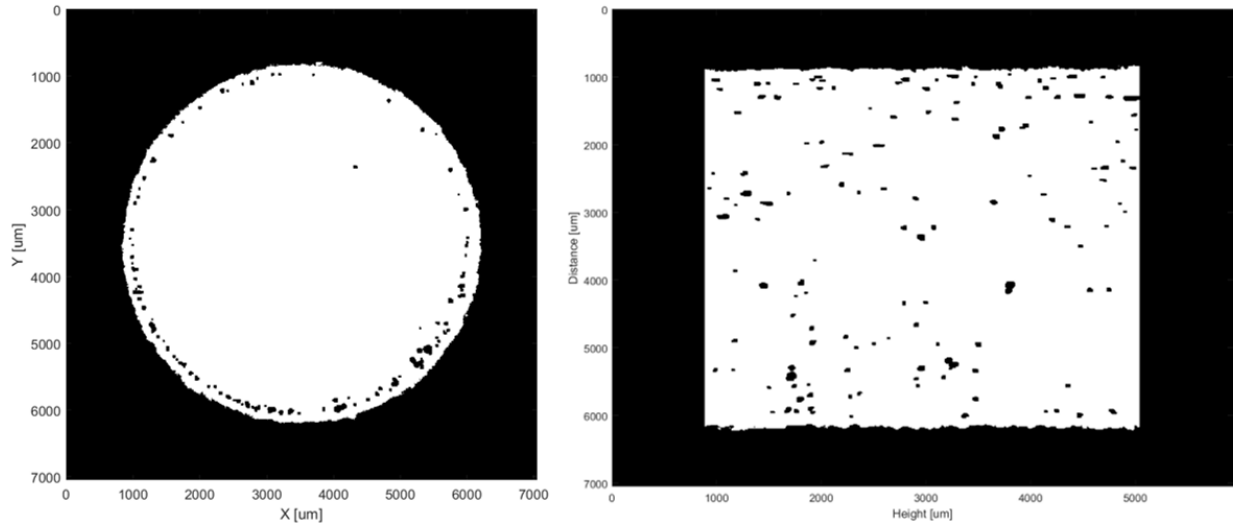
Figure K 7. Minimum intensity projection images from CT analysis. Build variables correspond to sample I.D. 3-4.

Parameters for sample I.D. 5-1

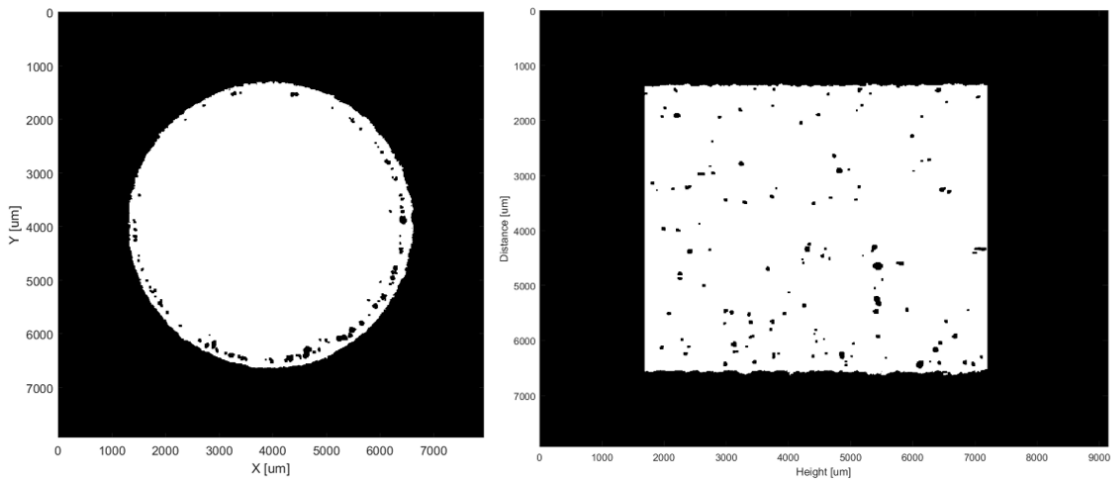| Power	275 W
Border power	250 W
Fill contour offset	100%
Hatch compensation	25%
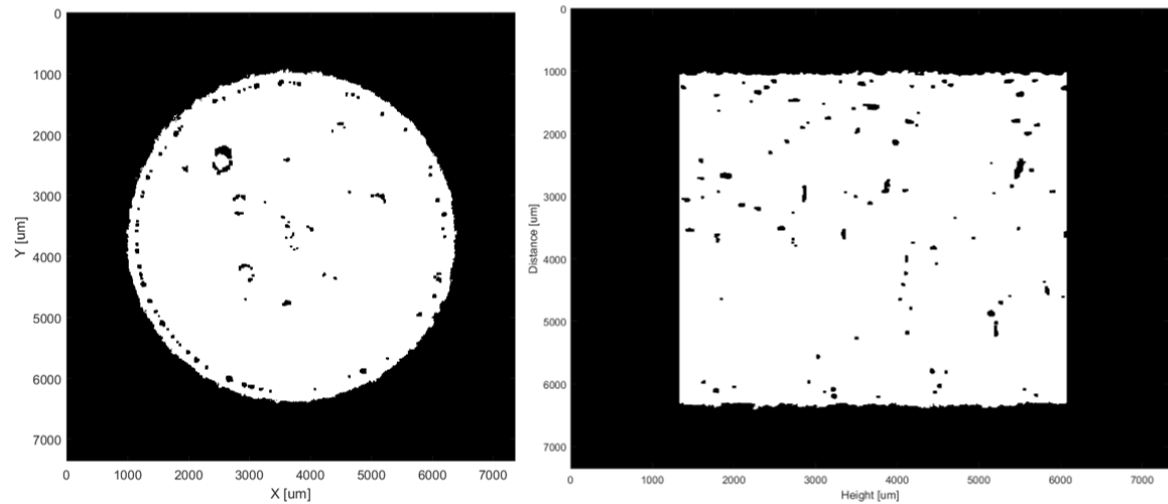
Figure K 8. Minimum intensity projection images from CT analysis. Build variables correspond to sample I.D. 5-1.

302

Parameters for sample I.D. 5-2

Power	275 W
Border power	275 W
Fill contour offset	100%
Hatch compensation	25%
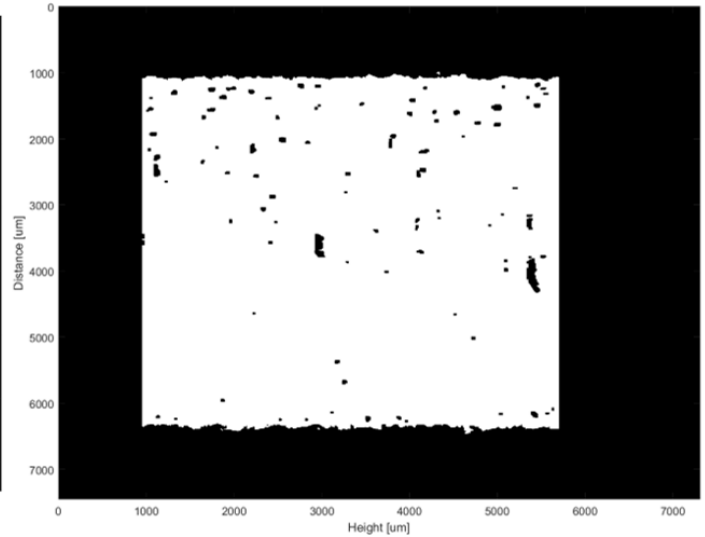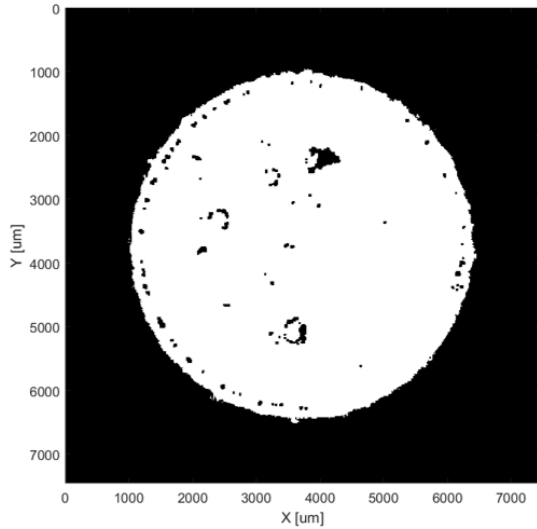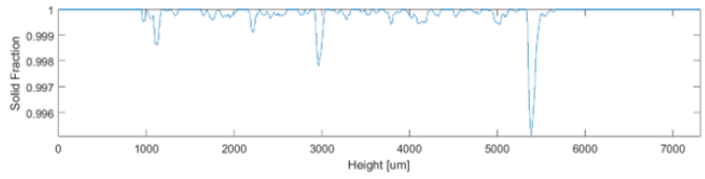
Figure K 9. Minimum intensity projection images from CT analysis. Build variables correspond to sample I.D. 5-2.

Parameters for sample I.D. 5-3

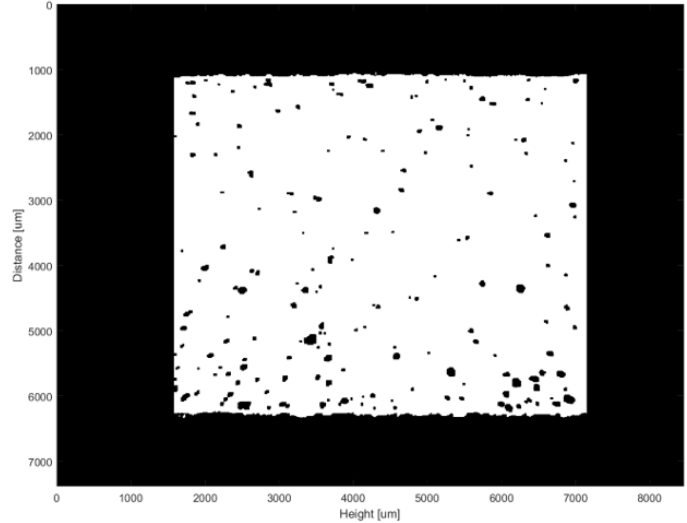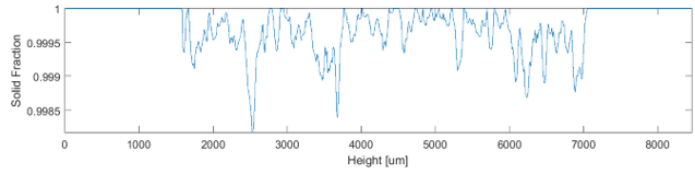| Power	275 W
Border power	250 W
Fill contour offset	100%
Hatch compensation	25%
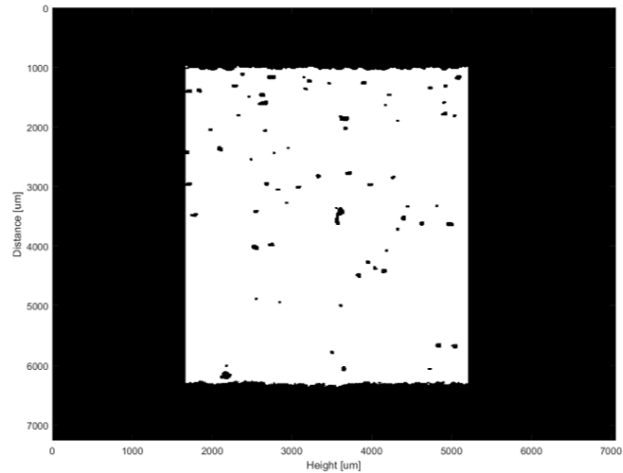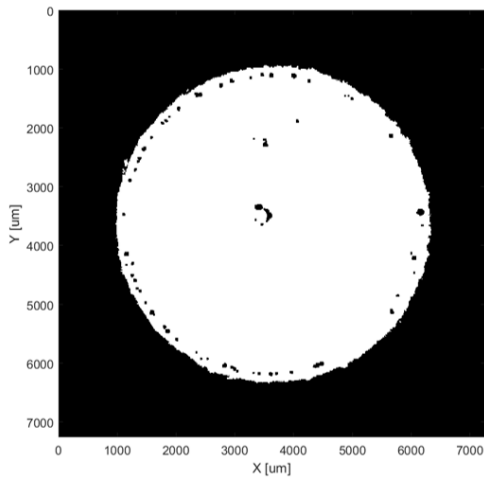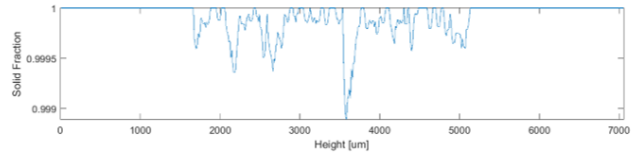
Figure K 10. Minimum intensity projection images from CT analysis. Build variables correspond to sample I.D. 5-3.

Parameters for sample I.D. 5-4

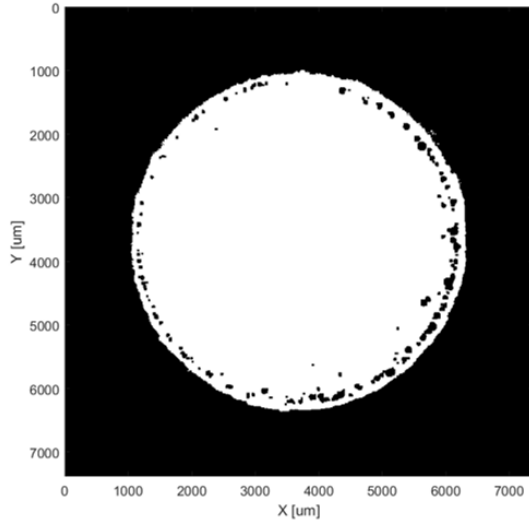| Power	275 W
Border power	250 W
Fill contour offset	100%
Hatch compensation	25%

Figure K 11. Minimum intensity projection images from CT analysis. Build variables correspond to sample I.D. 5-4.

Parameters for sample I.D. 7-1

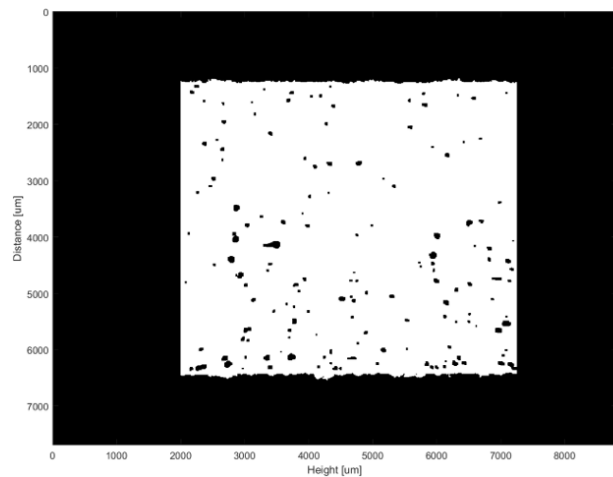| Power	300 W
Border power	250 W
Fill contour offset	100%
Hatch compensation	25%

Figure K 12. Minimum intensity projection images from CT analysis. Build variables correspond to sample I.D. 7-1.

Parameters for sample I.D. 7-3

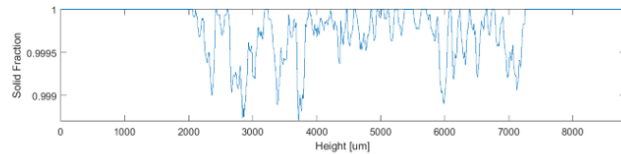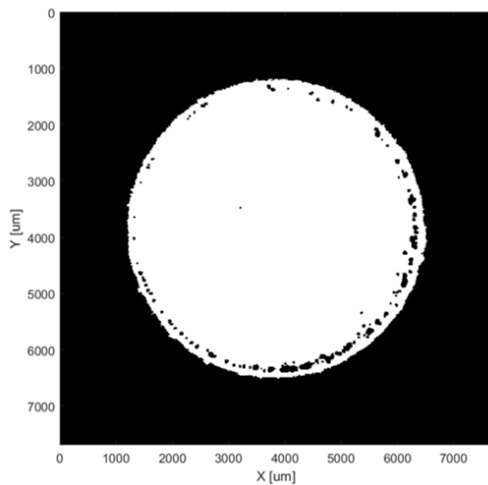| Power	300 W
Border power	250 W
Fill contour offset	100%
Hatch compensation	25%

Figure K 13. Minimum intensity projection images from CT analysis. Build variables correspond to sample I.D. 7-3.

Parameters for sample I.D. 7-4

Power	300 W
Border power	275 W
Fill contour offset	100%
Hatch compensation	25%

Figure K 14. Minimum intensity projection images from CT analysis. Build variables correspond to sample I.D. 7-4.

Parameters for sample I.D. 9-2

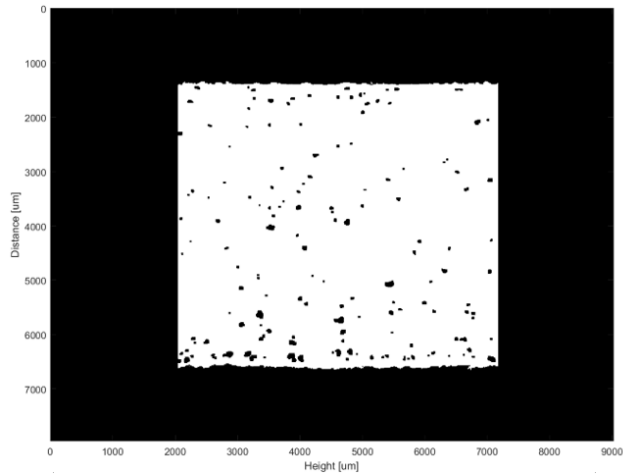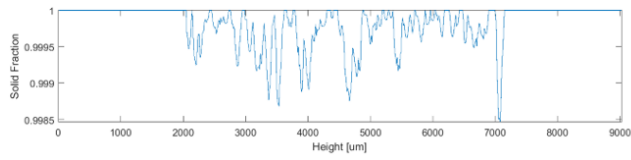| Power	275 W
Border power	275 W
Fill contour offset	50%
Hatch compensation	50%

Figure K 15. Minimum intensity projection images from CT analysis. Build variables correspond to sample I.D. 9-2.

Parameters for sample I.D. 9-3

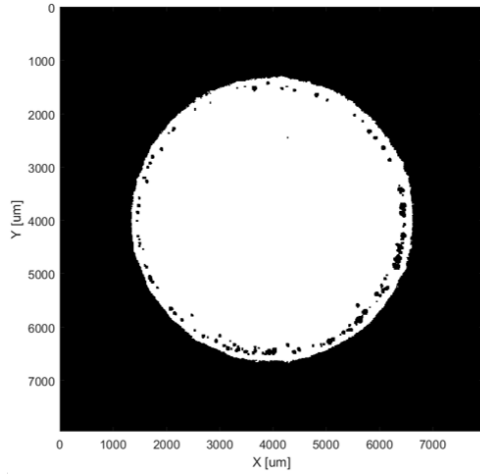| Power	275 W
Border power	250 W
Fill contour offset	50%
Hatch compensation	50%

Figure K 16. Minimum intensity projection images from CT analysis. Build variables correspond to sample I.D. 9-3.

Parameters for sample I.D. 9-4

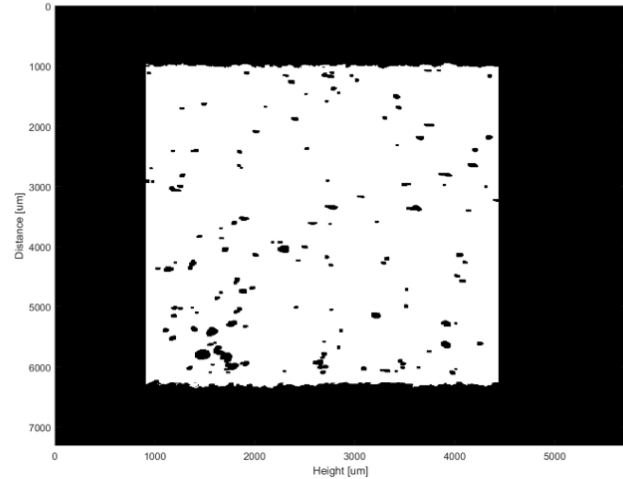| Power	275 W
Border power	275 W
Fill contour offset	50%
Hatch compensation	50%

Figure K 17. Minimum intensity projection images from CT analysis. Build variables correspond to sample I.D. 9-4.

Parameters for sample I.D. 11-2

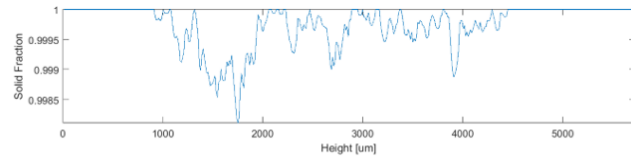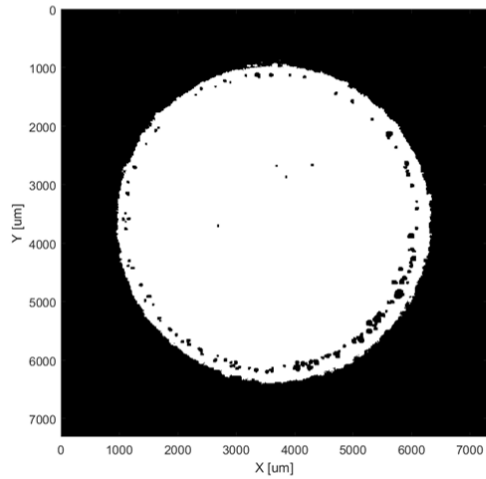| Power	300 W
Border power	275 W
Fill contour offset	50%
Hatch compensation	50%

Figure K 18. Minimum intensity projection images from CT analysis. Build variables correspond to sample I.D. 11-2.

Parameters for sample I.D. 11-4

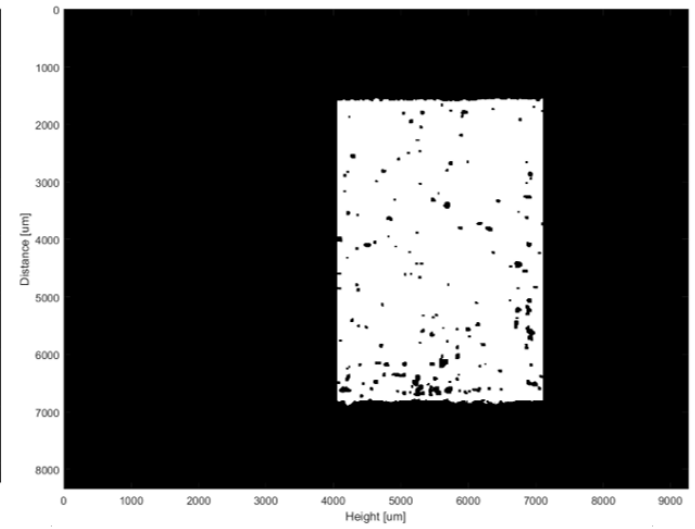| Power	300 W
Border power	275 W
Fill contour offset	50%
Hatch compensation	50%

Figure K 19. Minimum intensity projection images from CT analysis. Build variables correspond to sample I.D. 11-4.

Parameters for sample I.D. 13-1

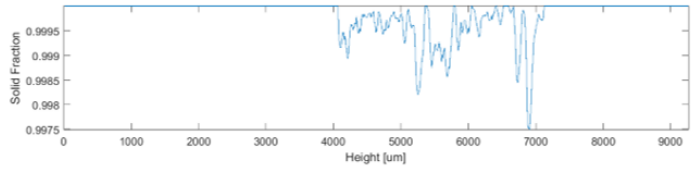| Power	275 W
Border power	250 W
Fill contour offset	100%
Hatch compensation	50%

Figure K 20. Minimum intensity projection images from CT analysis. Build variables correspond to sample I.D. 13-1.

Parameters for sample I.D. 13-2

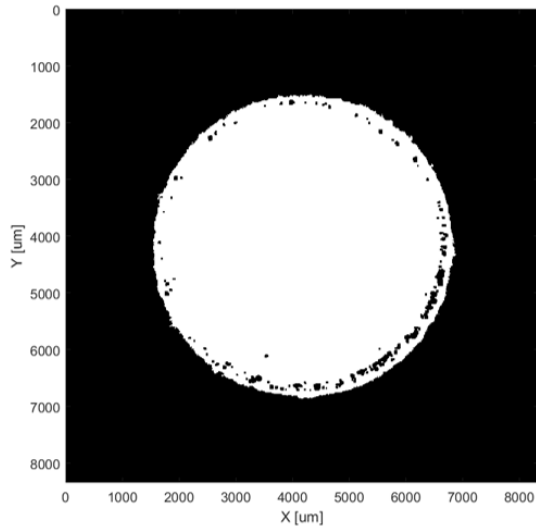| Power	275 W
Border power	275 W
Fill contour offset	100%
Hatch compensation	50%

Figure K 21. Minimum intensity projection images from CT analysis. Build variables correspond to sample I.D. 13-2.

Parameters for sample I.D. 13-3

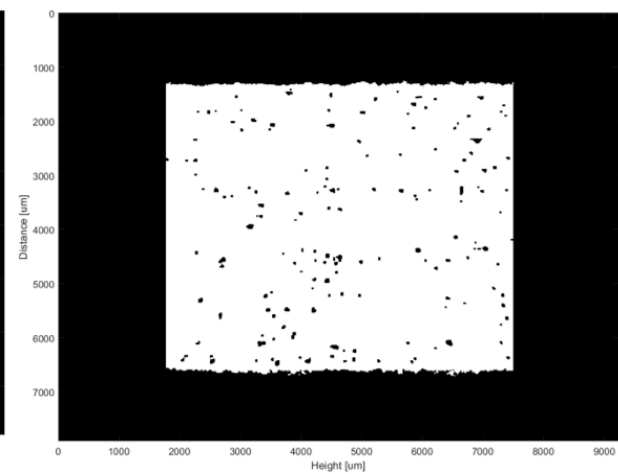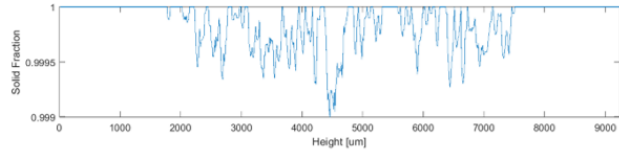| Power	275 W
Border power	250 W
Fill contour offset	100%
Hatch compensation	50%

Figure K 22. Minimum intensity projection images from CT analysis. Build variables correspond to sample I.D. 13-3.

Parameters for sample I.D. 13-4

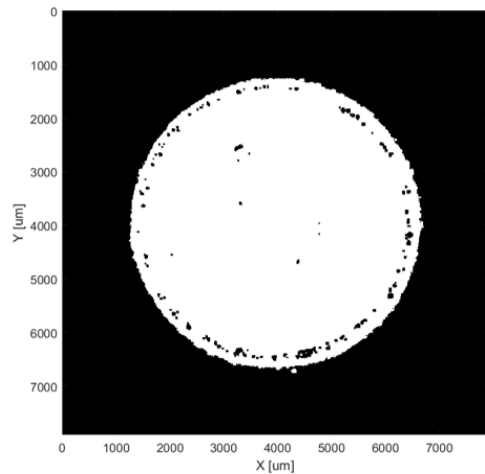|	
Power	275 W
Border power	275 W
Fill contour offset	100%
Hatch compensation	50%

Figure K 23. Minimum intensity projection images from CT analysis. Build variables correspond to sample I.D. 13-4.

Parameters for sample I.D. 15-1

Power	300 W
Border power	250 W
Fill contour offset	100%
Hatch compensation	50%

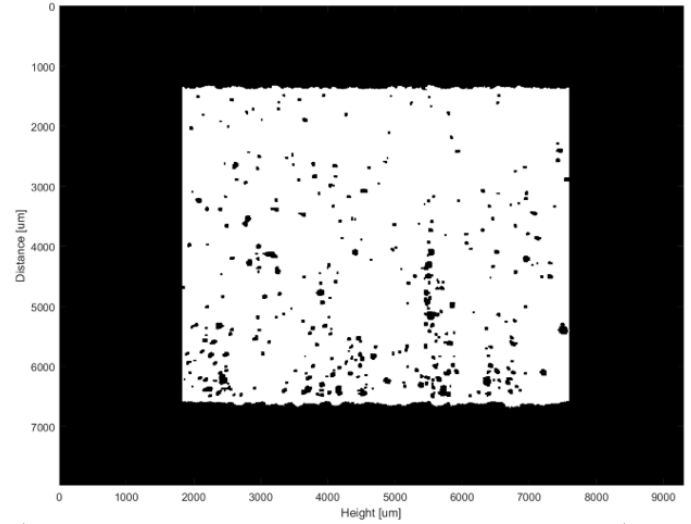**Figure K 24. Minimum intensity projection images from CT analysis. Build variables correspond to sample I.D. 15-1.**

Parameters for sample I.D. 15-2

Power	300 W
Border power	275 W
Fill contour offset	100%
Hatch compensation	50%

Figure K 25. Minimum intensity projection images from CT analysis. Build variables correspond to sample I.D. 15-2.

Parameters for sample I.D. 15-3

Power	300 W
Border power	250 W
Fill contour offset	100%
Hatch compensation	50%

Figure K 26. Minimum intensity projection images from CT analysis. Build variables correspond to sample I.D. 15-3.

311

Parameters for sample I.D. 15-4

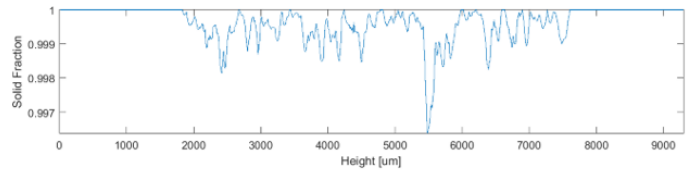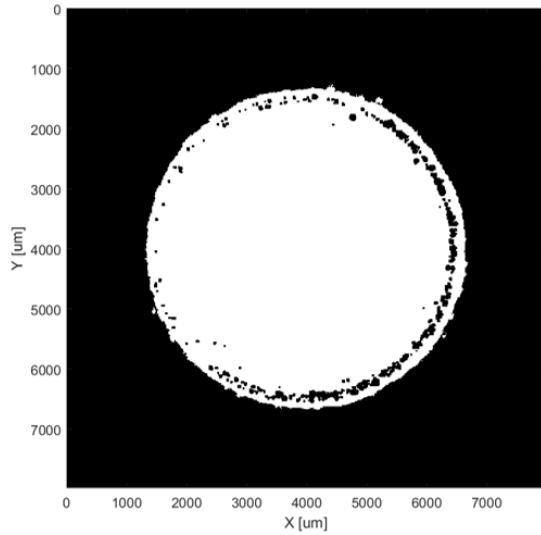| Power	300 W
Border power	275 W
Fill contour offset	100%
Hatch compensation	50%

Figure K 27. Minimum intensity projection images from CT analysis. Build variables correspond to sample I.D. 15-4.

Appendix L:
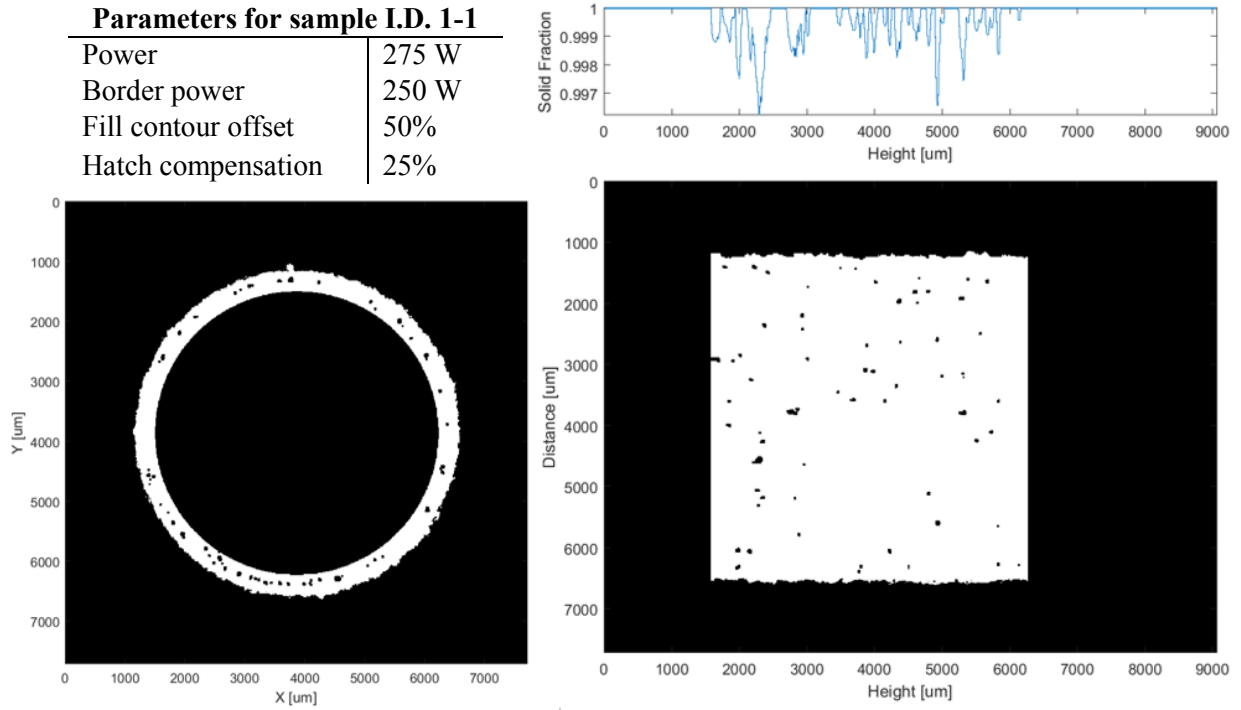
CT Analysis Results (Core Removed) for Chapter 5

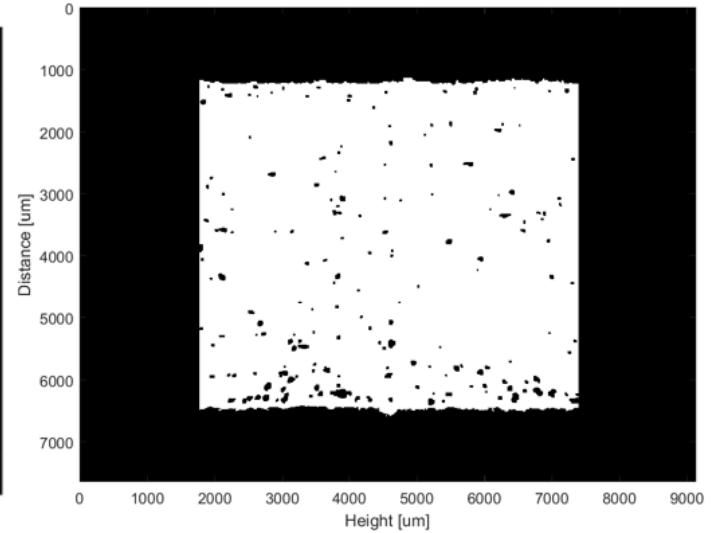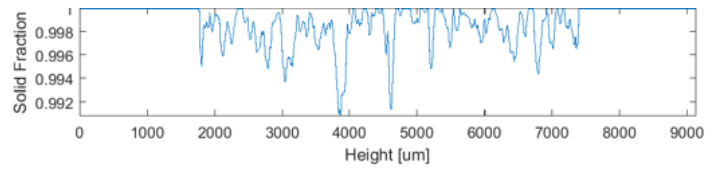| Parameters for sample I.D. 1-1	
Power	275 W
Border power	250 W
Fill contour offset	50%
Hatch compensation	25%

Figure L 1. **Minimum intensity projection images from CT analysis. Build variables correspond to sample I.D. 1-1.**

Parameters for sample I.D. 1-2

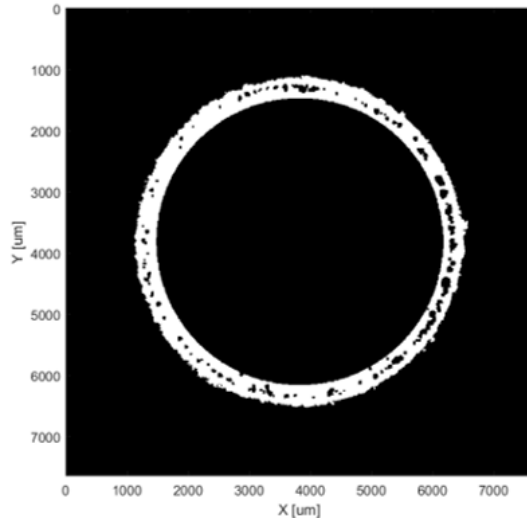| Power	275 W
Border power	275 W
Fill contour offset	50%
Hatch compensation	25%

Figure L 2. Minimum intensity projection images from CT analysis. Build variables correspond to sample I.D. 1-2.

Parameters for sample I.D. 1-3

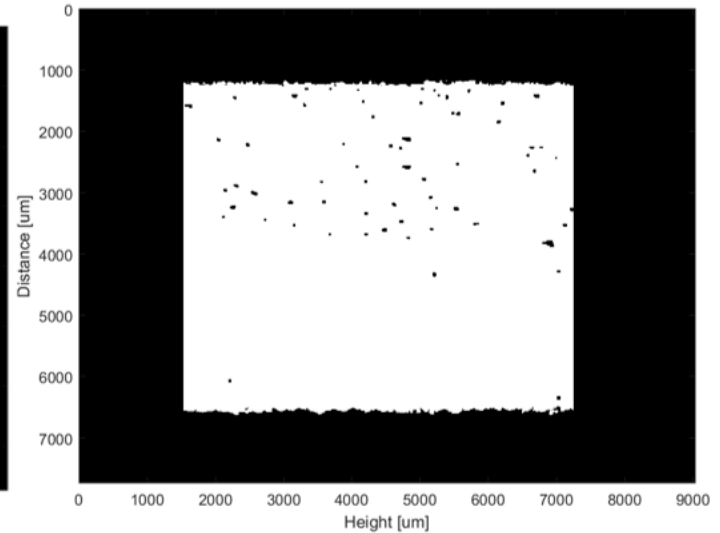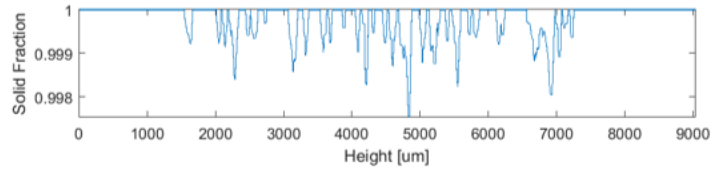| Power	275 W
Border power	250 W
Fill contour offset	50%
Hatch compensation	25%

Figure L 3. Minimum intensity projection images from CT analysis. Build variables correspond to sample I.D. 1-3.

Parameters for sample I.D. 1-4

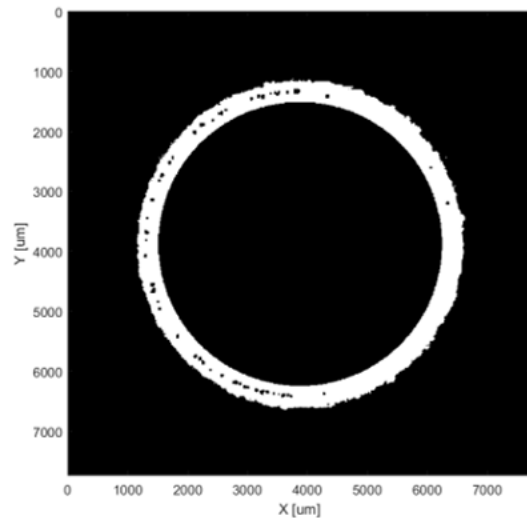| Power	275 W
Border power	275 W
Fill contour offset	50%
Hatch compensation	25%

Figure L 4. Minimum intensity projection images from CT analysis. Build variables correspond to sample I.D. 1-4.

Parameters for sample I.D. 3-1

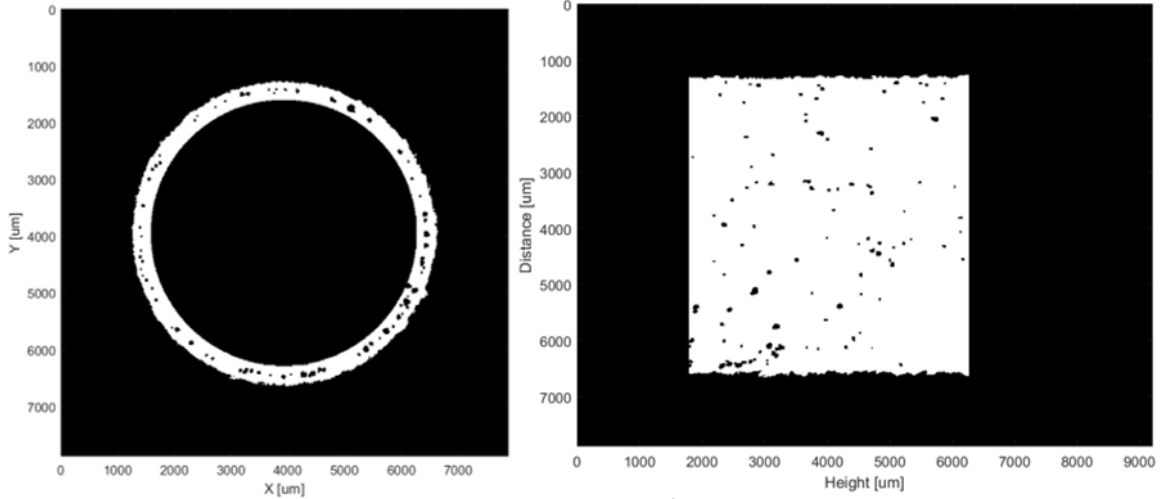| Power	300 W
Border power	250 W
Fill contour offset	50%
Hatch compensation	25%

Figure L 5. Minimum intensity projection images from CT analysis. Build variables correspond to sample I.D. 3-1.

315

Parameters for sample I.D. 3-3

Power	300 W
Border power	250 W
Fill contour offset	50%
Hatch compensation	25%

Figure L 6. Minimum intensity projection images from CT analysis. Build variables correspond to sample I.D. 3-3.

Parameters for sample I.D. 3-4

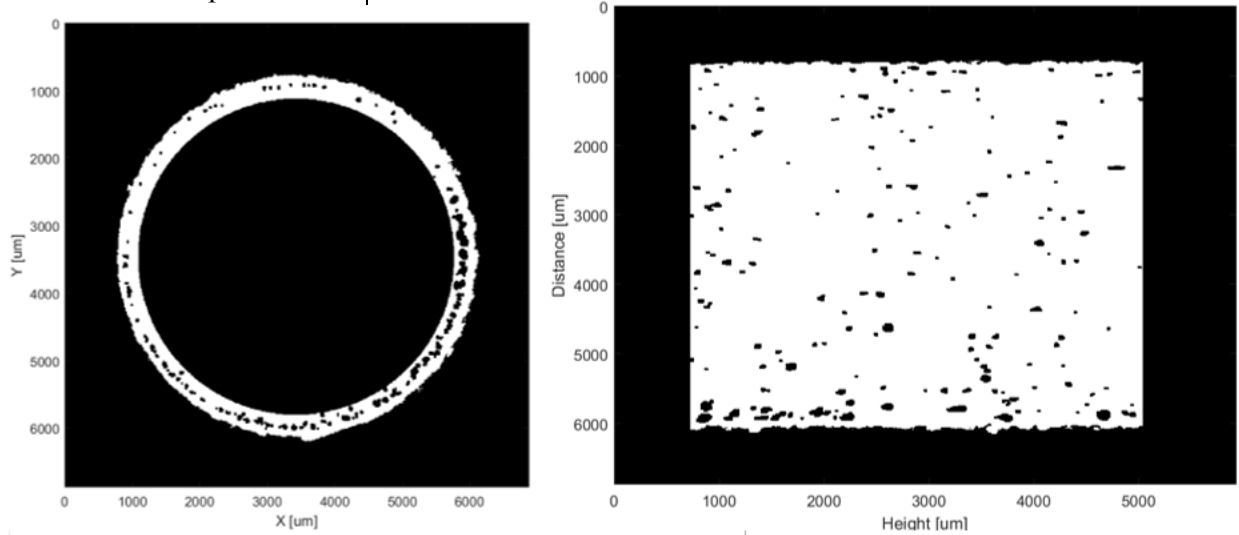|	
Power	300 W
Border power	275 W
Fill contour offset	50%
Hatch compensation	25%

Figure L 7. Minimum intensity projection images from CT analysis. Build variables correspond to sample I.D. 3-4.

Parameters for sample I.D. 5-1

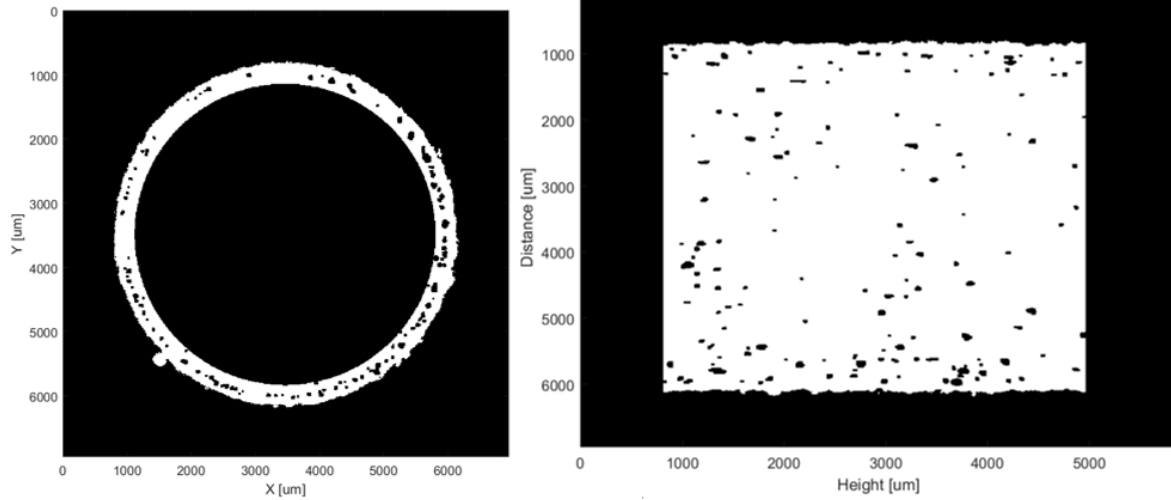| Power	275 W
Border power	250 W
Fill contour offset	100%
Hatch compensation	25%

Figure L 8. Minimum intensity projection images from CT analysis. Build variables correspond to sample I.D. 5-1.

Parameters for sample I.D. 5-2

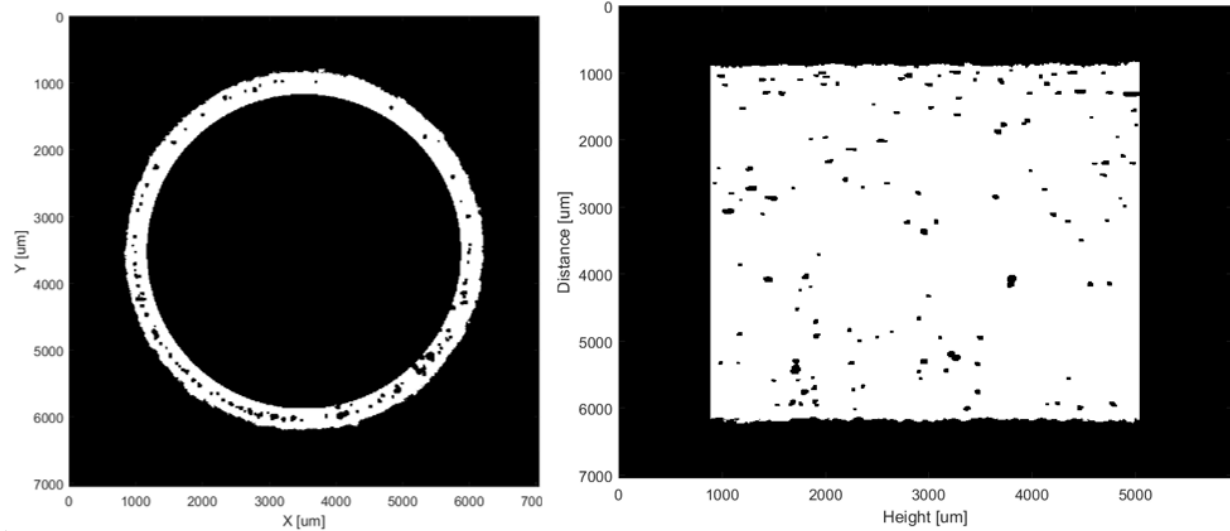| Power	275 W
Border power	275 W
Fill contour offset	100%
Hatch compensation	25%

Figure L 9. Minimum intensity projection images from CT analysis. Build variables correspond to sample I.D. 5-2.

Parameters for sample I.D. 5-3

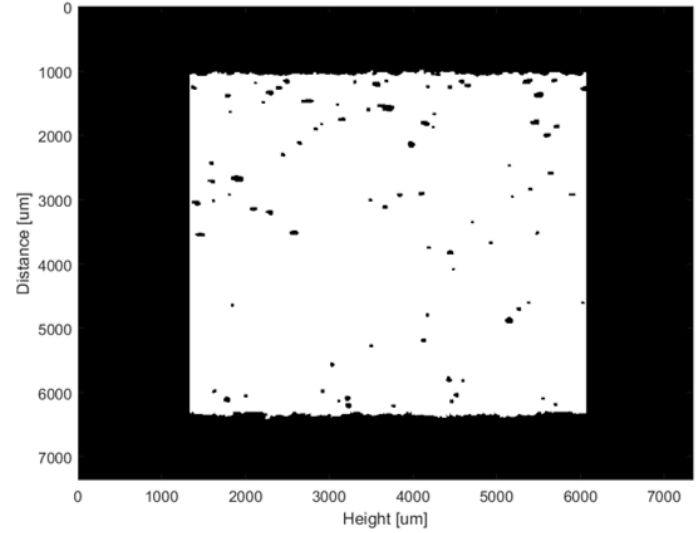| Power	275 W
Border power	250 W
Fill contour offset	100%
Hatch compensation	25%

Figure L 10. Minimum intensity projection images from CT analysis. Build variables correspond to sample I.D. 5-3.

Parameters for sample I.D. 5-4

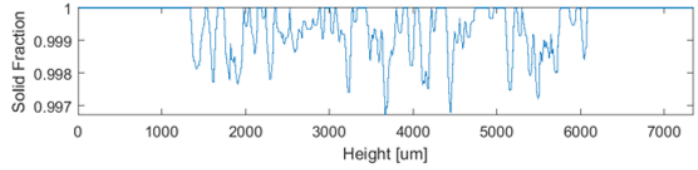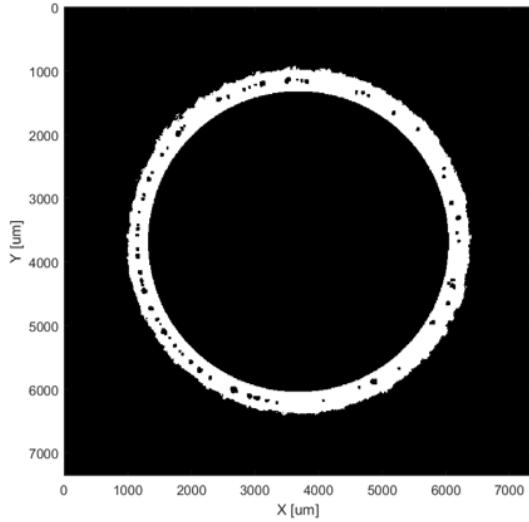| Power	275 W
Border power	250 W
Fill contour offset	100%
Hatch compensation	25%

Figure L 11. Minimum intensity projection images from CT analysis. Build variables correspond to sample I.D. 5-4.

Parameters for sample I.D. 7-1

Power	300 W
Border power	250 W
Fill contour offset	100%
Hatch compensation	25%

Figure L 12. Minimum intensity projection images from CT analysis. Build variables correspond to sample I.D. 7-1.

Parameters for sample I.D. 7-3

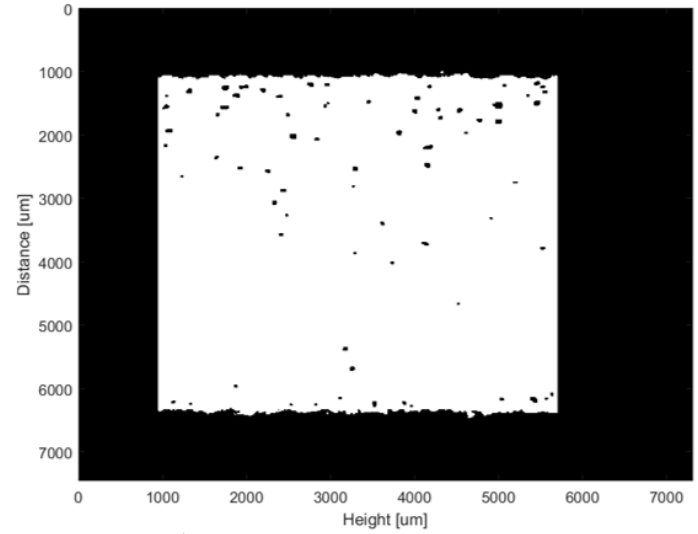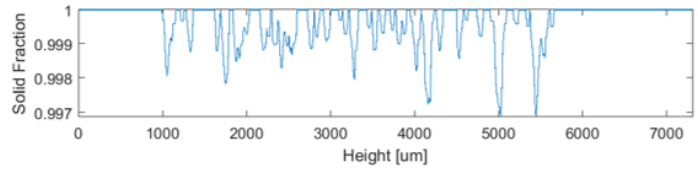| Power	300 W
Border power	250 W
Fill contour offset	100%
Hatch compensation	25%

Figure L 13. Minimum intensity projection images from CT analysis. Build variables correspond to sample I.D. 7-3.

Parameters for sample I.D. 7-4

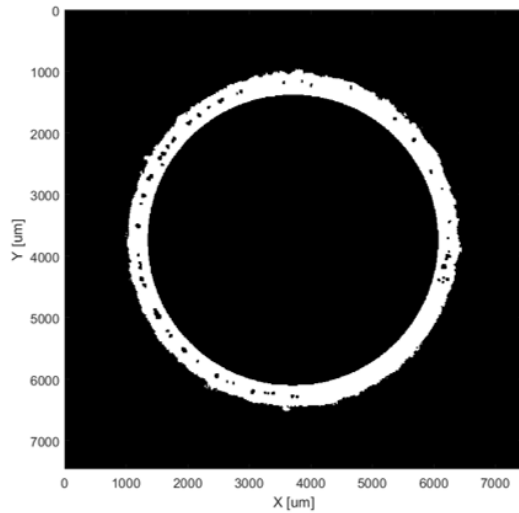| Power	300 W
Border power	275 W
Fill contour offset	100%
Hatch compensation	25%

Figure L 14. Minimum intensity projection images from CT analysis. Build variables correspond to sample I.D. 7-4.

Parameters for sample I.D. 9-2

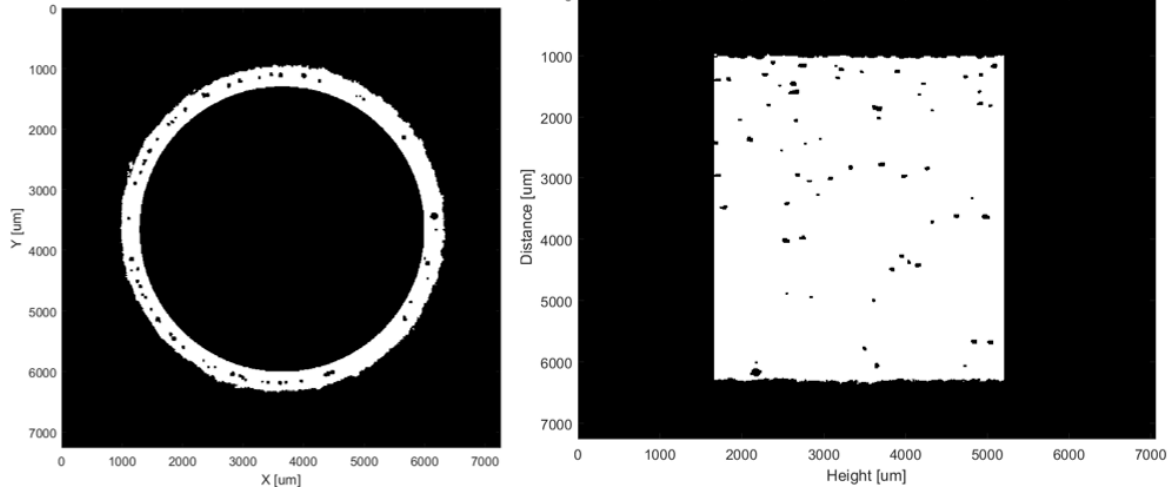| Power	275 W
Border power	275 W
Fill contour offset	50%
Hatch compensation	50%
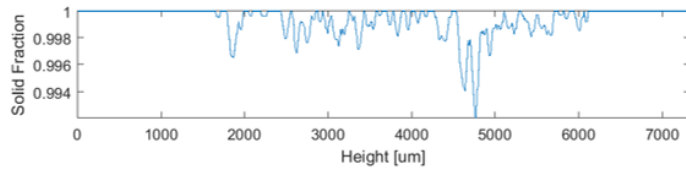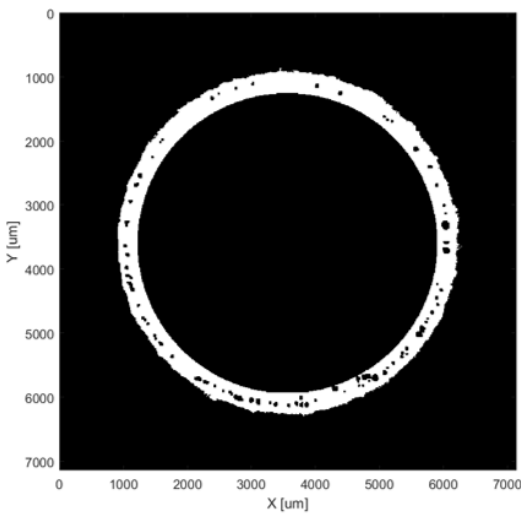
Figure L 15. Minimum intensity projection images from CT analysis. Build variables correspond to sample I.D. 9-

320

2.

Parameters for sample I.D. 9-3

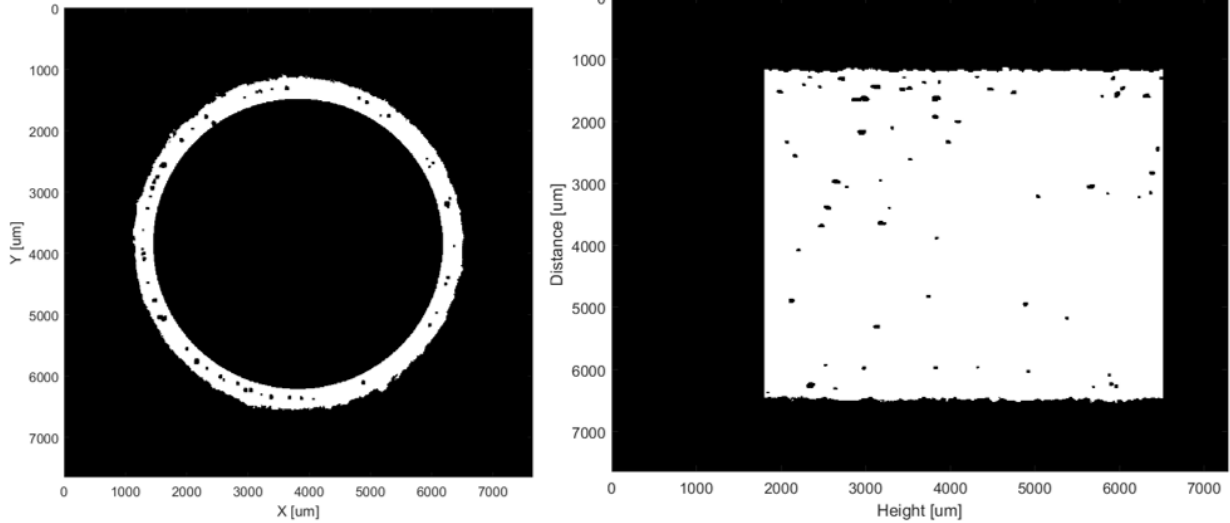|	
Power	275 W
Border power	250 W
Fill contour offset	50%
Hatch compensation	50%
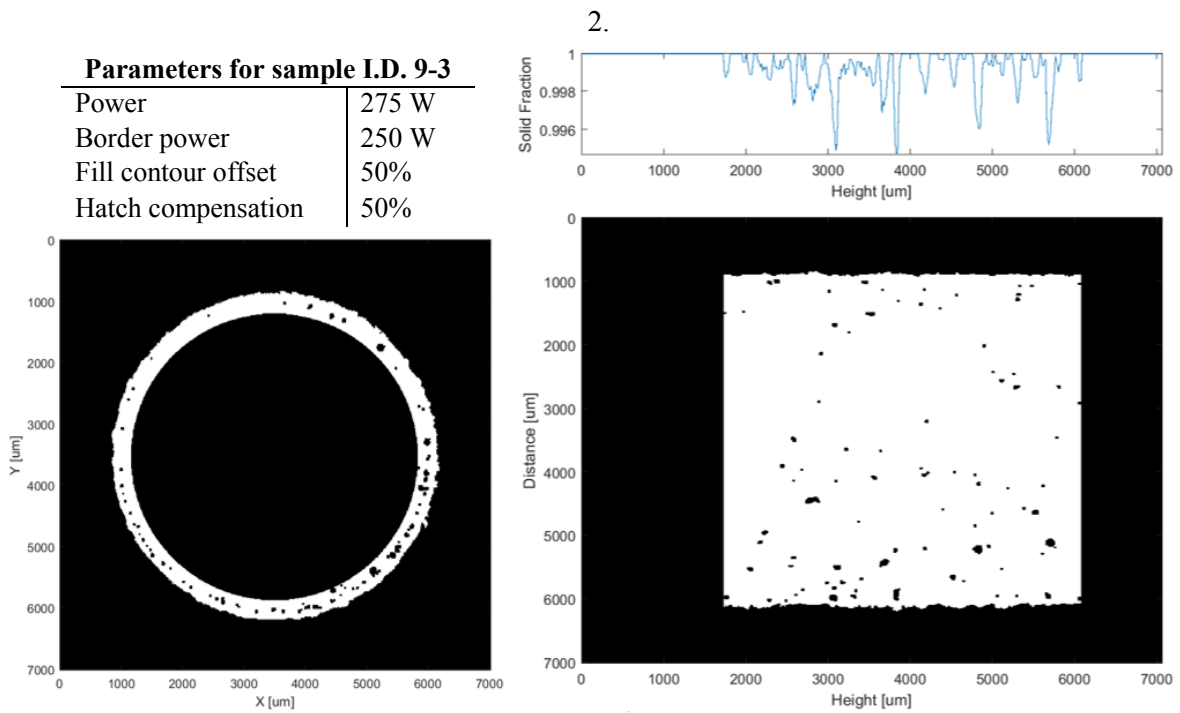
Figure L 16. Minimum intensity projection images from CT analysis. Build variables correspond to sample I.D. 9-3.

Parameters for sample I.D. 9-4

Power	275 W
Border power	275 W
Fill contour offset	50%
Hatch compensation	50%

Figure L 17. Minimum intensity projection images from CT analysis. Build variables correspond to sample I.D. 9-4.

Parameters for sample I.D. 11-2

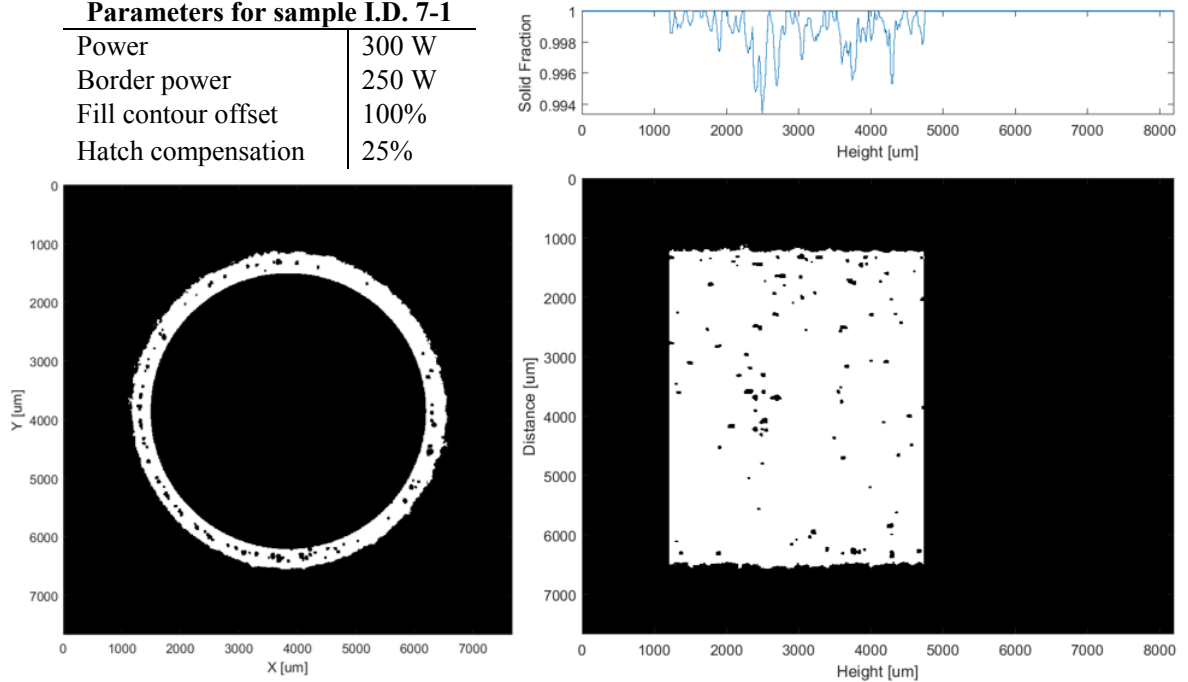| Power	300 W
Border power	275 W
Fill contour offset	50%
Hatch compensation	50%

Figure L 18. Minimum intensity projection images from CT analysis. Build variables correspond to sample I.D. 11-2.

Parameters for sample I.D. 11-3

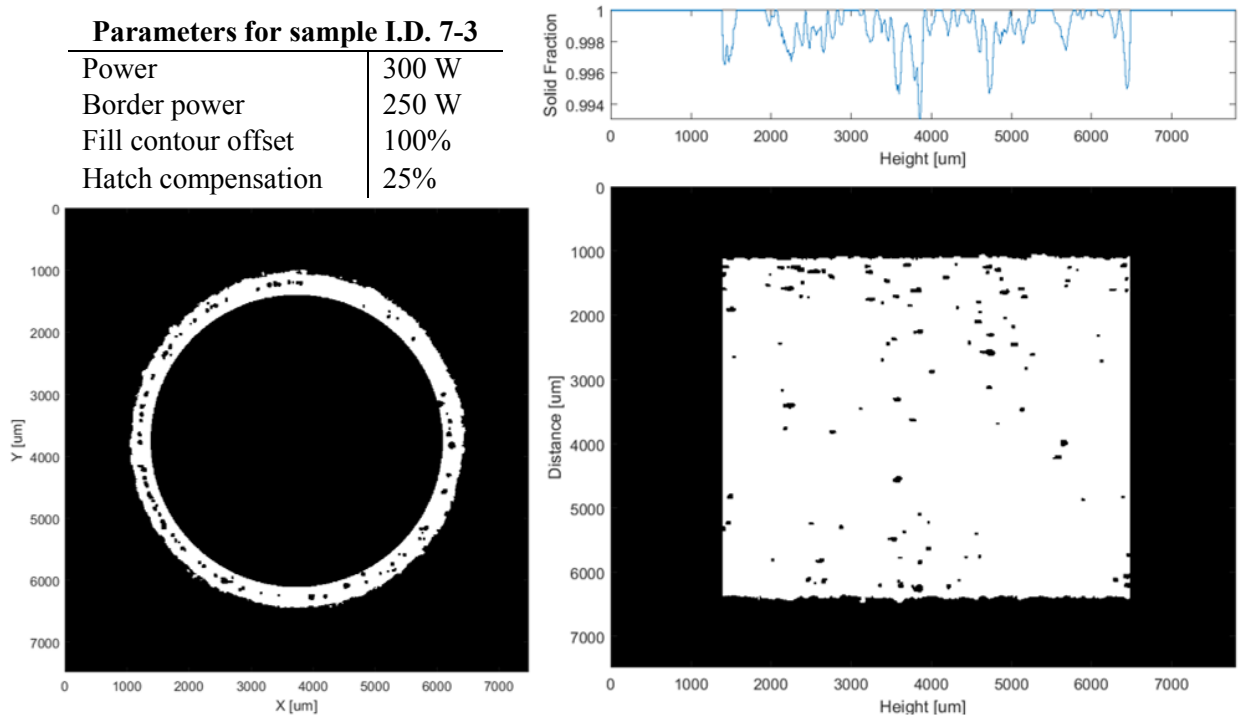| Power	300 W
Border power	250 W
Fill contour offset	50%
Hatch compensation	50%

Figure L 19. Minimum intensity projection images from CT analysis. Build variables correspond to sample I.D. 11-3.

Parameters for sample I.D. 11-4

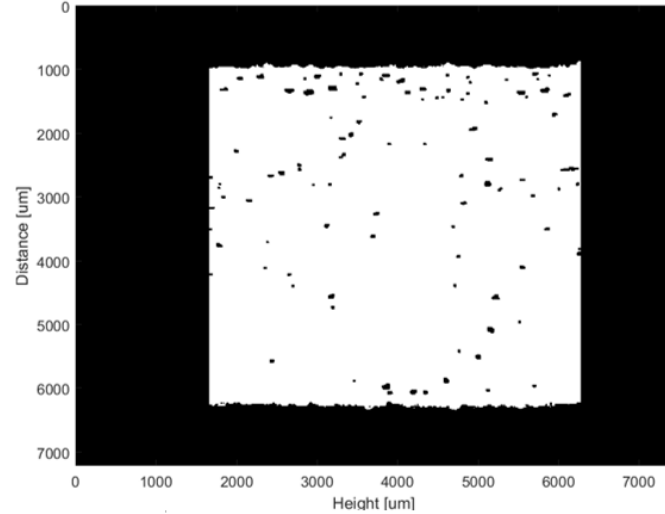| Power	300 W
Border power	275 W
Fill contour offset	50%
Hatch compensation	50%

Figure L 20. Minimum intensity projection images from CT analysis. Build variables correspond to sample I.D. 11-4.

Parameters for sample I.D. 13-1

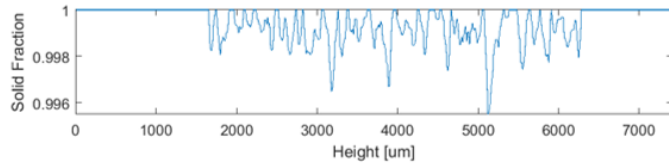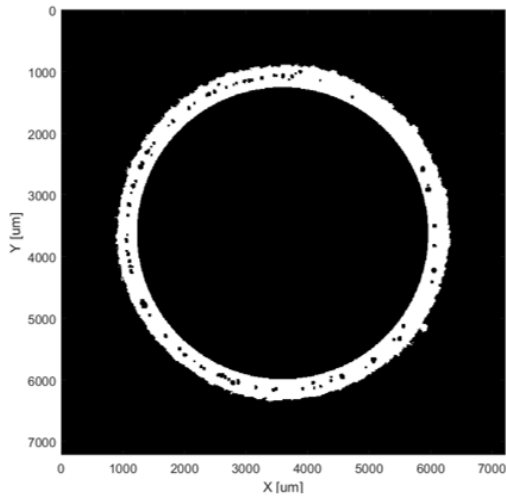| Power	275 W
Border power	250 W
Fill contour offset	100%
Hatch compensation	50%

Figure L 21. Minimum intensity projection images from CT analysis. Build variables correspond to sample I.D. 13-1.

323

Parameters for sample I.D. 13-2

Power	275 W
Border power	275 W
Fill contour offset	100%
Hatch compensation	50%

Figure L 22. Minimum intensity projection images from CT analysis. Build variables correspond to sample I.D. 13-2.

Parameters for sample I.D. 13-3

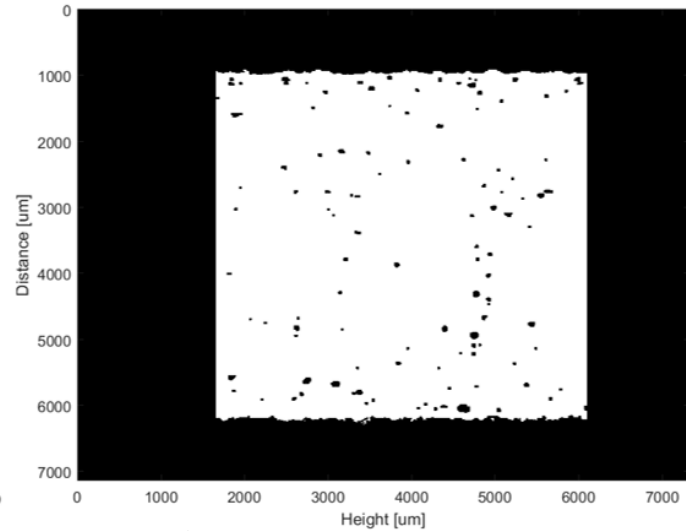| Power	275 W
Border power	250 W
Fill contour offset	100%
Hatch compensation	50%
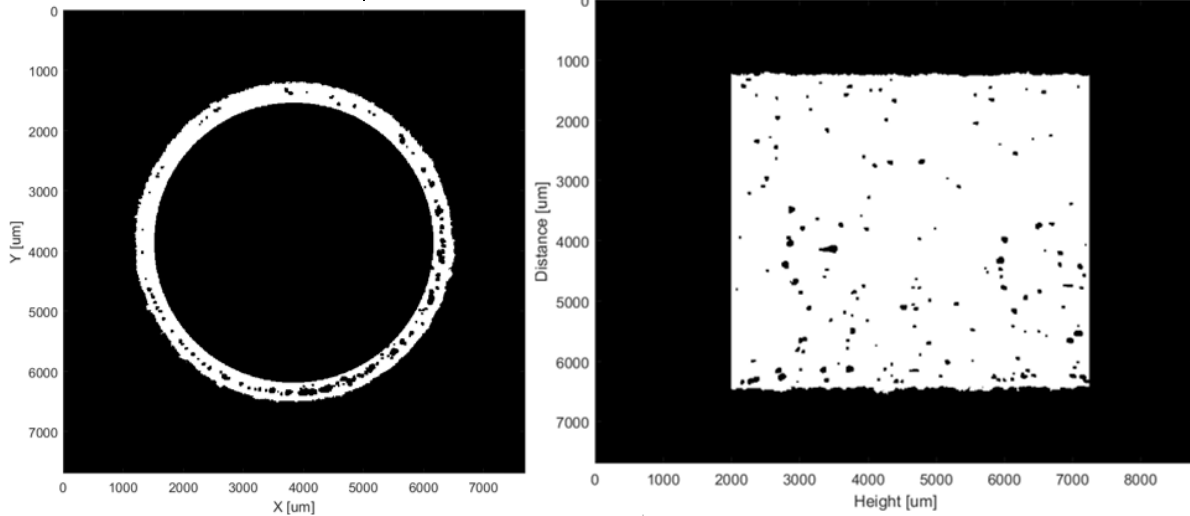
Figure L 23. Minimum intensity projection images from CT analysis. Build variables correspond to sample I.D. 13-3.

Parameters for sample I.D. 13-4

Power	275 W
Border power	275 W
Fill contour offset	100%
Hatch compensation	50%
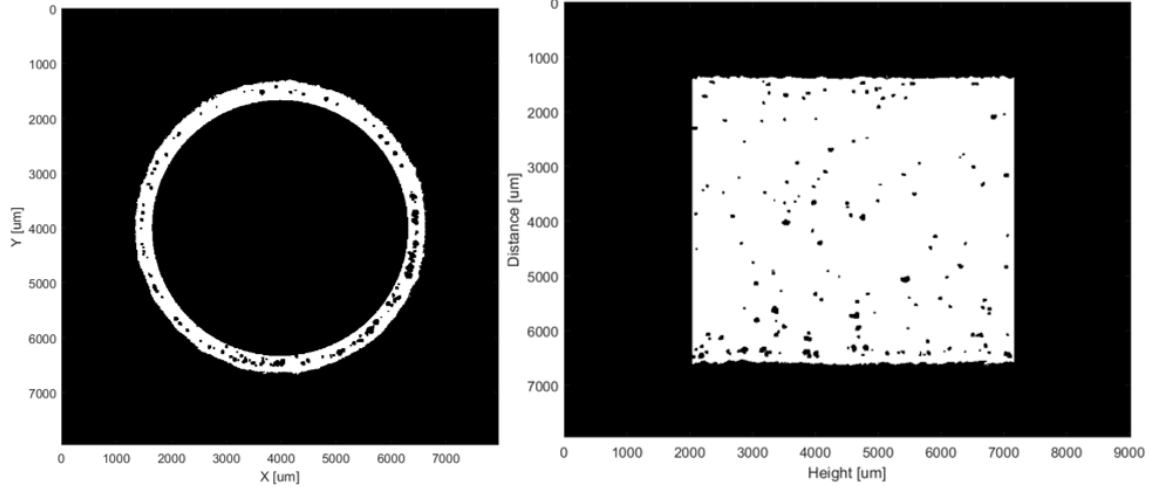
Figure L 24. Minimum intensity projection images from CT analysis. Build variables correspond to sample I.D. 13-4.

Parameters for sample I.D. 15-1

Power	300 W
Border power	250 W
Fill contour offset	100%
Hatch compensation	50%
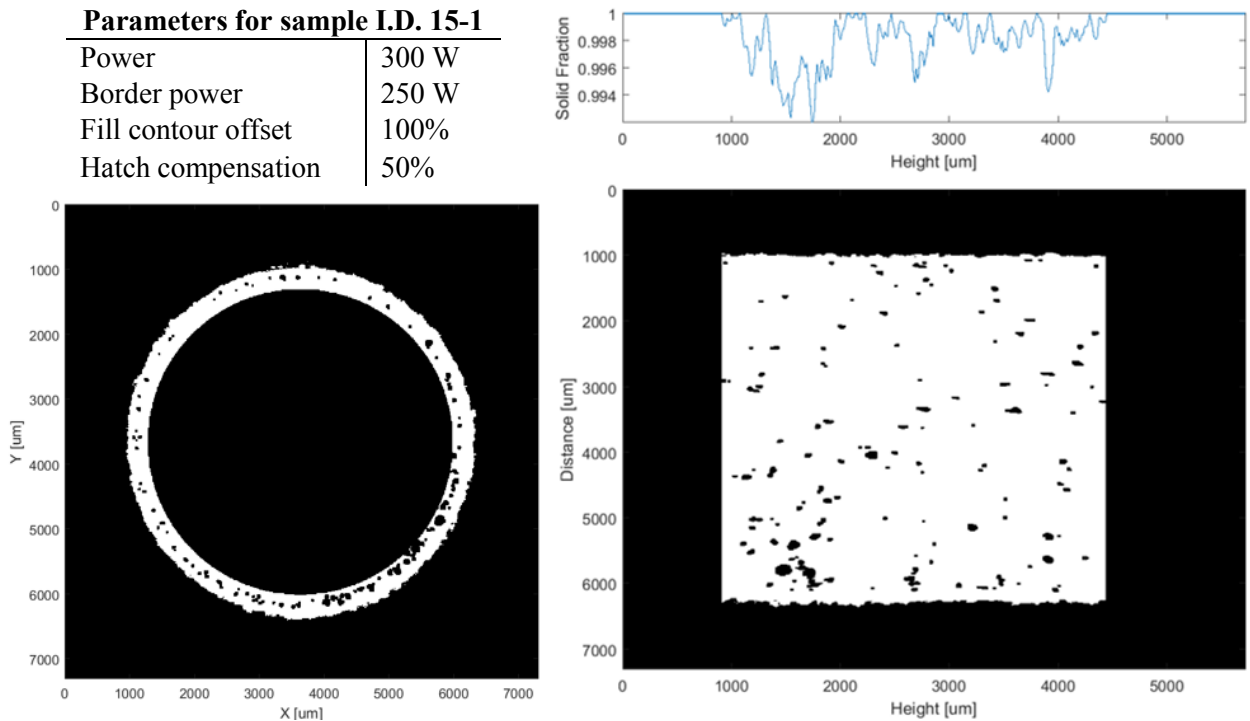
Figure L 25. Minimum intensity projection images from CT analysis. Build variables correspond to sample I.D. 15-1.

Parameters for sample I.D. 15-2
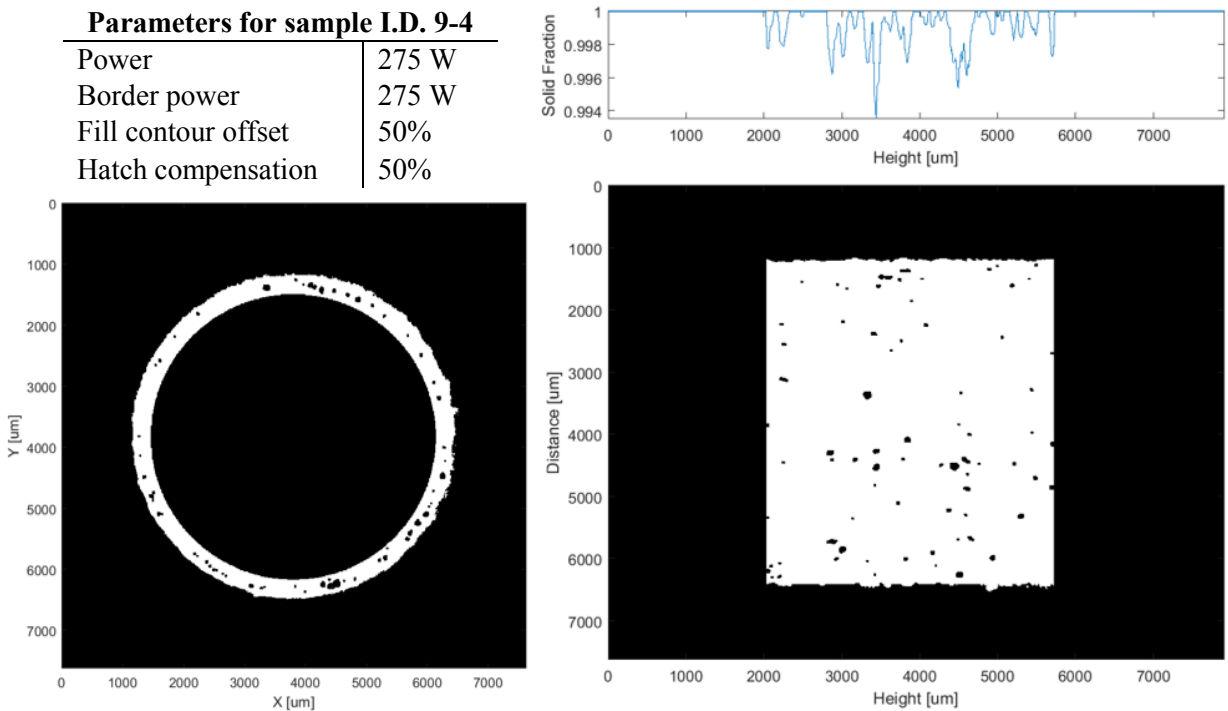
Power	300 W
Border power	275 W
Fill contour offset	100%
Hatch compensation	50%
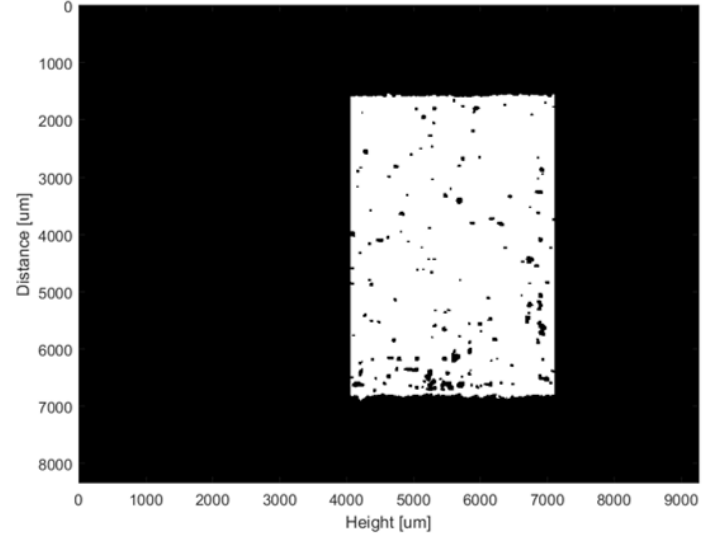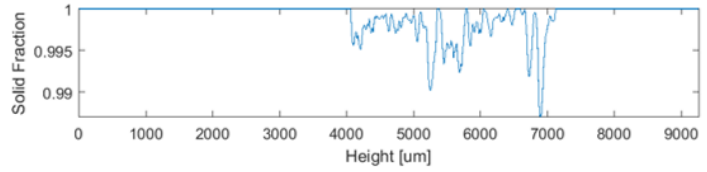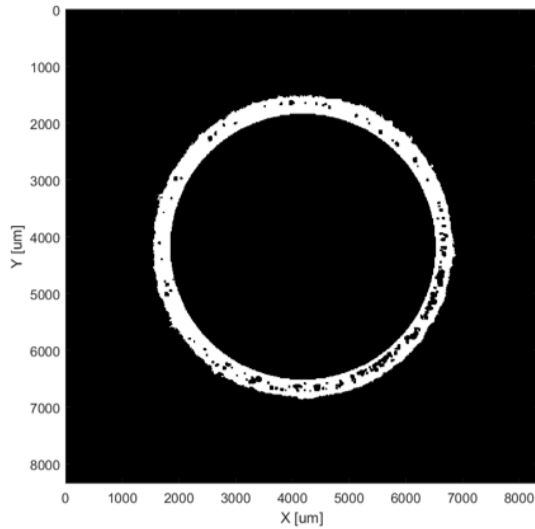
Figure L 26. Minimum intensity projection images from CT analysis. Build variables correspond to sample I.D. 15-2.

Parameters for sample I.D. 15-3

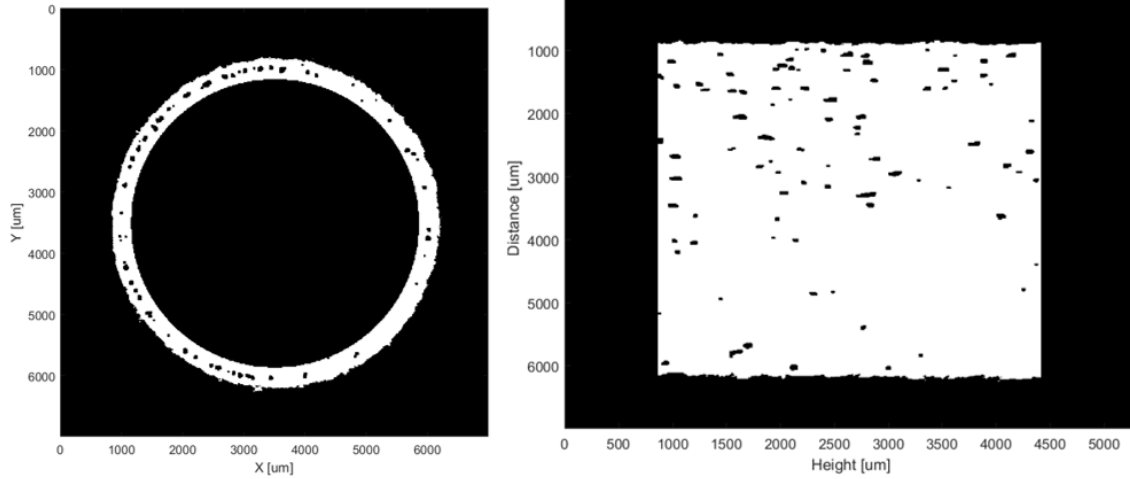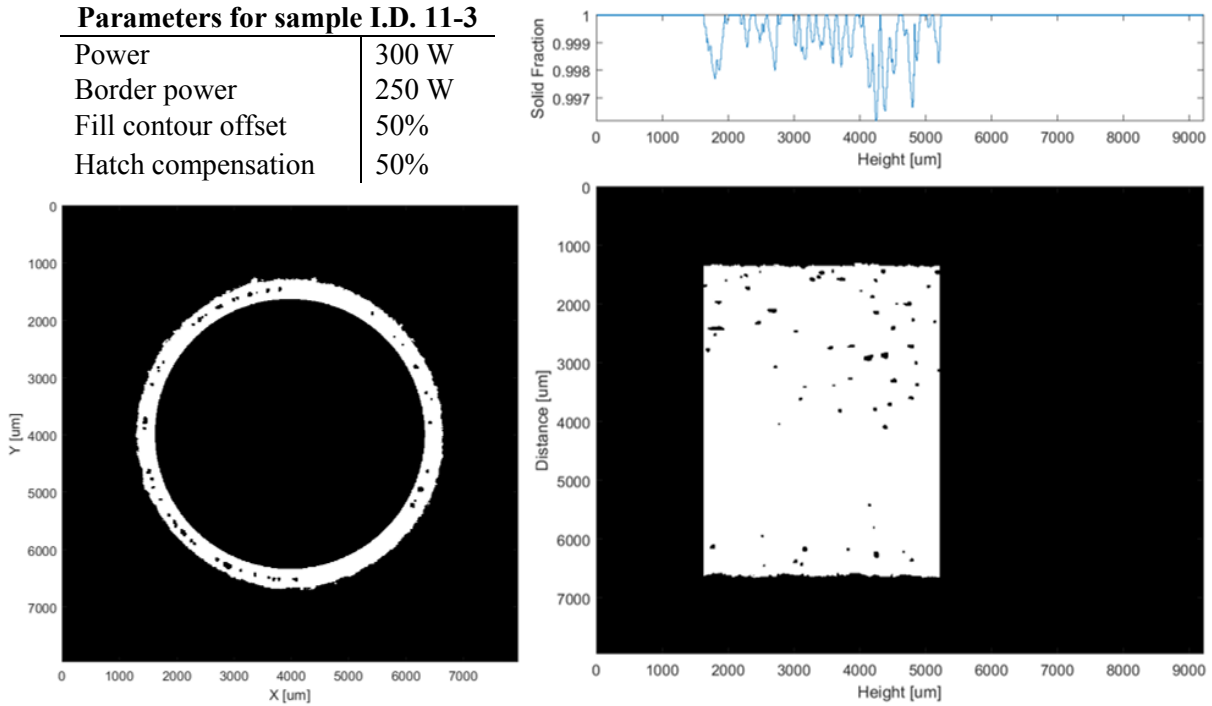| Power	300 W
Border power	250 W
Fill contour offset	100%
Hatch compensation	50%

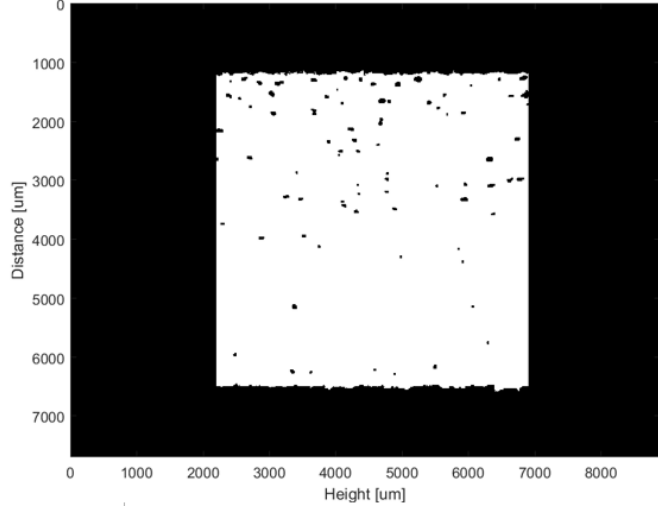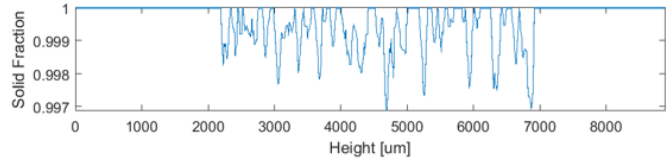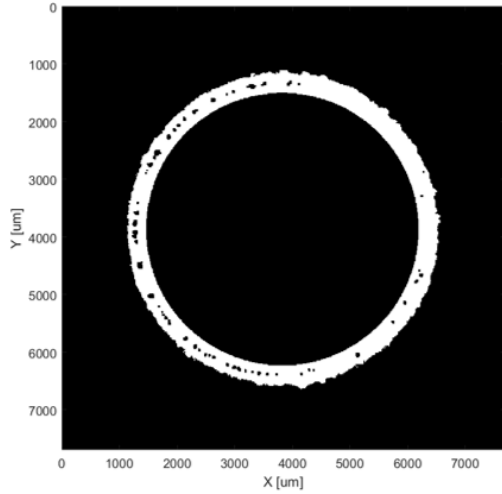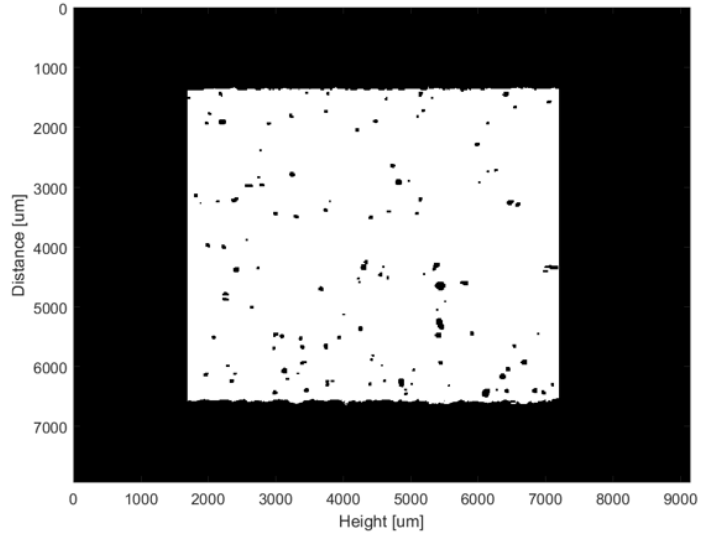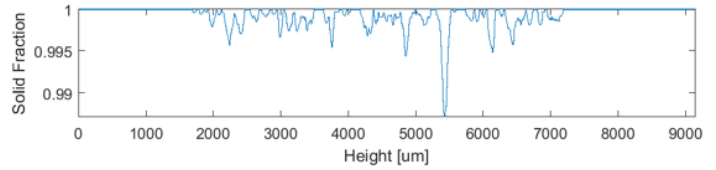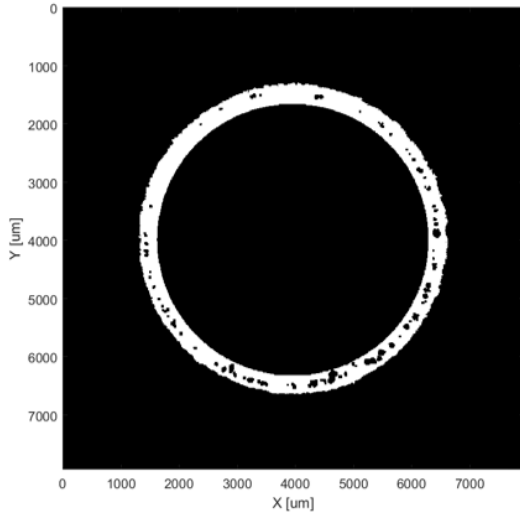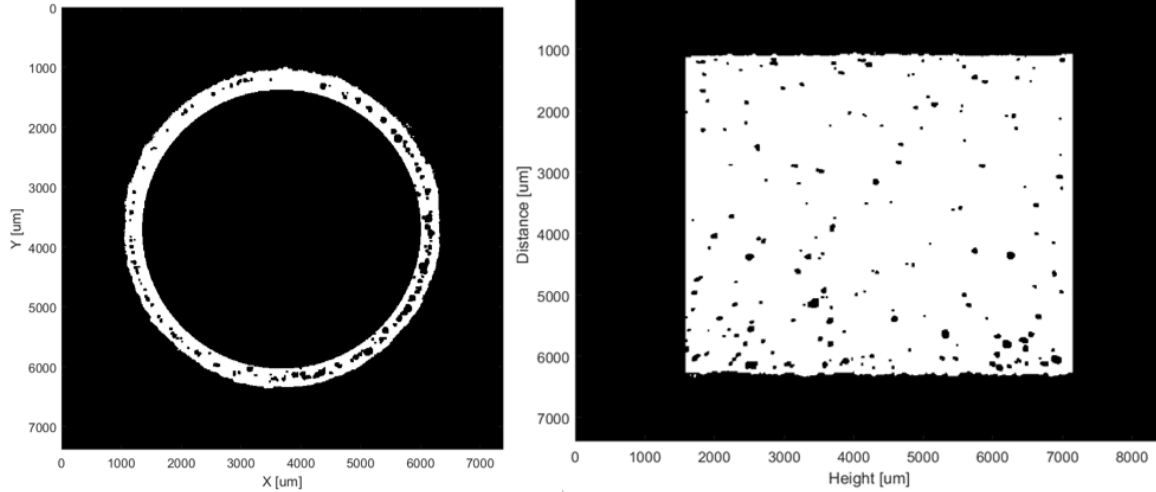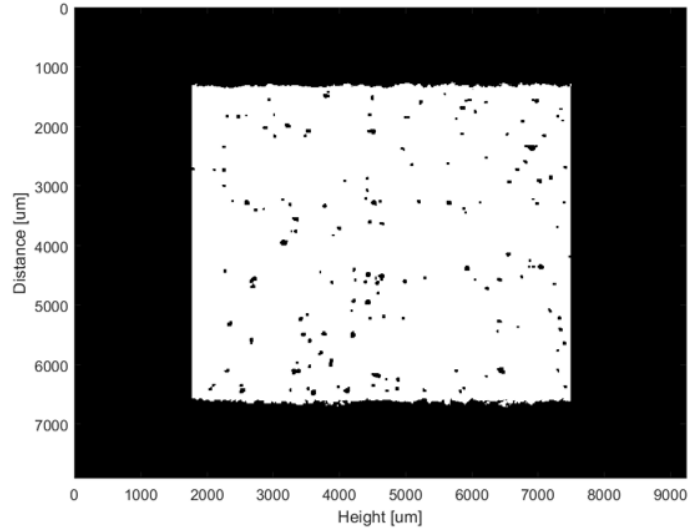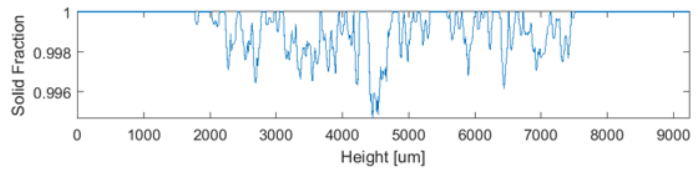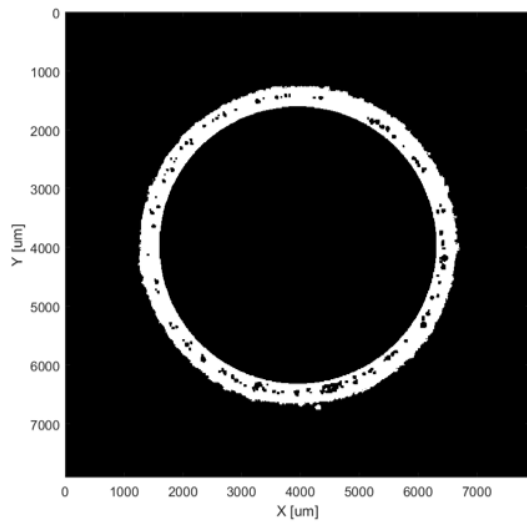**Figure L 27. Minimum intensity projection images from CT analysis. Build variables correspond to sample I.D. 15-3.**

Parameters for sample I.D. 15-4

Power	300 W
Border power	275 W
Fill contour offset	100%
Hatch compensation	50%
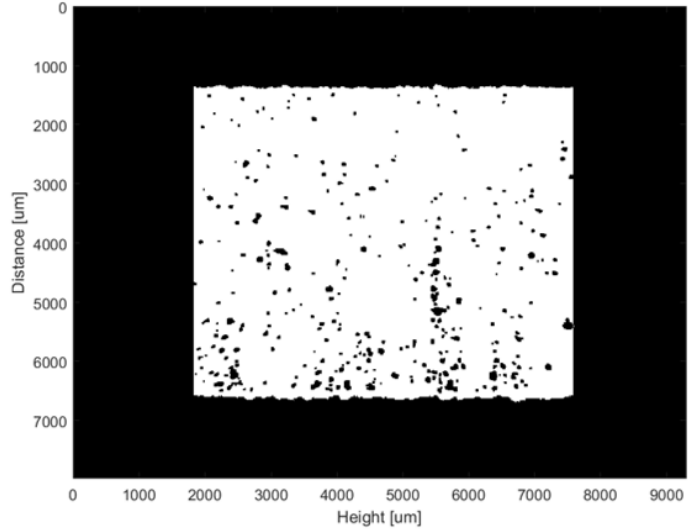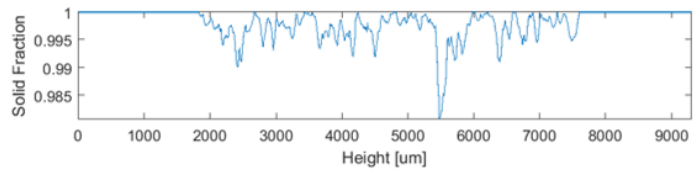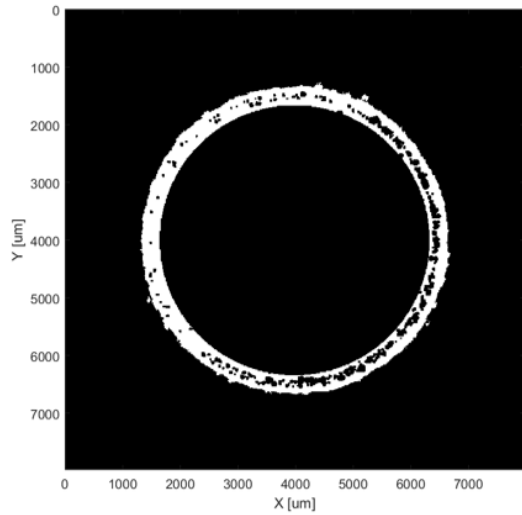
Figure L 28. Minimum intensity projection images from CT analysis. Build variables correspond to sample I.D. 15-4.

Appendix M:

Raw Data for Statistical Analysis of Chapter 5

Table M 1. Raw data input for the MATLab code. Values correspond to the variable 'perf' within the code.

Hatch Compensation [%]	Fill Contour Offset [%]	Laser Power [W]	Border Power [W]	Batch	Full Solid Fraction	Border Only Solid Fraction
25	50	275	250	1	0.999861	0.99942
25	50	275	250	2	0.999887	0.999645
25	50	275	275	1	0.999642	0.998125
25	50	275	275	2	0.999793	0.998917
25	50	300	250	1	0.999557	0.997681
25	50	300	250	2	0.999674	0.998296
25	50	300	275	1	NaN	NaN
25	50	300	275	2	0.999744	0.998669
25	100	275	250	1	0.999757	0.999168
25	100	275	250	2	0.99982	0.9992
25	100	275	275	1	0.999752	0.999431
25	100	275	275	2	0.999826	0.999431
25	100	300	250	1	0.999747	0.998691
25	100	300	250	2	0.999781	0.998889
25	100	300	275	1	NaN	NaN
25	100	300	275	2	0.99979	0.999067
50	50	275	250	1	NaN	NaN
50	50	275	250	2	0.999826	0.999122
50	50	275	275	1	0.999764	0.998934
50	50	275	275	2	0.999793	0.999012
50	50	300	250	1	NaN	NaN
50	50	300	250	2	0.999791	0.999176
50	50	300	275	1	0.999716	0.998638
50	50	300	275	2	0.999828	0.999239
50	100	275	250	1	0.999758	0.998746
50	100	275	250	2	0.999667	0.998264
50	100	275	275	1	0.999592	0.997944
50	100	275	275	2	0.999666	0.998263
50	100	300	250	1	0.999585	0.99793
50	100	300	250	2	0.999773	0.998852

Table M 1 (cont'd). Raw data input for the MATLab code. Values correspond to the variable 'perf' within the code.

Hatch Compensation [%]	Fill Contour Offset [%]	Laser Power [W]	Border Power [W]	Batch	Full Solid Fraction	Border Only Solid Fraction
50	100	300	275	1	0.99948	0.997284
50	100	300	275	2	0.999404	0.996933

Appendix N:

MATLab Code for Statistical Analysis of Chapter 5

```
%% Initializing

clear all; close all; clc;

%Loading perf table
%Format is HATCH COMP. | Fill Contour Offset. | Power | Border Poewr |
%Batch | Solid Fraction
% WHERE ... can be any other miscellaneous columns
load('MATLab.mat');

%My Solver
%%{
%Required constants
a = length(unique(perf(:,1))); % Number of hatch compensation levels
b = length(unique(perf(:,2))); % Number of fill contour offset levels
c = length(unique(perf(:,3))); % Number of power levels
d = length(unique(perf(:,4))); % Number of border power levels
n = length(unique(perf(:,5))); % Number of batches
index = length(perf(1,:));     % Column number where perf is.



%% ANOVA

A = perf(:,3); %Power
B = perf(:,4); %Border Power
C = perf(:,2); %Fill contour Offset
D = perf(:,1); %Hatch compensation
N = perf(:,5);


denn = perf(:,length(perf(1,:))-1);

[p, t, stats, terms] = anovan(denn,{A B C D},'model','full' ,'varnames',{'A', 'B',
'C', 'D'});
alpha = 0.05;
significance = p < alpha;
t(1,8) = cellstr(strcat('Significant at alpha =',num2str(alpha),'?'));
t(2:length(significance)+1,8) = num2cell(significance);
cell2table(t)
scatter(perf(:,6),stats.resid)
xlabel('Actual Solid Fraction')
ylabel('Model Residual')
title('Plot of Residuals vs Actual Values')
Rsq = 1-(cell2mat(t(end-1,2))/cell2mat(t(end-
1,3)))/(cell2mat(t(end,2))/cell2mat(t(end,3)))

%%{
%%
%Reduced
```

```matlab
%[p, t, stats,terms] = anovan(denn,{A B C D},'model',[1 0 0 0 ; 0 1 0 0 ; 0 0 1 0;0
0 0 1 ; 1 1 0 0 ; 1 0 1 0; 1 0 0 1 ; 0 1 1 0 ; 0 1 0 1 ; 0 0 1 1 ; 1 1 1 0 ; 1 1 0
1 ; 1 0 1 1; 0 1 1 1; 1 1 1 1],'varnames',{'A', 'B', 'C', 'D'}, 'alpha', .05);
% [p, t, stats,terms] = anovan(denn,{A B C D},'model',[1 0 0 0 ; 0 1 0 0 ; 0 0 1
0;0 0 0 1 ; 1 1 0 0 ; 1 0 0 1],'varnames',{'A', 'B', 'C', 'D'}, 'alpha', .05);
[p, t, stats,terms] = anovan(denn,{A B C D},'model',[1 0 0 0 ; 0 1 0 0 ; 0 0 1 0 ;
0 0 0 1 ; 1 1 0 0 ; 1 0 1 0 ; 1 0 0 1 ; 0 1 1 0 ; 0 1 0 1 ; 0 0 1 1; 1 1 1 0 ; 1 1
0 1 ; 1 0 1 1 ; 0 1 1 1 ; 1 1 1 1],'varnames',{'A', 'B', 'C', 'D'}, 'alpha', .05);
[p, t, stats,terms] = anovan(denn,{A B C D},'model',[1 0 0 0 ; 0 1 0 0 ; 0 0 1 0 ;
0 0 0 1 ; 1 1 0 0 ; 1 0 1 0 ; 1 0 0 1 ; 0 1 1 0 ; 0 1 0 1 ; 0 0 1 1; 1 1 1 0 ; 1 1
0 1 ; 1 0 1 1 ; 0 1 1 1],'varnames',{'A', 'B', 'C', 'D'}, 'alpha', .05);

alpha = 0.05;
significance = p < alpha;
t(1,8) = cellstr(strcat('Significant at alpha =',num2str(alpha),'?'));
t(2:length(significance)+1,8) = num2cell(significance);
cell2table(t)

Rsq = 1-(cell2mat(t(end-1,2))/cell2mat(t(end-
1,3)))/(cell2mat(t(end,2))/cell2mat(t(end,3)))
%}
```

Appendix O:
MATLab Code for Importing the Finite Element Model into COMSOL

To use this code, COMSOL with MATLab integration is required

```matlab
function out = model
%
% MODEL_20180723.m
%
% Model exported on Jul 25 2018, 19:50 by COMSOL 5.3.0.260.

import com.comsol.model.*
import com.comsol.model.util.*

model = ModelUtil.create('Model');

model.modelPath('C:\Users\Msam\Documents\Henry\COMSOL\2018-07');

model.label('MODEL_20180723.mph');

model.comments(['Untitled\n\n']);

model.param.set('P', '300[W]', 'Power');
model.param.set('D_l', '30 [um]', 'Layer Thickness');
model.param.set('t_e', '70 [us]', 'Exposure Time');
model.param.set('t_drill', '10[us]');
model.param.set('D_p', '70 [um]', 'Point Distance');
model.param.set('r', '35 [um]', 'Laser Spot Radius');
model.param.set('Tsol', '1450 [degC]', 'Solidus Temperature');
model.param.set('Tmelt', '1460 [degC]', 'Liquidus Temperature');
model.param.set('a', '0.01', '% Conductivity as powder');
model.param.set('b', '1', '% Conductivity as solid');
model.param.set('w', 'r*sqrt(2)/2', 'Characteristic Radius');
model.param.set('T_inf', '20 [degC]', 'Environmental Temperature');
model.param.set('Io', 'P/(pi*w^2)', 'Intensity Scale Factor (Laser)');
model.param.set('A_rho', '0.7', 'Hemispherical Reflectivity');
model.param.set('A_a', '(1-A_rho)^0.5', 'Arbitrary Constant');
model.param.set('A_epsilon', '2/3', 'Packed Density');
model.param.set('A_L', 'D_l', 'Powder Bed Thickness');
model.param.set('A_lambda', 'A_beta*A_L', 'Optical Thickness');
model.param.set('A_beta', '1.5*(1-A_epsilon)/(A_epsilon*A_D2)', 'Extinction Coefficient');
model.param.set('A_D', '(1-A_a)*(1-A_a-A_rho*(1+A_a))*exp(-2*A_a*A_lambda)-(1+A_a)*(1+A_a-
A_rho*(1-A_a))*exp(2*A_a*A_lambda)', 'Arbitrary Constant');
model.param.set('A_D2', '24[um]', 'Particle Size');
model.param.set('x0', '0.3 [mm]', 'Initial X-Position of Laser');
model.param.set('y0', '0 [mm]', 'Initial Y-Position of Laser');
model.param.set('height', '10', 'Substrate height, in terms of # of layers');
model.param.set('A_As', 'A_rho*A_a/(4*A_rho-3)/A_D*((1-A_rho^2)*exp(-A_lambda)*((1-A_a)*exp(-
2*A_a*A_lambda)+(1+A_a)*exp(2*A_a*A_lambda))-2*(1-A_rho)*(3+A_rho*exp(-2*A_lambda)))-3*(1-
A_rho)^2*exp(-A_lambda)/(4*A_rho-3)', '[UNUSED] Residual Radiation on Substrate');

model.component.create('comp1', true);

model.component('comp1').geom.create('geom1', 3);

model.result.table.create('evl3', 'Table');
model.result.table.create('evl2', 'Table');

model.func.create('an1', 'Analytic');
model.func.create('an2', 'Analytic');
model.func.create('an3', 'Analytic');
```

```
model.func.create('an4', 'Analytic');
model.func.create('an9', 'Analytic');
model.func.create('an5', 'Analytic');
model.func.create('an6', 'Analytic');
model.func.create('an7', 'Analytic');
model.func.create('an10', 'Analytic');
model.func('an1').label('Gaussian Pulse');
model.func('an1').set('funcname', 'gp');
model.func('an1').set('expr', 'Io*exp(-2*x^2/w^2 [1/m^2]) [m^2/W]');
model.func('an1').set('plotargs', {'x' '-2*r' '2*r'});
model.func('an2').label('Radius');
model.func('an2').set('funcname', 'radius');
model.func('an2').set('expr', '((x[m]-pX(t[s]))^2+(y[m]-y0)^2)^0.5[1/m]');
model.func('an2').set('args', {'x' 'y' 't'});
model.func('an2').set('argunit', 'm, m, s');
model.func('an2').set('fununit', 'm');
model.func('an2').set('plotargs', {'x' '-6[mm]' '6[mm]'; 'y' '0' '0'; 't' '1' '1'});
model.func('an3').label('Laser Flux Input');
model.func('an3').set('funcname', 'laser');
model.func('an3').set('expr', 'gp(radius(x[m],y[m],t[s])) [m^2/W]');
model.func('an3').set('args', {'x' 'y' 't'});
model.func('an3').set('argunit', 'm,m,s');
model.func('an3').set('fununit', 'W/m^2');
model.func('an3').set('plotargs', {'x' '-6[mm]' '6[mm]'; 'y' '-6[mm]' '6[mm]'; 't' '0' '0'});
model.func('an4').label('Dimensionless Power Density Flux');
model.func('an4').set('funcname', 'A_q');
model.func('an4').set('expr', '((A_a*A_rho*((A_rho*exp(-2*A_lambda) + 3)*(2*A_a*exp(-
2*A_a*(A_lambda - A_beta*z))*(A_a + A_rho*(A_a + 1) - 1) + 2*A_a*exp(2*A_a*(A_lambda -
A_beta*z))*(A_a + A_rho*(A_a - 1) + 1)) - exp(-A_lambda)*(A_rho^2 - 1)*(2*A_a*exp(-
2*A_a*A_beta*z)*(A_a - 1) + 2*A_a*exp(2*A_a*A_beta*z)*(A_a + 1))))/(A_D*(4*A_rho - 3)) -
((3*A_rho - 3)*(exp(-A_beta*z) + A_rho*exp(A_beta*z - 2*A_lambda)))/(4*A_rho - 3))');
model.func('an4').set('args', {'z'});
model.func('an4').set('argunit', 'm');
model.func('an4').set('plotargs', {'z' '0' 'D_l'});
model.func('an9').label('Fraction Absorbed');
model.func('an9').set('funcname', 'A_Q');
model.func('an9').set('expr', 'A_rho*A_a/(4*A_rho-3)/A_D*((1-A_rho^2)*exp(-A_lambda)*((1-
A_a)*exp(-2*A_a*x)+(1+A_a)*exp(2*A_a*x))-(3+A_rho*exp(-2*A_lambda))*((1+A_a-A_rho*(1-
A_a))*exp(2*A_a*(A_lambda-x))+(1-A_a-A_rho*(1+A_a))*exp(2*A_a*(x-A_lambda))))-3*(1-
A_rho)*(exp(-x)-A_rho*exp(x-2*A_lambda))/(4*A_rho-3)');
model.func('an9').set('plotargs', {'x' '0' 'A_lambda'});
model.func('an5').label('X-Position of Laser');
model.func('an5').set('funcname', 'pX');
model.func('an5').set('expr', '(x0+D_p*floor(t[s]/(t_e+t_drill))) [1/m]');
model.func('an5').set('args', {'t'});
model.func('an5').set('plotargs', {'t' '0' 't_e*150'});
model.func('an6').label('Y-Position of Laser');
model.func('an6').set('funcname', 'pY');
model.func('an6').set('expr', 'y0 [1/m]');
model.func('an6').set('args', {'t'});
model.func('an6').set('plotargs', {'t' '0' '1'});
model.func('an7').label('Drill delay');
model.func('an7').set('funcname', 'drill');
model.func('an7').set('expr', '1-floor(t[s]/(t_e))');
model.func('an7').set('args', {'t'});
model.func('an7').set('periodic', true);
model.func('an7').set('periodicupper', 't_e+t_drill');
model.func('an7').set('argunit', 's');
model.func('an7').set('plotargs', {'t' '0' '(t_e+t_drill)*3'});
model.func('an10').set('expr', 'A_Q(0)-A_Q(A_lambda)');

model.component('comp1').mesh.create('mesh1');
model.component('comp1').mesh.create('mesh2');

model.component('comp1').geom('geom1').create('blk1', 'Block');
model.component('comp1').geom('geom1').feature('blk1').label('Substrate');
```

```
model.component('comp1').geom('geom1').feature('blk1').set('size', {'1.5[mm]' '0.5 [mm]'
'D_l*height'});
model.component('comp1').geom('geom1').create('blk2', 'Block');
model.component('comp1').geom('geom1').feature('blk2').label('Substrate - Scan Area');
model.component('comp1').geom('geom1').feature('blk2').set('pos', {'0.125 [mm]' '0' '0'});
model.component('comp1').geom('geom1').feature('blk2').set('size', {'1.25[mm]' '140[um]'
'D_l*height'});
model.component('comp1').geom('geom1').create('ext1', 'Extrude');
model.component('comp1').geom('geom1').feature('ext1').label('Powder Layer');
model.component('comp1').geom('geom1').feature('ext1').setIndex('distance', 'D_l', 0);
model.component('comp1').geom('geom1').feature('ext1').selection('inputface').set('blk1(1)',
[4]);
model.component('comp1').geom('geom1').feature('ext1').selection('inputface').set('blk2(1)',
[4]);
model.component('comp1').geom('geom1').create('igf1', 'IgnoreFaces');
model.component('comp1').geom('geom1').feature('igf1').selection('input').set('fin(1)', [6 10
12 17 19]);
model.component('comp1').geom('geom1').run;

model.component('comp1').view.create('view2', 'geom1');
model.view.create('view3', 2);
model.view.create('view4', 3);
model.view.create('view5', 2);

model.component('comp1').material.create('mat1', 'Common');
model.component('comp1').material('mat1').propertyGroup('def').func.create('pw1',
'Piecewise');
model.component('comp1').material('mat1').propertyGroup('def').func.create('pw2',
'Piecewise');
model.component('comp1').material('mat1').propertyGroup('def').func.create('pw3',
'Piecewise');
model.component('comp1').material('mat1').propertyGroup('def').func.create('pw4',
'Piecewise');

model.component('comp1').physics.create('ht', 'HeatTransfer', 'geom1');
model.component('comp1').physics('ht').create('temp1', 'TemperatureBoundary', 2);
model.component('comp1').physics('ht').feature('temp1').selection.set([3]);
model.component('comp1').physics('ht').create('hs1', 'HeatSource', 3);
model.component('comp1').physics('ht').feature('hs1').selection.all;
model.component('comp1').physics('ht').create('bhs1', 'BoundaryHeatSource', 2);
model.component('comp1').physics('ht').feature('bhs1').selection.set([8]);
model.component('comp1').physics('ht').create('sym1', 'Symmetry', 2);
model.component('comp1').physics('ht').feature('sym1').selection.set([2 7]);
model.component('comp1').physics.create('dode', 'DomainODE', 'geom1');
model.component('comp1').physics('dode').create('dode2', 'DistributedODE', 3);
model.component('comp1').physics('dode').feature('dode2').selection.set([1]);
model.component('comp1').physics('dode').create('init2', 'init', 3);
model.component('comp1').physics('dode').feature('init2').selection.all;

model.component('comp1').mesh('mesh1').create('edg1', 'Edge');
model.component('comp1').mesh('mesh1').create('map1', 'Map');
model.component('comp1').mesh('mesh1').create('swe1', 'Sweep');
model.component('comp1').mesh('mesh1').create('edg2', 'Edge');
model.component('comp1').mesh('mesh1').create('map2', 'Map');
model.component('comp1').mesh('mesh1').create('swe2', 'Sweep');
model.component('comp1').mesh('mesh1').create('ftet1', 'FreeTet');
model.component('comp1').mesh('mesh1').create('ftet2', 'FreeTet');
model.component('comp1').mesh('mesh1').feature('edg1').selection.set([9 12 13]);
model.component('comp1').mesh('mesh1').feature('edg1').create('size1', 'Size');
model.component('comp1').mesh('mesh1').feature('map1').selection.set([9]);
model.component('comp1').mesh('mesh1').feature('swe1').selection.geom('geom1', 3);
model.component('comp1').mesh('mesh1').feature('swe1').selection.set([2]);
model.component('comp1').mesh('mesh1').feature('edg2').create('dis1', 'Distribution');
model.component('comp1').mesh('mesh1').feature('swe2').selection.geom('geom1', 3);
model.component('comp1').mesh('mesh1').feature('ftet1').selection.geom('geom1', 3);
model.component('comp1').mesh('mesh1').feature('ftet1').selection.set([1]);
model.component('comp1').mesh('mesh1').feature('ftet1').create('size1', 'Size');
```

```
model.component('comp1').mesh('mesh1').feature('ftet2').selection.geom('geom1', 3);
model.component('comp1').mesh('mesh1').feature('ftet2').create('size1', 'Size');
model.component('comp1').mesh('mesh1').feature('ftet2').feature('size1').selection.geom('geom
1', 3);
model.component('comp1').mesh('mesh2').create('edg1', 'Edge');
model.component('comp1').mesh('mesh2').create('map1', 'Map');
model.component('comp1').mesh('mesh2').create('swe1', 'Sweep');
model.component('comp1').mesh('mesh2').create('edg2', 'Edge');
model.component('comp1').mesh('mesh2').create('map2', 'Map');
model.component('comp1').mesh('mesh2').create('swe2', 'Sweep');
model.component('comp1').mesh('mesh2').create('ftet1', 'FreeTet');
model.component('comp1').mesh('mesh2').create('ftet2', 'FreeTet');
model.component('comp1').mesh('mesh2').feature('edg1').selection.set([9 12 13]);
model.component('comp1').mesh('mesh2').feature('edg1').create('size1', 'Size');
model.component('comp1').mesh('mesh2').feature('map1').selection.set([9]);
model.component('comp1').mesh('mesh2').feature('swe1').selection.geom('geom1', 3);
model.component('comp1').mesh('mesh2').feature('swe1').selection.set([2]);
model.component('comp1').mesh('mesh2').feature('edg2').selection.set([1 6 22 25]);
model.component('comp1').mesh('mesh2').feature('edg2').create('dis1', 'Distribution');
model.component('comp1').mesh('mesh2').feature('edg2').create('size1', 'Size');
model.component('comp1').mesh('mesh2').feature('edg2').feature('dis1').selection.set([]);
model.component('comp1').mesh('mesh2').feature('swe2').selection.geom('geom1', 3);
model.component('comp1').mesh('mesh2').feature('ftet1').create('size1', 'Size');
model.component('comp1').mesh('mesh2').feature('ftet1').feature('size1').selection.geom('geom
1', 3);
model.component('comp1').mesh('mesh2').feature('ftet1').feature('size1').selection.set([1]);
model.component('comp1').mesh('mesh2').feature('ftet2').selection.geom('geom1', 3);
model.component('comp1').mesh('mesh2').feature('ftet2').create('size1', 'Size');
model.component('comp1').mesh('mesh2').feature('ftet2').feature('size1').selection.geom('geom
1', 3);

model.result.table('evl3').label('Evaluation 3D');
model.result.table('evl3').comments('Interactive 3D values');
model.result.table('evl2').label('Evaluation 2D');
model.result.table('evl2').comments('Interactive 2D values');

model.component('comp1').view('view2').label('xz');
model.component('comp1').view('view2').set('locked', true);
model.view('view3').axis.set('xmin', -6.643772940151393E-5);
model.view('view3').axis.set('xmax', 0.0027443491853773594);
model.view('view3').axis.set('ymin', -5.519290061783977E-5);
model.view('view3').axis.set('ymax', 8.034996571950614E-4);
model.view('view3').axis.set('abstractviewlratio', -0.044291820377111435);
model.view('view3').axis.set('abstractviewrratio', 0.8295661211013794);
model.view('view3').axis.set('abstractviewbratio', -0.16725121438503265);
model.view('view3').axis.set('abstractviewtratio', 1.434847354888916);
model.view('view3').axis.set('abstractviewxscale', 2.862308519979706E-6);
model.view('view3').axis.set('abstractviewyscale', 2.862308519979706E-6);
model.view('view5').axis.set('xmin', -1.5016680117696524E-4);
model.view('view5').axis.set('xmax', 0.0016501666978001595);
model.view('view5').axis.set('ymin', -2.500001573935151E-5);
model.view('view5').axis.set('ymax', 5.250000394880772E-4);
model.view('view5').axis.set('abstractviewlratio', -0.10011120140552521);
model.view('view5').axis.set('abstractviewrratio', 0.10011111944913864);
model.view('view5').axis.set('abstractviewbratio', -0.05000003054738045);
model.view('view5').axis.set('abstractviewtratio', 0.05000003054738045);
model.view('view5').axis.set('abstractviewxscale', 1.8333334992348682E-6);
model.view('view5').axis.set('abstractviewyscale', 1.8333334992348682E-6);

model.component('comp1').material('mat1').label('Invar');
model.component('comp1').material('mat1').propertyGroup('def').func('pw1').label('Density');
model.component('comp1').material('mat1').propertyGroup('def').func('pw1').set('funcname',
'rho');
model.component('comp1').material('mat1').propertyGroup('def').func('pw1').set('arg', 't');
model.component('comp1').material('mat1').propertyGroup('def').func('pw1').set('extrap',
'interior');
```

```
model.component('comp1').material('mat1').propertyGroup('def').func('pw1').set('pieces',
{'25' '1450' '7902-0.41*t'; '1460' '2400' '7977-0.566*t'; '1450' '1460' '7977-0.566*1460'});
model.component('comp1').material('mat1').propertyGroup('def').func('pw1').set('argunit',
'degC');
model.component('comp1').material('mat1').propertyGroup('def').func('pw1').set('fununit',
'kg/m^3');
model.component('comp1').material('mat1').propertyGroup('def').func('pw2').label('Thermal
Conductivity');
model.component('comp1').material('mat1').propertyGroup('def').func('pw2').set('funcname',
'kb');
model.component('comp1').material('mat1').propertyGroup('def').func('pw2').set('arg', 't');
model.component('comp1').material('mat1').propertyGroup('def').func('pw2').set('extrap',
'interior');
model.component('comp1').material('mat1').propertyGroup('def').func('pw2').set('pieces',
{'25' '1450' '4.821+0.01438*t'; '1460' '2400' '5.432+0.01296*t'; '1450' '1460'
'5.432+0.01296*1460'});
model.component('comp1').material('mat1').propertyGroup('def').func('pw2').set('argunit',
'degC');
model.component('comp1').material('mat1').propertyGroup('def').func('pw2').set('fununit',
'W/(m*K)');
model.component('comp1').material('mat1').propertyGroup('def').func('pw3').label('Enthalpy');
model.component('comp1').material('mat1').propertyGroup('def').func('pw3').set('funcname',
'H');
model.component('comp1').material('mat1').propertyGroup('def').func('pw3').set('arg', 't');
model.component('comp1').material('mat1').propertyGroup('def').func('pw3').set('extrap',
'interior');
model.component('comp1').material('mat1').propertyGroup('def').func('pw3').set('pieces',
{'25' '1450' '-104.5+0.519*t'; '1460' '2400' '-334.7+0.8*t'; '1450' '1460' '-
334.7+0.8*1460'});
model.component('comp1').material('mat1').propertyGroup('def').func('pw3').set('argunit',
'degC');
model.component('comp1').material('mat1').propertyGroup('def').func('pw3').set('fununit',
'J/g');
model.component('comp1').material('mat1').propertyGroup('def').func('pw4').label('Specific
Heat');
model.component('comp1').material('mat1').propertyGroup('def').func('pw4').set('funcname',
'Cp');
model.component('comp1').material('mat1').propertyGroup('def').func('pw4').set('arg', 't');
model.component('comp1').material('mat1').propertyGroup('def').func('pw4').set('pieces',
{'25' '1450' 'd(H(t),t)'; '1450' '1460' '40'; '1460' '2400' 'd(H(t),t)'});
model.component('comp1').material('mat1').propertyGroup('def').func('pw4').set('argunit',
'degC');
model.component('comp1').material('mat1').propertyGroup('def').func('pw4').set('fununit',
'J/(g*K)');
model.component('comp1').material('mat1').propertyGroup('def').set('thermalconductivity',
{'kb(T)*(a+u*(b-a))' '0' '0' '0' 'kb(T)*(a+u*(b-a))' '0' '0' '0' 'kb(T)*(a+u*(b-a))'});
model.component('comp1').material('mat1').propertyGroup('def').set('density', 'rho(T)');
model.component('comp1').material('mat1').propertyGroup('def').set('heatcapacity', 'Cp(T)');

model.component('comp1').physics('ht').prop('AmbientSettings').set('T_amb', 'T_inf');
model.component('comp1').physics('ht').feature('init1').set('Tinit', 'T_inf');
model.component('comp1').physics('ht').feature('temp1').set('T0', 'T_inf');
model.component('comp1').physics('ht').feature('hs1').set('Q0', '-
A_beta*laser(x,y,t)*A_q(D_l*height+D_l-z)*(z<=D_l+D_l*height)*(A_beta*(D_l*height+D_l-
z)<=A_lambda)*drill(t)');
model.component('comp1').physics('ht').feature('bhs1').set('Qb', '(1-A_rho)*(A_Q(0)-
A_Q(A_lambda))*laser(x,y,t)*drill(t)');
model.component('comp1').physics('ht').feature('bhs1').active(false);
model.component('comp1').physics('dode').label('Solidification History');
model.component('comp1').physics('dode').prop('ShapeProperty').set('order', 0);
model.component('comp1').physics('dode').prop('Units').set('SourceTermQuantity',
'dimensionless');
model.component('comp1').physics('dode').feature('dode1').set('f', 'u-
nojac(if(T>Tmelt,1,u))');
model.component('comp1').physics('dode').feature('dode1').set('da', 0);
model.component('comp1').physics('dode').feature('dode2').set('f', 'u-1');
model.component('comp1').physics('dode').feature('dode2').set('da', 0);
```

```
model.component('comp1').physics('dode').feature('dode2').active(false);
model.component('comp1').physics('dode').feature('init2').set('u', 'if(z>D_l*height,0,1)');

model.component('comp1').mesh('mesh1').label('Manual');
model.component('comp1').mesh('mesh1').feature('edg1').feature('size1').set('custom', 'on');
model.component('comp1').mesh('mesh1').feature('edg1').feature('size1').set('hmax', 'r/4');
model.component('comp1').mesh('mesh1').feature('edg1').feature('size1').set('hmaxactive',
true);
model.component('comp1').mesh('mesh1').feature('edg1').feature('size1').set('hmin', 'r/4');
model.component('comp1').mesh('mesh1').feature('edg1').feature('size1').set('hminactive',
true);
model.component('comp1').mesh('mesh1').feature('edg2').feature('dis1').set('type',
'predefined');
model.component('comp1').mesh('mesh1').feature('edg2').feature('dis1').set('elemcount', 10);
model.component('comp1').mesh('mesh1').feature('edg2').feature('dis1').set('elemratio',
0.35);
model.component('comp1').mesh('mesh1').feature('ftet1').feature('size1').set('custom', 'on');
model.component('comp1').mesh('mesh1').feature('ftet1').feature('size1').set('hgrad', 1.2);
model.component('comp1').mesh('mesh1').feature('ftet1').feature('size1').set('hgradactive',
true);
model.component('comp1').mesh('mesh1').feature('ftet2').active(false);
model.component('comp1').mesh('mesh1').feature('ftet2').feature('size1').set('hauto', 3);
model.component('comp1').mesh('mesh1').run;
model.component('comp1').mesh('mesh2').label('Auto');
model.component('comp1').mesh('mesh2').feature('edg1').feature('size1').set('custom', 'on');
model.component('comp1').mesh('mesh2').feature('edg1').feature('size1').set('hmax', 'r*2');
model.component('comp1').mesh('mesh2').feature('edg1').feature('size1').set('hmaxactive',
true);
model.component('comp1').mesh('mesh2').feature('edg1').feature('size1').set('hmin', 'r*2');
model.component('comp1').mesh('mesh2').feature('edg1').feature('size1').set('hminactive',
true);
model.component('comp1').mesh('mesh2').feature('edg2').feature('dis1').active(false);
model.component('comp1').mesh('mesh2').feature('edg2').feature('dis1').set('type',
'predefined');
model.component('comp1').mesh('mesh2').feature('edg2').feature('dis1').set('elemcount', 10);
model.component('comp1').mesh('mesh2').feature('edg2').feature('dis1').set('elemratio',
0.35);
model.component('comp1').mesh('mesh2').feature('edg2').feature('size1').set('custom', 'on');
model.component('comp1').mesh('mesh2').feature('edg2').feature('size1').set('hmax', 'D_l');
model.component('comp1').mesh('mesh2').feature('edg2').feature('size1').set('hmaxactive',
true);
model.component('comp1').mesh('mesh2').feature('edg2').feature('size1').set('hmin', 'D_l');
model.component('comp1').mesh('mesh2').feature('edg2').feature('size1').set('hminactive',
true);
model.component('comp1').mesh('mesh2').feature('map2').active(false);
model.component('comp1').mesh('mesh2').feature('swe2').active(false);
model.component('comp1').mesh('mesh2').feature('ftet1').feature('size1').set('hauto', 9);
model.component('comp1').mesh('mesh2').feature('ftet2').active(false);
model.component('comp1').mesh('mesh2').feature('ftet2').feature('size1').set('hauto', 3);
model.component('comp1').mesh('mesh2').run;

model.study.create('std1');
model.study('std1').create('time', 'Transient');

model.sol.create('sol1');
model.sol('sol1').study('std1');
model.sol('sol1').attach('std1');
model.sol('sol1').create('st1', 'StudyStep');
model.sol('sol1').create('v1', 'Variables');
model.sol('sol1').create('t1', 'Time');
model.sol('sol1').feature('t1').create('se1', 'Segregated');
model.sol('sol1').feature('t1').create('d1', 'Direct');
model.sol('sol1').feature('t1').create('i1', 'Iterative');
model.sol('sol1').feature('t1').create('i2', 'Iterative');
model.sol('sol1').feature('t1').create('ps1', 'PreviousSolution');
model.sol('sol1').feature('t1').create('ta1', 'TimeAdaption');
model.sol('sol1').feature('t1').feature('se1').create('ss1', 'SegregatedStep');
```

```
model.sol('sol1').feature('t1').feature('se1').create('ss2', 'SegregatedStep');
model.sol('sol1').feature('t1').feature('se1').create('ll1', 'LowerLimit');
model.sol('sol1').feature('t1').feature('se1').feature.remove('ssDef');
model.sol('sol1').feature('t1').feature('i1').create('mg1', 'Multigrid');
model.sol('sol1').feature('t1').feature('i2').create('mg1', 'Multigrid');
model.sol('sol1').feature('t1').feature.remove('fcDef');
model.sol.create('sol2');
model.sol('sol2').study('std1');

model.result.dataset.create('cpl1', 'CutPlane');
model.result.dataset.create('cpl2', 'CutPlane');
model.result.create('pg1', 'PlotGroup3D');
model.result.create('pg2', 'PlotGroup3D');
model.result.create('pg3', 'PlotGroup3D');
model.result.create('pg4', 'PlotGroup3D');
model.result.create('pg5', 'PlotGroup2D');
model.result.create('pg6', 'PlotGroup2D');
model.result('pg1').create('vol1', 'Volume');
model.result('pg1').create('surf1', 'Surface');
model.result('pg1').create('mesh1', 'Mesh');
model.result('pg1').create('slc1', 'Slice');
model.result('pg2').create('vol1', 'Volume');
model.result('pg2').create('mesh1', 'Mesh');
model.result('pg3').create('vol1', 'Volume');
model.result('pg3').create('surf1', 'Surface');
model.result('pg3').create('mesh1', 'Mesh');
model.result('pg3').create('slc1', 'Slice');
model.result('pg4').create('surf1', 'Surface');
model.result('pg5').create('surf1', 'Surface');
model.result('pg5').feature('surf1').create('hght1', 'Height');
model.result('pg6').create('surf1', 'Surface');
model.result('pg6').feature('surf1').create('hght1', 'Height');
model.result.export.create('anim1', 'Animation');

model.study('std1').feature('time').set('tlist', 'range(0,t_e/16,16*t_e)');
model.study('std1').feature('time').set('mesh', {'geom1' 'mesh1'});

model.sol('sol1').attach('std1');
model.sol('sol1').feature('v1').set('clist', {'range(0,t_e/16,16*t_e)'});
model.sol('sol1').feature('t1').set('tlist', 'range(0,t_e/16,16*t_e)');
model.sol('sol1').feature('t1').set('maxorder', 2);
model.sol('sol1').feature('t1').set('estrat', 'exclude');
model.sol('sol1').feature('t1').feature('se1').feature('ss1').set('segvar', {'comp1_u'});
model.sol('sol1').feature('t1').feature('se1').feature('ss2').label('Temperature T');
model.sol('sol1').feature('t1').feature('se1').feature('ss2').set('segvar', {'comp1_T'});
model.sol('sol1').feature('t1').feature('se1').feature('ss2').set('linsolver', 'd1');
model.sol('sol1').feature('t1').feature('se1').feature('ss2').set('subdamp', 0.8);
model.sol('sol1').feature('t1').feature('se1').feature('ss2').set(...
                                           'subjtech', 'onevery');
model.sol('sol1').feature('t1').feature('se1').feature('ll1').set(...
                                        'lowerlimit', 'comp1.T 293.15');
model.sol('sol1').feature('t1').feature('d1').set('linsolver', 'pardiso');
model.sol('sol1').feature('t1').feature('i1').label(...
                                  'Algebraic Multigrid Solver (ht)');
model.sol('sol1').feature('t1').feature('i2').label(...
                                  'Geometric Multigrid Solver (ht)');
model.sol('sol1').feature('t1').feature('ps1').set('prevcomp', {'comp1_u'});
model.sol('sol1').feature('t1').feature('ps1').set('linsolver', 'd1');
model.sol('sol1').feature('t1').feature('ta1').active(false);
model.sol('sol1').feature('t1').feature('ta1').set('globalminpar', 20);
model.sol('sol1').feature('t1').feature('ta1').set('ngenlocal', 8);
model.sol('sol1').feature('t1').feature('ta1').set('eefunctime', ...
                       'sqrt(comp1.Tx^2+comp1.Ty^2+comp1.Tz^2)');
model.sol('sol1').feature('t1').feature('ta1').set('samplepts', 'range(0,1/16,1)');
model.sol('sol1').feature('t1').feature('ta1').set('consistentrestart', 'bweuler');
model.sol('sol1').feature('t1').feature('ta1').set('tadapsol', 'sol2');
model.sol('sol1').feature('t1').feature('ta1').set(...
```

```
      'tadapmesh', {'mesh3' 'mesh4' 'mesh5' 'mesh6' 'mesh7' 'mesh8' 'mesh9' ...
      'mesh10' 'mesh11' 'mesh12'});
model.sol('sol1').runAll;
model.sol('sol2').label('Refined Mesh Solution 1');
model.sol('sol2').runAll;

model.result.dataset('cpl1').set('quickplane', 'xz');
model.result.dataset('cpl2').set('quickplane', 'xy');
model.result.dataset('cpl2').set('quickz', '330[um]');
model.result.dataset('cpl2').set('spacevars', {'cpl1x' 'cpl1y'});
model.result.dataset('cpl2').set('normal', {'cpl1nx' 'cpl1ny' 'cpl1nz'});
model.result('pg1').label('Temperature (ht)');
model.result('pg1').feature('vol1').active(false);
model.result('pg1').feature('vol1').set('rangecoloractive', true);
model.result('pg1').feature('vol1').set('rangecolormin', 293.1499999999997);
model.result('pg1').feature('vol1').set('rangecolormax', 1460);
model.result('pg1').feature('vol1').set('resolution', 'normal');
model.result('pg1').feature('surf1').label('Surface');
model.result('pg1').feature('surf1').set('rangecoloractive', true);
model.result('pg1').feature('surf1').set('rangecolormin', 273);
model.result('pg1').feature('surf1').set('rangecolormax', 1460);
model.result('pg1').feature('surf1').set('resolution', 'normal');
model.result('pg1').feature('mesh1').set('elemcolor', 'none');
model.result('pg1').feature('slc1').active(false);
model.result('pg1').feature('slc1').set('resolution', 'normal');
model.result('pg2').label('Solidification History');
model.result('pg2').feature('vol1').set('expr', 'u');
model.result('pg2').feature('vol1').set('unit', '1');
model.result('pg2').feature('vol1').set('descr', 'Dependent variable u');
model.result('pg2').feature('vol1').set('smooth', 'none');
model.result('pg2').feature('vol1').set('resolution', 'normal');
model.result('pg2').feature('mesh1').set('elemcolor', 'none');
model.result('pg3').label('Melt Pool Size');
model.result('pg3').feature('vol1').set('rangecoloractive', true);
model.result('pg3').feature('vol1').set('rangecolormin', 293.1499999999997);
model.result('pg3').feature('vol1').set('rangecolormax', 1460);
model.result('pg3').feature('vol1').set('rangedataactive', true);
model.result('pg3').feature('vol1').set('rangedatamin', 1460);
model.result('pg3').feature('vol1').set('rangedatamax', 10000);
model.result('pg3').feature('vol1').set('resolution', 'normal');
model.result('pg3').feature('surf1').active(false);
model.result('pg3').feature('surf1').set('expr', 'T>=1460');
model.result('pg3').feature('surf1').set('unit', '');
model.result('pg3').feature('surf1').set('descr', 'T>=1460');
model.result('pg3').feature('surf1').set('resolution', 'extrafine');
model.result('pg3').feature('surf1').set('smooth', 'everywhere');
model.result('pg3').feature('surf1').set('resolution', 'extrafine');
model.result('pg3').feature('mesh1').active(false);
model.result('pg3').feature('mesh1').set('elemcolor', 'none');
model.result('pg3').feature('slc1').active(false);
model.result('pg3').feature('slc1').set('quickxmethod', 'coord');
model.result('pg3').feature('slc1').set('quickx', '0.3[mm]');
model.result('pg3').feature('slc1').set('interactive', true);
model.result('pg3').feature('slc1').set('shift', 8.2E-4);
model.result('pg3').feature('slc1').set('rangecoloractive', true);
model.result('pg3').feature('slc1').set('rangecolormin', 293.1499999999997);
model.result('pg3').feature('slc1').set('rangecolormax', 1460);
model.result('pg3').feature('slc1').set('rangedataactive', true);
model.result('pg3').feature('slc1').set('rangedatamin', 1460);
model.result('pg3').feature('slc1').set('rangedatamax', 10000);
model.result('pg3').feature('slc1').set('resolution', 'normal');
model.result('pg4').feature('surf1').set('expr', 't_e');
model.result('pg4').feature('surf1').set('unit', 's');
model.result('pg4').feature('surf1').set('descr', 'Exposure Time');
model.result('pg4').feature('surf1').set('resolution', 'normal');
model.result('pg5').set('data', 'none');
model.result('pg5').feature('surf1').set('data', 'cpl1');
```

```
model.result('pg5').feature('surf1').set('looplevel', [257]);
model.result('pg5').feature('surf1').set('expr', 'comp1.T');
model.result('pg5').feature('surf1').set('rangecoloractive', true);
model.result('pg5').feature('surf1').set('rangecolormin', 293.15);
model.result('pg5').feature('surf1').set('rangecolormax', 1460);
model.result('pg5').feature('surf1').set('rangedataactive', true);
model.result('pg5').feature('surf1').set('rangedatamin', 1460);
model.result('pg5').feature('surf1').set('rangedatamax', 5274.570796151467);
model.result('pg5').feature('surf1').set('resolution', 'normal');
model.result('pg5').feature('surf1').feature('hght1').active(false);
model.result('pg5').feature('surf1').feature('hght1').set('scale', 1.7347E-7);
model.result('pg5').feature('surf1').feature('hght1').set('view', 'view4');
model.result('pg5').feature('surf1').feature('hght1').set('scaleactive', false);
model.result('pg6').set('data', 'none');
model.result('pg6').feature('surf1').set('data', 'cpl2');
model.result('pg6').feature('surf1').set('looplevel', [257]);
model.result('pg6').feature('surf1').set('expr', 'comp1.T');
model.result('pg6').feature('surf1').set('rangecoloractive', true);
model.result('pg6').feature('surf1').set('rangecolormin', 293.15);
model.result('pg6').feature('surf1').set('rangecolormax', 1460);
model.result('pg6').feature('surf1').set('rangedataactive', true);
model.result('pg6').feature('surf1').set('rangedatamin', 1460);
model.result('pg6').feature('surf1').set('rangedatamax', 60000);
model.result('pg6').feature('surf1').set('resolution', 'normal');
model.result('pg6').feature('surf1').feature('hght1').active(false);
model.result('pg6').feature('surf1').feature('hght1').set('scale', 1.7347E-7);
model.result('pg6').feature('surf1').feature('hght1').set('scaleactive', false);
model.result.export('anim1').label('Solidification Animation');
model.result.export('anim1').set('plotgroup', 'pg2');
model.result.export('anim1').set('target', 'player');
model.result.export('anim1').set('framesel', 'all');
model.result.export('anim1').set('showframe', 2);
model.result.export('anim1').set('shownparameter', '6E-4');
model.result.export('anim1').set('title', 'on');
model.result.export('anim1').set('legend', 'on');
model.result.export('anim1').set('logo', 'off');
model.result.export('anim1').set('options', 'off');
model.result.export('anim1').set('fontsize', '9');
model.result.export('anim1').set('customcolor', [1 1 1]);
model.result.export('anim1').set('background', 'color');
model.result.export('anim1').set('axisorientation', 'on');
model.result.export('anim1').set('grid', 'on');
model.result.export('anim1').set('axes', 'on');
model.result.export('anim1').set('showgrid', 'on');

model.sol('sol1').clearSolutionData;
model.sol('sol2').clearSolutionData;

model.label('MODEL_20180723.mph');

out = model;
```

Appendix P:
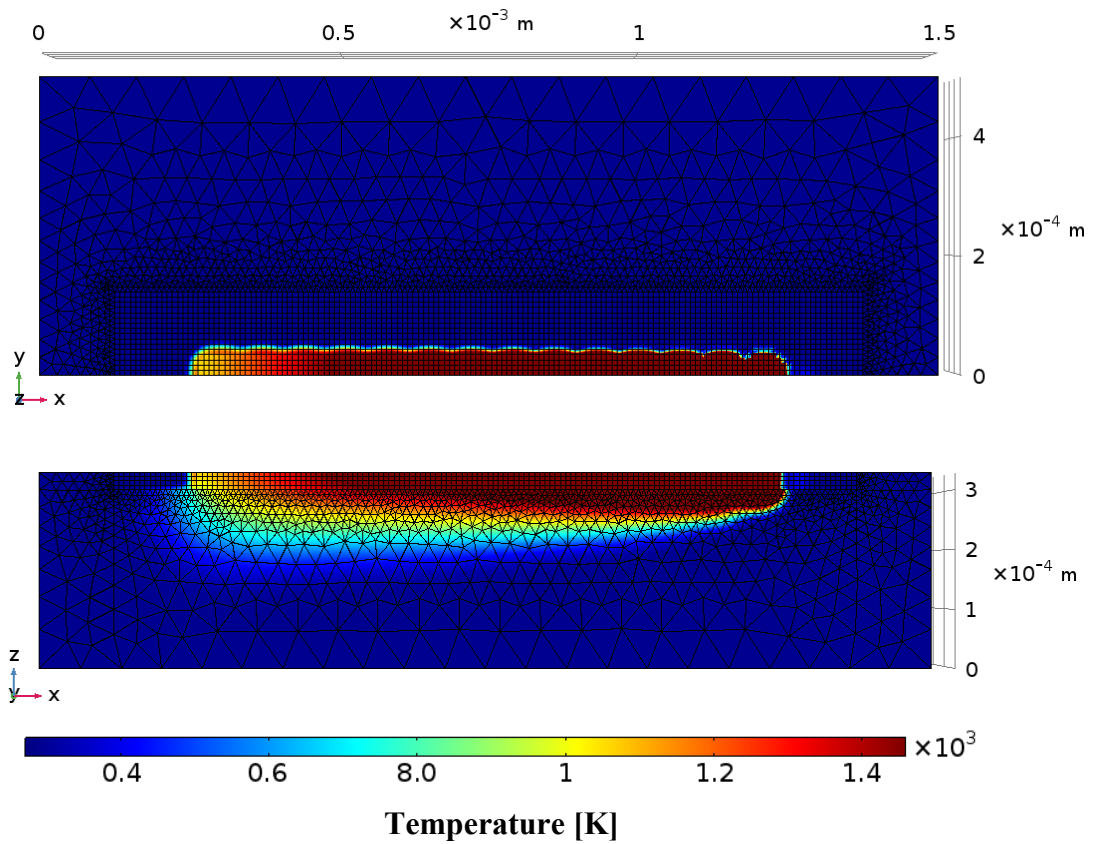# COMSOL Simulation Results

Figure P 1. Top and side view of the results for temperature at a time equal to 16 exposure points (0.00112 s). Simulation build variables equal those of sample 5 from Table 29.
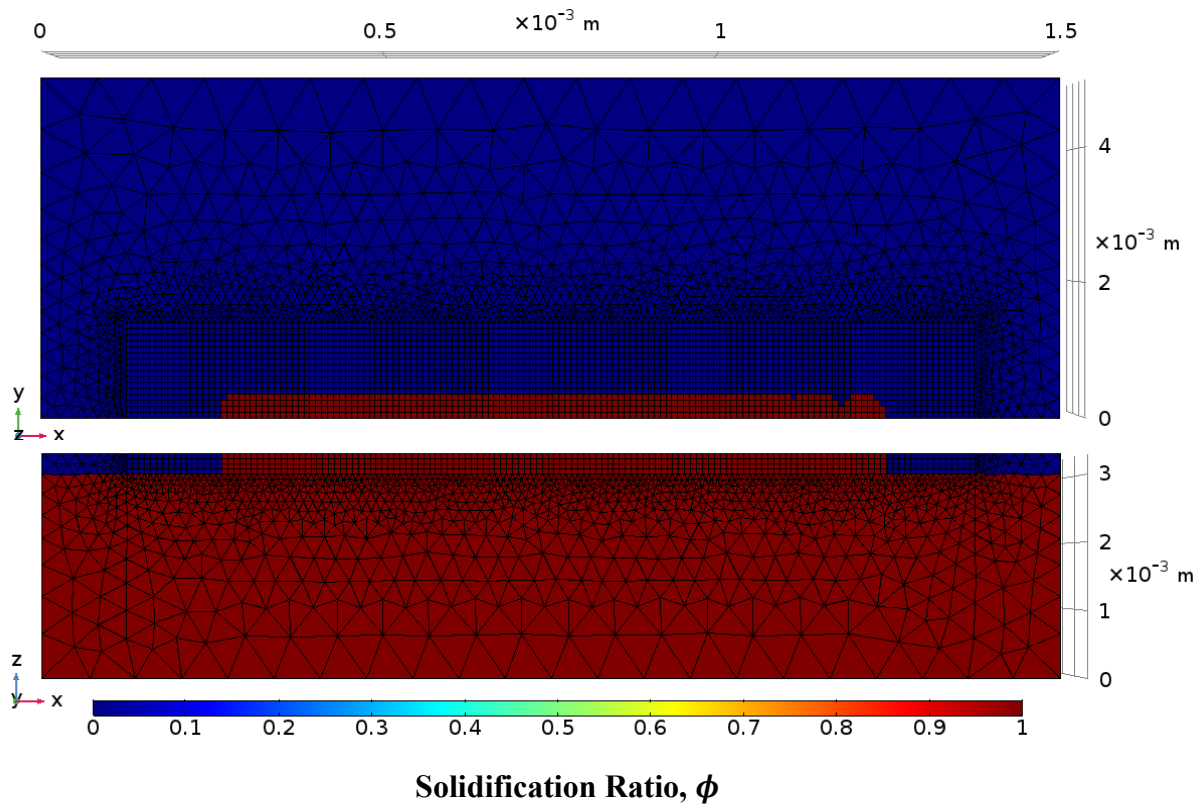
Figure P 2. Top and side view of the solidification ratio at a time equal to 16 exposure points (0.00112 s). Simulation build variable selection equal those of sample 5 from Table 29.
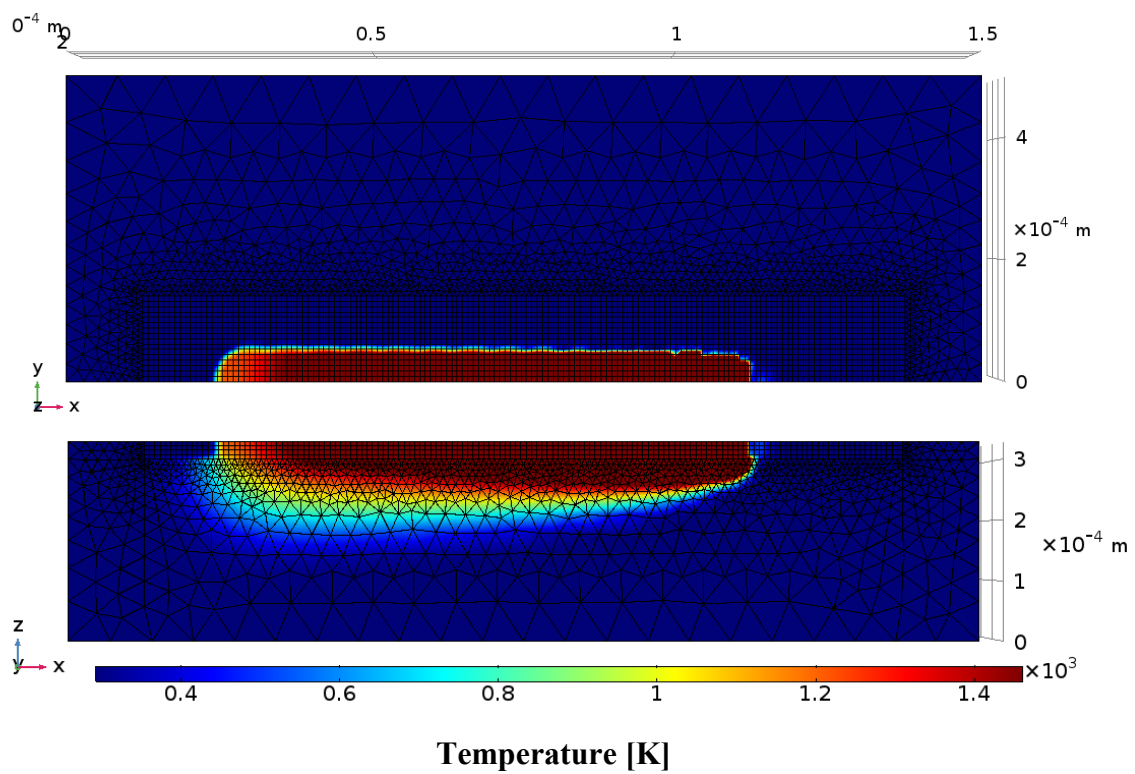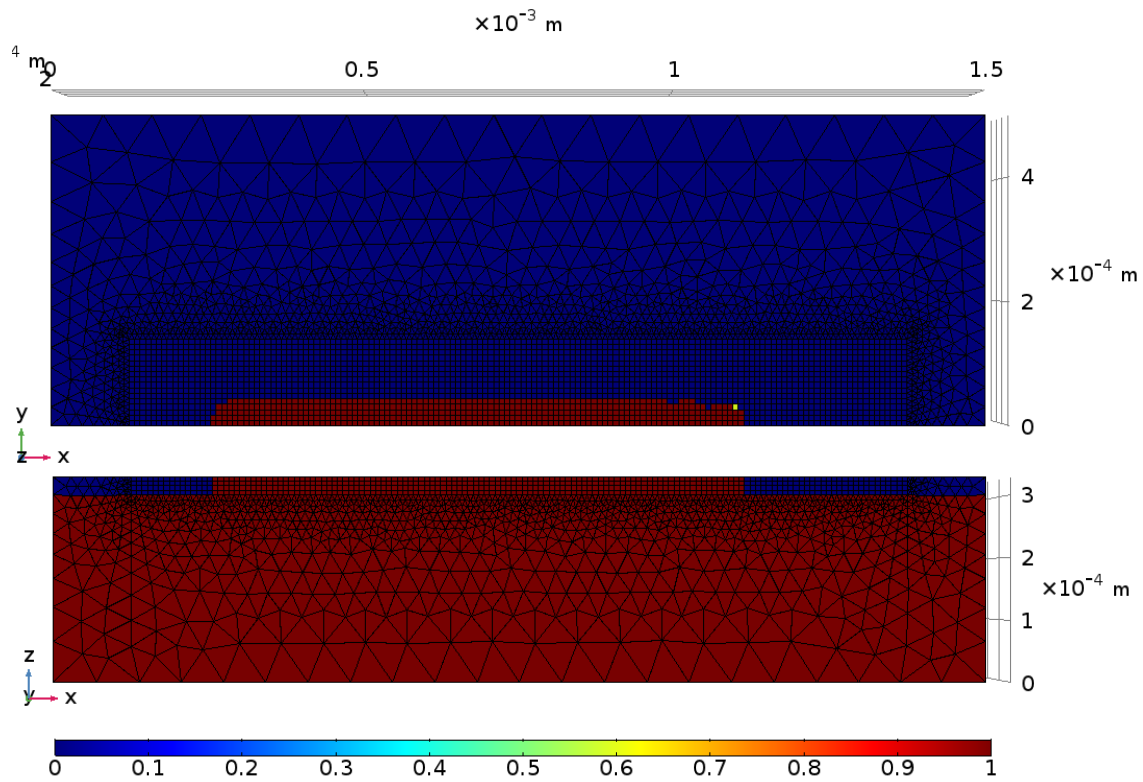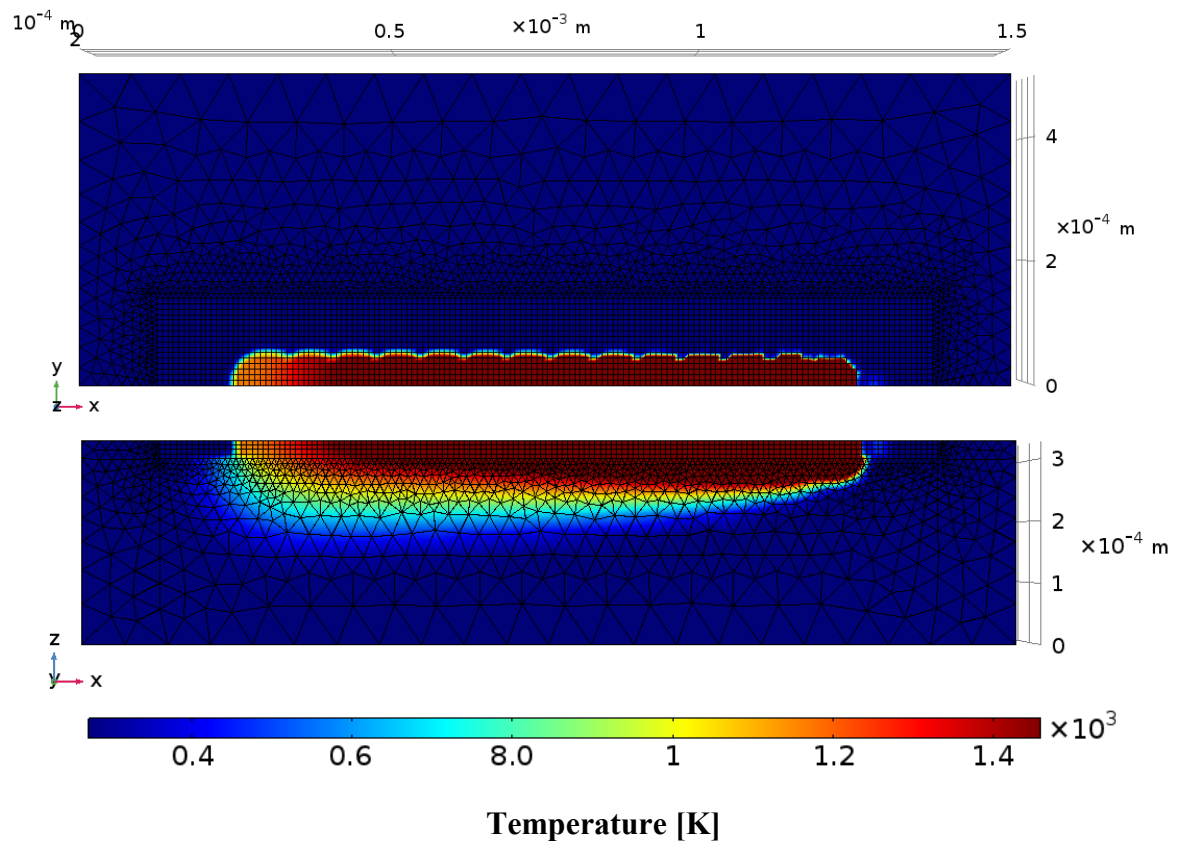
Figure P 3. Top and side view of the results for temperature at a time equal to 16 exposure points (0.00112s). Simulation build variables equal those of sample 20 from Table 29.
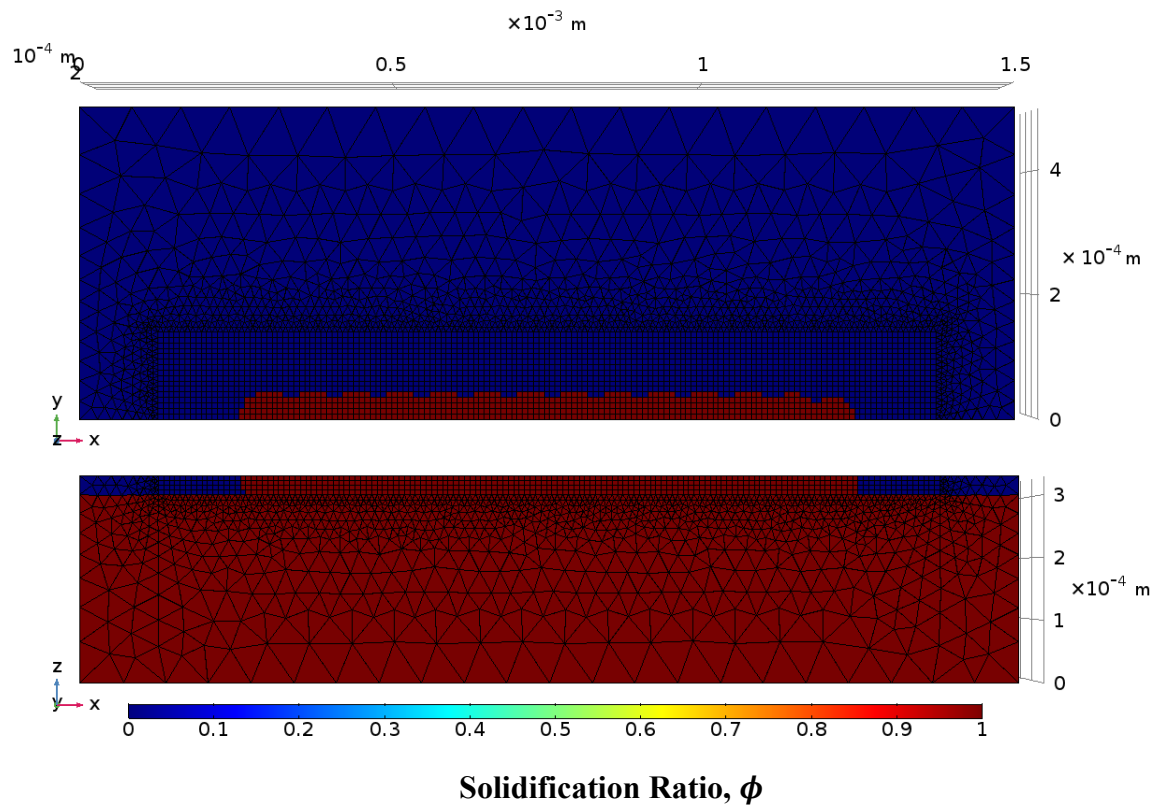
Solidification Ratio, ϕ

Figure P 4. Top and side view of the solidification ratio at a time equal to 16 exposure points (0.00112 s). Simulation build variable selection equal those of sample 20 from Table 29.
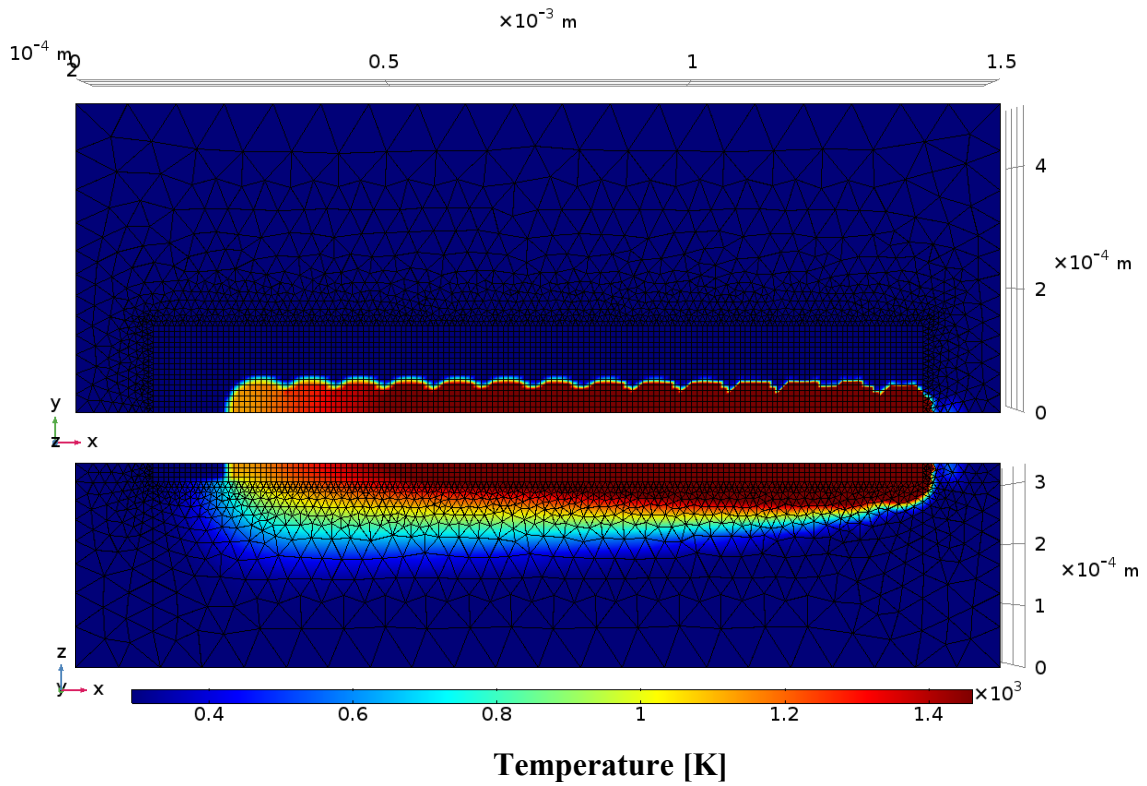
Figure P 5. Top and side view of the results for temperature at a time equal to 16 exposure points (0.00112 s). Simulation build variables equal those of sample 23 from Table 29.

Figure P 6. Top and side view of the solidification ratio at a time equal to 16 exposure points (0.00112 s). Simulation build variable selection equal those of sample 23 from Table 29.
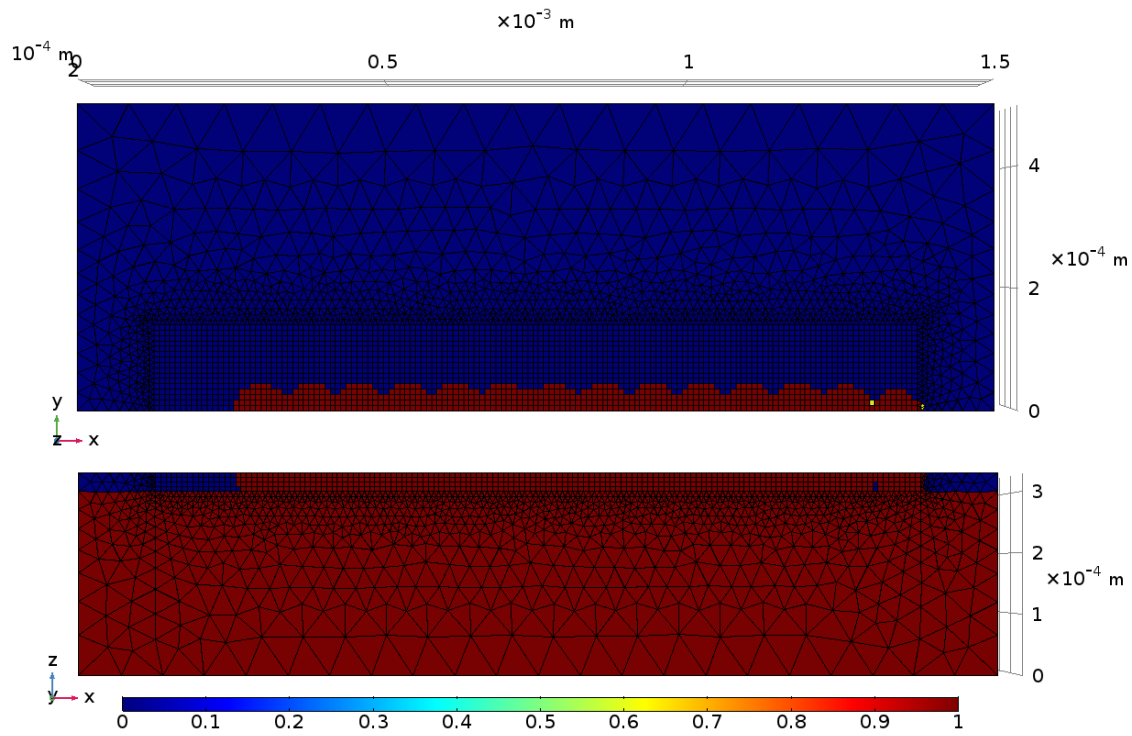
Figure P 7. Top and side view of the results for temperature at a time equal to 16 exposure points (0.00112 s). Simulation build variables equal those of sample 26 from Table 29.

Solidification Ratio, ϕ

Figure P 8. Top and side view of the solidification ratio at a time equal to 16 exposure points (0.00112 s). Simulation build variable selection equal those of sample 26 from Table 29.
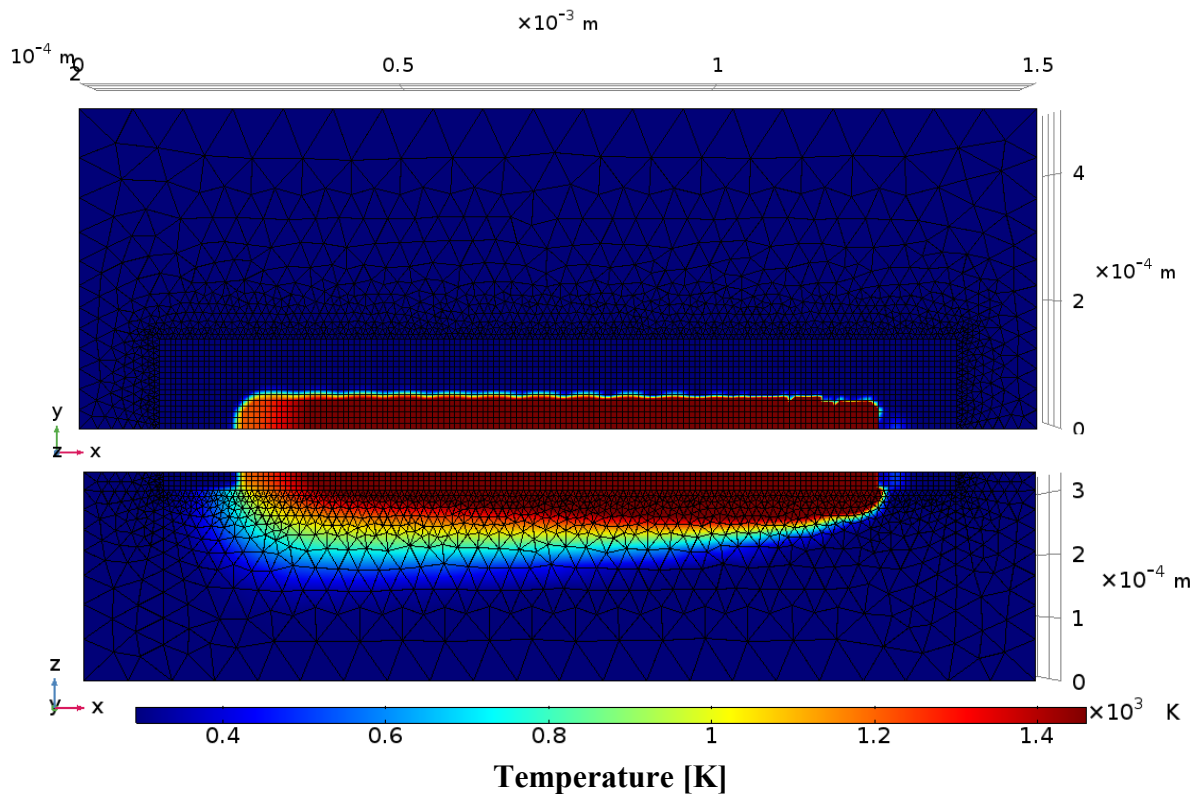
Figure P 9. Top and side view of the results for temperature at a time equal to 16 exposure points (0.00112 s). Simulation build variables equal those of sample 32 from Table 29.
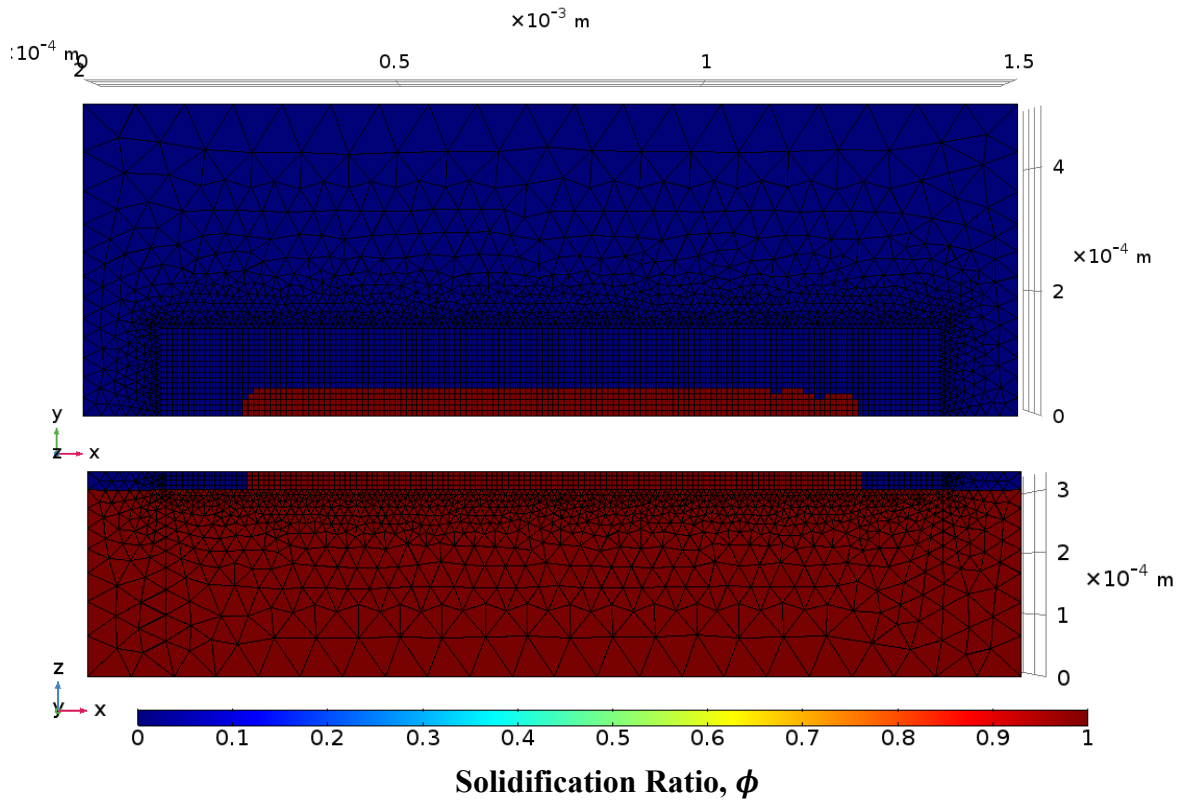
Figure P 10. Top and side view of the solidification ratio at a time equal to 16 exposure points (0.00112 s). Simulation build variable selection equal those of sample 32 from Table 29.
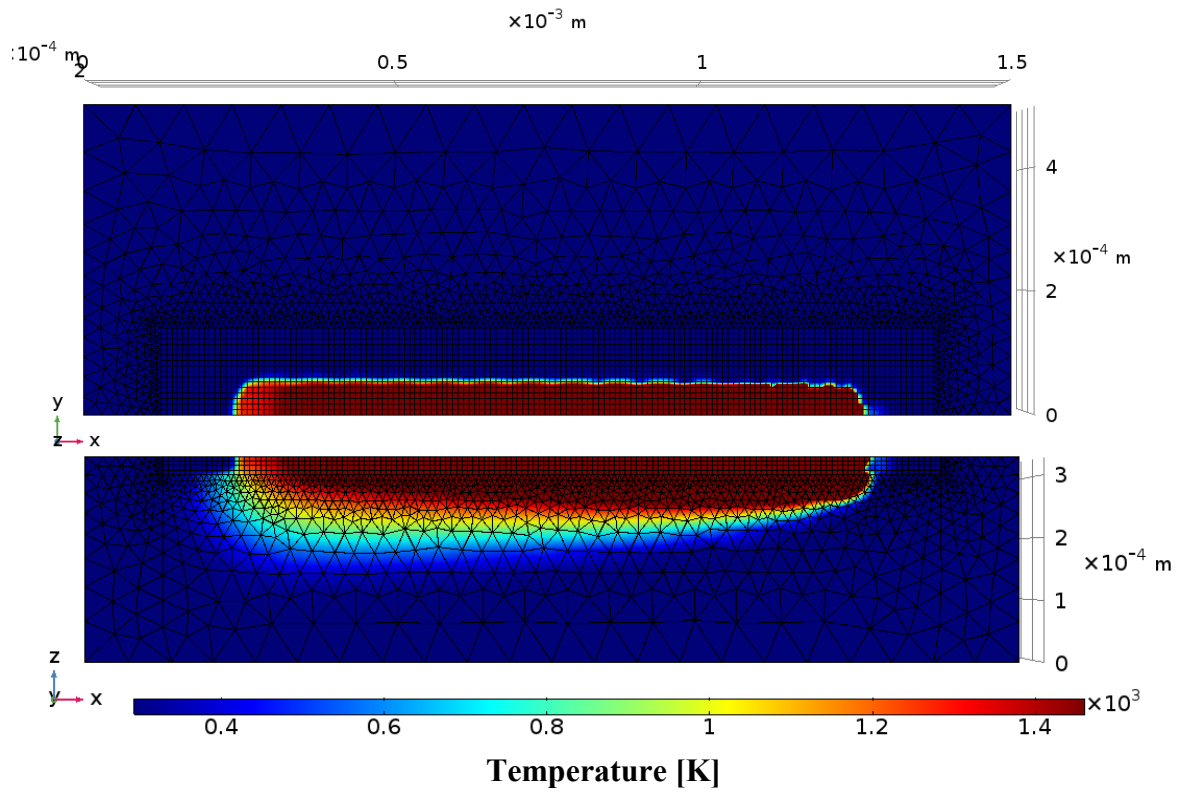
Figure P 11. Top and side view of the results for temperature at a time equal to 16 exposure points (0.00112 s). Simulation build variables equal those of sample 50 from Table 29.

Figure P 12. Top and side view of the solidification ratio at a time equal to 16 exposure points (0.00112 s). Simulation build variable selection equal those of sample 50 from Table 29.